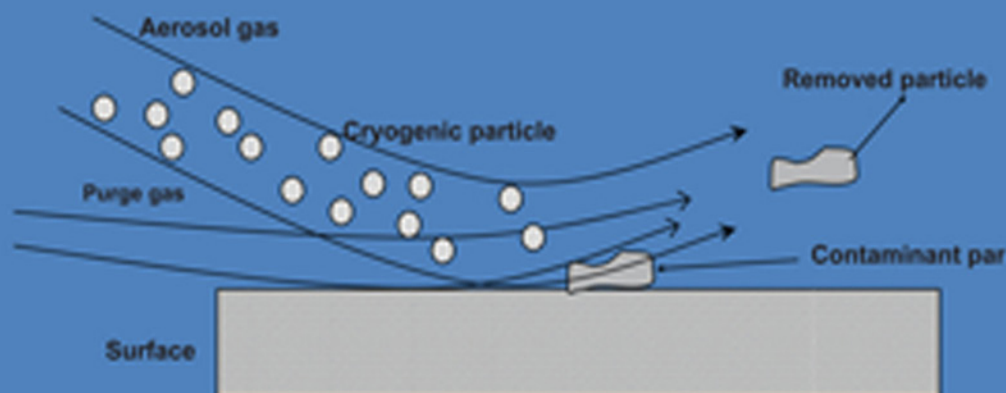


# PARTICLE ADHESION AND REMOVAL



Edited by K.L. Mittal and Ravi Jaiswal



# Particle Adhesion and Removal

**Scrivener Publishing**  
100 Cummings Center, Suite 541J  
Beverly, MA 01915-6106

**Adhesion and Adhesives: Fundamental and Applied Aspects**

The topics to be covered include, but not limited to, basic and theoretical aspects of adhesion; modeling of adhesion phenomena; mechanisms of adhesion; surface and interfacial analysis and characterization; unraveling of events at interfaces; characterization of interphases; adhesion of thin films and coatings; adhesion aspects in reinforced composites; formation, characterization and durability of adhesive joints; surface preparation methods; polymer surface modification; biological adhesion; particle adhesion; adhesion of metallized plastics; adhesion of diamond-like films; adhesion promoters; contact angle, wettability and adhesion; superhydrophobicity and superhydrophilicity. With regards to adhesives, the Series will include, but not limited to, green adhesives; novel and high-performance adhesives; and medical adhesive applications.

**Series Editor:** Dr. K.L. Mittal  
1983 Route 52,  
P.O. Box 1280, Hopewell Junction, NY 12533, USA  
Email: [usharmittal@gmail.com](mailto:usharmittal@gmail.com)

*Publishers at Scrivener*  
Martin Scrivener ([martin@scrivenerpublishing.com](mailto:martin@scrivenerpublishing.com))  
Phillip Carmical ([pcarmical@scrivenerpublishing.com](mailto:pcarmical@scrivenerpublishing.com))

# Particle Adhesion and Removal

Edited by

**K.L. Mittal and Ravi Jaiswal**



**WILEY**

Copyright © 2015 by Scrivener Publishing LLC. All rights reserved.

Co-published by John Wiley & Sons, Inc. Hoboken, New Jersey, and Scrivener Publishing LLC, Salem, Massachusetts.  
Published simultaneously in Canada.

No part of this publication may be reproduced, stored in a retrieval system, or transmitted in any form or by any means, electronic, mechanical, photocopying, recording, scanning, or otherwise, except as permitted under Section 107 or 108 of the 1976 United States Copyright Act, without either the prior written permission of the Publisher, or authorization through payment of the appropriate per-copy fee to the Copyright Clearance Center, Inc., 222 Rosewood Drive, Danvers, MA 01923, (978) 750-8400, fax (978) 750-4470, or on the web at [www.copyright.com](http://www.copyright.com). Requests to the Publisher for permission should be addressed to the Permissions Department, John Wiley & Sons, Inc., 111 River Street, Hoboken, NJ 07030, (201) 748-6011, fax (201) 748-6008, or online at <http://www.wiley.com/go/permission>.

**Limit of Liability/Disclaimer of Warranty:** While the publisher and author have used their best efforts in preparing this book, they make no representations or warranties with respect to the accuracy or completeness of the contents of this book and specifically disclaim any implied warranties of merchantability or fitness for a particular purpose. No warranty may be created or extended by sales representatives or written sales materials. The advice and strategies contained herein may not be suitable for your situation. You should consult with a professional where appropriate. Neither the publisher nor author shall be liable for any loss of profit or any other commercial damages, including but not limited to special, incidental, consequential, or other damages.

For general information on our other products and services or for technical support, please contact our Customer Care Department within the United States at (800) 762-2974, outside the United States at (317) 572-3993 or fax (317) 572-4002.

Wiley also publishes its books in a variety of electronic formats. Some content that appears in print may not be available in electronic formats. For more information about Wiley products, visit our web site at [www.wiley.com](http://www.wiley.com).

For more information about Scrivener products please visit [www.scrivenerpublishing.com](http://www.scrivenerpublishing.com).

Cover design by Exeter Premedia Services

***Library of Congress Cataloging-in-Publication Data:***

ISBN 978-1-118-83153-3

Printed in the United States of America

10 9 8 7 6 5 4 3 2 1

# Contents

---

<b>Preface</b>	<b>xv</b>
<b>Part 1: Particle Adhesion: Fundamentals</b>	<b>1</b>
<b>1 Fundamental Forces in Particle Adhesion</b>	<b>3</b>
<i>Stephen Beaudoin, Priyanka Jaiswal, Aaron Harrison, Jennifer Laster, Kathryn Smith, Melissa Sweat, and Myles Thomas</i>	
1.1 Introduction	3
1.2 Various Forces in Particle Adhesion	4
1.2.1 Capillary Forces	4
1.2.2 van der Waals Forces	27
1.2.3 Electrostatic Forces	49
1.3 Summary	69
References	70
<b>2 Mechanics of Particle Adhesion and Removal</b>	<b>81</b>
<i>Goodarz Ahmadi</i>	
2.1 Introduction	81
2.2 Models	83
2.2.1 Particle Adhesion and Detachment Models	83
2.2.2 Rough Particles Adhesion	89
2.2.3 Charge Distribution	90
2.2.4 Electrostatic Forces	92
2.2.5 Capillary Force	93
2.2.6 Hydrodynamic Forces and Torque	93
2.2.7 Particle Detachment Models	95
2.3 Simulations Results	96
2.4 Summary and Conclusions	99
Acknowledgements	100
References	100

<b>3</b>	<b>Microscopic Particle Contact Adhesion Models and Macroscopic Behavior of Surface Modified Particles</b>	<b>105</b>
	<i>Katja Mader-Arndt, Zinaida Kutelova and Jürgen Tomas</i>	
3.1	Introduction	105
3.2	Constitutive Contact Models	107
3.2.1	Elastic Contact Deformation	113
3.2.2	Elastic-plastic Contact Deformation	115
3.2.3	Plastic Contact Deformation	118
3.2.4	Unloading	119
3.3	Macroscopic Powder Behavior – Continuum Mechanics Approach	121
3.4	Surface Modification to Alter the Adhesion Properties	124
3.4.1	Surface Free Energy: Dispersion and Polar Components	124
3.4.2	Glass Surface Cleaning Prior to Silanization	125
3.4.3	Silanization	127
3.5	Experimental Measurements of the Adhesion Forces	130
3.5.1	Single Particle Adhesion Measurements	130
3.5.2	Shear Testing – Macromechanical Approach	140
3.6	Summary and Conclusions	146
	Acknowledgements	147
	List of Symbols	147
	References	148
<b>4</b>	<b>Characterization of Single Particle Adhesion: A Review of Recent Progress</b>	<b>157</b>
	<i>Armin Saeedi Vahdat and Cetin Cetinkaya</i>	
4.1	Introduction	157
4.2	Background	159
4.2.1	Adhesion Models	160
4.2.2	Measurement Methods	161
4.2.3	Non-contact Adhesion Characterization of Single Particles	161
4.2.4	Particle Adhesion to Nano-film Coated Surfaces	162
4.2.5	Non-contact Particle Manipulation	164
4.2.6	Molecular-scale Characterization Challenges in Biological Adhesion	165
4.3	Recent Developments	167
4.3.1	Nonlinear Dynamics in Adhesion Characterization of Micro-Particles	167



4.3.2	Adhesion Characterization of Monolayer Graphene by Vibrational Spectroscopy	177
4.3.3	Controllable Rolling Motion of Micro-Spherical Particles in SAW Fields	184
4.4	Conclusions and Remarks	193
	Acknowledgments	194
	List of Symbols	194
	References	196
<b>Part 2: Particle Removal Techniques</b>		<b>201</b>
<b>5</b>	<b>High Intensity Ultrasonic Cleaning for Particle Removal</b> <i>Sami B. Awad and Nadia F. Awad</i>	<b>203</b>
5.1	Introduction	204
5.2	Ultrasound and Ultrasonics	204
5.2.1	Ultrasound Waves	205
5.2.2	Factors Hindering the Transmission of Ultrasound Waves	206
5.2.3	Principal Mechanism of High Power Ultrasound	206
5.3	Cavitation Phenomenon	207
5.3.1	Cavitations and Micro-streaming	207
5.3.2	Frequency and Cavitation Abundance	209
5.3.3	Types of Cavitations	210
5.4	Generation of Ultrasound – Transducers	211
5.4.1	Gas-driven Transducers	211
5.4.2	Liquid-driven Transducers	212
5.4.3	Electromechanical Transducers	213
5.4.4	Transducer Assembly	215
5.4.5	Ultrasonic Immersible Transducers	216
5.5	Ultrasonic Generators	217
5.5.1	Power Requirements	217
5.5.2	Multi-Frequency Ultrasonic Systems	217
5.6	Principles of Ultrasonic Cleaning for Particle Removal	219
5.6.1	Cleaning Process Parameters	221
5.7	Determination of Residual Particles on Surfaces	223
5.8	Ultrasonic Aqueous Cleaning Equipment and Process	225
5.9	Precision Cleaning	228
5.10	Contaminants	228

5.11	Ultrasonic Cavitation Forces and Surface Cleaning	230
5.11.1	Requirements to Produce Cavitations	231
5.12	Cleaning Chemistry	232
5.12.1	Selection of Ultrasonic Cleaning Chemicals	234
5.12.2	Maximizing the Overall Cleaning Effect	235
5.13	Mechanism of Cleaning	236
5.13.1	Particle Removal	236
5.13.2	Particle Removal Mechanism	236
5.13.3	Prevention of Particle Re-deposition	237
5.13.4	Cleaning Chemistry and Particle Removal	238
5.14	Cavitation Erosion	238
5.15	Summary	239
	References	239
<b>6</b>	<b>Megasonic Cleaning for Particle Removal</b>	<b>243</b>
	<i>Manish Keswani, Rajesh Balachandran, and Pierre Deymier</i>	
6.1	Introduction	243
6.1.1	Wafer Cleaning	244
6.2	Principles of Megasonic Cleaning	247
6.2.1	Acoustic Streaming	248
6.2.2	Acoustic Cavitation	251
6.3	Particle Removal Mechanisms During Megasonic Cleaning	259
6.4	Types of Megasonic Systems	262
6.5	Particle Removal and Feature Damage in Megasonic Cleaning	264
6.6	Summary	274
	References	274
<b>7</b>	<b>High Speed Air Jet Removal of Particles from Solid Surfaces</b>	<b>281</b>
	<i>Kuniaki Gotoh</i>	
7.1	Introduction	281
7.2	Fundamental Characteristics of the Air Jet	282
7.3	Fundamentals of Air Jet Particle Removal	286
7.3.1	Definition of Parameters and Removal Efficiency	286
7.3.2	Effect of Pressure Drop $\Delta P_n$ and Distance $d$ on Removal Efficiency $\eta$	288
7.3.3	Effect of Impinging Angle $\theta$	290

7.3.4	Effect of Scan Speed of Air Jet	294
7.3.5	Other Parameters Affecting the Removal Efficiency	295
7.4	New Methods Using Air Jet	300
7.4.1	Pulsed-jet Method	300
7.4.2	Vibrating Air Jet Method	304
7.5	Summary and Prospect	307
	List of Symbols	308
	References	309
<b>8</b>	<b>Droplet Spray Technique for Particle Removal</b>	<b>313</b>
	<i>James T. Snow, Masanobu Sato and Takayoshi Tanaka</i>	
8.1	Introduction	313
8.2	Droplet Impact Phenomena	314
8.2.1	Impact on Solid Surface	315
8.2.2	Crown Formation	317
8.2.3	Impact on Liquid Film	318
8.3	Cleaning Process Window	318
8.3.1	Theoretical Studies	319
8.3.2	Experimental Studies	320
8.4	Droplet Spray Technique for Semiconductor Wafer Cleaning	324
8.4.1	Initial Studies	324
8.4.2	Droplet Distribution Optimization	325
8.4.3	Advanced Spray	329
8.5	Summary	331
	References	331
<b>9.</b>	<b>Laser-Induced High-Pressure Micro-Spray Process for Nanoscale Particle Removal</b>	<b>337</b>
	<i>Daehwan Ahn, Changho Seo and Dongsik Kim</i>	
9.1	Introduction	337
9.1.1	Nanoscale Contamination Control	337
9.1.2	Review of Physical Cleaning Methods	338
9.2	Concept of Droplet Opto-Hydrodynamic Cleaning (DOC)	340
9.3	Micro-Spray Generation by LIB	343
9.4	Mechanisms of Particle Removal by Laser-Induced Spray Jet	344
9.5	Generation of Micro-Spray Jet	345

9.5.1	Experimental Setup	345
9.5.2	Hydrodynamic Phenomena	346
9.6	Nanoscale Particle Removal	352
9.6.1	Experimental Setup	352
9.6.2	Optimization of Micro-Spray Jet	352
9.6.3	Effect of Process Parameters	355
9.6.4	Sub-100 nm Particle Cleaning	357
9.7	Summary	360
	References	360
<b>10</b>	<b>Wiper-Based Cleaning of Particles from Surfaces</b>	<b>365</b>
	<i>Brad Lyon and Jay Postlewaite</i>	
10.1	Introduction	366
10.1.1	Why Wipe?	366
10.1.2	Particle Cleanliness	367
10.2	Basic Mechanism of Wiping for Cleaning of Particles and Other Contaminants	371
10.2.1	Why Wiping Works	371
10.2.2	Wiping Mechanisms for Particle Removal	373
10.2.3	Contamination Types	378
10.3	Various Types of Wipers	379
10.3.1	Fabric Construction	381
10.3.2	Edge Type	385
10.3.3	Selecting a Cleanroom Wiper	388
10.4	Proper Ways to Carry Out Wiping or How to Use Wipers Properly	390
10.4.1	The Purpose of Wiping	390
10.4.2	Wiping Methods	393
10.4.3	Introductory Training Example for Wiper-Based Particle Cleaning	395
10.5	Characterization of Wipers	396
10.5.1	Methods to Assess Wiper Particle and Fiber Contamination Levels	396
10.6	Results Obtained Using Wiping	398
10.6.1	Test Method	399
10.6.2	Experimental Setup	400
10.6.3	Data Collection	401
10.6.4	Results	401
10.6.5	Comments	405

10.7	Future Directions	405
10.7.1	Nanotechnology	405
10.7.2	Microfiber Technology	405
10.8	Summary	406
	References	408
<b>11</b>	<b>Application of Strippable Coatings for Removal of Particulate Contaminants</b>	<b>411</b>
	<i>Rajiv Kohli</i>	
11.1	Introduction	411
11.2	Coating Description	412
11.2.1	Coating Properties	412
11.3	Types of Strippable Coatings	413
11.3.1	Solvent-Based Coatings	413
11.3.2	Water-Based Coatings	415
11.3.3	Coatings for Removal of Radioactive Contamination	418
11.3.4	Hazardous Materials Cleaning	422
11.3.5	UV Curable Coatings	422
11.4	Issues with Strippable Coatings	426
11.5	Precision Cleaning Applications	427
11.5.1	Optical Surfaces	427
11.5.2	Other Applications	435
11.5.3	Non-Optical Cleaning Applications	436
11.6	Summary	443
	Disclaimer	443
	References	443
<b>12</b>	<b>Cryo-aerosol Cleaning of Particles from Surfaces</b>	<b>453</b>
	<i>Souvik Banerjee</i>	
12.1	Introduction	453
12.2	History of Cryo-aerosol Cleaning	455
12.3	Thermodynamics of Cryo-aerosol Processes	456
12.3.1	Thermodynamics of CO <sub>2</sub> Aerosol Process	457
12.3.2	Thermodynamics of Ar/N <sub>2</sub> Cryogenic Aerosol System	460
12.4	Cleaning Mechanism	461
12.5	Factors Affecting Cleaning Performance	462
12.5.1	Moisture Control	463
12.5.2	Control of Electrostatic Charging	463

12.5.3	Airflow Management	465
12.5.4	Aerosol Particle Size Control	466
12.5.5	Gas Purity	468
12.6	Results Obtained by Cryoaerosol Cleaning	469
12.7	Summary and Prospects	473
	References	474

<b>13</b>	<b>Supercritical Carbon Dioxide Cleaning: Relevance to Particle Removal</b>	<b>477</b>
	<i>Rajiv Kohli</i>	
13.1	Introduction	477
13.2	Surface Cleanliness Levels	478
13.3	Dense Phase Fluids	479
13.3.1	Supercritical Carbon Dioxide	482
13.4	Principles of Supercritical CO <sub>2</sub> Cleaning	489
13.4.1	Cleaning Systems	490
13.4.2	Costs	491
13.5	Advantages and Disadvantages of Supercritical CO <sub>2</sub> Cleaning	493
13.5.1	Advantages	493
13.5.2	Disadvantages	495
13.6	Applications	496
13.6.1	Cleaning Spacecraft Components and Planetary Protection	497
13.6.2	Cleaning of Printing Rollers	498
13.6.3	Carbon Nanotubes	498
13.6.4	Soil Cleaning with Ionic Liquids and SCCO <sub>2</sub>	499
13.6.5	Conservation of Historical Art Objects and Structures	499
13.6.6	Sterilization	500
13.6.7	Monitoring of SCCO <sub>2</sub> Precision Cleaning Processes with the Quartz Crystal Microbalance	502
13.7	Summary and Conclusions	502
	Acknowledgement	503
	Disclaimer	503
	References	503

<b>14 The Use of Surfactants to Enhance Particle Removal from Surfaces</b>	<b>519</b>
<i>Brian Grady</i>	
14.1 Introduction	519
14.2 Solid-Solid Interactions	520
14.3 Introduction to Surfactants	524
14.4 Surfactant Adsorption at Solid Surfaces	529
14.5 Surfactants and Particulate Removal	535
14.6 Prospects	539
14.7 Summary	540
Acknowledgements	540
References	540
Index	543





## Preface

---

The importance of particle adhesion and removal is quite manifest in many areas of human endeavor (ranging from microelectronics to optics, and space to biomedical). A complete catalog of modern precision and sophisticated technologies where removal of particles from surfaces is of cardinal importance will be prohibitively long, but the following eclectic examples should suffice to underscore the concern about particles on a variety of surfaces where particulate contamination is a *bête noire*. In the semiconductor world of ever-shrinking dimensions, particles which, just a few years ago, were cosmetically undesirable but functionally innocuous, are now “killer” defects. As device sizes get smaller, there will be more and more concern about smaller and smaller particles. In the information storage technology, the gap between the head and the disk is very narrow, and if a particle is trapped in the gap this can have very grave consequences. The implications of particulate contamination on sensitive optical surfaces are all too manifest. So the particulate contamination on surfaces is an anathema from functional, yield, and reliability points of view. With the burgeoning interest in nanotechnologies, the need to remove nano and sub-nano particles will be more and more intense. Apropos, it should be mentioned that in some situations, particle adhesion is a desideratum. For example, in photocopying the toner particles must adhere well to obtain photocopies, but these should not adhere to wrong places otherwise the result will be a dirty photocopy. Here also one can see the importance of particle removal.

One of us (KLM) has edited a series of books called “Particles on Surfaces: Detection, Adhesion and Removal” but the last volume (Volume 9) was published in 2006. Since 2006 there has been an enormous level of research activity, particularly in removing nanosize particles, and thus it was obvious that recent developments needed consolidation and this provided the vindication for the present book. This book was conceived with the core purpose of providing a comprehensive and easily accessible

reference source covering important aspects/ramifications of particle adhesion and removal, with emphasis on recent developments in understanding nanoparticle adhesion mechanism(s) and their removal. All signals indicate that R&D activity in the arena of removal of nanometer size particles will continue unabated.

Now coming to this book (containing 14 chapters), it is divided into two parts: Part 1: Particle Adhesion: Fundamentals, and Part 2: Particle Removal Techniques. The topics covered include: Fundamental forces in particle adhesion; mechanics of particle adhesion and removal; microscopic particle adhesion models and surface modified particles; characterization of single particle adhesion; high intensity ultrasonic removal of particles; megasonic cleaning for particle removal; high speed air jet removal of particles; droplet spray technique for particle removal; laser-induced high-pressure micro-spray technique for particle removal; wiper-based cleaning of particles; application of strippable coatings for removal of particulate contaminants; cryogenic cleaning of particles; supercritical carbon dioxide cleaning; relevance to particle removal; and use of surfactants to enhance particle removal.

This book represents the cumulative contribution of many internationally renowned subject matter experts in the domain of particle adhesion and removal. The book reflects the state-of-the-art with special attention to recent and novel developments.

The book containing bountiful information on the fundamental and applied aspects of particle adhesion and removal provides a unified and comprehensive source. It should serve as a portal for the neophyte and a commentary on the recent developments for the veteran. The book should be of interest to researchers in academia and R&D, manufacturing, and quality control personnel in microelectronics, aerospace, automotive, optics, solar panels, pharmaceutical, biomedical, equipment cleaning and wafer reclaiming industries. Essentially, anyone involved in or concerned with removal of particles should find this book of immense value. Also, we hope that this book will serve as a fountainhead for new ideas pertaining to particle removal.

## **Acknowledgements**

Now comes the pleasant task of thanking those who made this book possible. First and foremost, we are deeply thankful to the authors for their interest, enthusiasm, cooperation and contribution without which this

book would not have seen the light of day. Also we are much appreciative of Martin Scrivener (Scrivener Publishing) for his steadfast interest in and continued support for this book project.

K.L. Mittal  
Hopewell Junction, NY, USA  
E-mail: [ushaRmittal@gmail.com](mailto:ushaRmittal@gmail.com)

Ravi Jaiswal  
Varanasi, UP, India  
E-mail: [ravi.jaiswal@gmail.com](mailto:ravi.jaiswal@gmail.com)

October 25, 2014



**Part 1**  
**PARTICLE ADHESION:**  
**FUNDAMENTALS**



# Fundamental Forces in Particle Adhesion

Stephen Beaudoin<sup>1</sup>, Priyanka Jaiswal<sup>2</sup>, Aaron Harrison<sup>1</sup>, Jennifer Laster<sup>1</sup>,  
Kathryn Smith<sup>1</sup>, Melissa Sweat<sup>1</sup>, and Myles Thomas<sup>1</sup>

<sup>1</sup>*School of Chemical Engineering, Purdue University,  
W. Lafayette, IN, USA,* <sup>2</sup>*Department of Applied Chemistry & Polymer Technology,  
Delhi Technological University (formerly Delhi College of Engineering),  
New Delhi, India*

---

## Abstract

van der Waals, capillary, and electrostatic forces acting at the interface between a particle and a surface drive the adhesion behavior of the particles. If one can describe the nature and the strength of these forces as a function of the properties of the two interacting solids and the intervening medium, it is possible to predict and, in many cases, to control particle adhesion. This chapter focuses on the factors that influence the nature and strength of the forces, the fundamental theories that describe them, and the relevant mathematical expressions required to quantify them, with a caveat that the analysis presented is limited to systems with ideal geometry. Specifically, more advanced analysis, which may account for aspects such as roughness, non-uniform shape, deformation, and other complicating aspects, is not treated.

**Keywords:** Particle adhesion, van der Waals force, Hamaker constant, electrostatic force, double layer, capillary force, surface tension, surface energy.

## 1.1 Introduction

Particle adhesion influences many areas of science and engineering, including semiconductor fabrication, pharmaceuticals, cosmetics, mining, separations, petroleum production, surface coating, and food processing, to name a few. In the context of this chapter, adhesion is an interfacial

---

\*Corresponding author: sbeaudoi@purdue.edu

phenomenon which appears when two solid bodies, one of which is of colloidal dimensions, approach each other closely. As the two surfaces approach, a complex interplay of van der Waals, electrostatic, and capillary forces drives the resulting behavior. Thorough knowledge of these surface forces is essential to understanding particle adhesion.

## 1.2 Various Forces in Particle Adhesion

In most applications of practical interest, the forces that control the adhesion between solid particles and solid surfaces are van der Waals (dipole) forces, electrostatic forces, and forces resulting from any liquid bridges due to capillaries or adsorbed molecular water between the two solids. Depending on the composition of the particle, the solid, and the ambient medium (air of varying relative humidity or aqueous solution are of interest here), the relative importance of these may change. This chapter provides an overview of these varying forces.

### 1.2.1 Capillary Forces

When a solid particle of characteristic dimension on the order of 100 micrometers or smaller is in contact with a solid surface in a gaseous medium (air), the relative humidity (RH) of the air is a critical factor in the relative importance of the forces that will influence the adhesion between the particle and surface [1, 2]. Specifically, water molecules in humid air will minimize their free energy by adsorbing on surfaces at low humidity and by condensing onto surfaces at higher humidity, if the surfaces of interest are sufficiently hydrophilic [3–8]. If condensed moisture forms liquid bridges between a particle and a surface, the capillary forces resulting from these liquid bridges will generally be the controlling forces in the particle adhesion [9]. The behavior of adsorbed water molecules has been studied using gravimetric methods, ellipsometry, nuclear magnetic resonance (NMR), atomic force microscopy (AFM) and the surface force apparatus (SFA), among others [3–8, 10–19].

#### 1.2.1.1 Forces Across a Curved Liquid Interface

When a solid surface comes in contact with a liquid medium, the difference in the magnitude of the net cohesive forces between the liquid molecules (*i.e.*,  $F_{l-l}$ ), and the net adhesion force between the liquid and the solid molecules (*i.e.*,  $F_{s-l}$ ) initiates the formation of a liquid meniscus at the solid/liquid interface. The nature of the curvature of the liquid meniscus



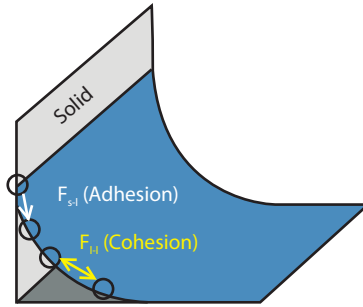


**Figure 1.1** Meniscus formation on a solid plate partially immersed in a wetting liquid.

(concave or convex) depends on which force,  $F_{s-l}$  (concave) or  $F_{l-l}$  (convex) is dominant. This leads to the phenomenon of wetting or de-wetting of the surface. Figure 1.1 shows an example of a liquid climbing on a solid plate. In this case,  $F_{s-l} > F_{l-l}$ . Solid surfaces which have  $F_{s-l} > F_{l-l}$  are known as high energy surfaces. If the liquid is an aqueous solution, these are known as hydrophilic surfaces. If the liquid is non-aqueous, they are known as lyophilic surfaces. Such surfaces facilitate wetting. Mica, silicon dioxide, metals, and oxidized surfaces in general are typically hydrophilic. Solid surfaces in which  $F_{s-l} < F_{l-l}$  are known as low energy surfaces. If the liquid is an aqueous solution, these are the hydrophobic surfaces. If the liquid is non-aqueous, they are the lyophobic surfaces. They facilitate de-wetting. Most organic surfaces, including most polymers, are hydrophobic. The surface energy of such materials can be increased by surface modifications (*e.g.*, surface oxidation achieved *via* ultraviolet radiation, plasma discharge, laser irradiation, etc.) to enhance their hydrophilicity [20].

#### 1.2.1.1.1 Surface Tension Force Acting at a Solid/Liquid Interface

The origin of surface tension is the unbalanced intermolecular force acting on the liquid molecules at the surface. The molecules present in the bulk of the liquid experience no net intermolecular force as they are surrounded by molecules of similar properties and hence are in a low energy state. However, the liquid molecules present at a liquid/solid or liquid/air interface are in an unbalanced or high energy state as they experience a net intermolecular force resulting from the difference in properties of the molecules in the different media. This leads to the development of the surface tension force. The surface tension ( $\gamma$ ) is quantified as the net surface tension force acting on a unit length of the liquid/solid or liquid/air interface. Figure 1.2 is a schematic of a spherical particle in contact with a solid

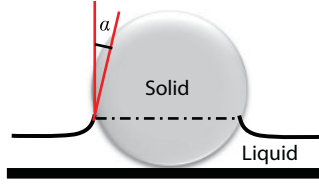


**Figure 1.2** Schematic showing surface tension force acting at the solid/liquid interface.

surface through a liquid medium. The surface tension force,  $F_{st}$ , acting on the solid/liquid boundary (the dotted line) can be obtained as

$$F_{st} = \int \gamma dl = \gamma (\cos(\alpha)) l_{wetted} \quad (1.1)$$

where  $\alpha$  is the angle of inclination of the liquid meniscus from the vertical, and  $l_{wetted}$  is the perimeter of the meniscus boundary on the solid surface.

#### 1.2.1.1.2 Capillary Pressure Force Acting Across a Curved Liquid Interface

The micro-/nano-contacts between two solid surfaces act as active sites for condensation in a humid environment if the RH is above a critical value. When condensed moisture comes in contact with the solid surfaces, a liquid meniscus is formed in the contact region bridging the two solid surfaces, as shown in Figure 1.3.

Menisci form through two methods on solid surfaces: the spontaneous condensation of a vapor in a confined space (otherwise known as capillary condensation) and, for non-volatile liquids, the combination of adsorbed layers (on the two adhering surfaces) merged into a meniscus. A meniscus induces a pressure difference across the liquid-vapor interface, as shown in Figure 1.4, where the pressure on the liquid side of the meniscus is lower than that in the surrounding vapor. This pressure difference is described by the Young-Laplace equation

$$\Delta P = \gamma_l \left( \frac{1}{r_n} + \frac{1}{r_p} \right) \quad (1.2)$$

where  $\Delta P$  is the pressure difference across the meniscus (the Laplace pressure),  $\gamma_l$  is the surface tension of the liquid condensate, and  $r_n$  and  $r_p$  are the two principal radii of curvature (ROC) of the liquid bridge between the surfaces [21]. The Laplace pressure acts over an area,  $A$ , and induces a force that pulls the two surfaces together increasing the total adhesion

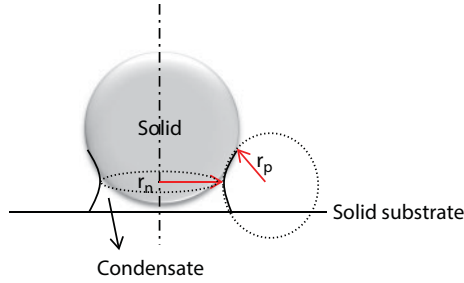


**Figure 1.3** A liquid bridge surrounding a solid particle in contact with a flat substrate.

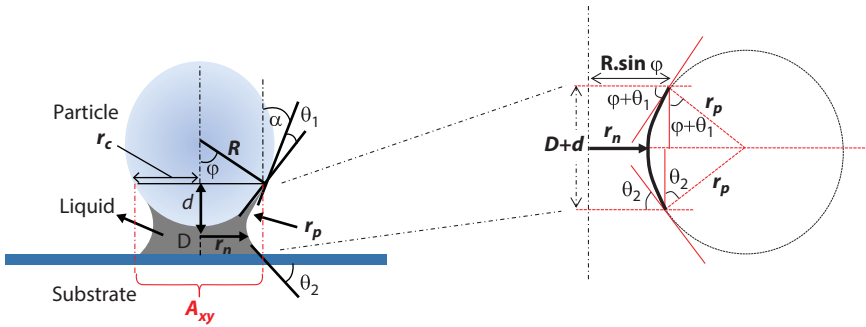


**Figure 1.4** A spherical particle adhering onto a flat substrate with a liquid bridge formed at the solid-solid interface. The meniscus geometry is shown on the right.

force [9]. The normal surface tension force around the circumference of the meniscus (Equation 1.1) also contributes to the force, but it is usually small compared to the pressure-induced force and is often not considered for micro-scale particles [9].

The following relations can be obtained for the geometry shown:

$$D + d = r_p (\cos(\varphi + \theta_1) + \cos(\theta_2)) \quad (1.3)$$

$$r_p = \frac{D + d}{(\cos(\varphi + \theta_1) + \cos(\theta_2))} \quad (1.4)$$

where  $d$  is the height of the particle inside the liquid bridge, and  $D$  is the separation distance, as shown in Figure 1.4,  $\theta_1$  and  $\theta_2$  are the contact angles of the liquid with the sphere (1) and the flat substrate (2), and  $\varphi$  is the half angle subtended at the center of the sphere by the wetted area of the sphere (this is also known as the ‘embracing’ or ‘filling’ angle).

The ROC,  $r_p$ , can also be obtained from the geometry shown in Figure 1.4:

$$\begin{aligned}
r_n &= R \sin(\varphi) - \left( r_p - r_p \sin(\varphi + \theta_1) \right) \\
&= R \left( \sin(\varphi) - \left( \frac{D+d}{R} \right) \left( \frac{1 - \sin(\varphi + \theta_1)}{\cos(\varphi + \theta_1) + \cos(\theta_2)} \right) \right)
\end{aligned} \quad (1.5)$$

where  $R$  is the particle radius. The equilibrium capillary pressure force,  $F_{cp}$ , is found by multiplying the Laplace pressure by the interaction area using the Young-Laplace equation [22]

$$F_{cp} = A_{xy} \gamma_l \left( \frac{1}{r_p} + \frac{1}{r_n} \right) = \pi r_c^2 \gamma_l \left( \frac{\cos(\varphi + \theta_1) + \cos(\theta_2)}{D+d} + \frac{1}{r_n} \right) \quad (1.6)$$

where  $r_c$  is the radius of the contact circle at the solid particle/liquid/air interface, and is given by:

$$r_c = R \sin(\varphi) \quad (1.7)$$

For a large sphere ( $R \gg D$  and  $R \gg d$ ), the following approximations can be made:

- I. The embracing angle,  $\varphi$ , will be very small in comparison to the contact angle,  $\theta_1$
- II.  $\varphi \left( = \cos^{-1} \left( \frac{R-d}{R} \right) = \cos^{-1} \left( 1 - \frac{d}{R} \right) \right)$  will be very small, hence  $\varphi + \theta_1 \approx \theta_1$
- III.  $r_c$  can be obtained using the geometry shown in Figure 1.4,

$$r_c = R \sin(\varphi) = \sqrt{R^2 - (R-d)^2} \sim \sqrt{2Rd} \quad (1.8)$$

- IV.  $r_n \gg r_p$  from Equations 1.4 and 1.5, therefore  $1/r_n$  in Equation 1.6 can be neglected.

The final expression for the capillary pressure force between a large spherical particle and a planar surface, using the above approximations, can be obtained as:

$$F_{cp}^{R \gg D, R \gg d} = 2\pi R \gamma_l \left( \frac{\cos(\theta_1) + \cos(\theta_2)}{1 + \frac{D}{d}} \right) \quad (1.9)$$

When the spherical particle and the substrate are in contact ( $D = 0$ ), the capillary force will attain a maximum:

$$F_{cp_{max}}^{R \gg D, R \gg d} = 2\pi R\gamma_l (\cos(\theta_1) + \cos(\theta_2)) = 4\pi R\gamma_l \cos(\theta) \quad (\text{if } \theta_1 = \theta_2 = \theta) \quad (1.10)$$

It is apparent from Equation 1.10 that the capillary force for the case of a large spherical particle in contact with a flat substrate is humidity independent (as  $d$ , a humidity-dependent parameter which quantifies the height of the liquid bridge, gets canceled out); and hence the capillary force in this case is a function of only the particle size and the surface tension. This has also been shown experimentally [22]. However, the capillary forces for small particles have strong humidity dependence [6, 23].

Most parameters, except  $d$ , in Equation 1.9 are usually available to calculate the capillary force between a sphere and a flat plate. The estimation of  $d$  requires knowledge of the embracing angle ( $\varphi$ ) or the volume of the liquid bridge ( $V$ ).

a) *Relation between  $d$  and  $\varphi$*

It is apparent from the geometry shown in Figure 1.4 that

$$d = R(1 - \cos(\varphi)) = 2R\sin^2\left(\frac{\varphi}{2}\right) \approx \frac{R\varphi^2}{2} \quad \text{for small } \varphi \quad (1.11)$$

The embracing angle  $\varphi$  will be very small for large spheres or for small liquid bridge volume.

b) *Relation between  $d$  and  $V$*

The following relation exists between  $d$  and the liquid bridge volume  $V$  [24]

$$d = \sqrt{D^2 + V / (\pi R)} - D \quad (1.12)$$

For the case of small separation distance  $D$ ,  $d \approx \sqrt{V / (\pi R)}$ .

For the case of large separation distance  $D$ ,

$$d = D \left( \left[ 1 + V / (\pi R D^2) \right]^{1/2} - 1 \right) \approx V / (2\pi R D)$$

The total capillary force acting between a sphere and a flat plate can be determined by combining the capillary pressure force (Equation 1.9) with the surface tension force (Equation 1.1) [25]

$$F_{st} = 2\pi R\gamma_l \cos(\alpha) = 2\pi R\gamma_l \sin(\varphi) \sin(\varphi + \theta_1) \quad (1.13)$$

where  $\alpha \left( = \frac{\pi}{2} - (\varphi + \theta_1) \right)$  is the angle of the liquid meniscus (at the particle/liquid/air interface) from the vertical as shown in Figure 1.4. Finally,

$$F_{tot}^{sphere-plate} = 2\pi R\gamma_l \left( \frac{\cos(\theta_1) + \cos(\theta_2)}{1 + \frac{D}{d}} \right) + 2\pi R\gamma_l \sin(\varphi) \sin(\varphi + \theta_1) \quad (1.14)$$

The filling angle  $\varphi$  is still unknown, but can be estimated by the Kelvin equation, which relates the equilibrium ROC of the meniscus to the ambient relative humidity (RH) [26, 27]

$$\left( \frac{1}{r_n} + \frac{1}{r_p} \right) = \frac{R_g T \ln(RH)}{\gamma_l V_m} \quad \text{or} \quad \left( \frac{1}{r_n} + \frac{1}{r_p} \right)^{-1} = r_k = \frac{\gamma_l V_m}{R_g T \ln(RH)} \quad (1.15)$$

where  $r_k$  is the so-called 'Kelvin radius.' Specifically, by substituting Equations 1.4 and 1.5 into Equation 1.15, one may determine  $\varphi$  numerically based on Equation 1.16, and then solve Equations 1.6 and 1.14 to determine  $F_{cp}$  and  $F_{tot}$

$$\frac{R_g T \ln(p/p_0)}{\gamma_l V} = \frac{\cos(\theta_1 + \alpha) + \cos(\theta_2)}{D + R(1 - \cos(\alpha))} - \frac{1}{R \sin(\alpha)} \quad (1.16)$$

where  $p$  = the partial pressure of water at the system conditions and  $p_o$  = the vapor pressure of water at these conditions. The magnitude of  $2r_k$  gives the maximum separation distance between two adhering bodies over which capillary condensation can take place (*i.e.*, the range of the capillary forces). For instance, the value of  $2r_k$  for water ( $\gamma_l = 74 \text{ mN/m}$ ) at room temperature ( $T = 298 \text{ K}$ ) is  $[1.08/\ln(RH)] \text{ nm}$ . Figure 1.5 shows the maximum separation distance for capillary condensation as a function of RH at this temperature. If the RH is below 50%, the maximum separation distance ( $2r_k$ ) for capillary condensation is roughly  $\sim 2 \text{ nm}$ . Virtually all substrates generally have root-mean-squared (RMS) surface roughness greater than 2 nm. For this reason, unless there is substantial complementarity between the roughness on the particle and surface such that the peaks on one surface fit into the valleys on the opposing surface, capillary condensation (and correspondingly capillary forces) between particles and solid surfaces are generally negligible when the RH is below 50%.

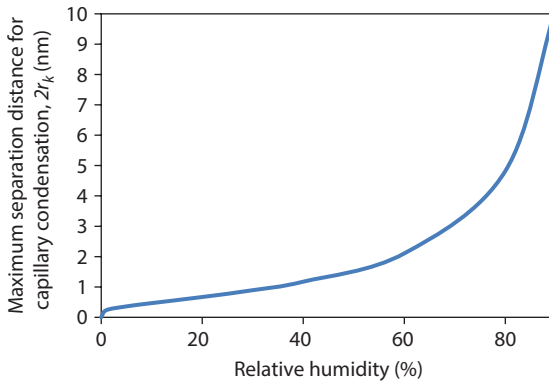


**Figure 1.5** Maximum separation distance between two solid surfaces to allow capillary condensation as a function of RH at room temperature.

It is important to note that the Kelvin equation applies to systems containing continuum or bulk liquid water (systems in which the water in the liquid phase has the density and surface tension of bulk liquid water). Adsorbed moisture in molecular form still has an impact on adhesion, but the Kelvin equation is inappropriate for describing the behavior in such systems. Water has an effective diameter of roughly 0.37 nm [21]. At 30% RH, the liquid bridge between two solid surfaces would have a characteristic Kelvin radius corresponding to  $\sim 3$  water molecules. At 50% RH, this number increases to somewhere between 4 and 5 water molecules. In either case, the argument that such a small amount of water would behave like ‘bulk’ water, exhibiting surface tension effects in the same manner as bulk water, is tenuous.

The Young-Laplace and Kelvin equations are almost universally used to predict the capillary force between macroscopic bodies [1, 6, 11, 28–37]. Butt and Kappal summarize these capillary forces for smooth systems, such as plane-plane, sphere-plane, cone-plane, sphere-sphere, and cone-cone geometries [37]. Furthermore, with only slight modifications, these equations can also model the dependence of the capillary force on the surface roughness [35, 38, 39] and heterogeneity [38].

The conditions in which the surface tension force should be considered when calculating the total capillary force have been demonstrated through numerical simulation in an idealized modeling framework, as shown in Figure 1.6 [40]. This figure shows computational values of the total capillary force, the surface tension force, and the capillary pressure force, for three differently-sized spherical particles interacting with a flat surface. For

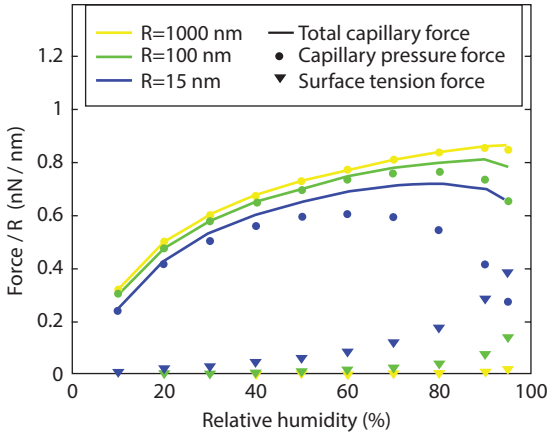


**Figure 1.6** Theoretical capillary pressure ( $F_{cp}$ ), surface tension ( $F_{st}$ ), and total capillary forces ( $F_{tot}$ ) between a sphere and flat surface separated by  $3\text{\AA}$ . Reproduced with permission [40].

ease of comparison, the total force is normalized by the particle radius. The relevant region of RH to be considered in this figure is the region with  $\text{RH} > 50\%$ , as this is the condition where condensed moisture can be well-represented as continuum. In this region, it can be seen that the surface tension force (inverted triangles) makes a negligible contribution to the overall force (solid lines) when the particle size is above 1000 nm. When the particle radius is 100 nm, the surface tension force contribution to the overall force is no longer negligible, and when the particle is nano-scale and the RH is high, the surface tension force and the capillary pressure force make comparable contributions to the overall force.

### 1.2.1.2 Effects of RH on Capillary Forces

Capillary forces resulting from condensed moisture between hydrophilic surfaces generally increase continuously with increasing humidity to a maximum and then decrease, while humidity has little effect on adhesion when one or both of the interacting surfaces are hydrophobic [2, 3, 6–8, 18, 19, 32, 41–43]. Frequently, the increase in adhesion with increasing RH continues until RH attains roughly 50%, after which the force becomes independent of further RH increases or drops with such increases [3, 6, 32, 43]. Figures 1.7 and 1.8 show such results in two AFM-based studies. The magnitude of these changes is influenced by the geometry and composition of the surfaces (or the asperities on the surfaces) in contact [5–7, 15–17].



These behaviors have been attributed to: 1) variations in the radii of curvature of the menisci of condensed moisture between non-uniform features (asperities) of the interacting surfaces; 2) variations in the thickness of any adsorbed molecular water films; 3) the complexity of the local separation distance between the interacting surfaces due to the complementarity of the asperities/topography of the surfaces (basically, how well do the asperities on the two surfaces fit together and how does this influence the accessibility of condensed moisture to elements of the interacting surfaces); 4) changes in the cantilever tip geometry as a result of dulling during multiple tip-substrate interactions (unique to AFM-based studies); 5) composition-driven variations in the contact angles of water on both the probe and substrate, leading to local variations in capillary forces; and 6) dissolution and reaction of surface species on the two interacting surfaces [5]. While these effects do have an influence on the observed behavior, a true description over the entire range of humidity requires a detailed consideration of the form of water at the interface between the particle and surface. Specifically, the Young-Laplace and Kelvin equations are of great utility for equilibrated systems where: 1) moisture is present on a surface in sufficient quantity that it maintains the properties of bulk water, 2) the radius of the particle is much greater than both  $r_n$  and  $r_p$ , and 3) the volume of the liquid bridge is approximately constant [37]. However, as the size of the particle approaches the nanoscale, the validity of these criteria is disputable, throwing into question the applicability of these continuum models.

In Figures 1.7 and 1.8, the fact that the dependence of the adhesion force on RH is different for hydrophilic and hydrophobic surfaces is to be expected. However, the maxima in adhesion force observed in the hydrophilic systems are not consistent with existing continuum models. The Kelvin equation typically predicts a monotonic increase in adhesion force with increasing RH. It also predicts radii of curvature on the order of a few molecular diameters for equilibrated menisci at low RH. For example, at 20 °C and 50% RH, the Kelvin radius for water is 0.8 nm [9]. With an effective diameter of approximately 0.37 nm [9], water is thus expected to form a meniscus with less than 3 molecules. Such a constraint considerably stretches the intra- and intermolecular bonds within the liquid. To further illustrate this discrepancy, it has been shown that when the mechanical properties of water dictate the change in surface tension on a nanoscale in water-induced capillary systems, the Kelvin equation is only applicable above 45% RH at best [44]. Below 45% RH, the macroscopic or continuum assumptions in the Young-Laplace and Kelvin equations oversimplify the existence, formation, and magnitude of capillary forces on the nanoscale, especially for polar liquids.

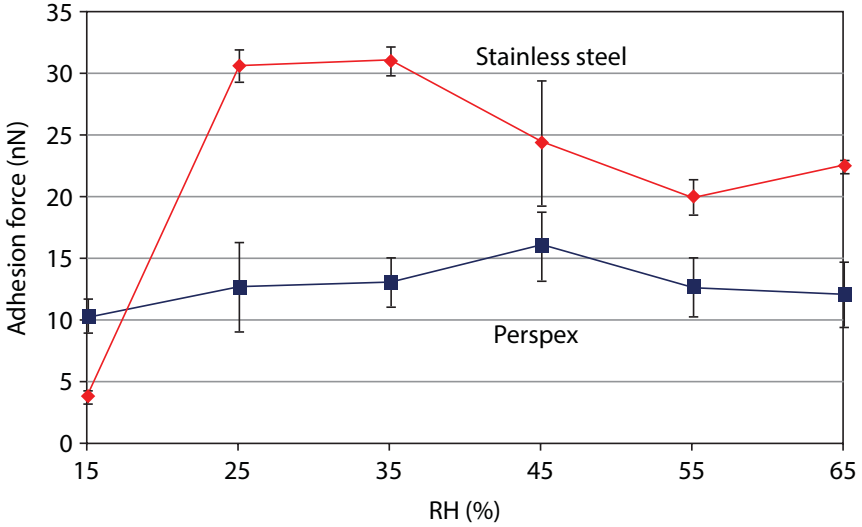


**Figure 1.7** Measured adhesion forces between  $\text{Si}_3\text{N}_4$  AFM cantilevers with nanoscale radii of curvature ( $\sim 20$  nm) and stainless steel (hydrophilic) and Perspex® (hydrophobic) surfaces. Each data point is the average of 1200 measurements [42].

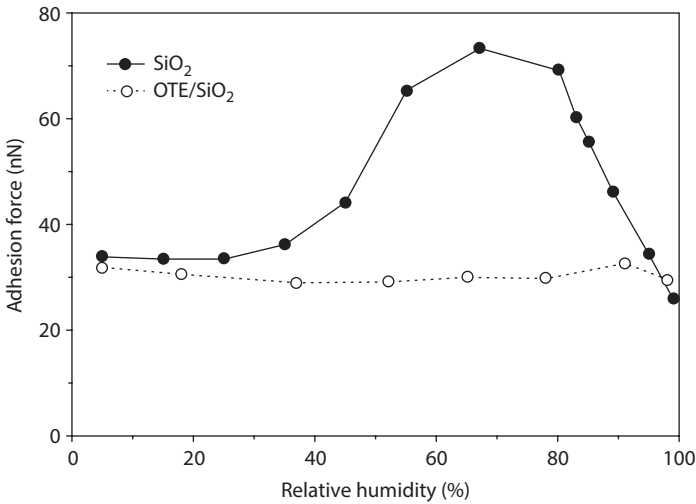


**Figure 1.8** Measured adhesion forces as a function of humidity for  $\text{SiO}_2$  (hydrophilic) and OTE/ $\text{SiO}_2$  (hydrophobic) surfaces against  $\text{Si}_3\text{N}_4$  AFM probes. OTE = hydrophobic *N*-octadecyltrimethoxysilane coating over  $\text{SiO}_2$ . Reproduced with permission [6].

### 1.2.1.2.1 Effects of High RH on Adhesion Forces

At sufficiently high humidity (>80%), particle adhesion forces are observed to decrease, as can be seen in Figures 1.7 and 1.8. This is attributed to a combination of factors. First, strongly adsorbed water on a hydrophilic substrate prevents the close approach of the particle and surface. At the higher RH, the liquid bridge can wet a larger fraction of the particle, as the condensed moisture can span a greater distance between the two surfaces. The liquid bridge can also be extended to a greater distance along the substrate. As the extent of the condensed liquid around the particle grows, the values of  $r_p$  and  $r_n$  in Equation 1.6 become large which drives the capillary force down. This makes it easier for the adsorbed water to hold the particle away from the surface. When the RH attains 100%, a continuous water layer forms at the solid/solid interface. This completely eliminates the liquid neck and hence the capillary force at the solid contacts, and it screens the van der Waals interactions between the adhering solid surfaces.

### 1.2.1.2.2 Effects of Low RH on Adhesion Forces

At humidity levels below 45%, molecular-scale representations of the behavior of water are required to explain the role of water in particle adhesion. For this purpose, several approaches have been applied successfully. First, a combination of coarse lattice-gas (LG) models, grand canonical Monte Carlo (GCMC) simulations, and thermodynamic integration techniques has been used to predict the effects of adsorbed moisture between an AFM probe and a hydrophilic surface [8, 45–51]. In these studies, vapor molecules ( $c_i$ ) are allowed to occupy sites on a 3D lattice spanning the interstitial space between the two bodies, as shown schematically (in 2D) in Figure 1.9. The lattice spacing is generally one molecular diameter, each site may be either fully occupied or unoccupied, and molecules are only allowed to interact with their nearest neighbors (NN). Each molecule has its own chemical potential,  $\mu$ , and the interaction between a molecule and its NN is

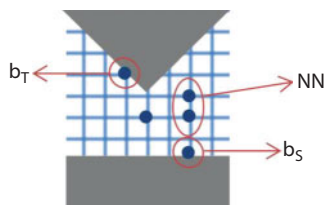


**Figure 1.9** Schematic of grand canonical Monte Carlo lattice-gas model.

described using an intermolecular attraction energy,  $\varepsilon$ . If a molecule's NN is either of the two solid surfaces in consideration, the top or the bottom surface (particle or substrate), binding energies of  $b_T$  or  $b_s$  are imposed.

The total energy of such a system,  $H$ , is given by:

$$H = -\varepsilon \sum_{i,j=NN} c_i c_j - b_T \sum_{i=\text{top boundary}} c_i - b_s \sum_{i=\text{bottom boundary}} c_i - \mu N \quad (1.17)$$

where  $N$  is the total number of molecules in the system or the total number of occupied sites [52]. The chemical potential is related to RH by

$$\mu = k_B T \ln RH + \mu_c \quad (1.18)$$

where  $\mu_c$  is the chemical potential at the gas-liquid transition. For a 3D LG system,  $\mu = 3\varepsilon$  [53].

To determine whether or not a molecule is removed from, added to, or moved to a lattice site, one calculates the change in the total energy of the system ( $\Delta H$ ) resulting from the proposed molecular change. If  $\Delta H$  is negative (i.e., the change is energetically favorable), the removal, addition or relocation of the molecule is accepted. If  $\Delta H$  is positive, the removal, addition or relocation of the molecule occurs with a given probability. This Monte Carlo process is repeated hundreds of thousands of times, which allows the system to reach 'equilibrium' [52]. The capillary force resulting from this *molecularly adsorbed, non-continuum water* is calculated by integrating the partial derivative of the excess number of molecules relative to the bulk system ( $N_{ex}$ ) with respect to changes in the separation distance between the two surfaces ( $h$ ) for a fixed  $\mu$  and  $T$  [45]:

$$F_p = \int_{-\infty}^{\mu} \left( \frac{\partial N_{ex}}{\partial h} \right)_{\mu'} d\mu' \quad (1.19)$$

Many of the effects of molecularly adsorbed water between an AFM probe and a substrate have been predicted with this LG GCMC model (Equations 1.17–1.19) [54]. Additionally, the effects of RH on the pull-off force between AFM cantilevers and substrates of varying hydrophilicity can be predicted qualitatively with this method. Specifically, a maximum in the adhesion force is predicted around 30% RH for a strongly hydrophilic tip; a plateau above 34% is predicted for a hydrophobic tip, due to the interaction of two confined layers of water; and a monotonic increase is predicted for a slightly hydrophilic tip [46, 55]. All of these behaviors have been verified experimentally [3, 11, 30, 32, 56, 57]. The LG GCMC

model has also demonstrated that nanoscale roughness on either the tip or the substrate dramatically influences the force-RH curve [48, 51]. For example, for a smooth tip and a smooth surface, a single maximum is seen in the plot of the adhesion (pull-off) force as a function of RH. However, when a rough tip and rough surface are simulated, several local maxima are predicted [51, 52]. The LG GCMC model is computationally simple, and its ability to provide molecular insight into the onset of true capillary forces makes it very attractive [52].

A drawback of the LG GCMC model is that it does not account for molecular shape, dipole moments, or long-range electrostatic interactions. To consider these effects, adhesion forces between AFM probes and surfaces at low RH have also been modeled using molecular dynamics (MD) techniques, which can incorporate these more realistic conditions [58]. The formation and breakage of a true liquid meniscus between an AFM probe and a surface at high (70%) RH was predicted in this manner based on the density profile of water molecules from MD snapshots on a 3D lattice [58]. In other work with a hydrophilic AFM probe tip against a hydrophilic surface, an oscillatory force was predicted as the tip was withdrawn from the surface, indicative of the role of confined layers of molecular water on the adhesion. This simulation also recreated a global maximum in the pull-off force around 20% RH, which correlates with experimental values for gold and mica surfaces [59]. These recent studies are promising approaches to understanding the molecular origin of capillary forces at low RH.

In addition to LG GCMC and MD simulations, density functional theory (DFT) [46, 60, 61] and computational fluid dynamics (CFD) [62, 63] simulations have been used to describe the effect of RH on adhesion. Like the MD simulations, the DFT simulations are computationally less demanding than the LG GCMC model. However, they do not account for strongly adsorbed layers or fluctuations in the meniscus at high RH (the region of transition from water with continuum-like density to vapor with gas-like density) [61].

A final approach to modeling capillary forces at low RH stems from an observation that adsorbed water can form ice-like, monolayer structures on smooth, hydrophilic materials (*e.g.*, mica and silicon dioxide) [10]. This phenomenon has been attributed to the surface having an isosteric heat of adsorption greater than the latent heat of condensation for water [57]. Since the number of hydrogen bonds per water molecule is greater in ice than in the liquid (a monolayer of ice-like molecules is expected to have a higher surface energy than liquid water), the surface tension of liquid water, therefore, should not be expected to account for the total

adhesion force between a particle and an ice-inducing surface. By considering van der Waals forces (described later) to account for the surface energy of ice-like molecular water, and the capillary forces (predicted using the Young-Laplace and Kelvin adhesion models), the experimentally observed adhesion behavior of ultra-smooth hydrophilic surfaces against AFM probes as a function of RH has been modeled effectively, including the prediction of an adhesion maximum at roughly 30% RH as shown in Figure 1.7 [30, 64].

### 1.2.1.3 Effects of Bulk Liquid Water on Capillary Forces in Idealized Systems

In systems where the RH is high enough to assure the presence of liquid water, but in which the adhesion between the water and the interacting solid surfaces is not so strong as to limit the closeness of approach of the two surfaces, a number of idealized continuum models may be used to obtain analytical expressions for capillary forces and to describe the effect of the condensed moisture. This section shows derivations of the analytical expressions for capillary forces for systems with ideal geometries.

#### 1.2.1.3.1 Parallel Plates

As a starting point, Figure 1.10 shows two parallel plates of different materials separated by a thin liquid film of thickness,  $d$ . The meniscus of the film is cylindrical in shape with the primary ROC,  $r_p$ , and the secondary ROC,  $r_n (= \infty)$ . The capillary pressure force for this system can be obtained from a modified version of Equation 1.6:

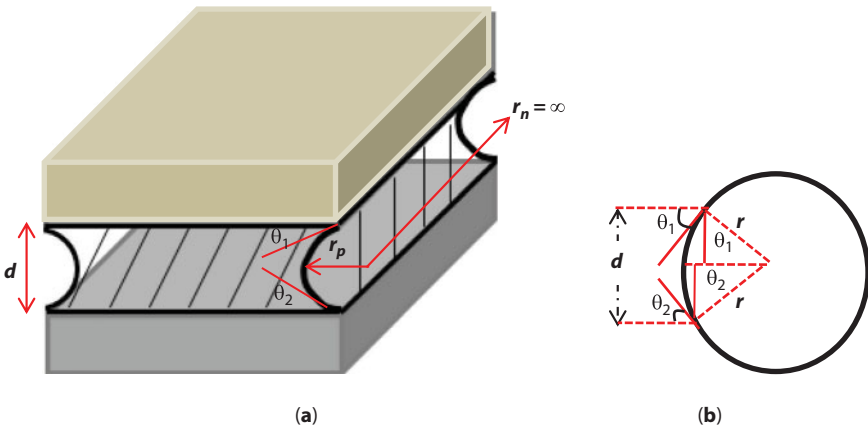


**Figure 1.10** (a) Two parallel plates made of different materials separated by a thin sheet of liquid film, (b) expanded view of the geometry at the liquid film meniscus.

$$F_{cp} = A_{xy}\gamma_l \left( \frac{1}{r_p} + \frac{1}{r_n (= \infty)} \right) = \frac{A_{xy}\gamma_l}{r_p} \tag{1.20}$$

where  $A_{xy}$  is the wetted area of the plate.

The ROC,  $r_p$ , of the film meniscus can be related to the film thickness,  $d$ , using geometry shown in Figure 1.10b:

$$d = r_p (\cos(\theta_1) + \cos(\theta_2)) \tag{1.21}$$

where  $\theta_1$  and  $\theta_2$  are the contact angles of the liquid against the two plates. Finally, the capillary pressure force for this system can be determined as:

$$F_{cp} = \frac{A_{xy}\gamma_l (\cos(\theta_1) + \cos(\theta_2))}{d} \tag{1.22}$$

If both plates shown in Figure 1.10a are made of the same material with the liquid contact angle  $\theta_1 = \theta_2 = \theta$ , the capillary force between them can be determined as:

$$F_{cp} = \frac{2A_{xy}\gamma_l \cos(\theta)}{d} \tag{1.23}$$

Figure 1.11 shows a schematic of two plates of the same material, separated by a liquid column of height,  $d$ , and radius,  $R$ . The contact angle of the liquid with each plate is  $\theta$ . The capillary pressure force between these plates can be obtained using Equations 1.6 and 1.23:

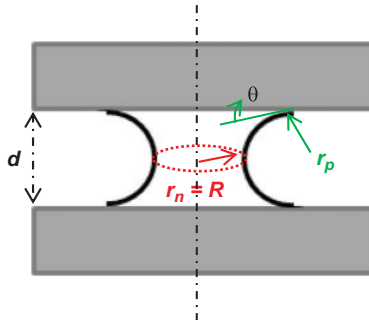


**Figure 1.11** Two parallel plates of same material linked by a columnar liquid bridge.

$$F_{cp} = A_{xy}\gamma_l \left( \frac{2\cos(\theta)}{d} - \frac{1}{R} \right) = \pi R^2 \gamma_l \left( \frac{2\cos(\theta)}{d} - \frac{1}{R} \right) \quad (1.24)$$

where  $A_{xy}$  is the wetted area of the plate, and can be approximated to  $\pi R^2$  [22].

If the radius of the liquid column is much larger than the column height (i.e.,  $R \gg d$ ),

$$F_{cp} \sim \frac{2\pi R^2 \gamma_l \cos(\theta)}{d} \quad (1.25)$$

The surface tension force acting on the plate in this case can be obtained using Equation 1.26:

$$F_{st} = \gamma_l \cos(\pi/2 - \theta) l_{\text{wetted}} = 2\pi R \gamma_l \sin(\theta) \quad (1.26)$$

The total capillary force acting between the plates can be determined by combining the capillary pressure force with the surface tension force:

$$F_{\text{tot}} = \pi R^2 \gamma_l \left( \frac{2\cos(\theta)}{d} - \frac{1}{R} \right) + 2\pi R \gamma_l \sin(\theta) \quad (1.27)$$

#### 1.2.1.3.2 Two Spherical Particles Linked by a Liquid Bridge

Figure 1.12 shows a schematic of two spherical particles of radii  $R_1$  and  $R_2$ , separated by distance  $D$  and linked by a liquid column with radii of curvature  $r_p$  and  $r_n$  and height  $(D+d_1+d_2)$ . The ROC,  $r_p$ , can be determined using geometry shown in Figure 1.12.

$$r_p = \frac{D + d_1 + d_2}{\cos(\varphi_1 + \theta_1) + \cos(\varphi_2 + \theta_2)} \quad (1.28)$$

where  $d_1$  and  $d_2$  are the heights of the two spherical particles inside the liquid bridge,  $\theta_1$  and  $\theta_2$  are the contact angles of the liquid with the spheres, and  $\varphi_1$  and  $\varphi_2$  are the 'embracing' angles for the spheres.

The ROC,  $r_n$ , can also be obtained from the geometry shown:

$$\begin{aligned} r_n &= R_1 \sin(\varphi_1) - r_p (1 - \sin(\varphi_1 + \theta_1)) \\ &= R_1 \left( \sin(\varphi_1) - \left( \frac{D + d_1 + d_2}{R_1} \right) \left( \frac{1 - \sin(\varphi_1 + \theta_1)}{\cos(\varphi_1 + \theta_1) + \cos(\varphi_2 + \theta_2)} \right) \right) \end{aligned} \quad (1.29)$$



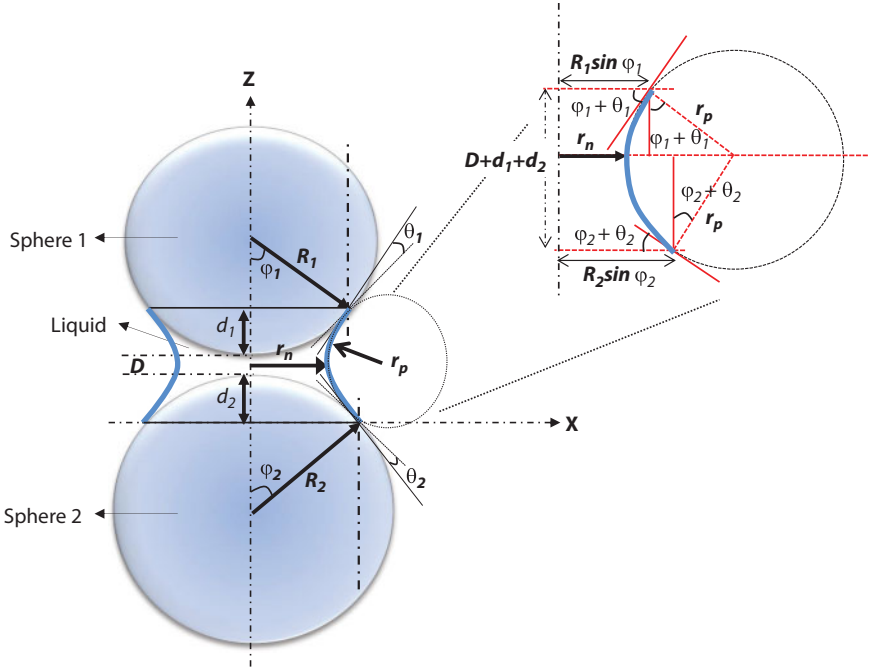


**Figure 1.12** Two spherical particles linked by a liquid bridge. Detail of the meniscus is at the right.

Now the general expression for the capillary force between two spherical particles can be obtained using the Young-Laplace equation as:

$$F_{cp} = A_{xy}\gamma_l \left( \frac{1}{r_p} + \frac{1}{r_n} \right) = \pi r_c^2 \gamma_l \left( \frac{\cos(\varphi_1 + \theta_1) + \cos(\varphi_2 + \theta_2)}{D + d_1 + d_2} + \frac{1}{r_n} \right) \quad (1.30)$$

where  $r_c$  is the radius of the contact circle at the solid particle/liquid/air interface.

The capillary force in Equation 1.30 can be calculated if either the particle depths into the liquid bridge ( $d_1$  and  $d_2$ ) or the embracing angles ( $\varphi_1$  and  $\varphi_2$ ) are known as they both are related according to:

$$d_1 = R_1(1 - \cos(\varphi_1)) \quad \text{and} \quad d_2 = R_2(1 - \cos(\varphi_2)) \quad (1.31)$$

When the volume of the liquid bridge,  $V$ , is known, the capillary force can be calculated. First, the expression for the volume of the liquid bridge is [65, 66]:

$$V = \int_0^{D+d_1+d_2} \pi r^2(z) dz - \frac{\pi}{6} \left( d_1 \left( 3R_1^2 \sin^2(\varphi_1) + d_1^2 \right) + d_2 \left( 3R_2^2 \sin^2(\varphi_2) + d_2^2 \right) \right) \quad (1.32)$$

where  $r(z) = r_n + r_p - \sqrt{r_p^2 - (z - r_p \cos(\theta_2 + \varphi_2))^2}$

Next, the following apparent geometric relation can be obtained from Figure 1.12.

$$R_2 \sin(\varphi_2) - R_1 \sin(\varphi_1) = r_p \left( \sin(\varphi_1 + \theta_1) - \sin(\varphi_2 + \theta_2) \right) \quad (1.33)$$

The embracing angles can now be calculated using Equations 1.29-1.30, and then the total force can be predicted using Equation 1.27.

For large spheres ( $R_1$  and  $R_2 \gg D$ , and  $R_1$  and  $R_2 \gg d$ ), the following approximations can be made:

- I. The embracing angles,  $\varphi_1 \left( = \cos^{-1} \left( 1 - \frac{d_1}{R_1} \right) \right)$  and  $\varphi_2 \left( = \cos^{-1} \left( 1 - \frac{d_2}{R_2} \right) \right)$  will be very small, and hence  $\varphi_1 + \theta_1 \approx \theta_1$  and  $\varphi_2 + \theta_2 \approx \theta_2$
- II.  $r_n \gg r_p$  from Equations 1.25 and 1.26, therefore  $1/r_n$  in Equation 1.30 can be neglected.

The final expression for the capillary pressure force between two large spherical particles linked by a liquid bridge can be obtained using the above approximations in Equation 1.30

$$F_{cp}^{R_1, R_2 \gg D, R_1, R_2 \gg d} = \pi r_c^2 \gamma_l \left( \frac{\cos(\theta_1) + \cos(\theta_2)}{D + d_1 + d_2} \right) \quad (1.34)$$

If both spheres are identical (*i.e.*,  $R_1 = R_2 = R$ ;  $\theta_1 = \theta_2 = \theta$ , and  $d_1 = d_2 = d$ ), Equation 1.34 can be reduced to

$$F_{cp}^{R \gg D, R \gg d} = \frac{2\pi R \gamma_l \cos(\theta)}{1 + D/2d} \quad (1.35)$$

The parameter  $d$  can be determined from the known embracing angle using Equation 1.31. It can also be estimated if the volume of the liquid bridge,  $V$ , is given using the following relation [67]:

$$d = \sqrt{\frac{D^2}{4} + \frac{V}{2\pi R}} - \frac{D}{2} \quad (1.36)$$

For the case of small separation distance  $D$ ,  $d \approx \sqrt{V/(2\pi R)}$

For the case of large separation  $D$ ,

$$d = \frac{D}{2} \left( \left[ 1 + 2V/(\pi R D^2) \right]^{1/2} - 1 \right) \approx V/(2\pi R D)$$

### 1.2.1.3.3 Non-spherical Particles Against a Flat Surface

Particle shape can influence the capillary forces by changing the geometrical parameters of the liquid meniscus generated at the solid/solid interface in a humid environment. Figure 1.13 (top) shows simulated geometries of five idealized AFM cantilever probes, and Figure 1.13 (bottom) shows predicted capillary forces, based on the Kelvin-Laplace equation, between a flat substrate and these AFM probes [40]. As noted above, the RH levels at which the Kelvin-Laplace equation may be applied are strictly limited by the ability of the two surfaces to approach each other. In this case, where the surface is a theoretical, atomically flat surface and the cantilever tip is assumed to have perfect geometry and no roughness, the Kelvin-Laplace predictions are appropriate at lower RH levels than would be appropriate for realistic systems. The shapes of the simulated AFM probes are assumed to be (a) spherical, (b) polynomial with flat tip, (c) conical, (d) truncated conical, and (e) polynomial with curved tip. As can be seen in Figure 1.13 (bottom), particle geometry has a strong impact on the capillary forces, emphasizing the importance of adequate modeling of the particle geometry for reliable prediction of these forces.

### 1.2.1.4 *Effects of Bulk Liquid Water on Capillary Forces Using Non-ideal Meniscus Shapes*

The prediction of capillary forces for non-ideal solid/solid contacts in a humid environment requires a proper accounting of the irregularity in geometry, roughness and material properties of the adhering objects, and the resulting shape of the liquid meniscus formed between them. Even for cases when interacting solid objects are ideally shaped, it is not necessarily true that the meniscus has an ideal shape as was assumed in the calculations considered above. Most theoretical models assume a circular profile for the liquid meniscus, *i.e.*, the ROC ( $r_p$ ) in Fig. 1.4 is assumed to be

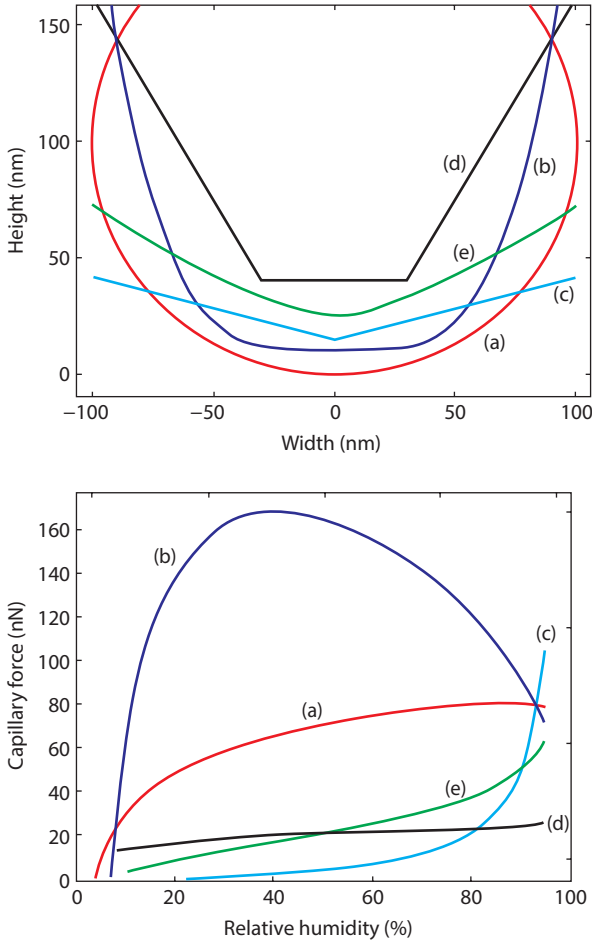


**Figure 1.13** Top: Assumed AFM probe shapes in capillary force calculations: (a) sphere ( $R = 100 \text{ nm}$ ), (b) polynomial with flat tip,  $z = k_v x^4 [k_v = 2 \times 10^{21}]$ , (c) cone (cone angle  $\beta = 15^\circ$ ), (d) truncated cone ( $R = 30 \text{ nm}$  and cone angle,  $\beta = 60^\circ$ ), (e) polynomial with curved tip,  $z = k_e x^3 / 2 (k_e = 1500)$ ; Bottom: Calculated capillary forces for AFM probes against a flat surface at particle–surface separation distance of  $3 \text{ \AA}$ . Reproduced with permission [40].

the same at every point on the liquid meniscus. However, this assumption is rarely true and can give significant deviation, especially for small particles or nano-contacts at high humidity [40]. For such systems, precise predictions of capillary forces can be made by computing in a sequential, point-by-point manner across the liquid meniscus. This can be done by expressing  $r_p$  and  $r_n$  as [68]

$$r_p = \frac{\left(1 + \left(\frac{dx}{dy}\right)^2\right)^{3/2}}{d^2 x / dy^2} \text{ and } r_n = x \left(1 + \left(\frac{dx}{dy}\right)^2\right)^{1/2} \quad (1.37)$$

The expression for the capillary force can now be written using the general form of the Young-Laplace equation:

$$F_{cp} = \gamma_l \left( \frac{d^2 x / dy^2}{\left(1 + \left(\frac{dx}{dy}\right)^2\right)^{3/2}} + \frac{1}{x \left(1 + \left(\frac{dx}{dy}\right)^2\right)^{1/2}} \right) A_{xy} \quad (1.38)$$

Equation 1.38 can be solved with proper boundary conditions for the given solid/solid system to obtain the meniscus profile  $x(y)$  and the capillary force,  $F_{cp}$ .

For the case of a spheroidal particle in contact with a flat plate, as shown in Figure 1.14, the following boundary conditions can be used to solve Equation 1.38

$$\left(\frac{dx}{dy}\right)_{x=X_1} = 1 / \tan(\varphi + \theta_1), \quad \left(\frac{dx}{dy}\right)_{x=X_2} = -1 / \tan(\theta_2) \quad \text{and} \quad X_1 = R \sin(\varphi),$$

$$x(y = 0) = X_2.$$

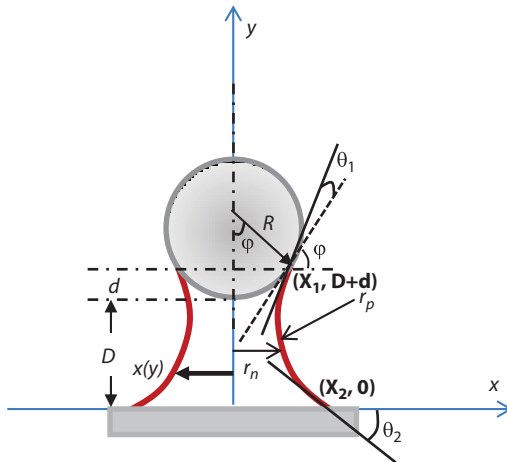


Figure 1.14 Schematic of a sphere adhered onto a flat plate with a liquid bridge.

The solution of Equation 1.38 with these boundary conditions will lead to the derivation of the meniscus profile  $= f(y, \varphi, F_{cp}, R, \gamma, \theta_1, \theta_2)$ . Finally, the expression for the capillary force between a sphere and a flat plate, accounting for the non-uniform ROC, can be obtained using the following condition in the derived meniscus profile:

$$x(y = D + d) = R \sin(\varphi) \quad (1.39)$$

where  $d = R(1 - \cos(\varphi))$ , and  $\varphi$  is the embracing angle.

The value of  $\varphi$  needs to be known to calculate the capillary force. If  $\varphi$  is not given but the volume of the liquid bridge ( $V$ ) is known, the following relation between  $V$  and  $\varphi$  can be obtained.

$$V = \int_0^{D+d} \pi x^2(y) dy - \frac{\pi}{6} d (3R^2 \sin^2(\varphi) + d^2) \quad (1.40)$$

Equations 1.38 and 1.40 can now be solved together to calculate  $\varphi$  and the capillary force.

#### 1.2.1.5 Concluding Remarks

- a. The formation of liquid bridges (due to moisture condensation) at the solid/solid interface leads to the existence of capillary forces.
- b. The total capillary force is the combination of the surface tension force and the capillary pressure force. The capillary pressure force, which originates due to the pressure difference across the liquid/vapor meniscus developed at the solid/solid interface, dominates over the surface tension force.
- c. The Kelvin diameter ( $2r_k$ ) is defined as the maximum separation distance between the adhering solid surfaces over which the moisture condensation takes place. Since the Kelvin diameter for even the most strongly wetting surfaces is  $< 2$  nm (which is on the order of the roughness height for most substrates) for  $RH < 50\%$ , any adhesion enhancement with  $RH$  at levels below 50% cannot be attributed to continuum moisture effects.
- d. The strength of the capillary force depends on the  $RH$ , the nature of the adhering substrates, and the temperature. The capillary forces resulting from the condensed

moisture between hydrophilic surfaces generally increase with increasing RH, while humidity has little effect on adhesion when one or both of the interacting surfaces are hydrophobic.

- e. The magnitude of the capillary force also depends on the geometries of the adhering solid bodies. Relevant analytical expressions to predict capillary forces for the systems with ideal geometries (plate-plate, sphere-plate, and sphere-sphere) have been derived. The approach to determine capillary forces for non-ideal geometries has also been discussed.

### 1.2.2 van der Waals Forces

van der Waals forces result when dipoles in the surface regions of two interacting bodies respond to electromagnetic radiation propagating between the surfaces of the bodies. These forces are significant over separation distances up to 40 nm, depending on the properties of the medium between the bodies. There are two approaches used to describe these forces, Hamaker's pairwise additive approach and the Lifshitz continuum approach.

#### 1.2.2.1 Hamaker's Pairwise Additive Method

Hamaker's approach for determining van der Waals forces between particles and surfaces begins with the energy of interaction between two particles (of radii  $R_1$  and  $R_2$ ) containing  $\rho_1$  and  $\rho_2$  atoms per  $\text{cm}^3$ , as shown in Figure 1.15. The interaction energy between the two spheres, or any spherically symmetric pair of bodies, is [69–75]

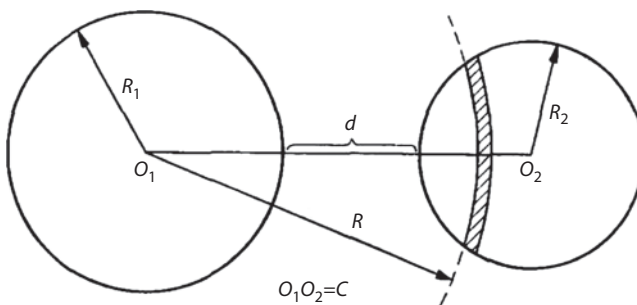


**Figure 1.15** Diagram of two spherical particles experiencing mutual vdW interaction [76]. Reprinted with permission.

$$E = - \int_{V_1} dV_1 \int_{V_2} dV_2 \frac{\rho_1 \rho_2 \zeta_{12}}{|\mathbf{r}|^6} \quad (1.41)$$

where  $dV_1$ ,  $dV_2$ ,  $V_1$ , and  $V_2$  are the volume elements and total volumes, respectively, of the two particles;  $|\mathbf{r}|$  is the separation distance between  $dV_1$  and  $dV_2$ ; and  $\zeta_{12}$  is the vdW or Hamaker constant, a purely material-dependent quantity. To evaluate the double integral in Equation 1.41, one considers the interaction energy experienced at point  $P$  in Figure 1.16. In this case, the surface  $ABC$  is given by

$$\text{surface}(ABC) = \int_0^{2\pi} d\phi \int_0^{\theta_0} d\theta r^2 \sin(\theta) \quad (1.42)$$

where  $\theta_0$  is found by using the Law of Cosines,

$$R_1^2 = R^2 + r^2 - 2rR \cos(\theta_0) \rightarrow \cos(\theta_0) = \frac{R^2 + r^2 - R_1^2}{2rR} \quad (1.43)$$

After substituting Equation 1.43 into Equation 1.42, one obtains

$$\text{surface}(ABC) = \pi \frac{r}{R} \left[ R_1^2 - (R-r)^2 \right] \quad (1.44)$$

Thus, a volume element (*i.e.*,  $dV_1$  or  $dV_2$ ) is

$$dV_i = \left\{ \pi \frac{r}{R_i} \left[ R_1^2 - (R_i - r)^2 \right] \right\} dr \quad (1.45)$$

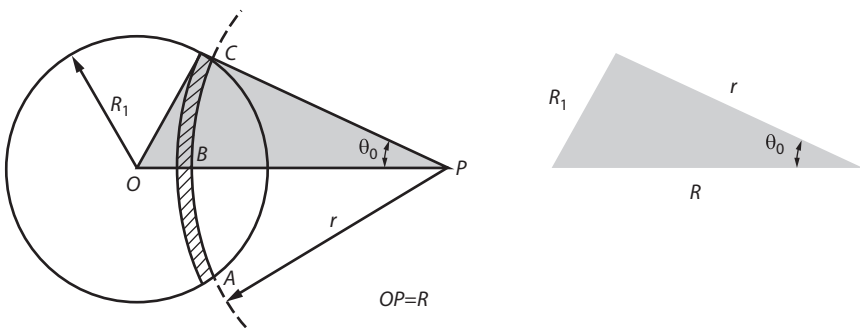


**Figure 1.16** Diagram illustrating the geometry associated with the vdW interaction energy experienced at point  $P$  [76]. Adapted with permission.



Finally, the potential energy of an atom or molecule located at point  $P$  is

$$E_p = - \int_{R_p-R_1}^{R_p+R_1} \frac{\rho_1 \zeta_{1P}}{r^6} \left\{ \pi \frac{r}{R_p} \left[ R_1^2 - (R_p - r)^2 \right] \right\} dr \quad (1.46)$$

To incorporate a second sphere of radius  $R_2$  and centered around point  $P$ , this geometric procedure is repeated and the double integration in Equation 1.42 is repeated between opposing volume elements (in a pairwise fashion). The resulting expression for the interaction energy between two spheres is

$$E = \frac{-\pi^2 \rho_1 \rho_2 \zeta_{12}}{6} \left\{ \frac{2R_1 R_2}{C^2 - (R_1 + R_2)^2} + \frac{2R_1 R_2}{C^2 - (R_1 - R_2)^2} + \ln \left( \frac{C^2 - (R_1 + R_2)^2}{C^2 - (R_1 - R_2)^2} \right) \right\} \quad (1.47)$$

where  $C = R_1 + R_2 + d$ , and  $d$  is the separation distance between particles 1 and 2. Equation 1.47 may be recast

$$E = \frac{-A}{12} \left\{ \frac{y}{x^2 + xy + x} + \frac{y}{x^2 + xy + x + y} + 2 \ln \left( \frac{x^2 + xy + x}{x^2 + xy + x + y} \right) \right\} \quad (1.48)$$

where  $x = \frac{d}{(2R_1)}$ ,  $y = \frac{R_2}{R_1}$ , and  $A = \pi^2 \rho_1 \rho_2$ . This  $A$  is the so-called Hamaker constant.

When the separation distance between the particles is much smaller than the size of either particle (*i.e.*,  $|\mathbf{r}| \ll R_{particle}$ ), Equation 1.48 is readily transformed to describe the vdW interaction between a sphere and an infinite flat plate ( $R_2 \gg R_1$ ,  $y \rightarrow \infty$ ):

$$E_{\text{sphere-plate}}(x) = \frac{-A}{12} \left\{ \frac{1}{x} + \frac{1}{x+1} + 2 \ln \left( \frac{x}{x+1} \right) \right\} \quad (1.49)$$

To obtain the force of interaction between a sphere and a flat plate, differentiate Equation 1.49 with respect to separation distance  $d$ :

$$F_{\text{sphere-plate}}(x) = \frac{-A}{24R_1} \left\{ \frac{2}{x} - \frac{1}{x^2} - \frac{2}{x+1} - \frac{1}{(x+1)^2} \right\} \quad (1.50)$$

When  $x \ll 1$ , which is the case for a particle in contact with a flat plate, this expression simplifies even further to [9]

$$F_{\text{sphere-plate}}(d) = \frac{-A}{12x^2} = \frac{-AR_1}{6d^2} \quad (1.51)$$

Similarly, the expression for the vdW forces for other regular geometries can also be derived using Hamaker's pairwise additivity. The vdW force between unit areas of the two opposing parallel plates is derived as

$$F_{\text{plate-plate}}(d) / \text{Area} = \frac{-A}{6\pi d^3} \quad (1.52)$$

The vdW force between two spherical particles of radii  $R_1$  and  $R_2$  is given as

$$F_{\text{sphere-sphere}}(d) = \frac{-A}{6d^2} \left( \frac{R_1 R_2}{R_1 + R_2} \right) \quad (1.53)$$

These limiting-case results owe their simplicity to Hamaker's assumption of pairwise additivity of vdW interactions. This means each volume element  $dV_{1,i}$  interacts with a second volume element  $dV_{2,j}$  over a distance  $r_{ij}$ , and there is no accounting for the effect of many-body interactions—e.g. reflected electromagnetic (EM) waves caused by the presence of neighboring atoms or molecules, known as the *polarizability effect*—nor is the retardation effect (*i.e.*, the phase lag induced during transmission of the electric field between interacting elements) considered.

#### 1.2.2.1.1 Calculating the Hamaker Constant: Approximate Forms Using Pairwise Schemes

When a pairwise approach is taken to describing van der Waals forces, the Hamaker constant is often expressed in terms of a combination of Keesom, Debye, and London interactions. Keesom interactions are interactions between polar molecules with permanent dipoles (dipole-dipole interactions). Debye interactions are interactions between polar molecules and non-polar molecules (dipole-induced dipole interactions) or between pairs of polar molecules when the molecules induce dipoles in each other. London interactions are between pairs of non-polar molecules and non-polar molecules (induced dipole-induced dipole interactions; dispersion interactions).

The Keesom interaction energy is described by

$$W_{Keesom}(r) = -\frac{\left(\frac{p_2^2}{3kT}\right) p_1^2}{(4\pi\epsilon_0\epsilon)^2 r^6} = -\frac{p_1^2 p_2^2}{3(4\pi\epsilon_0\epsilon)^2 kTr^6} = -\frac{C_{orient}}{r^6} \quad (1.54)$$

where  $W_{Keesom}(r)$  = Keesom interaction energy,  $C_{orient} = \frac{p_1^2 p_2^2}{3(4\pi\epsilon_0\epsilon)^2 kT}$ , the

$p_i$  are the dipole moments of the interacting molecules,  $\epsilon_0$  = permittivity of vacuum,  $\epsilon$  = permittivity of medium between molecules,  $T$  = temperature,  $r$  = intermolecular separation distance.

The Debye interaction energy between a polar molecule (molecule 1) and a non-polar molecule (molecule 2) is described by

$$W_{Debye}(r) = -\frac{\alpha_{0,2} p_1^2}{(4\pi\epsilon_0\epsilon)^2 r^6} = -\frac{C_{Ind}}{r^6} \quad (1.55)$$

where  $W_{Debye}(r)$  = Debye interaction energy,  $C_{ind} = \frac{\alpha_{0,2} p_1^2}{(4\pi\epsilon_0\epsilon)^2}$ , and  $\alpha_{0,2}$  =

the induced polarizability of molecule 2. In the same way, dipole-induced dipole interactions between two polar molecules (the polar molecule can induce a dipole in the other) can be given as

$$W_{Debye}(r) = -\frac{\alpha_{0,2} p_1^2 + \alpha_{0,1} p_2^2}{(4\pi\epsilon_0\epsilon)^2 r^6} = -\frac{C_{Ind}}{r^6} \quad (1.56)$$

where  $\alpha_{0,1}$  = induced polarizability of molecule 1.

The London dispersion interaction energy between two similar molecules is

$$W_{London\ dispersion}(r) = -\frac{\left(\frac{3}{4}\right) \alpha_0^2 h\nu}{(4\pi\epsilon_0\epsilon)^2 r^6} = -\frac{C_{Disp}}{r^6} \quad (1.57)$$

where  $C_{Disp} = \frac{\left(\frac{3}{4}\right) \alpha_0^2 h\nu}{(4\pi\epsilon_0\epsilon)^2}$ ,  $h$  = Planck's constant, and  $\nu$  = the frequency of

the electromagnetic waves associated with the dipole. For two dissimilar atoms/molecules, the London dispersion energy is

$$W_{London\ dispersion}(r) = -\frac{3}{2} \frac{a_{0,1} a_{0,2} h \nu_1 \nu_2}{(4\pi\epsilon_0\epsilon)^2 r^6 (\nu_1 + \nu_2)} = -\frac{C_{Disp}}{r^6} \quad (1.58)$$

$$\text{where } C_{Disp} = \frac{3}{2} \frac{a_{0,1} a_{0,2} h \nu_1 \nu_2}{(4\pi\epsilon_0\epsilon)^2 (\nu_1 + \nu_2)}.$$

When Hamaker constants are determined in this manner, they are calculated analogously to the form in Equation 1.41

$$E = -\int_{V_1} dV_1 - \int_{V_2} dV_2 \frac{C_{orient} + C_{Ind} + C_{Disp}}{r^6} = -\int_{V_1} dV_1 - \int_{V_2} dV_2 \frac{\left(\frac{A}{\pi^2}\right)}{r^6} \quad (1.59)$$

It should be noted that when Hamaker constants are determined using this pairwise additive approach, it is assumed that the electromagnetic field propagating between the two interacting objects moves quickly relative to the time that dipoles reorient in the objects. When the separation distance between the interacting bodies is larger than roughly 5 nm in gaseous environments, this assumption begins to fail and dipoles within the interacting surfaces can recover before the reflected field from the opposing surface arrives. This assumption fails at closer separation distances in condensed media, where the propagation of electric fields is slower. In such cases, the van der Waals forces are considered to be ‘retarded,’ and the extent of the retardation is related to the properties of the medium between the bodies [9, 77]. When vdW forces are retarded, the various components of the force (Keesom, Debye, London dispersion) are affected differently. Specifically, the dispersion forces, which are the dominant forces at close separations, tend to fade, becoming proportional to  $1/r^7$  rather than  $1/r^6$ . In such cases, the overall vdW force begins to follow the  $1/r^7$  pattern. As separation distance continues to increase to the point where the dispersion forces are no longer dominant, one finds that the forces driven by permanent dipoles (Keesom and Debye), assume a dominant role. Their electronic configuration does not change, and as such their dependence on the propagation of electric field through the medium does not change. This causes the vdW force to resume a  $1/r^6$  behavior [9].

### 1.2.2.2 Lifshitz’ Continuum Approach to van der Waals Forces

In 1954, Lifshitz developed a rigorous method, derived on the basis of quantum electrodynamics, for predicting vdW interactions between bulk

condensed-phase media by treating these as continua and relating the fluctuating EM fields of the approaching bodies to their complex dielectric permittivity functions (dielectric functions). These functions are defined according to

$$\varepsilon(\omega) = \varepsilon'(\omega) + i\varepsilon''(\omega) \quad (1.60)$$

where  $\varepsilon'$  is the real component of the dielectric permittivity,  $\varepsilon''$  is the imaginary component of the dielectric permittivity, and  $\omega$  is the frequency of the propagating electromagnetic field between the surfaces of the interacting bodies. It has been shown that the imaginary part of the permittivity is always positive and determines the energy dissipation of a wave propagating through a medium [78–89].

The geometry used as the basis for the development of this approach is illustrated in Figure 1.17.

Dzyaloshinskii, Lifshitz, Pitaevskii and Hamermesh (DLPH) used quantum field theory methods in statistical physics to validate Lifshitz' original approach and prove that vdW interactions can be quantified based on purely macroscopic considerations [79]. The resulting DLPH theory formulae for the vdW energy of interaction between two condensed-phase, semi-infinite, planar media, separated by a small distance  $D$ , across an intervening medium  $m$  are

$$E_{LmR}(D) = -\frac{k_B T}{8\pi D^2} \sum_{n=0}^{\infty} \int_{r_n}^{\infty} x \ln \left[ (1 - \bar{\Delta}_{Lm} \bar{\Delta}_{Rm} e^{-x}) (1 - \Delta_{Lm} \Delta_{Rm} e^{-x}) \right] dx \quad (1.61)$$

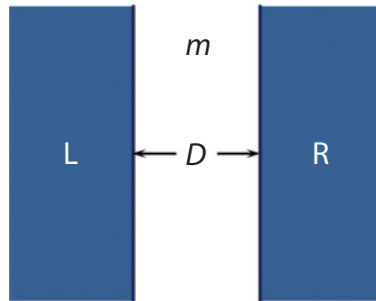


**Figure 1.17** Two semi-infinite media separated by distance  $D$ , interacting across intervening medium  $m$ .

$$\bar{\Delta}_{ji} = \frac{x_i \epsilon_j - x_j \epsilon_i}{x_i \epsilon_j + x_j \epsilon_i} \text{ and } \Delta_{ji} = \frac{x_i \mu_j - x_j \mu_i}{x_i \mu_j + x_j \mu_i} \quad (1.62)$$

$$x_i^2 = x^2 + \left( \frac{2D\xi_n}{c} \right)^2 (\epsilon_i \mu_i - \epsilon_m \mu_m) \quad (1.63)$$

$$\text{and } \xi_n = \frac{2\pi k_B T}{\hbar} n, \quad n = 0, \pm 1, \pm 2, \dots \quad (1.64)$$

where  $k_B$  = the Boltzmann constant,  $T$  = the system temperature,  $\hbar$  = the reduced Planck constant,  $c$  = the speed of light (in air),  $r_n$  = the ratio of the electromagnetic (EM) radiation travel time (to pass between the interacting bodies) to the EM fluctuation lifetime,  $\xi_n$  = the complex frequency of EM radiation (*i.e.*,  $\omega = i\xi$ ), and  $\epsilon_i$  and  $\mu_i$  = the complex dielectric permittivity and complex magnetic susceptibility functions of the interacting materials (*i.e.*, the index  $i = \mathbf{L}, \mathbf{R}$ , or  $m$ ). The prime on the summation operator in Equation 1.60 indicates that for  $n = 0$  (*i.e.*, the zero-frequency term) the sum is multiplied by  $1/2$ .

To derive the formula for the sphere-plane system geometry, the Derjaguin Transformation is applied to Equation 1.61 [90]. The Derjaguin Transformation relates the interaction force between two spheres to the energy per unit area of two flat plates at the same separation distance

$$F(D) = 2\pi \left( \frac{R_1 R_2}{R_1 + R_2} \right) W(D) \quad (1.65)$$

where  $F(D)$  is the sphere-sphere interaction force at separation distance  $D$ ,  $R_1$  and  $R_2$  are the radii of the spheres, and  $W(D)$  is the interaction energy per unit area of flat plates at the same separation distance  $D$ . Per this transform, if oppositely curved surfaces are at a separation distance  $D$  that is small in comparison to the radii  $R_1, R_2$  of the bodies, the interaction force between the curved surfaces can be approximated as an interaction between parallel flat plates. This transform is appropriate for micro-scale spheroidal contact within the separation distance from a surface where vdW forces are important. Applying this transform to Equation 1.61 yields the interaction energy between two spheres:

$$E_{\mathbf{LmR}}(D; R_1, R_2) = -\frac{k_B T}{4D} \left( \frac{R_1 R_2}{R_1 + R_2} \right) \sum_{n=0}^{\infty} r_n \sum_{q=1}^{\infty} \frac{1}{q^2} \quad (1.66)$$

$$\times \int_1^{\infty} \left[ (\bar{\Delta}_{\mathbf{Lm}} \bar{\Delta}_{\mathbf{Rm}})^q + (\Delta_{\mathbf{Lm}} \Delta_{\mathbf{Rm}})^q \right] e^{-r_n p q} dp$$

$$\bar{\Delta}_{ji} = \frac{s_i \varepsilon_j - s_j \mu_i}{s_i \varepsilon_j + s_j \varepsilon_i} \quad \text{and} \quad \Delta_{ji} = \frac{s_i \mu_j - s_j \mu_i}{s_i \mu_j + s_j \mu_i} \quad (1.67)$$

$$s_i = \sqrt{p^2 - 1 + \frac{\varepsilon_i \mu_i}{\varepsilon_m \mu_m}} \quad (1.68)$$

Note that the variable of integration, which was  $x$  in Equation 1.61, is now  $p$  in Equation 1.66. For very small values of  $r_n$ , which arise for situations involving bodies in contact, the argument of the natural logarithm in Equation 1.61 approaches zero, and the function is no longer analytical. To avoid this difficulty, the variable transformation  $x \rightarrow p$  has been introduced, and the range of integration has changed correspondingly from  $[r_n, \infty)$ , for which  $r_n$  can be arbitrarily small, to  $[1, \infty)$ . Note also that the functions  $\varepsilon_i$  and  $\mu_i$  are complex. In order to evaluate Equation 1.61, the integrand must be complex-differentiable. Complex-valued functions often contain points, zeroes, poles, asymptotes, and other features at which they are not complex-differentiable in Cartesian coordinates. To avoid difficulties associated with this situation, the second infinite summation, the second Riemann zeta function, sometimes denoted  $\zeta(2)$ , is used in Equation 1.66. This allows the integrand in Equation 1.61 to be mapped onto a space over which it is complex-differentiable over the range of integration. The effect of introducing  $\zeta(2)$  is that integrand of Equation 1.66 no longer involves a natural logarithm.

For a spherical particle in contact with a planar surface,  $R_2 \rightarrow \infty$  and Equation 1.66 becomes

$$E_{\text{LmR}}(D; R) = -\frac{k_B T}{4D} R \sum_{n=0}^{\infty} r_n \sum_{q=1}^{\infty} \frac{1}{q^2} \times \int_1^{\infty} \left[ (\bar{\Delta}_{\text{Lm}} \bar{\Delta}_{\text{Rm}})^q + (\Delta_{\text{Lm}} \Delta_{\text{Rm}})^q \right] e^{-r_n p q} dp \quad (1.69)$$

For non-permanently magnetic materials, the  $\mu_i$ 's are all simply unity. This means the magnitudes of the  $\Delta_{ji}$ 's depend only on the difference between  $s_i$  and  $s_j$ . When all of the materials comprising the system have relatively similar dielectric characteristics, the difference between  $s_i$  and  $s_j$  is small and is made even smaller by the Riemannian exponent  $q$ . The net effect is that the  $(\Delta_{\text{Lm}} \Delta_{\text{Rm}})^q$  term in Equation 1.69 can often be omitted, so that the interaction energy becomes

$$E_{\text{LmR}}(D; R) = -\frac{k_B T}{4D} R \sum_{n=0}^{\infty} r_n \sum_{q=1}^{\infty} \frac{1}{q^2} \times \int_1^{\infty} (\bar{\Delta}_{\text{Lm}} \bar{\Delta}_{\text{Rm}})^q e^{-r_n p q} dp \quad (1.70)$$

The vdW interaction force of a sphere-plane system may be found by differentiating Equation (1.70) with respect to separation distance  $D$  as

$$F_{LmR}(D;R) = -\frac{k_B T}{4D^2} R \sum_{n=0}^{\infty} r_n^2 \sum_{q=1}^{\infty} \frac{1}{q} \times \int_1^{\infty} p \left( \bar{\Delta}_{Lm} \bar{\Delta}_{Rm} \right)^q e^{-r_n p q} dp \quad (1.71)$$

In this expression, the Hamaker constant, which is actually a coefficient that varies with the separation distance between the two bodies, is

$$A_{LmR}(D) = \frac{3k_B T}{2} R \sum_{n=0}^{\infty} r_n^2 \sum_{q=1}^{\infty} \frac{1}{q} \times \int_1^{\infty} p \left( \bar{\Delta}_{Lm} \bar{\Delta}_{Rm} \right)^q e^{-r_n p q} dp \quad (1.72)$$

Before these formulae can be utilized to calculate the vdW force, the complex dielectric permittivities  $\epsilon(i\xi)$  of  $L$ ,  $R$ , and  $m$  must be known. Unfortunately, the exact functional forms of  $\epsilon(i\xi)$  are rarely known, and in general one must resort to approximation techniques or other simplifications to evaluate their integral relations [9, 78, 79, 83, 85, 91–103]. It has been shown that only the imaginary part  $\epsilon''$  of the dielectric permittivity is needed for the determination of  $\epsilon$ , via the Kramers-Kronig formula [79, 104].

$$\epsilon(i\xi) = 1 + \frac{2}{\pi} \int_0^{\infty} \frac{\omega \epsilon''(\omega)}{\omega^2 + \xi^2} d\omega \quad (1.73)$$

Thus, if experimental optical data are available over a sufficient range of angular frequencies  $\omega$ , then the interaction force can be calculated beginning with numerical evaluation of Equation 1.73.

A common criticism of the Lifshitz approach to determination of van der Waals forces is that one must measure dielectric responses at all frequencies across the entire EM spectrum for all materials involved in the adhesion system. This is not the case. Rather, one can collect each material's spectral information from a set of discrete sampling frequencies [9, 79, 85, 88]. This sampling occurs at  $n$  frequencies, beginning with the 'zero frequency' (*i.e.*,  $n = 0$ ) of static polarizability, which gives the (static) dielectric constant. For  $n = 1, 2, \dots$ , the sampling frequencies are evenly spaced such that the photon energy of each is a multiple of thermal energy, *viz.*

$$\left( n + \frac{1}{2} \right) \hbar \omega = 2\pi n k_B T \quad (1.74)$$

These sampling frequencies are known as Matsubara frequencies. Figure 1.18 illustrates the Matsubara frequency distribution across the EM spectrum. As can be seen, there is an increase in sampling frequency with



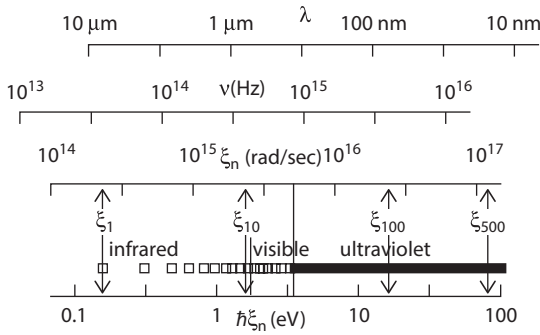


**Figure 1.18** Distribution of Matsubara frequencies across the EM spectrum (based on [88]). Reprinted with permission.

**Table 1.1** Relative Contributions of EM Spectral Regions to Overall Interaction\*

Spectral Region	Value of $n$	Percentage Contribution
Static	0	23
Infrared	1–11	13
Visible	12–24	15
Ultraviolet	25–∞	49

\*For Polystyrene-Water-Polystyrene

photon energy. This allows certain spectral regions (specifically, the UV) to make greater contributions to the overall energy or force of interaction for a system. Table 1.1 provides an example of the breakdown of these contributions per spectral region [105].

As mentioned above, the dielectric function of a material is a complex function

$$\varepsilon(\omega) = \varepsilon_1(\omega) + i\varepsilon_2(\omega), \text{ or } \varepsilon(\omega) = \varepsilon'(\omega) + i\varepsilon''(\omega) \quad (1.75)$$

where the real part of  $\varepsilon(\omega)$ ,  $\varepsilon_1(\omega)$ , describes the speed of light within a medium, and the imaginary part,  $\varepsilon_2(\omega)$ , describes the absorption of light in the medium. When describing how radiation propagates through a medium, it is more common to use the refractive index ( $n$ ) because this quantity can be measured experimentally.  $\varepsilon(\omega)$  is related to  $n(\omega)$  via

$$n(\omega) = \sqrt{\varepsilon(\omega)} \quad (1.76)$$

which makes  $\mathbf{n}$  a complex function, according to

$$\mathbf{n}(\omega) = \hat{n}(\omega) + i\kappa(\omega) \quad (1.77)$$

where  $\hat{n}(\omega)$  is the real part of  $\mathbf{n}$ , and  $\kappa(\omega)$  is the imaginary part. By combining Equations 1.75–1.77, one obtains expressions for the real and imaginary components of  $\varepsilon$

$$\varepsilon_1(\omega) = \hat{n}^2(\omega) - \kappa^2(\omega) \quad (1.78)$$

$$\varepsilon_2(\omega) = 2\hat{n}(\omega)\kappa(\omega) \quad (1.79)$$

Because  $\varepsilon(\omega)$  is a complex function, it can be recast in terms of complex frequency, *i.e.*,

$$\omega = \omega_R + i\xi \quad (1.80)$$

where both  $\omega_R$  and  $\xi$  are strictly real variables.  $\varepsilon(\omega)$  can be expanded in terms of these variables and an appropriate function of time as [88]

$$\varepsilon(\omega) = 1 + \int_0^\infty f(t) e^{i\omega t} dt = 1 + \int_0^\infty f(t) e^{i\omega_R t} e^{-\xi t} dt \quad (1.81)$$

and  $\varepsilon(\omega)$  has the following properties [88]:

1. For  $\xi > 0$  (i.e. on the upper half of the complex-frequency plane,  $i\xi$  versus  $\omega_R$ ),  $\varepsilon(\omega)$  must remain finite.
2. On the  $\varepsilon(\omega)$ -axis (i.e.  $\xi = 0$ ),  $\varepsilon_1(\omega_R)$  is an even function while  $\varepsilon_2(\omega_R)$  is an odd function.
3. On the  $i\xi$ -axis (i.e.  $\varepsilon(\omega) = 0$ ),  $\varepsilon(i\xi)$  is a purely real function while  $\varepsilon_2(i\xi) = 0$ .
4. For  $\xi > 0$ ,  $\varepsilon(i\xi)$  decreases monotonically with increasing  $\xi$ .

Based on these essential properties, the Kramers-Kronig (K-K) Transformation relates  $\varepsilon(i\xi)$  and  $\varepsilon_2(\omega)$ , according to Equations 1.73, 1.78, and 1.79. This transformation provides the necessary conversion between experimental measurements conducted at real frequencies  $\omega_R$  and the  $\varepsilon(i\xi)$ -function used for the computation of interaction forces.

During the determination of  $\varepsilon(\omega)$ ,  $\varepsilon(\omega)$  is not directly measured. Instead, reflectance and transmittance data are collected in terms of  $\mathbf{n}$  (i.e.  $\hat{n}$  and  $\kappa$ ), and then these are converted to  $\varepsilon(\omega)$ , using Equations 1.78 and 1.79, or to  $\varepsilon(i\xi)$ , using additionally Equation 1.73. Figures 1.19 and 1.20, combined with Equations 1.78 and 1.79, show how  $\mathbf{n}$ , and consequently  $\varepsilon(\omega)$ ,

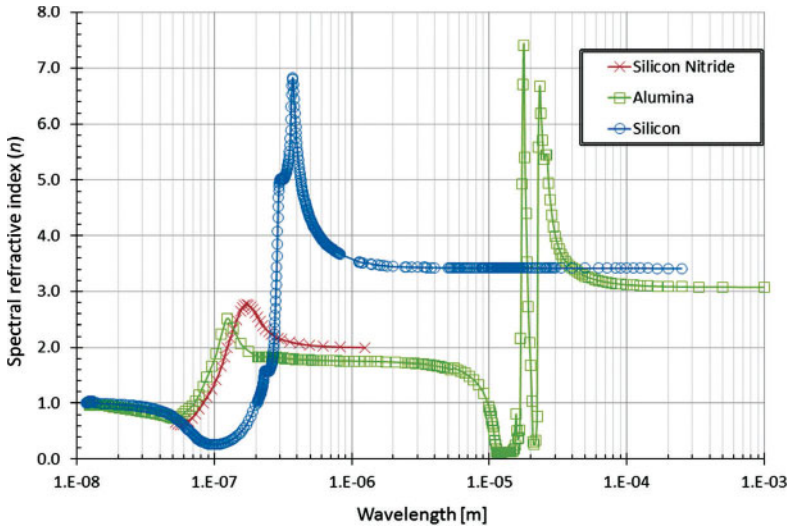


Figure 1.19 Experimentally-determined spectral refractive index ( $\hat{n}$ ) as a function of incident radiation wavelength. Data from [106–108].

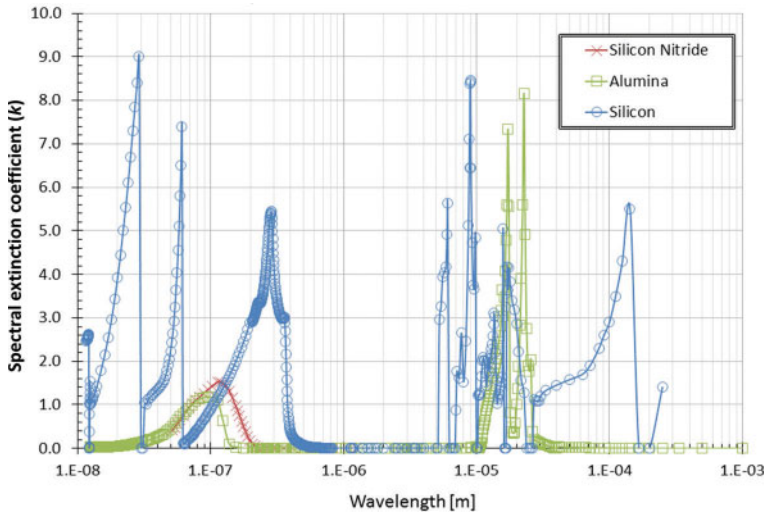


Figure 1.20 Experimentally-determined extinction coefficient ( $\kappa$ ) as a function of incident radiation wavelength. Data from [106–108].

can undergo enormous changes in magnitude even for extremely small differences in the incident radiation wavelength. For this reason, modeling  $\varepsilon(\omega)$  is impractical. By transforming spectroscopic data using the K-K Transformation in Equation 1.73, it becomes possible to represent  $\varepsilon(i\xi)$  with more straightforward functional forms.

This approach, and others that rely on relations between the values of  $\varepsilon(\omega)$  over a full spectrum of  $\omega$  are full spectral methods for evaluating the Hamaker coefficient.

#### 1.2.2.2.1 Approximating the Functional Form of $\varepsilon(i\xi)$ for Use in Lifshitz Theory

A myriad of techniques have been formulated for approximating the functional form of  $\varepsilon(i\xi)$ . For the most part, these approaches [81, 109–113] are similar in that they characterize materials using their static dielectric constants  $\varepsilon_0$  and a small number of characteristic, zero-bandwidth absorption peaks (typically within the visible and/or ultraviolet portions of the EM spectrum) whose wavelengths and intensities can be deduced from discrete sets of experimental data [9, 88]. Approximate methods of this sort have proven useful in semi-quantitative applications when a high level of precision is not required [105].

An alternate, yet not exclusive, approach is to assume a functional form for  $\varepsilon(\omega)$  or  $\varepsilon(i\xi)$ , and then iterate upon this form by checking it against experimental data. What appear commonly in the literature [94, 99, 114–118] are expressions ‘derived’ on the basis of quantum mechanical arguments within dispersion theory. The expression perhaps most commonly employed, which was originally proposed by Parsegian and Ninham, uses a series of damped harmonic oscillators to fit piecewise spectral data of several types and has the following general form [84, 88, 96, 102, 115, 116, 119–124]

$$\varepsilon(i\xi) = 1 + \frac{f_0}{\xi^2} + \frac{h_0}{g_0 + \xi} + \sum_j \frac{f_j}{\xi^2 + g_j\xi + \omega_{R,j}^2} \quad (1.82)$$

The first term following unity in Equation 1.82 is the contribution from free electrons (present only in metals), the second term is from the orientation of a permanent dipole (present only in polar liquids, such as water), and the remaining terms are from peaks in the infrared (IR), visible (vis), and ultraviolet (UV) spectral regions [105]. The difficulty in using Equation 1.82 is that the minimum number of terms, and consequently the values of the parameters  $f_0$ ,  $h_0$ ,  $g_0$ ,  $f_j$ ,  $g_j$  and  $\omega_{R,j}$  needed to represent  $\varepsilon(i\xi)$  with sufficient accuracy are unknown. In an attempt to address this

difficulty, others have put forth another (simpler) functional form, which requires knowledge of only a single zero-bandwidth absorption peak and the static dielectric constant [9, 88]

$$\varepsilon(i\xi) = \begin{cases} \varepsilon_0, & \text{for } \xi_n = 0 \\ 1 + \frac{C_j}{1 + (\xi_n/\omega_{R,j})^2}, & \text{for } \xi_n > 0 \end{cases} \quad (1.83)$$

which corresponds to only three parameters per material. The constants  $C_j$  and  $\omega_{R,j}$  are fitting parameters and/or can be obtained by constructing Cauchy plots from experimental spectroscopic data for each material. From optical theory, any single absorption peak of zero bandwidth can be represented mathematically (in terms of  $\omega$ ) by

$$\varepsilon(\omega) = 1 + \frac{C_{SR}}{1 - (\omega/\omega_{SR})^2} = \hat{n}^2(\omega) \quad \text{or} \quad (1.84)$$

$$\hat{n}^2 - 1 = C_{SR} + \left( \hat{n}^2 - 1 \right) \left( \omega/\omega_{SR} \right)^2 \quad (1.85)$$

In Equations 1.84 and 1.85, the subscript ‘‘SR’’ stands for ‘‘spectral region,’’ meaning, for example, if the peak being represented exists in the infrared (IR) spectral region, then one would use the parameters  $C_{IR}$  and  $\omega_{IR}$ . Examination of Equation 1.85 reveals that a plot of the quantities  $\hat{n}^2 - 1$  versus  $(\hat{n}^2 - 1)\omega^2$ , known as a Cauchy plot, will be linear, whose intercept and slope can be used to determine values of  $C_{SR}$  and  $\omega_{SR}$ .

Two other common ways to calculate the Hamaker coefficient include the simple spectral (SS) method, and the Tabor-Winterton (TW) approximation [77, 109, 119, 120, 125–127]. In the SS method, the dielectric response function,  $\varepsilon(i\xi)$ , is represented by a model based on a damped oscillator [77, 119, 120, 125, 127]. For many dielectrics it is assumed that

$$\varepsilon(i\xi) = 1 + \frac{C_{IR}}{1 + \left( \frac{\xi}{\omega_{IR}} \right)^2} + \frac{C_{UV}}{1 + \left( \frac{\xi}{\omega_{UV}} \right)^2} \quad (1.86)$$

where  $C_{IR}$  and  $C_{UV}$  are the absorption strengths in the IR and UV range and  $\omega_{IR}$  and  $\omega_{UV}$  represent the characteristic absorption frequencies in the IR and UV range.  $C_{IR}$  and  $C_{UV}$  are parameters used to fit physical property

data such as  $\xi$  and  $\varepsilon(i\xi)$ .  $C_{UV}$  and  $\omega_{UV}$  can also be determined from Cauchy plots of refractive index and frequency.  $C_{IR}$  is then estimated by

$$C_{IR} = \varepsilon_o - C_{UV} - 1 \quad (1.87)$$

The TW method uses indices of refraction to approximate the dielectric response of a material [9, 109, 126, 127]. The TW method determines Hamaker coefficients based on

$$A_{123} = \frac{3\pi\hbar\nu_e}{4\sqrt{2}} \frac{\left[ (n_{vis0,1}^2 - n_{vis0,2}^2)(n_{vis0,3}^2 - n_{vis0,2}^2) \right]}{\left[ (n_{vis0,1}^2 + n_{vis0,2}^2)^{1/2} (n_{vis0,3}^2 + n_{vis0,2}^2)^{1/2} \left( (n_{vis0,1}^2 + n_{vis0,2}^2)^{1/2} + (n_{vis0,3}^2 + n_{vis0,2}^2)^{1/2} \right) \right]} \quad (1.88)$$

where  $n_{vis0,j}$  is the limiting index of refraction for energy in the visible range for material  $j$ . The characteristic absorption frequency,  $\eta_e$ , is assumed to be equivalent for all three materials. It is typically accepted that Hamaker coefficients can be measured or predicted accurately to within 10% using these techniques.

### 1.2.2.3 Experimental Methods to Measure Hamaker Constants

Hamaker coefficients,  $A_{132}$ , quantify the van der Waals interaction between materials 1 and 2 in a medium, 3. If there is no medium (i.e., measured in a vacuum), the Hamaker coefficient would be denoted as  $A_{12}$ . For cohesive interaction between two materials of the same composition in a vacuum, the Hamaker coefficient would be denoted as  $A_{11}$ . The Hamaker constant depends on the ability of the two interacting materials to reflect the incoming electric field from the opposing material; on the permittivity of the intervening medium; and on the separation distance between the two interacting surfaces. When ‘measuring’ Hamaker constants, one may use the continuum approaches outlined above, which require evaluation of the dielectric responses of the interacting materials over a range of frequencies of incident radiation. If one wishes to measure the Hamaker constant directly, then one typically employs methods to measure the interaction force at conditions where van der Waals forces are the dominant forces. One then uses a van der Waals force model to describe the force and a value for the Hamaker constant is extracted. When such methods are employed, the shape, roughness, and possibly the deformation, of the interacting surfaces typically have an effect on the value of the constant that is determined. Whether using a continuum approach or a direct force measurement approach, the Hamaker

constant is better considered a Hamaker *coefficient*, so as to acknowledge the changes that can be encountered in this parameter. During direct measurement of Hamaker coefficients, either atomic force microscopy (AFM), the surface forces apparatus (SFA), or surface energy measurements are employed.

When AFM force measurements are made to determine Hamaker coefficients, a cantilever mounted with a particle or pre-manufactured tip is carefully lowered toward a surface. When the van der Waals forces between the cantilever and the surface are strong enough, the cantilever “snaps” into contact. The cantilever is then pushed into the surface until it reaches a previously determined deflection or vertical displacement. Next, the cantilever is pulled away from the surface. The force required to pull the cantilever out of contact with the surface (the pull-off force) is taken as the adhesion force. Usually many pull-off forces are determined at several locations on the surface to obtain a representative force distribution (*e.g.*, [128]). When relating AFM-measured forces to the Hamaker coefficient, it is often assumed that the surfaces are smooth and that the AFM cantilever tip is hemispherical [129]. However, it is often the case that the geometry is complicated and/or that the surface

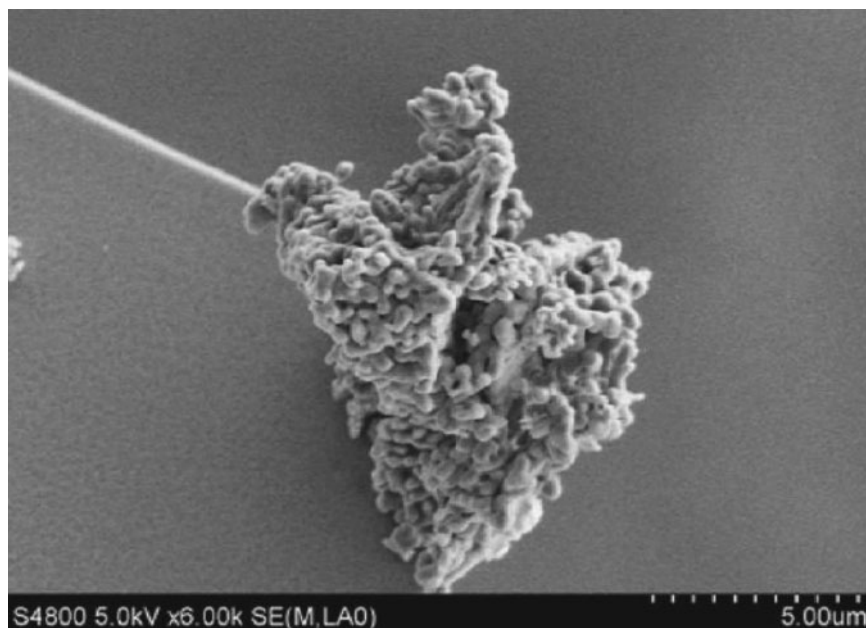


**Figure 1.21** Field-emission SEM micrograph of an alumina particle mounted on the tip of an AFM cantilever. Reproduced with permission [132].

roughness is significant, as seen in Figure 1.21. In an attempt to more accurately characterize the Hamaker coefficient, the geometries of the tips are often characterized by either reverse imaging [130] or scanning electron microscopy [11, 130, 131], while the surface roughness is often estimated based on AFM topographical images [132]. Mathematical models and simulators have been developed to extract Hamaker coefficients from these more realistic descriptions of the interacting surfaces by ascribing all of the measured interaction force to van der Waals force and using an appropriate relationship, such as Equations 1.50-1.53, to model this force [132–136].

Figure 1.22 demonstrates another experimental approach to measure the Hamaker coefficients for the silicon nitride/ruthenium system in air [128]. A well-defined pyramidal probe made of silicon nitride and a flat substrate made of ruthenium were used. The geometrical parameters of the silicon nitride probe were characterized using scanning electron microscopy (SEM). The surface roughnesses of the interacting bodies were measured using atomic force microscopy (AFM) in scanning mode. The interaction force between the pyramidal silicon nitride probe and the flat ruthenium surface in the vdW force regime was measured using AFM as a function of the separation distance between them. The pyramidal silicon nitride probe is loaded onto the AFM cantilever, and the cantilever is

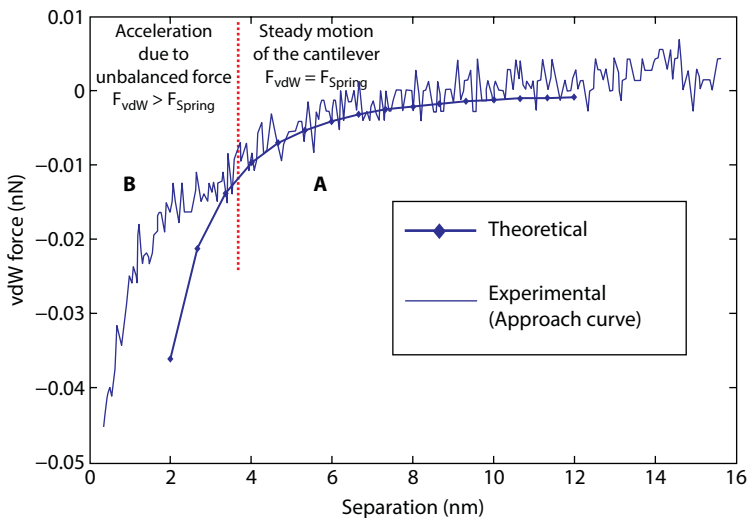


**Figure 1.22** Calculated and measured vdW forces between a silicon nitride pyramidal probe and a flat ruthenium substrate in air as a function of separation distance. The approach curve is an average of 5 measured curves.



brought towards the underlying ruthenium surface during the AFM force measurement. The ‘approach curve’ in Figure 1.22 shows the measured probe-surface interaction force as a function of separation distance, and is divided into two regimes. In regime A, the probe-surface separation distance is larger than 4 nm. This shows the region where the slope of the approach curve ( $dF/dx$ ) is less than the spring constant of the AFM cantilever, and therefore the vdW force is balanced by the cantilever’s spring force. In the regime B the separation distance is less than 4 nm. Here, the slope of the approach curve ( $dF/dx$ ) is greater than the spring constant of the AFM cantilever, and therefore the cantilever accelerates towards the underlying substrate and ‘snaps’ into contact. The behavior in this region is not considered to be well-described by Newtonian mechanics, and hence the information in this regime is not analyzed. The data in regime A are used in conjunction with theoretical van der Waals force models to allow the ‘effective’ Hamaker coefficient to be extracted as a fitting parameter.

Some of the main disadvantages of AFM measurements are that force measurements are generally made at multiple locations, and geometries and local topographies are difficult to characterize [132]. One main advantage of using the AFM to determine adhesion forces is that it has a high force resolution and can yield reasonably accurate Hamaker coefficients if the geometries and surface roughnesses are appropriately characterized.

The surface forces apparatus (SFA) was developed by Tabor and Winterton, and Israelachvili [109, 137–139]. With this technique, a piezoelectric tube is used to control the separation distance between two crossed cylinders. The distance between the cylinders is calculated using optical techniques. As the separation distance is varied using the piezoelectric tube for sub-nanometer control, the interaction force causes a deflection in a Hookean cantilever spring holding one of the cylinders. Based on the spring constant of the cantilever and the change in separation distance caused by the interaction force, the magnitude of the interaction force is determined. The primary advantage of the SFA technique is that it can measure the interactions of macroscopic surfaces including van der Waals and longer-range forces. The requirement of the crossed cylinder geometry is the primary disadvantage of the method.

The work of adhesion may be presented as a function of the system Hamaker constant, or as a function of the surface energies of the interacting materials. Equation 1.89 shows the work of adhesion ( $W$ ) for a material with itself (the work of cohesion) in terms of the Hamaker constant, while Equation 1.90 shows the same work of cohesion expressed in terms of surface energy.

$$W = \frac{A_{ii}}{12\pi D^2} \quad (1.89)$$

$$W = 2\gamma \quad (1.90)$$

where  $\gamma$  is the surface energy of the solid of interest. Equations 1.89 and 1.90 may be combined to yield a simplified approximation for the Hamaker coefficient

$$A_{ii} = 24\pi D^2 \gamma \quad (1.91)$$

If one assumes that the closest possible separation distance between two surfaces is approximately 0.165 nm [9], one may approximate the Hamaker coefficient to within  $\sim 20\%$  using

$$A_{ii} \approx 2.1 \times 10^{-21} \gamma \quad (1.92)$$

Equation 1.92 is applicable to nonpolar and weakly polar substances, but severely underestimates Hamaker coefficients for polar compounds, such as water. Surface energy may be obtained through a variety of methods [140, 141]. Calorimetry and inverse gas chromatography can also be applied if powders are of interest.

#### 1.2.2.3.1 Determination of Solid Surface Energy

When contact angle goniometry is used to determine surface energy, the Owens and Wendt method [142] is frequently used, although other methods also exist [141]. This approach begins with Young's equation,

$$\gamma_{lv} \cos(\theta) = \gamma_{sv} - \gamma_{sl} - \pi_e \quad (1.93)$$

where  $\theta$  is the contact angle formed by the liquid on the solid;  $\gamma_{ij}$  is the surface energy of one phase against a second; subscripts s, l, and v represent the solid, liquid, and vapor phases; and  $\pi_e$  is the equilibrium pressure of the adsorbed vapor on the solid. This is depicted in Figure 1.23.

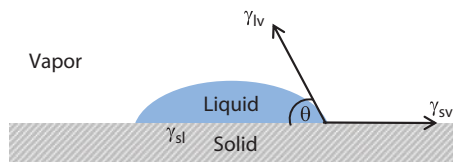


**Figure 1.23** Schematic of surface energies, and hence forces encountered in contact angle goniometry.

The equilibrium pressure is generally neglected if the contact angle is greater than zero [143]. As an approximation, the surface energy is often broken into dispersion (d) and polar (p) components [144]

$$\gamma_i = \gamma_i^d + \gamma_i^p \quad (1.94)$$

After taking the geometric mean of the solid and liquid surface energies, one may reduce Equation 1.94 to obtain

$$\gamma_{sl} = \gamma_{sv} + \gamma_{lv} - 2\sqrt{\gamma_s^d \gamma_l^d} - 2\sqrt{\gamma_s^p \gamma_l^p} \quad (1.95)$$

When Equation 1.95 is rearranged and combined with Young's equation, the following useful expression emerges

$$\frac{\cos(\theta) + 1}{2} \left( \frac{\gamma_{lv}}{\sqrt{\gamma_l^d}} \right) = \sqrt{\gamma_s^p} \left( \sqrt{\frac{\gamma_l^p}{\gamma_l^d}} \right) + \sqrt{\gamma_s^d} \quad (1.96)$$

For many liquids, the approximated 'polar' and 'dispersion' components of the surface energy are known. Hence, Equation 1.96 may be regarded as a linear function.

Typically, a plot of  $\frac{\cos(\theta) + 1}{2} \left( \frac{\gamma_{lv}}{\sqrt{\gamma_l^d}} \right)$  against  $\sqrt{\frac{\gamma_l^p}{\gamma_l^d}}$  yields a straight line with a slope equal to the square root of the polar component of the solid surface energy, and a y-intercept equal to the square root of the dispersion component of the solid surface energy, according to

$$\text{Slope} : \sqrt{\gamma_s^p}; \text{Intercept} : \sqrt{\gamma_s^d} \quad (1.97)$$

The most frequently used method of obtaining contact angles involves static contact angles. With this technique, a single drop of a liquid is placed on a clean surface of interest. The contact angle between the solid and liquid phases is then measured directly. A variety of well-characterized liquids with varying 'polar' and 'dispersion' surface energy components are typically examined on a single solid. The reverse can also be true – where the liquids are examined against solids of known properties, but this is less common. The results for the cosine of the contact angles versus surface tension of the liquids are plotted as in Figure 1.24. Note that  $\gamma_c$  is the critical surface tension, which corresponds to the solid surface tension.

Obtaining solid surface energies through contact angle measurements is possible. Goniometers are typically very easy to maintain, and experiments

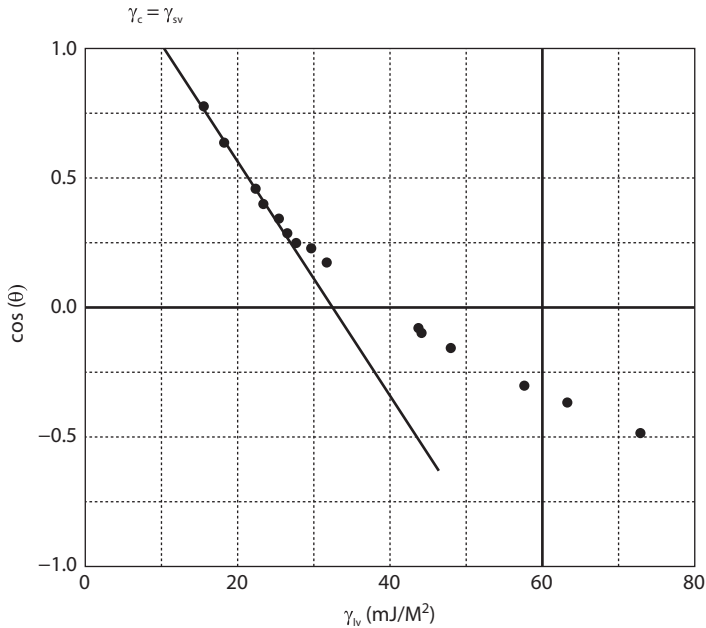


**Figure 1.24** Representative graphical determination of surface tension of a solid (paraffin wax), using a range of liquids. Reproduced with permission [145].

may be performed relatively quickly. Users require minimal training, though interpreting the results and ensuring care in operation requires an appreciation of the inherent difficulties in contact angle goniometry [140]. Generally, only small volumes of liquid are necessary, though operators may wish to use up to six different liquids per unknown surface [142]. The surfaces should be clean and flat, as any contaminants or particulates may distort the results. Similarly, a curved, rough, or deformable surface may adversely affect the contact angles [140]. Volatile liquids may present difficulty, as measurements should be taken in the absence of effects of evaporation. Solids should be uniform and homogeneous to avoid misleading results [140]. The principal drawback to this method of obtaining Hamaker constants is in the many assumptions and estimations that limit the accuracy of the approach to  $\sim 20\%$  [9]. Contact angles and their relevance to surface energy (and hence, adhesion) have been studied in many systems (*e.g.*, polymers, proteins and surfactants) relevant to both pure and applied science [140, 146]. The microelectronics industry is especially concerned with adhesion as it relates to cleaning. Contact angles may be used in this context to evaluate surface cleanliness [147–149].

#### 1.2.2.4 Concluding Remarks

- a. van der Waals forces result when dipoles in the surface regions of two interacting bodies respond to electromagnetic radiation propagating between the adhering surfaces. These forces are significant over separation distances up to 40 nm.
- b. The vdW force can be considered to be comprised of three components: Keesom (dipole-dipole interactions), Debye (dipole-induced dipole interactions), and London (induced dipole-induced dipole interactions *a.k.a.* dispersion interactions). Since the London interactions are always present, the vdW force exists for all systems.
- c. There are two approaches used to describe vdW forces: a) Lifshitz' continuum approach, b) Hamaker's pairwise additive approach. Lifshitz' approach requires knowledge of a series of electrodynamic constants for the interacting materials which are often not readily available. Hamaker's approach consolidates all the electrodynamic constants into a single constant known as 'Hamaker constant' which depends on the nature of the interacting materials and the intervening medium. While this simplifies analysis, the value of the Hamaker 'constant' changes with separation distance, and it should be considered a Hamaker 'coefficient'.
- d. Hamaker constants can be measured using scanning probe methods (*e.g.*, SFA and AFM) using substrates with ideal geometries and smooth surfaces in a controlled environment.
- e. Hamaker constants can also be estimated from the surface energies which can be determined from a variety of methods such as contact angle goniometry, microcalorimetry, and inverse gas chromatography

### 1.2.3 Electrostatic Forces

Electrostatic forces between particles and surfaces can be substantial in both dry and aqueous environments. They can be important when the particles are up to hundreds (or more) nm apart, depending on the charge on the particles and surfaces and the composition and dielectric properties of the intervening medium. Similarly, depending on the properties of the particles, surfaces, and intervening medium, electrostatic forces may be the controlling forces in particle adhesion at particle-surface separation

distances less than 20 nm. In general, however, they are usually not the dominant forces until particle-surface separation distances are greater than this distance. Descriptions of electrostatic particle adhesion forces vary depending on whether or not the particles are in solution or in air environments. In both cases it is necessary that the particles possess the ability to respond to an electric field, either by virtue of having a potential that is different from that of an opposing surface, or by having a charge that interacts with an opposing charge or a field from an opposing surface.

### 1.2.3.1 *Electrostatic Forces in a Dry Environment: Coulomb's Law and the Method of Images*

In the simplest representation, electrostatic forces between charged particles in a gaseous ambient are modeled assuming that the particles are point charges whose behavior is described by Coulomb's Law. Here, the coulombic electrostatic force,  $F_C$ , felt between two point charges,  $Q_1$  and  $Q_2$ , separated by a distance,  $r$ , can be described by

$$F_C = \frac{Q_1 Q_2}{4\pi \epsilon r^2} \quad (1.98)$$

where  $Q_i$  are the distinct point charges on the opposing points  $i$ ,  $r$  is the distance between the two point charges, and  $\epsilon$  is the permittivity of the medium between the two point charges. For a polarizable medium the permittivity is related to  $\epsilon_0$  by its dielectric constant,  $\kappa$ , according to

$$\epsilon = \kappa \epsilon_0 \quad (1.99)$$

Figure 1.25 (top) shows a schematic of two spherical particles. In this case, we assume sphere 1 is a conductive particle with radius  $a$  and potential  $V_1$ , with a fixed charge  $q_1$  at its center. Sphere 2 is a second, conductive sphere with radius  $b$ , potential  $V_2$ , and a fixed charge  $q_2$  at its center. The force between these two spheres may be written in terms of their potentials according to

$$F_{ES,V} = \frac{1}{2} \left( \frac{\partial c_{11}}{\partial d} V_1^2 + 2 \frac{\partial c_{12}}{\partial d} V_1 V_2 + \frac{\partial c_{22}}{\partial d} V_2^2 \right) \quad (1.100)$$

where  $F_{ES,V}$  is the electrostatic force between the spheres when the potential of the spheres is maintained constant,  $c_{ii}$  is the self-capacitance of either sphere,  $c_{ij}$  is the mutual capacitance of the spheres,  $\frac{\partial c_{ij}}{\partial d}$  is the change in

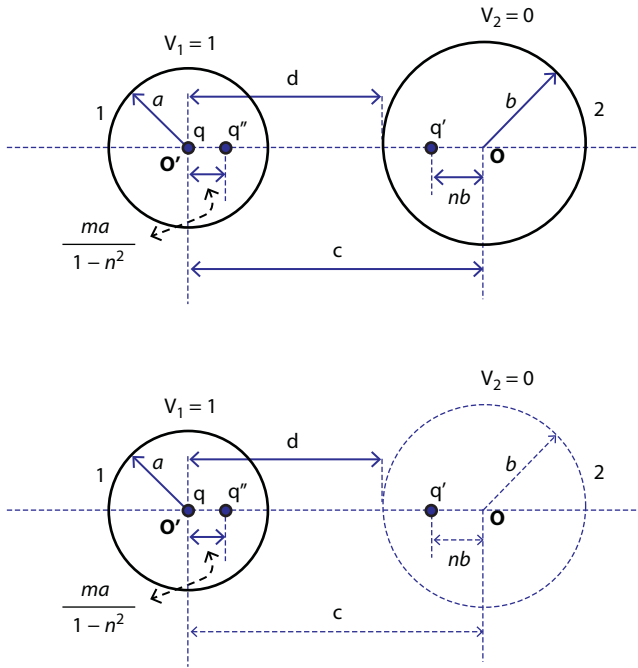


**Figure 1.25** (Top) Image charges induced between 2 conductive spheres. (Bottom) Image charges induced between a conductive sphere and a conducting plane.

the capacitance with separation distance between the spheres, and  $V_i$  is the potential of each sphere [150]. If the charges on the spheres are maintained constant but the potentials may vary, the electrostatic force is written

$$F_{ES,Q} = \frac{1}{2} \left( \frac{\partial s_{11}}{\partial d} Q_1^2 + 2 \frac{\partial s_{12}}{\partial d} Q_1 Q_2 + \frac{\partial s_{22}}{\partial d} Q_2^2 \right) \quad (1.101)$$

where  $F_{ES,Q}$  is the electrostatic force between the spheres when the charge of the spheres is maintained constant,  $s_{ii}$  is the self-elasticance of either sphere,  $s_{ij}$  is the mutual elasticance of the spheres,  $\frac{\partial s_{ij}}{\partial d}$  is the change in the elasticance with separation distance between the spheres, and  $Q_i$  is the charge on each sphere [150].

A simplified method to solve Equations 1.100 and 1.101 uses the *method of images* [150–152]. For purposes of illustration, assume that sphere 2 in the top of Figure 1.25 is conductive and is grounded, so as to have a potential  $V_2 = 0$ . Assume further that the potential on the spheres is maintained

constant and the centers of the two spheres are separated by a distance  $c$ . The magnitude of the charge  $q_1$  is

$$q_1 = 4\pi\epsilon a V_1 = q \quad (1.102)$$

An image charge,  $q'_1$ , of opposite sign to  $q_1$ , is induced in sphere 2. The magnitude of this charge is

$$q'_1 = 4\pi\epsilon a V_1 \frac{b}{c} = 4\pi\epsilon V_1 n a = q' \quad (1.103)$$

where  $n = \frac{b}{c}$ . This charge is placed at a distance  $\frac{b^2}{c} = nb$  to the left of the center of sphere 2,  $\mathbf{O}$ . To restore sphere 1 to unit potential, a second image charge,  $q''$ , is placed in sphere 1.  $q''$  has a charge opposite to that on  $q'$  and has a magnitude

$$q'' = \frac{a q'}{(c - nb)} = \frac{4\pi\epsilon V_1 m n a}{(1 - n^2)} \quad (1.104)$$

where  $m = \frac{a}{c}$ . This charge is placed at a distance  $\frac{a^2}{(c - nb)} = \frac{ma}{(1 - n^2)}$

to the right of the center of sphere 1,  $\mathbf{O}'$ . This process of images is repeated *ad infinitum*, placing sequentially smaller charges at distances sequentially placed between the center of each sphere and its leading edge. Figure 1.25 (bottom) shows the relevant geometry to determine the interaction force between a sphere and a plate, based on this method. In this case, the radius of sphere 2 is made infinite to create a system of a sphere interacting with a flat plate, with

$$c - d = b \rightarrow \infty, \quad n \rightarrow 1, \quad m \rightarrow 0, \quad \text{and} \quad \frac{m}{|1 - n|} = \frac{a}{d} \quad (1.105)$$

After the radius of sphere 2 is allowed to go to  $\infty$ , it is possible to sum the induced charges on the sphere and plate to obtain the self- and mutual-capacitances for the interacting objects ( $c_{11}$  and  $c_{12}$ ) according to

$$\begin{aligned} c_{11} &= 4\pi\epsilon V_1 a \left[ 1 + \frac{a}{2d} + \frac{a^2}{4d^2 - a^2} + \dots \right]; \\ c_{12} &= -c_{11} = -4\pi\epsilon V_1 a \left[ 1 + \frac{a}{2d} + \frac{a^2}{4d^2 - a^2} + \dots \right] \end{aligned} \quad (1.106)$$



$c_{22}$  is not relevant for the grounded conductive plane. Solving Equation 1.100 using the expressions in Equation 1.106, one obtains the following relation for the electrostatic force between the sphere and plane [150, 153]

$$\begin{aligned} F_{ES,V} &= \frac{1}{2} \left( \frac{\partial c_{11}}{\partial d} V_1^2 \right) = -2\pi\epsilon a^2 V_1^2 \left\{ \frac{1}{2d^2} + \frac{8ad}{(4d^2 - a^2)^2} \right\} \\ &= -2\pi\epsilon R_1^2 V_1^2 \left\{ \frac{1}{2d^2} + \frac{8R_1 d}{(4d^2 - R_1^2)^2} \right\} \end{aligned} \quad (1.107)$$

where  $R_1$  is the radius of sphere 1 and  $d$  is the sphere-plane separation distance.

Equation 1.107 describes the electrostatic component of the adhesion between a particle and substrate assuming that the charge on the particle can be approximated as a fixed charge at the center of the particle and assuming that the sphere and plate are conductors.

### 1.2.3.2 Contact Electrification

In the case of contact electrification, in which a charge is transferred onto a dielectric particle as a result of contact between the particle and a conductive surface, it is appropriate to reevaluate Equation 1.100 in light of the region of the particle surface over which the transferred charge is trapped [151, 154–156]. In this case, one first relates the capacitance between the sphere and plane to the trapped charge, according to [157]

$$C = \frac{Q}{V} = 4\pi\epsilon R \left( 1 + \frac{R}{2d} + \dots \right), \text{ or } V = \frac{Q}{4\pi\epsilon R \left( 1 + \frac{R}{2d} + \dots \right)} \quad (1.108)$$

where  $Q$  is the total trapped charge on the sphere. The trapped charge on the sphere is localized in a region with an effective radius that is far smaller than that of the original sphere, as shown in Figure 1.26. Using  $R_{eff}$  from Figure 1.26 in place of  $R$  in Equations 1.107 and 1.108, one obtains an expression for the electrostatic force due to the trapped charge

$$F_{ES,V,local} = -\frac{Q^2}{2\pi\epsilon} \left( \frac{d^2}{(2d + R_{eff})^2} \right) \left\{ \frac{1}{d^2} + \frac{8R_{eff}d}{(4d^2 - R_{eff}^2)^2} + \dots \right\} \quad (1.109)$$

where  $F_{ES,V,local}$  is the electrostatic force resulting from the localized trapped charge on the dielectric sphere. The first term in Equation 109 results from the interaction between the conductive plane and the fixed charge on the sphere with effective radius  $R_{eff}$  while the second and subsequent terms describe the effects of induced images in the plane and sphere. For a dielectric sphere, charges are trapped and these higher-order terms are not relevant. The final expression therefore becomes (consistent with Coulomb's law) [151, 154–156]

$$F_{ES,V,local} = -\frac{Q^2}{2\pi\epsilon(2d + R_{eff})^2} \quad (1.110)$$

It is important to note that this approximate expression considers that the charge originally distributed over a chord whose length is twice the contact radius that would be calculated based on contact deformation models ( $R_{eff}$  in Figure 1.26) can be described as though it were uniformly distributed over a sphere with radius  $R_{eff}$  [151, 154–156]. It is not unreasonable to expect that the radius of the effective sphere on the right hand side of Figure 1.26 should be substantially smaller than that predicted based on contact deformation, and indeed this is the case. In a study of the contact electrification of polystyrene spheres and their interactions with a grounded plane, Gady *et al.* determined that  $R_{eff}$  in Equation 1.110 was  $\sim 1/3$  the value expected from contact deformation [154]. Another important outcome of this analysis is the realization that the expressions for adhesion force between a particle and a flat plane are the same when the particle and sphere are both conductors as when one of the two is an insulator. However, the higher order terms that appear in the image method for

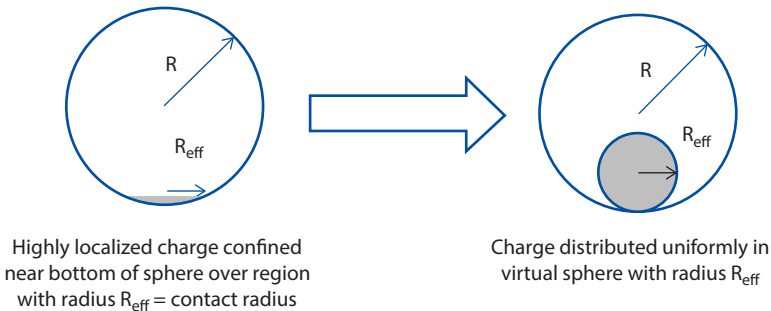


**Figure 1.26** Effective radius of region of trapped charge (shaded region) on dielectric sphere.

the case of a conductive particle and plane can be neglected when one or the other (particle or plane) is a non-conductor.

1.2.3.3 General Determinations of Electrostatic Force in Dry Systems

In the case where a charged conductive particle is very close to a surface, the expressions above run into problems because the separation distance between the particle center and the plane goes to zero in the denominator of the force expressions. Recasting the problem in spherical or bispherical coordinates avoids this problem [153, 158, 159]. Figure 1.27 shows the relevant system of two spheres that are used to establish the spherical coordinates. The radii of the spheres are denoted by  $a_i$ , the total charges on the spheres by  $Q_i$ , and the dielectric constants of the spheres by  $k_i$ . The Gauss electric potential at any point  $r$  due to the two spheres is given by

$$\Phi(r) = K \int \frac{dQ}{R} = K \int \frac{\sigma_1(t) dt}{|r - a_1(t)|} + K \int \frac{\sigma_2(t) dt}{|r - h - a_2(t)|}; \quad K = \frac{1}{4\pi\epsilon} \quad (1.111)$$

where  $\sigma_i$  is the charge density on the surface of sphere 1,  $K = \frac{1}{4\pi\epsilon}$ , and  $\epsilon$  is

the permittivity of the intervening medium between the spheres. To solve Equation 1.111, the potential is first expanded about the center of each sphere and appropriate boundary conditions are applied.

The expansions produce

$$\Phi(r) = \sum_{l=0}^{\infty} A_{1,l} \frac{r^l}{a_1^{2l+1}} P_l \cos(\beta) + \sum_{l=0}^{\infty} \sum_{m=0}^{\infty} A_{2,m} \frac{(l+m)!}{m!!} \frac{r^l}{h^{l+m+1}} P_l \cos(\beta) \quad \text{for } r < a_1 \quad (1.112)$$

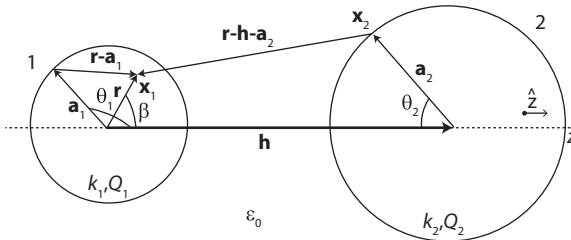


Figure 1.27 Two interacting dielectric spheres for evaluating the electrostatic force between dielectric spheres in spherical coordinates. Reproduced with permission [159].

$$\Phi(r) = \sum_{l=0}^{\infty} A_{1,l} \frac{1}{r^{l+1}} P_l \cos(\beta) + \sum_{l=0}^{\infty} \sum_{m=0}^{\infty} A_{2,m} \frac{(l+m)!}{m!l!} \frac{r^l}{h^{l+m+1}} P_l \cos(\beta)$$

for  $r > a_1$  (1.113)

where  $A_{i,m} = 2\pi K a_i^{m+2} \int_0^{\pi} \sin(\theta_i) d\theta_i \sigma_i(\theta_i) P_m \cos(\theta_i)$ , and the  $P_m$  are Legendre polynomials. The boundary conditions are:

1. The electric potential vanishes as the distance from the spheres goes to infinity,
2. The electrical potential is continuous across the surface of each sphere as a result of the tangential component of the electric field being equal on both sides of the sphere surface,

$$-\frac{1}{r} \frac{\partial f}{\partial \beta} \Big|_{r=a_1^-} = -\frac{1}{r} \frac{\partial f}{\partial \beta} \Big|_{r=a_1^+} \quad (1.114)$$

3. Because there is a permanent charge on the surface of each sphere, the normal component of the electric field is not discontinuous across the sphere surface

$$4\pi K \sigma_1 = \frac{\partial f}{\partial r} \Big|_{r=a_1^-} - \frac{\partial f}{\partial r} \Big|_{r=a_1^+} \quad (1.115)$$

4. The free charge of the surface of each sphere causes the normal component of the dielectric displacement field to be discontinuous across the sphere surface

$$4\pi K \sigma_{f,1} = \frac{\partial f}{\partial r} \Big|_{r=a_1^-} - \frac{\partial f}{\partial r} \Big|_{r=a_1^+} = \text{const.} \quad (1.116)$$

With these boundary conditions, one obtains

$$A_{1,j_1} = KQ_1 \delta_{j_1,0} - \frac{(k_1-1)j_1}{(k_1+1)j_1+1} \frac{a_1^{2j_1+1}}{h^{j_1+1}} KQ_2 + \frac{(k_1-1)j_1}{(k_1+1)j_1+1}$$

$$\left( \sum_{j_2=0}^{\infty} \sum_{j_3=0}^{\infty} \frac{(k_2-1)j_2}{(k_2+1)j_2+1} \frac{(j_1+j_2)! (j_2+j_3)!}{j_1! j_2! j_2! j_3!} \left[ \frac{a_1^{2j_1+1} a_2^{2j_2+1}}{h^{j_1+2j_2+j_3+2}} \right] A_{1,j_3} \right) \quad (1.117)$$

Ultimately, the force between the two spheres becomes

$$F_{12} = -\frac{1}{K} \sum_{l=0}^{\infty} A_{1,l} A_{1,l+1} \frac{(k_1 + 1)(l + 1) + 1}{(k_1 - 1)a_1^{2l+3}} \quad (1.118)$$

To simulate the force between a sphere and a flat plate,  $a_2$  is allowed to become large. By varying the dielectric constants,  $k_1$  or  $k_2$ , dielectric or conductive materials may be simulated. Specifically, when its dielectric constant approaches 1, the material behaves as a dielectric, while as its dielectric constant becomes large, the material behaves as a conductor.

Equation 1.118 may be rearranged to produce

$$F_{12} = K \frac{Q_1 Q_2}{h^2} - Q_1 \sum_{m=1}^{\infty} \sum_{l=0}^{\infty} A_{1,l} \frac{(k_2 - 1)m(m + 1)(l + m)!}{(k_2 + 1)m + 1} \frac{a_2^{2m+1}}{l!m! h^{2m+l+3}} - \frac{1}{K} \sum_{l=1}^{\infty} A_{1,l} A_{1,l+1} \frac{(k_1 + 1)l + 1}{(k_1 - 1)a_1^{2l+3}} \quad (1.119)$$

The first term in Equation 1.119 is the force between two nonpolarizable spheres, which is modeled as point charges  $Q_1$  and  $Q_2$  separated by a distance  $h$ . When  $l = 0$  in Equation 1.119, the force becomes

$$F_{12} = K \frac{Q_1 Q_2}{h^2} - Q_2^2 \sum_{m=1}^{\infty} \sum_{l=0}^{\infty} \frac{(k_2 - 1)m(m + 1)}{(k_2 + 1)m + 1} \frac{a_2^{2m+1}}{h^{2m+3}} \quad (1.120)$$

which describes that force between a charged polarizable sphere 2 and a nonpolarizable sphere 1, which is modeled as a point charge [159]. Figure 1.28 shows normalized interaction forces between spheres interacting as a function of their dielectric constants and normalized separation distance. In this figure, the interaction forces are normalized to those between perfect dielectric spheres (point charges), the separation distance,  $d$ , is calculated

according to  $d = \frac{h - (a_1 + a_2)}{a_1}$ , the radii of the spheres are  $a_1$  and  $a_2$ , charges on the spheres are fixed according to  $\frac{Q_2}{Q_1} = 3$ , and the radii of the spheres are fixed according to  $\frac{a_2}{a_1} = 1$ . Negative forces are attractive in this figure.

What is of particular interest here is that spheres with the charge of the same sign can be attractive at close separation distances, and the magnitude of the attraction increases as the spheres become more conductive.

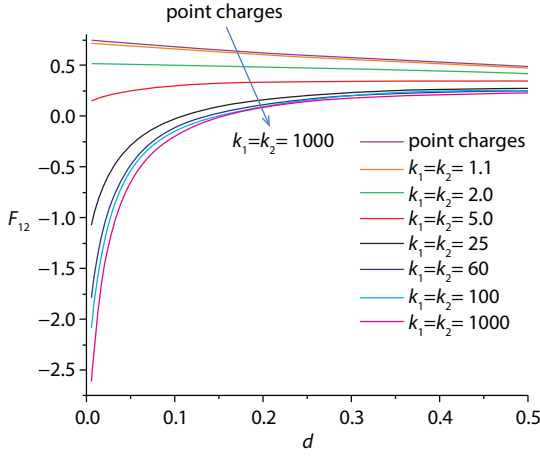


**Figure 1.28** Normalized interaction forces between spheres as a function of the dielectric properties and normalized separation distance  $d$  between the spheres. Reproduced with permission [159].

Figure 1.29 shows an alternative approach to calculating the electrostatic interaction force, based on recasting the problem in bispherical coordinates [153, 158]. On the left-hand portion of this figure,  $a_1$  and  $a_2$  are the radii of sphere 1 and sphere 2;  $a$  is half the separation distance between the two foci (the filled circles within each sphere);  $s$  is the surface-surface separation;  $h$  is the center-center separation;  $c_1$  and  $d_1$  are inverse point separations with respect to sphere 1; and  $a_2$  and  $d_2$  are inverse point separations with respect to sphere 2. On the right-hand portion of this figure, it is shown how the position of an arbitrary point X can be described in terms of the variables  $\eta$ ,  $\xi$  and  $\phi$ . In this case

$$d_1 c_1 = a_1^2, \quad d_2 c_2 = a_2^2 \tag{1.121}$$

$$\eta \equiv -\ln\left(\frac{r_1}{r_2}\right), \quad \xi \equiv \theta_1 - \theta_2,$$

The surface of sphere 1 is defined by  $\eta = \eta_1$ , where  $\eta_1$  is a positive constant. The surface of sphere 2 is defined by  $\eta = \eta_2$  where  $\eta_2$  is a positive constant. The bispherical coordinates are defined by [153, 158, 160]

$$x = \frac{a \sin(\xi) \cos(\phi)}{\cosh(\eta) - \cos(\xi)}; \quad y = \frac{a \sin(\xi) \sin(\phi)}{\cosh(\eta) - \cos(\xi)}; \quad z = \frac{a \sinh(\eta)}{\cosh(\eta) - \cos(\xi)} \tag{1.122}$$

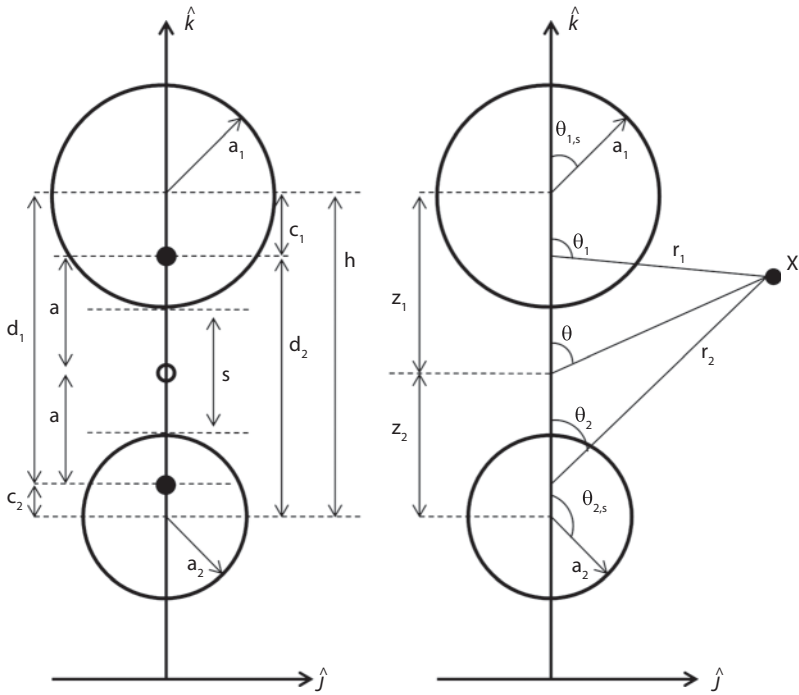


**Figure 1.29** Two interacting spheres as represented in classical Cartesian framework (left) and after being converted to bispherical coordinates (right). The  $\theta_{i,s}$  are the polar angles of each sphere  $i$ , the  $r_i$  are the distances from the point  $X$  to the foci of each sphere  $i$ , and the  $z_i$  are the separations of the centers of each sphere  $i$  from the origin. Redrawn with permission [158].

The spatial parameters  $\eta, \xi$  can be determined in terms of the spatial parameters on the left side of Figure 1.29, according to

$$\cosh(\eta_1) = \sqrt{1 + \frac{a^2}{a_1^2}} = \frac{h^2 + a_1^2 - a_2^2}{2a_1h}; \quad \cosh(\eta_2) = \sqrt{1 + \frac{a^2}{a_2^2}} = \frac{h^2 + a_2^2 - a_1^2}{2a_2h} \quad (1.123)$$

$$\begin{aligned} \cos(\xi) &= \cosh(\eta_1) - \frac{a \sinh(\eta_1)}{a \coth(\eta_1) + a_1 \cos(\theta_{1,s})} \\ &= \cosh(\eta_2) - \frac{-a \sinh(\eta_2)}{-a \coth(\eta_2) + a_2 \cos(\theta_{2,s})} \end{aligned} \quad (1.124)$$

The distance  $a$  is related to the center-to-center separation  $h$  [158]

$$a = \sqrt{\frac{h^4 + (a_1^2 - a_2^2)^2 - 2h^2(a_1^2 + a_2^2)}{4h^2}} \quad (1.125)$$

In the limit where sphere 1 will interact with a flat plate instead of sphere 2, as shown in Figure 1.30,  $a_2 \rightarrow \infty$  in Equations 1.120–1.122. In this case [158]

$$a = \sqrt{s(s + 2a_1)}; \eta_1 = \cosh^{-1}\left(1 + \frac{s}{a_1}\right); \text{ and } \eta_2 = 0 \quad (1.126)$$

Finally, along the flat plane in Figure 1.30, one defines [158]

$$\rho^2 \equiv x^2 + y^2; \cos(\zeta) = \frac{\rho^2 - a^2}{\rho^2 + a^2} = \frac{\rho^2 - s(s + 2a_1)}{\rho^2 + s(s + 2a_1)} \quad (1.127)$$

One can evaluate the electric potential at any point in space due to the presence of the spheres, according to [158]

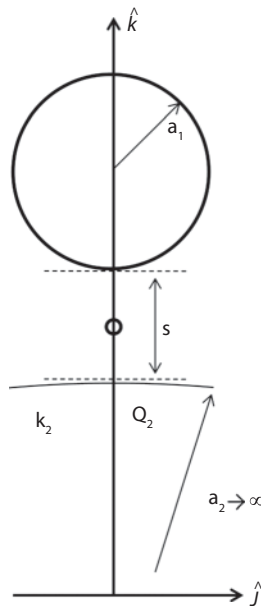


**Figure 1.30** Two interacting spheres when bottom sphere has radius approaching  $\infty$ , to approximate a sphere interacting with a flat plate. Redrawn with permission [158].



$$\Phi(r) = K \int \frac{dQ}{R} = K \int \frac{dQ_1}{R_1} + K \int \frac{dQ_2}{R_2}; K = \frac{1}{4\pi\epsilon} \quad (1.128)$$

where  $\Phi(r)$  is the electrical potential at  $r$ ,  $Q_i$  is the total charge (sum of free surface and bound charges) on each sphere  $i$ , and  $R_i$  is the radius of each sphere  $i$ . Finally, after solving the potential and charge distributions in bispherical coordinates, one solves for the electrostatic force on sphere 1 due to the flat plate [158]

$$F_{12} = K \int dQ_1(\mathbf{x}) \int dQ_2(\mathbf{x}_2) \frac{x - x_2}{|x - x_2|^3} = \hat{k} \int dQ_1 \frac{\partial \Phi_2^{(out)}}{\partial z} \quad (1.129)$$

where  $\Phi_2^{(out)}$  is the potential between the flat plate and the sphere. When the charge on sphere 1 and the potential between the plate and the sphere are written in terms of bispherical coordinates and substituted into Equation 1.129, one obtains

$$\begin{aligned} F_{12} &= - \int_0^\pi \frac{\sigma_1 \cos(\xi) a^2 \sin(\xi) d\xi}{(\cosh(\eta_1) - \cos(\xi))^2} 2\pi \frac{\sqrt{\cosh(\eta_1) - \cos(\xi)}}{a} \times \\ &\sum_{n=0}^{\infty} f_n \left( \frac{n}{2} P_{n-1}(\cos(\xi)) e^{\eta_1} - \left( n + \frac{1}{2} \right) P_n(\cos(\xi)) + \frac{n+1}{2} P_{n+1}(\cos(\xi)) e^{-\eta_1} \right) \Phi_{2,n} \\ &= - \frac{1}{K} \sum_{n=0}^{\infty} f_n \left( \frac{n}{2} \Phi_{1,n-1} e^{\eta_1} - \left( n + \frac{1}{2} \right) \Phi_{1,n} + \frac{n+1}{2} \Phi_{1,n+1} e^{-\eta_1} \right) \Phi_{2,n} \end{aligned} \quad (1.130)$$

where

$$\cos(\xi) = \frac{x^2 + y^2 - s(s + 2a_1)}{x^2 + y^2 + s(s + 2a_1)}; a = \sqrt{s(s + 2a_1)}; f_n = e^{-\left(\frac{n+1}{2}\right)(\eta_1 + \eta_2)};$$

$P_i(\cos(\xi))$  is the  $i^{\text{th}}$  Legendre polynomial with argument

$$\cos(\xi); \Phi_{i,n} = 2\pi a K \int_0^\pi \frac{\sigma_i \cos(\xi') \sin(\xi') d\xi'}{(\cosh(\eta_i) - \cos(\xi'))^2} P_n(\cos(\xi')); \xi' = \xi \text{ on the}$$

surface of sphere 2. When the results of Equations 1.120 and 1.130 were compared for cases of a charged particle interacting with either a grounded conductive plane or a dielectric plane, they agreed well [158, 159].

A final approach to be considered when evaluating particle adhesion to surfaces is the most general [153]. The relevant geometry to be considered is shown in Figure 1.31. In this case, the force between a conductive plate and a particle is [153]

$$F_V = \frac{V^2}{2R} \frac{dC}{d\xi} \text{ or } F_Q = \frac{Q^2}{2RC^2} \frac{dC}{d\xi} \tag{1.131}$$

where  $F_V$  is the particle-plane interaction force when the particle is maintained at constant potential,  $F_Q$  is the particle-plane interaction force when the particle is maintained at constant charge,  $V$  is the particle potential,  $Q$  is the particle charge (total charge),  $C$  is the capacitance of the particle-plane system,  $\xi = \frac{h}{R}$ ,  $h$  = the particle-plane separation distance, and  $R$  = the particle radius. The capacitance is defined according to

$$C = \frac{Q}{V} \tag{1.132}$$

The charge on the particle is written as a function of the normal electric field along the grounded plane

$$Q = -2\pi\epsilon R^2 \sinh^2(\eta_0) \int_0^\pi E_G(\theta) \frac{\sin(\theta)}{(\cosh(\eta) - \cos(\theta))^2} d\theta \tag{1.133}$$

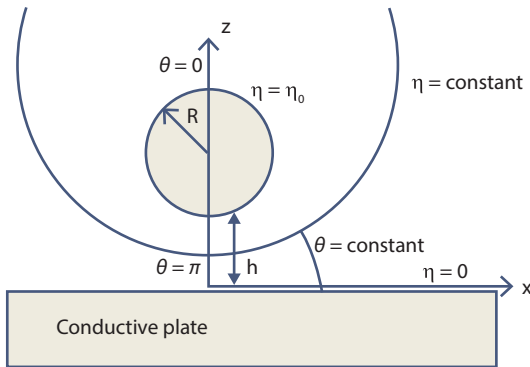


**Figure 1.31** Bispherical geometry for the adhesion between a particle and flat plate. Redrawn with permission [153].

where  $E_G(\theta)$  is the normal electric field along the grounded plane. The potential on the grounded plane is

$$\Phi(\eta = 0, \theta) = 0 \quad (1.134)$$

while the potential on the particle is

$$\Phi(\eta = \eta_0, \theta) = V \quad (1.135)$$

The potential in space resulting from the particle and plane can then be written as

$$\Phi(\eta, \theta) = V \sum_{n=0}^{\infty} \frac{2\sqrt{2}}{e^{(1+2n)\eta_0} - 1} \sqrt{\cosh(\eta) - \cos(\theta)} P_n(\cos(\theta)) \sinh \left[ \left( n + \frac{1}{2} \right) \eta \right] \quad (1.136)$$

and the normal electric field along the ground plane becomes

$$E_G(\theta) = -\frac{\sqrt{2}V}{R} (1 - \cos(\theta))^{\frac{3}{2}} \operatorname{csch}(\eta_0) \sum_{n=0}^{\infty} \frac{(1+2n)P_n \cos(\theta)}{e^{(1+2n)\eta_0} - 1} \quad (1.137)$$

Equation 1.133 now can be combined with Equation 1.137 to produce a final expression for the charge on the particle

$$Q = \sum_{n=0}^{\infty} 2\sqrt{2}\pi\epsilon R V \frac{(1+2n)\sinh(\eta_0)}{e^{(\eta_0+2\eta_0n)} - 1} \int_0^{\pi} \frac{P_n(\cos(\theta))\sin(\theta)}{(1 - \cos(\theta))^{\frac{1}{2}}} d\theta \quad (1.138)$$

Finally, the capacitance can be written

$$C = 4\pi\epsilon R \sum_{n=0}^{\infty} \frac{2\sinh(\eta_0)}{e^{(1+2n)\eta_0} - 1} = 4\pi\epsilon R \sum_{n=0}^{\infty} \frac{2\sqrt{\zeta(2+\zeta)}}{e^{(1+2n)a \cosh(1+\zeta)} - 1} \quad (1.139)$$

When Equation 1.139 is substituted into Equation 1.131, the force on the sphere can be calculated. A drawback to this method is that as the separation distance between the particle and the plate decreases, the number of terms in the sum in Equation 1.139 that must be applied to obtain numerical convergence of the capacitance (and hence the force) can become unwieldy ( $\sim 10^6$ ). Approximate forms of Equations 1.131 and 1.139 that predict interaction forces to within  $\sim 5\%$  are [153]

$$C \approx 4\pi\epsilon R \left[ 1 + \frac{1}{2} \log \left( 1 + \frac{1}{\xi} \right) \right],$$

$$F_V \approx \pi\epsilon V^2 \left[ \frac{1}{\xi + \xi^2} \right], \quad F_Q \approx \frac{Q^2}{16\pi\epsilon R^2} \left[ \frac{1}{(\xi + \xi^2) \left( 1 + \frac{1}{2} \log \left( 1 + \frac{1}{\xi} \right) \right)^2} \right]$$

(1.140)

#### 1.2.3.4 Electrostatic Forces in Aqueous Environments

When immersed in an aqueous environment, solid materials attain a surface charge due to the adsorption of ions or the ionization of surface groups. These types of interactions are promoted by the high dielectric constant of water ( $\kappa_{\text{water}} = 80.1$  at  $T = 20^\circ\text{C}$ ). This induced surface charge is balanced by counter-ions in the solution to maintain charge neutrality. Therefore, an electrical double layer is formed consisting of the localized surface charge and a diffusely distributed cloud of ions, as shown schematically in Figure 1.32. Close to the charged surface, counter-ions in the solution are attracted electrostatically. This effect is opposed when the ions in solution are driven to distribute homogeneously in order to increase the entropy of the system [161]. This competition between electrostatic

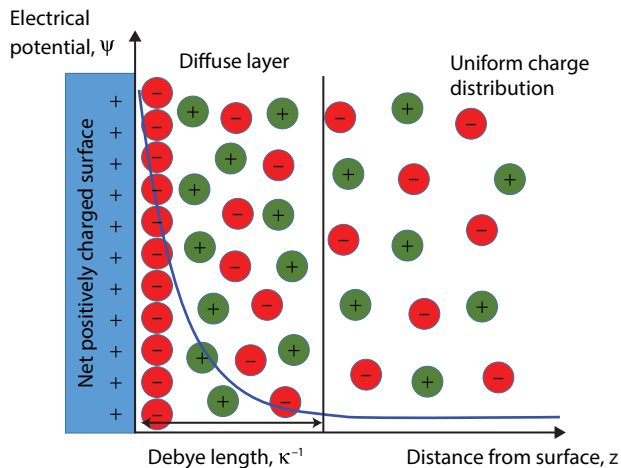


**Figure 1.32** Schematic showing key elements of the electrostatic double layer.

interactions and thermal motion of the ions leads to an outer diffuse layer of ions surrounding the surface. The thickness of the diffuse layer is a function of the concentration of ions present in the solution. The higher the ionic strength of the solution the thinner and denser the electrical double layer that is formed [162]. Not shown in Figure 1.32 is the zeta potential ( $\zeta$ -potential) in the double layer near the surface. The zeta potential is the potential at the slip-plane. When the particle moves in solution, some ions within the cloud are attracted to the particle with sufficient strength that they move with it. Others are farther away from the particle and are less strongly bound, so they do not move with it. The plane between the ions that move with the particle and those that do not move with the particle is called the slip-plane, and the potential on that plane is called the zeta potential.

The relationship between the electrostatic potential,  $\psi$ , and distance,  $z$ , from the charged surface is determined from the Poisson equation. For a single, planar surface

$$\nabla^2 \Psi = \frac{d^2 \Psi}{dz^2} = \frac{-4\Pi e}{\epsilon} [\rho_+(z) - \rho_-(z)] \quad (1.141)$$

where  $\rho_{\pm}(z)$  is the ionic charge density profile of the cations (+) and anions (-),  $e$  is the elementary charge of a proton ( $1.62 \times 10^{-19}$  C), and  $\epsilon$  is the permittivity of the solution [163]. The relationship of the ionic charge density,  $\rho$ , to the potential,  $\psi$ , follows from statistical mechanics and the Boltzmann distribution law

$$\rho_{\pm}(z) = \rho_s \exp\left(\frac{\mp e\Psi(z)}{k_B T}\right) \quad (1.142)$$

where  $\rho_s$  is the ionic charge density of the bulk solution,  $k_B$  is the Boltzmann constant, and  $T$  is the temperature. Equations 1.141 and 1.142 combine to constitute the Poisson-Boltzmann equation. If a dimensionless potential  $\Phi$  is defined according to

$$\Phi = \frac{e\Psi(z)}{k_B T} \quad (1.143)$$

the Poisson-Boltzmann equation can be simplified to

$$\frac{d^2 \Phi}{dz^2} = \kappa^2 \sinh \Phi(z) \quad (1.144)$$

The parameter  $k^{-1}$  is known as the Debye length, which is the characteristic length of the diffuse layer defined by

$$\kappa^{-1} = \left( \frac{8\Pi e^2 \rho_s}{\epsilon k_B T} \right)^{-1/2} \quad (1.145)$$

Because the ionic charge density is dependent on the potential, the Poisson-Boltzmann equation is a nonlinear second-order partial differential equation. For a planar geometry, the analytical solution of the Poisson-Boltzmann equation is

$$\Phi(z) = 2 \ln \left( \frac{1 + \gamma \exp(-\kappa z)}{1 - \gamma \exp(-\kappa z)} \right) \quad (1.146)$$

The constant,  $\gamma$ , is determined from one of two limiting boundary conditions, a constant surface potential or constant surface charge density.

Only for a planar geometry is an analytical solution to the Poisson-Boltzmann theory achieved. For a spherical geometry a numerical solution is required to solve the differential equation. However, when the surface potential is sufficiently low, a linearized form of the Poisson-Boltzmann equation can be used to approximate the electrostatic potential [164]. At small values of  $\Phi$ ,  $\sinh \Phi(z) \approx \Phi(z)$  and Equation 1.144 simplifies to

$$\frac{d^2 \Phi}{dz^2} = \kappa^2 \Phi \quad (1.147)$$

This is known as the Debye-Hückel approximation. The linearized Poisson-Boltzmann equation can be readily solved to give

$$\Phi(z) = \beta \exp(-\kappa z) \quad (1.148)$$

where  $\beta$  is a constant of integration. For the case of constant surface potential,  $\Phi_s$ , the potential can be expressed as

$$\Phi(z) = \Phi_s \exp(-\kappa z) \quad (1.149)$$

Additional approximations of the Poisson-Boltzmann distribution can be found from Derjaguin [90] and Hogg, Healy, and Fuerstenau [165]. A review covering a number of approximations to the Poisson-Boltzmann equation as well as a numerical evaluation of the nonlinear equation has

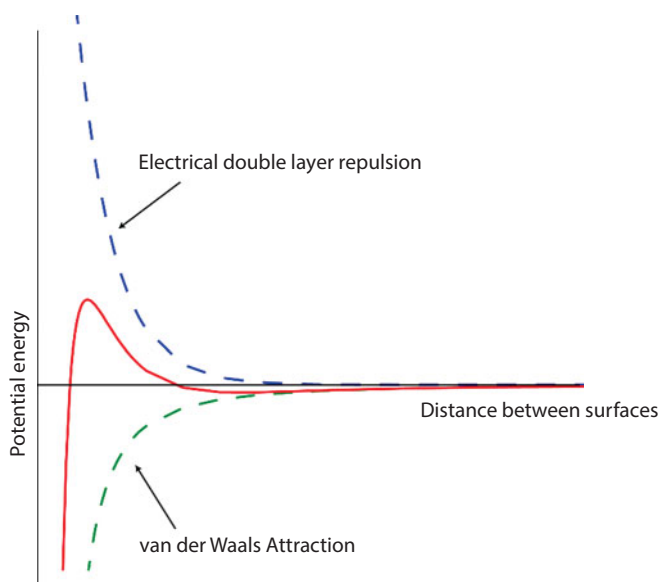


**Figure 1.33** Schematic representation of DLVO theory showing the balance between electrostatic repulsion and van der Waals attraction.

been published [166], in addition to solutions for surfaces with dissimilar charges or potentials [167].

Particle adhesion in an aqueous medium is governed by a balance between the van der Waals force of attraction and the electrostatic double layer force outlined above. Derjaguin and Landau [168] and Verwey and Overbeek [169] independently developed a theory for the stabilization of colloid dispersions based on the addition of these forces; this has come to be known as the DLVO theory. It is customary to describe the balance between the electrostatic double layer repulsion and the van der Waals attraction between colloidal particles in the form of an energy-distance diagram, as shown schematically in Figure 1.33. Because van der Waals forces follow a power law while electrostatic double layer forces follow an exponential relationship with respect to separation distance, the net interaction force has an interesting, characteristic shape.

#### 1.2.3.5 Concluding Remarks

- a. Adhesion interactions between particles and surfaces in dry environments are controlled by the charge and potential on both the particle and surface, by the conductivity of the particle and surface, and by the particle-surface separation

distance. Conductive particles have the ability to distribute charge throughout their volumes. When adhesion forces are modeled for conductive particles, the charge on the particle is described as a point charge at the particle center. When conductive particles interact with conductive surfaces, the method of images is commonly used to estimate the electrostatic component of the adhesion. This method leads to a series solution, with each term accounting for a subsequent 'image' within the particle or surface.

- b. Dielectric particles do not have the ability to distribute charge uniformly. As a result, any charge that becomes attached to a dielectric particle must stay where it attaches. When adhesion forces are calculated between a dielectric particle and a surface, the form of the final expression is the same as in the case of a conducting particle and surface, except that the terms corresponding to the various images are neglected.
- c. When particles and surfaces come into extremely close contact, the method of images is slightly inaccurate. To address this inaccuracy, the problem is recast in bispherical coordinates. The bispherical coordinate frame allows one to describe both the particle and surface using independent spherical coordinate frames and then to combine these frames into one frame, the bispherical frame. The bispherical descriptions of electrostatic particle adhesion forces provide more accurate descriptions of the adhesion force, although they are slightly more complex than simpler predictions using the method of images.
- d. Electrostatic interaction forces between particles and surfaces are generally described in two limits: a limit in which the potentials on the particle and surface are assumed constant and the charge on each can change, or one in which the charges on the particle and surface are assumed constant and the potential of each can change.
- e. In aqueous systems, particle adhesion to surfaces is described in terms of electrostatic double layers. These arise when ions in solution form loosely attracted ion clouds in the vicinity of the particle and surface. The interactions between these ion clouds then drive the electrostatic component of the particle adhesion. When the electrostatic and vdW forces are combined, the resulting force descriptions are known as DLVO theory, for Derjaguin, Landau, Verwey, and Overbeek, who developed it in parallel.



### 1.3 Summary

Adhesion forces between particles and surfaces are described in terms of electrostatic, van der Waals, and capillary forces, depending on the environmental conditions and the properties of the particle, surface, and medium. Electrostatic force descriptions are well developed in the limits of constant potential and constant charge systems, when the geometries of the particle and opposing surface are idealized. This is especially true in the case of conductors. Non-conductors require approximations to account for the varied location of fixed charges. The method of images provides approximate descriptions of the interaction forces, although more rigorous approaches also exist that involve recasting the problem in terms of bispherical coordinates. van der Waals forces are perhaps the best modeled from a computational/mathematical perspective. In an approximate sense, they can be considered as the combination of three types of interactions: those between fixed dipoles in the two interacting surfaces; those between fixed dipoles in one surface and induced dipoles in the opposing surface; and those between induced dipoles in the two interacting surfaces. These represent the so-called 'pairwise additive' approach to van der Waals forces. More rigorous approaches consider the propagation of energy between the two interacting surfaces, with the propagation driven by the dielectric properties of the two interacting objects and the intervening medium. This is the so-called 'Lifshitz continuum' approach. This approach can be difficult to apply due to the challenges associated with appropriate characterization of the dielectric properties of the materials involved, and as a result a number of approximate methods for calculating these properties have been introduced. These methods are generally based on models for oscillators interacting in an applied field, and they allow vdW forces to be calculated for a wider range of materials than would otherwise be possible. Capillary forces, when they exist, are the strongest of all of the forces considered here. They are driven by the interactions of condensed or physically adsorbed water between the particle and opposing surface. They are frequently described using the Kelvin equation, which relates the relative humidity, the surface tension of the liquid water, the system temperature, and the molar volume of the liquid water. While this equation is very effective when applied at high relative humidity conditions, its validity is questionable at relative humidity levels below 50%, where surface adsorbed moisture cannot appropriately be considered to have the properties of bulk water. Approaches that are based on atomistic and molecular dynamics simulations are under development that will more realistically describe the behavior in such situations.

## References

1. R. Jones, H. M. Pollock, J. A. S. Cleaver, and C. S. Hodges, Adhesion forces between glass and silicon surfaces in air studied by AFM: Effects of relative humidity, particle size, roughness, and surface treatment *Langmuir*, 18, 8045–8055 (2002).
2. M. A. Henderson, The interaction of water with solid surfaces: Fundamental aspects revisited *Surf. Sci. Rep.*, 46, 1–308 (2002).
3. D. Sedin and K. Rowlen, Adhesion forces measured by atomic force microscopy in humid air *Anal. Chem.*, 72, 2183–2189 (2000).
4. P. J. van Zwol, G. Palasantzas, and J. T. M. De Hosson, Influence of random roughness on the adhesion between metal surfaces due to capillary condensation *Appl. Phys. Lett.*, 91, 101905 (2007).
5. A. de Lazzar, M. Dreyer, and H. J. Rath, Particle–surface capillary forces *Langmuir*, 15, 4551–4559 (1999).
6. X. Xiao and L. Qian, Investigation of humidity-dependent capillary force *Langmuir*, 16, 8153–8158 (2000).
7. E. Charlaix and M. Ciccotti, Capillary condensation in confined media, in *Handbook of Nanophysics: Principles and Methods*, K. Sattler (Ed.), CRC Press, Boca Raton, FL (2010).
8. J. Jang, M. Yang, and G. Schatz, Microscopic origin of the humidity dependence of the adhesion force in atomic force microscopy *J. Chem. Phys.*, 126, 174705 (2007).
9. J. Israelachvili, *Intermolecular and Surface Forces*, 3rd ed. Academic Press Burlington, MA (2011).
10. J. Hu, X. D. Xiao, D. F. Ogletree, and M. Salmeron, Imaging the condensation and evaporation of molecularly thin films of water with nanometer resolution *Science*, 268, 267–269 (1995).
11. M. Farshchi-Tabrizia, M. Kappl, and H.-J. Butt, Influence of humidity on adhesion: An atomic force microscope study *J. Adhesion. Sci. Technol.*, 22, 181–203 (2008).
12. H. J. Butt, B. Cappella, and M. Kappl, Force measurements with the atomic force microscope: Technique, interpretation and applications *Surf. Sci. Reports.*, 59, 1–152, (2005).
13. J. Tamayo and R. García, Deformation, contact time, and phase contrast in tapping mode scanning force microscopy *Langmuir*, 12, 4430–4435 (1996).
14. L. Wang, The role of damping in phase imaging in tapping mode atomic force microscopy *Surface Sci.*, 429, 178–185 (1999).
15. R. P. Jaiswal and S. P. Beaudoin, Approximate scheme for calculating van der Waals interactions between finite cylindrical volume elements *Langmuir*, 28, 8359–8370 (2012).
16. K. Wendler, J. Thar, S. Zahn, and B. Kirchner, Estimating the hydrogen bond energy *J. Phys. Chem. A*, 114, 9529–9536 (2010).

17. P. L. Silvestrelli, Improvement in hydrogen bond description using van der Waals-corrected DFT: The case of small water clusters *Chem. Phys. Lett.*, 475, 285–288 (2009).
18. L. Qian, F. Tian, and X. Xiao, Tribological properties of self-assembled monolayers and their substrates under various humid environments *Tribol. Lett.*, 15, 169–176 (2003).
19. A. D. Zimon, *Adhesion of Dust and Powder*, 2nd ed., Consultants Bureau, New York (1982).
20. K. L. Mittal (Ed.), *Polymer Surface Modification: Relevance to Adhesion*, Vol. 5, CRC Press, Boca Raton, FL (2009).
21. A. Adamson and A. Gast, *Physical Chemistry of Surfaces*, 6th ed., pp. 4–48, John Wiley & Sons, New York (1967).
22. J. McFarlane and D. Tabor, Adhesion of solids and the effect of surface films *Proc. R. Soc. London A*, 202, 224–243 (1950).
23. L. Zitzler, S. Herminghaus, and F. Mugele, Capillary forces in tapping mode atomic force microscopy *Phys. Rev. B*, 66, 155436 (2002).
24. B. M. Moudgil, Effect of nanoscale roughness on adhesion force in dry and humid air, in: Proceedings AIChE World Congress on Particle Technology, Sydney (2002).
25. P. Lambert, A. Chau, A. Delchambre, and S. Régnier, Comparison between two capillary forces models *Langmuir*, 24, 3157–3163 (2008).
26. K. P. Galvin, A conceptually simple derivation of the Kelvin equation *Chem. Eng. Sci.*, 60, 4659–4660 (2005).
27. H. Yan, X.-S. Wang, and R.-Z. Zhu, Derivation of the Kelvin equation *Acta Physico-Chimica Sinica*, 25, 640–644 (2009).
28. L. R. Fisher and J. N. Israelachvili, Experimental studies on the applicability of the Kelvin equation to highly curved concave menisci *J. Colloid Interface Sci.*, 80, 528–541 (1981).
29. L. Fisher and J. N. Israelachvili, Direct of the effect of meniscus forces on adhesion: A study of the applicability of macroscopic thermodynamics to microscopic liquid interface *Colloids Surfaces*, 3, 303–319 (1981).
30. D. B. Asay and S. H. Kim, Effects of adsorbed water layer structure on adhesion force of silicon oxide nanoasperity contact in humid ambient *J. Chem. Phys.*, 124, 174712 (2006).
31. A. Fukunishi and Y. Mori, Adhesion force between particles and substrate in a humid atmosphere studied by atomic force microscopy *Adv. Powder Technol.*, 17, 567–580 (2006).
32. L. Xu, A. Lio, J. Hu, D. F. Ogletree, and M. Salmeron, Wetting and capillary phenomena of water on mica *J. Phys. Chem. B*, 102, 540–548 (1998).
33. S. Biggs, R. G. Cain, R. R. Dagastine, and N. W. Page, Direct measurements of the adhesion between a glass particle and a glass surface in a humid atmosphere *J. Adhesion Sci. Technol.*, 16, 869–885 (2002).
34. W. Stroud, J. Curry, and J. Cushman, Capillary condensation and snap-off in nanoscale contacts *Langmuir*, 17, 688–698 (2001).

35. A. Ata, Y. I. Rabinovich, and R. K. Singh, Role of surface roughness in capillary adhesion *J. Adhesion Sci. Technol.*, 16, 337–346 (2002).
36. M. P. Boer, Capillary Adhesion between elastically hard rough surfaces *Expl. Mech.*, 47, 171–183 (2007).
37. H.-J. Butt and M. Kappl, Normal capillary forces *Adv. Colloid Interface Sci.*, 146, 48–60 (2009).
38. H.-J. Butt, Capillary forces: Influence of roughness and heterogeneity *Langmuir*, 24, 4715–47221 (2008).
39. P. J. van Zwol, G. Palasantzas, and J. T. M. De Hosson, Influence of roughness on capillary forces between hydrophilic surfaces *Phys. Rev. E*, 78, 031601–031606 (2008).
40. O. H. Pakarinen, A. S. Foster, M. Paajanen, T. Kalinainen, J. Katainen, I. Makkonen, J. Lahtinen, and R. M. Nieminen, Towards an accurate description of the capillary force in nanoparticle-surface interactions *Model. Simul. Mater. Sci. Eng.*, 13, 1175–1186 (2005).
41. J. Tamayo and R. Garcia, Effects of elastic and inelastic interactions on phase contrast images in tapping-mode scanning force microscopy *Appl. Phys. Lett.*, 71, 2394–2396 (1997).
42. N. Zarate, A. Harrison, J. Litster, and S. Beaudoin, Effect of relative humidity on onset of capillary forces for rough surfaces *J. Colloid Interface Sci.*, 411, 265–272 (2013).
43. M. He, A. Szuchmacher Blum, D. E. Aston, C. Buenviaje, R. M. Overney, and R. Luginbühl, Critical phenomena of water bridges in nanoasperity contacts *J. Chem. Phys.*, 114, 1355–1360 (2001).
44. R. Digilov, Kelvin equation for menisci of nanosize dimensions, *Langmuir*, 16, 1424–1427 (2000).
45. J. Jang, G. Schatz, and M. Ratner, Capillary force on a nanoscale tip in dip-pen nanolithography *Phys. Rev. Lett.*, 90, 18–21 (2003).
46. J. Jang, G. C. Schatz, and M. Ratner, Capillary force in atomic force microscopy *J. Chem. Phys.*, 120, 1157–1160 (2004).
47. J. Jang, G. Schatz, and M. Ratner, How narrow can a meniscus be? *Phys. Rev. Lett.*, 92, 1–4 (2004).
48. J. Jang, M. A. Ratner, and G. C. Schatz, Atomic-scale roughness effect on capillary force in atomic force microscopy *J. Phys. Chem. B*, 110, 659–662 (2006).
49. J. Jang, J. Jeon, and S. Hwang, Monte Carlo study on the water bridge that produces the pull-off force in atomic force microscopy *Colloids Surfaces A*, 300, 60–64 (2007).
50. S. Han and J. Jang, A thermodynamic perturbation method to calculate surface forces in confined-fluid systems *Bull. Korean Chem. Soc.*, 27, 31–32 (2006).
51. J. Jang, J. Sung, and G. C. Schatz, Influence of surface roughness on the pull-off force in atomic force microscopy *J. Phys. Chem. C* 111, 4648–4654 (2007).

52. J. Jang and G. C. Schatz, Lattice gas Monte Carlo simulation of capillary forces in atomic force microscopy *J. Adhesion Sci. Technol.*, 24, 37–41 (2010).
53. R. Pandit, M. Schick, and M. Wortis, Systematics of multilayer adsorption phenomena on attractive substrates *Phys. Rev. B*, 26, 5112–5140 (1982).
54. J. Jang, G. C. Schatz, and M. Ratner, Liquid meniscus condensation in dip-pen nanolithography *J. Chem. Phys.*, 116, 3875–3886 (2002).
55. H. Shinto, K. Uranishi, M. Miyahara, and K. Higashitani, Wetting-induced interaction between rigid nanoparticle and plate: A Monte Carlo study *J. Chem. Phys.*, 116, 9500–9509 (2002).
56. O. Stukalov, C. Murray, A. Jacina, and J. R. Dutcher, Relative humidity control for atomic force microscopes *Rev. Sci. Instrum.*, 77, 033704 (2006).
57. D. Asay, A. Barnette, and S. Kim, Effects of surface chemistry on structure and thermodynamics of water layers at solid-vapor interfaces *J. Phys. Chem. C*, 113, 2128–2133 (2009).
58. H. J. Choi, J. Y. Kim, S. D. Hong, M. Y. Ha, and J. Jang, Molecular simulation of the nanoscale water confined between an atomic force microscope tip and a surface *Mol. Simul.*, 35, 466–472 (2009).
59. H. Kim, B. Smit, and J. Jang, Monte Carlo study on the water meniscus condensation and capillary force in atomic force microscopy *J. Phys. Chem. C*, 116, 21923–21931 (2012).
60. Y. Men, X. Zhang, and W. Wang, Capillary liquid bridges in atomic force microscopy: Formation, rupture, and hysteresis *J. Chem. Phys.*, 131, 184702 (2009).
61. P. B. Paramonov and S. F. Lyuksyutov, Density-functional description of water condensation in proximity of nanoscale asperity *J. Chem. Phys.*, 123, 084705 (2005).
62. H. Shinto, D. Komiyama, and K. Higashitani, Lattice Boltzmann study of capillary forces between cylindrical particles *Adv. Powder Technol.*, 18, 643–662 (2007).
63. H. Shinto, Computer simulation of wetting, capillary forces, and particle-stabilized emulsions: From molecular-scale to mesoscale modeling *Adv. Powder Technol.*, vol. 23, no. 5, 538–547 (2012).
64. D. B. Asay and S. H. Kim, Evolution of the adsorbed water layer structure on silicon oxide at room temperature *J. Phys. Chem. B*, 109, 16760–16763 (2005).
65. A. Payam and M. Fathipour, A capillary force model for interactions between two spheres *Particuology*, 9, 381–386 (2011).
66. D. Alguacil and L. Gauckler, Capillary forces between two solid spheres linked by a concave liquid bridge: Regions of existence and forces mapping *AIChE J.*, 55, 1103–1109 (2009).
67. Y. Rabinovich, M. Esayanur, and B. Moudgil, Capillary forces between two spheres with a fixed volume liquid bridge: Theory and experiment *Langmuir*, 21, 10992–10997 (2005).

68. W. Le-Feng, R. Wei-Bin, S. Li-Ning, and C. Li-Guo, Capillary forces between submillimeter spheres and flat surfaces at constant liquid volumes *Chinese Phys. Lett.*, 26, 126801 (2009).
69. F. London, Zur Theorie und systematik der molekularkräfte *Zeitschrift für Phys.*, 63, 245–279 (1930).
70. F. London, Über einiger eigenschaften und anwendungen der molekularkräfte *Zeitschrift Phys. Chemie*, B11, 222–251 (1930).
71. W. Heitler and F. London, Wechselwirkung neutraler atome und homöopolare bindung nach der quantenmechanik *Zeitschrift für Phys.*, 44, 455–472 (1927).
72. R. Eisenschitz and F. London, Über das verhältnis der van der Waalsschen kräfte zu den homöopolaren bindungskräften *Zeitschrift für Phys.*, 60, 491–527 (1930).
73. F. London, Die bedeutung der quantentheorie für die chemie *Naturwissenschaften*, 17, 516–529 (1929).
74. F. London, The general theory of molecular forces *Trans. Faraday Soc.*, 33, 8–26 (1937).
75. A. Jiemchoorj, First-principles calculations of long-range intermolecular dispersion forces, Ph.D. Thesis, Lingoping University, 2006.
76. H. C. Hamaker, The London-van der Waals attraction between spherical particles *Physica*, IV, 1058–1072 (1937).
77. J. Mahanty and B. W. Ninham, *Dispersion Forces*, Academic Press, New York (1976).
78. B. Davies, Calculation of van der Waals forces from dispersion relations *Chem. Phys. Lett.*, 16, 388–390 (1972).
79. I. E. Dzyaloshinskii, E. M. Lifshitz, L. P. Pitaevskii, and M. Hamermesh, General theory of van der Waals' forces *Uspekhi Fiz. Nauk (English Transl.)*, 73, 153–176 (1961).
80. J. S. Høye and I. Brevik, van der Waals force between dielectric plates derived from the quantum statistical mechanical path integral method *Physica A*, 259, 165–182 (1998).
81. D. Langbein, Non-retarded dispersion energy between macroscopic spheres *J. Phys. Chem. Solids*, 32, 1657–1667 (1971).
82. D. Langbein, The macroscopic theory of van der Waals attraction *Solid State Commun.*, 12, 853–855 (1973).
83. L.-H. Lee, (Ed.), *Fundamentals of Adhesion*, Plenum Press, New York (1991).
84. J. Mahanty and B. W. Ninham, Theory of dispersion interactions between macroscopic bodies *J. Chem. Soc. Faraday Trans. 2*, 71, 119–137 (1975).
85. E. M. Lifshitz, The theory of molecular attractive forces between solids *Sov. Phys. JETP*, 2, 73–83 (1956).
86. E. Elizalde and A. Romeo, Essentials of the Casimir effect and its computation *Am. J. Phys.*, 59, 711–719 (1991).
87. A. N. Kaufman, Equation of motion of a dielectric medium *Phys. Fluids*, 8, 935–938 (1965).

88. V. A. Parsegian, *van der Waals Forces: A Handbook for Biologists, Chemists, Engineers, and Physicists*, Cambridge University Press, Cambridge, UK (2006).
89. R. F. Rajter, R. H. French, W. Y. Ching, W. C. Carter, and Y. M. Chiang, Calculating van der Waals-London dispersion spectra and Hamaker coefficients of carbon nanotubes in water from ab initio optical properties *J. Appl. Phys.*, 101, 054303 (2007).
90. B. V. Derjaguin, Untersuchungen über die Reibung und Adhäsion, IV *Kolloid-Zeitschrift*, 69, 155–164 (1934).
91. J. E. Kiefer, V. A. Parsegian, and G. H. Weiss, An easily calculable approximation for the many-body van der Waals attraction between two equal spheres *J. Colloid Interface Sci.*, 57, 580–582 (1976).
92. J. E. Kiefer, V. A. Parsegian, and G. H. Weiss, Some convenient bounds and approximations for the many body van der Waals attraction between two spheres *J. Colloid Interface Sci.*, 67, 140–153 (1978).
93. G. Liuti and F. Pirani, Regularities in van der Waals forces: Correlation between the potential parameters and polarizability *Chem. Phys. Lett.*, 122, 245–250 (1985).
94. S. Nir, S. Adams, and R. Rein, Determination of dielectric dispersion by two methods and application to calculations of van der Waals forces *J. Colloid Interface Sci.*, 49, 196–203 (1974).
95. C. J. van Oss, M. K. Chaudhury, and R. J. Good, Interfacial Lifshitz-van der Waals and polar interactions in macroscopic systems *Chem. Rev.*, 88, 927–941 (1988).
96. G. H. Weiss, J. E. Kiefer, and V. A. Parsegian, Effects of dielectric inhomogeneity on the magnitude of van der Waals interactions *J. Colloid Interface Sci.*, 45, 615–625 (1973).
97. M. J. Sparnaay, Four notes on van der Waals forces: Induction effect, non-additivity, attraction between a cone and a flat plate (asperities), history *J. Colloid Interface Sci.*, 91, 307–319 (1983).
98. L. Bergström, A. Meurk, H. Arwin, and D. J. Rowcliffe, Estimation of Hamaker constants of ceramic materials from optical data using Lifshitz theory *J. Am. Ceram. Soc.*, 79, 339–348 (1996).
99. R. R. Dagastine, D. C. Prieve, and L. R. White, The dielectric function for water and its application to van der Waals forces *J. Colloid Interface Sci.*, 231, 351–358 (2000).
100. W. A. B. Donners, J. B. Rijnbout, and A. Vrij, Calculations of van der Waals forces in thin liquid films using Lifshitz' theory *J. Colloid Interface Sci.*, 60, 540–547 (1977).
101. C. E. Dykstra, Electrostatic interaction potentials in molecular force fields *Chem. Rev.*, 93, 2339–2353 (1993).
102. V. A. Parsegian and G. H. Weiss, Spectroscopic parameters for computation of van der Waals forces *J. Colloid Interface Sci.*, 81, 285–289, (1981).
103. S. Tcholakova, N. D. Denkov, R. Borwankar, and B. Campbell, van der Waals interaction between two truncated spheres covered by a uniform layer (deformed drops, vesicles, or bubbles) *Langmuir*, 17, 2357–2362 (2001).

104. B. V. Derjaguin, I. I. Abrikossova, and E. M. Lifshitz, Direct measurement of molecular attraction between solids separated by a narrow gap *Q. Rev. Chem. Soc.*, 10, 295–329 (1956).
105. D. C. Prieve and W. B. Russel, Simplified predictions of Hamaker constants from Lifshitz theory *J. Colloid Interface Sci.*, 125, 1, 1–13 (1988).
106. D. F. Edwards, Silicon (Si), in: *Handbook of Optical Constants of Solids*, vol. 1, E. D. Palik (Ed.), pp. 547–569, Elsevier/Academic Press, San Diego, CA (1985).
107. F. Gervais, Aluminum oxide ( $\text{Al}_2\text{O}_3$ ), in: *Handbook of Optical Constants of Solids*, Vol. 2, E. D. Palik (Ed.), pp. 761–774, Elsevier/Academic Press, San Diego, CA (1991).
108. H. R. Philipp, Silicon nitride ( $\text{Si}_3\text{N}_4$ ) (Noncrystalline), in: *Handbook of Optical Constants of Solids*, vol. 1, E. D. Palik (Ed.), pp. 771–774, Elsevier/Academic Press, San Diego, CA (1985).
109. D. Tabor and R. H. S. Winterton, The direct measurement of normal and retarded van der Waals forces *Proc. R. Soc. London Ser. A*, 312, 435–450 (1969).
110. B. V. Derjaguin, P. N. Lebedev's ideas on the nature of molecular forces *Sov. Phys. Uspekhi*, 10, 108–111 (1967).
111. J. N. Israelachvili, The calculation of van der Waals dispersion forces between macroscopic bodies *Proc. R. Soc. London. Ser. A*, 331, 39–55 (1972).
112. V. A. Parsegian, Long-range van der Waals Forces, in: *Physical Chemistry: Enriching Topics from Colloid and Surface Science*, H. van Olphen and K. J. Mysels (Eds.), Theorex, La Jolla, CA (1975).
113. J. T. Duniec, J. Mahanty, and B. W. Ninham, Effect of spatial dispersion on van der Waals interactions between molecules *Solid State Commun.*, 21, 899–902 (1977).
114. M. A. Bevan and D. C. Prieve, Direct measurement of retarded van der Waals attraction *Langmuir*, 15, 7925–7936 (1999).
115. D. Gingell and V. A. Parsegian, Prediction of van der Waals interactions between plastics in water using the Lifshitz theory *J. Colloid Interface Sci.*, 44, 456–463 (1973).
116. V. A. Parsegian and G. H. Weiss, On van der Waals interactions between macroscopic bodies having inhomogeneous dielectric susceptibilities *J. Colloid Interface Sci.*, 40, 35–41 (1972).
117. E. R. Smith, D. J. Mitchell, and B. W. Ninham, Deviations of the van der Waals energy for two interacting spheres from the predictions of Hamaker theory *J. Colloid Interface Sci.*, 45, 55–68 (1973).
118. N. G. van Kampen, B. R. A. Nijboer, and K. Schram, On the macroscopic theory of van der Waals forces *Phys. Lett. A*, 26, 307–308 (1968).
119. B. W. Ninham and V. A. Parsegian, van der Waals forces across triple-layer films *J. Chem. Phys.*, 52, 4578–4587 (1970).
120. B. W. Ninham and V. A. Parsegian, van der Waals forces: Special characteristics in lipid-water systems and a general method of calculation based on the Lifshitz theory *Biophys. J.*, 10, 646–663 (1970).



121. B. W. Ninham and V. A. Parsegian, van der Waals interactions in multilayer systems *J. Chem. Phys.*, 53, 3398–3402 (1970).
122. V. A. Parsegian and B. W. Ninham, Toward the correct calculation of van der Waals interactions between lyophobic colloids in an aqueous medium *J. Colloid Interface Sci.*, 37, 332–341 (1971).
123. V. A. Parsegian and B. W. Ninham, Generalization of the Lifshitz result for two semi-infinite media *J. Theor. Biol.*, 38, 101–109 (1973).
124. V. A. Parsegian and G. H. Weiss, Dielectric anisotropy and the van der Waals interaction between bulk media *J. Adhesion*, 3, 259–267 (1972).
125. D. Hough and L. White, The calculation of hamaker constants from Lifshitz theory with applications to wetting phenomena *Adv. Colloid Interface Sci.*, 14, 3–41 (1980).
126. H. D. Ackler, R. H. French, and Y. M. Chiang, Comparisons of Hamaker constants for ceramic systems with intervening vacuum or water: from force laws and physical properties *J. Colloid Interface Sci.*, 179, 460–469 (1996).
127. S. Eichenlaub, C. Chan, and S. Beaudoin, Hamaker constants in integrated circuit metalization *J. Colloid Interface Sci.*, 248, 389–397 (2002).
128. R. Jaiswal and S. P. Beaudoin, Nanoparticle adhesion models: Applications in particulate contaminant removal from extreme ultraviolet lithography photomasks *J. Adhesion Sci. Technol.*, 25, 781–797 (2011).
129. C. Argento and R. H. French, Parametric tip model and force-distance relation for Hamaker constant determination from atomic force microscopy *J. Appl. Phys.*, 80, 6081–6090 (1996).
130. S. Yang, H. Zhang, and S. M. Hsu, Correction of random surface roughness on colloidal probes in measuring adhesion *Langmuir*, 23, 1195–1202 (2007).
131. E. R. Beach, G. W. Tormoen, J. Drelich, and R. Han, Pull-off force measurement between rough surfaces by atomic force microscopy *J. Colloid Interface Sci.*, 247, 84–99 (2002).
132. R. P. Jaiswal, G. Kumar, C. M. Kilroy, and S. P. Beaudoin, Modeling and validation of the van der Waals force during the adhesion of nanoscale objects to rough surfaces: A detailed description *Langmuir*, 25, 10612–10623 (2009).
133. K. Cooper, A. Gupta, and S. P. Beaudoin, Simulation of particle adhesion: Implications in chemical mechanical polishing and post chemical mechanical polishing cleaning *J. Electrochem. Soc.*, 148, G662–G667 (2001).
134. G. Kumar, S. Smith, R. Jaiswal, and S. Beaudoin, Scaling of van der Waals and electrostatic adhesion interactions from the micro- to the nano-scale *J. Adhesion Sci. Technol.*, 22, 407–428 (2008).
135. G. Kumar and S. Beaudoin, Undercut removal of micrometer-scale particles from surfaces *J. Electrochem. Soc.*, 153, G175–G181 (2006).
136. S. Eichenlaub, A. Gelb, and S. Beaudoin, Roughness models for particle adhesion *J. Colloid Interface Sci.*, 280, 289–98 (2004).
137. J. N. Israelachvili and D. Tabor, The measurement of van der Waals dispersion forces in the range 1.5 to 130 nm *Proc. R. Soc. London A*, 331, 19–38 (1972).

138. J. N. Israelachvili and D. Tabor, van der Waals forces: theory and experiment *Prog. Surf. Membrane Sci.*, 7, pp. 1–55, (1973).
139. J. Israelachvili and G. Adams, Measurement of forces between two mica surfaces in aqueous electrolyte solutions in the range 0–100 nm *J. Chem. Soc. Faraday Trans. 74*, 975–1001 (1978).
140. D. Y. Kwok and A. W. Neumann, Contact angle measurement and contact angle interpretation *Adv. Colloid Interface Sci.*, 81, 167–249 (1999).
141. F. Etzler, Determination of the surface free energy of solids *Rev. Adhesion Adhesives*, 1,3–45 (2013).
142. D. Owens and R. Wendt, Estimation of the surface free energy of polymers *J. Appl. Polym. Sci.*, 13, 1741–1747 (1969).
143. F. Fowkes and W. Zisman, The spreading of liquids on low energy surfaces. I. Polytetrafluoroethylene *J. Colloid Sci.*, 5, 514–531 (1950).
144. F. Fowkes, Attractive forces at interfaces *Ind. Eng. Chem.*, 56 (12) 40–52 (1964).
145. S. Siboni, C. Della Volpe, D. Maniglio, and M. Brugnara, The solid surface free energy calculation; II. The limits of the Zisman and of the ‘equation-of-state’ approaches *J. Colloid Interface Sci.*, 271, 454–72, (2004).
146. Y. Chen, C. Helm, and J. Israelachvili, Molecular mechanisms associated with adhesion and contact angle hysteresis of monolayer surfaces *J. Phys. Chem.*, 95, 10736–10747 (1991).
147. D. F. O’Kane and K. L. Mittal, Plasma cleaning of metal surfaces *J. Vac. Sci. Technol.*, 11, 567–569 (1974).
148. D.L. Williams and T.M. O’Byron, Cleanliness verification on large surfaces, in: *Developments in Surface Contamination and Cleaning*, Vol. 6, R. Kohli and K.L. Mittal (Eds.), pp. 163–181, Elsevier, Oxford, England (2013).
149. N. S. Tambe and B. Bhushan, Micro/nanotribological characterization of PDMS and PMMA used for BioMEMS/NEMS applications *Ultramicroscopy*, 105, 238–247 (2005).
150. W. Smythe, *Static and Dynamic Electricity*, 2nd ed., McGraw-Hill, New York (1950).
151. B. Gady, D. Schleef, R. Reifenberger, and D. S. Rimai, The interaction between micrometer-size particles and flat substrates: A quantitative study of jump-to-contact *J. Adhesion*, 67, 291–305 (1998).
152. D. Griffiths, *Introduction to Electrodynamics*, Prentice Hall, Upper Saddle River, NJ (1999).
153. J. Crowley, Simple expressions for force and capacitance for a conductive sphere near a conductive wall, in Proceedings of the Electrostatics Society of America Annual Meeting on Electrostatics, 1–15 (2008).
154. B. Gady, R. Reifenberger, D. S. Rimai, and L. P. DeMejo, Contact electrification and the interaction force between a micrometer-size polystyrene sphere and a graphite surface *Langmuir*, 13, 2533–2537 (1997).
155. B. L. Gady, Measurement of interaction forces between micrometer-sized particles and flat surfaces using an atomic force microscope, Ph.D. thesis, Purdue University, West Lafayette, IN (1996).

156. B. Gady, D. Schleeff, R. Reifenberger, D. Rimai, and L. DeMejo, Identification of electrostatic and van der Waals interaction forces between a micrometer-size sphere and a flat substrate *Phys. Rev. B*, 53, 8065–8070 (1996).
157. P. Lorrain and D. Corson, *Electromagnetic Fields and Waves*, 2nd ed., W. H. Freeman and Co., San Francisco (1970).
158. A. Khachatourian, H.-K. Chan, A. J. Stace, and E. Bichoutskaia, Electrostatic force between a charged sphere and a planar surface: A general solution for dielectric materials *J. Chem. Phys.*, 140, 074107 (2014).
159. E. Bichoutskaia, A. L. Boatwright, A. Khachatourian, and A. J. Stace, Electrostatic analysis of the interactions between charged particles of dielectric materials *J. Chem. Phys.*, 133, 024105 (2010).
160. G. Arfken, *Mathematical Methods for Physicists*, 2<sup>nd</sup> ed., pp. 115–170, Academic Press, Orlando, FL (1970).
161. J. Hansen and H. Löwen, Effective interaction between electrical double layers *Annu. Rev. Phys. Chem.*, 51, 209–242 (2000).
162. C. J. van Oss, *Interfacial Forces in Aqueous Media*, pp. 51–69, CRC Press, Boca Raton, FL (2008).
163. R. van Roji, Electrostatics in liquids: From electrolytes and suspensions towards emulsions and patchy surfaces *Physica A* 389, 4317–4331 (2010).
164. J. Stankovich and S. Carnie, Interactions between two spherical particles with nonuniform surface potentials: The linearized Poisson-Boltzmann theory *J. Colloid Interface Sci.*, 216, 329–347 (1999).
165. R. Hogg, T. Healy, and D. Fuerstenau, Mutual coagulation of colloidal dispersions *Trans. Faraday Soc.*, 62, 1638–1651 (1966).
166. S. Carnie, D. Chan, and J. Stankovich, Computation of forces between spherical colloidal particles: Nonlinear Poisson-Boltzmann theory *J. Colloid Interface Sci.*, 165, 116–128 (1994).
167. D. McCormack, S. Carnie, and D. Chan, Calculations of electric double-layer force and interaction free energy between dissimilar surfaces *J. Colloid Interface Sci.*, 169, 177–196 (1995).
168. B. V. DeJaguin and L. D. Landau, Theory of the stability of strongly charged lyophobic sols and of the adhesion of strongly charged particles in solution of electrolytes *Acta Physicochim. URSS*, 14, 633–662 (1941).
169. E. J. W. Verwey and J. Th. G. Overbeek, *Theory of the Stability of Lyophobic Colloids*, Elsevier, Amsterdam (1948).



# Mechanics of Particle Adhesion and Removal

Goodarz Ahmadi

Department of Mechanical and Aeronautical Engineering,  
Clarkson University, Potsdam, NY, USA

---

## Abstract

An overview of mechanics of particle adhesion and removal is provided. Different adhesion models are outlined and the effect of electrostatic forces on particle adhesion and detachment is discussed. The criteria for incipient rolling and sliding detachments and electrostatic lifting removal are described. The bumpy particle model for analyzing adhesion and detachment of compact non-spherical particles is described. Particular attention was given to detachment of particles in turbulent airflows. A turbulence burst model for evaluating the peak air velocity near the substrate is described and used. The critical shear velocities for detaching particles of different sizes under different conditions are discussed. The electric field strength needed for electrostatic removal of particles with different charges is also evaluated. Comparisons of the model predictions with the available experimental data are also presented.

**Keywords:** Particle adhesion, detachment, bumpy particles, surface roughness.

## 2.1 Introduction

Nano- and micro-particle adhesion and removal are important in a variety of industrial and environmental applications. In particular, removal of fine particles from surfaces is of great concern in semiconductor, pharmaceutical and xerographic industries. Some recent studies have also shown connection between increase in indoor air pollution and particle resuspension from common floorings.

---

*E-mail:* gahmadi@clarkson.edu

---

K.L. Mittal and Ravi Jaiswal (eds.) Particle Adhesion and Removal, (81–104)  
2015 © Scrivener Publishing LLC

Extensive reviews of particle adhesion and removal were provided by Corn [1], Krupp [2], Visser [3], Tabor [4] and Bowling [5]. Accordingly, the van der Waals force is the main cause for particle adhesion to surfaces under dry conditions. The JKR adhesion model developed by Johnson, Kendall and Roberts [6] includes the effects of the surface energy and surface deformation. Using the Hertzian profile assumption, Derjaguin, Muller and Toporov [7] developed the so-called DMT model. More recent developments on particle adhesion models were presented by Tsai *et al.* [8], Maugis [9] and Rimai *et al.* [10]. Additional related articles on particle adhesion and removal can be found in the books edited by Mittal [11–12], and Quesnel *et al.* [13].

Re-entrainment of particles from plane surfaces was reported by Corn [1] and Corn and Stein [14]. Punjraath and Heldman [15] studied the particle resuspension mechanisms through a series of wind tunnel experiments. Healy [16], Sehmel [17], Smith *et al.* [18], Hinds [19] and Nicholson [20] provided reviews of resuspension processes. Particle detachment mechanisms in turbulent flows were studied by Cleaver and Yates [21]. Additional advances on particle resuspension processes were reported by Reeks and Hall [22], Wen and Kasper [23], Wang [24], Tsai *et al.* [25], and Soltani and Ahmadi [26–29], and Ibrahim *et al.* [30].

Nearly all earlier works were concerned with resuspension of ideal smooth spherical particles and smooth surfaces. Real particles are, however, irregular and bumpy. Greenwood and Williamson [31] suggested that the contact deformation depend on the topography of the surface. Greenwood and Tripp [32] improved the Hertz contact model by taking into account the effect of roughness. Soltani and Ahmadi [27] studied the effect of surface roughness on particle detachment mechanisms. Rimai and Quesnel [33] and Quesnel *et al.* [34] studied the adhesion of irregularly-shaped particles to plane substrate. Detailed experimental measurements of particle detachment in wind tunnels were reported by Wen and Kasper [23], Braaten *et al.* [35], Wu *et al.* [36], Nicholson [37], Ibrahim *et al.* [30,38], Krauter and Biermann [39] and Goldasteh *et al.* [40–42], among others.

Studies on adhesion of charged particles were reported by Derjaguin and Smilga [43], Davis [44], Kottler *et al.* [45] and Mastrangelo [46]. Donald [47,48] showed the strong dependence of adhesion force on the presence of an external electric field. Goel and Spencer [49] analyzed the effect of electrostatic and van der Waals forces on adhesion of toner particles. Detachment of charged toner particles under the action of an electric field was studied by Hays [50,51]. The effect of electrostatic forces on the adhesion of electrophotographic toners to photoconductor in xerographic

printers was studied by Lee and Jaffe [52]. A set of experiments to quantify the relative contributions of nonelectrostatic and electrostatic forces to the net adhesion force were performed by Mizes [53]. Soltani and Ahmadi [29] evaluated the minimum critical shear velocity needed to remove different size particles taking into account the electrostatic forces.

The importance of the capillary force on particle adhesion was noted by a number of researchers. Hinds [19] reported the expression for adhesion force at different values of relative humidity. Zimon [54] experiments indicated that the effect of capillary condensation on adhesion force begins to appear at air relative humidity above 50%. Luzhnov [55] performed experiments on factors affecting the capillary forces. Podczeczek *et al.* [56], Busnaina and Elsaywy [57] and Tang and Busnaina [58] reported the results of their study on the effect of relative humidity on particle adhesion and removal. Ahmadi *et al.* [59] studied the effect of the capillary force on the minimum critical shear velocities needed for removing different size spherical particles from surfaces. More recently, Goldasteh *et al.* [40–42] introduced the Monte Carlo approach to account for the random variations of parameters that affect the adhesion and detachment of particles.

In this chapter, the fundamentals of particle adhesion and detachment are reviewed, and the hydrodynamic particle resuspension is described. The importance of electrostatic and capillary forces is discussed. Sample simulation results are presented and compared with the available experimental data. Most natural particles are rough and irregular in shape. The effect of small roughness, as well as large roughness (bumps) on particles resuspension is discussed. Attention is also given to the effects of electrostatic and capillary forces on rough particle detachment from plane surfaces. The Monte Carlo approach is also briefly outlined.

## 2.2 Models

### 2.2.1 Particle Adhesion and Detachment Models

Figure 2.1 shows the schematic of a particle of diameter  $d$  in contact with a flat surface. Here  $P$  is the external force exerted on the particle,  $a$  is the contact radius and  $F_{ad}$  is the adhesion force. The classical Hertz contact theory considers the elastic deformation of bodies in contact, but neglects the adhesion force. Several models for particle adhesion to flat surfaces were developed in the past that improved the Hertz model by including the effect of adhesion (van der Waals) force.

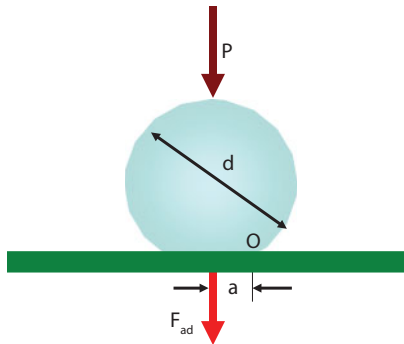


**Figure 2.1** Schematic of a spherical particle in contact with a plane.

### 2.2.1.1 JKR Model

Johnson-Kendall-Roberts [6] developed a model (The JKR Model) that included the effect of adhesion force on the deformation of an elastic sphere in contact with an elastic half space. Accordingly, the contact radius is given as

$$a^3 = \frac{d}{2K} \left[ P + \frac{3}{2} W_A \pi d + \sqrt{3\pi W_A d P + \left( \frac{3\pi W_A d}{2} \right)^2} \right] \quad (2.1)$$

Here  $W_A$  is the thermodynamic work of adhesion, and  $K$  is the composite Young's modulus given as

$$K = \frac{4}{3} \left[ \frac{1 - \nu_1^2}{E_1} + \frac{1 - \nu_2^2}{E_2} \right]^{-1} \quad (2.2)$$

In Equation (2.2),  $E_i$  is the elastic modulus,  $\nu$  is the Poisson ratio, and subscripts 1 and 2 refer to the materials of the particle and substrate, respectively.

In the absence of surface forces,  $W_A = 0$ , and Equation (2.1) is reduced to the classical Hertz model, i.e.,

$$a^3 = \frac{dP}{2K} \quad (2.3)$$



### 2.2.1.1.1 Pull-Off Force

The JKR model predicts that the force needed to remove the particle (the pull-off force) is given as

$$F_{po}^{JKR} = \frac{3}{4} \pi W_A d \quad (2.4)$$

### 2.2.1.1.2 Contact Radius at Zero Force

The contact radius at zero external force may be obtained by setting  $P = 0$  in Equation (2.1). That is,

$$a_0 = \left( \frac{3\pi W_A d^2}{2K} \right)^{\frac{1}{3}} \quad (2.5)$$

### 2.2.1.1.3 Contact Radius at Separation

The contact radius at separation is obtained by setting  $P = -F_{po}^{JKR}$  in Equation (2.1). The corresponding contact radius is given by

$$a = \left( \frac{3\pi W_A d^2}{8K} \right)^{\frac{1}{3}} = \frac{a_0}{4^{1/3}} \quad (2.6)$$

## 2.2.1.2 DMT Model

Derjaguin-Muller-Toporov [7] assumed the Hertz deformation and developed another model that included the effect of adhesion force. According to the DMT model, the pull-off force is given as

$$F_{Po}^{DMT} = \pi W_A d, \left( F_{Po}^{DMT} = \frac{4}{3} F_{Po}^{JKR} \right) \quad (2.7)$$

### 2.2.1.2.1 Contact Radius at Zero Force

The contact radius at zero external force is given as

$$a_0 = \left( \frac{\pi W_A d^2}{2K} \right)^{\frac{1}{3}} \quad (\text{Hertz contact radius under adhesion force}) \quad (2.8)$$

## 2.2.1.2.2 Contact Radius at Separation

The DMT model predicts that the contact radius at separation is zero, i.e.,

$$a = 0 \quad (\text{at separation}) \quad (2.9)$$

## 2.2.1.3 Maugis-Pollock Model

While the JKR and the DMT models assume elastic deformation, there are experimental data that suggest that in many cases plastic deformation occurs. Maugis-Pollock [60] developed a model that included the plastic deformation effects. Accordingly, the relationship between the contact radius and external force is given as

$$P + \pi W_A d = \pi a^2 H \quad (2.10)$$

where  $H$  is material hardness (at fully plastic contact) and

$$H = 3Y, \quad (2.11)$$

with  $Y$  being the yield strength of the material.

Note that variations of contact radius with particle diameter at equilibrium, i.e., in the absence of external force, for elastic and plastic deformations are different, (Rimai and co-workers [10], [33]) i.e.,

$$a_0 \sim d^{\frac{2}{3}} \text{ (elastic)}, a_0 \sim d^{\frac{1}{2}} \text{ (plastic)} \quad (2.12)$$

## 2.2.1.4 Nondimensional Forms

Nondimensional form of the relationship between contact radius and the external force and the corresponding moment as studied by Ziskind *et al.* [61] and Zhang and Ahmadi [62] are described in this section.

## 2.2.1.4.1 JKR Model

Equation (1) in nondimensional form may be restated as

$$a^{*3} = 1 - P^* + \sqrt{1 - 2P^*} \quad (2.13)$$

where the nondimensional external force and contact radius are defined as

$$P^* = -\frac{P}{\frac{3}{2}\pi W_A d}, \quad a^* = \frac{a}{\left(\frac{3\pi W_A d^2}{4K}\right)^{\frac{1}{3}}} \quad (2.14)$$

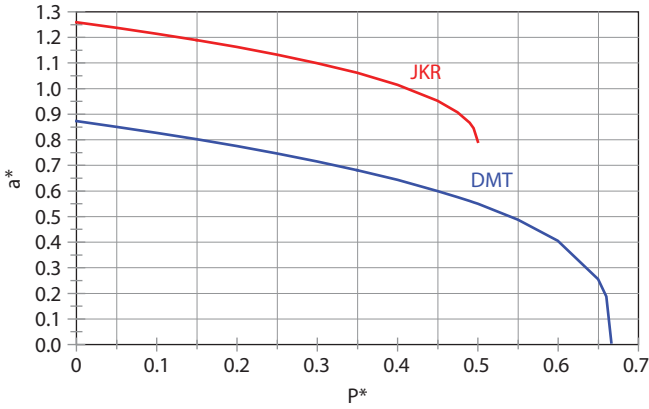


**Figure 2.2** Variations of contact radius with the exerted force.

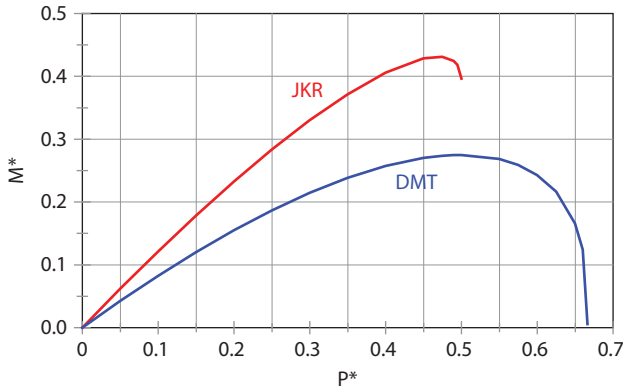


**Figure 2.3** Variations of resistance moment with the exerted force.

Variation of the nondimensional contact radius with the nondimensional force is shown in Figure 2.2. Note that for  $P^* = 0$ , Equation (2.13) and Figure 2.2 show that  $a_0 = 1.26$ .

The corresponding resistance moment about point O in Figure 2.1 as a function of nondimensional force is given as

$$M^{*JKR} = P^* a^* = P^* (1 - P^* + \sqrt{1 - 2P^*})^{1/3} \quad (2.15)$$

Figure 2.3 shows the variation of the resistance moment as predicted by the JKR model. The corresponding maximum resistance moment then is given by

$$M_{\max}^{*JKR} = 0.42 \quad (2.16)$$

and

$$P_{\max}^* = F_{po}^{*JKR} = \frac{F^{JKR}}{\frac{3\pi}{2}W_A d} = 0.5 \quad (2.17)$$

The maximum resistance moment at  $P^*$  is  $M^{*JKR} = 0.397$ . Also

$$P_{\max}^* a_0^* = 0.63 \quad (2.18)$$

#### 2.2.1.4.2 DMT Model

For the DMT model, the approximate expression for the contact radius is given as

$$a^3 \approx \frac{d}{2K}(P + \pi W_A d) \quad (2.19)$$

or

$$a^{*3} = \left(\frac{a}{3\pi W_A d^2 / 4K}\right)^3 = -P^* + \frac{2}{3} \quad (2.20)$$

Variation of the nondimensional contact radius with the nondimensional force as predicted by the DMT model is shown in Figure 2.2 and is compared with the JKR model. Note that for  $P^* = 0$ , Equation (2.20) and Figure 2.2 show that  $a_0^* = 0.874$ .

The corresponding resistance moment as a function of nondimensional force as predicted by the DMT model is given as

$$M^{*DMT} = P^*(2/3 - P^*)^{1/3} \quad (2.21)$$

The variation of the resistance moment as predicted by the DMT model is also shown in Figure 2.3. The corresponding maximum resistance moment is

$$M_{\max}^{*DMT} = 0.28 \quad (2.22)$$

Note also that the maximum force (the pull-off force) is given by

$$P_{\max}^* = F_{po}^{*DMT} = \frac{F^{DMT}}{\frac{3\pi}{2}W_A d} = \frac{2}{3} \quad (2.23)$$

and

$$P_{\max}^* a_0^* = 0.58 \quad (2.24)$$

Comparing Equations (2.16) and (2.22), it is seen that the JKR model predicts a larger resistance moment, i.e.,

$$M_{\max}^{*JKR} = 0.42 = 1.5M_{\max}^{*DMT}, \quad (M_{\max}^{DMT} = 0.28) \quad (2.25)$$

The resistance moment predicted by the JKR and the DMT models in dimensional form are given as

$$M_{\max}^{JKR} = 2.63 \frac{W_A^{\frac{4}{3}} d^{\frac{5}{3}}}{K^{\frac{1}{3}}}, \quad M_{\max}^{DMT} = 1.83 \frac{W_A^{\frac{4}{3}} d^{\frac{5}{3}}}{K^{\frac{1}{3}}} \quad (2.26)$$

### 2.2.2 Rough Particles Adhesion

Natural particles are hardly ever spherical, and are normally irregular and bumpy in shape. Adhesion of irregular shaped particles is relatively complex and far from being understood. Soltani and Ahmadi [29] proposed that compact particles with coarse roughness could be modeled as a sphere with a number of bumps. The bumps are then approximated to be hemispheres of radius  $\beta$ . The relationship among the radius of the bump,  $\beta$ , the number of bumps,  $N$ , and the particle diameter,  $d$ , is given as,

$$\beta = \frac{d}{n_b \sqrt{N}} \quad (2.27)$$

where  $n_b = 1, 2, \dots$  is the spacing between the bumps. (Note that,  $n_b = 1$  corresponds to the case that the bumps are in contact with no spacing.) A schematic of a bumpy particle in contact with a surface is shown in Figure 2.4.

Goel and Spencer [49] and Hays [50] reported that, on average, there are three asperities of a (toner) particle in contact with the substrate. Soltani and Ahmadi [29] and Ahmadi and Guo [63] used this assumption for developing their model of rough particle resuspension. Accordingly, the total pull-off force for detaching a bumpy particle from a surface is given as

$$f_{ad}^{JKR} = \frac{3}{2} \pi N_c W_A \beta \quad (2.28)$$

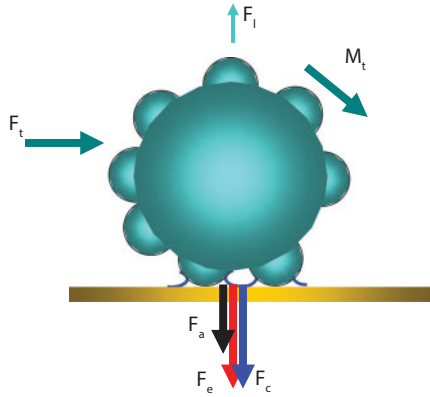


**Figure 2.4** Schematic of a bumpy particle in contact with a plane.

where  $N_c$  is the number of contact bumps (and typically  $N_c = 3$ ). Here the JKR adhesion model for each bump in contact with the substrate was used.

### 2.2.3 Charge Distribution

Aerosols acquire charges by a variety of mechanisms. Some of the charging mechanisms are well understood and others are not fully understood. In this section, the Boltzmann charge distribution and saturation field/diffusion charge distribution are outlined.

#### 2.2.3.1 Boltzmann Charge Distribution

Small particles in bipolar ionic atmosphere tend toward the Boltzmann charge distribution (Fuchs, [64]; Hinds, [19]; and Hidy, [65]). For a cloud of particles of diameter  $d$  under equilibrium condition at temperature  $T$ , the fraction  $f(n)$  of particles with  $n$  elementary electronic charges is given as,

$$f(n) = \frac{e^{-\frac{n^2 e^2}{dkT}}}{\sum_{n=-\infty}^{+\infty} e^{-\frac{n^2 e^2}{dkT}}} \quad (2.29)$$

where  $k$  is the Boltzmann constant ( $k = 1.38 \times 10^{-16}$  erg / K,  $e$  is the elementary unit of charge ( $e = 1.6 \times 10^{-19}$  Coulomb in SI unit, and  $= 4.8 \times 10^{-10}$

statcoulomb in cgs unit) and  $T$  is the temperature of the gas (degree K). The average number of absolute charges per particle is given as,

$$\bar{n} = \sum_{n=-\infty}^{+\infty} nf(n) \quad (2.30)$$

For particles larger than  $0.03 \mu\text{m}$ , the summation in (2.30) may be approximated as,

$$|\bar{n}| \approx 2.37\sqrt{d} \quad (2.31)$$

where  $d$  is particle diameter in  $\mu\text{m}$ . The average number of positive or negative charges carried by a particle then is  $|\bar{n}|/2$ . It should be emphasized that the Boltzmann charge distribution is for an ideal condition where aerosols have sufficient time to come to equilibrium with the positive and negative ions of the same concentration.

### 2.2.3.2 Diffusion and Field Charging

Small particles also get charged through diffusion and field charging mechanisms in a unipolar ionic environment. The approximate number of charges,  $n$ , acquired by a particle of diameter  $d$  by diffusion charging during a time  $t$  is given as (Hinds, [19]),

$$n_{diff} = \frac{dkT}{2e^2} \ln\left(1 + \frac{\pi d \bar{c}_i}{2kT} e^2 N_i t\right) \quad (2.32)$$

where  $\bar{c}_i = 2.4 \times 10^4$  cm/s is the mean thermal speed of the ions and  $N_i$  is the ion concentration (number of ions per volume). In the subsequent analysis, a typical value of  $N_i t \approx 10^8$  ion·s/cm<sup>3</sup> is used.

In the presence of a strong electric field  $E$ , the field charging becomes the main charging mechanism. After sufficient time, the saturation number of charges,  $n$ , acquired by a particle is given as ([19]),

$$n_{field} = \frac{3\varepsilon}{\varepsilon + 2} \frac{Ed^2}{4e} \quad (2.33)$$

where  $\varepsilon$  is the dielectric constant of the particle. It should be emphasized that Equations (2.32) and (2.33) are expressed in the cgs units. On the basis of the earlier studies of Hays [50], it is assumed that the charges carried by a particle are mainly concentrated on its bumps.

### 2.2.4 Electrostatic Forces

A brief summary of the electrostatic forces is presented in this section.

#### 2.2.4.1 Electrostatic Forces for Spherical Particles

The force acting on a charged particle near a conducting infinitely long plane substrate in the presence of an applied electric field is given approximately as (Hartmann *et al.* [66], Hidy [65], Cooper *et al.* [67], Fan and Ahmadi [68])

$$F_e = qE - \frac{q^2}{16\pi\epsilon_0 y^2} + \frac{qEd^3}{16y^3} - \frac{3}{128} \frac{\pi\epsilon_0 d^6 E^2}{y^4} \quad (2.34)$$

where  $\epsilon_0 = 8.859 \times 10^{-12} \text{ A} \cdot \text{s/V} \cdot \text{m}$  is the permittivity (dielectric constant of free space),  $d$  is the particle diameter,  $E$  is the imposed (constant) electric field strength,  $y$  is the distance of center of spherical particle from the surface, and  $q$  is the total charge on the particle. For a particle that carries  $n$  units of charge, the total electrical charge is given as,

$$q = ne \quad (2.35)$$

In Equation (2.34), the terms on the right-hand side are, respectively, the Coulomb force due to the applied electric field, the image force, the dielectrophoretic force and the polarization force. The Coulomb and dielectrophoretic forces can be either toward or away from the surface. While the image and polarization forces are always directed towards the surface. It should be pointed out that the dielectrophoretic force depends on the gradient of the electric field and the exact expression is geometry dependent. However, for a charged sphere near a conducting plane substrate in the presence of an imposed constant electric field, the expression given in (34) is a reasonable approximation. Note that in this case the dielectrophoretic force is generated by the gradient of the field from the image charge. Note that here the effect of contact potential induced electrical double layer force for particles in air is neglected.

#### 2.2.4.2 Electrostatic Forces for Bumpy Particles

For bumpy particles the electrostatic charges reside on the bumps. The corresponding electrostatic force acting on a charged bumpy particle as reported by Soltani and Ahmadi [29] is given as,



$$F_e = -1.5qE - \frac{q^2}{4\pi\epsilon_0} \left[ \frac{(1-3/N)^2}{d^2} + \frac{[(4n_b^2+1)(3/N)^2]}{3\beta^2(4n_b^2+1)^{3/2}} \right] - 72\pi\epsilon_0\beta^2 E^2. \quad (2.36)$$

The terms on the right-hand side of Equation (2.36) are, respectively, the combined effect of Coulomb and dielectrophoretic forces, the image force, and the polarization force. Unless stated otherwise, all the electrostatic forces are assumed to be directed toward the surface for evaluating the maximum force acting on the particle.

### 2.2.5 Capillary Force

Condensation of water vapor around the particle-substrate contact area forms a meniscus as shown in Figure 2.4 that leads to a capillary force. For a bumpy particle in contact with a substrate, the total capillary force then is given by,

$$F_c = 4\pi\sigma\beta N_c, \quad (2.37)$$

where  $\sigma$  is the surface tension of water ( $\sigma = 0.0735$  N/m, at room temperature). Here it is assumed that the liquid meniscus forms around the bump-substrate contact as shown in Figure 2.4 and the flattening effect of the bump is negligible. If liquid floods the contact area, submerges the bumps, and forms a film around the body of particle, then the capillary force for a spherical particle of diameter  $d$  given as

$$f_c = 2\pi\sigma d \quad (2.38)$$

should be used.

### 2.2.6 Hydrodynamic Forces and Torque

The hydrodynamic forces and torque acting on a particle in contact with a surface in a turbulent flow field are described in this section. Turbulent near-surface flows are characterized by formation of counter rotating coherent vortices and occasional bursts, which have profound effects on the particle detachment process. The peak instantaneous streamwise velocity experienced locally near the surface during the turbulent burst/inrush is given in wall units as (Soltani and Ahmadi, [28]),

$$u_M^+ = 1.72 y^+ \quad (2.39)$$

where the superscript '+' denotes a quantity stated in wall units. i.e.,

$$u^+ = \frac{u}{u^*}, y^+ = \frac{yu^*}{\nu} \quad (2.40)$$

where  $\nu$  is the kinematic viscosity of the fluid and  $u^*$  is the shear velocity.

The hydrodynamic drag force  $F_t$  acting on a spherical particle that is in contact with a smooth surface is given as,

$$F_t = \frac{C_D \pi f \rho_g d^2 V^2}{C_c} \quad (2.41)$$

where  $C_c$  is the Cunningham slip correction factor,  $f = 1.7009$  is the correction factor for the wall effect given by O'Neil [69],  $\rho_g$  is the air density at normal conditions,  $V$  is the mean air velocity at the centroid of the sphere, and  $C_D$  is the drag coefficient.

In Equation (2.41)  $C_D$  is the drag coefficient given in [19] as,

$$C_D = \frac{24}{\text{Re}_p} (1 + 0.15 \text{Re}_p^{0.687}) \quad \text{for } \text{Re}_p < 400. \quad (2.42)$$

Here  $\text{Re}_p$  is the particle Reynolds number defined as,

$$\text{Re}_p = \frac{dV}{\nu}, \quad (2.43)$$

where  $\nu$  is the kinematic viscosity of the fluid.

The hydrodynamic torque  $M_t$  acting on the particle is given by,

$$M_t = \frac{2\pi\mu f_m d^2 V}{C_c} \quad (2.44)$$

where  $f_m = 0.943993$  is the wall effect correction factor given by O'Neil [69]. Note that Equations (2.41) and (2.44) were derived for smooth spheres. Here, it is assumed that the hydrodynamic drag and torque acting on a bumpy particle in contact with a surface are given approximately by Equations (2.41) and (2.44). The lift force is typically quite small compared with the adhesion forces. In some earlier works (Soltani and Ahmadi [26–29]) the Saffman lift force was used to include the effect of the lift force on particle detachment.

## 2.2.7 Particle Detachment Models

Particles may be dislodged from a surface by rolling, sliding and electrostatic lifting.

### 2.2.7.1 Rolling Detachment Model

Figure 2.4 shows the schematic of the forces acting on the particle and their lines of action. It is assumed that the rough particles have three bumps in contact with the plane smooth substrate. The particle could be removed by breakup of one of the contact bumps and rolling with respect to the axis formed by connecting the centers of the other two contact bumps. It is assumed that the direction of the hydrodynamic drag force is perpendicular to the corresponding rolling axis. The onset of detachment with respect to a rolling axis (centerline of two bumps) is determined by the balance of torques generated by external and resistance forces (Soltani and Ahmadi [29]). i.e.,

$$M_t + F_t \frac{d}{2} \geq (F_{ad} + F_c + F_e)(0.58n_b \beta) \quad (2.45)$$

where  $F_{ad}$  is the pull-off force for the bumpy particle with three bumps in contact with the substrate as given by Equation (2.28). Here it is assumed that the adhesion force at the moment of incipient rolling is equal to the pull-off force. Due to symmetry, the lines of the action of adhesion force, capillary force and the electrical forces are located at the centroid of the triangle which connects the centers of the hemispherical contact bumps. The effect of the hydrodynamic lift force in Equation (2.45) is neglected.

### 2.2.7.2 Sliding Detachment Model

Wang [24] and Soltani and Ahmadi [26] studied the particle sliding detachment process. Accordingly, when the external force parallel to the surface becomes larger than the friction force, the particle will be detached and removed by sliding mechanism. When the effects of the electrical force and the capillary force are included, the condition for sliding detachment of the particle becomes,

$$F_t \geq k(F_{ad} + F_c + F_e) \quad (2.46)$$

where  $k$  is the coefficient of static friction for particle-substrate interface. Here, also the effect of the hydrodynamic lift force is neglected.

### 2.2.7.3 Electrostatic Particle Detachment

In the absence of hydrodynamic force, the onset for a charged particle to lift off from a substrate is controlled by balance of the adhesion force, the electrostatic force and the capillary force normal to the surface. Accordingly, the particle will be detached by electrostatic lifting if,

$$F_{ec} + F_{ed} \geq F_{ad} + F_{ei} + F_{ep} + F_c, \tag{2.47}$$

where  $F_{ec}, F_{ed}, F_{ei}, F_{ep}$ , respectively, are the standard Coulomb force ( $qE$ ), dielectrophoretic, image, and polarization forces.

## 2.3 Simulations Results

Sample results on particle removal are presented in this section. The critical shear velocities for resuspension of spherical graphite particles from a graphite substrate are shown in Figure 2.5. Here the results for JKR and Tsai-Pui-Lu (TPL) (Tsai et al., [8]) adhesion models are shown in this figure for comparison. Both the rolling and sliding removal mechanisms are considered. It is seen that the critical shear velocity increases sharply as particle size decreases. This is because the hydrodynamic forces

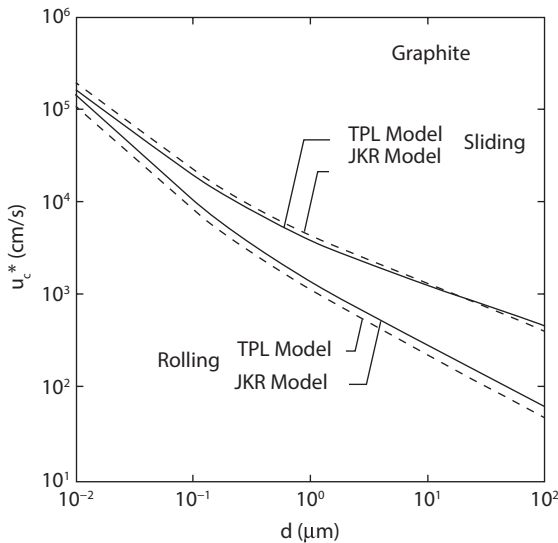
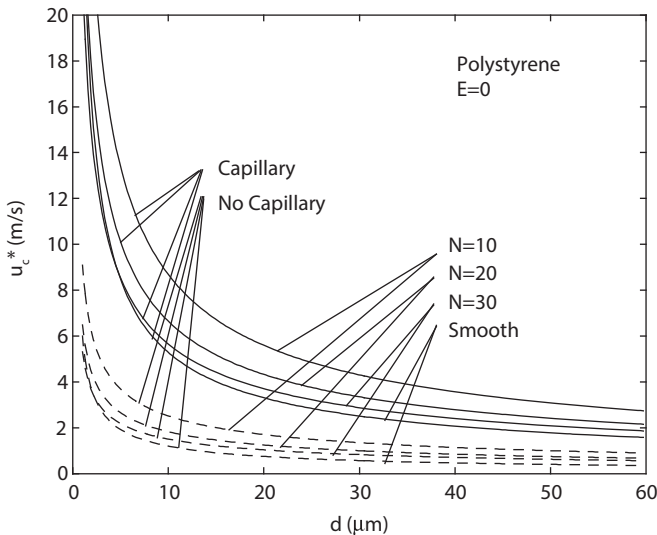


**Figure 2.5** Variations of the critical shear velocity with particle diameter for resuspension of spherical graphite particles from a graphite substrate.

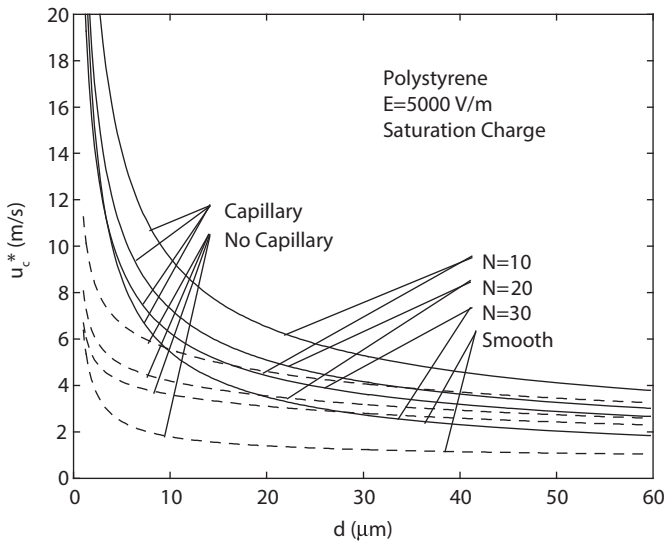
diminish as particle size decreases. Therefore, it is extremely difficult to remove nano-particles by hydrodynamic forces. Figure 2.5 also shows that the critical shear velocity for sliding detachment is much higher than that for rolling detachment. The JKR and TPL model predictions are also comparable.

Figure 2.6 shows the critical shear velocities for resuspension of neutral bumpy polystyrene particles with and without capillary force. The results for smooth spherical particle are also reproduced in this figure for comparison. Here, the rolling removal mechanism is considered and it is assumed that the contact bumps are one diameter apart. It is observed that the critical shear velocities in the presence of capillary force are higher than those obtained in the absence of capillary force for both smooth and bumpy particles. Figure 2.6 also shows that the critical shear velocity increases as the number of bumps decreases. i.e., when the particle becomes more irregular with smaller number of large bumps.

Figure 2.7 shows variations of the critical shear velocity with particle diameter for resuspension of particles that carry the saturation charge with and without capillary force in the presence of an electric field intensity of  $E = 5000$  kV/m. Simulation results for smooth and bumpy particles (with different numbers of bumps) are shown in this figure. Here, it is assumed that particles are removed by rolling. It is observed that the critical shear



**Figure 2.6** Variations of the critical shear velocity with particle diameter for resuspension of neutral polystyrene particles from a polystyrene substrate with and without capillary force for smooth and bumpy particles.  $N$  is the number of bumps.



**Figure 2.7** Variations of the critical shear velocity with particle diameter for resuspension of polystyrene particles with saturation charge from a polystyrene substrate with and without capillary for smooth and bumpy particles.  $N$  is the number of bumps.

velocities in the presence of capillary force are higher than those in its absence. Comparison of Figure 2.7 with Figure 2.6 shows that the electrostatic forces significantly increase the adhesion forces for both smooth and bumpy particles. As a result, the critical shear velocities needed to remove the particles increase accordingly. The relative increase of the critical shear velocity due to capillary in the presence of the electrostatic forces is not as large as that for the neutral particle. This further indicates the importance of electrostatic forces on particle adhesion and removal.

Hays [50] performed a series of experiment for electric detachment of charged toner particles from a nickel carrier bead. The toner particle charge was kept fixed at an average value of  $3 \times 10^{-14}$  C. Figure 2.8 compares the predicted critical electric detachment fields for bumpy particles with and without the capillary force with the experimental data of Hays [50]. It is observed that the detachment electric field increases significantly due to the presence of capillary force. Furthermore, the electric field intensity for particle detachment increases with the increase of the toner charge when the capillary force is present. In addition, the critical electric field intensity decreases with the increase of number of bumps both in the presence or absence of the capillary force.

Figure 2.8 also shows that the predicted detachment electric fields in the absence of capillary force are in reasonable agreement with the

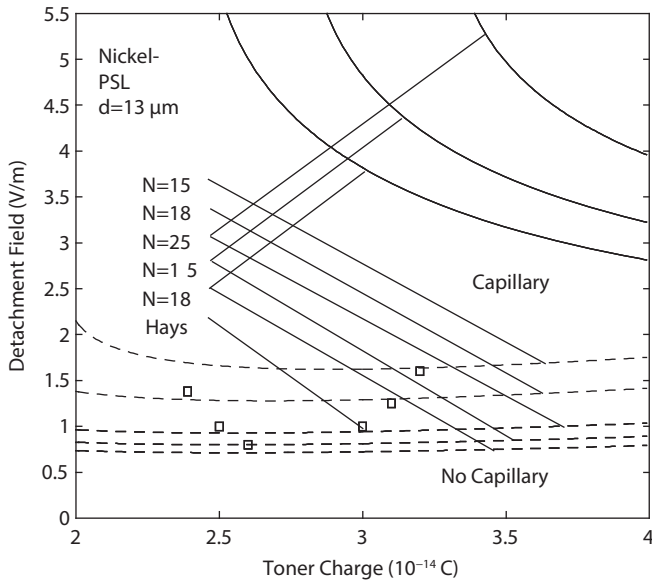


**Figure 2.8** Comparison of the electric detachment fields for bumpy particles with and without capillary force with the experimental data of Hays [50] for toner (polystyrene latex (PSL)) particles on a nickel carrier bead.  $N$  is the number of bumps.

experimental data for number of bumps in the range of 15 to 35 (Soltani and Ahmadi, [29]). While the precise number of bumps for toner particles modeled as bumpy spheres is not known,  $15 < N < 35$  is within the expected range.

Recently Goldasteh *et al.* [40–42] developed an improved Monte Carlo model for removal of rough particles that accounts for the random variations of parameters. It was found that the Monte Carlo simulation approach taking into account probabilistic distributions of surface roughness and particle size shows good agreement with the experimental data including those of Ibrahim *et al.* [30,38]

## 2.4 Summary and Conclusions

In this chapter, fundamentals of particle adhesion and removal were reviewed and particular attention was given to the effect of electrostatic and capillary forces. The available adhesion models were reviewed and the criteria for incipient rolling and sliding detachments as well as electrostatic lifting removal were described. Examples of predicted critical shear velocities for detaching particles of different sizes under different conditions

were discussed. The electric field strength needed for electrostatic removal of particles with different charges was also pointed out. Comparisons of the model predictions with the available experimental data were also presented. The presented results showed that:

- The critical shear velocity increases sharply as particle size decreases. Removal of nanometer size particles with hydrodynamical forces is rather difficult.
- The presence of electrostatic forces that are attractive significantly enhance the magnitude of the critical shear velocity needed to remove particles from a surface.
- Turbulent burst enhances the chance for particle removal from a surface.
- The presented models are in good agreement with the available experimental data.

## Acknowledgements

The financial support of the Environmental Protection Agency through the Center of Excellence of Syracuse University is gratefully acknowledged. Thanks are also given to Dr. Mehdi Soltani, Mr. Shigang Guo, Dr. Xinyu Zhang, Dr. Iman Goldasteh and Dr. Andrea Ferro for their contributions to various parts of this work.

## References

1. M. Corn, Adhesion of particles, in *Aerosol Science*, C. N. Davies (Ed.), pp. 359–392, Academic Press, New York (1966).
2. H. Krupp, Particle adhesion: Theory and experiment. *Adv. Colloid Interface Sci.*, 1, 111–140 (1967).
3. J. Visser, Adhesion of colloidal particles, in: *Surface and Colloid Science*, E. Matijevic (Ed.), Vol. 8, pp. 3–84, Plenum Press, New York (1976).
4. D. Tabor, Surface forces and surface interaction. *J. Colloid Interface Sci.*, 58, 2–13 (1977).
5. R.A. Bowling, An analysis of particle adhesion on semiconductor surfaces. *J. Electrochem. Soc.*, 132, 2208–2219 (1985).
6. K. L. Johnson, K. Kendall, and A. D. Roberts, Surface energy and contact of elastic solids. *Proc. Royal. Soc. Lond. Series A*, 324, 301–313 (1971).
7. B. V. Derjaguin, V. M. Muller, and Y. P. Toporov, Effect of contact deformation on the adhesion of particles. *J. Colloid Interface Sci.*, 53, 314–326 (1975).



8. C. J. Tsai, D. Y. H. Pui, and B. Y. H. Liu, Elastic flattening and particle adhesion. *Aerosol Sci. Technol.*, 15, 239–255 (1991).
9. D. Maugis, Adhesion of spheres: The JKR-DMT transition using a Dugdale model. *J. Colloid Interface Sci.*, 150, 243–269 (1992).
10. D. S. Rimai, L. P. DeMejo and W. Vreeland, The effect of Young's modulus on the surface-force-induced contact radius of spherical particles on polystyrene substrates. *J. Appl. Phys.*, 71, 2253–2258 (1992).
11. K. L. Mittal (Ed.) *Particles on Surfaces, 1–3: Detection, Adhesion and Removal*, Plenum Press, New York. (1988, 1989, 1991).
12. K. L. Mittal (Ed.) *Particles on Surfaces, 5–9: Detection, Adhesion and Removal*, CRC Press, Boca Raton, FL. (1999, 2002, 2003, 2006)
13. D.J. Quesnel, D.S. Rimai, and, and L.H. Sharpe (Eds.), *Particle Adhesion: Applications and Advances*, Taylor and Francis, New York (2001).
14. M. Corn and F. Stein, Re-entrainment of particles from plane surfaces. *J. Am. Ind. Hyg. Assoc.*, 26, 325–336 (1965).
15. J. S. Punjirath and D. R. Heldman, Mechanisms of small particle reentrainment from flat surfaces. *J. Aerosol Sci.*, 3, 429–440 (1972).
16. J. W. Healy, A review of resuspension models. In *Transuranics in Natural Environments*, M. G. White and P. B. Dunaway (Eds.), USERDA, Las Vegas, pp. 211–222. (1977).
17. G. A. Sehmel, Particle resuspension: A review. *Environment Intl.*, 4, 107–127 (1980).
18. W. J. Smith, F. W. Whicker and H. R. Meyer, Review and categorization of saltation, suspension and resuspension models, *Nuclear Safety*, 23, 685–699 (1982).
19. W. C. Hinds, *Aerosol Technology, Properties, Behavior and Measurement of Airborne Particles*, John Wiley and Sons, New York (1982).
20. K.W. Nicholson, A review of particle resuspension. *Atmospheric Environment*, 22, 2639–2651 (1988).
21. J. W. Cleaver, and B. Yates, Mechanism of detachment of colloidal particles from flat substrate in a turbulent flow. *J. Colloid Interface Sci.* 44, 464–474 (1973).
22. M. W. Reeks and D. Hall, On the resuspension of small particles by a turbulent flow. *J. Fluid Eng.*, 110, 165–171 (1988).
23. H. Y. Wen and J. Kasper, On the kinetics of particle re-entrainment from surfaces. *J. Aerosol Sci.*, 20, 483–498 (1989).
24. H. C. Wang, Effect of inceptive motion on particle detachment from surfaces. *Aerosol Sci. Technol.*, 13, 386–396. (1990).
25. C. J. Tsai, D. Y. H. Pui, and B. Y. H. Liu, Detachment of particles from disk surfaces of computer disk drives. *J. Aerosol Sci.*, 22, 737–746 (1991).
26. M. Soltani and G. Ahmadi, On particle adhesion and removal mechanisms in turbulent flows. *J. Adhesion Sci. Technol.*, 8, 763–785 (1994).
27. M. Soltani and G. Ahmadi, Particle detachment from rough surfaces in turbulent flows. *J. Adhesion*, 51, 105–123 (1995).

28. M. Soltani and G. Ahmadi, Direct numerical simulation of particle entrainment in turbulent channel flow. *Phys. Fluids*, 7A, 647–657 (1995).
29. M. Soltani and G. Ahmadi, Detachment of rough particles with electrostatic attraction from surfaces in turbulent flows, *J. Adhesion Sci. Technol.*, 13, 325–355 (1999).
30. A.H. Ibrahim, P.F. Dunn, and R.M. Brach, Microparticle detachment from surfaces exposed to turbulent air flow: Controlled experiments and modeling. *J. Aerosol Sci.*, 34, 765–782 (2003).
31. J. A. Greenwood and J. B. P. Williamson, Contact of nominally flat surfaces. *Proc. Roy. Soc. London A*, 295, 300–319. (1966).
32. J. A. Greenwood and J. H. Tripp, The elastic contact of rough spheres. *J. Appl. Mech.*, 67, 153–159 (1967).
33. D. S. Rimai and D. J. Quesnel, *Fundamentals of Particle Adhesion*. Global Press (Available through the Adhesion Society at Adhesionsociety.Org) (2001).
34. D. J. Quesnel, D. S. Rimai, and D.M., Schaefer, Aspects of particle adhesion and removal, in: *Developments in Surface Contamination and Cleaning: Fundamental and Applied Aspects*, R. Kohli and K.L. Mittal (Eds) pp. 475–501, William Andrew Publishing, Norwich, NY (2008).
35. D. Braaten, U. Paw and R. Shaw, Particle resuspension in a turbulent boundary layer observed and modeled. *J. Aerosol Sci.*, 21, 613–628 (1990).
36. Y.L. Wu, C.I. Davidson, and A.G. Russell, Controlled wind tunnel experiments for particle bounce off and resuspension. *Aerosol Sci. Technol.* 17, 245–262 (1992).
37. K.W. Nicholson, Wind tunnel experiments on the resuspension of particulate material. *Atmos. Environ. Part A.*, 27, 181–188 (1993).
38. A.H. Ibrahim, P.F. Dunn, and R.M. Brach, Microparticle detachment from surfaces exposed to turbulent air flow: Effects of flow and particle deposition characteristics. *J. Aerosol Sci.*, 35, 805–821 (2004).
39. P. Krauter, and A. Biermann, Reaerosolization of fluidized spores in ventilation systems. *Appl. Environ. Microbiol.* 73, 2165–2172 (2007).
40. I. Goldasteh, G. Ahmadi, and A. Ferro, A model for removal of compact, rough, irregularly shaped particles from surfaces in turbulent flows, *J. Adhesion*, 88, 766–786. (2012).
41. I. Goldasteh, G. Ahmadi, and A. Ferro, Monte Carlo simulation of micron size spherical particle removal and resuspension from substrate under fluid flow. *J. Aerosol Sci.*, 66, 62–71 (2013).
42. I. Goldasteh, G. Ahmadi, and A. Ferro, Wind tunnel study and numerical simulation of dust particle resuspension from indoor surfaces in turbulent flows, *J. Adhesion Sci. Technol.*, 27, 1563–1579 (2013).
43. B. V. Derjaguin, and V. P. Smilga, Electronic theory of adhesion. *J. Appl. Phys.*, 38, 4609–4616 (1967).
44. D. K., Davis, Surface charge and the contacts of elastic solids. *J. Phys. D: Appl. Phys.*, 6, 1017–1029 (1973).

45. W., Kottler, H. Krupp and H. Rabenhorst, Adhesion of electrically charged particles. *Z. Angew. Phys.*, 24, 219–223 (1968).
46. C. J. Mastrangelo, The effect of charge, size and shape of toner photoconductor adhesion in electrophotographic systems. *Photogr. Sci. Eng.*, 26, 194–197 (1982).
47. D. K. Donald, Electrostatic contribution to power-particle adhesion. *J. Appl. Phys.*, 40, 3013–3019 (1969).
48. D. K. Donald, Contribution of charge to powder particle adhesion, in *Recent Advances in Adhesion*, L. H. Lee (Ed.) Gordon and Breach, New York, pp. 129–143 (1973).
49. N. S. Goel and P. R. Spencer, Toner particle-photoreceptor adhesion, in *Adhesion Science and Technology*, L.H. Lee, (Ed.), Part B, Plenum Press, New York, pp. 763–829 (1975).
50. D. A. Hays, Electric field detachment of toner. *Photogr. Sci. Eng.*, 22, 232–235 (1978).
51. D. A. Hays, Electrostatics. Inst. Phys. Conf. Ser., The Institute of Physics, London and Bristol, 66, 237 (1983).
52. M. H. Lee and A. B. Jaffe, in: *Particles on Surfaces 1: Detection, Adhesion, and Removal*, K.L. Mittal, (Ed.), pp. 169–177, Plenum Press New York (1988).
53. H. A. Mizes, Adhesion of small particles in electric fields. *J. Adhesion Sci., Technol.* 8, 937–953 (1994).
54. A. D. Zimon, *Adhesion of Dust and Powder*. Consultants Bureau, New York (1982).
55. Y. M. Luzhnov, *Research in Surface Forces*, Izd. Nauka, Moscow (1967).
56. F. Podczeczek, J. M. Newton, and M. B. James, Influence of relative humidity of storage air on the adhesion and autoadhesion of micronized particles to particulated and compacted powder surfaces. *J. Colloid Interface Sci.*, 187, 484–491 (1997).
57. A.A. Busnaina and T. Elsayy, In: *Particle Adhesion: Applications and Advances*, D.J. Quesnel, D.S. Rimai and L.H. Sharpe (Eds.), Taylor and Francis, New York, pp. 391–409, (2001).
58. J. Tang and A.A. Busnaina, In: *Particle Adhesion: Applications and Advances*, D.J. Quesnel, D.S. Rimai and L.H. Sharpe (Eds.), Taylor and Francis, New York, pp. 411–419 (2001).
59. G. Ahmadi, S. Guo, , and X. Zhang, Particle adhesion and detachment in turbulent flows including capillary forces, *Particulate Sci. Technol.*, 25, 59–76 (2007).
60. D. Maugis and H. M. Pollock, Surface forces, deformation and adherence at metal microcontact. *Acta Metall.* 32, 1323–1334 (1984).
61. G. Ziskind, M. Fichman, and C. Gutfinger, Adhesion moment model for estimating particle detachment from a surface. *J. Aerosol Sci.* 28, 623–634 (1997).
62. X. Zhang and G. Ahmadi, Effects of capillary force and surface deformation on particle removal in turbulent flows, *J. Adhesion Sci. Technol.*, 21, 1581–1611 (2007).

63. G. Ahmadi, and S. Guo, Bumpy particle adhesion and removal in turbulent flows including electrostatic and capillary forces. *J. Adhesion*, 83, 289–311 (2007).
64. N. A. Fuchs, *The Mechanics of Aerosols*, Pergamon Press, Oxford (1964).
65. G. M. Hidy, *Aerosols, An Industrial and Environmental Science*, Academic Press, New York. (1984).
66. G. C. Hartmann, L. M. Marks, and C. C. Yang, Physical models for photoactive pigment electrophotography. *J. Appl. Phys.*, 47, 5409–5420 (1976).
67. D. W. Cooper, M. H. Peters, and R. J. Miller, Predicted deposition of sub-micron particles due to diffusion and electrostatics in viscous axisymmetric stagnation-point flow. *J. Aerosol Sci.*, 11, 133–143 (1989).
68. F. G. Fan and G. Ahmadi, On the sublayer model for turbulent deposition of aerosol particles in the presence of gravity and electric field. *Aerosol Sci. Technol.*, 21, 49–71 (1994).
69. M. E. O’Neil, A sphere in contact with a plane wall in a slow linear shear flow. *Chem. Eng. Sci.*, 23, 1293–1298 (1968).

# Microscopic Particle Contact Adhesion Models and Macroscopic Behavior of Surface Modified Particles

Katja Mader-Arndt\*, Zinaida Kutelova and Jürgen Tomas

*Mechanical Process Engineering, Department of Process Engineering and Systems Engineering, Otto von Guericke University Magdeburg, Magdeburg, Germany*

---

## Abstract

Attractive adhesion forces, and especially the van der Waals adhesion forces, are crucial for the product design of dry cohesive particles. These directly affect the flow properties of products. For this reason, a method for modifying the micro-mechanical properties of glass is presented in this chapter. The main focus at this juncture is the chemical surface modification of glass or silica particles.

A comparison between single particle and particle packing experiments is made to show how to characterize the surface properties. For single particle experiments the principles of atomic force microscopy (AFM) and nanoindentation are discussed. In contrast, particle packing experiments with a ring shear tester are conducted. Using the model system: dry, spherical glass particles, the results of these techniques are illustrated. Different micromechanical contact models are discussed with regard to the model-based back-calculation of shear- and nanoindentation results.

**Keywords:** Adhesion, contact model, surface energy, surface modification, powder properties, particles

## 3.1 Introduction

Adhesion forces play an important role in many industrial applications. Particularly in ranges where products are developed through product

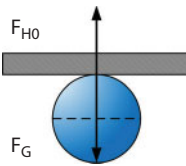
---

\*Corresponding author: katja.mader@ovgu.de

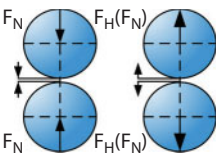
design, such as pelletizing in the pharmaceutical industry or the transport of powders in a silo, handling problems occur because of the adhesion effect. Cohesive powders consist of fine, ultrafine and nano-dispersed particles. This means the particle size ranges from micro- to nanometers [1]. With the decrease of particle size and stiffness, the specific surface of particles and thus the influence of the adhesion force increases. The strongest attractive forces between dry particles are the van der Waals adhesion forces [2, 3]. With decreasing particle sizes the characteristic attraction forces ( $F_{H0}$ ) exceed the weight forces ( $F_G$ ) by several orders of magnitude. This fact causes e.g. practical flow problems in powder handling or cleaning problems in silicon wafer processing (Table 3.1).

On the basis of the dimensionless elastic-plastic contact consolidation coefficient  $\kappa$ , the approximated linear adhesion force intensification  $F_H(F_N)$  of particles by contact flattening, can be evaluated (Table 3.2). This results from a preloading with a normal load  $F_N$  [6]. A stiff contact behavior with low pronounced adhesion potential is characterized by low values of the contact consolidation coefficient  $\kappa = 0 - 0.1$  and consequently  $F_H \approx F_{H0}$ . Similarly, with increasing flattening, the contact stiffness decreases  $\kappa$  and

**Table 3.1** Adhesiveness of fine, dry particles [4, 5].

	Particle size $d$ ( $\mu\text{m}$ )	Ratio $F_{H0}/F_G$	Degree of adhesiveness
	10 – 100	$1 - 10^2$	Slightly adhesive
	1 – 10	$10^2 - 10^4$	Adhesive
	0.01 – 1	$10^4 - 10^8$	Very adhesive

**Table 3.2** Evaluation of the adhesion force intensification [4].

	Particle size $d$ ( $\mu\text{m}$ )	Contact consolidation coefficient $\kappa$	Nature of the contact behavior
	1 – 100	0.1 – 0.3	Soft particle contact
	0.1 – 1	0.3 – 0.8	Very soft particle contact
	0.01 – 0.1	> 0.8	Extremely soft particle contact

the adhesion force  $F_H$  increases. The contact point is deformed to contact area with increasing adhesion potential. Macroscopically, this effect is experienced by the load-dependent increase of compression strength and shear resistance of fine-dispersed cohesive powders. This process is referred to as pre-consolidation. Because of this typical consolidation behavior of fine, dry and adhesive particles, the significant influence of the load-dependent adhesion force must be evaluated from microscopic point of view.

To influence the adhesion force, and thus the flow properties of bulk solids, different methods exist. For example, the usage of flow additives [5] can change the flow behavior from cohesive to free flowing. Besides, there is the possibility to modify the flow properties by a chemical functionalization method [7]. In this process the surface of the material is hydrophilized or hydrophobized by the method of silanization [8]. By this technique it is possible to directly control the adhesion forces between particles.

Therefore, the aim of the present work is to discuss the direct influence of the chemical modification of spherical glass particles in relation to the adhesion force. In order to characterize the particle properties various methods will be presented. For this purpose the characterization of material properties is distinguished between micro- and macroscopic determination. The microscopic assessment is discussed using the method of atomic force microscopy (AFM - direct adhesion force measurement) and nanoindentation (model-based back-calculation). Via shear measurements the macroscopic characterization of cohesive, surface functionalized bulk materials is explained. It is designed to bridge the gap between the microscopic and macroscopic contact behaviors of cohesive, fine, dry bulk solids by considering an elastic-plastic contact model with variable adhesion.

## 3.2 Constitutive Contact Models

The main focus in the following section is on the characteristic compliant contact of isotropic, dry, stiff, fine and monodispersed particles and substrates under the effect of a normal load. If the contact is continuously loaded a range of elastic deformations is yielded (section 3.2.1.). The transition to the elastic-plastic deformation is characterized by the yield point, see section 3.2.2. In section 3.2.3 the dominant plastic contact behavior, which is due to constant load and increasing deformation, is shown. At a defined load the contact is unloaded elastically, see section 3.2.4. The most important characteristics in terms of deformation effects during the particle-particle contact and the appropriate behavior are illustrated in Table 3.3.

Table 3.3 Overview of the considered contact models.

Authors	Year	Assumptions	Equations of the contact models
Tresca [32]	1868	yield criterion, maximum shear stress	$Y = 2 \cdot \tau_{\max} = \max\{ \sigma_1 - \sigma_2 ,  \sigma_2 - \sigma_3 ,  \sigma_3 - \sigma_1 \}$
Hertz [12]	1882	elastic, non-adhesive contact	$\left(\frac{p_{el}}{p_{\max}}\right)^2 = 1 - \left(\frac{r_K}{r_{K,el}}\right)^2$ $F_N(h_K) = \frac{2}{3} \cdot E^* \cdot \sqrt{r_{1,2} \cdot h_K^3}$
Huber [13]	1904	elastic contact with principal stresses	$\frac{\sigma_Y(r_K)}{p_{\max}} = -\frac{1-2 \cdot \nu}{3} \cdot \frac{r_{K,el}^2}{r_K^2} \cdot \left[ 1 - \left(1 - \left(\frac{r_K}{r_{K,el}}\right)^2\right)^{\frac{3}{2}} \right] - \sqrt{1 - \frac{r_K^2}{r_{K,el}^2}}$ for $r_K \leq r_{K,el}$ $\frac{\sigma_Y(r_K)}{p_{\max}} = -\frac{1-2 \cdot \nu}{3} \cdot \frac{r_{K,el}^2}{r_K^2}$ for $r_{K,el} \leq r_K$
von Mises [31]	1913	yield criterion, elastic strain energy	$Y = \sqrt{3 \cdot J_2} = \frac{1}{6} \left\{ (\sigma_1 - \sigma_2)^2 + (\sigma_2 - \sigma_3)^2 + (\sigma_3 - \sigma_1)^2 \right\}$
Abbott and Firestone [40], Greenwood and Tripp [41]	1933, 1970	fully plastic contact	$F = A \cdot H$ $A = 2 \cdot \pi \cdot r \cdot h_K$ $F_N(d) = 2 \cdot \pi^2 \cdot (\eta \cdot \beta \cdot \sigma)^2 \cdot H \cdot A \cdot E_2 \cdot \left(\frac{d}{\sigma}\right)$



Authors	Year	Assumptions	Equations of the contact models
Johnson, Kendall and Roberts [21]	1971	elastic contact, constant adhesion	$r_K^3 = \frac{3 \cdot r_{1,2}}{2 \cdot E^*} \left( F_N + F_{H,JKR} + \sqrt{2 \cdot F_{H,JKR} \cdot F_N + F_{H,JKR}^2} \right)$
Dahneke [20]	1975	elastic contact, variable adhesion	$F_H = F_{H0} + A_K \cdot p_{vdw} = \frac{C_{H,sls} \cdot r_{1,2}}{6 \cdot a_0^2} \cdot \left( 1 + \frac{2 \cdot h_K}{a_0} \right)$
Derjaguin, Muller and Toporov [18]	1975	elastic contact, constant adhesion	$F_{H0} = 4 \cdot \pi \cdot r_{1,2} \cdot \left( \sigma_{sg} - \frac{\sigma_{ss}}{2} \right)$
Maugis and Pollock [53]	1984	elastic-plastic contact, variable adhesion, unloading	$F_{N,Brittle} = \sigma_{ss} \cdot E^* \cdot \sqrt{\frac{F_N}{\pi \cdot p_f^3}} \quad F_{N,Ductile} = \pi \cdot r_{K,f}^2 \cdot \sigma_f$
Walton and Braun [54]	1986	plastic contact, unloading	$F_{N,load} = k_{N,1} \cdot h_K \quad F_{N,unload} = k_{N,2} \cdot (h_K - h_{K,E})$
Chang, Etsion and Bogy [36]	1987	elastic-plastic contact	$F = A \cdot K \cdot H \quad A = 2 \cdot \pi \cdot r \cdot h_K \quad K = 0.454 + 0.41V$
Thornton [43]	1991	elastic contact, constant adhesion, unloading	$\psi_{load}^3 = 1 - \frac{F_T + \mu_i \cdot \Delta F_N}{\mu_i \cdot F_N} \quad \psi_{unload}^3 = 1 - \frac{F_T^* - F_T + 2 \cdot \mu_i \cdot \Delta F_N}{2 \cdot \mu_i \cdot F_N}$

Table 3.3 Overview of the considered contact models (continued).

Authors	Year	Assumptions	Equations of the contact models
Sadd, Tai and Shukla [55]	1993	elastic contact, unloading	$F_{N,load} = \alpha_{load} \cdot h_K^p \cdot F_{N,unload} = \alpha_{unload} \cdot h_K^{p+q}$
Greenwood [23]	1997	elastic contact, variable adhesion	$\delta = \frac{r_{K,el}^2}{r} - k \cdot \left( \frac{r_{K,out}^2}{r} - \frac{r_{K,el}^2}{r} \right) \quad \sigma_0 = k \cdot \frac{2 \cdot E^*}{\pi \cdot r} \cdot \left( r_{K,out}^2 - r_{K,el}^2 \right)^{\frac{1}{2}}$
Thornton and Ning [56]	1998	elastic-plastic contact, variable adhesion, unloading	$F_{N,load} = \frac{2}{3} \cdot E^* \cdot \sqrt{r_{1,2} \cdot h_{K,Y}^3} + \pi \cdot p_f \cdot r_{1,2} \cdot (h_K - h_{K,Y})$ $F_{N,unload} = \frac{2}{3} \cdot E^* \cdot \sqrt{r_{1,2} \cdot (h_K - h_{K,U})^3}$
Tomas [58]	2000	elastic-plastic contact, variable adhesion	$F_H = F_{H0} + \left( \frac{\frac{P_{VdW}}{P_f}}{\frac{2}{3} + \frac{A_{pl} \cdot P_{VdW}}{(3 \cdot A_K) \cdot P_f}} + \frac{P_{VdW}}{\eta_K \cdot t} \right) \cdot (F_{H0} + F_N)$
Mesarović and Johnson [50, 22]	1985, 2000	elastic-plastic contact, fully elastic, unloading	$F_{pull-off} = \frac{2 \cdot \omega \cdot E^* \cdot a_0}{H}$ $\frac{F_1}{F_0} = \frac{F_1}{\pi \cdot a_0^2 \cdot P_0} = \frac{2}{\pi} \cdot \left[ \text{Arcsin} \left( \frac{a}{a_0} \right) - \frac{a}{a_0} \cdot \sqrt{1 - \left( \frac{a}{a_0} \right)^2} \right]$

Authors	Year	Assumptions	Equations of the contact models
Vu-Quoc, Zhang and Lesburg [49]	2000	elastic unloading	$\alpha - \alpha_{\text{res}} = \frac{(a^e)^2}{(C_R)_{F=F_{\text{max}}}} \cdot R \quad \text{for } F_{\text{max}} > F_Y$
Kogut and Etsion [38]	2002	elastic-plastic and fully plastic contact, FEM-based	$F = 1.03 \cdot F_Y \cdot \left( \frac{\delta}{\delta_Y} \right)^{1.425} \quad \text{for } 1 \leq \frac{\delta}{\delta_Y} \leq 6$ $F = 1.40 \cdot F_Y \cdot \left( \frac{\delta}{\delta_Y} \right)^{1.263} \quad \text{for } 6 \leq \frac{\delta}{\delta_Y} \leq 110$
Kogut and Komvopoulos [45]	2004	elastic unloading, indentation	$E_{R\delta} = \frac{\delta_i - \delta_r}{\delta_i}$
Jackson and Green [39]	2005	plastic contact, FEM-based	$F_N = \frac{4}{3} \cdot \left( \frac{R}{E} \right)^2 \cdot \left( \frac{C}{2} \cdot \pi \cdot S_Y \right)^3 \quad C = 1.295 \cdot \exp(0.736 \cdot \nu)$
Etsion, Kligerman and Kadin [51]	2005	elastic unloading, FEM-based	$F = F_{\text{max}} \cdot \left( \frac{h_{K,\text{el}}}{h_{K,\text{max}} - h_{K,0}} \right)^n \quad n = 1.5 \cdot \left( \frac{h_{K,\text{max}}}{h_{K,Y}} \right)^{-0.0331}$
Kadin, Kligerman and Etsion [52, 44]	2008	unloading	$dF(r) = 2 \cdot \pi \cdot r \cdot \frac{8 \cdot \Delta Y}{3 \cdot \varepsilon} \cdot \left[ (\Delta(r)+1)^{-3} - (\Delta(r)+1)^{-9} \right] dr$

Table 3.3 Overview of the considered contact models (continued).

Authors	Year	Assumptions	Equations of the contact models
Choi [46]	2008	unloading	$F_{\text{unload}} = \phi' \cdot \left( \frac{k}{E} \right)^{\frac{2}{5}} \cdot \rho^{\frac{3}{5}} \cdot D^2 \cdot V^{\frac{6}{5}} \quad k = \left[ \frac{(1-v_t^2) + (1-v^2) \cdot E_t}{E} \right]$
Li and Gu [47]	2009	elastic-plastic contact, extended unloading model of Thornton	$F_N = F_Y \cdot \left[ \frac{3}{2} \left( \frac{a}{a_Y} \right)^2 \cdot \left( \frac{p_0}{p_Y} \right) - \frac{1}{2} \cdot \left( \frac{p_0}{p_Y} \right)^3 \right]$ $F_{N,\text{unload}} = F_Y \cdot \left( \frac{a}{a_Y} \right)^3 \cdot \left( \frac{R_1}{R} + \frac{3 \cdot n \cdot R_1 \cdot B_n \cdot a^{2n-2}}{2n+1} \right)$ $B_n = \frac{2 \cdot 4 \cdot \dots \cdot 2n}{1 \cdot 3 \cdot \dots \cdot (2n-1)} \cdot \beta_n$

### 3.2.1 Elastic Contact Deformation

After the approach from an infinite distance to a minimum separation the two spherical contact partners or a particle and a substrate (see Figure 3.1 a) are in direct contact with a molecular minimum distance  $a_0$ . This surface distance can be calculated for van der Waals attraction and Born repulsion as the first derivative of molecular Lennard-Jones potential by setting it equivalent to zero. For an adhesive particle contact the characteristic attractive van der Waals adhesion force  $F_{H0}$  will be effective, see Eq. (3.1)

$$F_N(h_K) = -\frac{C_{H,sls} \cdot r_{1,2}}{6 \cdot (a_0 - h_K)^2} = -\frac{F_{H0} \cdot a_0^2}{(a_0 - h_K)^2} \quad (3.1)$$

The Hamaker constant  $C_{H,sls}$  [9] can be determined for the respective contact partners with solid-liquid-solid (sls) interactions included [10] in accordance with the Lifshitz theory [11]. The distance between the spheres without any contact deformation  $h_K = 0$  is equal to the minimum distance  $a_0$  between the contact partners.  $r_{1,2}$  describes the effective radius of the two spheres (for particle-substrate contact  $r_{1,2}$  is the radius of the particle) and  $F_{H0}$  the van der Waals force.

The elastic, non-adhesive contact between two particles with diameters  $d_1$  and  $d_2$  and the maximum elastic contact radius  $r_{K,el}$  was first described 1882 by Hertz [12]. The contact pressure  $p_{el}(r_k)$  within a circular contact

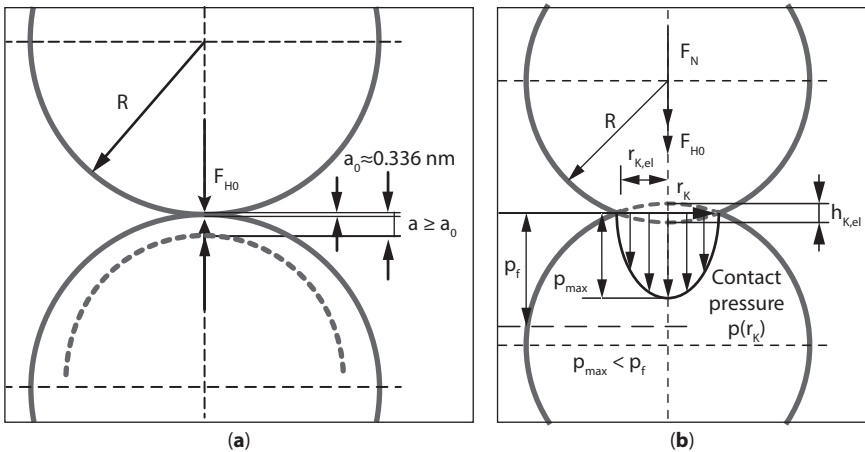


**Figure 3.1** Characteristic contact deformation of two spherical particles, a) approach, b) elastic contact deformation.

zone with the elastic contact radius  $r_{K,el}$  is assumed to be elliptically distributed (Eq. (3.2))

$$\left(\frac{p_{el}}{p_{max}}\right)^2 = 1 - \left(\frac{r_K}{r_{K,el}}\right)^2, \quad (3.2)$$

where  $r_K$  is the contact radius and  $p_{max}$  the maximum stress, see Figure 3.1 b).

The maximum contact stress  $p_{max}$  for the elastic deformation is always lower than the micro-yield strength  $p_f$ . If  $p_f$  is reached, the irreversible flow of the particulate materials starts. According to Hertz [12] the relation between the maximum elastic contact radius  $r_{K,el}$  and the normal force  $F_N$  can be described with Eq. (3.3)

$$r_{K,el} = \left(\frac{3 \cdot r_{1,2} \cdot F_N}{2 \cdot E^*}\right)^{\frac{1}{3}}. \quad (3.3)$$

For two different sized particles, the effective contact radius  $r_{1,2}$  is given by Eq. (3.4)

$$r_{1,2} = \left(\frac{1}{r_1} + \frac{1}{r_2}\right)^{-1}. \quad (3.4)$$

Thus, Hertz derived a non-linear, non-adhesive elastic normal force-displacement law, which also enables determination of the modulus of elasticity  $E$  and the Poisson ratio  $\nu$  with Eq. (3.5)

$$E^* = 2 \cdot \left(\frac{1-\nu^2}{E_1} + \frac{1-\nu^2}{E_2}\right)^{-1}. \quad (3.5)$$

Considering the principal stresses, which were introduced for the inner and outer contacts by Huber [13], the displacement of both contact partners is given by Eq. (3.6):

$$h_K = \frac{r_{K,el}^2}{r_{1,2}}. \quad (3.6)$$

Combining Eq. (3.5) and Eq. (3.6) leads to the normal force-displacement function of the non-linear Hertz law without adhesion (Eq. (3.7))

$$F_N(\mathbf{h}_K) = \frac{2}{3} \cdot E^* \cdot \sqrt{r_{1,2} \cdot h_K^3}. \quad (3.7)$$

In addition Lurje [14] and Chen *et al.* [15] described analytical and numerical contact models of spatial stress distributions within a sphere. Apparently, it is not possible to neglect the van der Waals forces between two particles so the existing model has often been modified. The additional contribution to the adhesion force was considered by Sperling [16], Derjaguin [17, 18], Dahneke [19, 20], Johnson [21, 22], Greenwood [23] and Peukert [24, 25, 26].

According to the DMT model by Derjaguin, Muller and Toporov [18, 27] Eq. (3.7) is enhanced with  $F_{H,DMT}$ . This model is suitable for small, rigid particles and substrates [27, 28, 29]. In 1971 Johnson, Kendall and Roberts also [21] developed a contact model with adhesion, the JKR theory. Contrary to the DMT model, in which half of the interaction force is assumed outside the contact, in the JKR theory the entire interaction force lies within the contact radius. The contact radius with a constant adhesion force  $F_{H,JKR}$  is given by Eq. (3.8):

$$r_K^3 = \frac{3 \cdot r_{1,2}}{2 \cdot E^*} \cdot \left( F_N + F_{H,JKR} + \sqrt{2 \cdot F_{H,JKR} \cdot F_N + F_{H,JKR}^2} \right). \quad (3.8)$$

According to Eq. (3.6) and Eq. (3.8) the normal force is (Eq. (3.9))

$$F_N = \frac{2}{3} \cdot E^* \cdot \sqrt{r_{1,2} \cdot h_K^3} - \sqrt{\frac{4 \cdot E^* \cdot F_{H,JKR}}{3} \cdot \sqrt{r_{1,2} \cdot h_K^3}}. \quad (3.9)$$

This model is suitable for relatively large and soft particles and substrates [28, 29, 30]. The normal force-displacement behavior for the presented models is shown in Figure 3.2.

### 3.2.2 Elastic-plastic Contact Deformation

The elastic-plastic contact deformation describes the transition from ideal elastic to ideal plastic material deformation. This occurs when the normal force  $F_N$  exceeds the yield point  $F_{N,Y}$ . The resulting elastic-plastic yield limit (Figure 3.3 b)) cannot be exceeded because of the incipient flow. Therefore, the yield limit is referred to as a dynamic stress limit function. The point

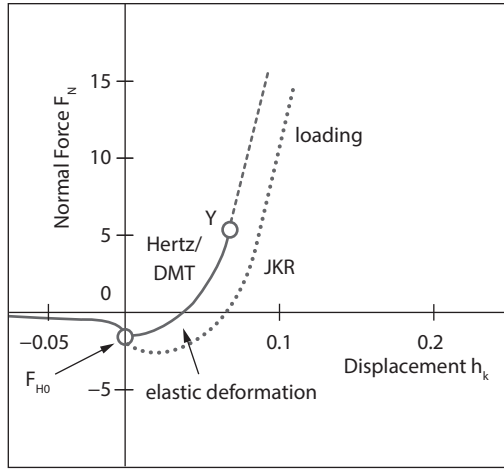


**Figure 3.2** Normal force-displacement behavior of the elastic contact. Hertz/DMT model compared with JKR theory.

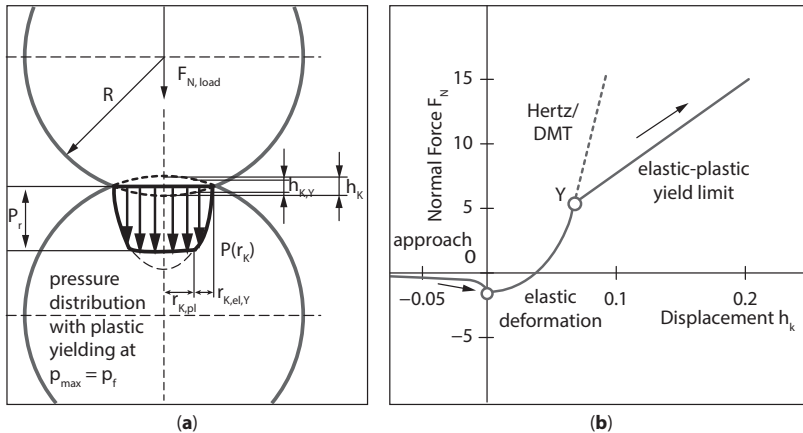


**Figure 3.3** Elastic-plastic contact, a) stress distribution of the elastic-plastic contact of two particles, b) normal force-displacement behavior with the elastic-plastic yield limit.

at which the material begins to flow depends on the flow pressure of the material. On loading of spherical/spherical or spherical/planar materials a circular contact area is formed as shown in Figure 3.3 a).

The maximum stress  $p_{max}$  is located in the middle of the circular area and is equal to the micro-yield strength  $p_f$  ( $p_{max} = p_f$ ). The formed plastic contact radius  $r_{K,pl}$  increases with increasing load. The internal compressive stresses in the outer part of the contact are smaller compared to the micro-yield stress, so that elastic deformation occurs in this area [22].



The literature contains two, widely used flow criteria to determine the micro-yield strength of deformable materials: the theory of von Mises [31] and Tresca [32]. The calculation of the yield point is based on Eq. (3.10)

$$Y = \sqrt{3 \cdot J_2} = \frac{1}{6} \left\{ (\sigma_1 - \sigma_2)^2 + (\sigma_2 - \sigma_3)^2 + (\sigma_3 - \sigma_1)^2 \right\}, \quad (3.10)$$

$\sigma_1, \sigma_2, \sigma_3$  represent the principal stresses and  $J$  the second invariant of the stress deviator [22].

On the contrary, in the Tresca criterion the maximum stress deviation or maximum shear stress  $\tau_{\max}$  is responsible for flow (Eq. (3.11)) [22, 33, 34]

$$Y = 2 \cdot \tau_{\max} = \max \left\{ |\sigma_1 - \sigma_2|, |\sigma_2 - \sigma_3|, |\sigma_3 - \sigma_1| \right\}. \quad (3.11)$$

The displacement-dependent elastic-plastic contact area ratio  $\kappa_A$  (Eq. (3.12)) describes the contribution of the circular inner plastic contact area  $A_{\text{pl}}$  and total contact area  $A_K$  including the annular elastic deformation [35]

$$\kappa_A = \frac{2}{3} + \frac{1}{3} \cdot \frac{A_{\text{pl}}}{A_K} = 1 - \frac{1}{3} \cdot \left( \frac{h_{K,Y}}{h_K} \right)^{\frac{1}{3}} = \frac{2}{3} \dots 1. \quad (3.12)$$

For an ideal elastic deformation  $\kappa_A$  is equal to 2/3 and for perfectly plastic deformation it is unity.

The effective normal force results for a particle-particle contact with adhesion into Eq. (3.13)

$$F_N(h_K) = \pi \cdot r_{1,2} \cdot p_f \cdot (\kappa_A - \kappa_p) \cdot h_K - F_{H0}. \quad (3.13)$$

$\kappa_p$  is the plastic repulsion coefficient (Eq. (3.14)), which depends on the van der Waals bond stress  $p_{\text{vdW}}$  within the contact area and the yield pressure at particle surface  $p_f$  due to stronger solid (covalent, metallic or ionic) bonds.

$$\kappa_p = \frac{p_{\text{vdW}}}{p_f} = \frac{C_{H,\text{sls}}}{6 \cdot \pi \cdot a_0^3 \cdot p_f} = \frac{4 \cdot \gamma_{\text{sls}}}{a_0 \cdot p_f} < 1, \quad (3.14)$$

with  $\gamma_{\text{sls}} \approx 0.25 - 50 \text{ mJ/m}^2$  surface energy (solid-liquid-solid) and consequently  $p_{\text{vdW}} \approx 3 - 600 \text{ MPa}$ , see for example [1].

### 3.2.3 Plastic Contact Deformation

The plastic deformation is defined as the irreversible dislocation of the molecular structure of the material. As described in section 3.2.2 the plastic deformation starts on exceeding the yield point. For a certain load, which depends on the material, the entire contact is dominantly plastically deformed. In Figure 3.4 the stress distribution for a plastic particle-particle contact is shown.

The stress distribution is linear and forms a purely plastic contact radius  $r_{K,pl}$ . This radius is calculated by means of the Pythagorean Theorem, therefore the normal force is given by Eq. (3.15)

$$F_N = p_f \cdot A_K = p_f \cdot \pi \cdot d_{1,2} \cdot h_K \quad (3.15)$$

There are several models in practice which describe the elastic-plastic and plastic contact deformations (see Table 3.3). Thus, Chang, Etsion and Bogy [36] developed in 1987 the CEB-model for the determination of the elastic-plastic contact. It describes the plastic deformation near the contact zone and the vertical stress distribution. The model identifies a discontinuity in the normal force and stiffness, as Chang verified in [37].

On the contrary, the Kogut and Etsion FEM-based model [38] illustrates the elastic-plastic and fully plastic deformation of materials. It describes the normal forces in the range of contact overlap [29]. However, the model is not suitable for large deformations. Jackson and Green found with further FEM studies that the ratio between the yield limit and the hardness changes [39]. Most of these contact models are based on the full plastically model of Abbott and Firestone from the year 1933 [40]. Originally, it was developed to describe erosion processes for the contact of rough material

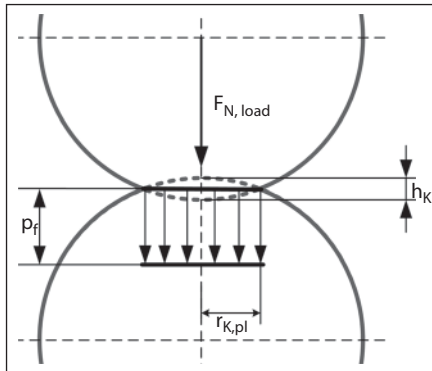


Figure 3.4 Stress distribution in a plastically deformed particle contact.

and a rigid plate. However, now it is used in the literature to characterize the deformation process of materials. A further development of this model is the theory of Greenwood and Tripp [41].

### 3.2.4 Unloading

In the literature a variety of models exist, which describe the unloading behavior of contacts. While Wu *et al.* [42] and Thornton [43] described the restitution and impact with unloading, Kadin *et al.* [44] specified the dependency on the residual surface roughness, Kogut and Komvopoulos [45] evaluated the mechanical properties at the indentation and Choi [46] characterized the damage due to eroding particles. Johnson [22] derived in 1985 an analytical model for the unloading of an elastic-plastic spherical contact considering a completely elastic unloading. In this model the curve runs along an extended parabolic Hertz-function (see Eq. (3.7)) between the unloading point U and the abscissa intersection point E (Figure 3.5 b)).

Li and Gu [47] extended the model of Thornton [43] for the unloading of an elastic-plastic contact of a deformable plate and a rigid sphere. Their analytical results are consistent with the finite element results of Yan and Li [48]. Further analytical models for unloading of relatively small and large contacts were published by Vu-Quoc *et al.* [49] as well as by Mesarovic and Johnson [50] in 2000. Etsion *et al.* [51] presented the first accurate solution for the unloading of an elastic-plastic spherical contact, which was based on FEM. Kadin *et al.* [52] extended this model considering the influence of adhesiveness.

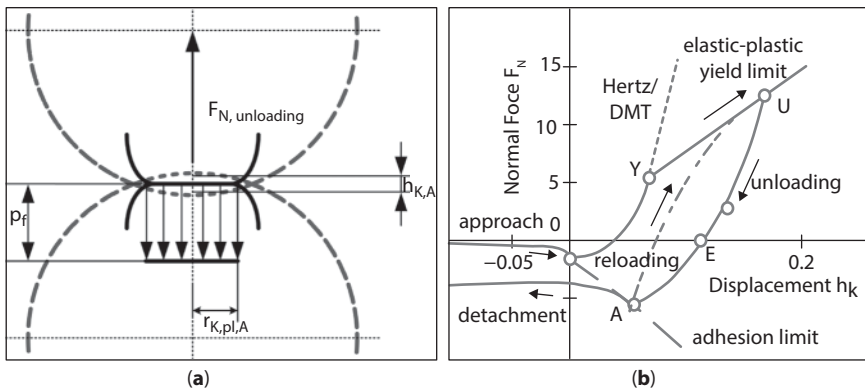


**Figure 3.5** Normal force-displacement behavior of a particle-particle contact on unloading, a) stress distribution for unloading, b) characteristic normal force-displacement behavior.

The following functions for unloading were specified by Maugis and Pollock [53], Walton and Braun [54], Sadd *et al.* [55] and Thornton and coworkers [56, 57]. In Figure 3.5 b) the extended parabolic Hertz-function for unloading is shown. After reaching the abscissa-intersection point E, the contact is ideally plastically deformed (see Figure 3.5 a)). The intersection between the abscissa and the unloading curve  $h_{K,E}$  is given by Eq. (3.16)

$$h_{K,E} = h_{K,U} - \sqrt[3]{h_{K,Y} \cdot h_{K,U}^2}. \quad (3.16)$$

The unloading curve runs along the points U-A (Eq. (3.17)) to the intersection  $h_{K,A}$  on the adhesion limit

$$F_{N,Unload} = \frac{2}{3} \cdot E^* \cdot \sqrt{r_{1,2} \cdot (h_K - h_{K,A})^3} - F_{H,A}. \quad (3.17)$$

The reloading curve runs between A-U with Eq. (3.18)

$$F_{N,Reload} = -\frac{2}{3} \cdot E^* \cdot \sqrt{r_{1,2} \cdot (h_{K,U} - h_K)^3} + F_{N,U}. \quad (3.18)$$

The adhesion force at the detachment point is calculated by a combination of the elastic-plastic yield limit (Eq. (3.13)), the adhesion force  $F_H = F_{H0} + A_K p_{vdW}$  and  $h_K = h_{K,A}$ , see Eq. (3.19)

$$F_{H,A} = F_{H0} + \pi \cdot r_{1,2} \cdot p_{vdW} \cdot h_{K,A}. \quad (3.19)$$

$p_{vdW}$  describes the acting van der Waals attraction with  $p_{vdW} = \kappa_p p_f$ ,  $\kappa_p$  is the plastic repulsion coefficient and  $p_f$  the solid surface strength due to covalent, metallic, ionic, hydrogen or van der Waals bonds.

The unloading and reloading hysteresis follows from the energy absorption or dissipation  $W_{diss}$  of the elastic-plastic contact, which is assumed as a lenticular area between unloading and reloading curves (see Eq. (3.20))

$$W_{diss} = \int_{h_{K,A}}^{h_{K,U}} F_{N,reload}(h_K) dh_K - \int_{h_{K,A}}^{h_{K,U}} F_{N,unload}(h_K) dh_K. \quad (3.20)$$

If the adhesion limit is reached, the contact partners detach from each other with an increasing surface distance  $a$  (see Eq. (3.21))

$$a = a_{F=0} + h_{K,A} - h_K. \quad (3.21)$$

The function is a short-ranged hyperbolic adhesion force curve with Eq. (3.22)

$$F_N(h_K) = -\frac{F_{H0} \cdot a_0^2}{(a_0 + h_{K,A} - h_K)^2} - \frac{\pi \cdot r_{1,2} \cdot \kappa_P \cdot P_f \cdot h_{K,A}}{(a_0 + h_{K,A} - h_K)^3} \cdot a_0^3, \quad (3.22)$$

and can be referred as pull-off force. At a few nanometers surface distance  $-h_K$  the normal force approach nearly zero,  $F_N \approx 0$ .

Each of the presented contact models can be applied for both the contact between particle-particle as well as for particle-substrate contacts by mathematical adaptation.

### 3.3 Macroscopic Powder Behavior – Continuum Mechanics Approach

The description of all the interactions between the single particles in a powder is a scientific challenge, because of the huge number of inter-particle forces that have to be taken into account [59]. Thus, in the powder mechanics the continuum mechanics approach is preferred. It considers the forces that are acting on a bulk volume element, which is large enough so that the local particle interactions between the single particles can be neglected [59].

In the powder mechanics the particle flow is described as irreversible plastic deformation within the bulk solid. This deformation is caused from internal shear stresses which somewhere within the powder (within any shear plane) cross a certain bulk material specific stress limit. In order to determine this stress limit, knowledge of the stress state inside the bulk element is required. The stress state can be described using as example a bulk solid element, at walls of which it is assumed that only normal forces ( $\sigma_v$  and  $\sigma_h$ ) are acting (Figure 3.6 a)). If one cuts one rectangular element from the powder element, and balances the forces, then after some transformations one obtains Eq. (3.23) and Eq. (3.24):

$$\sigma_\alpha = \frac{\sigma_v + \sigma_h}{2} + \frac{\sigma_v - \sigma_h}{2} \cos(2\alpha), \quad (3.23)$$

$$\tau_\alpha = \frac{\sigma_v - \sigma_h}{2} \sin(2\alpha). \quad (3.24)$$

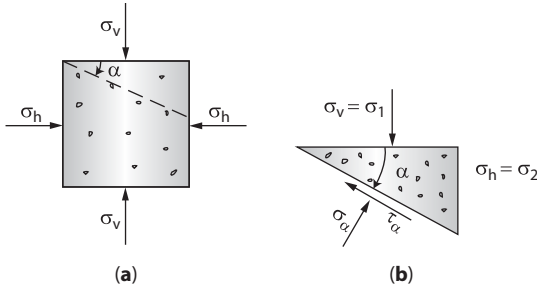


**Figure 3.6** a) Bulk solid element with vertical and horizontal forces acting on it ( $\sigma_v > \sigma_h$ ), b) rectangular powder element.

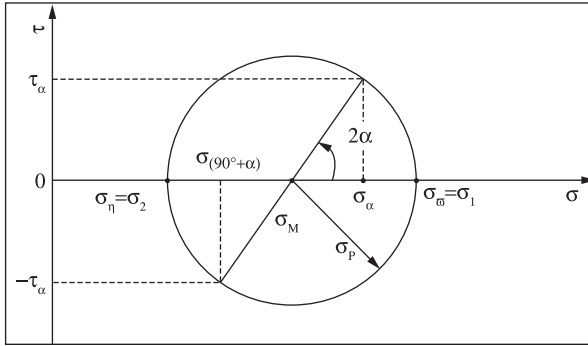


**Figure 3.7** Mohr circle, with which all stresses at every cross section within the powder specimen can be calculated, i.e.  $\tau = f(\sigma)$ ,  $\sigma_2 = f(\sigma_1)$  or  $\sigma_R = f(\sigma_M)$ . The center of the stress circle is  $\sigma_M = (\sigma_1 + \sigma_2)/2$  and the radius of the circle is  $\sigma_R = (\sigma_1 - \sigma_2)/2$ .

From these equations it is possible to calculate the normal stress  $\sigma_\alpha$  and the shear stress  $\tau_\alpha$  that are acting on the plane inclined by an angle  $\alpha$  (Figure 3.6 b)).

After some further transformations and elimination of the angles from the equations, one obtains the equation of a Mohr circle [60]. The stress state within the bulk element can be fully described by a Mohr circle (Figure 3.7).

In the Mohr circle  $\sigma_1$  is the major and  $\sigma_2$  is the minor principal stress. In the case of the bulk solid element shown in Figure 3.6 a) the major principal stress  $\sigma_1$  is the vertical stress  $\sigma_v$  and the minor stress  $\sigma_2$  is the horizontal stress  $\sigma_h$ .

As already mentioned, the flow of a powder is accompanied by irreversible plastic deformation. So, it is reasonable to measure the stress at which this plastic deformation occurs. This stress limit is called as the ‘yield limit’. In the solid mechanics this yield limit is specific for every material, and

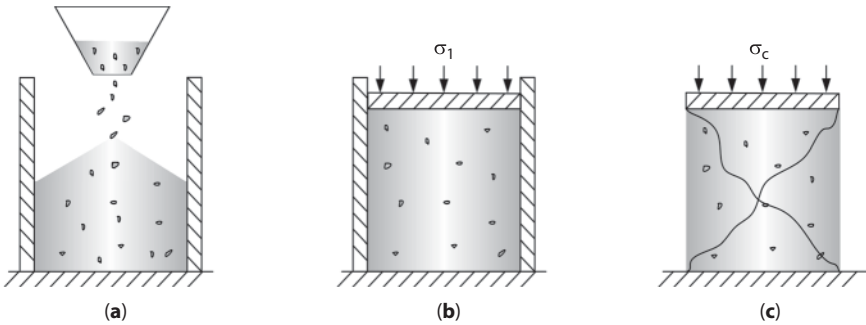


**Figure 3.8** Principle of uniaxial compression test: a) powder filling in a hollow cylinder with removable walls, b) powder consolidation at a certain normal stress  $\sigma_1$ , c) compression and powder breakage at stress  $\sigma_c$  (incipient flow).

can be found in the literature. In the case of bulk solids, however, there are many factors which influence this stress limit, like, for example, previous consolidation history, granulometric properties of the particles, and the adhesion forces.

The measurement of the stress at which powder begins to flow can be shown with one simple example - the uniaxial compression test (Figure 3.8). A hollow cylinder with removable walls is filled with a bulk solid powder (Figure 3.8 a)). Further, the powder is compressed and consolidated by applying a certain normal stress  $\sigma_1$  (Figure 3.8 b)). Then, the sample stress is released and the walls are removed. The consolidated sample is stressed again at an increasing normal force until it breaks (Figure 3.8 c)). The powder failure is referred to as ‘incipient flow’. The stress  $\sigma_c$  at which it breaks is called the uniaxial compressive strength. It defines the flow capability of the powder: the higher the compressive strength, the lower the powder flowability.

The most widely used flowability criterion is the Jenike [61] flow function  $ff_c$ , which is a correlation between the major principal stress  $\sigma_1$  and the uniaxial compressive strength  $\sigma_c$ . This flow function allows quantitative characterization of the powder flowability.

The evaluation of the powder flowability according to Jenike’s flow function is shown in Table 3.4.

To measure the flow properties of the powders shear testers are used e.g. translation shear tester, torsion shear tester, and ring shear tester. Nowadays, the most widely used shear testers are the ring shear testers, because they are easy to handle, they are very effective and only a little amount of material is required in comparison to other shear testers.

**Table 3.4** Classification of the flowability of powders according to Jenike [61] and Tomas [5].

Flow function $\mathit{ff}_c = \sigma_t/\sigma_c$	Powder behavior
$\mathit{ff}_c < 1$	not flowing, hardened
$1 < \mathit{ff}_c < 2$	very cohesive
$2 < \mathit{ff}_c < 4$	cohesive
$4 < \mathit{ff}_c < 10$	easy flowing
$\mathit{ff}_c > 10$	free-flowing

### 3.4 Surface Modification to Alter the Adhesion Properties

When a solid surface comes into contact with vapor, liquid or another solid, the interactions between them are influenced by the surface energetics of the system [62]. The surface free energy of solids is determined from the forces which act between the surface molecules [63]. It is possible to significantly influence the solid surface properties by modification with thin layers of appropriate compounds. These layers may be adsorbed, bound to, or coated on the surface [64].

#### 3.4.1 Surface Free Energy: Dispersion and Polar Components

Surface forces are of crucial relevance for adhesion and wetting phenomena. With respect to adhesion and surface energy, the van der Waals forces are of great importance [65]. According to Fowkes [66] the surface energy of solids and liquids represents all the attraction forces that act at the interface. It can be split into two components, in accordance with the interactions between the molecules: dispersion and polar interactions. The polar component results from Coulombic interaction between two permanent dipoles (Keesom force) and between one permanent dipole and an induced one (Debye force), from hydrogen bonding, and from Lewis acid-base interactions [67]. The dispersion component, on the other hand, is caused by random fluctuations in electron density within the molecule (London forces). Fowkes also assumed that the interactions at the surface were between intermolecular forces of the same type. While polar interactions occur only between polar surfaces, the dispersion interactions are present between all chemical groups.



The surface tension of liquids can be measured directly by a variety of measurement techniques (Du Noüy-Padday, Wilhelmy plate, pendant drop, spinning drop, bubble pressure etc. [68]). The surface free energy of solids, on the other hand, cannot be directly measured, but can be determined using test liquids with known surface tension. Nevertheless, a variety of techniques are available to determine the surface free energy of solids: contact angle methods, capillary penetration into columns of powder materials, particles sedimentation, with test inks, AFM [65,69].

Among the techniques to determine the solid surface free energy, experimentally the simplest way is to determine the wettability through contact angle measurements. The widely used liquid for contact angle measurements on complex surfaces is water. When a water droplet is placed on a high energy surface, it spreads on it, so that the surface is 'wetted' by the droplet. This happens because water-surface adhesion forces exceed the cohesive forces of bulk water [70]. The opposite behavior is observed in case of low energy surfaces. The droplet does not spread, but forms a spherical cap on the surface. This effect occurs because the interaction between the water molecules is stronger than the water-surface interactions. The first mentioned surfaces are known as hydrophilic, and the second ones as hydrophobic.

Contact angle measurements are most often realized using the static sessile drop method. It is an optical method which measures the contact angle which is formed on the three-phase contact line of the liquid and solid phase and the surrounding vapor or gas phase. The equilibrium of this three-phase system is described by the Young's equation [71]. A model based calculation of the solid surface free energy can be made using at least two test liquids (with known components of surface tension). The most widely used model for solids is the Owens, Wendt, Rabel and Kaelble model (OWRK model [72,73]). They extended the Fowkes model [74], which describes adequately only the dispersion interaction, and altered it to be applicable also for polar surfaces. Using at least two standard liquids, one polar and one purely dispersive, the surface free energy of the test solid can be calculated.

An effective method to alter the surface free energy of silica and glass is chemical modification with silanes. The functionalization process will be discussed in more detail later.

### 3.4.2 Glass Surface Cleaning Prior to Silanization

In order to prepare the glass surface for subsequent modification, it has to be cleaned from the adsorbed dirt, oils, or other contaminants. The removal of the above-mentioned materials from the surface can be done by chemical

cleaning [75]. The cleaning procedure is of crucial importance in the modification process for the formation of clean, complete monolayers. Therefore, in the literature a variety of chemical cleaning methods are reported, where acid, bases, and organic solvents at different temperatures are combined [76]. Groover [75] distinguishes between five different chemical cleaning types depending on the chemicals used: alkaline cleaning, emulsion cleaning, solvent cleaning, acid cleaning, and ultrasonic cleaning. Cras *et al.* [76] compared and qualitatively evaluated eight different cleaning techniques to prepare the glass surface for the silanization process. They applied different combinations of acids ( $\text{H}_2\text{SO}_4$ ,  $\text{HCl}$ ), bases ( $\text{NaOH}$ ,  $\text{KOH}$ ,  $\text{NH}_4\text{OH}$ ), methyl alcohol and hydrogen peroxide and used different temperatures and cleaning durations. The results were then evaluated based on contact angle of water on the substrate after cleaning and after coating. The contact angle after cleaning is an indication for the success of the surface cleaning. The contact angle after coating is indicative for the modification success and uniformity of the formed layers. Among the techniques they utilized, a mixture of  $\text{CH}_3\text{OH}$  and  $\text{HCl}$  in 1:1 ratio, followed by a rinse in concentrated  $\text{H}_2\text{SO}_4$  both at ambient temperature was found to yield the best results. Nevertheless, the cleaning procedure with peroxymonosulfuric acid (the so called 'piranha' solution or Caro's acid), which is a mixture of  $\text{H}_2\text{SO}_4$  and  $\text{H}_2\text{O}_2$  in 3:1 ratio, find the widest application for glass surface preparation for silanization [77,78,79,80]. The charring effect of the sulfuric acid is supplemented in this case by the formation of elemental oxygen that oxidizes the produced carbon to  $\text{CO}_2$ . Therefore, the piranha solution completely eliminates organic contaminants. In addition, the piranha hydroxylates the treated surface, and, as already mentioned, a high density of OH-groups is a prerequisite for a successful silanization process.

The cleaning procedure with peroxymonosulfuric acid is shown in Figure 3.9.

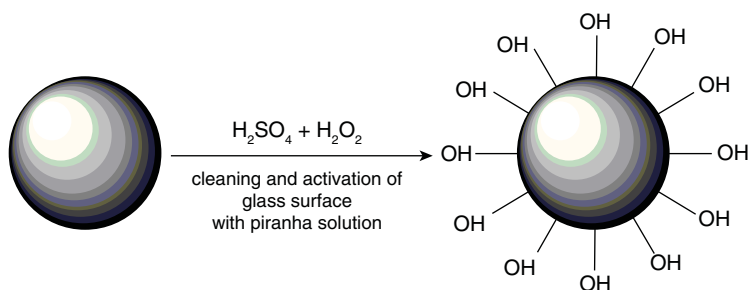


**Figure 3.9** Cleaning and hydroxylation of glass particle surface with peroxymonosulfuric acid as a preparation step for the silanization process.

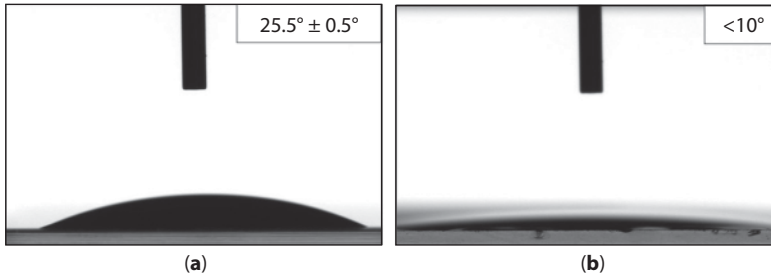


**Figure 3.10** a) Static contact angle between water droplet and non-cleaned glass slide, b) static contact angle between water droplet and glass slide cleaned with piranha solution.

Heating the solution in order to enhance the oxidizing activity is also possible. As a result of this cleaning process the surface becomes extremely hydrophilic (water contact angle lower than  $10^\circ$  [81]).

A comparison between the static contact angles on a cleaned and non-cleaned glass surface, measured using the sessile drop technique, with an OCA 15plus instrument (Data Physics Instruments GmbH, Germany), can be seen in Figure 3.10.

### 3.4.3 Silanization

Silanization is widely used to modify silica or glass surfaces. The silanes are applied for a wide range of applications as: coupling agents, adhesion promoters, silicate stabilizers, crosslinking agents, hydrophobizing and dispersing agents [82,83]. The silanes are organic silicon chemicals that possess at least one easily hydrolyzable group (halogen, alkoxy, hydroxyl, etc.) that reacts with the substrate. They also have an organic radical, which is bonded to the treated substrate and moderates its physical interactions.

The silanes that are used to modify the surface energy can be hydrophilic or hydrophobic [70]. Arkles [70] gives the following classification of the hydrophilic silanes presented in order of increasing hydrophilicity: polar, non-hydrogen bonding; polar, hydrogen bonding; hydroxylic; ionic-charged. The hydrophobic silanes, on the other hand, have a low energy organic radical (hydrocarbon or fluorocarbon chain, phenyl radical etc.), which reduces the surface energy by replacing the highly polar OH-groups.

In recent years fluorinated silanes have been of great interest for glass surface modification. After the modification with such silanes the surface becomes not only hydrophobic, but lipophobic as well [84]. The reason for this lies in the fact that due to the high electronegativity of fluorine, the polarizability of this atom is reduced. This results in decreased charge

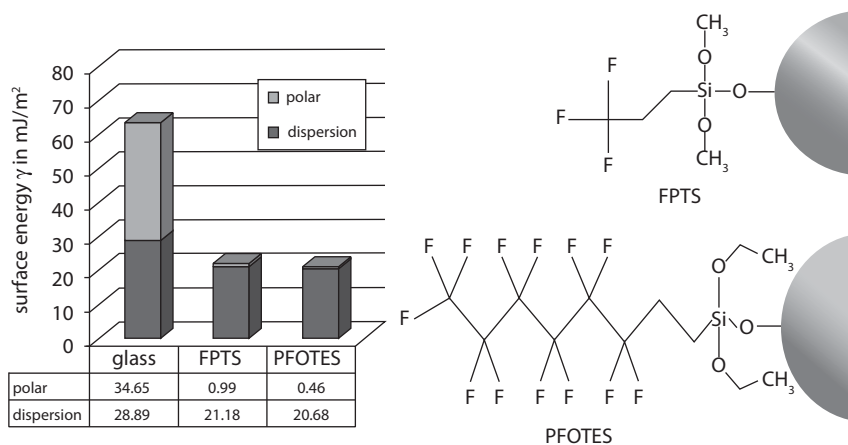


**Figure 3.11** Surface energy of untreated glass surface and glass surface modified with 1H,1H,2H,2H-Perfluorooctyltriethoxysilane (PFOTES) and 3,3,3-Trifluoropropyltrimethoxysilane (FPTS). The surface energy is calculated using the OWRK model and contact angles measured with two reference liquids: water as a polar liquid and  $\alpha$ -bromonaphthalene as purely dispersion liquid.

fluctuations (instantaneous dipole-induced dipole), responsible for the London dispersion force, and consequently result in low intermolecular interactions [85]. Figure 3.11 shows the surface energy of glass slides modified with fluorinated silanes. It is obvious that attachment of fluorocarbon chains to the surface not only almost entirely eliminated the surface polar interactions, but also reduced the dispersion interactions. This phenomenon was also observed by Linder and Ariast [64], who investigated the effect of the chain length of the fluorocarbon silane on the dispersion component of surface energy.

They discovered a slight decrease in the dispersion component of surface energy with increasing length of the fluorocarbon chain.

If the effect of surface hydrophobicity or hydrophilicity is coupled with surface roughness, a fabrication of superhydrophilic or superhydrophobic surfaces (alternatively ultraphilic and ultraphobic) is enabled [86,87,88]. The roughness affects the surface wettability by increasing the water contact angle on hydrophobic surfaces and decreasing it on hydrophilic ones [89,90]. If a water droplet is placed on an ultrahydrophobic surface it beads up, whereas on ultrahydrophilic surface a water droplet forms a very low or vanishing contact angle. Both this water repellency and outstanding wettability are advantageous for the fabrication of self-cleaning surfaces. The interactions between a water droplet and an ultrahydrophobic surface are so low that if the surface is inclined

the water droplet rolls off and carries the surface contamination with it. The self-cleaning effect of ultrahydrophilic surfaces is accomplished by means of film formation, which can easily flow and wash away the undesired particles.

#### 3.4.3.1 Silanization Techniques

There are different techniques for silanes deposition. The modification reaction can take place either in liquid or in vapor phase. The reaction in vapor phase is called chemical vapor deposition (CVD). The CVD reaction is carried out in an adsorption apparatus, where either dynamic or static adsorption procedures can be applied. Although the vapor phase reaction is preferred on industrial scale, for laboratory-scale modification the liquid phase deposition is more easily applicable.

There is a variety of solvents, aqueous and organic, which can be used for the liquid phase modification [91]. The silanes are extremely moisture sensitive. When the modification is carried out in an aqueous solvent, immediate hydrolysis and condensation takes place. The hydrolyzed silane molecules form hydrogen bonds with each other. This leads to a building of large polymerizates, which are then physi- or chemisorbed on the surface. Thus, the modification process under these conditions results in thick and difficult to control multilayers. Other disadvantage of this coating technique is its low reproducibility due to the difficulty in controlling hydrolysis process.

That is why utilization of dry organic solvents is preferable. In the absence of water the hydrolysable silane groups hydrolyze directly from the OH-groups present on the substrate surface. In dry conditions, the tri-functional silanes tend to form highly ordered films, the so called self-assembled monolayers (SAMs). In a SAM the molecules that form the film interact with the neighboring molecules and with the surface. In this way, if the hydroxyl concentration on the surface is high enough, closed and dense monolayers can be built [91].

There are various dry organic solvents (polar and nonpolar) that can be used for SAM deposition. McGovern *et al.* [92] tested eleven different solvents and their efficiency for the deposition of a tri-functional chlorosilane on a glass surface. They found that the densest film was created when dry toluene was utilized. In Figure 3.12 is shown as an example the deposition of chlorodimethylphenylsilane (CDMPS) in dry solvent (anhydrous toluene).

The silanization is applicable for both planar surfaces and particles. The modification of planar surfaces can be carried out through dip

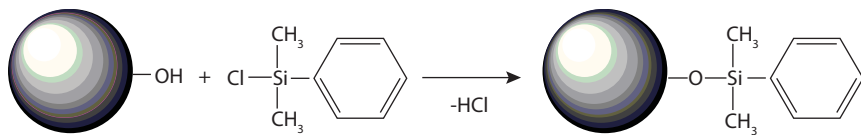


**Figure 3.12** Anhydrous deposition of silanes using the example of chlorodimethylphenylsilane (CDMPS).

coating; as for particles, the particles are stirred in the reagent solution. After the modification the majority of the silane groups are just physically attached to the surface, so for a chemical anchoring one additional high temperature curing step is needed to insure that the functional groups are covalently linked [93]. When modification of particles is carried out, different treatment times can be applied. Forny *et al.* [94] investigated the effect of the reaction time on the degree of hydrophobicity and the water adsorption capacity of the glass particles modified with trimethylchlorosilane. They found that one hour treatment was sufficient to induce surface hydrophobicity, but it is preferable to allow longer reaction times.

## 3.5 Experimental Measurements of the Adhesion Forces

In the following we discuss the different methods of adhesion force determination. In the case of single particle contacts, the atomic force microscopy (AFM) and nanoindentation technique are presented. For the characterization of particle packing, the principle of ring shear measurement is explained.

### 3.5.1 Single Particle Adhesion Measurements

The first part of the experimental section describes adhesion force determination via single particle measurements. Two different methods are presented. For the direct adhesion force measurement the AFM method is briefly discussed. The disadvantage of this method is the insufficient resolution of the displacement. The second method is the nanoindentation, which offers a high force- and displacement resolution. To evaluate the results of this indirect adhesion force measurement method the contact model 'stiff particles with soft contacts' is used for back-calculations.

### 3.5.1.1 Atomic Force Microscopy - Direct Adhesion Force Measurement

One possibility to determine the adhesion force between two bodies is the spring balance method. This was realized by Bradley [95] and later by Derjaguin *et al.* [96], Black *et al.* [97], Rouweler and Overbeek [98], Israelachvili and Tabor [99, 100], Israelachvili and Adams [101] and Israelachvili [10]. However, for very small particles this method is not suitable [102]. For determination of the adhesion force between two particles in the micrometer range, the method of atomic force microscopy (AFM) is appropriate.

AFM is applied in many fields of materials science, surface engineering and biology. Not only because of its capability to scan a surface with high resolution, but also its ability to determine local material properties makes this method indispensable in science [103]. Thus, by recording force-displacement curves, material properties, such as adhesion force  $F_H$ , modulus of elasticity  $E$ , Hamaker constant  $C_{H,sls}$  or hardness  $H$  can be determined [104]. In this case, the forces between the AFM tip and the surface are smaller than 1 nN [105].

The method was developed in 1986 by Binnig *et al.* [106]. It is a further development of the scanning tunneling microscope (STM). For STM measurements it is necessary that the surfaces are electrical conductors. But with an AFM it is possible to investigate both electrical conductors and insulators on the atomic scale. AFM measurements, in general, are carried out to determine the deflection of the flexible cantilever [106]. Figure 3.13 represents schematically the set-up of an atomic force microscope.

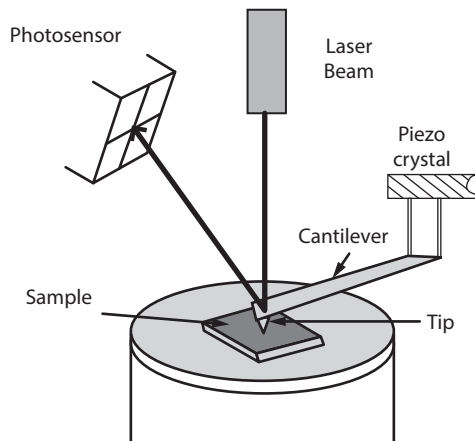


Figure 3.13 Schematic layout of an atomic force microscope (AFM)

During an AFM measurement, a tip attached to the cantilever moves against the sample in normal direction. After that the vertical position of the tip and the deflection of the cantilever are recorded and converted into a force-displacement curve.

For adhesion force determination between glass particles and modified glass slides, the colloid probe technique has been used. It was established in 1991. The pioneers of this method were Ducker and Butt. The technique involves direct attachment of the particle to be examined to the cantilever. While Ducker *et al.* [107] stuck silica spheres to a tipless cantilever, Butt [108] used glass spheres.

The advantage of this methodology is (for spherical particles with a defined radius) that the sensitivity of the measurement increases with a higher total adhesion force. Therefore, it is possible to quantify different chemically modified particles, which were attached to the cantilever [104]. The attachment of the particle is preferably carried out using an adhesive [109]. In Figure 3.14 a), a scanning electron micrograph (SEM) of a bonded glass particle ( $d_{50} = 12 \mu\text{m}$ ) is shown.

Figure 3.14 b) illustrates the deflection signal of the cantilever and the resulting force-separation curve. In the approach range between the colloidal sample and the surface, without any contact, cantilever deflection is non-measurable. With further loading, the attractive adhesion forces increase proportionally to the deflection of the cantilever. If the cantilever spring force exceeds the adhesion force at contact, the cantilever springs back to the equilibrium position and  $F_H$  (Figure 3.14 b)) describes the resulting detachment- /adhesion force.

Below the method of atomic force microscopy with the colloidal probe technique shall be described as an example of adhesion force determination

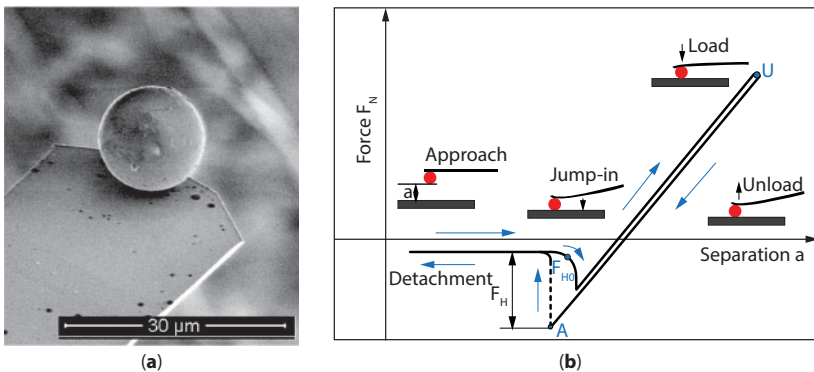


**Figure 3.14** a) Scanning electron micrograph of a bonded glass particle ( $d_{50} = 12 \mu\text{m}$ ), b) AFM force-separation curve of a particle-substrate contact.



for chemically modified glass particles. For the present study an AFM (Asylum Research MFP 3DTM AFM) was used. The experiments were carried out under an ambient temperature of  $23.4 \pm 0.3$  °C and a relative humidity of  $15.9 \pm 0.7$  %. The mean particle size of the glass particles used was  $d_{50} = 17.4$   $\mu\text{m}$ . The exact diameter of each particle was determined using SEM. To evaluate the surface roughness of the samples (RMS roughness = 0.8 nm), a non-contact AFM (XE-100, Park Systems) was used. By using a two-component adhesive (Araldite, epoxy), the particle was glued to the cantilever which is described in [109]. The applied cantilever (NSC35/tipless/AlBS), Schaefer Technology GmbH (Germany), had a length of 90  $\mu\text{m}$ . To determine the spring constant of the cantilever, the thermal noise method was used [110]. This resulted in a spring constant of 10.47 N/m.

To determine adhesion forces between a glass particle and a glass slide, the slides were functionalized as described in section 3.4.3. Subsequently, the respective force-displacement curves of the particle-substrate contact were measured. For this, the method of force mapping with 10 x10 points was applied in a range of 50  $\mu\text{m}$  x 50  $\mu\text{m}$  three times. The measurement velocity for this experiment was 1  $\mu\text{m/s}$ . Figure 3.15 illustrates the results of the realized adhesion force measurements. For this purpose, the mean value was calculated for all of the 300 individual measurements.

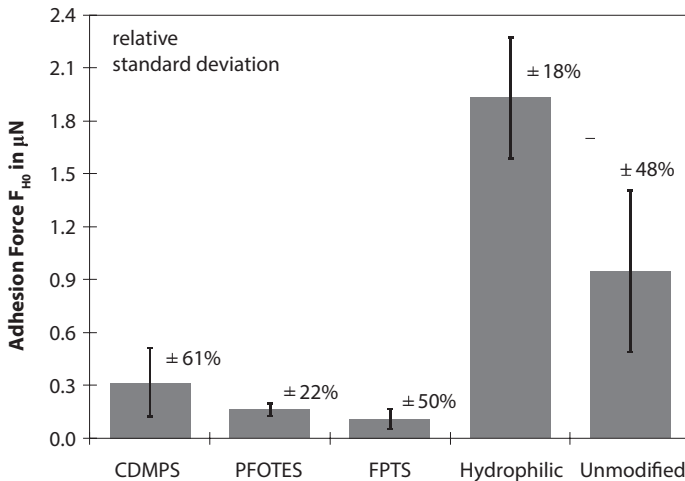


**Figure 3.15** Results of the adhesion force measurements between an unmodified glass particle ( $d_{50} = 17.3$   $\mu\text{m}$ ) and chemically modified glass surfaces. Types of functionalization: CDMPs - Chlorodimethylphenylsilane; PFOTES - 1H,1H,2H,2H-Perfluorooctyltriethoxysilane, FPTS - 3,3,3-Trifluoropropyltrimethoxysilane, Hydrophilic - cleaned with peroxymonosulfuric acid, Unmodified [111].

The largest adhesion force was found for the hydrophilic contact. It amounts to 1.93  $\mu\text{N}$  with a relative standard deviation of 18 % which is due to the polarity of the surface groups, which adsorb during the purification process with peroxymonosulfuric acid. This means that the deposition of the hydroxyl groups on glass surfaces increases the van der Waals attraction forces because of the hydrophilicity. With an increase in non-polarity of the silane groups, the hydrophobicity of the contact increases with decrease in the measured adhesion force. The silanes with the fluoroalkyl group, FPTS and PFOTES, show the lowest adhesion forces with  $F_{\text{HO,FPTS}} = 0.11 \mu\text{N}$  and  $F_{\text{HO,PFOTES}} = 0.16 \mu\text{N}$ . This corresponds to the expected results. From contact angle measurements of differently functionalized surfaces (see section 3.4.2), we obtained contact angles of  $88.7^\circ \pm 2.2^\circ$  for FPTS and  $106.8^\circ \pm 0.8^\circ$  for PFOTES. Thus, they represent the most hydrophobic silanes applied with the smallest adhesion forces [111].

### 3.5.1.2 *Nanoindentation - Model-based Adhesion Force Determination*

The disadvantage of AFM measurements is the dependence on the cantilever stiffness. This limits the weight and size of the particles to be investigated. Moreover, the force range is limited [109]. To close the gap between the required load range and the resolution of the atomic force microscopy, the method of nanoindentation is effective. In contrast to the direct adhesion force determination by AFM, the technique for model-based characterization of micromechanical material properties is presented using nanoindentation. For the back-calculations of the indirect adhesion force measurement the model 'stiff particles with soft contact' (described in section 3.2) is used.

The investigations in materials science in recent years show that contacts between materials are very dependent on the mechanical properties of the materials [22,112]. For this reason, various indentation and compression tests for the measurement of the mechanical contact properties were performed [113]. The resulting method of nanoindentation allows investigation of contact surfaces in the nanometer range and the recording of appropriate force-displacement curves. In addition, characteristics such as hardness  $H$ , modulus of elasticity  $E$  [105,114,115], flow behavior  $f_f$  [116,117,118,119,120] and adhesion force  $F_H$  [111] can be determined.

The respective properties of particles or surfaces were investigated by indenter compression tests [121,122]. For the attachment of the particle to the indenter the colloidal probe was applied for the nanoindentation [109].

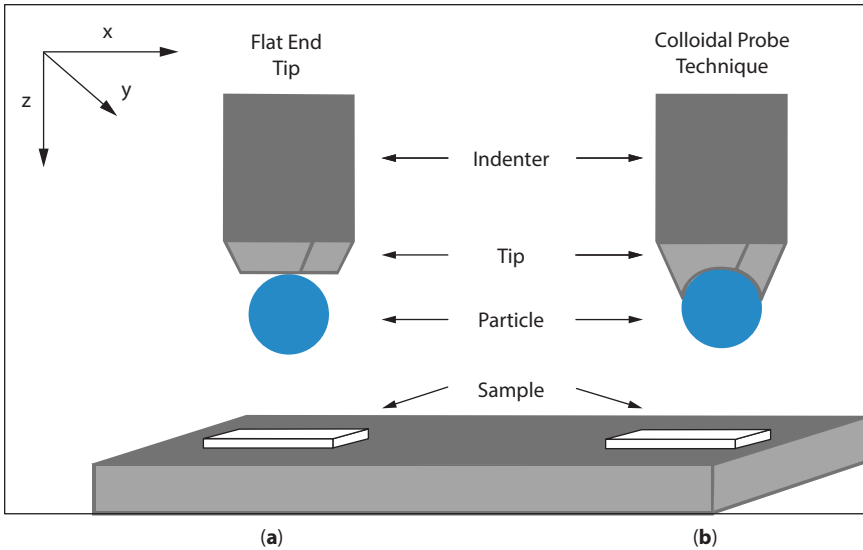


**Figure 3.16** Comparison of nanoindentation measurements, a) flat end tip, particle adhered due to the attraction forces, b) particle is fixed on the tip by colloidal probe technique.

A particle is attached to the end of the tip of diamond indenter. Two options are available to fix the particle. In the first case the particle adhered to the indenter underside due to the acting adhesion forces (Figure 3.16 a)). If the size of the particle is too large and the weight force exceeds the adhesion force, the particle has to be fixed to the tip (Figure 3.16 b)). In the following, only the method of colloidal probe technique is elucidated.

The preparation method was first published by Fuchs *et al.* [109]. The following example illustrates the preparation of the tip, the implementation of experiment and the model-based evaluation of a nanoindentation measurement. As a reference, a spherical, (cube corner diamond tip, Hysitron Inc.) attached glass particle, see Figure 3.17 a), and a glass slide are used on a three-sided pyramidal tip. These exemplify the particle-plate contact, as it was described in section 3.5.1.1.

In the first step a cavity is cut into the diamond tip (Figure 3.17 b)) with a focused ion beam system (FEI Helios 600). The hole formed an ideal contact surface for the particle because of its diameter ( $d_{\text{hole}} < d$ ).

Since the hole diameter is also smaller than the depth of the hole, the contact area between the particle and tip is only formed by a circular ring. Based on this, the particle is attached to the tip by means of an AFM (XE-100, PSIA) and photosensitive acrylate-based adhesive (DIC Europe GmbH, Austria). The AFM is used as a micromanipulator for the

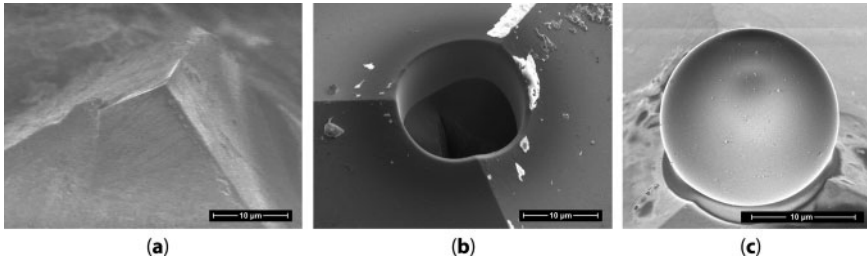


**Figure 3.17** Scanning electron micrographs (Zeiss Ultra 55) of a) three-sided pyramidal diamond cube corners tip (Hysitron Inc.) [123], b) cut hole using focused ion beam, c) glued glass particle (adhesive: DIC Europe GmbH, Austria).

positioning of the particle. The evaluation of the quality of prepared tips is done using SEM images (Zeiss Ultra 55), see Figure 3.17 c).

While piranha cleaning solution is used for AFM measurements, the cleaning method is different for the nanoindentation. Due to the organic additives of the acrylate glue and the resulting detachment of the particle using the peroxymonosulfuric acid, the samples were cleaned by oxygen plasma. The particles were cleaned for 30 s with this method. The functionalization of glass surfaces was done as described in section 3.4.3. For the measurements, a TriboIndenter from Hysitron Inc. was used.

Thus both single-sided and double-sided modified contacts were investigated. The maximum penetration depth was 32 nm. The measured values can be used to record the mean force-displacement curves. All experiments were performed at an ambient temperature of  $22.8 \pm 0.3$  °C and a relative humidity of  $29.6 \pm 0.4$  %.

In Figure 3.18 a) comparison of the normal force-displacement curves for the mean values of three different types of surface modifications are presented.

In the following section the applications of the contact model ‘stiff particles with soft contacts’ and the model-based back-calculations of the material properties are discussed for these force-displacement curves.

Based on Hertz [12] and according to Eq. (3.25) the elastic contact radius is

$$r_{K,el} = \sqrt{h_K \cdot r_{1,2}}. \quad (3.25)$$

For a particle diameter of  $d = 17.4$  µm and a maximum contact flattening of  $h_K = 32$  nm it follows that the elastic contact radius is  $r_{K,el} = 0.53$  µm for the three differently modified particles. From the measurements, which

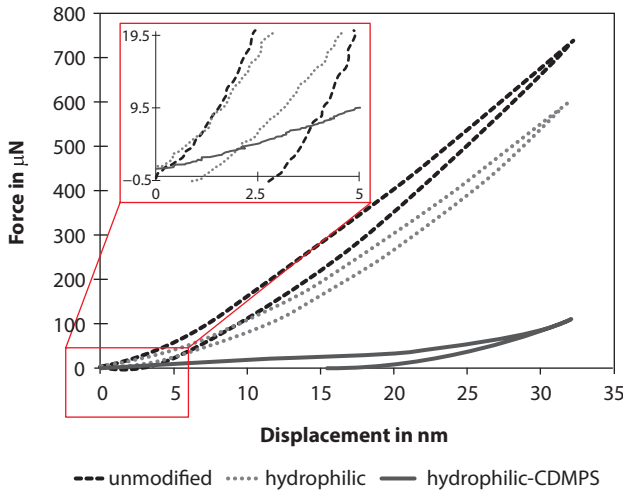


**Figure 3.18** Comparison of the normal force-displacement behavior for differently functionalized glass particles and surfaces during a nanoindentation measurement. Unmodified: untreated glass particles and glass slide; hydrophilic: treated with oxygen plasma; hydrophobic: functionalized with chlorodimethylphenylsilane. The zoom-in view shows the intersection of the curves and the abscissa. This intercept characterizes the residual plastic deformation [111].

are shown in Figure 3.18, it is not possible to divide clearly into the elastic and the elastic-plastic contact deformation because the whole curve is ‘bent’. Otherwise in the theory, the elastic-plastic yield limit is linear and only the elastic range is bent. Nevertheless, to determine the yield point, we have plotted the x-axis with  $\sqrt[3]{x}$ . Consequently, a linearized curve with the slope  $a_1$  can be achieved, see Figure 3.19 b).

From a linear regression of the measured values  $F_N = f(h_K^{3/2})$  and therefore  $a_1$ , the effective modulus of elasticity  $E^*$  results in Eq. (3.26)

$$E^* = 3 \cdot a_1 \cdot \sqrt{\frac{2}{r_{1,2}}} \tag{3.26}$$

The deformation in normal direction leads to a lateral strain of the particle. From the Poisson ratio for glass ( $\nu = 0.25$ ) [124] the modulus of elasticity  $E$  can be determined as follows:

$$E = \frac{1-\nu^2}{2} \cdot E^* \tag{3.27}$$

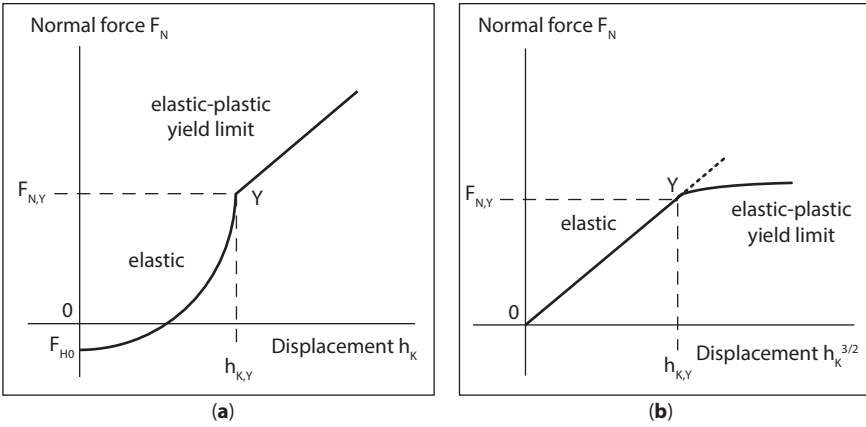


**Figure 3.19** a) Normal force-displacement behavior of the elastic contact, b) linearized normal force-displacement behavior of the elastic contact.

Furthermore, the force  $F_{N,Y}$  and the contact flattening  $h_{K,Y} = (h_{K,Y}^{3/2})^{2/3}$  at the yield point Y can be estimated. Through Eq. (3.28) the mean contact stiffness for loading in the elastic range might be approached as secant contact stiffness,

$$k_{N,el,Sec} = \frac{2 \cdot F_{N,Y}}{h_{K,Y}}. \tag{3.28}$$

Because of the relatively wide elastic deformation range in the present example, and significantly high values of the yield limit obtained [125,126,127,128], the elastic-plastic yield limit can be determined by Eq. (3.29):

$$\begin{aligned} F_N(h_K) &= \frac{\pi}{2} \cdot r_{1,2} \cdot p_f \cdot (\kappa_A - \kappa_p) \cdot (h_K - h_{K,Y}) + F_{N,Y} - F_{H0} \\ &= a_2 \cdot (h_K - h_{K,Y}) + b_2. \end{aligned} \tag{3.29}$$

Additionally the displacement at yield point  $h_{K,Y}$  is used to supplement Eq. (3.13).

The linear regression of the experimentally determined yield limit provides the slope  $a_2$  and the intercept  $b_2$ . This leads to the characteristic adhesion force  $F_{H0}$ :

$$F_{H0} = F_{N,Y} - b_2, \tag{3.30}$$

to the characteristic micro-yield strength  $p_f$ :

$$p_f = \frac{E^*}{\pi} \sqrt{\frac{h_{k,Y}}{2 \cdot r_{1,2}}}, \quad (3.31)$$

the elastic-plastic contact stiffness  $k_{N,el-pl}$ :

$$k_{N,el-pl} = a_2 = \frac{\pi}{2} \cdot r_{1,2} \cdot p_f \cdot (\kappa_A - \kappa_p) \quad (3.32)$$

and the plastic repulsion coefficient  $\kappa_p$ :

$$\kappa_p = \kappa_A - \frac{2 \cdot a_2}{\pi \cdot r_{1,2} \cdot p_f}. \quad (3.33)$$

The unloading in the compression test leads to elastic recovery of the contact. The intercept of the abscissa  $E$  for  $F_N = 0$ , see Figure 3.20, describes the residual plastic displacement  $h_{k,E}$ .

The elastic-plastic contact consolidation coefficient  $\kappa$  (see Eq. (3.34)) denotes the current contact stiffness and the increase in the adhesion force  $F_H$  (Eq. (3.35)) on subjecting to a pre-consolidation force  $F_N$  [1, 35]

$$\kappa = \frac{\kappa_p}{\kappa_A - \kappa_p} \quad (3.34)$$

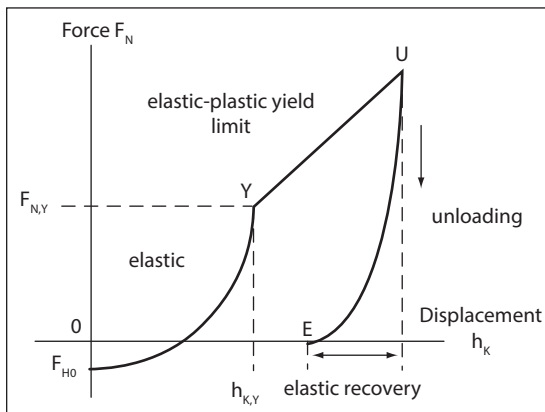


**Figure 3.20** Force-displacement curve for the elastic-plastic contact on unloading.

**Table 3.5** Model-based determination of material properties of functionalized glass beads.

Material property	Unmodified	Hydrophilic (O <sub>2</sub> -plasma)	Hydrophobic (CDMPS)
Elastic contact stiffness $k_{N,el}$ in N/mm	24.2	13.2	13.7
Elastic-plastic contact stiffness $k_{N,el-pl}$ in N/mm	25.4	20.6	12.2
Characteristic adhesion force $F_{H0}$ in nN	157.9	105.9	59.0
Micro-yield strength $p_F$ in MPa	1336.5	720.2	715.0
Modulus of elasticity $E$ in kN/mm <sup>2</sup>	113.9	89.0	83.2
Elastic-plastic contact consolidation coefficient $\kappa$	0.012	0.022	0.023
Plastic deformation in nm	2.9	1.2	0.8

and

$$F_H(F_N) = (1 + \kappa) \cdot F_{H0} + \kappa \cdot F_N. \quad (3.35)$$

Table 3.5 presents the specific material properties investigated for differently modified particles.

The contact of the unmodified particles shows the stiffest contact behavior. In contrast, the hydrophobic contact illustrates a relatively compliant behavior. Furthermore, the decrease of the plastic deformation from unmodified to hydrophilic and hydrophobic can be observed. The deposited silane layer provides an increase of the elastic contact range for the constant contact flattening. Additionally, the smallest adhesion force  $F_{H0}$  was determined for the CDMPS-coated surfaces. This is due to the non-polarity of the silane groups. By comparing the calculated elastic-plastic contact consolidation coefficients  $\kappa$  with Table 3.2, the unmodified contact shows the stiffest particle behavior followed by hydrophilic- and hydrophobic contact.

### 3.5.2 Shear Testing – Macromechanical Approach

The particle flowability is governed by friction between the particles, which depends on the adhesion forces. As already mentioned, in case of dry, fine



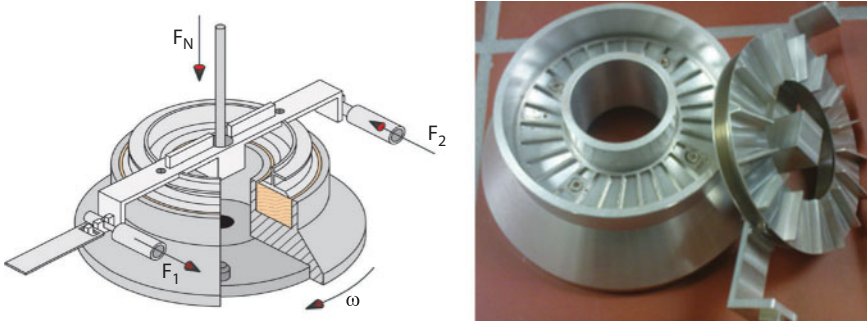


**Figure 3.21** Schulze Ring shear tester RST-XS.s (left) and a shear cell XS-Mr (right) with a volume of 30 ml [130].

particles the most important forces are the van der Waals attraction forces. Using the macroscopic bulk powder approach, it is also possible to state that the van der Waals forces act between the particles in the bulk solid. The adhesion force can be back-calculated from the shear test results using of the contact model ‘stiff particles with soft contacts’ [129].

To measure the macroscopic bulk powder properties, ring shear testers can be used. The ring shear test procedure will be explained using the example of a Schulze ring shear tester RST-XS.s [130]. The main part of the shear tester is the shear cell (Figure 3.21), which is filled with the sample to be measured. The shear cell has asperities on its lid and its bottom, which are protruding inside the sample. The aim is to avoid any friction between the bottom or the lid and the sample. In this way, the shearing inside the powder is induced only by the friction between the particles.

The shear test procedure consists of three steps: pre-consolidation, pre-shear, and shear. The first step is very short and implies consolidation of the powder by applying a certain normal stress  $\sigma_{pre}$  onto the lid. After that without releasing the powder from the applied normal stress the pre-shearing begins (Figure 3.22). The ‘pre-shearing’ continues until the shear force reaches a constant value, i.e. a steady state flow. After this, the sample is unloaded and then sheared again but under lower stress  $\sigma_{sh}$  ( $\sigma_{pre} > \sigma_{sh}$ ). This step is called ‘shear’. At the preshear step the stress is higher than during the shear step, the sample is considered to be overconsolidated. The shearing continues until the powder breaks, i.e. incipient flow. So far one has obtained two points from the yield locus. To measure further points from the yield locus the ‘preshear-shear’ procedure is repeated several times and each time the stress at the shear step is increased. When the points of incipient and stationary flows are entered in the  $\sigma, \tau$ -diagram and connected together the yield locus is obtained. To construct the flow function

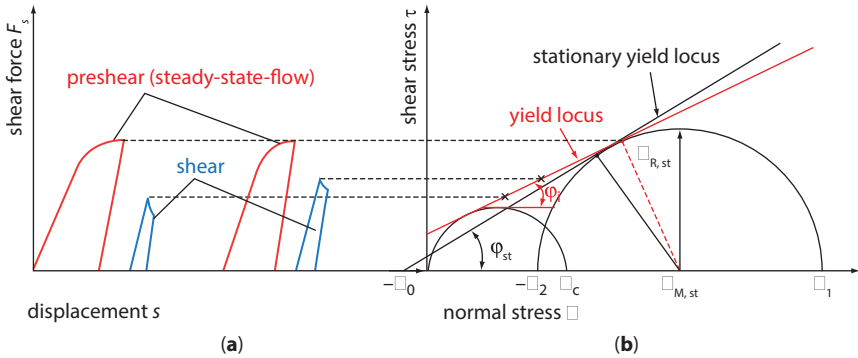


**Figure 3.22** a) Shear force-displacement diagram during the shear test for determining the yield locus. The ‘preshear’ curves show the course of shear force and the reaching of steady state flow. The ‘shear’ curves describe the incipient flow. b) Corresponding Mohr circles which represent the stress state inside the measured sample. The big circle defines the consolidation stress (the major principal stress  $\sigma_1$ ) and the smaller circle defines the unconfined yield strength  $\sigma_c$ .

$f_c$  minimum two yield loci have to be determined, but normally not less than four.

In Figure 3.23 the consolidation functions (sometimes called flow functions) of unmodified, hydrophobic and hydrophilic glass particles are shown. They are measured at four different pre-consolidation stresses  $\sigma_{pre} = 2, 4, 8$  and  $16$  kPa. Obviously, the hydrophobic glass particles have the best and hydrophilic ones the worst flowability. The slope of the consolidation function is defined by the adhesion between the particles, i.e., the steeper the slope, the higher the adhesion force and vice versa. This is due to the surface energy (respectively the adhesion force Figure 3.15), which in case of highly polar OH-groups is the highest.

Besides the yield locus also other important characteristics of a bulk solid can be measured with the shear testing such as: bulk density  $\rho_b$ , angle of internal friction  $\varphi_p$ , which represents the friction between the particles at the moment when the powder breaks - the incipient flow (the slope of the yield locus), stationary angle of internal friction  $\varphi_{st}$ , which characterizes the cohesive steady-state flow, the effective angle of internal friction  $\varphi_e$  (cohesionless steady-state flow), the isostatic tensile strength  $\sigma_0$  which is equal to the tensile or adhesion force between particles in an unconsolidated powder [131].

As already mentioned it is possible to back-calculate the adhesion force between particles in the bulk powder from the shear tests making a reverse micro-macro transition. For this purpose, the contact model ‘stiff particles with soft contacts’ will be used.

The evaluation of the shear test implies first the determination of the stationary yield locus. Both the incipient flow and the stationary flow are cohesive [4,132]. The stationary yield locus can be described using the radius and center stresses (Eq. (3.36) and (3.37)) of the larger/right one Mohr circle (see Figure 3.22) [131]

$$\sigma_{R,st} = \frac{\sigma_1 - \sigma_2}{2}, \quad (3.36)$$

$$\sigma_{M,st} = \frac{\sigma_1 + \sigma_2}{2}. \quad (3.37)$$

The stationary yield locus can be approximated as a linear function with an intercept  $b_1$ , which follows from the micro-macro transition of a representative adhesive and frictional particle contact see Eq. (3.38):

$$\sigma_{R,st} = \sin \varphi_{st} \cdot (\sigma_{M,st} + \sigma_0) = a_1 \cdot \sigma_{M,st} + b_1. \quad (3.38)$$

By a linear regression, the stationary angle of internal friction  $\varphi_{st}$  (Eq. (3.39)) and the isostatic tensile strength  $\sigma_0$  (Eq. (3.40)) can be calculated as:

$$\varphi_{st} = \arcsin(a_1), \quad (3.39)$$

$$\sigma_0 = \frac{b_1}{\sin \varphi_{st}}. \quad (3.40)$$

The next step is to determine the compression function. The compression function describes the powder compressibility in dependence of the major principal consolidation stress  $\sigma_1$  [5]. To describe the characteristic compression function one assumes an isentropic compression, i.e. during the compression the arrangement of the random packing is not changed or a regular packing is not obtained. The powder compressibility can also be related to the powder flowability - the more compressible the powder, the more compliant is the particle contact and the lower the flowability

$$\rho_b = \rho_{b,0} \cdot \left( \frac{1}{1 + \sin \varphi_{st}} \right)^n \cdot \left( 1 + \frac{\sigma_1}{\sigma_0} \right)^n. \quad (3.41)$$

After taking the logarithm of this function and transforming it to a linear regression function (see Eq. (3.42)):

$$\ln \rho_b = n \cdot \ln \left( 1 + \frac{\sigma_1}{\sigma_0} \right) + \ln \rho_{b,0} - \ln (1 + \phi_{st})^n = n \cdot \ln x + b_2 \quad (3.42)$$

where  $x = (1 + \sigma_1/\sigma_0)$  is a dimensionless stress, and the slope  $n$  and the intercept  $b_2$  of the function can be calculated. The slope  $n$  is called compressibility index. It has a significant physical meaning, and its evaluation is given by Tomas [131]. From the intercept  $b_2$  the bulk density of the powder before the compression can be calculated: the bulk density  $\rho_{b,0}$  of the loose, unconsolidated particle packing is Eq. (3.43):

$$\rho_{b,0} = \exp \left[ b_2 + n \cdot \ln (1 + \sin \phi_{st}) \right]. \quad (3.43)$$

Then the porosity of a loose, unconsolidated packing  $\epsilon_0$  is given as Eq. (3.44):

$$\epsilon_0 = 1 - \frac{\rho_{b,0}}{\rho_s} \quad (3.44)$$

where  $\rho_s$  is the solid density of the particles.

Now, making a reverse micro-macro transition, and under certain conditions explained in [133, 4], it is possible to back-calculate the characteristic adhesion force  $F_{H0}$  of one representative unconsolidated particle contact (see Eq. (3.45)) [131]:

$$F_{H0} = \frac{\epsilon_0}{1 - \epsilon_0} \cdot \sigma_0 \cdot d_{50}^2. \quad (3.45)$$

From the mean angle of internal friction  $\varphi_i$  and the stationary angle of internal friction  $\varphi_{st}$  also the elastic-plastic contact consolidation coefficient  $\kappa$  can be calculated:

$$\kappa = \frac{\tan \varphi_{st}}{\tan \varphi_i} - 1 \quad (3.46)$$

and also the plastic repulsion coefficient  $\kappa_p$  ( $\kappa_A \approx 5/6$ )

$$\kappa_p = \frac{\kappa}{1 + \kappa} \cdot \kappa_A. \quad (3.47)$$

Eq. (3.35) shows the linearized adhesion force as a function of the normal pre-consolidation force  $F_N$ , which acts between the particles depending on

the major principal consolidation stress. The term  $\kappa \cdot F_{H0}$  describes the additional instantaneous contact consolidation as a response to the application of the adhesion force  $F_{H0}$  at unconsolidated state  $F_N = 0$  (see Eq. (3.48)):

$$F_N = \frac{\varepsilon}{1 - \varepsilon} \cdot \sigma_1 \cdot d_{50}^2 \tag{3.48}$$

where  $\varepsilon$  is the porosity as a function of  $\sigma_1$ .

In Figure 3.24 is shown the mean adhesion force  $F_{H0}$  of one representative unconsolidated particle contact back-calculated from the shear test results shown in Figure 3.23.

From the graph one can see that the surface modification with silanes has caused a decrease of the adhesion force between the modified surfaces, when compared to the adhesion force of unmodified particles. The surface hydrophilization, on the other hand, has led to an increased particle adhesion. The results from the back-calculation are in good agreement with the results from the direct measurement of the adhesion force via AFM (see Figure 3.15).

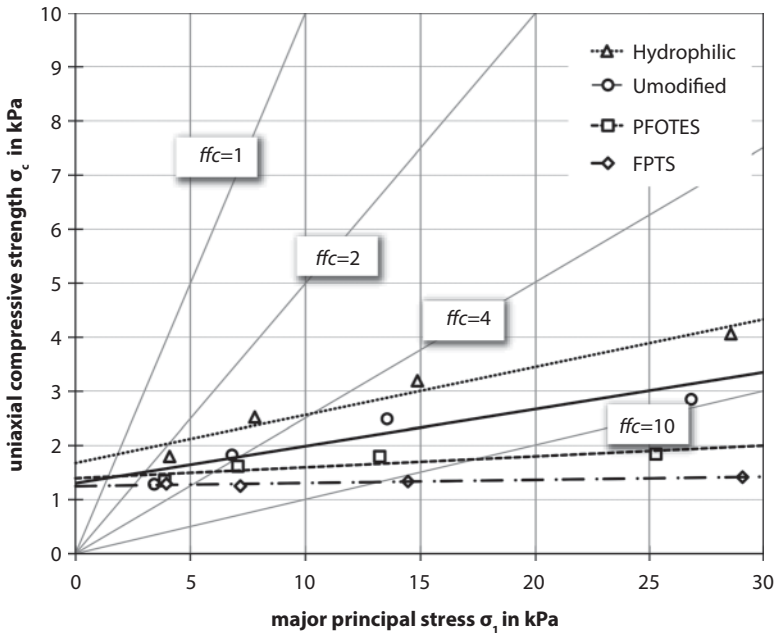


**Figure 3.23** Consolidation function  $ff_c$  (see Table 3.4) of unmodified, hydrophobic glass particles modified with fluoroalkylsilanes (PFOTES and FPTS) and hydrophilic particles. The mean particle size  $d_{50}$  is ca. 7  $\mu\text{m}$ .

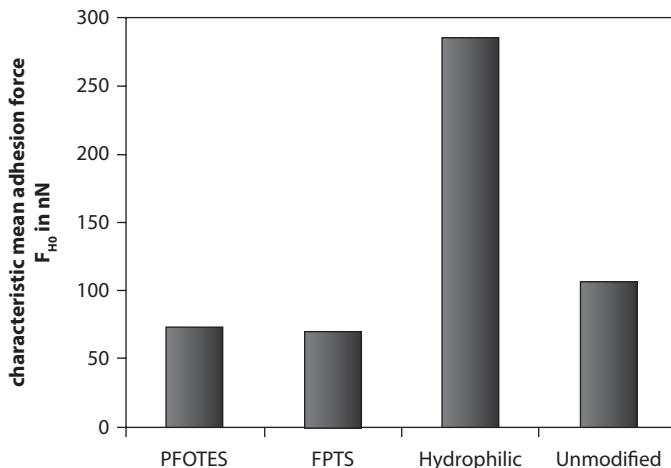


**Figure 3.24** Mean adhesion force of two particles from a particles packing back-calculated from shear test results using the contact model 'stiff particles with soft contacts'. The mean adhesion force is back-calculated for particles modified with: PFOTES - 1H,1H,2H,2H-Perfluorooctyltriethoxysilane; FPTS - 3,3,3-Trifluoropropyltrimethoxysilane; Hydrophilic- cleaned with peroxymonosulfuric acid.

### 3.6 Summary and Conclusions

The change in micro- and macroscopic properties of particles has a substantial influence on their handling, i.e. product design, transport, conveying and packing. Based on single particle experiments an extensive analysis of contact models for the contact of spherical, smooth, dry, fine and isotropic particles and substrates under normal load was presented. Different contact deformations such as elastic, elastic-plastic, plastic and unloading were considered.

To determine the macroscopic material properties in a particle packing, the shear testing technique was presented. In this context, the basics of shear experiments and the determination of physical properties using the contact model 'stiff particles with soft contacts' were discussed.

The modification of glass surfaces was carried out by hydrophilization and hydrophobization. This was done with glass particles from Potters Europe GmbH (Spheriglass 5000 CP00) as a reference. Hydrophilic particles were produced by a chemical cleaning process with peroxymonosulfuric acid. The hydrophobic particles were obtained with the wet chemical silanization process. Furthermore, the methods of surface energy determination and contact angle measurements were explained.

To determine the physical properties such as van der Waals adhesion force the methods of atomic force microscopy, nanoindentation and ring shear experiments were presented. Based on the example of modified glass particles the evaluation of material properties for direct adhesion measurements (AFM) and model-based back-calculation (nanoindentation, shear cell measurements) with the model ‘stiff particles with soft contacts’ was shown.

In conclusion, it is possible to change the flowability and physical properties of bulk solids with chemical surface modification. The characterization methods presented for these fine and nano-scaled particles are suitable with the introduced model ‘stiff particles with soft contacts’. The single particle- and particle packing experiments show the same contact behavior as demonstrated for unmodified, hydrophilic and hydrophobic glass particles.

## Acknowledgements

The authors would like to thank the Surface and Materials Technology Group at the University of Siegen. The support from Dr. T. Staedler and R. Fuchs with respect to the fundamentals and implementation of atomic force microscopy and nanoindentation measurements was especially appreciated during the collaboration of the priority program 1486 ‘PiKo - Particles in contact’. The authors also acknowledge the German Research Foundation (DFG) for their financial support.

## List of Symbols

Symbol	Unit	Description
$A$	$\text{nm}^2$	particle contact area
$a_0$	nm	molecular minimum distance
$C_{\text{H,sls}}$	J	Hamaker constant according to Lifshitz [11]
$d$	$\mu\text{m}$	particle diameter
$d_{50}$	$\mu\text{m}$	mean particle diameter
$E$	$\text{kN/mm}^2$	modulus of elasticity
$E^*$	$\text{kN/mm}^2$	effective modulus of elasticity
$F_{\text{H}}$	nN	adhesion force (in general)
$F_{\text{H0}}$	nN	adhesion force at contact point
$F_{\text{N}}$	nN	normal force
$H$	$\text{kN/mm}^2$	hardness

$h_K$	nm	overlap zone
$k_N$	N/m	contact stiffness in normal direction
$p$	kPa	contact pressure
$p_f$	MPa	plastic micro-yield strength of particle contact
$p_{vdW}$	MPa	van der Waals bond stress
$r$	$\mu\text{m}$	particle radius
$r_K$	nm	contact radius
$\gamma$	$\text{mJ/m}^2$	surface energy
$\varepsilon$	-	porosity
$\kappa$	-	elastic-plastic contact consolidation coefficient
$\kappa_A$	-	elastic-plastic contact area ratio
$\kappa_p$	-	plastic repulsion coefficient
$\nu$	-	Poisson ratio
$\varphi_e$	deg	effective angle of internal friction
$\varphi_i$	deg	angle of internal friction
$\varphi_{st}$	deg	stationary angle of internal friction
$\rho_b$	$\text{kg/m}^3$	bulk density
$\rho_s$	$\text{kg/m}^3$	solid density
$\sigma_\alpha$	kPa	normal stress
$\sigma_h$	kPa	horizontal stress
$\sigma_M$	kPa	center stress of Mohr circle
$\sigma_r$	kPa	radius stress of Mohr circle
$\sigma_v$	kPa	vertical stress
$\sigma_0$	kPa	isostatic tensile strength of the unconsolidated powder
$\sigma_1$	kPa	major principal stress
$\sigma_2$	kPa	minor principal stress
$\tau_\alpha$	kPa	shear stress

## References

1. J. Tomas, Adhesion of ultrafine particles - A micromechanical approach, *Chem. Eng. Sci.*, 62, 1997–2010 (2007).
2. K. Borho, R. Polke, K. Wintermantel, H. Schubert and K. Sommer, Produkteigenschaften und Verfahrenstechnik, *Chem. Ing. Tech.*, 63, 792–808 (1991).
3. H. Rumpf, Grundlagen und Methoden des Granulierens, *Chem. Ing. Tech.*, 30, 144–158 (1958).
4. J. Tomas, Produkteigenschaften ultrafeiner Partikel - Mikromechanik, Fließ- und Kompressionsverhalten kohäsiver Pulver, *Abhandlungen der Sächsischen Akademie der Wissenschaften zu Leipzig, Technikwissenschaftliche Klasse*, 1(3), 1–46 (2009).



5. J. Tomas and S. Kleinschmidt, Improvement of flowability of fine cohesive powders by flow additives, *Chem. Eng. Technol.*, 32, 1470–1483 (2009).
6. J. Tomas, Assessment of mechanical properties of cohesive particulate solids - Part 1: Particle contact constitutive model, *Particulate Sci. Technol.*, 19, 95–110 (2001).
7. Z. Kutelova, H. Mainka, K. Mader, W. Hintz and J. Tomas, Glass spheres: Functionalization, surface modification and mechanical properties, In: *Surface Effects in Solid Mechanics, Advanced Structured Materials*, H. Altenbach and N. F. Morozov (Eds.), pp. 95–104, Springer, Berlin (2013).
8. E. Plueddemann, *Silane Coupling Agents*, Plenum Press, New York (1991).
9. H. Hamaker, The London - van der Waals attraction between spherical particles, *Physica*, 4, 1058–1072 (1937).
10. J. Israelachvili, *Intermolecular and Surface Forces*, Academic Press, London (1992).
11. E. Lifshitz, The theory of molecular attractive forces between solids, *Soviet Physics (JETP)*, 2, 73–83 (1956).
12. H. Hertz, Über die Berührung fester elastischer Körper, *J. Reine Angew. Math.*, 92, 156–171 (1882).
13. M. Huber, Zur Theorie der Berührung fester elastischer Körper, *Ann. Phys.*, 14, 153–163 (1904).
14. A. Lurje, *Räumliche Probleme der Elastizitätstheorie*, Akademieverlag, Berlin (1963).
15. Y. Chen, A. Best, T. Haschke, W. Wiechert and H.-J. Butt, Stress and failure at mechanical contacts of microspheres under uniaxial loading, *J. Appl. Phys.*, 101, 084908–1–084908–6 (2007).
16. G. Sperling, Eine Theorie der Haftung von Feststoffteilchen an Festkörpern, PhD, University of Karlsruhe, Germany (1964).
17. B. Derjaguin, Untersuchungen über die Reibung und Adhäsion, IV - Theorie des Anhaftens kleiner Teilchen, *Kolloid Zeitschrift*, 69, 155–164 (1934).
18. B. Derjaguin, V. Muller and U. Toporov, Effect of contact deformations on the adhesion of particles, *J. Colloid Interface Sci.*, 53, 314–326 (1975).
19. B. Dahneke, The influence of flattening on the adhesion of particles, *J. Colloid Interface Sci.*, 40, 1–13 (1972).
20. B. Dahneke, Further measurements of the bouncing of small latex spheres, *J. Colloid Interface Sci.*, 51, 58–65 (1975).
21. K. Johnson, K. Kendall and A. Roberts, Surface energy and the contact of elastic solids, *Proc. Roy. Soc. London*, A 324, 301–313 (1971).
22. K. Johnson, *Contact Mechanics*, Cambridge University Press, London (1985).
23. J. Greenwood, Adhesion of elastic spheres, *Proc. Roy. Soc. London*, A 453, 1277–1297 (1997).
24. M. Götzinger and W. Peukert, Particle adhesion force distributions on rough surfaces, *Langmuir*, 20, 5298–5303 (2004).
25. Q. Li, V. Rudolph and W. Peukert, London-van der Waals adhesiveness of rough particles, *Powder Technol.*, 161, 248–255 (2006).

26. H. Zhou and W. Peukert, Modelling adhesion forces between deformable bodies by FEM and Hamaker summation, *Langmuir*, 24, 1459–1468 (2008).
27. V. Muller, V. Yuschenko and B. Derjaguin, On the influence of molecular forces on the deformation of an elastic sphere and its sticking to a rigid plane, *J. Colloid Interface Sci.*, 77, 91–101 (1980).
28. D. Maugis, Adhesion of spheres: The JKR-DMT transition using a Dugdale model, *J. Colloid Interface Sci.*, 150, 243–272 (1992).
29. H. Eid and N. Joshi, A model of contact with adhesion of a layered elastic-plastic microsphere with a rigid flat surface, *J. Tribology*, 133, 031406–1–031406–5 (2011).
30. Y. I. Rabinovich, J. J. Adler, M. S. Esayanur, A. Ata, B. M. Moudgil and R. K. Singh, Capillary forces between surfaces with nanoscale roughness, *Adv. Colloid Interface Sci.*, 96, 213–230 (2002).
31. R. von Mises, Mechanik des festen Körpers im plastischen deformablen Zustand, *Nachrichten von der Gesellschaft der Wissenschaften zu Göttingen, Mathematisch-physikalische Klasse*, 582–592 (1913).
32. H. Tresca, Mémoire sur l'écoulement des corps solides soumis à de fortes pressions, *C.R. Acad. Sci. Paris*, 59, 754–758 (1864).
33. A. Castellanos, The relationship between attractive interparticle forces and bulk behaviour in dry and uncharged fine powders, *Adv. Phys.*, 54, 263–376 (2005).
34. M. Stieß, Die Druckbeanspruchung von elastischen und inelastischen Kugeln bis zum Bruch, PhD dissertation, University of Karlsruhe, Germany (1976).
35. J. Tomas, Assessment of mechanical properties of cohesive particulate solids - Part 2: Powder flow criteria, *Particulate Sci. Technol.*, 19, 111–129 (2001).
36. W. Chang, I. Etsion and D. Bogy, An elastic-plastic model for the contact of rough surfaces, *J. Tribology*, 109, 257–263 (1987).
37. W. Chang, An elastic-plastic contact model for a rough surface with an ion-plated soft metallic coating, *Wear*, 212, 229–237 (1997).
38. L. Kogut and I. Etsion, Elastic-plastic contact analysis of a sphere and a rigid flat, *J. Appl. Mech.*, 69, 657–662 (2002).
39. R. Jackson and I. Green, A finite element study of elasto-plastic hemispherical contact against a rigid flat, *J. Tribology*, 127, 343–354 (2005).
40. E. Abbott and F. Firestone, Specifying surface quality: A method based on accurate measurement and comparison, *Mech. Eng.*, 55, 569–572 (1933).
41. J. Greenwood and J. Tripp, The contact of two nominally flat rough surfaces, *Proc. Inst. Mech. Eng.*, 185, 625–633 (1970).
42. C. Wu, C. Thornton and L. Li, Rebound behavior of spheres during elastic-plastic oblique impacts, *Int. J. Mod. Phys.*, B22, 1095–1102 (2008).
43. C. Thornton, Interparticle sliding in the presence of adhesion, *J. Phys. D.: Appl. Phys.*, 24, 1942–1946 (1991).
44. Y. Kadin, Y. Kligerman and I. Etsion, Unloading of elastic-plastic contact of rough surfaces, *J. Mech. Phys. Solids*, 54, 2652–2674 (2006).

45. L. Kogut and K. Komvopoulos, Analysis of the spherical indentation cycle for elastic-perfectly plastic solids, *J. Mater. Res.*, 19, 3641–3653 (2004).
46. S. Choi, Foreign object damage behavior in a silicon nitride ceramic by spherical projectiles of steels and brass, *Mater. Sci. Eng.*, 497, 160–167 (2008).
47. L. Li and J. Gu, An analytical solution for the unloading in spherical indentation of elastic-plastic solids, *Int. J. Eng. Sci.*, 47, 452–462 (2009).
48. S. Yan and L. Li, Finite element analysis of cyclic indentation of elastic-perfectly plastic half-space by a rigid sphere, *J. Mech. Eng.*, 217, 505–514 (2003).
49. L. Vu-Quoc, X. Zhang and L. Lesburg, A normal force-displacement model for contacting spheres accounting for plastic deformation: Force-driven formulation, *J. Appl. Mech.*, 67, 363–371 (2000).
50. S. Mesarovic and K. Johnson, Adhesive contact of elastic-plastic spheres, *J. Mech. Phys. Solids*, 48, 2009–2033 (2000).
51. I. Etsion, Y. Kligerman and Y. Kadin, Unloading of an elastic-plastic loaded spherical contact, *Inter. J. Solids Structures*, 42, 3716–3729 (2005).
52. Y. Kadin, Y. Kligerman and I. Etsion, Loading-unloading of an elastic-plastic adhesive spherical microcontact, *J. Colloid Interface Sci.*, 321, 242–250 (2008).
53. D. Maugis and H. Pollock, Surface forces, deformation and adherence at metal microcontacts, *Acta Metall.*, 32, 1323–1334 (1984).
54. O. Walton and R. Braun, Viscosity, granular-temperature, and stress calculations for shearing assemblies of inelastic, frictional disks, *J. Rheology*, 30, 949–980 (1986).
55. M. Sadd, Q. Tai and A. Shukla, Contact law effects on wave propagation in particulate materials using distinct element modeling, *Inter. J. Non-Linear Mech.*, 28, 251–265 (1993).
56. C. Thornton and Z. Ning, A theoretical model for the stick/bounce behaviour of adhesive, elastic-plastic spheres, *Powder Technol.*, 99, 154–162 (1998).
57. C. Thornton and K. Yin, Impact of elastic spheres with and without adhesion, *Powder Technol.*, 65, 153–166 (1991).
58. J. Tomas, Particle adhesion fundamentals and bulk powder consolidation, *Powder Handling Proc.*, 12, 131–138 (2000).
59. D. Schulze, *Powders and Bulk Solids - Behavior, Characterization, Storage and Flow*, Springer, Berlin (2008).
60. H. Schubert, E. Heidenreich, F. Liepe and T. Neeße, *Mechanische Verfahrenstechnik*, Deutscher Verlag für Grundstoffindustrie, Leipzig (1990).
61. A. Jenike, Storage and Flow of Solids, Eng. Expl. Station Report No. 123, University of Utah, Salt Lake City, Utah (1964).
62. I. Grimsey, J. Feeley and P. York, Analysis of the surface energy of pharmaceutical powders by inverse gas chromatography, *J. Pharm. Sci.*, 91, 571–583, (2002).
63. R. van de Grampel, W. Ming, A. Gildenpfennig, W. van Gennip, J. Laven, J. Niemantsverdriet, H. Brongersma, G. de With and R. van der Linde,

- The outermost atomic layer of thin films of fluorinated polymethacrylates, *Langmuir*, 20, 6344–6351 (2004).
64. E. Lindner and E. Ariast, Surface free energy characteristics of polyfluorinated silane films, *Langmuir*, 8, 1195–1198 (1992).
  65. J. Vojtěchovská and L. Kvítek, Surface energy - Effects of physical and chemical surface properties, *Chemica*, 44, 25–48 (2005).
  66. F. M. Fowkes, Additivity of intermolecular forces at interfaces. I. Determination of the contribution to surface and interfacial tensions of dispersion forces in various liquids, *J. Phys. Chem.*, 67, 2538–2541 (1963).
  67. M. J. Schwuger, *Lehrbuch der Grenzflächenchemie*, Georg Thieme, New York (1996).
  68. Kibron Inc., The World Leader in Surface Tension Instrumentation, <http://www.kibron.com/surface-tension/measurement-techniques>, [Accessed 16 07 2013].
  69. F. Etzler, Determination of the surface free energy of solids: A critical review, *Rev. Adhesion Adhesives*, 1, 3–45 (2013).
  70. B. Arkles, Hydrophobicity and hydrophilicity and silane surface modification, Report from Gelest Inc., 1–80 (2011).
  71. L. White, On deviations from Young's equation, *J. Chem. Soc., Faraday Trans. 1*, 73, 390–398 (1997).
  72. D. Owens and R. Wendt, Estimation of the surface free energy of polymers, *J. Appl. Polym. Sci.*, 13, 1741–1747 (1969).
  73. W. Rabel, Einige Aspekte der Benetzungstheorie und ihre Anwendung auf die Untersuchung und Veränderung der Oberflächeneigenschaften von Polymeren, *Farbe und Lacke*, 77, 997–1005 (1971).
  74. F. Fowkes, Calculation of work of adhesion by pair potential summation, *J. Colloid Interface Sci.*, 28, 493–505 (1968).
  75. M. Groover, *Fundamentals of Modern Manufacturing: Materials, Processes and Systems*, John Wiley & Sons (2010).
  76. J. J. Cras, C. A. Rowe-Taitt, D. A. Nivens and F. S. Ligler, Comparison of chemical cleaning methods of glass in preparation for silanization, *Biosensors Bioelectronics*, 14, 683–688 (1999).
  77. R. Wilson and D. Schiffrin, Use of fluorescamine for the spectrofluorimetric investigation of primary amines on silanized glass and indium tin oxide-coated glass, *Analyst*, 120, 175–178 (1995).
  78. Q. Chen, S. Bae and S. Granick, Directed self-assembly of a colloidal kagome lattice, *Nature*, 469, 381–384 (2011).
  79. R. Iyer and A. Niroomand, Method to clean substrate and improve photore-sist profile, US patent 6383723 B1 (2002).
  80. C. Halliwell and A. Cass, A factorial analysis of silanization conditions for the immobilization of oligonucleotides on glass surfaces, *Anal. Chem.*, 73, 2476–2483 (2001).
  81. H.-J. Butt, K. Graf and M. Kappl, *Physics and Chemistry of Interfaces*, Wiley-VCH, Weinheim (2006).

82. K. Mittal (Ed.), *Silanes and Other Coupling Agents*, Vol. 4, CRC Press, Boca Raton, FL (2007).
83. K. Mittal (Ed.), *Silanes and Other Coupling Agents*, Vol. 5, CRC Press, Boca Raton, FL (2009).
84. N. Yoshino, T. Sato, K. Miyao, M. Furukawa and Y. Kondo, Synthesis of novel highly heat-resistant fluorinated silane coupling agents, *J. Fluorine Chem.*, 127, 1058–1065 (2006).
85. D. M. Lemal, Perspective on fluorocarbon chemistry, *J. Org. Chem.*, 69, 1–11 (2004).
86. Y. Cheng, D. Rodak, C. Wong and C. Hayden, Effects of micro- and nano-structures on the self-cleaning behaviour of lotus leaves, *Nanotechnology*, 17, 1359–1362 (2006).
87. A. Marmur, The lotus effect: Superhydrophobicity and metastability, *Langmuir*, 20, 3517–3519 (2004).
88. I. Parkin and R. Palgrave, Self-cleaning coatings, *J. Mater. Chem.*, 15, 1689–1695 (2005).
89. P. Olin, S. Lindström, T. Pettersson and L. Wågberg, Water drop friction on superhydrophobic surfaces, *Langmuir*, 29, 9079–9089 (2013).
90. R. Blossey, Self-cleaning surfaces - Virtual realities, *Nature Materials*, 2, 301–306 (2003).
91. P. van der Voort and E. F. Vansant, Silylation of the silica surface: A review, *J. Liq. Chrom. Rel. Technol.*, 19, 2723–2752 (1996).
92. M. E. McGovern, K. M. R. Kallury and M. Thompson, Role of solvent on the silanization of glass with octadecyltrichlorosilane, *Langmuir*, 10, 3607–3614 (1994).
93. E. Vansant, P. van der Voort and K. Vrancken, *Characterization and Chemical Modification of the Silica Surface*, Elsevier, Amsterdam (1995).
94. L. Forny, I. Pezron, K. Saleh, P. Guigon and L. Komunjer, Peculiar adsorption of water by hydrophobized glass beads, *Colloids Surfaces A*, 270–271, 263–269 (2005).
95. R. Bradley, The cohesive force between solid surfaces and the surface energy of solids, *Philos. Mag.*, 13, 853–862 (1932).
96. B. Derjaguin, I. Abrikosova and E. Lifshitz, Direct measurement of molecular attraction between solids separated by a narrow gap, *Quarterly Rev. Chemical Soc.*, 10, 295–329 (1956).
97. W. Black, J. de Jongh, J. Overbeek and M. Sparnaay, Measurements of retarded van der Waals forces, *Trans. Faraday Soc.*, 56, 1597–1608 (1960).
98. G. Rouweler and J. Overbeek, Dispersion forces between fused silica objects at distances between 25 and 350 nm, *Trans. Faraday Soc.*, 67, 2117–2121 (1971).
99. J. Israelachvili and D. Tabor, The measurement of the van der Waals dispersion forces in the range 1.5 to 130 nm, *Proc. Roy. Soc. London*, A 331, 19–38 (1972).
100. J. Israelachvili and D. Tabor, Van der Waals forces. Theory and experiment, In: *Progress in Surface and Membrane Science*, J. F. Danielli, M. D. Rosenberg

- and D. A. Cadenhead (Eds.), vol. 7, pp. 1–55, Academic Press, New York (1973).
101. J. Israelachvili and G. Adams, Measurements of the forces between two mica surfaces in aqueous electrolyte solutions in the range 0–100 nm, *J. Chem. Soc. Faraday Trans. I* 74, 975–1001 (1978).
  102. R. Tykhoniuk, J. Tomas, S. Luding, M. Kappl and H.-J. Butt, Ultrafine cohesive powders: From interparticle contacts to continuum behaviour, *Chem. Eng. Sci.*, 62, 2843–2864 (2007).
  103. J. Drelich and K. L. Mittal (Eds.), *Atomic Force Microscopy in Adhesion Studies*, CRC Press, Boca Raton, FL (2005).
  104. H.-J. Butt, B. Capella and M. Kappl, Force measurements with the atomic force microscope: Technique, interpretation and applications, *Surf. Sci. Rep.*, 59, 1–152 (2005).
  105. B. Bhushan (Ed.), *Handbook of Micro/Nano Tribology*, CRC Press, Boca Raton, FL (1999).
  106. G. Binnig, C. Quate and C. Gerber, Atomic force microscopy, *Phys. Rev. Lett.*, 56, 930–933 (1986).
  107. W. Ducker, T. Senden and R. Pashley, Direct measurement of colloidal forces using an atomic force microscope, *Nature*, 353, 239–241 (1991).
  108. H.-J. Butt, Measuring electrostatic, van der Waals, and hydration forces in electrolyte solutions with an atomic force microscope, *Biophys. J.*, 60, 1438–1444 (1991).
  109. R. Fuchs, J. Meyer, T. Staedler and X. Jiang, Sliding and rolling of individual micrometre sized glass particles on rough silicon surfaces, *Tribology, Materials, Surfaces & Interfaces* 7, 103–107 (2013).
  110. R. Proksch, T. Schäffer, J. Cleveland, R. Callahan and M. Viani, Finite optical spot size and position corrections in thermal spring constant calibration, *Nanotechnology*, 15, 1344–1350 (2004).
  111. K. Mader-Arndt, Z. Kutelova, R. Fuchs, J. Meyer, T. Staedler, W. Hintz and J. Tomas, Single particle contact vs. particle packing behavior: Model based analysis of chemically modified glass particles, *Granular Matter*, DOI 10.1007/s10035-013-0478-9, January 2014.
  112. S. Timoshenko, *History of Strength of Materials*, McGraw-Hill, New York (1953).
  113. C. Schuh, Nanoindentation studies of materials, *Mater. Today*, 9(5), 32–40 (2006).
  114. W. Oliver and G. Pharr, An improved technique for determining hardness and elastic modulus using load and displacement sensing indentation experiments, *J. Mater. Res.*, 7, 1564–1583 (1992).
  115. W. Oliver and G. Pharr, Measurement of hardness and elastic modulus by instrumented indentation: Advances in understanding and refinements to methodology, *J. Mater. Res.*, 19, 3–20 (2004).
  116. A. Fisher-Cripps, *Nanoindentation*, Springer, New York (2004).

117. M. Oyen and R. Cook, Load-displacement behavior during sharp indentation of viscous-elastic-plastic materials, *J. Mater. Res.*, 18, 139–150 (2003).
118. B. Storakers and P.-L. Larsson, On Brinell and Boussinesq indentation of creeping solids, *J. Mech. Phys. Solids*, 42, 307–332 (1994).
119. B. Lucas and W. Oliver, Indentation power-law creep of high-purity indium, *Metall. Mater. Trans.*, 30A, 601–610 (1999).
120. H. Takagi, M. Dao, M. Fujiwara and M. Otsuka, Experimental and computational creep characterization of Al-Mg solid-solution alloy through instrumented indentation, *Philos. Mag.*, 83, 3959–3976 (2003).
121. X. Li and B. Bhushan, A review of nanoindentation continuous stiffness measurement technique and its application, *Mater. Charact.*, 48, 11–36 (2002).
122. K. Mussert, W. Vellinga, A. Bakker and S. van der Zwaag, A nano-indentation study on the mechanical behaviour of the matrix material in an AA 6061-Al<sub>2</sub>O<sub>3</sub> MMC, *J. Mater. Sci.*, 37, 789–794 (2002).
123. Hysitron. Inc.: Tip Selection Guide, [http://hysitron.com/LinkClick.aspx?fileticket=bcq5arPC\\_GE%3d&tabid=429](http://hysitron.com/LinkClick.aspx?fileticket=bcq5arPC_GE%3d&tabid=429) [Accessed 25 07 2013]
124. H. Czichos and M. Hennecke, *Hütte - Das Ingenieurwissen*, Springer, Berlin (2008).
125. S. Antonyuk, J. Tomas, S. Heinrich and L. Mörl, Breakage behaviour of spherical granulates by compression, *Chem. Eng. Sci.*, 60, 4031–4044 (2005).
126. S. Antonyuk, S. Heinrich, J. Tomas, N. G. Deen, M. S. van Buijtenen and J. A. M. Kuipers, Energy absorption during compression and impact of dry elastic-plastic spherical granules, *Granular Matter*, 12, 15–47 (2010).
127. P. Müller and J. Tomas, Compression behavior of moist spherical zeolite 4A granules, *Chem. Eng. Technol.*, 35, 1677–1684 (2012).
128. P. Müller, M. Seeger and J. Tomas, Compression and breakage behavior of  $\gamma$ -Al<sub>2</sub>O<sub>3</sub> granules, *Powder Technol.*, 237, 125–133 (2013).
129. J. Tomas, Mechanics of nanoparticle adhesion - A continuum approach, In: *Particles on Surfaces 8: Detection, Adhesion and Removal*, K. L. Mittal (Ed.), pp. 183–229, CRC Press, Boca Raton, FL (2003).
130. D. Schulze, Powder testers and software, <http://www.dietmar-schulze.de/leafxss.pdf> [Accessed 03 10 2013].
131. J. Tomas, Product design of cohesive powders mechanical properties, compression and flow behavior, *Chem. Eng. Technol.*, 27, 605–618 (2004).
132. O. Molerus, *Schüttgutmechanik - Grundlagen und Anwendungen in der Verfahrenstechnik*, Springer, Heidelberg (1985).
133. J. Tomas, Fundamentals of cohesive powder consolidation and flow, *Granular Matter*, 6, 75–86 (2004).





# Characterization of Single Particle Adhesion: A Review of Recent Progress

Armin Saeedi Vahdat and Cetin Cetinkaya\*

*Photo-Acoustics Research Laboratory, Center for Advanced Materials Processing,  
Department of Mechanical and Aeronautical Engineering, Clarkson University,  
Potsdam, NY, USA*

---

## Abstract

While over past several decades, one-dimensional adhesion behavior of micro-objects has been extensively studied both experimentally and analytically, the analytical and experimental studies for two-dimensional adhesion behavior have been rather limited. Considering the critical role of rolling motion of micro-/nano-scale round objects in adhesion and detachment, this void is somewhat surprising. In this chapter, some recent experimental and analytical developments in the adhesion characterization of nano-/micro-scale objects are reviewed with a special emphasis on non-contact methods for single particle measurements and associated two-dimensional adhesion models. In addition, recent works on nonlinear effects in adhesion bonds, thin layers adhesion characterization and micro-scale objects manipulation techniques are covered and some additional research in these fields is identified. Finally, potential applications of the mentioned works are discussed.

**Keywords:** Adhesion bond, work of adhesion characterization, micro-particles nonlinear dynamics, non-contact techniques, monolayer graphene, micro-particle manipulation, particle rocking motion, rolling resistance, Surface Acoustic Wave (SAW)

## 4.1 Introduction

At nano/micrometer scales, compared to several other types of forces (e.g. inertia, gravity, electromagnetic, and electrostatic), adhesion, a weak

---

\*Corresponding author: [cetin@clarkson.edu](mailto:cetin@clarkson.edu)

intermolecular interaction (van der Waals force), often dominates the deformation and dynamics of biological and/or engineered small-scale objects. Understanding and characterizing the interactions of micro-scale objects (e.g. micro-particles, liposome vesicles, biological cells and other morphologically similar entities), with their environments and with each other, is critically important in various industries, such as digital/additive manufacturing, pharmaceutical manufacturing, semiconductor manufacturing, biomedical devices, sensors, and food processing.

Adhesion characterization of nano-/micro-scale objects is a challenge due mainly to issues associated with their effective handling and manipulation as well as uncertainty about the nature of contacts and interfaces due to the small length-scale of the associated objects and the low force levels involved. To understand particle–substrate interactions at micro-scale, the development of application-specific experimental techniques and models is often required. At present, several statistical adhesion measurement techniques for multi-particle systems based on centrifugal, aerodynamic and hydrodynamic forces, impact–spectrum and ultrasonic vibration are utilized for adhesion characterization of micro-scale object systems [1]. In the centrifuge technique, the adhesion restitution force and/or moment acting on particles is obtained by measuring the centrifugal force required for detaching particles from a rotating substrate. In the aerodynamic and hydrodynamic techniques, the adhesion force is determined by measuring the threshold force generated by flow to detach particles from the substrate. In the impact–spectrum technique, the particles are detached from the substrate by the impact force exerted at the opposite side of the substrate and the detachment force due to resulting surface acceleration is measured. In the ultrasonic vibration approach, the frequency and hence the force required to detach particles from substrate using an ultrasonic probe is measured. It is noteworthy that in all these statistical adhesion measurements, the adhesion characterization is performed by measuring the detachment force required to detach particles from the substrates. Detachment process is often a result of interactions of a number of complex events due to its disruptive nature, leading to energy release, plastic deformation, finite amplitude deformation, and mass transfer at nano-/micro-scale. Consequently, in addition to their statistical nature, the accuracy of resulting work of adhesion extraction from detachment-based techniques suffers.

Adhesion bond between a particle and a surface plays a key role in the motion and adhesion of particles on surfaces and the strength/stability of networks of adhered round objects (e.g. particles, powders, biological cells, and nanotubes) in a wide spectrum of applications at nano-/micro-scale.

In recent years, single particle adhesion measurement techniques for accurate adhesion characterization of micro-scale objects have attracted attention to address the shortcomings of various statistical techniques based on measurement in multi-particle systems. Moreover, while one-dimensional adhesion behavior of micro-objects (out-of-plane) has been extensively studied both experimentally and analytically, only limited attention has been paid to the analytical and experimental studies for two-dimensional (in-plane) adhesion behavior. Considering the critical role of rolling motion of micro-/nano-scale round objects in adhesion and detachment, the current situation needs attention and, at the same time, creates research opportunities. In this chapter, some recent experimental and analytical developments in the adhesion characterization of nano-/micro-scale objects are reviewed with a special emphasis on non-contact methods and associated two-dimensional adhesion models. In addition, recent works on nonlinear effects in adhesion bonds, thin layers adhesion characterization and micro-scale objects manipulation techniques are covered and some additional research in these fields is identified. Finally, a number of potential applications of the presented works are discussed.

In this chapter, following a brief background to the subject matter in Section 4.2, various experimental and analytical progresses in adhesion characterization are reviewed. In Section 4.3, micro-particles adhesion characterization based on nonlinear dynamics of micro-particles using a non-contact vibrational spectroscopy technique is discussed. Also, a novel technique for adhesion characterization of thin layers (monolayer graphene) using a non-contact vibrational spectroscopy approach is introduced and its advantages over previously reported techniques are discussed. Afterwards, a non-contact technique is introduced for controllable rolling motion of micro-particles using surface acoustic wave (SAW) fields. Finally, in Section 4.4, following a brief concluding discussion, some drivers and research needs for future developments are identified and discussed.

## 4.2 Background

In the past decade or so, in addition to the traditional approaches discussed above, particle adhesion and force–displacement characterization studies for individual particles with the aid of AFM (Atomic Force Microscopy) probes and micro-manipulators have also been reported [2–5]. The main disadvantage of an axial AFM-based detachment technique, in addition to its disruptive nature, is that in such experiments the particle has to be fixed and/or glued to the tip of a probe; therefore, it is essentially a destructive

approach applicable to “relatively” large particles. Without fixing the particle to the tip, two interfaces (particle–substrate and particle–tip) need to be characterized independently, leading to complications in the work of adhesion extraction.

#### 4.2.1 Adhesion Models

At present, several adhesion models for nano-/micro-particles are available. Since 1971, a number of continuum mechanics-based models describing the out-of-plane adhesion force–displacement behavior (one-dimensional adhesion theories) between micro-particles and substrates have been reported and found applications in the interpretation of AFM based force–displacement measurements [6–9]. One-dimensional adhesion theories describing the out-of-plane adhesion force–displacement behavior are well-characterized, and a unifying framework establishing the transition between the existing theories and their applicability zones for the ranges of an external load and an elasticity parameter was introduced in 1997 [9].

The adhesion theories often assume that the interacting surfaces are smooth at the atomic level. However, it is known that finite surface roughness decreases the contact area and consequently reduces the adhesion between the contacting surfaces. The key difficulty in taking the irregularity of a surface into consideration in adhesion models is the technical challenges associated with the accurate characterization of its topology and/or additive materials. Moreover, such irregularities substantially affect the local mechanics. As a result of various emerging industrial applications, in recent years, there has been renewed interest in surface roughness effect, and adhesion reduction due to surface roughness has been studied experimentally and theoretically [10–14]. Besides the out-of-plane motion of a particle on substrate, understanding the in-plane rocking (leaning prior to free rolling) and free-rolling motions of particle on substrate are found significant due to their critical importance in particle removal and attachment. As detachment requires a detailed understanding of complicated local physics stemming from the disruptive nature of the detachment phenomenon, detachment-free methods (such as restitution-based techniques) are often desirable. In addition, the detachment-free approach allows the study of various external effects (such as temperature, humidity, electric field) on a specific adhesion bond in a controllable manner. Unlike the one-dimensional adhesion models for characterizing the out-of-plane adhesion force–displacement behavior, the characterization of the in-plane rocking/rolling motions and the associated restitution moment resisting

the in-plane motion requires a two-dimensional adhesion theory which recently has been experimentally and theoretically explored and studied [15–17].

#### 4.2.2 Measurement Methods

As extensively reported in the literature [1], there exist many adhesion measurement techniques for multi-particle systems, based on centrifugal effect, aerodynamic and hydrodynamic forces, impact–spectrum, and ultrasonic vibration. In all these statistical adhesion measurement approaches, the adhesion is characterized by measuring the detachment force required to detach particles from substrates. Due to the disruptive nature of the process, detachment process is often a result of interactions of a number of complex physical effects, such as energy release, plastic deformation, finite amplitude deformation, and mass transfer at nano-/micro-scale. Complexity associated with these processes leads to accuracy issues. Since its inception, the uses of a Quartz Crystal Microbalance (QCM) in adhesion characterization have been considered and reported, even though it is commonly used to determine minute mass (per unit area) deposition on its shear-mode quartz crystal resonator and the viscoelastic properties of its material by measuring the shift in the damped resonance (central) frequency of its resonator. Unlike the aforementioned methods, QCM requires no particle detachment. As reported in [18], its use as a tool to understand the adhesion of biologically functionalized polystyrene micro-particles on substrates was demonstrated and a mechanical model was presented to study the pivot-point vibration of such particles on a QCM resonator to scan the bond-rupture events for biomedical diagnostics. The QCM-based method proposed in [18] is a detachment-based technique and resulting work of adhesion could include substantial error due to complexity and disruptive nature of the detachment phenomenon. However, based on [15,19], the work of adhesion of raw/coated particles can be extracted considering the pivot-point vibration of such particles on a QCM resonator.

#### 4.2.3 Non-contact Adhesion Characterization of Single Particles

In recent years, single particle non-contact adhesion measurement techniques have attracted attention for accurate adhesion characterization of micro-scale objects as these methods target to eliminate the disadvantages of the contact and destructive as well as statistical techniques.

In [15,19], based on non-invasive external excitation (ultrasonic base or air-coupled) and non-contact laser interferometric sensing, a non-contact and non-destructive adhesion characterization method was introduced for observing the dynamic behavior of individual adhesive micro-particles experiencing pre-rolling in-plane and out-of-plane motions on flat substrates from their dynamic responses. The main advantage of the utilization of a laser interferometer (vibrometer) in this individual particle adhesion characterization approach is its ability to acquire surface nanometer-level transient displacements at high frequency vibrations (up to GHz) in a non-contact manner with high accuracy. In this approach a particle subjected to an external excitation undergoes nonlinear and coupled dynamics in in-plane and out-of-plane directions and, because of adhesion and associated local elastic deformation, experiences restitution force and moments resisting its out-of-plane displacement described by several continuum mechanics models [9] and the in-plane (rocking and/or rolling) angular displacement [20], respectively. At micro-scale, this restitution moment along with the rotational inertia of the particle results in a free oscillatory vibrational (rocking) motion of the particle with respect to the center of its contact area [15,19]. Nonlinear and coupled dynamics of a particle can result in various vibrational modes in the experimentally obtained spectral domains of the particles which can lead to an ambiguity in adhesion characterization. In order to accurately characterize the interfacial interactions as well as the work of adhesion using the observed dynamic behavior of particles subjected to external excitations, a two-dimensional mathematical model describing the nonlinear and coupled out-of-plane and in-plane motions of the particle subjected to external elastic wave is required. A novel technique to generate and detect the high frequency acoustic modes of individual micrometer-sized spheres using focused ultra-short laser pulses was proposed recently as a tool for quality control of spherical elastic particles [21]. Also in nano-scale range, the vibrations of nano-scale surface-supported gold particles were studied using optical spectroscopy and time-resolved X-ray scattering [22].

#### 4.2.4 Particle Adhesion to Nano-film Coated Surfaces

In a wide spectrum of applications, nano-films between particles and surfaces are present. Their presence could significantly affect the surface properties and, consequently, the adhesion properties of nano-/micro-scale objects are modified by such films. While such intermediate layer is often considered to weaken the adhesion bond, it indeed could have the primer effect for enhancing adhesion to unprecedented levels. For instance, due

to unusually high surface energy of graphene (Gr), integrating monolayer graphene into nano-/micro-scale devices offers potential in several practical applications, such as flexible electronics, transparent electrodes, biosensors [23] and nano-mechanical devices [24,25]. The high flexibility of monolayer Gr and its capability to conform to a surface in comparison to multilayer Gr sheets was proposed as a possible explanation for considerably high work of adhesion value for monolayer Gr sheets. Also in biomimetic systems applications, thin layers are created by immobilizing receptor proteins (such as streptavidin, P-selectin) on flat substrates to interact with ligand proteins (such as biotin and PSGL-1) immobilized on the surface of elastic particles and flat rafts to study/understand the ligand–receptor interactions in biological entities adhesion process. For functional integration of nano-films (such as Gr) into nano-/micro-scale devices, understanding and characterization of the interfacial adhesion properties of the nano-film coated substrates is essential. Monolayer Gr, a sheet of carbon atoms uniformly arranged in a hexagonal honeycomb lattice, has attracted considerable attention in scientific and engineering communities due to its unusual mechanical (strength), electrical (conductivity with high electron mobility), optical (transparency) and thermal properties. The potential of the use of Gr in nano-/micro-scale devices using tools compatible with current semiconductor manufacturing methods has far-reaching practical implications. However, various properties of Gr and its interactions with other materials are currently either not accurately characterized or poorly understood despite the extent of the reported research on theoretical and computational (molecular dynamics) simulations.

Recently, a number of studies [26–28] on the work of adhesion of monolayer/multilayer Gr with other materials have been reported. In 2010, Zong *et al.* [26] proposed an AFM (Atomic Force Microscopy)-based technique to measure the local adhesion strengths of Gr sheets on a silicon dioxide ( $\text{SiO}_2$ ) wafer by depositing gold and silver rigid nano-particles at the Gr- $\text{SiO}_2$  interface. With an AFM, the trapped particles heights and the circular blisters diameters were measured and used along with a membrane mechanics model to extract the adhesion energy (work of adhesion) of multilayer Gr- $\text{SiO}_2$  interface as  $W_{\text{Gr-SiO}_2} = 151 \pm 28 \text{ mJ/m}^2$  using an underestimated value for average Young's modulus of Gr ( $E = 0.5 \text{ TPa}$ ). In 2012, Bunch and Dunn [27], using an increased value for average Young's modulus of monolayer Gr as  $E \approx 1 \text{ TPa}$ , corrected this value to  $W_{\text{Gr-SiO}_2} = 300 \text{ mJ/m}^2$ . In 2011, Keonig *et al.* [28] reported a value for the work of adhesion of the Gr- $\text{SiO}_2$  interface using a pressurized blister method with Gr sheets on  $\text{SiO}_2$  substrate including an array of predefined wells. The deflection

and delamination of the blister under pressure were measured with an AFM and were used along with a mechanics-based analysis of the blister configuration for determining the work of adhesion of Gr sheets to SiO<sub>2</sub>. Work of adhesion values of  $W_{Gr-SiO_2} = 450 \pm 20$  mJ/m<sup>2</sup> for monolayer Gr and  $W_{Gr-SiO_2} = 310 \pm 30$  mJ/m<sup>2</sup> for multilayer (2–5) Gr sheets exfoliated on SiO<sub>2</sub> wafers were reported. In calculations for extracting Gr adhesion energy (the work of adhesion of the Gr–SiO<sub>2</sub> interface) using this technique, the mechanical properties of monolayer Gr are required:  $E \approx 1$  TPa is taken as Young's modulus of Gr and it is stated that this value was verified by the measured value of  $E t_e = 347$  N/m where  $t_e$  is the effective thickness of monolayer Gr. Poisson's ratio of Gr is taken as  $\nu = 0.16$ , the same as that of graphite. However, recently even a higher value for the Young's modulus of Gr has been reported. For single and bilayer graphene sheets, the Young's modulus is reported as 2.4 and 2 TPa, respectively [29].

In 2012, Yoon *et al.* [30] reported the adhesion energy of monolayer Gr grown on copper substrate using chemical vapor deposition (CVD) process by employing the double cantilever beam fracture mechanics testing. In their measurements, the Gr layer is glued with epoxy to the target substrate, and the work of adhesion is extracted from the delamination force of Gr from the copper substrate as  $720 \pm 70$  mJ/m<sup>2</sup>. This high work of adhesion between monolayer Gr and copper substrate is attributed to increase in the electronic density at the Gr–metal interface. In the reported studies, in addition to the disadvantages of the destructive and contact techniques, the mechanical properties of the Gr which are not quite known yet play a key role in the adhesion energy calculations. A non-destructive external excitation and non-contact technique independent of Gr mechanical properties is necessary to accurately determine the adhesion energy of Gr layer and to avoid the disadvantages of the previous methods. In a recent work [31], as discussed in Section 4.3.2 in detail, a novel method is introduced as an alternative adhesion energy characterization approach for Gr by employing a non-contact vibrational spectroscopy approach along with a mathematical formulation which eliminates the dependency of Gr adhesion energy on its mechanical properties.

#### 4.2.5 Non-contact Particle Manipulation

Manipulation/transport and rolling of single micro-particles have implications in a wide range of applications from particle detachment/removal, pick and place of micro-objects [32–34], surface properties mapping to motility of biological cells (e.g. leukocyte rolling) [35–37]. Non-contact



manipulation and transport of individual micro-particles on dry surfaces, especially at micro-meter length scale, is often desirable, as in contact-based approaches, unintended interactions related to elasticity of materials, multi-point contacts, electrostatic charge transfer and liquid meniscus formation (capillary effect) [38] create complications in resolving experimental data [32]. Non-contact techniques are required to be developed to manipulate/transport single micro-particle on dry substrates. Recently, using a cantilever metal tapered strip (ultrasonic actuator), transportation of small mechanical components due to flexural ultrasonic vibration modes of the actuator was reported [39]. Currently, the out-of-plane force–displacement characteristics of the particle–surface adhesion bond are well-established and several models have been proposed and utilized [9]. Also using a two-dimensional adhesion model (including both out-of-plane and rocking displacements), the presence of a restitution moment resisting the free-rolling of the particle has been demonstrated computationally and experimentally [15, 19, 20] while coupling between out-of-plane and rolling modes has only been partially resolved. Dynamics of micro-particles on flat substrates is affected by various particle–surface interaction mechanisms. In addition to capillary effect [38, 40] and electrostatic charges [41, 42], friction of micro-/nano-particles during rolling and spinning motions on flat substrates is of great interest [5]. For characterization purposes, a mathematical model describing the coupled out-of-plane and free-rolling motions of particle is required to characterize the particle–surface interaction mechanisms during the rolling of the particles. Note that the non-uniform surface properties and distribution of electrostatic charge packs on the surfaces of particles and substrates result in anisotropic adhesion behavior of particles on substrates. Therefore, surface properties mapping is essential using non-contact techniques since in the contact techniques the surface properties of particles and substrates can be modified by contact.

#### **4.2.6 Molecular-scale Characterization Challenges in Biological Adhesion**

Several studies indicate that the interactions of biological cells with each other and their environments play a key role in the formation of multicellular organisms, elimination of viruses and bacteria by the immune system [43] and detection of cancerous cells [44]. Many biological phenomena, such as cell adhesion and cell migration, are directly affected by the interactions of cells with their neighbors and extracellular

substrates [45]. Recent studies report that adhesion of biological cells is a well-orchestrated, highly interactive phenomenon mediated by the specific binding of receptors and ligand molecules anchored in membrane of cell [46,47]. Understanding the cell adhesion is of a significant value in bioengineering applications, since controlling the cell adhesion is a requirement to organize cells in a synthetic matrix [45]. In addition to the specific and strong molecular interactions in cell adhesion, physical forces including repulsion force due to the presence of the glycocalyx in cells as well as gravity, van der Waals, Coulomb and hydration forces [43,48] also contribute to the cell adhesion process. Since biological cells are complex live entities and the active and passive phenomena both contribute to the cell adhesion process, study of the adhesion of cells using a living cell is extremely challenging and it cannot be meaningfully described by the theories developed for the contact mechanics of inactive (non-living) matters [43,49]. Therefore, one possible approach to understand the cell adhesion is to separately study each adhesion process contributing to the cell adhesion by isolating it from other adhesion processes. Simplified cell models (cell-free models) can be employed to separately study/characterize the influences of each process in the cell adhesion. For instance, a giant liposome with no embedded protein molecules in its membrane can be a proper model to study the adhesion and viscoelastic properties of the cell membrane free from the ligand–receptor interaction influences. Bio-materials such as liposomes are soft and their viscoelastic properties play an important role in their adhesion properties since the elastic energy of the deforming particles restricts the spreading/flattening of soft materials on substrates induced by adhesion force. Developing effective methods to characterize the mechanical properties of materials is significant. On the other hand, a biotin-coated polystyrene latex (PSL) particle in contact with a substrate coated with a monolayer of streptavidin protein could be a good model to separately study the ligand–receptor interactions (catch bonds formation) free from the cell membrane mechanics influences and other complexities of living cells. A liposome with embedded protein molecules in its membrane leads to a more complex cell behavior, including both ligand–receptor interactions and cell membrane mechanical contributions to its adhesion process. Such a cell model can be employed for a better understanding of the cell adhesion, since the possible coupling and contributions of the ligand–receptor interactions and cell membrane mechanics in adhesion can be explored. There is need for the development of novel experimental and mathematical tools that can be utilized for various cell models to determine mechanical and adhesion properties of cells in contact with surfaces.

## 4.3 Recent Developments

### 4.3.1 Nonlinear Dynamics in Adhesion Characterization of Micro-Particles

It has been shown that the vibrational base excitation of particle–surface bonds and the response of particle to such excitation can be used for adhesion characterization [15,19,50]. In this section, the adhesion properties of micro-spherical particles on flat vibrating substrates are characterized using experimentally obtained dynamic responses of particles subjected to external pulsative excitations. By relating the experimentally observed natural frequencies in the spectral domains of particles to the stiffness of the adhesion bond, the particle–substrate adhesion property (work of adhesion) was extracted recently [15,19]. However, in [51] it is reported that nonlinear and coupled dynamics of a vibrating particle can result in complicated spectral responses for its free vibrational rocking motion, leading to an uncertainty in the extraction of adhesion property. In the experimental spectral responses of some of vibrating particles, in addition to their predicted rocking resonance frequencies, additional resonance peaks in the vicinity of the doubles of these predicted frequencies have been observed and reported [50,51]. Previously, the doubling effect was also observed and reported with no analysis [17]. To understand and explain the rocking resonance frequency doubling effect, a two-dimensional mathematical model describing the coupled dynamics of a micro-spherical particle in the out-of-plane and in-plane coordinates was developed and reported [50]. Using the presented dynamic model, the work of adhesion values for micro-spherical particles can be extracted from their experimentally determined rocking resonance frequencies without the ambiguity caused by the double resonance peaks [50].

#### 4.3.1.1 Two-Dimensional Particle Adhesion Models

An overview of two-dimensional adhesion models is presented. Despite many models available in the literature for the out-of-plane motion of a spherical particle, only a few analytical and experimental studies have been reported for two-dimensional (in-plane and out-of-plane) motion of particle along with the restitution force and moment resisting particle motion and their relation to the adhesion property of the adhesion bond [15,20,50]. Below one such model is described and discussed. As depicted in Figures 4.1(a) and 1(b), the out-of-plane and in-plane motions of an adhesive micro-particle are described by the elastic out-of-plane displacement of the

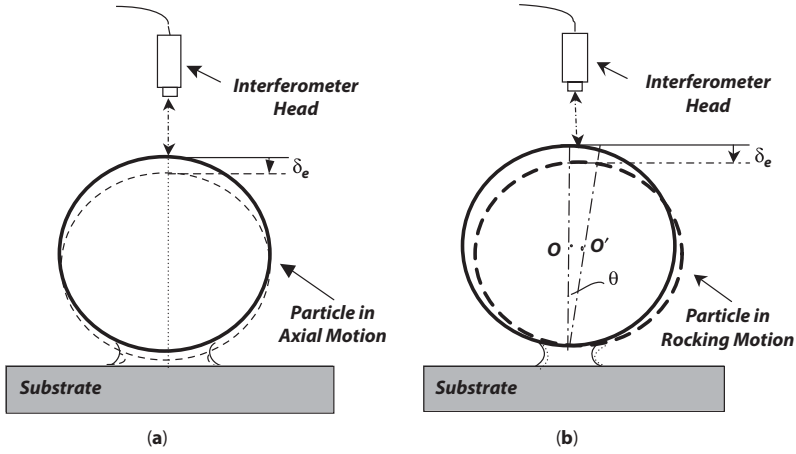


**Figure 4.1** Schematics of (a) purely out-of-plane (axial), and (b) purely in-plane (rocking) motions of a spherical particle subjected to base excitation.

center of the particle ( $\delta$ ) and rocking angle of the particle ( $\theta$ ) with respect to the substrate normal, respectively, as the coordinates of its motion. In the Johnson-Kendall-Roberts (JKR) adhesion theory, the out-of-plane restitution force  $F_R(a)$  opposing the axial (out-of-plane) motion of the spherical particle on a flat substrate is expressed as [6]:

$$F_R(a) = \frac{K a^3}{r} - a^{3/2} \sqrt{6\pi W_A K} \tag{4.1}$$

where  $r$  is the radius of the particle,  $W_A$  the work of adhesion of the particle–substrate interface,  $a$  the radius of the contact area, and  $K = \frac{4}{3}((1 - \nu_p^2)/E_p + (1 - \nu_s^2)/E_s)^{-1}$  the stiffness coefficient of the particle–substrate adhesion bond (here  $E_s$  and  $E_p$  are the Young’s moduli and  $\nu_s$  and  $\nu_p$  the Poisson’s ratios of the isotropic substrate and particle materials, respectively). In addition to the out-of-plane restitution force ( $F_R$ ), this bond creates a restitution moment opposing the free rolling motion of the particle. The restitution moment and the rotational inertia of the particle result in free vibrational rocking motion of the particle with respect to its contact. Employing a two degree-of-freedom adhesion theory, the restitution moment,  $M_R(a, \delta, \theta)$ , was previously approximated as [20]:

$$M_R(a, \delta, \theta) \approx 6\pi W_A \left( \frac{a}{a_0} \right)^{3/2} r(r - \delta) \sin(\theta) \tag{4.2}$$

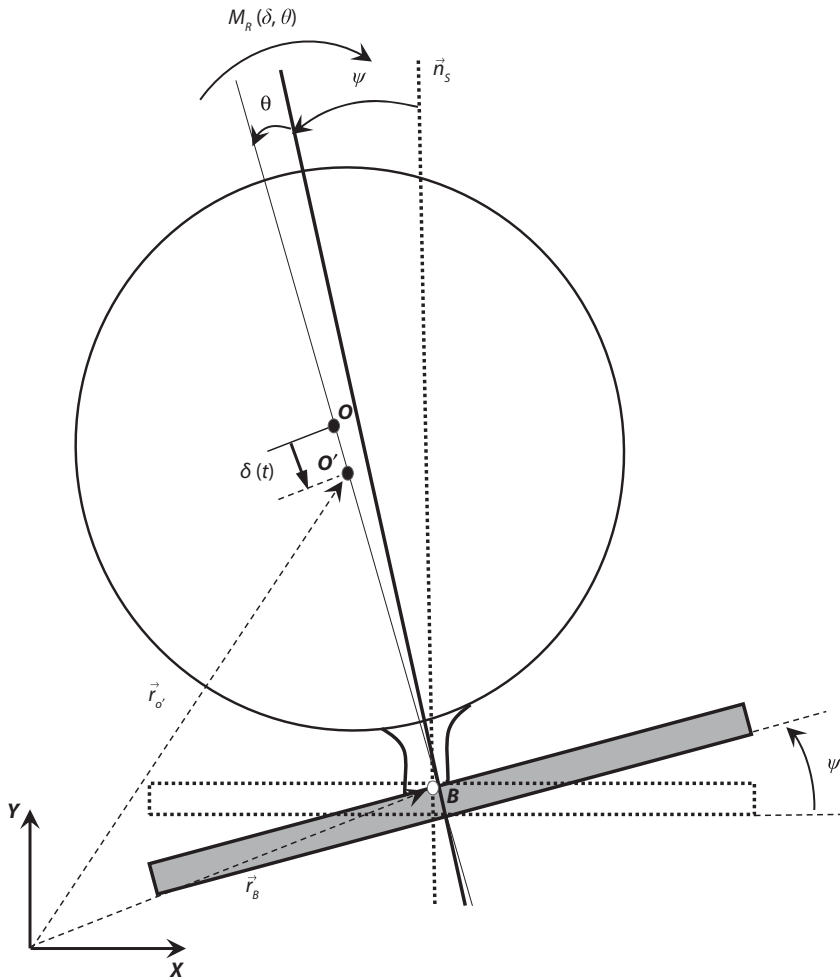


**Figure 4.2** The independent coordinates of the proposed two-dimensional mathematical model for the simultaneous out-of-plane ( $\delta$ ) and in-plane ( $\theta$ ) motions of a spherical particle on a vibrating surface (not to scale).

where  $a_0 = (6\pi r^2 W_A / K)^{1/3}$  is the contact area radius at static equilibrium position ( $\delta^*$ ).  $F_R$  and  $M_R$  are expressed as a function of  $\delta$  using the geometric relationship  $\delta = \frac{a^2}{r} \left( 1 - \frac{2}{3} \left( \frac{a_0}{a} \right)^{3/2} \right)$  [52]. Assuming a low amplitude out-of-plane vibration and a low-amplitude rocking motion around the surface normal, for a spherical particle depicted in Figure 4.2, the linearized out-of-plane  $f_a$  and in-plane  $f_r$  resonance frequencies are thus extracted as:

$$f_a = \frac{1}{2\pi} \sqrt{\frac{K_a^*}{m}} = \frac{1}{2\pi} \sqrt{\frac{27}{20\rho r^3} \left( \frac{3W_A K^2 r^2}{4\pi^2} \right)^{1/3}} \quad (4.3)$$

$$f_r = \frac{1}{2\pi} \sqrt{\frac{K_r^*}{I_B}} = \frac{1}{2\pi} \sqrt{\frac{6\pi W_A r(r-\delta^*)}{I_{O'} + m(r-\delta^*)^2}} \quad (4.4)$$

where  $m$  and  $\rho$  are the mass and the mass density of the particle, respectively,  $I_{O'}$  and  $I_B$  are the mass moments of inertia of the particle about axis respectively passing through  $O'$  and  $B$  and parallel to axis  $Z$ , and  $K_a^*$  and  $K_r^*$  are linearized out-of-plane and in-plane stiffnesses of particle–substrate adhesion bond respectively. Using Equations 4.3 and 4.4 for polystyrene latex (PSL) particles with an average diameter of 21.4  $\mu\text{m}$  ( $\rho_p = 1050 \text{ kg/m}^3$ ,  $E_p = 2.77 \text{ GPa}$ , and  $\nu_p = 0.33$ ) on a flat polished silicon substrate ( $\rho_s = 2329 \text{ kg/m}^3$ ,  $E_s = 127 \text{ GPa}$ , and  $\nu_s = 0.28$ ) and considering  $W_A = 23.5 \text{ mJ/m}^2$  as reported in [53], the linearized rocking and out-of-plane resonance frequencies are calculated as  $f_r = 38.57 \text{ kHz}$  and  $f_a = 1.98 \text{ MHz}$ , respectively. Note that the resonance frequencies of the in- and out-of-plane modes of motion are well separated.

#### 4.3.1.2 Experimental Observations of Nonlinear Particle Vibrations

As reported in [15,17], a set of experiments were conducted to acquire the transient responses of a set of PSL particles on a silicon substrate to an impulsive external excitation in order to characterize the adhesion property of the particle–substrate adhesion bond. The instrumentation diagram of a typical experimental set-up is depicted in Figure 4.3 as detailed in [50]. In the reported experiments, a number of NIST-traceable spherical PSL particles with an average diameter of 21.4  $\mu\text{m}$  were dry-deposited on a polished silicon substrate. In order to eliminate the possible electrostatic force interaction, the particle and substrate were showered with ions using a single point ionizer [50] to neutralize the particle and substrate. First, several single particles oscillating at different locations of the silicon substrate were identified for measurements as some particles were strongly fixed to the surface with no relative motion with respect to the substrate [54]. The laser spot of the fiber interferometer with an approximate diameter of 0.5  $\mu\text{m}$  was focused on the top of the particle using the objective of the optical microscope. The transient out-of-plane responses of the substrate at a set of four substrate measurement points around each particle and the top of each particle were acquired, digitalized, and recorded with

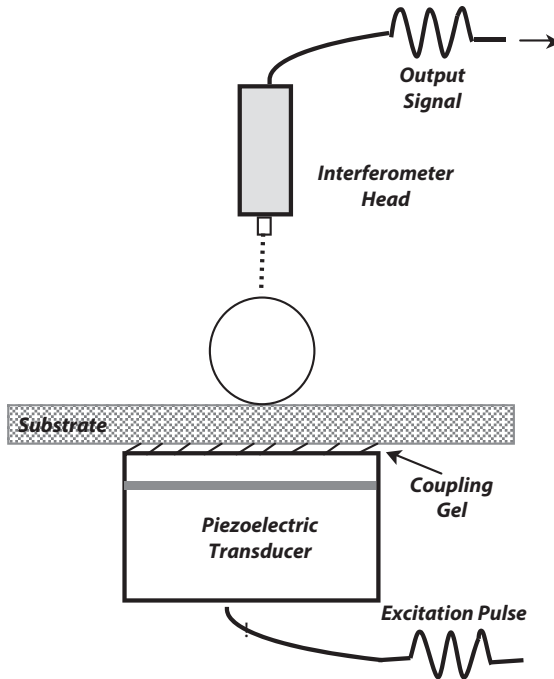


Figure 4.3 Schematic of the base excitation experimental set-up (close-up).

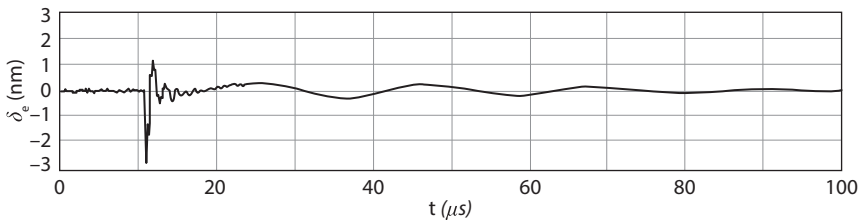
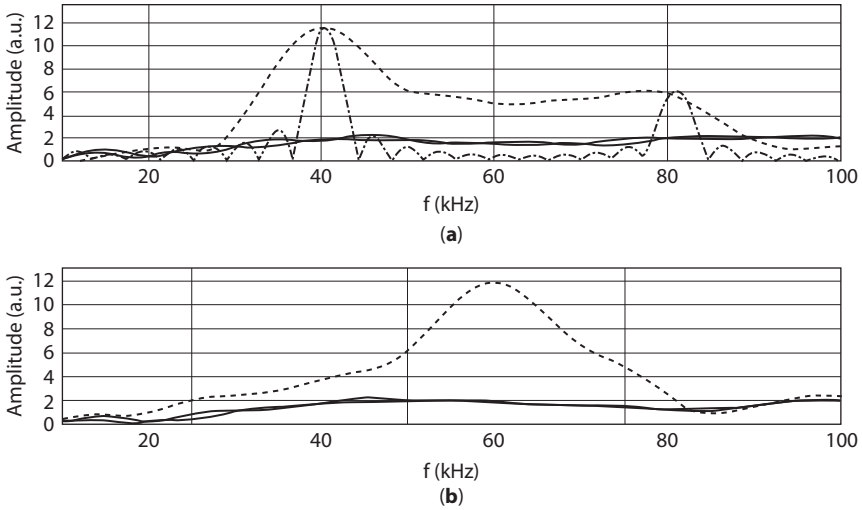


Figure 4.4 Experimentally obtained temporal response of particle I subjected to base excitation applied from  $t_1 = 10.50 \mu s$  to  $t_2 = 17.50 \mu s$ .

a digitizing oscilloscope for signal processing. The procedure was repeated for several particles on the same substrate within a few minutes. The temporal responses of a set of five PSL particles (as depicted in Figure 4.4 for Particle I) were acquired and transformed into the spectral domain using the Fast Fourier Transform (FFT) routine (as depicted in Figure 4.5 (a) for Particle I (dashed thick lines)) for determining their resonant structures. A pair of peaks for each particle in its spectral response is observed as follows; Particle I (at 40.41 and 78.15 kHz), II (at 45.16 and 82.70 kHz),



**Figure 4.5** Comparisons of experimental spectral responses of the substrates (solid thin lines) and particle I (dashed thick line) (a) with those computationally obtained from the integration of the proposed model (dot-dashed thin line). A particle exhibiting no whirling motion is included (b).

III (at 36.55 and 64.4 kHz) and IV (at 40.86 and 78.56 kHz). However for Particle V, only a single peak in the frequency range of interest was observed at 60.14 kHz (Figure 4.5 (b)). These observed resonance frequencies are absent in the substrate responses as depicted in Figures 4.5 (a) and (b) (solid thin lines), respectively, indicating they are due to the particle–substrate bond. Experimental evidence for frequency doubling is also observed in a previous work [17] for polyvinylpyrrolidone (PVP) micro-particles (see Figures 4.7.c (37.80 kHz and 75.40 kHz), 7.e (22.51 kHz and 45.50 kHz), 7.f (24.50 kHz and 45.20 kHz) and 7.g (22.51 kHz and 43.52 kHz) of reference [17]) without identifying the frequency doubling effect and/or its causes. Moreover, in the spectral responses included in [17], the amplitude of the rocking resonance frequency for each particle and its double are considerably different.

#### 4.3.1.3 *Mathematical Modeling for Nonlinear Dynamics of Particle Vibration*

Modeling is essential in adhesion characterization. The observed rocking frequency doubling phenomenon results in ambiguity in extracting the adhesion property based on the experimentally obtained spectral domains [50]. For accurate characterization of particle–substrate adhesion and to



resolve the ambiguity in the frequency doubling phenomenon, coupled dynamics of the vibrating particle should be studied. To this end, here the vibrational motion of an adhesive spherical particle on a moving flat substrate is considered (Figure 4.2). The equations of motion are derived assuming the particle experiences in-plane and out-of-plane vibrations under base excitation and no particle detachment occurs during motion, that is, neither free-rolling nor sliding occurs during experiments. Below, these nonlinear coupled equations of motion are employed to explain the experimentally observed frequency doubling phenomenon and to determine the value of work of adhesion. In this model, the effect of the adhesion bond is modeled as an out-of-plane restitution force  $F_R(\delta)$  and an in-plane restitution moment  $M_R(\delta, \theta)$  (Figure 4.2) [50]. The equations of motion for the particle are derived with respect to the fixed global coordinate system  $(X, Y)$  with the corresponding unit vectors  $\hat{i}, \hat{j}$ . As reported in [50], the in-plane and out-of-plane equations of motion of an adhesive spherical particle with a radius  $r$  and a mass  $m$  on a vibrating flat substrate are derived as:

$$m\ddot{\delta} + F_R(\delta) = m\left(\ddot{Y}\cos(\psi + \theta) - (r - \delta)(\dot{\psi} + \dot{\theta})^2 - \ddot{X}\sin(\psi + \theta)\right) \quad (4.5)$$

$$\begin{aligned} I_O(\ddot{\psi} + \ddot{\theta}) + M_R(\delta, \theta) &= m(r - \delta)(\ddot{X}\cos(\psi + \theta) + 2\dot{\delta}(\dot{\psi} + \dot{\theta}) \\ &+ \ddot{Y}\sin(\psi + \theta) - (r - \delta)(\dot{\psi} + \dot{\theta})) \end{aligned} \quad (4.6)$$

For the external excitation of a short pulse, the governing equations for the motion observed following excitation are simplified for its purely free vibrational motion:

$$m\ddot{\delta} - m\delta\dot{\theta}^2 + F_R(\delta) = -mr\dot{\theta}^2 \quad (4.7)$$

$$(I_O + m(r - \delta)^2)\ddot{\theta} - (2m(r - \delta)\dot{\delta})\dot{\theta} + M_R(\delta, \theta) = 0 \quad (4.8)$$

As reported in [50], Eq. 4.8 is linear with respect to  $\theta(t)$  and practically independent of  $\delta(t)$ . As a result, the dynamics of the rocking motion ( $\theta(t)$ ) is dominated by its linear terms and its harmonic response could be approximated as  $\theta(t) = \Theta \sin(\omega_r t)$  where  $\Theta$  and  $\omega_r$  are the amplitude and resonance frequency of the rocking motion, respectively. Substituting the approximated harmonic solution  $\theta(t)$  in Eq. 4.7, the right-hand side of the resulting equation, acting as an external excitation term, becomes

$$mr\dot{\theta}^2 = mr\omega_r^2\Theta^2\cos^2(\omega_r t) = \frac{1}{2}mr\omega_r^2\Theta^2(1 + \cos(2\omega_r t)) \quad \text{and forces the}$$

system to oscillate at an additional frequency which is double of the rocking frequency  $\omega_r$ . Due to the nonlinear coupling, the pure rocking motion can excite the out-of-plane displacement  $\delta(t)$  with a frequency of  $2\omega_r$ . According to [15], since in the experiments the interferometer detects the total out-of-plane displacement of the top of a particle as it oscillates, the measured out-of-plane displacement  $\delta_e(t)$  is a combination of the in- and out-of-plane displacement components as:

$$\delta_e(t) \approx (\delta(t) - \delta^*) + 2r(1 - \cos \theta(t)) \quad (4.9)$$

Consequently, it is concluded that since the rocking motion appears as the argument of the cosine function, the resonance frequency of the rocking motion cannot be seen in the spectral domain unless a non-zero leaning angle  $\theta_0(\dots)$  with un-specified arguments is present and is added to the approximated solution  $\theta(t)$  as  $\theta_m(t) = \Theta \sin(\omega_r t) + \theta_0(\dots)$  which leads to the out-of-plane displacement oscillating not only at  $2\omega_r$ , but also at  $\omega_r$ . The term  $\theta_0(\dots)$  causes the rocking resonance frequency doubling effect and attests that the rocking motion occurs around an inclined axis with respect to the substrate normal which in a three-dimensional dynamic model implies the existence of whirling-like motion of particle. Based on the developed two-dimensional dynamic model, the whirling-like motion is due to an inclined rocking motion of a particle and/or the nonlinear component coming from the presence of the nonlinear damping term in Eq. 4.7. In Figure 4.5(a) (dashed thick lines) the experimentally observed spectral domain of particle I experiencing whirling-like motion is shown. However, Figure 4.5(b) (dashed thick line) shows the experimentally observed spectral domain of a particle with no whirling motion.

#### 4.3.1.4 Numerical Simulations

Numerical simulations are often utilized to compare the responses of models to those of the physical systems, and to extract model parameters from experimental data. In order to extract the leaning angles and work of adhesion values for particle–substrate systems using equations of motion and experimental results, Eqs. 4.5 and 4.6 are numerically integrated in time considering substrate and particle materials properties and substrate translation motion as reported in [50]. The transient responses of the dynamic out-of-plane motion with respect to  $\delta^*$  ( $\delta_d(t) = \delta(t) - \delta^*$ ) are determined numerically as illustrated in Figure 4.6 for particle I. According to Figure 4.6, the dynamic out-of-plane response  $\delta_d(t)$  of the particle has a natural period of  $T_d = 0.50 \mu\text{s}$ . The in-plane transient response of particle

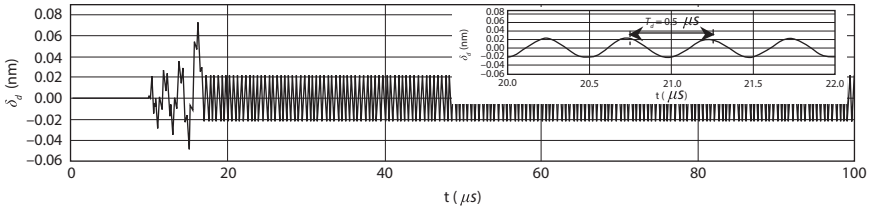


**Figure 4.6** Temporal response of the out-of-plane motion of particle I obtained from the computational simulations. A close-up of the response with its natural period  $T_d = 0.50 \mu\text{s}$  is shown in the inset.

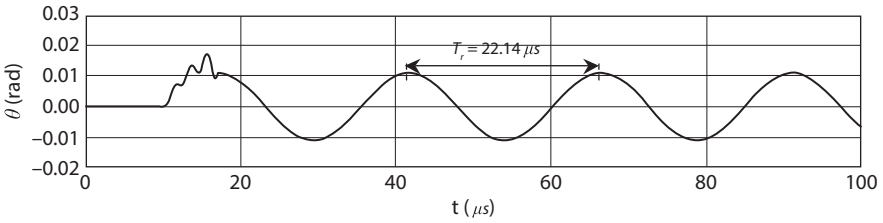


**Figure 4.7** Temporal response of the in-plane motion of particle I extracted from the computational simulation with a natural period  $T_r = 22.14 \mu\text{s}$ .

$\theta(t)$  is also determined numerically (Figure 4.7) for the same particle. The in-plane transient response  $\theta(t)$  has a natural period of  $T_r = 22.14 \mu\text{s}$  (Figure 4.7). The total depression of the particle top  $\delta_e(t)$  is calculated by substituting numerically determined  $\delta_d(t)$  and  $\theta(t)$  into Eq. 4.9. The numerically determined  $\delta_e(t)$  for each particle is transformed into the spectral domain to obtain their frequency contents. However, as discussed before, in order to observe both rocking resonance frequency and its double in the spectral domain, the particle has to experience leaning rocking motion with respect to the substrate normal. As depicted in Figure 4.8 for particle I, the value of leaning angle  $\theta_0(\dots)$  affects the ratio of the amplitudes of the rocking resonance frequency and its doubled frequency in the spectral domain. It is seen in Figure 4.8 that when  $\theta_0 = 5.1 \text{ mrad}$ , the amplitudes ratio of the rocking resonance frequency and its double in the spectral domain agrees with that of the experimental spectral response, indicating  $\theta_0 = 5.1 \text{ mrad}$  is a reasonable approximation for the leaning angle for the particle I [50]. It is noteworthy that since the amplitudes of the rocking resonance frequency and its double are almost the same in the substrate spectral domains (solid thin lines in Figures 4.5 (a) and (b)), in [50], it is concluded that the energy pumped in the system at these

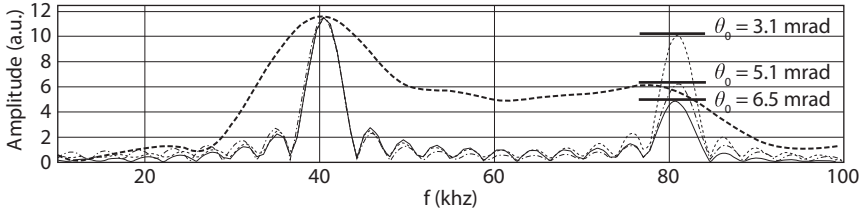


**Figure 4.8** The influence of the whirling (leaning) angles ( $\theta_0 = 3.1$  mrad (dashed thin line),  $\theta_0 = 5.1$  mrad (dot-dashed thin line) and  $\theta_0 = 6.5$  mrad (solid thin line)) on the amplitude ratios of rocking frequency and its double peaks (1.13, 1.87, 2.43, respectively) for particle I. The dashed thick line corresponds to the experimentally observed spectral response of the particle.

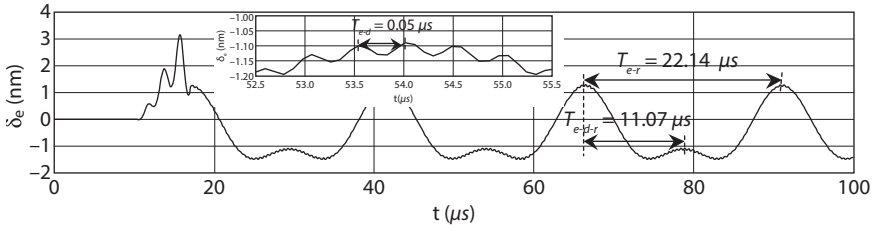


**Figure 4.9** Temporal response of the total out-of-plane depression  $\delta_e(t)$  of particle I extracted from the computational simulations. The low frequency component of the total response possesses a natural period of  $T_{e-r} = 22.14 \mu s$ . The high frequency component of  $\delta_e(t)$  response with a natural period of  $T_{e-d} = 0.50 \mu s$  is shown in the inset.

frequencies is approximately the same, and thus the amplitude difference at these frequencies in the spectral domain of particles is related only to the dynamic motion of the particle. Using the approximated leaning angles values, the total depression of the particles  $\delta_e(t)$  with whirling-like motion is calculated for particle I (Figure 4.9). In Figure 4.9, as predicted, the natural periods of  $\delta_d(t)$  and the rocking  $\theta(t)$  and its doubled natural frequencies responses are clearly seen in the  $\delta_e(t)$  response ( $T_{e-d} = T_d = 0.50 \mu s$ ,  $T_{e-r} = T_r = 22.14 \mu s$  and  $T_{e-d-r} = 0.5T_r = 11.07 \mu s$ ). Also the values of work of adhesion for particles are extracted from simulation by matching the rocking resonance frequency of the simulation to the experimentally obtained ones. The work of adhesion values are extracted for the particle set (Particles I-IV) as  $W_A = 25.9, 32.5, 22.0$  and  $26.5 \text{ mJ/m}^2$ , respectively. These values are consistent with the reported value of  $W_A = 23.5 \text{ mJ/m}^2$  calculated directly from the Hamaker constants of the particle and substrate materials in the literature [53].

In conclusion, in [50,51], it is demonstrated that the coupled vibrational dynamics of micro-spherical particles on vibrating flat substrates can be employed for accurate characterization of adhesion property of particle–substrate system. For some of vibrating particles, unanticipated resonance peaks at or around the doubles of the predicted rocking natural frequencies were observed in the experimentally obtained spectral domains. The proposed model describes the nonlinear coupled in-plane and out-of-plane motions, and paves the way to the derivation of a set of nonlinearly coupled equations of motion. From the analysis of the equations of motion, it is concluded that nonlinear coupling between the in-plane and out-of-plane modes of motion is the source of doubled rocking resonance frequencies observed in the experimental data. It was explained that for both the rocking resonance frequency and its double to be created in experiments, the particle must experience rocking motion around an inclined (tilted) axis with respect to the surface normal. This leaning rocking motion implies the presence of whirling-like motion of particles in the reported experiments when the frequency doubling effect is observed. The excitation modes/mechanisms and/or nonlinear coupling effects could cause a whirling-like motion of particles. Additionally, a set of computational simulations for the rocking and out-of-plane motions of micro-spherical particles excited by impulsive loads were conducted. It is shown that, by matching the amplitude ratios of the rocking resonance frequency and its double in the simulated responses to the experimentally obtained ones, the leaning angles of whirling particles can be approximated. The larger the amplitude ratio of the rocking resonance frequency to the doubled rocking resonance frequency is, the larger the leaning angle for the particle during whirling-like motion is. The extracted work of adhesion values by matching the rocking resonance frequency values of simulations and experimental results are in good agreement with the expected theoretical value for the particle and substrate materials.

#### **4.3.2 Adhesion Characterization of Monolayer Graphene by Vibrational Spectroscopy**

The presence of nano-films on a surface affects the adhesion interactions between the surface and adhering objects, and poses challenges for adhesion characterization. In this section, some recent findings on the effects of nano-films on surface adhesion characterization are summarized. In [31], the transient responses of a set of PSL micro-particles on an ultrasonically

excited  $\text{SiO}_2$  substrate with a monolayer Gr grown with CVD process are utilized to determine the work of adhesion of the Gr- $\text{SiO}_2$  interfaces. Following an approach similar to the ones discussed in Section 4.3.1.2, in [31] the rocking resonance frequencies of the particles are determined from their acquired transient responses and a mathematical formulation is reported to relate these resonance frequencies to the work of adhesion of the Gr-PSL interfaces and consequently to the work of adhesion of the Gr- $\text{SiO}_2$  interfaces. It is noted that this non-contact and non-destructive technique requires no knowledge of the mechanical properties of substrate materials, namely, Gr and/or  $\text{SiO}_2$ .

#### 4.3.2.1 *Experimental Studies*

The main utility of the vibrational spectroscopy experimental set-up discussed below is to acquire the transient response of a micro-spherical particle on a vibrating substrate for determining the locations of frequency peaks in its spectral response to characterize the adhesion energy. In the reported study [31], the Gr/ $\text{SiO}_2$  substrate with dry-deposited PSL micro-particles was subjected to an impulsive external excitation (Figure 4.10 and see Figure 4.2 for particle model). The instrumentation diagram of the set-up employed was originally reported in [15,19] and the key components were described in [31]. In the reported experiments, NIST-traceable spherical PSL particles with an average diameter of 21.4  $\mu\text{m}$  were dry-deposited on a monolayer Gr sheet grown by CVD and transferred on the 285 nm-thick polished  $\text{SiO}_2$  layer on a silicon (Si) substrate. With the procedure explained in detail in [31], a set of waveforms were acquired for each particle in the sample set. In the reported study, in addition to the particle response waveforms, the transient out-of-plane responses of the substrate at two substrate measurement points around each particle in the sample set were acquired, averaged, digitalized, and recorded with the digitizing oscilloscope for further signal processing.

#### 4.3.2.2 *Mathematical Model for Dynamics of a Particle on a Nano-film Coated Surface*

In a recent study [31], a mathematical model for understanding the dynamics of a particle on a nano-film coated surface is presented. As depicted in Figure 4.2, the out-of-plane and in-plane modes of motion of an adhesive micro-particle are described by the elastic out-of-plane displacement of the center of the particle ( $\delta$ ) and the rocking angle of the particle with respect to the substrate normal ( $\theta$ ), respectively. Employing a two

degree-of-freedom adhesion model, the restitution moment,  $M_R(a, \delta, \theta)$ , was previously approximated [20] and later modified [50] for the reported work as below:

$$M_R(a, \delta, \theta) \approx 6\pi W_A r (r - \delta) \left( a/a_0 \right)^{3/2} \sin(\theta) \quad (4.10)$$

where  $W_A$  is the work of adhesion between the particle and substrate material,  $a$  the contact area radius of the spherical particle and substrate,  $r$  the radius of the particle and  $a_0 = (6\pi r^2 W_A / K)^{1/3}$  the radius of the contact area at static equilibrium with the stiffness coefficient of the adhesion bond  $K = \frac{4}{3}((1 - \nu_p^2) / E_p + (1 - \nu_s^2) / E_s)^{-1}$  ( $E_s$  and  $E_p$  are the Young's moduli and  $\nu_s$  and  $\nu_p$  the Poisson's ratios of the isotropic substrate and particle materials, respectively). It is noted that the effect of the harder material in determining  $K$  becomes negligible when the difference between Young's moduli is large. In [50], assuming a low amplitude vibration in the out-of-plane and in-plane directions and using the restitution moment in the in-plane direction, the linearized in-plane resonance frequency of a rocking particle with respect to the center of the contact area (point  $B$  in Figure 4.2) is expressed as:

$$f_r = \frac{1}{2\pi} \sqrt{\frac{6\pi W_A r (r - \delta^*)}{I_{O'} + m(r - \delta^*)^2}} \approx \frac{1}{2\pi} \frac{1}{r^{3/2}} \sqrt{\frac{45 W_A}{14 \rho}} \quad (4.11)$$

where  $m$  and  $\rho$  are the total mass and the mass density of the particle material, respectively,  $I_{O'} = 2mr^2/5$  is the mass moment of inertia of the spherical particle about the axis passing through  $O'$  (the center of the particle) and perpendicular to particle surface and  $\delta^*$  is the out-of-plane displacement of the center of the particle in the static equilibrium position of the particle.

A PSL micro-spherical particle adhering to monolayer Gr on  $\text{SiO}_2$  layer interacts with Gr at short and with  $\text{SiO}_2$  at larger distances, as depicted in Figure 4.10. In order to accurately include the contributions of the  $\text{SiO}_2$  surface and the monolayer Gr in the adhesion interactions between the substrate and the particle, in general, a more involved adhesion model is needed. However, in the current study, since the particle-substrate separation distance is nearly tripled because of the Gr layer in between, it is assumed that the adhesion energy between particle and substrate is due primarily to PSL and Gr interactions even though, as discussed below, the long range PSL- $\text{SiO}_2$  interaction are detected as well.

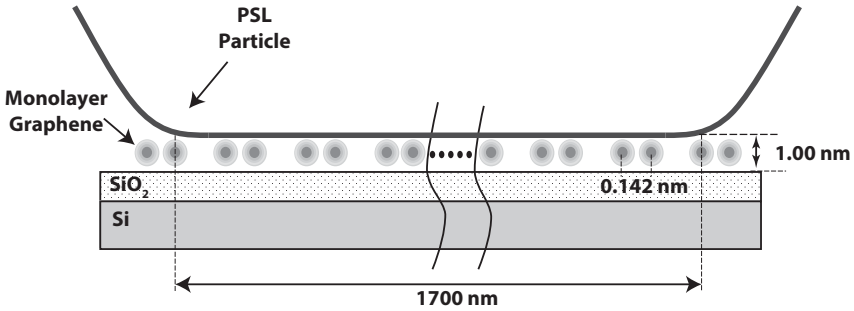


**Figure 4.10** Schematic of the contact zone of the PSL particle adhering to monolayer graphene on a silicon dioxide substrate. The diameter of the contact area of the PSL-Gr interface is determined by using  $W = 1160 \text{ mJ/m}^2$ .

Utilizing the measured rocking resonance peaks in the acquired spectral domain responses of the PSL particles on the Gr/SiO<sub>2</sub> substrate, the work of adhesion of the Gr-SiO<sub>2</sub> interface can be extracted with no knowledge of the Hamaker constant and mechanical properties of Gr, as described below. The work of adhesion between two dissimilar Materials 1 and 2 is defined as [52]:  $W_{12} = (A_1 A_2)^{1/2} / 12\pi z_{12}^2$  where  $A_1$  and  $A_2$  are the Hamaker constants of Materials 1 and 2, respectively, and  $z_{12}$  is the separation distance between the two material surfaces. In the current study, the three materials are dealt with, namely PSL, SiO<sub>2</sub> and Gr. Here  $A_1$  is for the Hamaker constant of PSL (Material 1),  $A_2$  for SiO<sub>2</sub> (Material 2), and  $A_3$  for Gr as Material 3. From the ratio  $W_{23}/W_{12}$ ,  $A_3$  (for Gr) is expressed in terms of  $A_1$  (PSL),  $W_{12}$  (for the PSL-SiO<sub>2</sub> interface) and  $W_{23}$  (for the Gr-SiO<sub>2</sub> interface) as follows:  $A_3 = A_1 (W_{23}/W_{12})^2 (z_{23}/z_{12})^4 = (12\pi z_{23}^2 W_{23})^2 / A_2$  where  $z_{23}$  is the separation distance between the Gr and SiO<sub>2</sub> surfaces. From Eq. 4.11, the rocking motion resonance frequency of a spherical PSL particle on the Gr surface is related to the work of adhesion value

of the PSL-Gr interface as:  $f_{13} = \frac{1}{2\pi r_1^{3/2}} \sqrt{45W_{13}/14\rho_1}$  where  $\rho_1$  and  $r_1$  are the mass density and the radius of the spherical PSL particle, respectively, and, using  $W_{13} = (A_1 A_3)^{1/2} / 12\pi z_{13}^2$ , this resonance frequency is expressed in terms of the Hamaker constants of PSL and Gr ( $A_1$  and  $A_3$ )

as:  $f_{13} = \frac{1}{2\pi r_1^{3/2}} \sqrt{\frac{15 A_1^{1/2} A_3^{1/2}}{56 \pi z_{13}^2 \rho_1}}$  where  $z_{13}$  is the separation distance between the Gr and PSL surfaces. To eliminate  $A_3$ , the relationship derived above for the Hamaker constant of Gr ( $A_3$ ) is substituted into  $f_{13}$  and the resulting equation is solved for  $W_{23}$  to express the work of adhesion of the Gr-SiO<sub>2</sub> interface ( $W_{23}$ ) in terms of  $A_2/A_1$  as:



$$f_{13} = \frac{1}{2\pi} \frac{z_{23}}{r_1^{3/2} z_{13}} \sqrt{\frac{45}{14} \frac{W_{23}}{\rho_1} \left( \frac{A_1}{A_2} \right)^{1/2}}$$

or

$$W_{23} = \frac{56}{45} \pi^2 \rho_1 r_1^3 f_{13}^2 \left( \frac{z_{13}}{z_{23}} \right)^2 \left( \frac{A_2}{A_1} \right)^{1/2} \quad (4.12)$$

For the Hamaker constant of  $\text{SiO}_2$ , here the average of its reported experimental values [52],  $A_2 = 5.5 \times 10^{-20}$  J, is employed. Since no experimental value is reported for PSL [52], the average of reported analytically approximated values for polystyrene,  $A_1 = 7.25 \times 10^{-20}$  J, is utilized in the calculations below. In recent AFM studies [55, 56], the equilibrium separation distance between Gr and  $\text{SiO}_2$  is reported in a range of  $z_{23} = 0.42\text{--}0.90$  nm, however, from the interlayer spacing in bulk graphite it is often taken as 0.34nm [56]. In the following calculation, its lowest measured value of  $z_{23} = 0.42\text{nm}$  (reported in [55]) is used, as it is the closest to its reported theoretical value. In addition, error in AFM measurements and its sensitivity to environmental conditions are known, as reported in [55]. It is noted that since  $\text{SiO}_2$  surface is highly polished, no surface roughness effect on the equilibrium separation distance between Gr and  $\text{SiO}_2$  is anticipated. Below, the equilibrium separation distance between PSL and Gr surfaces is taken as  $z_{13} = 0.43$  nm [57]. As a result, the value of  $W_{23}$  is approximated in terms of the ratio  $\alpha = (z_{13}/z_{23})^2 = 1.048$ , which is nearly unity, as:

$$W_{23} \approx \frac{56}{45} \pi^2 \alpha \rho_1 r_1^3 f_{13}^2 \left( \frac{A_2}{A_1} \right)^{1/2} .$$

Under ambient temperature of 297 K and a relative humidity of 15%, the transient response of each PSL particle in the sample set to the surface vibration is acquired (see Figure 4.11 as a representative) as detailed in [31] and transformed into the spectral domain using a Fast Fourier Transform (FFT) routine for determining its frequency content (see Figure 4.12) and,

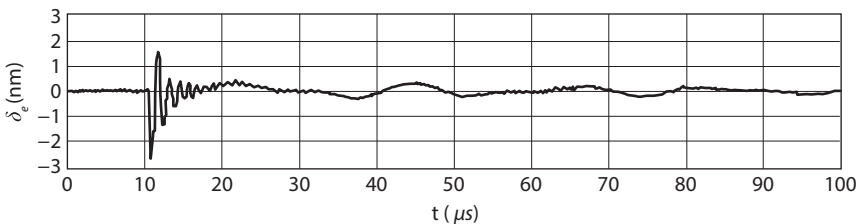


**Figure 4.11** Sample experimental temporal response of a rocking micro-particle.

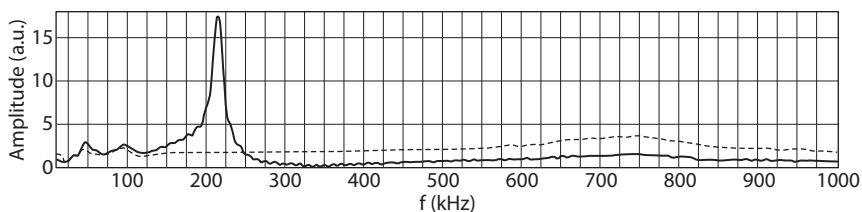


**Figure 4.12** Sample experimental spectral response of the substrate (dashed thin line) and a rocking micro-particle (solid thick line).

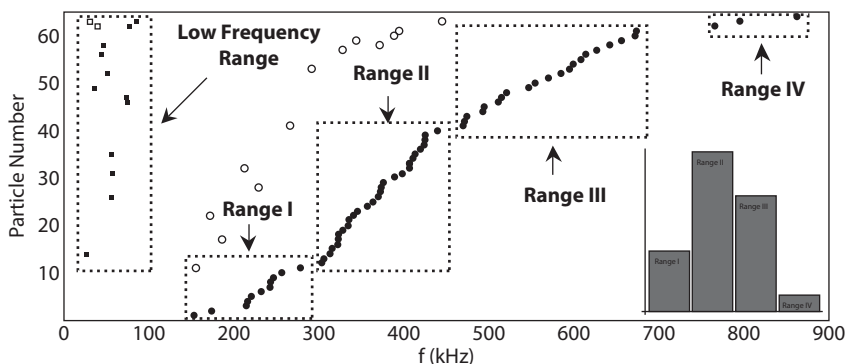


**Figure 4.13** Vibrational spectra for determining Gr/SiO<sub>2</sub> interface adhesion energies. Frequency peaks observed in the experimentally obtained spectral domain of particles, including graphene-SiO<sub>2</sub> interactions with PSL particles. The inset shows the distribution of the number of particles in each measured frequency range.

consequently, its resonance peaks. The extracted resonance peaks for the sample set are summarized in Figure 4.13, in which an empty circle corresponds to the rocking resonance frequency for a particle experiencing whirling-like motion whereas a filled circle is for marking the double of its rocking resonance frequency. It is observed that the acquired peak frequencies occur in two distinct zones. In addition to their dense, uniform grouping in a *low frequency zone* (20–88 kHz), four resonance frequency ranges in a *high frequency zone* (150–870 kHz), as depicted in Figure 4.13, are identified: in the range of  $f_I = 152.7\text{--}278.4$  kHz (Range I, 17.2% of the particles in the sample set),  $f_{II} = 303.0\text{--}439.4$  kHz (Range II, 45.3%),  $f_{III} = 469.6\text{--}673.6$  kHz (Range III, 32.8%) and  $f_{IV} = 766.0\text{--}862.7$  kHz (Range IV, 4.7%) and are used in the following adhesion characterization analysis.

Based on the relationship  $f_{13} \approx \frac{1}{2\pi r_1^{3/2}} \sqrt{45W_{13}/14\rho_1}$ , derived above, for the PSL sample set, using the measured frequency peaks ( $f_{13}$ ) for each particle in *the high frequency zone*, the work of adhesion ranges for the PSL-Gr interface are obtained in the four identified frequency ranges in *the high frequency zone* as  $W_{13} = W_{\text{PSL-Gr}} = 92\text{--}306$  mJ/m<sup>2</sup> (I), 362–762 mJ/m<sup>2</sup> (II), 871–1792 mJ/m<sup>2</sup> (III), and 2317–2939 mJ/m<sup>2</sup> (IV). From these values, utilizing Eq. 4.12, the ranges for the work of adhesion between SiO<sub>2</sub> and Gr are extracted as follows:  $W_{23} = W_{\text{SiO}_2\text{-Gr}} = 84\text{--}279$  mJ/m<sup>2</sup> (I), 331–696 mJ/m<sup>2</sup> (II), 797–1641 mJ/m<sup>2</sup> (III), and 2122–2692 mJ/m<sup>2</sup> (IV) [31]. To better understand the origins of the observed frequencies in the *low frequency zone* (20–88 kHz) depicted in Figure 4.13, in which hollow and filled squares in the *low frequency zone* represent the same frequency concepts as empty and filled circles represented in the *high frequency zone*, an analysis is carried out as detailed in [31] and it is concluded that *the low frequency zone* corresponds to PSL and SiO<sub>2</sub> interaction across the monolayer Gr. While this long-range interaction between the surfaces of the PSL particle and the SiO<sub>2</sub> substrate would easily be masked by the strong short-range Gr-PSL interactions in static or quasi-static measurements using an AFM, the results reported here indicate that in the spectral response of a micro-particle under dynamic excitation conditions it is well separated from the resonance frequencies due to short range (Gr-PSL) interactions and thus it is observable.

In conclusion, employing a non-contact vibrational spectroscopy technique, values of local work of adhesion of Gr-SiO<sub>2</sub> interface are extracted and grouped into four ranges (with their mean values in parentheses) as  $W_{23} = W_{\text{SiO}_2\text{-Gr}} = 84\text{--}279$  (182) mJ/m<sup>2</sup> (I); 331–696 (487) mJ/m<sup>2</sup> (II); 797–1641 (1160) mJ/m<sup>2</sup> (III); and 2122–2692 (2368) mJ/m<sup>2</sup> (IV). The low average values of the work of adhesion in Ranges I and II can be attributed to the geometric irregularities (such as wrinkles, surface roughness, and chemical/electronic imperfections) on the interface of Gr with other surfaces and/or to the fact that, in some areas, Gr is multi-layered. Due to its low population density (three out of a sample set of 64 particles), data points in Range IV are assumed as outliers. It is, therefore, concluded that, as it is the highest determined value, Range III with 797–1641 (1160) mJ/m<sup>2</sup> corresponds to the monolayer Gr-SiO<sub>2</sub> substrate interface with minimal imperfections. It is known that the measured adhesion energy of a multi-layer Gr film tends to decrease with the number of its sub-layers, as increased layer stiffness leads to reduced compliance [28].

### 4.3.3 Controllable Rolling Motion of Micro-Spherical Particles in SAW Fields

In a recent study [58], a non-contact controlled directional rolling motion of individual adhesive micro-spherical particles on a dry substrate subjected to two orthogonal Surface Acoustic Wave (SAW) fields has been demonstrated for the first time for particle manipulation/transportation and surface properties mapping purposes. In this sub-section, for particle manipulation/transport and surface properties mapping purposes, a method for the controlled directional rolling motion of individual well-characterized micro-spheres on a dry and polished substrate subjected to Surface SAW fields is summarized. For characterization purposes, a two-dimensional mathematical model including a linear dissipation mechanism for accounting for the collective effect of possible dissipation mechanisms is developed and presented for predicting the rolling distance of the particle subjected to single SAW pulse. The equations of motion extracted in the proposed mathematical model are integrated numerically for simulating the rolling trajectory of the particle under a characterized SAW field. By comparing the computationally and experimentally obtained rolling travel distances, it is shown that the average equivalent rolling damping coefficient can be approximated from the experimental results.

#### 4.3.3.1 *Experimental Observations of SAW-Driven Rolling Motion of Micro-Particles*

The non-contact and controlled rolling motion is essential for scanning the surface properties of an individual micro-particle. Here, an experimental setup designed to create SAW field on the surface of substrate in two perpendicular directions in order to directionally roll micro-spherical particles in a controllable and non-contact manner is described. In the reported experiments, trains of perpendicular SAW pulses on a dry soda-lime glass plate are generated using two acoustic wedges with mounted piezoelectric ultrasonic transducers as depicted in the instrumentation diagram in Figure 4.14. Two piezoelectric ultrasonic transducers with a central frequency of 2.25 MHz are placed on right-angle faces of wedges to create longitudinal wave fields in the wedges. The transducers are sequentially excited by square electrical pulses generated by a pulser/receiver unit. In the reported experiments, NIST-traceable spherical PSL particles with diameter of 21.4  $\mu\text{m}$  were dry-deposited on the cleaned substrate. In order to eliminate residual electrostatic charge effects, the substrate surface and

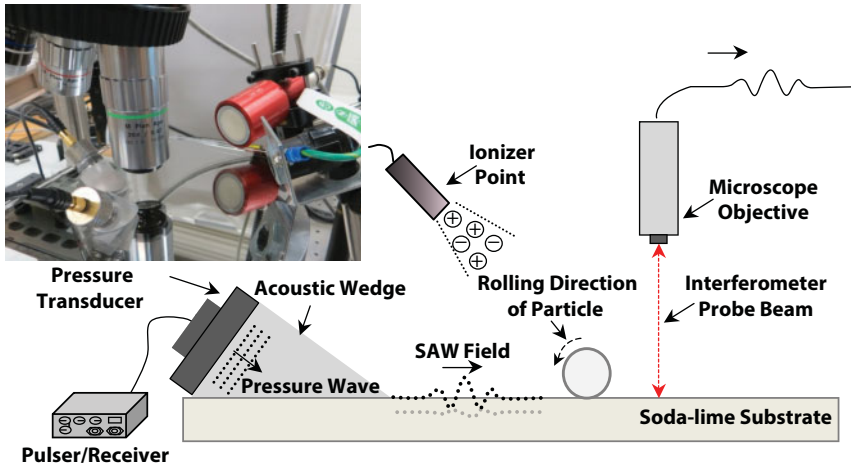


**Figure 4.14** Schematic of the instrumentations of the SAW generation experiment and non-contact laser interferometry measurement device. Inset is a photograph of the experimental set-up.

particles were charge-neutralized by showering with ions using a single point ionizer as shown in Figure 4.14. The laser interferometry setup used in [50] was used for detecting the out-of-plane transient displacement of the surface of the substrate  $u_y$  as a result of SAW excitation (Figure 4.14). The laser beam of the fiber interferometer unit is transmitted through the microscope objective, allowing real-time observation of the location of detecting laser beam on the surface. A number of locations of a individual PSL particle during rolling motion on surface of substrate subjected to SAW (see Figure 4.14 and Figure 4.15) were recorded. The transient out-of-plane response  $u_y$  of the substrate at a measurement point on the substrate (see inset of Figure 4.16) was acquired, digitalized, and recorded with the digitizing oscilloscope for signal processing. The in-plane displacement  $u_x$  of the substrate due to SAW is determined mathematically from the experimental out-of-plane displacement measurement  $u_y$  since the in-plane and out-of-plane displacements in the harmonic SAW field are related and expressed, respectively, as  $u_x(X, t) = F(\gamma_R) \exp(i\gamma_R (X - c_R t))$  and  $u_y(X, t) = G(\gamma_R) \exp(i\gamma_R (X - c_R t))$  in which  $\gamma_R$  and  $c_R$  are the wave-number and phase velocity for the Rayleigh wave on substrate surface. Considering the in-plane ( $u_x$ ) and out-of-plane ( $u_y$ ) displacements, as depicted in Figure 4.16, the trajectory of a point on the surface is elliptical and retrograde with respect to the Rayleigh wave propagation direction.

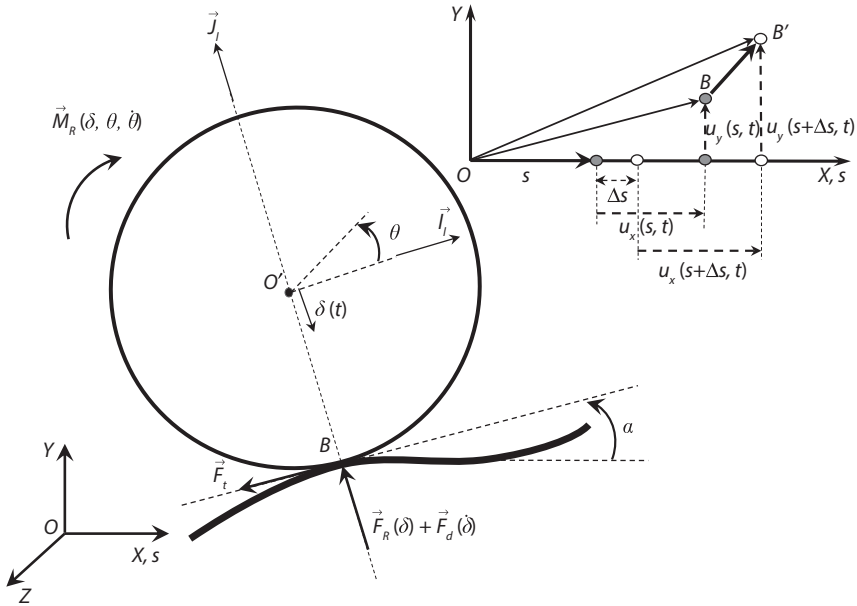


**Figure 4.15** Schematics of the SAW-excited two-dimensional motion of an adhesive spherical particle on a flat substrate in the out-of-plane ( $\delta$ ) and rolling ( $\theta$ ) coordinates (not to scale). Inset represents the mapping of the substrate element starting at the local coordinate  $s$  under the SAW displacement field ( $u_x, u_y$ ) at a time instance.

For a SAW propagating in the positive direction of  $X$  axis (Figure 4.16), the trajectory of a point on the surface of the substrate is a counterclockwise elliptical motion [59]. In current particle manipulation study, two orthogonal SAW sources, named as Source I and Source II, are placed in the directions of  $X$  and  $Z$  axes, respectively, to generate SAW pulses in the orthogonal directions for steering a particle on the surface plane. In the first experiment, under square electrical pulses with amplitude of 300 V from the pulser/receiver unit, SAW trains including 16 and 6 pulses (a total of 22 pulses) are launched in  $X$  and  $Z$  directions from Sources I and II, respectively and as depicted in Figure 4.17, each SAW pulse rolls the PSL particle by a particular distance toward its excitation source. The rolling distances of the particle between two consecutive stations are shown as a bar chart in the inset (a) of Figure 4.17 as well. It must be noted that the SAW pulses are triggered manually with an approximate frequency of 1 Hz in the experiments. It is observed that under identical SAW pulses, particle rolling distances and/or directions vary, and the particle rolling direction is deviated from the exact SAW propagation directions (Figure 4.17).

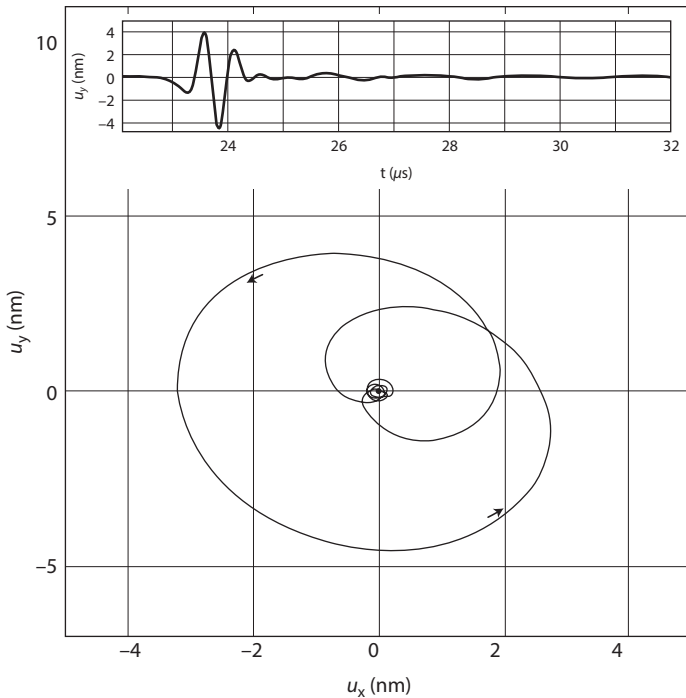


**Figure 4.16** The counter-clockwise trajectory of a point on the substrate surface subjected to a pulsatile SAW field. An acquired out-of-plane ( $u_y$ ) waveform for the out-of-plane motion of the substrate is shown in the inset.

These variations in rolling distances and directions are attributed to the local variations in the mechanical and surface properties of the particle and substrate surface which result in anisotropic adhesion properties and varying dissipation rates during rolling of the particle. In addition, presence of electrical charge patches on the nonconductive substrate and particle (PSL) could affect rolling distance and direction of particle even though, in the reported experiments, an attempt for charge-neutralization was made. In particle–substrate interactions, a number of mechanical dissipation mechanisms, leading to observed finite rolling distances, could be in effect. Irreversibility of the adhesion bond formation and breakage during rolling leads to energy dissipation in the form of photon and/or elastic wave propagation from the adhesion bond zone into the substrate and/or particle body [60]. Additionally, viscoelasticity of the particle and substrate materials could be responsible for mechanical hysteresis loss of particle energy during rolling of particle [61].

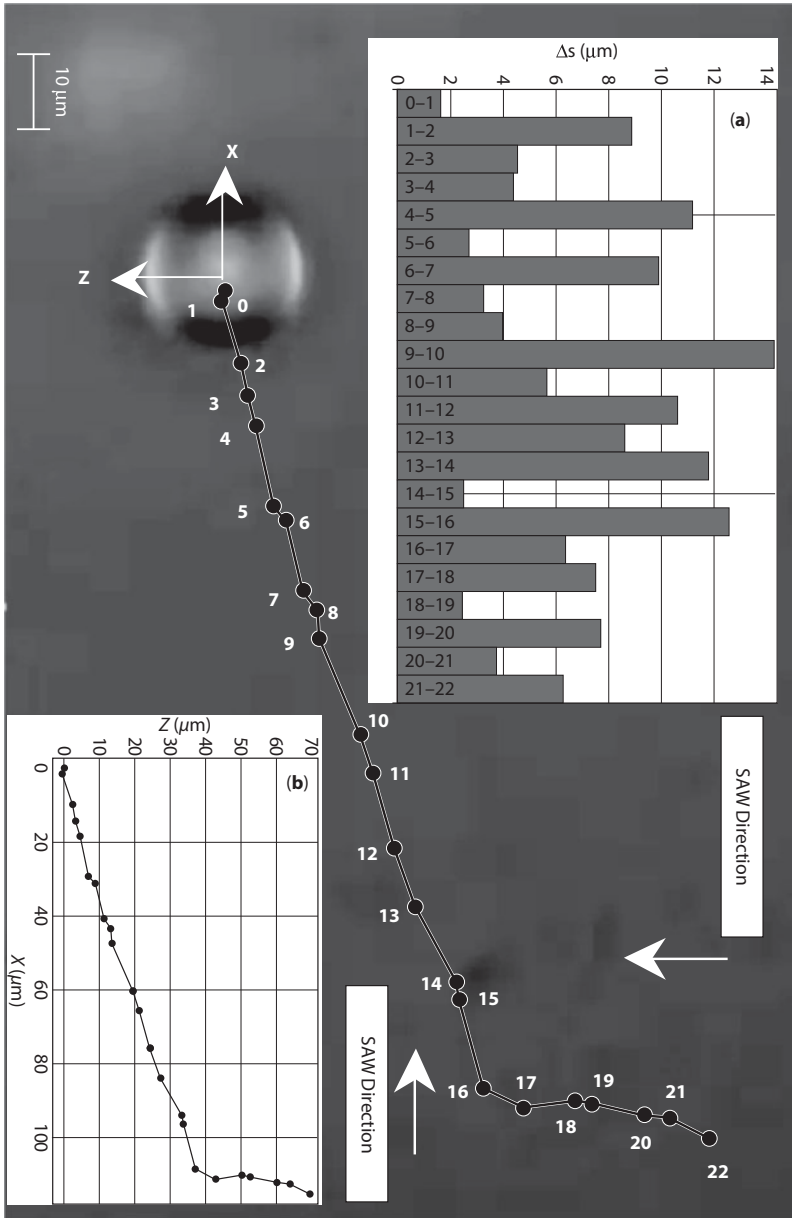


**Figure 4.17** Trajectory of the center of a spherical particle (contact point) during rolling under the two orthogonal pulsatile SAW fields (using 300 V amplitude in pulser/receiver unit) after 22 pulses = 16 in SAW direction X and 6 in SAW direction Z. In the inset (a), the bar represents the rolling distance following each pulse and in inset (b) the trajectory of the particle center after each SAW pulse is shown as a series of station points (0, 1, 2 . . . 22).



#### 4.3.3.2 Mathematical Modeling of the Rolling Motion of a Micro-Particle in SAW Fields

A mathematical model provides a context for extracting adhesion property. In the two-dimensional mathematical model for predicting the rolling distance of a spherical particle with a radius  $r$  and a mass  $m$  on a substrate surface subjected to the SAW field (Figure 4.15),  $\theta(t)$  and  $\delta(t)$  coordinates represent the rotation angle of the center of the spherical particle with respect to substrate surface and the total out-of-plane displacement in  $B-O'$  orientation, respectively. Employing Newton's second law for the particle model represented in Figure 4.15 in local coordinate system directions ( $\vec{j}_l$  and  $\vec{i}_l$  directions) and considering the moment balance about point  $O'$ , the equations of motion are extracted directly as:

$$\begin{aligned} -m g \vec{j} \cdot \vec{j}_l + |\vec{F}_R(\delta)| + |\vec{F}_d(\dot{\delta})| &= m \vec{a}_{O'} \cdot \vec{j}_l \\ -m g \vec{j} \cdot \vec{i}_l - |\vec{F}_t| &= m \vec{a}_{O'} \cdot \vec{i}_l \\ -(r - \delta) |\vec{F}_l| - |\vec{M}_R(\delta, \theta, \dot{\theta})| &= I_{O'} (\ddot{\theta} + \ddot{\alpha}) \end{aligned} \quad (4.13)$$

where  $I_{O'}$  is the mass moment of inertia about the axis passing through particle center ( $O'$ ) and parallel to  $Z$  direction,  $\vec{F}_t$  the friction force at the center of the contact point ( $B$ ) and  $g$  is the gravitational acceleration. Note that these equations of motion are derived assuming no sliding and/or detachment occurs during rolling of the particle.

Based on the JKR model [6, 9], the particle-substrate adhesion bond in the out-of-plane direction is modeled as a restitution force  $F_R(\delta)$ . The damping force  $F_d(\dot{\delta})$  is modeled as an axial linear damper proportional to the out-of-plane motion of the particle as  $F_d(\dot{\delta}) = c_d \dot{\delta}$  where  $c_d$  is the equivalent axial damping coefficient (Figure 4.15). The damping moment resisting the particle rolling on the surface (Figure 4.15) is modeled as a torsional linear damper proportional to the rolling velocity of the particle as  $M_R(\delta, \theta, \dot{\theta}) = c \dot{\theta}$  where  $c$  is the equivalent rolling damping coefficient. Since the out-of-plane displacement of the particle center  $\delta$  is substantially smaller than the particle radius  $r$  ( $r \gg \delta$ ) the out-of-plane restitution of the nonlinear adhesion bond is approximated as a linear axial spring,  $F_R(\delta) = K_a^* \delta$ . The linearized out-of-plane stiffness, as previously

reported [50], is expressed as  $K_a^* = \frac{9}{5} \left( \frac{3\pi W_{12} r^2 K^2}{4} \right)^{1/3}$  where  $W_{12}$  is the work of adhesion between the particle and substrate materials and  $K$  is the stiffness coefficient of the adhesion bond  $K = \frac{4}{3} ((1 - \nu_p^2)/E_p + (1 - \nu_s^2)/E_s)^{-1}$

(here  $E_s$  and  $E_p$  are the Young's moduli and  $\nu_s$  and  $\nu_p$  the Poisson's ratios of the isotropic substrate and particle materials, respectively). As shown in Figure 4.15 and its inset, the coordinate  $s(t)$  representing the position of the center of the contact area ( $B$ ) (assuming no slip and no detachment) is related to the rotation angle  $\theta$  during rolling as:

$$\dot{s} \sqrt{\left(1 + \frac{\partial u_x}{\partial s}\right)^2 + \left(\frac{\partial u_y}{\partial s}\right)^2} \approx -(r - \delta) \dot{\theta} \quad (4.14)$$

The rotation angle  $\alpha(s, t)$  of the normal of the substrate surface with respect to the global coordinate system ( $X$ - $Y$ - $Z$ ) (Figure 4.15) due to the propagation of SAW pulse is obtained as:

$$\alpha(s, t) \approx \frac{\partial u_y(s, t) / \partial s}{1 + \partial u_x(s, t) / \partial s} \quad (4.15)$$

The acceleration vector of point  $O'$  with respect to the global coordinate system is written as follows:

$$\vec{a}_{O'} = \vec{a}_B + \vec{\Omega} \times \vec{r}_{O'/B} + \dot{\vec{\Omega}} \times \vec{r}_{O'/B} + 2\vec{\Omega} \times \dot{\vec{r}}_{O'/B} + (\vec{a}_{O'/B})_{rel} \quad (4.16)$$

where  $(\vec{a}_{O'/B})_{rel}$  is the relative acceleration of point  $O'$  with respect to point  $B$ . The angular velocity and acceleration of local coordinate system with respect to the global coordinate system is expressed as  $\vec{\Omega} = \dot{\alpha} \vec{k}_l$  and  $\dot{\vec{\Omega}} = \ddot{\alpha} \vec{k}_l$  where  $\vec{k}_l$  is the unit vector of the local coordinate system in the  $Z$  direction. Taking  $\vec{i}, \vec{j}, \vec{k}$  as the unit vectors of the global ( $X$ - $Y$ - $Z$ ) coordinate system, the position vector of the center of the particle with respect to the contact point ( $B$ ) in the local and global coordinate systems ( $\vec{r}_{O'/B}$ ) is written as:  $\vec{r}_{O'/B} = (r - \delta)(\cos \alpha \vec{j} - \sin \alpha \vec{i})$ . Consequently, the acceleration terms in Eq. 4.16 are calculated. Substituting the acceleration terms into Eq. 4.13 after eliminating the  $|\vec{F}_t|$  term from Eq. 4.13 and taking the linearized restitution forces and moments, the equations of motion in the coordinates  $\delta$  and  $s$  result in:

$$\begin{aligned} m \ddot{\delta} + c_a \dot{\delta} + k \delta = m(g \cos \alpha - (r - \delta) \dot{\alpha}^2 - (r - \delta) \left(\frac{\partial \alpha}{\partial s}\right)^2 \dot{s}^2 \\ - 2(r - \delta) \dot{\alpha} \frac{\partial \alpha}{\partial s} \dot{s} + \frac{\partial u_y}{\partial s} \ddot{s} + \frac{\partial^2 u_y}{\partial s^2} \dot{s}^2 + 2 \frac{\partial^2 u_y}{\partial s \partial t} \dot{s} + \ddot{u}_y) \end{aligned} \quad (4.17)$$

$$\begin{aligned}
 & I_o \left( \ddot{a} + \ddot{\theta} + \frac{\partial a}{\partial s} \ddot{s} + 2 \frac{\partial^2 a}{\partial s \partial t} \dot{s} + \frac{\partial^2 a}{\partial s^2} \dot{s}^2 \right) + c \dot{\theta} \\
 & = m(r - \delta) \left[ \begin{aligned}
 & g \sin \alpha + \left( 1 + \frac{\partial u_x}{\partial s} - (r - \delta) \frac{\partial a}{\partial s} \right) \ddot{s} \\
 & + \frac{\partial^2 u_x}{\partial s^2} \dot{s}^2 + 2 \frac{\partial^2 u_x}{\partial s \partial t} \dot{s} - (r - \delta) \frac{\partial^2 a}{\partial s^2} \dot{s}^2 \\
 & - 2(r - \delta) \frac{\partial^2 a}{\partial s \partial t} \dot{s} - (r - \delta) \ddot{a} + 2 \dot{\delta} \left( \dot{a} + \frac{\partial a}{\partial s} \dot{s} \right) + \ddot{u}_x
 \end{aligned} \right] \quad (4.18)
 \end{aligned}$$

#### 4.3.3.3 Numerical Simulations of SAW-Driven Rolling Motion of Micro-Particles

In [58], numerical simulation results supporting the experimental observations are presented. For obtaining particle rolling trajectories, the coupled equations of motion (Eqs. 4.17 and 4.18) are numerically integrated in time with the following values for the mass density, Young's modulus and Poisson's ratio of a PSL particle:  $\rho_p = 1050 \text{ kg/m}^3$ ,  $E_p = 2.77 \text{ GPa}$ , and  $\nu_p = 0.33$ , and those for the soda-lime substrate:  $\rho_s = 2440 \text{ kg/m}^3$ ,  $E_s = 72 \text{ GPa}$ , and  $\nu_s = 0.22$ , respectively. The value for the Hamaker constant for PSL,  $A_1$ , from analytical calculations is reported in the literature in the range of  $A_1 = 6.6 \times 10^{-20} - 7.9 \times 10^{-20} \text{ J}$  and the experimentally determined value reported in the literature [52] for  $\text{SiO}_2$ ,  $A_2$  is in the range of  $A_2 = 5 \times 10^{-20} - 6 \times 10^{-20} \text{ J}$ . Using reported ranges for  $A_1$  and  $A_2$ , the corresponding range for the work of adhesion of PSL- $\text{SiO}_2$  interface with a separation distance of  $d = z_{12} = 0.40 \text{ nm}$  is calculated as  $W_A = 9.52 - 11.41 \text{ mJ/m}^2$  and the Hamaker constant for soda-lime glass is approximated to that of  $\text{SiO}_2$ , and, in the reported simulations, an average value of  $W_{12} = 10.46 \text{ mJ/m}^2$  is used.

In the reported experiments [58], it is observed that particle rolling distance is finite and short compared to the particle diameter as the particle halts rolling after travelling a certain distance, implying the presence of dissipation resisting particle rolling motion (Figure 4.17). In the present mathematical formulation, an equivalent linear dissipation model (represented by  $c \dot{\theta}$  in Eq. 4.18) is employed. Due to dissipation, the particle rolls a particular distance on the surface before it stops and this distance converges to a finite value in the long-time limit. As shown in Figure 4.18 for the particle rolling behavior depicted in Figure 4.17, the convergence

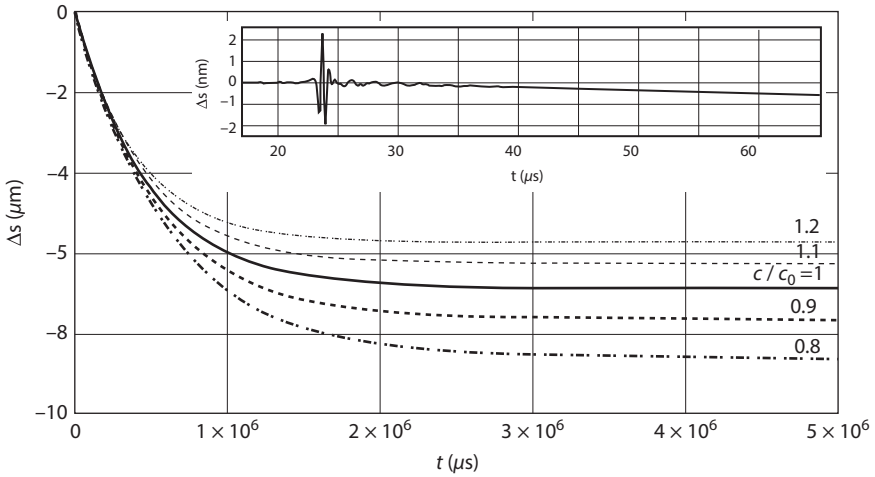


**Figure 4.18** The trajectories of the contact point of PSL particle on long-time scale obtained numerically considering various linear damping coefficients as  $c/c_0 = 1$  (solid thick line), 0.8 (dot-dashed thick line), 0.9 (dashed thick line), 1.1 (dashed thin line) and 1.2 (dot-dashed thin line). In inset, the waveform on short-time scale is shown.

of  $s(t)$  (particle rolling distance) changes as the location-dependent parameters during rolling of the particle are in effect. Thus, the equivalent rolling damping coefficient  $c$  in Eq. 4.18 is approximated by matching the numerically and experimentally obtained rolling distances of the particle, and, as depicted in Figure 4.18, an average damping coefficient of  $c_0 = 2.7 \times 10^{-21} \text{ Nms/rad}$  is obtained based on the resulting average rolling distance of  $\overline{\Delta s} = 6.8 \text{ }\mu\text{m}$  under a square electrical pulse with amplitude of 300 V for particle behavior depicted in Figure 4.17. As indicated in Figure 4.18, the rolling distance expectedly decreases with increasing damping.

For the average rolling distances of  $\overline{\Delta s} = 1.9 \text{ }\mu\text{m}$  and  $\overline{\Delta s} = 1.2 \text{ }\mu\text{m}$  obtained in second and third experiments under square electrical pulses with amplitude of 200 V, average damping coefficient of  $c_0 = 2.5 \times 10^{-21} \text{ Nms/rad}$  and  $c_0 = 4.0 \times 10^{-21} \text{ Nms/rad}$  are calculated for particle behavior. Note that in the represented bar chart of Figure 4.17 (inset (a)), the rolling distance is  $\Delta s_j = s_{j-1} - s_j$  for the  $j$ -th step. It is observed that under identical SAW excitations, the rolling directions and distances of the particle can deviate from the wave propagation direction, indicating anisotropic property distribution on the particle and substrate surfaces, which can be attributed to non-uniformly distributed electrical charge patches on the associated surfaces.

The particle–substrate contact point ( $B$ ) follows the motion of the substrate due to the pre-rolling adhesion bond as the wave field passes by, and due to the rotational momentum build-up during this initial interaction, the particle begins rolling in the opposite direction of the wave propagation direction after a critical leaning angle is reached (as demonstrated in the dynamic response of the particle–substrate contact point in inset of Figure 4.18) [16]. Here it is demonstrated that the particle rolling distance can be controlled by varying the amplitude of the square electrical pulse.

## 4.4 Conclusions and Remarks

In this chapter, a review of the recent developments in adhesion characterization in nano-/micro-scale with a special focus on non-contact methods and two-dimensional adhesion models is provided. Various experiments and analytical and computational progresses have been reviewed and the current state of understanding in the one-dimensional and two-dimensional adhesion characterization is summarized. Some challenge areas are highlighted and emerging approaches to address the needs for more accurate adhesion characterization are discussed. It is noted that while analytical and modeling works have been well developed for the one-dimensional (out-of-plane) case, analytical and experimental studies, especially for two-dimensional adhesion behavior of micro-objects, are still lacking. Recent literature on the nonlinear effects in adhesion bonds is also covered and needs for additional research in this field is discussed.

Finally, some drivers and research areas for future developments are identified as follows:

- (i) Soft materials and their interactions with micro-particles and nano-features: the need for understanding the effects of adhesion on soft materials,
- (ii) Complexities of adhesion in biological systems: features at various length-scales (molecular to cell membrane) interplay with the surface energy to create complex mechanical behavior. Cells sense their environment due to such interactions and change their (stiffness) properties. Understanding adhesion in this process will be a key to many practical applications.
- (iii) Detailed surface property mapping applications: geometric, mechanical and adhesion property mapping at high resolutions is needed to support detailed modeling studies.

Experimental techniques and novel analytical/mathematical tools are needed.

- (iv) Effects of patched charges on particle surfaces on their adhesion behavior: the effect of non-uniform charge fields is a neglected area in the detailed dynamics of micro-particles and their interactions with boundaries and with each other. It appears that such interactions have far-reaching implications from desert storms to copying/printing applications.

## Acknowledgments

The senior author acknowledges NSF, Xerox, Intel, SEMATECH, Pfizer, Praxair, U.S. Army Research Office, as well as CAMP (Center for Advanced Materials Processing) for their generous financial support for his research program over the years. The authors are grateful for financial support through two recent grants from the National Science Foundation (NSF): *GOALI: Mapping of Charge Distribution on a Non-Uniformly Charged Toner Particle for Determining Fundamental Contributors of Adhesion Force* (Award Number: 1066877) from the NSF Division of Chemical, Bioengineering, Environmental, and Transport Systems (CBET), and *Dynamic Bio-Mechanical Properties of Ligand-Receptor Bonds* (Award Number: 1200839) from the NSF Civil, Mechanical and Manufacturing Innovation Division (CMMI).

## List of Symbols

$W_{ij}$ :	Work of adhesion between surfaces $i$ and $j$
$E_i$ :	Young's modulus of material $i$
$\nu_i$ :	Poisson's ratio of material $i$
$A_i$ :	Hamaker constant of material $i$
$z_{ij}$ :	Separation distance between surfaces $i$ and $j$
$K$ :	Stiffness of the particle–substrate adhesion bond
$\rho$ :	Mass density of particle
$m$ :	Mass of the particle
$r$ :	Radius of the un-deformed spherical particle
$g$ :	Gravitational acceleration
$t_e$ :	Effective thickness
$t$ :	Time

- $a$ : Radius of particle–substrate contact area  
 $a_0$ : Radius of particle–substrate contact area at static equilibrium position  
 $s(t)$ : Coordinate representing the position of the center of the particle–substrate contact area ( $B$ )  
 $\delta(t)$ : Out-of-plane displacement of the center of the particle  
 $\delta^*$ : Static equilibrium position of the particle measured from the undeformed radius of the particle  
 $\delta_e(t)$ : Experimentally measured total out-of-plane displacement (suppression) of top of the particle.  
 $\delta_d(t)$ : Elastic out-of-plane displacement of the center of the particle with respect to static equilibrium position ( $\delta^*$ )  
 $\theta$ : Rocking/Rolling angle of the particle with respect to the substrate normal as coordinate of in-plane motion.  
 $\psi$ : Rotation angle of the substrate at the contact point with respect to  $X, Y, Z$   
 $\Theta$ : Amplitude of rocking (in-plane) motion  
 $\omega_r$ : Angular frequency of rocking (in-plane) motion  
 $\theta_0(\dots)$ : Non-zero leaning angle of rocking motion with un-specified arguments  
 $\alpha$ : Rotation angle of the normal of the substrate at center of the contact area ( $B$ ) with respect to  $X, Y, Z$   
 $\vec{\Omega}, \vec{\dot{\Omega}}$ : Angular velocity and acceleration of local coordinate system with respect to the global coordinate system  
 $F_R$ : Restitution force against out-of-plane motion due to the particle–substrate adhesion bond  
 $M_R$ : Restitution moment against rocking motion due to the particle–substrate adhesion bond  
 $\vec{F}_d$ : Out-of-plane damping force  
 $\vec{F}_t$ : Friction force at the center of the contact point ( $B$ )  
 $c_d$ : Equivalent axial damping coefficient  
 $c$ : Equivalent rolling damping coefficient  
 $K_a^*$ : Linearized out-of-plane stiffness of particle–substrate adhesion bond  
 $K_r^*$ : Linearized in-plane stiffness of particle–substrate adhesion bond  
 $f_a$ : Linearized out-of-plane resonance frequency  
 $f_r$ : Linearized in-plane resonance frequency  
 $O$ : The position of the center of mass of the particle prior to any motion (rotational and axial displacements)  
 $O'$ : The position of the center of mass of the particle in its displaced/excited position

- $B$ : Center point of the particle–substrate contact zone  
 $B'$ : Contact point corresponding to the original position  $s + \Delta s$  at time  $t$  in the global coordinate system  
 $\vec{r}_{O'}$ : Position vector of point  $O'$  in  $X, Y, Z$   
 $\vec{r}_B$ : Position vector of point  $B$  in  $X, Y, Z$   
 $I_{O'}$ : The mass moment of inertia about axis passing through  $O'$  and parallel to  $Z$   
 $I_B$ : The mass moment of inertia about axis passing through  $B$  and parallel to  $Z$   
 $\vec{a}_{O'}$ : Acceleration vector of center of the particle ( $O'$ ) in the X-Y coordinate system.  
 $\vec{a}_B$ : Acceleration of point ( $B$ ) in the X-Y coordinate system.  
 $(\vec{a}_{O'/B})_{rel}$ : Relative acceleration of point  $O'$  with respect to point  $B$   
 $\vec{r}_{O'/B}$ : Position vector of the center of the particle ( $O'$ ) with respect to the contact point ( $B$ ) in the local and global coordinate systems  
 $\vec{n}_s$ : Normal vector along the out-of-plane motion direction ( $\overline{BO'}$ )  
 $X, Y, Z$ : Fixed global coordinate system (with  $\vec{i}, \vec{j}, \vec{k}$  as its unit vectors)  
 $\vec{i}_l, \vec{j}_l$ : Unit vectors of local coordinate system fixed to  $O'$  perpendicular and tangent to  $BO'$  direction  
 $u_x, u_y$ : In-plane and out-of-plane displacements of the substrate due to SAW  
 $\gamma_R$ : Wavenumber of Rayleigh surface wave on the substrate  
 $c_R$ : Phase velocity of Rayleigh surface wave on the substrate

## References

1. F. Podczek, *Particle-Particle Adhesion in Pharmaceutical Powder Handling*, Imperial College Press, London (1998).
2. L. O. Heim, J. Blum, M. Preuss and H. J. Butt, Adhesion and friction forces between spherical micrometer-sized particles, *Phys. Rev. Lett.* 83, 3328–3331 (1999).
3. S. Saito, H. T. Miyazaki, T. Sato and K. Takahashi, Kinematics of mechanical and adhesional micromanipulation under a scanning electron microscope, *J. Appl. Phys.* 92, 5140 (2002).
4. M. Sitti, Atomic force microscope probe based controlled pushing for nanotribological characterization, *IEEE/ASME Trans. Mechatron.* 9, 343–349 (2004).
5. B. Sumer and M. Sitti, Rolling and spinning friction characterization of fine particles using lateral force microscopy based contact pushing, *J. Adhesion Sci. Technol.* 22, 481–506 (2008).



6. K. Johnson, K. Kendall and A. Roberts, Surface energy and the contact of elastic solids, *Proc. Royal Soc. London Series. A.* 324, 301–313 (1971).
7. B. V. Derjaguin, V. M. Muller and Y. P. Toporov, Effect of contact deformations on the adhesion of particles, *J. Colloid Interface Sci.* 53, 314–326 (1975).
8. D. Maugis, Adhesion of spheres: The JKR-DMT transition using a Dugdale Model, *J. Colloid Interface Sci.* 150, 243–269 (1992).
9. K. Johnson and J. Greenwood, An adhesion map for the contact of elastic spheres, *J. Colloid Interface Sci.* 192, 326–333 (1997).
10. Y. I. Rabinovich, J. J. Adler, A. Ata, R. K. Singh and B. M. Moudgil, Adhesion between nanoscale rough surfaces: II. Measurement and comparison with theory, *J. Colloid Interface Sci.* 232, 17–24 (2000).
11. Y. I. Rabinovich, J. J. Adler, A. Ata, R. K. Singh and B. M. Moudgil, Adhesion between nanoscale rough surfaces: I. Role of asperity geometry, *J. Colloid Interface Sci.* 232, 10–16 (2000).
12. B. Persson, Adhesion between elastic bodies with randomly rough surfaces, *Phys. Rev. Lett.* 89, 245502 (2002).
13. B. Persson, Adhesion between an elastic body and a randomly rough hard surface, *Eur. Phys. J. E.* 8, 385–401 (2002).
14. A. Peressadko, N. Hosoda and B. Persson, Influence of surface roughness on adhesion between elastic bodies, *Phys. Rev. Lett.* 95, 124301 (2005).
15. M. D. M. Peri and C. Cetinkaya, Rolling resistance moment of microspheres on surfaces, *Philos. Mag.* 85, 1347–1357 (2005).
16. W. Ding, A. Howard, M. D. M. Peri and C. Cetinkaya, Rolling resistance moment of microspheres on surfaces: Contact measurements, philosophical magazine. 87, 5685–5696 (2007).
17. I. Akseli, M. Miraskari, H. Zhang, W. Ding and C. Cetinkaya, Non-contact rolling bond stiffness characterization of polyvinylpyrrolidone (PVP) particles, *J. Adhesion Sci. Technol.* 25, 407–434 (2011).
18. Y. J. Yuan and R. Jia, Study on pivot-point vibration of molecular bond-rupture events by quartz crystal microbalance for biomedical diagnostics, *Int. J. Nanomed.* 7, 381 (2012).
19. M. Peri and C. Cetinkaya, Non-contact microsphere–surface adhesion measurement via acoustic base excitations, *J. Colloid Interface Sci.* 288, 432–443 (2005).
20. C. Dominik and A. Tielens, Resistance to rolling in the adhesive contact of two elastic spheres, *Philos. Mag. A.* 72, 783–803 (1995).
21. T. Dehoux, T. Kelf, M. Tomoda, O. Matsuda, O. Wright, K. Ueno, Y. Nishijima, S. Juodkakis, H. Misawa and V. Tournat, Vibrations of microspheres probed with ultrashort optical pulses, *Opt. Lett.* 34, 3740–3742 (2009).
22. V. Kotaidis, T. Dekorsy, S. Ibrahimkuty, D. Issenmann, D. Khakhulin and A. Plech, Vibrational symmetry breaking of supported nanospheres, *Phys. Rev. B.* 86, 100101 (2012).
23. W. Choi, I. Lahiri, R. Seelaboyina and Y. S. Kang, Synthesis of graphene and its applications: A review, *Crit. Rev. Solid State Mater. Sci.* 35, 52–71 (2010).

24. J. S. Bunch, A. M. van der Zande, S. S. Verbridge, I. W. Frank, D. M. Tanenbaum, J. M. Parpia, H. G. Craighead and P. L. McEuen, Electromechanical resonators from graphene sheets, *Science* 315, 490–493 (2007).
25. J. C. Meyer, A. K. Geim, M. I. Katsnelson, K. S. Novoselov, T. J. Booth and S. Roth, The structure of suspended graphene sheets, *Nature* 446, 60–63 (2007). Available at <http://dx.doi.org/10.1038/nature05545>
26. Z. Zong, C. Chen, M. R. Dokmeci and K. Wan, Direct measurement of graphene adhesion on silicon surface by intercalation of nanoparticles, *J. Appl. Phys.* 107, 026104 (2010).
27. J. S. Bunch and M. L. Dunn, Adhesion mechanics of graphene membranes, *Solid State Commun.* 152, 1359–1364 (2012).
28. S. P. Koenig, N. G. Boddeti, M. L. Dunn and J. S. Bunch, Ultrastrong adhesion of graphene membranes, *Nat. Nanotechnol.* 6, 543–546 (2011).
29. J. U. Lee, D. Yoon and H. Cheong, Estimation of young's modulus of graphene by raman spectroscopy, *Nano Lett.* 12, 4444–4448 (2012).
30. T. Yoon, W. C. Shin, T. Y. Kim, J. H. Mun, T. Kim and B. J. Cho, Direct measurement of adhesion energy of monolayer graphene as-grown on copper and its application to renewable transfer process, *Nano Lett.* 12, 1448–1452 (2012).
31. A. S. Vahdat and C. Cetinkaya, Adhesion energy characterization of monolayer graphene by vibrational spectroscopy, *J. Appl. Phys.* 114, 143502 (2013). Available at <http://dx.doi.org/10.1063/1.482428>
32. B. K. Chen, Y. Zhang and Y. Sun, Active release of microobjects using a MEMS microgripper to overcome adhesion forces, *J. Microelectromech. Syst.* 18, 652–659 (2009).
33. B. K. Chen, Y. Zhang, D. D. Perovic and Y. Sun, MEMS microgrippers with thin gripping tips, *J. Micromech. Microeng.* 21, 105004 (2011).
34. Y. Zhang, B. K. Chen, X. Liu and Y. Sun, Autonomous robotic pick-and-place of microobjects, *IEEE Trans. Robot.* 26, 200–207 (2010).
35. M. Bok, H. Li, L. Y. Yeo and J. R. Friend, The dynamics of surface acoustic wave-driven scaffold cell seeding, *Biotechnol. Bioeng.* 103, 387–401 (2009).
36. L. S. Cheung, P. S. Raman, E. M. Balzer, D. Wirtz and K. Konstantopoulos, Biophysics of selectin–ligand interactions in inflammation and cancer, *Phys. Biol.* 8, 015013 (2011).
37. S. Choi, J. M. Karp and R. Karnik, Cell sorting by deterministic cell rolling, *Lab Chip* 12, 1427–1430 (2012).
38. P. H. Schade and J. S. Marshall, Capillary effects on a particle rolling on a plane surface in the presence of a thin liquid film, *Exp. Fluids* 51, 1645–1655 (2011).
39. X. Zhu and J. Hu, Ultrasonic drive of small mechanical components on a tapered metal strip, *Ultrasonics* 53, 417–422 (2013).
40. H. Butt and M. Kappl, Normal capillary forces, *Adv. Colloid Interface Sci.* 146, 48–60 (2009).
41. M. Takeuchi, Adhesion forces of charged particles, *Chem. Eng. Sci.* 61, 2279–2289 (2006).

42. J. W. Kwek, I. U. Vakarelski, W. K. Ng, J. Y. Heng and R. B. Tan, Novel parallel plate condenser for single particle electrostatic force measurements in atomic force microscope, *Colloids Surf. A* 385, 206–212 (2011).
43. S. F. Fenz and K. Sengupta, Giant vesicles as cell models, *Integr. Biol.* 4, 982–995 (2012).
44. R. M. Gaikwad, M. E. Dokukin, K. S. Iyer, C. D. Woodworth, D. O. Volkov and I. Sokolov, Detection of cancerous cervical cells using physical adhesion of fluorescent silica particles and centripetal force, *Analyst* 136, 1502–1506 (2011).
45. B. Ladoux and A. Nicolas, Physically based principles of cell adhesion mechanosensitivity in tissues, *Rep. Prog. Phys.* 75, 116601 (2012).
46. E. Reister-Gottfried, K. Sengupta, B. Lorz, E. Sackmann, U. Seifert and A. Smith, Dynamics of specific vesicle-substrate adhesion: From local events to global dynamics, *Phys. Rev. Lett.* 101, 208103 (2008).
47. A. Carré and K. L. Mittal (Eds.), *Surface and Interfacial Aspects of Cell Adhesion*, CRC Press, Boca Raton, FL (2011).
48. P. Bongrand, Ligand-receptor interactions, *Rep. Prog. Phys.* 62, 921 (1999).
49. E. Sackmann and R. F. Bruinsma, Cell adhesion as wetting transition? *Chem. Phys. Chem.* 3, 262–269 (2002).
50. A. Saeedi Vahdat, S. Azizi and C. Cetinkaya, Nonlinear dynamics of adhesive micro-spherical particles on vibrating substrates, *J. Adhesion Sci. Technol.* 27, 1712–1726 (2012). Available at <http://dx.doi.org/10.1080/01694243.2012.751521>
51. A. S. Vahdat, S. Azizi and C. Cetinkaya, Doubling of rocking resonance frequency of an adhesive microparticle vibrating on a surface, *Appl. Phys. Lett.* 101, 101602 (2012). Available at <http://dx.doi.org/10.1063/1.4751109>
52. J. N. Israelachvili, *Intermolecular and Surface Forces*, 3<sup>rd</sup> edition, Academic press, Waltham, MA (2011).
53. J. Visser, On Hamaker constants: A comparison between Hamaker constants and Lifshitz-van der Waals constants, *Adv. Colloid Interface Sci.* 3, 331–363 (1972).
54. M. D. M. Peri and C. Cetinkaya, Rotational motion of microsphere packs on acoustically excited surfaces, *Appl. Phys. Lett.* 86, 194103 (2005).
55. M. Ishigami, J. Chen, W. Cullen, M. Fuhrer and E. Williams, Atomic structure of graphene on SiO<sub>2</sub>, *Nano Lett.* 7, 1643–1648 (2007).
56. Z. H. Aitken and R. Huang, Effects of mismatch strain and substrate surface corrugation on morphology of supported monolayer graphene, *J. Appl. Phys.* 107, 123531 (2010)
57. S. Frankland, V. Harik, G. Odegard, D. Brenner and T. Gates, The stress-strain behavior of polymer-nanotube composites from molecular dynamics simulation, *Composites Sci. Technol.* 63, 1655–1661 (2003).
58. A. Saeedi Vahdat and C. Cetinkaya, Directional rolling motion of micro-particles in surface acoustic wave fields, submitted for publication, *Granul. Mat.* (2014).

59. K. F. Graff, *Wave Motion in Elastic Solids*, Dover Publications, New York (1991).
60. Y. Chen, C. Helm and J. Israelachvili, Molecular mechanisms associated with adhesion and contact angle hysteresis of monolayer surfaces, *J. Phys. Chem.* 95, 10736–10747 (1991).
61. N. V. Brilliantov and T. Pöschel, Rolling friction of a viscous sphere on a hard plane, *EPL* 42, 511 (1998).

**Part 2**  
**PARTICLE REMOVAL**  
**TECHNIQUES**



# High Intensity Ultrasonic Cleaning for Particle Removal

Sami B. Awad\* and Nadia F. Awad

*Ultrasonic Apps LLC, Houston, Texas, USA*

---

## Abstract

The high intensity ultrasonic technology has evolved over the past four decades. Different frequencies were developed, and are now industrially available in the range from 20 kHz to 1 MHz. Current electromechanical ultrasound technology with a sweep frequency band provides a uniform ultrasonic activity throughout the cleaning or reaction vessel which was a major limitation in the earlier technology. The two main mechanical forces generated in liquids that effectively clean component surfaces are cavitation shock and acoustic streaming. Both are generated as a result of the direct interaction of high frequency sound waves with liquids to create micro-vacuum bubbles that grow to critical sizes and then implode. The intensity of each varies with the frequency used and the power supplied ( $W/cm^2$ ) to the transducers.

Cleaning of components in different industrial applications with high intensity ultrasonics is strictly based on mechanical actions through a series of energy transformations. The same ultrasonic transducer technology is widely used in other applications such as emulsification, atomization, defoaming, sonochemical reactions and also in plastic welding, soldering and removal of biocontaminants. Very high frequency ultrasound ( $> 1$  MHz) with moderate to very low power is being used in sonar, therapeutics and medical diagnostics.

This chapter covers an important aspect of particle removal i.e., how to quantify it using ultrasonic extraction of residual particles on the surface after cleaning. For small particles determination, background noise caused by particles shed from the test containers is a big concern and is addressed.

**Keywords:** Sound waves, ultrasonics, precision cleaning, power ultrasound, high intensity ultrasound, transducers, multi-frequency, surface decontamination, cleaning chemicals, cavitation, micro-streaming, particle removal

---

\*Corresponding author: sawad@ultrasonicapps.com

## 5.1 Introduction

Acoustics, the science of sound, dates back to Pythagoras in the 6th century BC, who found that a vibrating string produces harmonious tones when the ratios of the lengths of the strings are whole numbers. Sir Francis Galton constructed a whistle producing ultrasound in 1893. The first technological application of ultrasound was an attempt to detect submarines in 1917 by Paul Langevin [1]. The piezoelectric effect, discovered by Jacques and Pierre Curie in 1880 [2] was useful in transducers to generate and detect ultrasonic waves in air as well as in water [3].

In 1917 the British admiralty commissioned physicist Lord Rayleigh [4] to investigate the probable cause of accelerated deterioration to ship propellers with the advent of higher rotational speeds. The search for the cause of this ship propeller destruction led to the discovery of the damage source as cavitation. Rayleigh's research led to the discovery of the effects of cavitation, and confirmed the existence of cavitation that was previously established in 1894 by the renowned Irish engineer and physicist named Osbourne Reynolds. Independently, in 1895 R.E. Froude identified the cavitation phenomenon and named it the cavitation of water. He noticed that high velocity flow of propellers generates low pressure areas and liquid changes phase to vapor accordingly. Froude observed that cavitation appeared to manifest itself when the mean negative pressure exceeds about 46.5 kPa [4,5].

## 5.2 Ultrasound and Ultrasonics

The frequency of sound waves audible to human ear ranges from 20 Hz to 20 kHz. The sound waves having frequencies greater than 20 kHz are called ultrasonics or earlier called supersonics. The term supersonic is generally used nowadays for sound waves having velocities greater than that of audible sound (Figure 5.1). Ultrasonics is the application of ultrasound. There are many applications using high intensity ultrasonic energy [6].

Applications of ultrasonics are in a wide range of chemical and engineering areas like cleaning, plastic bonding, spot welding, materials forming, chemical processing, compaction of powdered metals, enhanced filtration, and sonochemical reactions [7,8,9]. The terms high power or high intensity are used interchangeably throughout the text and have the same meaning.

Ultrasound is an oscillating sound pressure wave with a frequency greater than the upper limit of the human hearing range. Ultrasound thus is not separated from 'normal' (audible) sound based on differences in



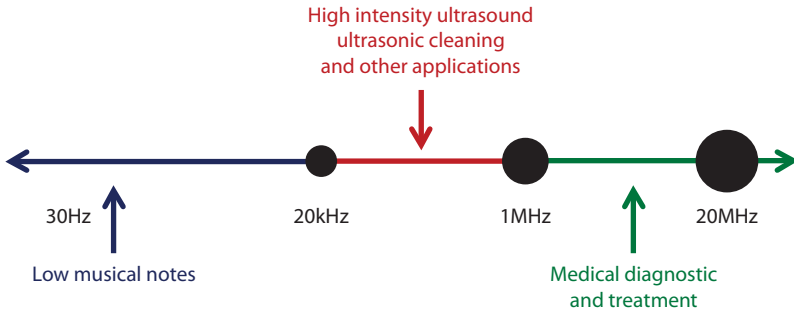


Figure 5.1 Sound frequency ranges for different applications.

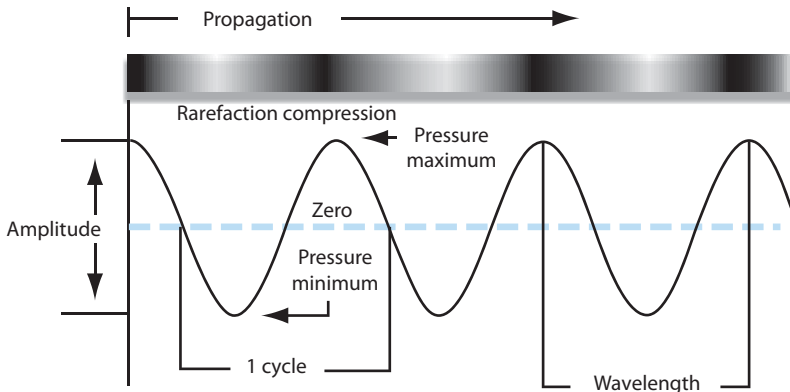


Figure 5.2 Sinusoidal sound wave compression and rarefaction propagation.

physical properties, only the fact that humans cannot hear it. Although this limit varies from person to person, it is approximately 20 kHz in healthy, young adults. Ultrasound devices operate with frequencies from 20 kHz up to 20 MHz (Figure 5.1).

### 5.2.1 Ultrasound Waves

Figure 5.2 shows various phenomena which are defined as:

Longitudinal waves – are waves in which the displacement of the medium is in the same direction as, or the opposite direction to, the direction of the wave.

Compression wave – is a shock wave that compresses the medium through which it is transmitted.

Rarefaction – is a decrease in density and pressure in a medium, such as air, caused by the passage of a sound wave.

Transverse waves – are waves in which the direction of displacement is perpendicular to the direction of propagation.

The speed of sound wave is directly related to the density of material. Denser and more rigid materials have a higher transmission velocity.

### 5.2.2 Factors Hindering the Transmission of Ultrasound Waves

Several factors are responsible for dampening or impeding of sound waves such as reflection, refraction, absorption and attenuation.

Reflection – is the change in direction of a wave front at an interface between two different media so that the wave front returns into the medium from which it originated.

Refraction – is the turning or bending of sound wave when it passes from one medium into another of different density.

Absorption – is the partial loss in energy of sound waves passing through a medium.

Attenuation - is the decrease in a wave's intensity resulting from absorption, reflection, and refraction.

### 5.2.3 Principal Mechanism of High Power Ultrasound

The fundamental effect of ultrasound on a liquid is to impose an acoustic pressure ( $P_a$ ) in addition to the hydrostatic pressure already acting on the medium. The acoustic pressure is a sinusoidal wave dependent on time ( $t$ ), frequency ( $f$ ), and the maximum pressure amplitude of the wave ( $P_{a\max}$ ) [10].

$$P_a = P_{a\max} \sin(2\pi ft)$$

The maximum pressure amplitude of the wave ( $P_{a\max}$ ) is directly proportional to the power input of the transducer. At low intensity (amplitude), the pressure wave induces motion and mixing within the liquid, so-called acoustic streaming. At higher intensities, the local pressure in the expansion phase of the cycle falls below the vapor pressure of the liquid, causing tiny bubbles to grow (created from the existing gas nuclei within the liquid). A further increase in intensity generates negative transient pressure within the liquid that enhances the bubble growth [11].

During the compression cycle, the bubbles shrink and their contents are dissipated back into the liquid. However, since the surface area of the bubble is now larger, so the entire vapor is not absorbed back into the liquid and thus the bubble grows over a number of cycles. Within a critical size range the oscillation of the bubble wall matches that of the applied

frequency of the sound waves causing the bubble to implode during the compression cycle [12].

### 5.3 Cavitation Phenomenon

The process of compression and rarefaction (Figure 5.2) of the medium molecules and the consequent collapse of the bubbles comprises the well-known phenomenon of cavitation, the most important effect in high power ultrasonics. The conditions within these imploding micro-bubbles can be dramatic, with localized temperatures of 5000°C and pressures of up to 1000 atmospheres, which, in turn, produces very high shear energy waves and turbulence in the cavitation zone [7,13]. The work published by Lorimer and Mason [14] shows that the bubble size is inversely proportional to the frequency. Therefore, low frequency ultrasound (16–100 kHz) generates large cavitation bubbles resulting in high temperatures and pressures in the cavitation zone. As the frequency increases, the cavitation zone becomes less violent and in the megahertz range almost no cavitation is observed and the main mechanism is acoustic streaming. While medical imaging operates at frequencies in the megahertz range, most ultrasonic equipment in industrial applications (such as processing of chemicals, processing of food and general cleaning) operate at 16 to ~500 kHz. High intensity cavitations can be generated within this frequency range.

Cavitations are generated in the order of microseconds. At 20 kHz frequency, it is estimated that the pressure is about 35–70 kPa and the transient localized temperatures are about 5000°C, with the velocity of micro-streaming around 400 km/h (Table 5.1). Several factors have great influence on the cavitation intensity and abundance in a given medium. Among these factors are the ultrasonic waveform, its frequency and the power amplitude. Other critical factors are the physical properties of the liquid medium, including viscosity, surface tension, density and vapor pressure, the medium temperature and the liquid flow, whether laminar or turbulent, and dissolved gases.

#### 5.3.1 Cavitations and Micro-streaming

When high energy ultrasonic waves (20 kHz to about 500 kHz (@ about 0.3 – 3 W/cm<sup>2</sup>) travel in a liquid or in a solution, the waves interact with liquid medium to generate highly dynamic agitated solution. In the process, high intensity ultrasonic waves create micro-vapor / vacuum bubbles in the liquid medium, which grow to maximum size proportional to the applied ultrasonic frequency and then violently implode, releasing their energies. This

**Table 5.1** Frequency range for submicrometer and nano-particle removal

Frequency, kHz	Cavitation Size $\mu\text{m}$ & Intensity	Microstreaming Velocity	Boundary layer/ $\mu\text{m}$
20–30	125 $\uparrow$ Potential	$\sim 50$ m/s	$\uparrow$ 4.4
40	75 Erosion	$>100$ m/s	2.82
65–80	42		
90–95			
100–125			
130–135	23		
140–190			
200–250			1.6
400	} Sub-micrometer and Nano Particle Removal		
0.8–1 MHz			0.594

Note: The arrow in the second column represents the intensity.

phenomenon is known as cavitation implosion. The higher the frequency, the smaller is the cavity size with lower implosion energy. At 20 kHz the bubble size is roughly 125  $\mu\text{m}$  in diameter (Table 5.1). At a higher frequency of 70 kHz, the total time from nucleation to implosion is estimated to be about one-third of that at 25 kHz. The size of a vacuum bubble is a function of the sound wavelength and becomes smaller at higher frequencies. For example, at 140 kHz it is estimated to be about half the size of cavitations generated at 70 kHz and much smaller at 200 kHz. Meanwhile, at higher frequencies, the minimum amount of energy required to produce ultrasonic cavities is higher and must be above the cavitation threshold. In other words, the ultrasonic waves must have enough pressure amplitude to overcome the natural molecular bonding forces and the natural elasticity of the liquid medium in order to grow cavities. For water, at ambient temperature, the minimum amount of energy needed to be above the threshold was found to be about 0.3 and 0.5  $\text{W}/\text{cm}^2$  (per transducer radiating surface) for 20 kHz and 40 kHz, respectively.

Cavitation shock wave intensity becomes milder with the increase in frequency. At frequencies greater than 400 kHz the cavitation size becomes very small and generates much weaker implosions. The ultrasound wave energy is being transformed in liquids to mainly acoustic streaming, which

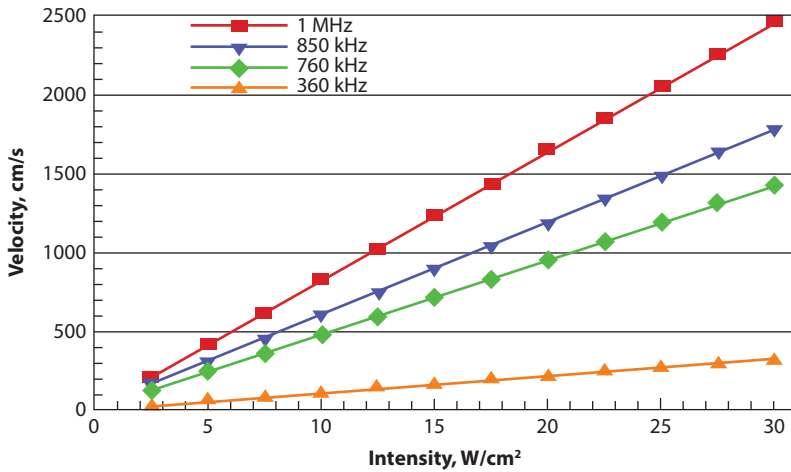


Figure 5.3 Effects of acoustic frequency and intensity on streaming velocity.

tends to become stronger with the increase in frequency. At one MHz and higher frequencies, energy is mainly transformed into a directional acoustic streaming.

Table 5.1 illustrates the inverse relation between cavitation size, acoustic streaming and boundary layer thickness.

Bakhtari *et al.* [15] have presented the effect of acoustic frequency and amplitude (represented as intensity) on streaming velocity (Figure 5.3).

From the data one can conclude that at 360 kHz the increase in power intensity does not have dramatic effect on velocity as it does at 760 kHz and higher frequencies. It is apparent that at 360 kHz cavitation is still dominant and the extra energy is being transformed to more powerful cavitation implosions.

### 5.3.2 Frequency and Cavitation Abundance

At low frequencies of 20–30 kHz, a smaller number of cavitations with larger sizes and higher energies are generated. Much smaller cavitations with moderate to lower energies are formed as frequency increases. Frequencies of 20–40 kHz are more appropriate for cleaning heavy and large size components, while frequency of 60–80 kHz is recommended for cleaning delicate surfaces such as thin optics. Frequencies of 130 kHz and 200 kHz are recommended for cleaning ultra-delicate components such as thin glass or silicon wafers and tiny electronic components or highly polished aluminum surfaces. The latter two ranges are good for the rinsing

steps with all cleaning applications. For example, at 60–80 kHz, the cavitation abundance is high enough and mild enough to remove detergent films and submicrometer particles in the rinsing step without inflicting damage to surfaces. The 35–45 kHz frequency range was found to be appropriate for a wide range of industrial components such as automotive parts and steel molds.

As indicated before, cavitations are more abundant at higher frequencies. For example, about 60 to 70 % more cavitation sites per unit volume of liquid are generated at 70 kHz than at 40 kHz. This is because the size of the micro-cavities decreases at higher frequencies [7]. Therefore, one would expect that at higher frequency, at a given energy level, the scrubbing intensity would be milder, particularly on soft, thin or delicate surfaces. In general, selecting the proper frequency for a particular application is critical and must be carefully investigated.

### 5.3.3 Types of Cavitations

In the present context, cavitations are produced when a liquid is subjected to a high intensity ultrasonic wave. During the rarefaction portion of the ultrasonic wave cycle, when the pressure in the wave is low, gas pockets may form and expand. Such gas pockets are of two types: (1) those dissolved or trapped in minute bubbles in the liquid or on surfaces in contact with the liquid, and (2) vapors of the liquid itself. The first of these types produces gaseous cavitation with relatively low intensity. The second type, called vaporous cavitation, is of fairly high intensity. Gaseous cavitation involves gases dissolved or entrapped in the liquid or existing on surfaces in contact with the liquid. Vaporous cavitation involves gases from the vaporization of the liquid itself. Most liquids contain nuclei at which cavitation bubbles originate. These nuclei may consist of dispersed dust particles, protrusions on immersed surfaces, and minute gas bubbles. In fact, unless especially treated, most liquids contain dissolved or entrained gases [16,17].

Not all phenomena associated with cavitation appear to be explained completely by either vaporous or gaseous cavitation. If the pressure within the cavity is lower than the vapor pressure of the liquid during the expansion phase, the bubble is a result of fragmentation due to the tensile stress imposed by the ultrasonic wave being equal to the tensile strength of the liquid. This type of cavitation is very intense. The tensile strength of the liquid imposes an upper limit on the amplitude of the stress of the ultrasonic wave used to produce cavitation [7,9,18,19,20].

Some effects produced in the presence of cavitations include increased chemical reactions, erosion of surfaces, rupture or fragmentation of

suspended particles, emulsification of liquid mixtures, and dispersion of small particles in the liquid. The importance of cavitations in ultrasonic processing has prompted considerable amount of research and many publications with respect to the physics and associated effects of this phenomenon [7,8,21].

Various factors influence the onset and intensities of the cavitation bubbles. These factors include the sizes of the nuclei, ambient pressure, amount of dissolved gases, vapor pressure, viscosity, surface tension, and the frequency and duration of the ultrasonic energy.

In some cases, ultrasonic cleaning may be attributed, in part, to the promotion of chemical reactions between the contaminants and the cleaning chemicals. When the contaminant is a part of the material to be cleaned or embedded in, cavitation force alone is insufficient to remove the embedded contaminants [22]. The use of ultrasonics in industrial cleaning has two main requirements: a cleaning chemical and a source of high-energy vibrations (the ultrasound). The vibration energy source is called a transducer which transfers the vibration (after amplification) to the so-called sonotrode (or probe) or to a diaphragm which is typically the bottom or the sides of a stainless steel tank. There are two main types of transducers: piezoelectric and magnetostrictive. Piezoelectric transducers are the most commonly used in commercial scale applications due to their scalability, i.e., the maximum power per single transducer is generally higher than that of magnetostrictive transducers.

## 5.4 Generation of Ultrasound – Transducers

Ultrasonic energy is generated and detected by devices called transducers. By definition a transducer is a “device that is actuated by power from one system to supply power in any other form to another system”; that is, a transducer converts energy from one form to another.

Ultrasonic transducers are oscillatory systems that are able to transform mechanical or electrical energy to sound waves. There are three main types of transducers: gas-driven, liquid-driven, and electromechanical. The most common type is electromechanical based on magnetostrictive or more often piezoelectric technology.

### 5.4.1 Gas-driven Transducers

These are, quite simply, whistles with high frequency output. The generation of ultrasound via whistles dates back to the work of F. Galton in the

nineteenth century who was interested in establishing the threshold levels of the human hearing. He produced a whistle that generated sound of known frequencies and was able to determine that the approximate limit of human hearing was 18 kHz. The mechanical method is rarely used due to its very limited applications.

### 5.4.2 Liquid-driven Transducers

In essence, this type of transducer is a “liquid whistle” and generates cavitation via the motion of a liquid rather than a gas. Process material is forced at high velocity by the homogeniser pump through a special orifice from which it emerges as a jet which impacts upon a steel blade (Figure 5.4). There are two ways in which cavitation can occur at this point. Firstly through the Venturi effect as the liquid rapidly expands into a larger volume on exiting the orifice and secondly via the blade which is caused to vibrate by the process liquid flowing over it. The relationship between orifice and blade is critically controlled to optimise blade activity. The required operating pressure and throughput are determined by the use of different sized orifices or jets and the velocity can be varied to achieve the necessary particle size or degree of dispersion.

With no moving parts, other than a pump, the system is rugged and durable. When a mixture of immiscible liquids is forced through the orifice and across the blade, cavitation produces extremely efficient homogenization [12].

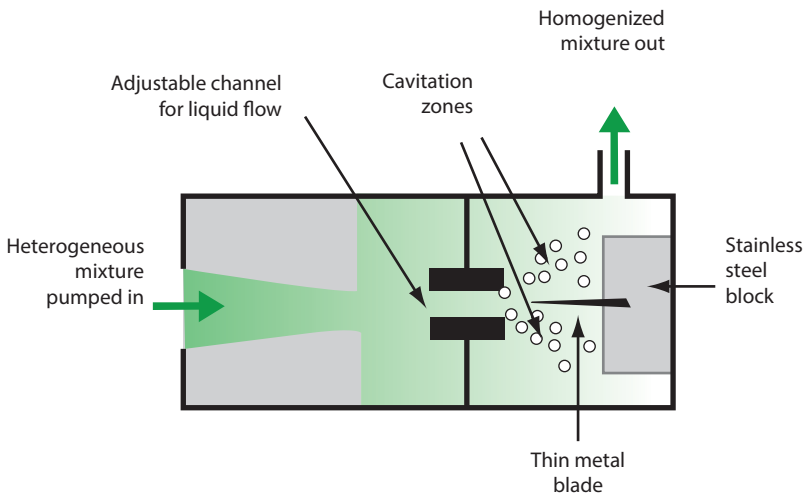


Figure 5.4 Liquid-driven transducer.



### 5.4.3 Electromechanical Transducers

The two main types of electromechanical transducers are based on either the piezoelectric or the magnetostrictive effect. The most commonly used of which are piezoelectric transducers, generally employed to power the bath and probe type sonicator systems. Although more expensive than mechanical transducers, electromechanical transducers are by far the most versatile.

#### 5.4.3.1 Piezoelectric Transducers

Piezoelectric effect discovered by the Curie brothers in 1880 [2] is related to the electric charges developed on the surfaces of certain types of crystals when the crystals are subjected to pressure or tension. The magnitude of the potential difference so developed is proportional to the applied pressure. The converse effect is also possible i.e. if a potential difference is applied to the opposite faces of a crystal, then a change in dimension (i.e. a mechanical contraction or expansion) in the other faces would take place according to the direction of potential difference. The example of crystals in which this effect is best observed are quartz, tourmaline, Roche salt, etc. The inverse effect in which a voltage impressed across two surfaces of a piezoelectric crystal induces stresses in the material is presently the most commonly used method for generating ultrasonic energy in commercially available systems.

It was the introduction of the first polarized ceramic, barium titanate, in 1947, which revolutionized the industrial applications for ultrasonics by permitting higher power generation and significantly reduced device costs [1].

Modern transducers (Figure 5.5) are based on ceramics containing piezoelectric materials. These materials cannot be obtained as large single

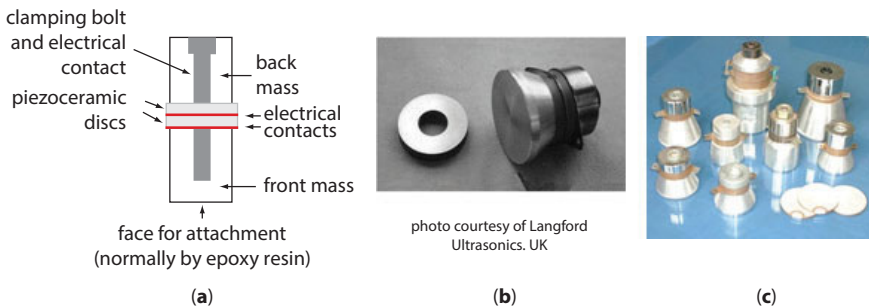


**Figure 5.5** Piezoelectric Transducer Assemblies: (a) basic diagram of transducer assembly, (b) piezo ring disc and assembly, (c) different designs of transducer assemblies.

crystals and so, instead, they are ground with binders and sintered under pressure at above  $1000^{\circ}\text{C}$  to form ceramic discs. Cooling from above their ferroelectric transition temperature in a magnetic field aligns the crystal-lites of the ceramic. Such transducers can be produced in different shapes and sizes. The most frequently used piezoceramic is composed of lead zirconate titanate (commonly referred to as PZT).

Most of the piezoceramic disc materials have a natural resonance frequency and possibly a multiple of secondary resonance points at higher frequencies. For example, a 40 kHz piezoceramic disc produces secondary resonance points at 70 and at 170 kHz. Maximum energy transformation is at best at the primary natural resonance frequency. To run two frequencies requires a generator which is in effect has two sets of circuits linked by a switch or programmable logic controller. The piezoelectric transducer (PZT) assembly is the most widely used configuration in the cleaning and plastic welding applications. The PZT assembly can generate a wide range of frequencies from about 20 kHz to the megasonic range.

#### 5.4.3.2 Magnetostrictive Transducers

Magnetostrictive transducers feature a ferrous core and a two-step sound wave emission process provides power to the core to create electromagnetic field which vibrates a metal plate creating the ultrasound waves. Typical frequencies produced are in lower frequency range from 16 to 25 kHz and are especially suited for heavy duty industrial processing at high operating temperatures [23,24]. Magnetostrictive transducers (Figure 5.6) were the first to be used on an industrial scale to generate high power ultrasound. This type of transducer is a device which uses laminated nickel

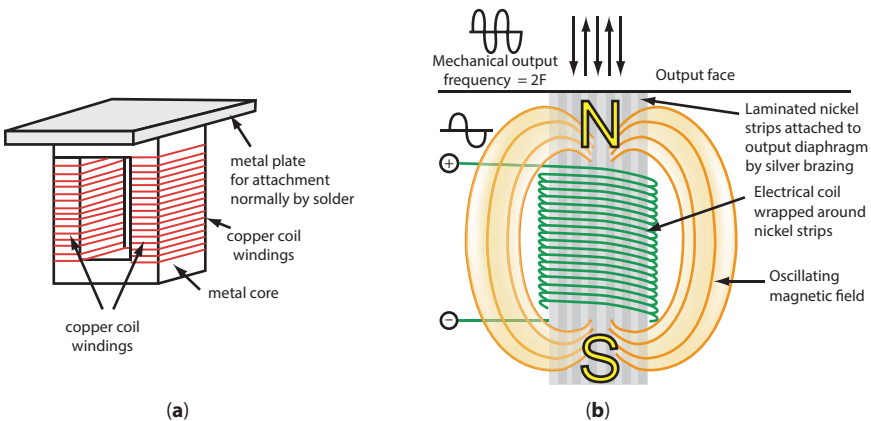


**Figure 5.6** Magnetostrictive transducers: (a) diagram of transducer components (b) schematic of magnetic forces which oscillate the metal plate.

core which reduces in size when placed in a magnetic field and returns to normal dimensions when the field is removed (magnetostriction). When the magnetic field is applied as a series of short pulses to a magnetostrictive material it vibrates at the same rate as the applied pulse. To maximize the effect, two such transducers are wound and connected in a loop.

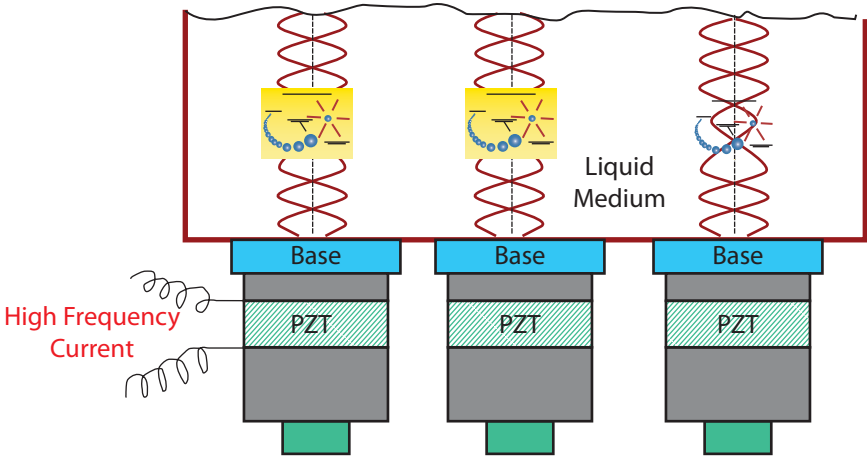
The major advantages of magnetostrictive systems are that they are of an extremely robust and durable construction and provide very large driving forces. There are however two disadvantages, firstly the upper limit to the frequency range is about 100 kHz, beyond which the metal cannot respond fast enough to the magnetostrictive effect. Secondly there are significant losses in energy due to heating which reduces the electrical efficiency.

#### 5.4.4 Transducer Assembly

Whether it is magnetostrictive or electrostrictive transducer to produce positive or negative pressure waves in the aqueous medium, a mechanical vibrating device is required. Ultrasonic manufacturers have made use of high-frequency transducer assemblies bonded onto to a diaphragm to build ultrasonic cleaning tanks of various sizes. The diaphragm can be the bottom or the side wall of a tank or a vessel. The bonded transducers, being activated by a high-frequency electrical generator, vibrate at their resonance frequency inducing vibration of the diaphragm. This amplified vibration is the source of positive and negative pressure waves that propagate through the solution in the tank. When transmitted through liquids, these pressure waves create the cavitation process.

The diaphragm can be designed to work at multiple frequencies by varying the supplied frequencies to the transducers which push them off of their natural frequency. This only works to a limited degree as every transducer has a natural frequency at which it will resonate best. If the transducer is pushed too far off its natural frequency a good part of the supplied energy will transform into thermal energy, meaning inefficient energy transformation process [25].

By connecting the transducers to an electrical generator that puts out a high frequency signal [20 to 500 kHz] the transducer generates longitudinal waves which rapidly induces compression and rarefaction waves in the liquid (Figure 5.2). During the rarefaction cycle the liquid expands against its natural tensile forces at multiple points. At every point a vacuum cavity is created. These cavities will continuously grow larger. When the cavity reaches a critical size the cavity can no longer retain its shape. The micro-cavity collapses violently and creates a transient temperature of 5,000° C and a jet stream that impacts against whatever object is in its vicinity.



Courtesy of Ultrasonic Apps LLC

**Figure 5.7** Ultrasonic PZT Transducer Assembly Bonded onto the bottom of a tank.

Multi-millions of these micro-cavities or micro-bubbles are created and collapse per second in an active ultrasonic tank.

Typical piezoelectric transducer assemblies are normally mounted on the bottom and/or the sides of cleaning tanks (Figure 5.7).

#### 5.4.5 Ultrasonic Immersible Transducers

A boxed immersible transducer (Figure 5.8) is simply a welded sealed stainless steel box usually about 3–4 inches high and with various lengths and widths. The transducers are bonded to the upward facing surface. A watertight coaxial cable connects the transducer to the generator. The transducer can be placed in any still tank and will turn it into an ultrasonic active tank.

A second type of immersibles is known by its tubular designs. Typically it is a long cylinder with one (or two transducer) assembly mounted at one end. The length of the cylinder is a multiple of  $\frac{1}{2}$  the wavelength of the ultrasound wave. The design with two head assemblies [26] has one transducer assembly mounted at each end of the cylinder and is known as the push-pull transducer. The push-pull is made of titanium or stainless steel rod with specific length and diameter. The ultrasonic waves generated along the rod axis propagate perpendicularly to the resonating surface. The radial propagating waves interact with liquid medium to generate cavitation implosions.



**Figure 5.8** Immersible Transducers Block Boxes (left) and Rods (right).

## 5.5 Ultrasonic Generators

An ultrasonic generator (Figure 5.9) comprises a complex electrical circuitry that energizes the transducers. The generator transforms the electrical energy from the power source into high voltage, high frequency electromagnetic waves for efficiently energizing the transducers at the desired frequencies. When the transducers receive the signal, they respond by changing shape as long as the signal is applied. The natural resonance of the transducer determines the needed frequency of the generator. Since the response range of the transducer is narrow, the signal from the generator must be close to the response range of the transducer.

### 5.5.1 Power Requirements

The general ultrasonic power requirement for almost all active tank cleaning applications, expressed in terms of electrical-input wattage to the transducer, is in the range of  $0.35 - 0.75 \text{ W/cm}^2$  of the radiating surface. In common terminology, it translates to  $50 - 125 \text{ W}$  per gallon of liquid.

### 5.5.2 Multi-Frequency Ultrasonic Systems

A single frequency tank has a set of bonded transducers powered by a generator that matches the natural resonance frequency of the transducers (Figure 5.9). Multi-frequency ultrasonic cleaning tanks are of 3 basic types. Type 1 is a tank that has 2 or more independent sets of transducers bonded to the tank. Each set of transducers is powered by its own matching generator and the frequency is fixed. The running frequency is determined by which set of transducers is operational at a given time. A tank that has both 40 and 70 kHz transducers will run at either 40 or 70 kHz



**Figure 5.9** Ultrasonic Tank and Generator.

independently or both run at both 40 kHz and 70 kHz simultaneously. This can be controlled either by a manual switch or by a Programmable Logic Control for automatic operation. The limitations of such a system are the physical constraints that are imposed by the tank size and the bonding area for the transducers that is available. It is possible to run both frequencies at the same time but cautious must be taken to avoid too much power in the tank that can cause damage to delicate parts. In other words, it can cause cavitation erosion to the surfaces of the part. Power intensity control is a must for this type of system to prevent such potential damage.

A second type of multi-frequency cleaning system is a system that has one set of transducers bonded onto the tank and the generator that is capable of generating multi-high frequencies simultaneously. It has a Programmable Logic Control that switches the frequencies from one to another as programmed. In most cases only one frequency at a time can be present in the ultrasonic tank.

There is a third type of system that combines both of the above, and that is a system that has the ability to run banks of transducers [i.e., 2, 4, or 6, out of 12 ] at a particular frequency for a specified time. This system can be run in either mode and has the added advantage of limiting the total power, thus avoiding part damage.

The multi-frequency system creates multi-size cavitations within a tank. With a multiplicity of wavelengths, high-stress regions are brought close together. Destructive interference by reflections from the surface of the cleaning chemical or from large surfaces placed in the tank is less of a problem than it is with single-frequency operation. If one wavelength is canceled by destructive interference, activity still continues at the remaining frequencies. The intensity of the energy at each frequency must be above the cavitation threshold. The cavitation threshold increases as frequency *increases*. The total energy consumed is necessarily higher than that for

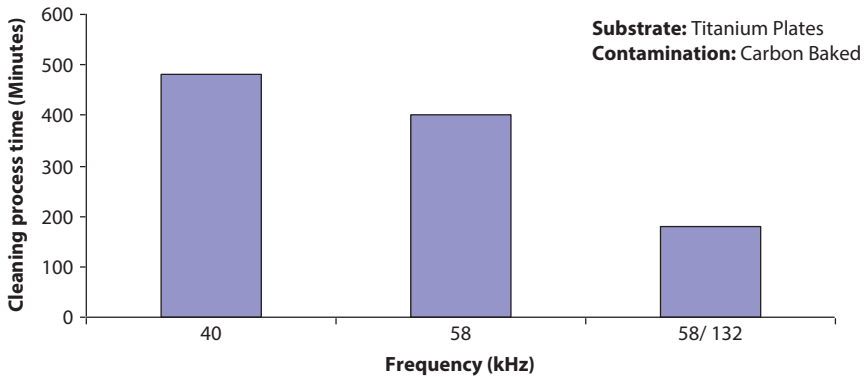


**Figure 5.10** Cleaning Time vs. Single and Dual Frequencies.

single-frequency units, but the additional power of the multi-frequency units is generally better distributed.

It has been reported a dual frequency system (58 / 132 kHz) displays significantly higher cleaning efficiency for the tested substrates / contaminants (Figure 5.10). Advantages of the combined frequencies include a decrease in the process time, enhancement of the cleanliness level, and optimization of the equipment configuration by reducing the number of cleaning steps [26].

## 5.6 Principles of Ultrasonic Cleaning for Particle Removal

The main scrubbing force in cleaning and particle removal is the shock waves (Figure 5.11). A micro-cavity is formed and implodes through at least three steps: nucleation, growth and violent collapse or implosion. The transient micro cavities (or vacuum bubbles or vapor voids), ranging from 50 to 150  $\mu\text{m}$  in diameter at 25 kHz, are produced during the sound wave's half cycles. During the rarefaction phase of the sound wave, the liquid molecules are extended outward against and beyond the liquid natural physical elasticity / bonding/ attraction forces, generating vacuum nuclei that continue to grow to a maximum. Then violent collapse occurs during the compression phase of the wave. It is believed that the latter phase is augmented by the enthalpy of formation and the degree of mobility of the molecules, as well as by the hydrostatic pressure of the medium.

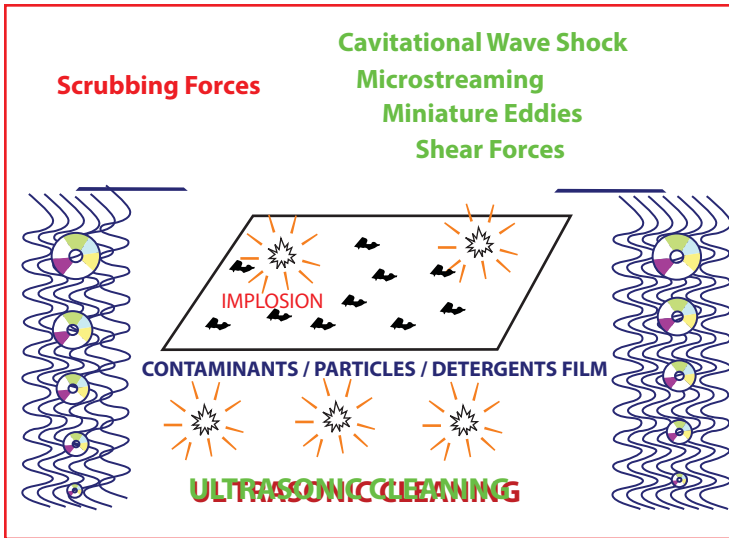


Figure 5.11 Micro-Bubble Formation and Scrubbing Forces.

In general, ultrasonic cleaning consists of immersing an object in a suitable liquid medium, agitating or sonicating the medium with high-frequency (18 to 500 kHz) sound waves for a brief interval of time (usually a few minutes), rinsing with clean solvent or water, and drying. The mechanism underlying this process is one in which microscopic bubbles in the liquid medium implode or collapse under the pressure of agitation to produce shock waves, which impinge on the surface of the part and, through a scrubbing action, displace or loosen particulate matter from the surface. The process by which these bubbles collapse or implode is known as cavitation.

Ultrasonic cleaning has, however, been used to great advantage for extremely tenacious deposits, such as corrosion deposits on metals. In any case, cavitation forces can be controlled; thus, with proper selection of critical cleaning parameters, ultrasonics can be used successfully in virtually any cleaning application that requires removal of small particulates. The effectiveness of ultrasonic energy in cleaning materials may be attributed to phenomena which accompany cavitation. These include (1) development of stress between the cleaning chemical and the contaminated surface, (2) agitation and dispersion of contaminant throughout the cleaning chemical, (3) promotion of chemical reactions at the contaminated surfaces, and (4) effective penetration of the cleaning chemical into pores and crevices.



Cavitation implosion at a liquid-solid interface imposes severe stresses on the solid surface such that, in time, the surface may itself become severely eroded. When a surface containing a contaminant is exposed to cavitation, these stresses operate to disperse the contaminant. The intensity of the stress when cavitation occurs is a function of the vapor pressure of the liquid, the gas content of the liquid, and the adhesion force between the liquid and the surface [21].

Adhered particles that are removed from the surface are immediately subjected to the violent activity of cavitation bubbles. These particles are, thus, propelled with high initial accelerations and are dispersed throughout the cleaning chemical. Further, the agitation provides a scrubbing action which promotes the removal of particle contaminant. Such contaminants may be loose, fine particles or materials that dissolve or emulsify in the cleaning chemical.

Organic contaminants are removed by two main mechanisms. The first is by solubilization in an organic solvent. Degree of solubilization in various cleaning solvents is directly related to their molecular structure. The second mechanism is by displacement / emulsification with surfactants. Surfactants are capable of displacing and encapsulating various types of contaminants such as oils, greases and organometallics.

A very important aspect of ultrasonic cleaning is its ability to draw contaminants out of very small pores and crevices. Therefore, by combining the proper cleaning chemical with properly selected sound frequency has made it possible to remove sub-micrometer and nanometer particles. Ultrasonic cleaning (20 kHz – 450 kHz) is especially due to cavitation. Cavitation is also the key to homogenization and is due to the dispersion of materials in cleaning liquids. On the other hand, megasonic (> 850 kHz) removal of nano and submicrometer size particles is basically due to high velocity acoustic streaming.

### 5.6.1 Cleaning Process Parameters

The cavitation intensity in a sonic field is largely determined by three factors [27]:

1. The frequency and amplitude of the radiating wave.
2. The colligative properties of the medium, including vapor pressure, surface tension, density, and viscosity
3. The rheological properties of the liquid, including static condition, turbulent flow, and laminar flow.

### 5.6.1.1 *Frequency and Amplitude*

The radiating wave frequencies most commonly used in ultrasonic cleaning, 18- 450 kHz, lie just above the audible frequency range. In any cleaning system, however, the harmonics of the fundamental frequency, together with vibrations originating at the tank walls and liquid surface, produce audible sound. Thus, an operating system that is fundamentally ultrasonic will nonetheless be audible

Moreover, ultrasonic intensity is an integral function of the frequency and amplitude of a radiating wave; therefore, a 20-kHz radiating wave will be approximately twice in intensity than a 40-kHz wave for any given average power output.

The amplitude of the radiating wave is directly proportional to the electrical energy that is applied to the transducer. In order for cavitation to be produced in a liquid medium, the amplitude of the radiating wave must have a certain minimum value, which is usually rated in terms of electrical input power to the transducer. No cavitation can occur below this threshold value, and the use of electrical power over and above the minimum level results not in more intense cavitation activity but rather in an increase in the overall quantity of cavitation bubbles. The minimum power requirement for the production of cavitation varies greatly with the colligative properties and temperature of the liquid as well as with the nature and concentration of dissolved substances.

### 5.6.1.2 *The Colligative Properties of the Liquid*

The intensity with which cavitation takes place in a liquid medium varies greatly with the colligative properties of the medium [27], which include vapor pressure, surface tension, viscosity, and density, as well as any other property that is related to the number of atoms, ions, or molecules in the medium. In ultrasonic cleaning applications, the surface tension and the vapor pressure characteristics of the cleaning chemical play the most significant roles in determining cavitation intensity and, hence, cleaning effectiveness.

The energy required to form a cavitation bubble in a liquid is proportional to both its surface tension and vapor pressure. Thus, the higher the surface tension of the liquid, the greater will be the energy required to produce a cavitation bubble, and, consequently, the greater will be the shock-wave energy produced when the bubble collapses. In pure water, for example, whose surface tension is about 72 mN/m cavitation is produced with difficulty at ambient temperature in contrast to a water solution of a surfactant.

It is, however, produced easily when a surface-active agent is added to the liquid, thus reducing the surface tension to about 30 mN/m. In the same manner, when the vapor pressure of the liquid is low, as is the case with cold water, cavitation is difficult to produce but becomes easier as the temperature is increased.

### 5.6.1.3 *The Rheological Properties of the Liquid*

The flow characteristics, or rheological properties, of the cleaning chemical play a highly significant role in ultrasonic cleaning applications.

Static liquid conditions, for example, are highly conducive to the formation of standing wave patterns that characterize intense ultrasonic fields, and hence it would seem likely that cavitation intensity would be maximized under such conditions.

In fact, however, optimum performance is seldom achieved in static fields, since continuous purification of the cleaning chemical either by overflow or by recycle filtration process that necessitates cleaning chemical change of up to 50% of the total bath volume per minute is often a prerequisite to effective cleaning. And, contrary to what one might anticipate under such conditions, little or no cavitation activity is lost to this liquid flow when it is properly introduced into the bath. In fact, improvement in overall surface impingement and homogeneity of cleaning can be realized with this method.

It becomes clear that there are many process parameters affecting the cleaning process outcome and thus it takes time and effort to scale up and fine-tune a cleaning process [28].

## 5.7 **Determination of Residual Particles on Surfaces**

The recent dramatic rise in cleanliness requirements for certain components in the automotive industry e.g. in the brake systems and fuel-injection systems was due to the new designs for safer and fuel efficient mechanisms. Small particles can clog very the new small precise orifices and can cause performance failures. The industry cannot afford to identify possible failures at a relatively late stage. Therefore, the standard VDA ISO/FDIS 16232 (2006) 'Road Vehicles – Cleanliness of Components of Fluid Circuits / Particle Mass Determination by Gravimetric Analysis' was developed which describes methods that can comply with the cleanliness requirements.

In measuring residual particles using an offline laser LPC (liquid particle counter), it is important to use an extraction apparatus that produces

a very low background count when subjected to ultrasonics. Ultrasonics is usually applied to help extract the very small residual particles from surfaces. Most of the test containers shed particles from their own materials when subjected to low frequency ultrasonics. High background counts normally reduce the degree of confidence in the final count results. Pyrex glass beakers are typically used for the extractions. This is not the optimum material of choice. A study was performed to find the right material for the ultrasonic extraction apparatus that generates the lowest background count when subjected to ultrasonics at different frequencies.

Borosilicate glass (Pyrex), quartz and stainless steel were evaluated (Figure 5.12). There were significant differences in the results obtained from containers made from different materials. It was evident that the physical and/or the chemical composition of the apparatus surface as well as the condition of apparatus surface are important determining factors in the cumulative number of the background count. Ultrasonic frequency and power amplitude were also significant contributing factors. The data showed that electropolished stainless steel (Figure 5.13) gives relatively low background readings at high ultrasonic frequency (132 kHz, 100% power) when compared to the particle shedding from the quartz material (Figure 5.14) or the Pyrex glass [29].

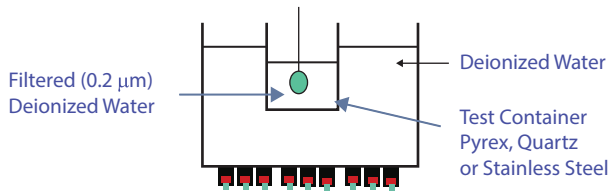


**Figure 5.12** Ultrasonic apparatus for extraction of residual particles on cleaned parts.

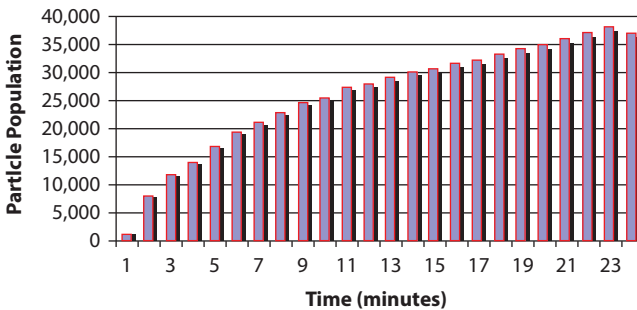


**Figure 5.13** Total particles generated by the quartz beaker material, in a 10 ml sample, measured by laser counter (0.5 – 20 μm).

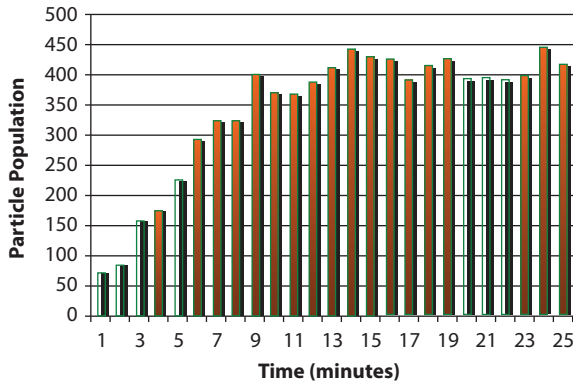


**Figure 5.14** Total particles generated by the electropolished stainless steel beaker material, in a 10 ml sample, measured by laser counter (0.5 – 20  $\mu\text{m}$ ).

## 5.8 Ultrasonic Aqueous Cleaning Equipment and Process

In designing a cleaning system (Figure 5.15), one must give primary consideration to the size, configuration, and capacity of the ultrasonic tank so that this structure will be able to accommodate the parts to be cleaned in sufficient quantity to fulfill production requirements.

A typical ultrasonic aqueous batch cleaning system consists of at least four stations: ultrasonic wash tank, minimum of two separate (or reverse cascading) water rinse tanks and heated re-circulated clean air for drying. In the wash and the rinse tanks the ultrasonic transducers are bonded onto the outside of the bottom surface or onto the outside of the sidewalls. The immersible transducers are normally installed inside the tank on the bottom or the side walls. Immersible transducers are usually preferred in very large tanks. Two types of immersible transducers (Figure 5.8) are commercially available in various sizes and frequencies. The traditional sealed metal box contains a multi-transducer system and the tubular immersible transducer, which is powered by one or two transducer assemblies at one or both ends [26].

Prior to selecting equipment, it is imperative that an effective cleaning process be first developed and then the number and the size of the stations are determined based on production demand, total process time and space limitation.

Typical tank size ranges from 10 liters to 2,500 liters, based on the size of the parts, production throughput and the required drying time. The whole

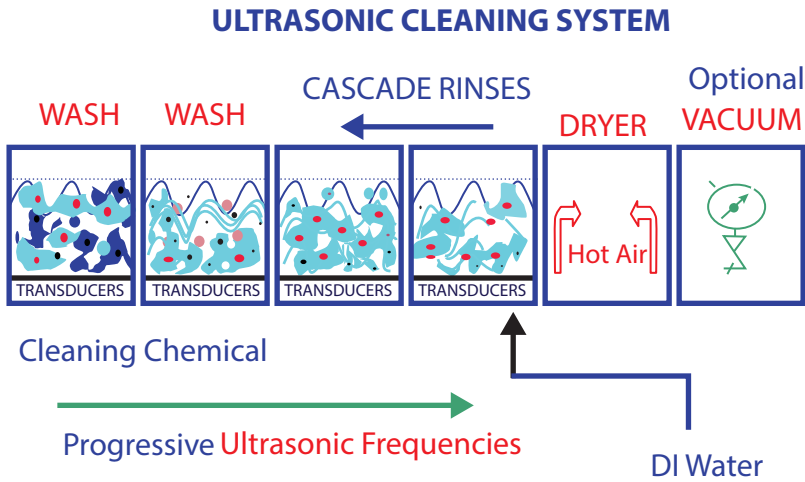


**Figure 5.15** Ultrasonic Aqueous Cleaning System. Courtesy of Ultrasonic Apps LLC.

machine can be enclosed to provide a cleanroom environment meeting class 10,000 and possibly down to class 100 cleanroom specifications according to Fed Standard 209B . Process control and monitoring equipment consists of flow-controls, chemical feed-pumps, in-line particle count, Total Organic Compounds (TOC) measurement, pH, turbidity, conductivity, refractive index, etc. The tanks are typically made of corrosion resistant stainless steel or electropolished stainless steel. Titanium nitride coated stainless steel or similarly coated with hard chromium or zirconium is used to extend the lifetime of the radiating surface in the tanks or the immersible transducers. The hard coat seems to delay the natural surface erosion over the long time use of the tanks. Other materials are also used such as quartz, poly(vinyl chloride), polypropylene or titanium to construct tanks for special applications.

The number and the size of stations are determined based on the required process time. For example, some cleaning systems include an extra station for corrosion inhibitors or solvent displacement. The cleaning process can be automated to include computerized transport systems able to run different processes for various parts simultaneously. Another advantage of automation is monitoring all the process controls and keeping the process parameters in check.

Every individual cleaning application has its own set of variables, such as the number of parts per load, the orientation and spacing of these parts, and the fixturing or racking arrangements.

The majority of ultrasonic cleaning systems, which were developed in the 1950s, were operated at 18 to 40 kHz, 18 kHz is the lowest frequency, Up until the late 1980s most of the commercially available systems operated at 25 to 40 kHz.

Cleaning was one of the earliest industrial applications of high power ultrasonics. Objects to be cleaned are placed in a bath full of cleaning chemical which is violently agitated by a number of ultrasonic transducers. The liquid may be a neat cleaning chemical or a water based cleaning chemical depending on the application.

Performance and reliability of an ultrasonic system depend on the design and construction of the transducers and generators. The overall cleaning effectiveness depends on the cleaning liquid. The size of the tank depends on the size of the parts being cleaned. The numbers of transducers and generators are determined by the tank size and the desired power amplitude intensity. The choice of the cleaning solution depends on the material of the parts being cleaned and the contaminants to be removed.

High power ultrasonic cleaning of components is used in many industries, including automotive, aerospace, semiconductor, disk drive, medical, dental, electronic, optical, and other industries. Cleaning is carried out primarily by cavitation in the cleaning chemical. The cavitation activity not only produces kinetic motion but also brings fresh cleaning chemical close to the contaminants where the contaminants are either solublized or dispersed as very fine encapsulated particles.

Water based and many other cleaning chemicals are used as cleaning media. Cleaning agents are selected based on their ability to combine cavitation activity with chemical action. The effectiveness of cleaning depends on the type of stress generated between the contaminant and the cleaning chemical, severity of agitation, increase of attraction between the contaminant and cleaning chemical, gas content of the liquid, and the potential for promoting desirable chemical reaction at the interface. When a surface with a contaminant is exposed to cavitation, intensity of stress generated depends on the vapor pressure of the cleaning chemical, the gas content of the liquid, and the adhesion force between the liquid and the surface [21].

Operation of ultrasonic cleaners at discrete frequencies has some advantages. High-intensity cavitation forms in local regions rather than throughout the cleaning tank. This concentration of cavitation permits operation at relatively low power input per unit volume of cleaning chemical. The disadvantage is that parts to be cleaned must be located in the high-stress region of the cleaning chemical. Intensities in other regions may not be sufficient for satisfactory cleaning. Materials closest to the radiating surface will receive the greatest benefit from the cleaning activity. These surfaces

may shield materials located behind them with respect to the radiating surface. Placing the radiating surfaces at angles to large surfaces minimizes the shielding effect and increases exposure to cavitations.

As with any other application of ultrasonic energy, the same basic principles govern the effectiveness of an ultrasonic cleaning operation. These principles involve the choice of cleaning system and the choice of cleaning chemical. Some cleaning chemicals will react unfavorably with some types of soils and actually make it more difficult to disperse the contaminants ultrasonically. Some chemical suppliers have developed effective specialty cleaning chemicals for cleaning various classes of materials and can provide not only the proof data but also commercial products which are often sold under trade names that indicate the applications for which they are suited. Cleaning chemicals for ultrasonic cleaning are discussed more fully in a later section.

Hindrances to the proper distribution of energy to surfaces *to be* cleaned may sometimes be subtle. Any coating or obstacle that prevents the ultrasonic energy from acting on a component using a suitable cleaning chemical is a detriment to effective cleaning. Piling too many items into a cleaning tank obviously is a poor practice [22].

## 5.9 Precision Cleaning

Precision or critical cleaning of components or substrates is the complete removal of undesirable contaminants to a desired preset level, without introducing new contaminants in the process [24]. The preset level is normally the minimum level at which no adverse effects take place in a subsequent operation. To achieve the desired cleanliness level, it is critical not to introduce new contaminant(s) into the cleaning process. For example, in an aqueous cleaning process, it is important to have high quality rinse water and minimum of two rinse steps. Otherwise, residual detergent and/or salts from the rinsing water will be the new contaminants. Re-contamination of cleaned parts with outgassed residues produced from packaging or storing materials is another source [24].

### 5.10 Contaminants

Three general classes of common contaminants are organic, inorganic and particulate matter. Particles do not necessarily belong to a certain class and can be from either class or a mixture thereof. Insoluble particulate



contaminants can, for example, be divided into two groups: (1) water-wettable or hydrophilic particles, including metal particles, metal oxides, minerals, and inorganic dusts; and (2) non-water-wettable or hydrophobic particles, including plastic particles, smoke and carbon particles, graphite dust, and organic chemical dusts. Substrate surfaces, too, can be divided into hydrophilic and hydrophobic groups.

Contaminants of any class could be water soluble or water insoluble. Organic contaminants in most cases will be hydrophobic in nature, such as oils, greases, waxes, polymers, paints, adhesives or coatings.

Except for a very few, most inorganic materials or salts are insoluble in cleaning chemicals that are non-water-miscible. Water is the best universal cleaning liquid for organic or inorganic ionic materials. Water insoluble inorganics, such as polishing compounds made of oxides of aluminum, cerium or zirconium, require a more elaborate cleaning process.

Organic contaminants such as oils and greases can be classified into three general classes - long chain, medium chain, and short chain molecules. The physical and chemical characteristics are related to their structure and molecular geometry.

Insoluble particulate contaminants can, for example, be divided into two groups: inorganics such as silicates, metals and metal oxides, carbides, and organics such as plastics, cured adhesives and rubber.

Even a highly polished surface has a rugged surface that can hide nano-size particles in the crevices of the uppermost layer of surface imperfection [30] (Figure 5.16).

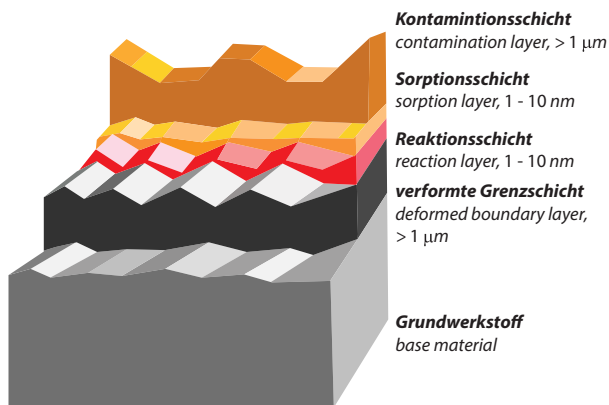


**Figure 5.16** A Metal surface magnified to show the peaks and valleys. Courtesy of Prof. Eng. B. Haase, Hochschule Bremerhaven, Germany. Typical layers above the metal base: Deformed boundary layer, > 1  $\mu\text{m}$ ; Reaction layer, 1 - 10 nm; Sorption layer, 1 - 10 nm; Contaminants layer, > 1  $\mu\text{m}$ .

## 5.11 Ultrasonic Cavitation Forces and Surface Cleaning

The scrubbing forces released from an implosion in close vicinity to the surface fragment or disintegrate the contaminants, allowing the detergent or the cleaning chemical to displace contaminants at a faster rate. The implosion also produces dynamic pressure waves, which carry the fragments away from the surface by the accompanying high-speed microstreaming current of the liquid molecules. The cumulative effect of millions of continuous tiny implosions in a liquid medium in an ultrasonic tank is what provides the necessary mechanical energy to break physically bonded micro- or nano-contaminants lying within the boundary layer (Figure 5.17) and / or speed up the hydrolysis of chemically bonded ones and enhance the solubilization of ionic contaminants. The chemical composition of the medium is an important factor in accelerating the removal rate of various contaminants.

Cleaning with ultrasonics offers several advantages over other conventional methods. Ultrasonic waves generate and evenly distribute cavitation implosions in a liquid medium. The released energies reach and penetrate deep into crevices, blind holes and areas that are inaccessible to other cleaning methods [4,5]. The removal of contaminants is consistent and uniform, regardless of the complexity and the geometry of the substrates.

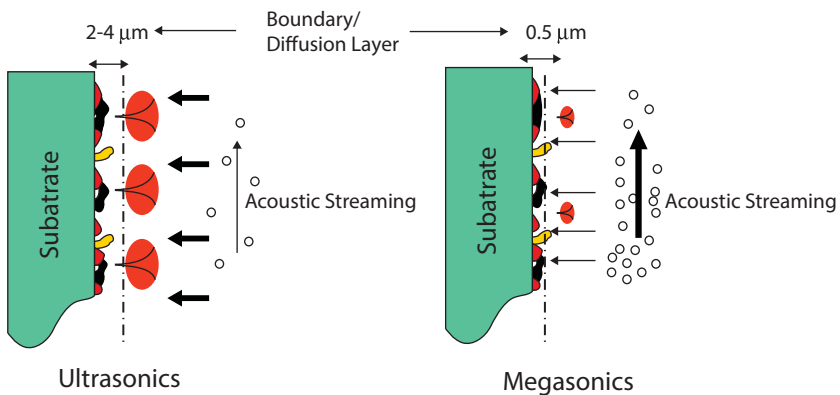


**Figure 5.17** Schematic showing cavitations vs. acoustic streaming. In the ultrasonic frequency range (left) cavitations are dominant while microstreaming is weak. In the megasonic frequency range (right) the acoustic streaming is dominant and cavitations are negligible (See Table 5.1). Courtesy of Ultrasonic Apps LLC.

## 5.11.1 Requirements to Produce Cavitations

### 5.11.1.1 Power Intensity

The intensity of the ultrasonic energy must exceed the intensity needed to promote cavitation in the cleaning chemical. In most cases, this is 0.1 – 0.3 W/cm<sup>2</sup>. The frequencies used in commercial equipment are 20–60 kHz, with 40 kHz being the most common. The power levels are commonly 60 – 100 W per gallon of tank capacity, regardless of the type of irradiating surface used. Conversion efficiency of electronic generator and transducer determines the power available to the cleaning solution.

A minimum level of ultrasound energy is needed to generate cavitation in a liquid.

The threshold to be about 0.05–0.3 W/cm<sup>2</sup> of the radiating surface at frequencies of 20 kHz and 40 kHz.

Currently available high power ultrasound frequencies range is from 20 kHz to 500 kHz. A frequency that is good for one application may not be good for another. The basic reason is that every application is unique in its nature with respect to material of construction, contaminants and the required cleanliness level. For example, cleaning of very thin fragile wafers requires higher frequencies while cleaning of automotive components requires lower frequency.

At the low end of 20 – 60 kHz, cavitation implosion energy is the main scrubbing force. While at the high end of one MHz, micro-streaming of the liquid molecules is the main force in fine cleaning. It is important to note that both types of forces exist at every frequency. Cavitation implosion energy is good for the removal of heavy contaminants while microstreaming is good for the removal of nanosize particulates.

There is a linear relationship between the generation of cavitation and microstreaming in liquids and applied frequency.

### 5.11.1.2 Degassing

When high-intensity ultrasonic energy is applied to liquids containing dissolved gases, the gases are released into pockets at intensity levels below that at which cavitation of the solution occurs. The bubbles that are formed are not caused by cavitation. They are transient, combining by coalescence, and rise to the surface at a rate dependent on the sizes of the bubbles and the viscosity of the liquid. When higher intensities are applied with the intention of producing cavitation, degassing occurs first. The rate of particle removal depends on the intensity of the ultrasound, the viscosity of the liquid, and the bubble size. If the intensity is too

high, the larger bubbles are shattered and move out at a lower rate. This phenomenon is sometimes used to remove gases from liquids to be used later for other purposes

Degassing of cleaning solutions is extremely important in achieving satisfactory cleaning results. Fresh solutions or solutions which have cooled must be degassed before proceeding with cleaning. Degassing is done after the chemical is added and is accomplished by turning the ultrasonic on and raising the liquid temperature. The time required for degassing varies considerably, based on tank capacity and solution temperature, and may range from several minutes for a small tank to an hour or more for a large tank. An unheated tank may require several hours to degas. Degassing is complete when small bubbles of gas cannot be seen rising to the surface of the liquid and a pattern of ripples can be seen.

### 5.11.1.3 *Compatible Cleaning Chemicals*

Not all cleaning chemicals will generate cavitations. Interferences can be from physical or chemical factors. The physical factors include viscosity, vapor pressure, surface tension, density, and gas absorption. Attenuations of the sound waves may occur in aqueous cleaning solutions that tend to form inverted micellar structures, viscous solutions and dual phase or multi-phase liquids. pH has minimal effect on generation of cavitations [28].

## 5.12 **Cleaning Chemistry**

*It is important to realize that the use of ultrasonic cavitations does not eliminate the need for proper cleaning chemicals and implementing and maintaining the proper process parameters [24,31].*

Furthermore, the chemical composition of the cleaning medium is a critical factor in achieving a complete removal of various contaminants and without inflicting any damage to the components.

In aqueous cleaning, the detergent contains a single or mixture of surfactants. Surfactants are long chain organic molecules with polar and non-polar sections in their chains. Surfactants can be ionic or non-ionic in nature, based on the type of functional groups attached to or part of their chains. When dissolved in water, surfactants form aggregates called micelles at a level above their critical micelle concentration (cmc). The micelles are composed of aggregates of hydrophilic moiety and hydrophobic portion of the surfactant molecules. They act as a cleaning chemical and encapsulate contaminants thus preventing them from re-deposition.

Cleaning with ultrasonics using only plain water is workable, but only for short period of time. In fact, cleaning is more complex in nature than just removing the contaminants away from the surface. Accumulation of contaminants and encapsulation / dispersion of contaminants are the determining factors for the effective lifetime of the cleaning medium and the cleaning results [24,28,32].

Reproducibility and consistency of the cleaning results are essential requirements for all successful cleaning processes. Cleaning chemistry, as part of the overall cleaning process, is a very crucial element in achieving such consistency [33]. Requirements for the selected cleaning chemical are many. It must cavitate well with ultrasonics and be compatible with the materials of the components to be cleaned. Other important properties are surface tension, stability, capability of emulsifying or separating oils, and effectiveness of dispersing or encapsulate of solid insoluble particles. An aqueous cleaning chemical must rinse freely and must be environmentally friendly. Disposal of used solutions is an important factor and must be addressed upfront when deciding on the appropriate chemical. As it sounds, an expert in the field better makes the selection decision.

Both aqueous and organic cleaning chemicals have advantages and disadvantages. Aqueous cleaning is universal and achieves better cleaning results. Organic cleaning solvents are good in removing organic contaminants but short on removing inorganic salts. Drying and protection of steel components are valid concerns. However, the current available technologies [32] offer in-process corrosion inhibitors to alleviate these concerns.

Power ultrasound enhances the effect of the cleaning chemicals. This is in part due to the mechanical scrubbing of general and bio-contaminants such as oils, protein or bacterial clumps residues on surfaces [11].

The role of aqueous chemistry is to displace oil, to solubilize it or emulsify organic and bio-contaminants, to encapsulate particles, to disperse and prevent re-deposition of contaminants after cleaning. Special aqueous formulations assisted with ultrasonics are being used to decontaminate post-operations surgical instruments, dental and medical devices and food processing equipment [32]. Some additives in the cleaning chemistries are used to assist in the process of breaking chemical bonding, removal of oxides, preventing corrosion, enhancing the physical properties of the surfactants, or to enhance the surface finish. Following cleaning, it is important to use deionized water or, RO water for rinsing the aqueous chemical in order to achieve spot-free surfaces. Minimum of two rinse steps is recommended.

### 5.12.1 Selection of Ultrasonic Cleaning Chemicals

Effective cleaning chemicals are essentially selected on the basis of (1) the chemical and physical nature of the contaminants to be removed; (2) compatibility with the substrate material(s); (3) environmental considerations, and (4) required cleanliness specifications. Therefore, in precision or fine cleaning no one chemical is good for all applications. Every case must be examined individually to determine the most effective and safe chemical [24].

Two main considerations in the process of selecting cleaning chemicals for use in ultrasonic cleaners are (1) chemical compatibility of the cleaning chemical with the materials to be cleaned and the materials of construction of the cleaning vessels, (2) how well it cavitates at different frequencies and (3) its effectiveness in removing contaminants.

There are several important factors that determine cavitation effectiveness in cleaning chemicals such as vapor pressure and viscosity. As the vapor pressure increases and the surface tension decreases the threshold for forming micro bubbles decreases. The intensity of the shock waves associated with the collapse of cavitating bubbles is a function of the ratio of maximum bubble size to minimum bubble size [34].

Dispersed materials of solid particles or gas bubbles, small point protrusions and rough surfaces form nuclei for the formation of cavitation bubbles. Therefore, the stresses that might be associated with cavitation in a given cleaning chemical are a major consideration in the choice of cleaning chemical. Its importance is related to the possible effects produced on the contaminated surface. For instance, high-power / high- cavitation intensity will erode plated and many coated surfaces. The effect can be minimized by using low surface tension cleaning chemicals to obtain the desired property of non-destructive stress levels. For example, high cavitation intensity is possible in water. A blend of surfactants will lower the surface tension and makes it possible to take advantage of the cleaning properties of the water and the surfactant blend at lower cavitation intensity.

A distinguishing characteristic of polar materials is a high dielectric constant. Nonpolar substances are characterized by a low dielectric constant and include materials such as hydrocarbons and their derivatives, which are comparatively inert. For a given polarity of cleaning chemical, a better penetration of the contaminants is obtained at lower molecular weights.

Other effects caused by cleaning chemicals include dissolution of base material, swelling of materials such as elastomeric coatings, and cracking and distorting of certain plastics. These are the considerations necessary to be regarded in choosing a cleaning chemical for material compatibility.

Other considerations in the choice of cleaning chemicals for ultrasonic cleaning include ability to dissolve or disperse the contaminant, and its ultrasonic transmission properties. Materials such as solvents with high vapor pressure will cavitate at a relatively low power intensity (low cavitation threshold) but will not produce high-intensity cavitation shock waves.

### 5.12.2 Maximizing the Overall Cleaning Effect

Three major contributors to maximize cleaning are 1) effective ultrasonic frequency and power amplitude 2) Cleaning chemical, and 3) temperature. All three produce a net combined effect in a cleaning process (Figure 5.18).

Cleaning chemical selection is extremely important to the overall success of the ultrasonic cleaning process. The selected chemical must be compatible with the base substrate being cleaned, cavitate well and should have the capability to remove the contaminants in concern. Best cleaning chemicals are those especially formulated for use with ultrasonics.

Temperature was mentioned earlier as being important to achieving maximum cavitation. The effectiveness of the cleaning chemical is also related to temperature. The cavitation effect is maximized in pure water at a temperature of approximately 50–70°C. Some cleaners were found to break down and lose their effectiveness if used at temperatures in excess of 80°C. The best practice is to use a chemical at its maximum recommended temperature not exceeding 90°C. Objects must not be allowed to rest on the bottom of the tank during the cleaning process, because heavy parts resting on the bottom of the tank will dampen or attenuate the transfer of the ultrasound waves into the cleaning liquid [35].

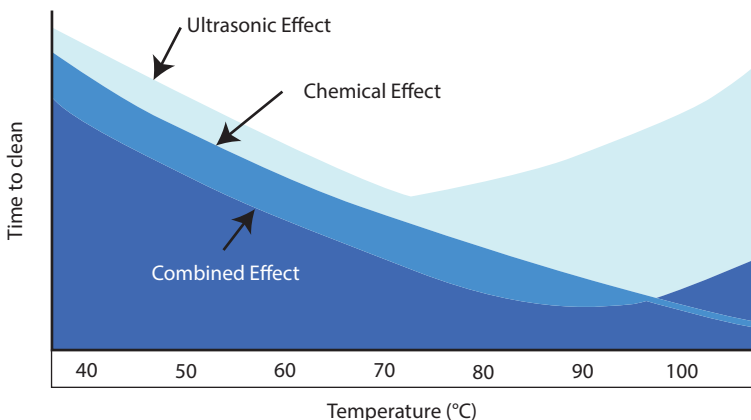


**Figure 5.18** Effect of ultrasonics and cleaning chemical on cleaning time.

## 5.13 Mechanism of Cleaning

The mechanism of removal of organic contaminants by detergent involves wetting of the contaminant as well as the substrate. This will result in increasing the contact angle between the contaminant and the surface and decreasing the surface area wetted with the hydrophobic contaminants such as oils and various organic and inorganic particles. This results in reducing the scrubbing energy needed for contaminant removal.

The ultrasonic cavitations play an important role in initiating and finishing the removal of such hydrophobic contaminants (e.g. oils, soils). The shock wave (and the micro-streaming currents) greatly speeds up the breaking of the contaminants. The removed contaminants are then encapsulated in the micellar aggregates, thus preventing their re-deposition. The net result is that ultrasonic cavitations accelerate the displacement of contaminants from the surface of the substrate and also facilitate their dispersion throughout the cleaning medium.

### 5.13.1 Particle Removal

Particles, in general, have irregular shapes. All the adhesion forces - van der Waals, electrical double layer, capillary and electrostatic - in theory are directly proportional in magnitude to the size of the particle [36,37]. One would expect that the force of detachment would decrease with the size of particles. However, the smaller particles are always more difficult to detach. This is mainly due to the lodging effect. Smaller particles tend to get trapped in the valleys of a rough surface, or in the boundary layer (see Figure 5.17).

### 5.13.2 Particle Removal Mechanism

The mechanism of particle removal involves shifting the free energy of detachment to be near zero. According to Gibbs adsorption equation, surfactants play a very important role in decreasing interfacial tension by adsorption at particle-substrate interface. The interfacial tension  $\gamma_{OB}$  and  $\gamma_{SB}$  will decrease and accordingly the force needed to detach the particles will decrease.

$$\Delta G = \gamma_{SB} + \gamma_{OB} - \gamma_{SO}$$

$\gamma_{SB}$ : Substrate-Bath interfacial energy,  $\gamma_{OB}$ : Soil-Bath interfacial energy,  
 $\gamma_{SO}$ : Substrate-Soil interfacial energy, O: Soil



The wettability of the surface plays an important role in achieving this step. The role of ultrasonic cavitation is to provide the necessary energy for the detachment (i.e. the removal force). At high frequency (100 kHz) ultrasonics, the detachment or the removal efficiency of very small size particles of one micrometer, measured in deionized water, was found to be 95 % versus 80 % at 40 kHz. This is expected in light of the fact that cavitation size is smaller at higher frequencies and can reach deeper into the surface valleys. One would then anticipate that by using a combination of the high frequency ultrasonics at 200 kHz or higher and using the appropriate cleaning chemical, the removal efficiency of sub-micrometer particles could be further optimized. Removal of nanoparticles requires frequencies of 400 kHz and higher. Powerful acoustic streaming is essential to accomplish such removal.

### 5.13.3 Prevention of Particle Re-deposition

Re-deposition of contaminants is not desirable and is inhibited by another mechanism, i.e., by forming a barrier between the removed contaminant and the cleaned surface. The adsorbed cleaning chemical layer on a surface provides a film barrier. In aqueous cleaning, a good surfactant system is capable of encapsulating contaminants within their micellar structure as depicted in Figure 5.19. Re-deposition of the encapsulated contaminants (soils) onto an adsorbed surfactant film on the surface is prevented via steric hindrance for nonionic surfactants, while anionic surfactants prevent re-deposition via electrical repulsive barrier. Encapsulation can be permanent or transient, based on the nature of the surfactant used. Transient encapsulation is superior to emulsification, as it allows better filtration and/or phase separation of contaminants. Therefore, allowing the increase in the soil load in a cleaning solution to reach a saturation point, without good filtration, will result in a significant decrease in

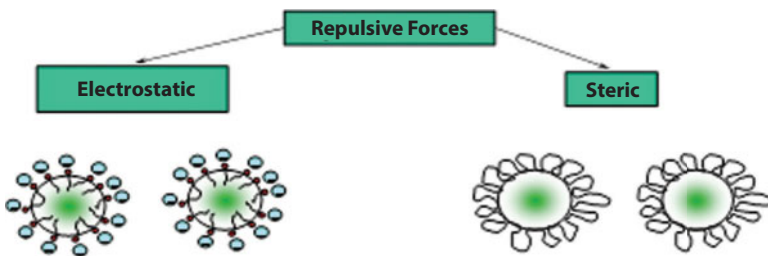


**Figure 5.19** Encapsulation of particles by surfactants keeps them sterically off surfaces or if particles are charged these will be kept apart by electrostatic repulsion.

the detergent cleaning efficiency, at which point the cleaning action may cease. To ensure steady cleaning efficiency, the dispersed contaminants must be removed by means of continuous filtration or separation of contaminants, along with maintaining the recommended concentration of the cleaning chemical.

#### 5.13.4 Cleaning Chemistry and Particle Removal

Two main steps take place in surface cleaning. The first step is the removal of contaminants and the second is to keep those contaminants from re-adhering to the surface. The removal of various contaminants involves different mechanisms, based on the nature and/or the class of the contaminant.

A crucial element in the removal of nano and sub-micrometer particles is prevention from re-deposition. Especially designed cleaning chemistry can achieve this crucial role. The cleaning chemical should be capable of encapsulating the removed particles and thus preventing their re-deposition on surfaces. Also a good cleaning chemical will displace the insoluble contaminants and leave a monomolecular film barrier on the surface to prevent particle deposition. The physical nature of the substrate and the degree of its surface finish are important factors in nano and sub-micrometer particle removal [38,39,40].

For example, a silicon wafer surface is different from that of an aluminum disc with respect to their physics, topography and finish. Plastics are another challenge when dealing with sub-micrometer particles because of the inherent strong static electrical charges. The attractive van der Waals forces have to be countered by repulsive interactions.

#### 5.14 Cavitation Erosion

High intensity ultrasonic fields are known to exert powerful forces that are capable of eroding even the hardest surfaces. Quartz, silicon, and alumina, for example, can be etched by prolonged exposure to ultrasonic cavitation, and “cavitation burn” has been encountered following repeated cleaning of glass surfaces. The severity of this erosive effect has, in fact, been known to preclude the use of ultrasonics in the cleaning of some sensitive delicate components. In Figure 5.20 the pictures vividly illustrate an aluminum surface before and after over-exposure for long time to 40 kHz ultrasonics in water. Under SEM it is clear that a very highly polished surface of aluminum wafer has in reality a rugged surface and has valleys where nano particles can reside. The surface is not exactly what we see with naked eye

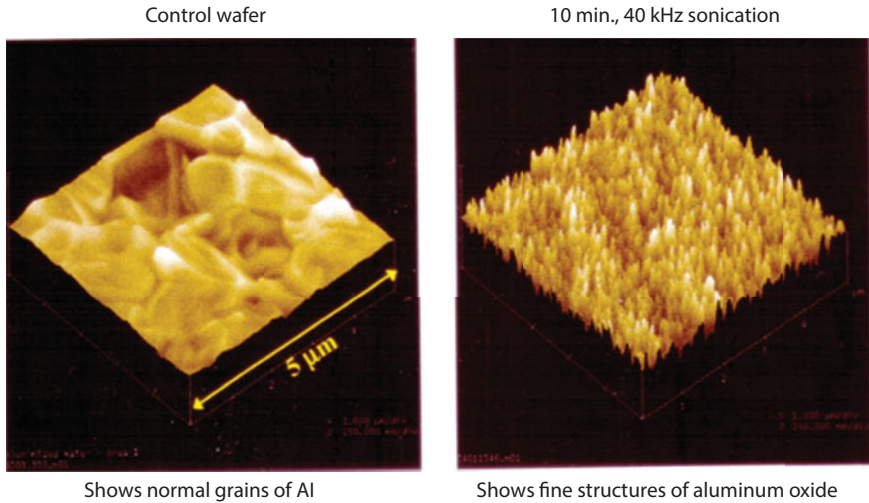


**Figure 5.20** Highly polished aluminum wafer before and after exposure to cavitations at 40 kHz for 10 min. in deionized water. Cavitation Erosion is obvious in the SEM micrograph on the right. Courtesy of Ultrasonic Apps LLC.

(photo to the left). Surface erosion is obvious in the photo to the right. The surface was exposed to ultrasonic cavitations at 40 kHz. For such surfaces of soft metals care must be taken to determine the right ultrasonic frequency, power and other process parameters to avoid surface erosion.

## 5.15 Summary

Three major contributors to optimum cleaning are 1) properly selected ultrasonic frequency applied at the optimum power amplitude 2) properly selected compatible cleaning chemical and 3) optimum cleaning process temperature. All three produce the net combined effect in a cleaning process. Effective removal of nano-particles requires the shearing action of high velocity micro-streams of liquid molecules produced at high frequencies > 850 kHz. Micro-encapsulation is a key for preventing potential re-deposition of contaminants on cleaned surfaces.

## References

1. R. W. B. Stephens, A historical review of ultrasonics, Proceedings Ultrasonics International, ICP Press, Guildford, UK, 9–19 (1975).

2. J. Curie and P. Curie, Development of pressure, polar electricity in crystals hemihedral inclined faces, *Comptes Rendus de l'Académie des Sciences*. 91, 294–295(1880).
3. P. Bruno, Power ultrasound in: *Electrochemistry: From Versatile Laboratory Tool to Engineering Solution*, chapter 1, John Wiley & Sons (2012).
4. Lord Rayleigh, Pressure developed in a liquid during the collapse of a spherical cavity, *Philosophical Magazine*, 34, 94–98 (1917).
5. E. A. Roger and A. Arndt, Cavitation in fluid machinery and hydraulic structures, *Rev. Fluid Mech.*, 13, 273–328 (1981).
6. A. Shoh, Industrial applications of ultrasound, in *Ultrasound: Its Chemical, Physical and Biological Effects*, K.S. Suslick (Ed.), 97–122, VCH, New York (1988).
7. K. S. Suslick, Homogeneous sonochemistry, in *Ultrasound: Its Chemical, Physical and Biological Effects*, K.S. Suslick (Ed). pp.123–159, VCH, New York (1988).
8. T. J. Mason and L. P. Lorimer, *Sonochemistry: Theory, Applications and Uses of Ultrasound in Chemistry*, Ellis Horwood, Chichester, UK (1988).
9. D. Ensminger, *Ultrasonics: Fundamentals, Technologies, and Applications*, third edition, CRC Press, Boca Raton, Florida, 1 -25 (2012).
10. S. Muthukumaran, S.E. Kentish, G.W. Stevens, and M. Ashokkumar, Application of ultrasound in membrane separation processes: A review. *Rev. Chem. Eng.*, 22, 155–194 (2006).
11. V. S. Moholkar, S. Rekveld, and M.M.C.G. Warmoeskerken, Modeling of the acoustic pressure fields and the distribution of the cavitation phenomena in a dual frequency sonic processor, *Ultrasonics*, 38, 666–670 (2000).
12. T. J. Mason, Power ultrasound in food processing - the way forward, in *Ultrasound in Food Processing*, M.J.W. Povey and T. J. Mason (Eds.), Blackie Academic & Professional, London, 105–126 (1998).
13. J. L. Laborde, C. Bouyer, J. P.Caltagirone and A. Gerard, Acoustic bubble cavitation at low frequencies. *Ultrasonics*, 36, 589–594 (1998).
14. J. P. Lorimer and T. J. Mason, Sonochemistry Part 1. The physical aspects. *Chem. Soc. Rev.*, 16, 239–274 (1987).
15. K. Bakhtari, R. O. Guldiken, P. Makaram, A. A. Busnaina, and J. G. Park, Experimental and numerical investigation of nano-particle removal using acoustic streaming and the effect of time, *J. Electrochem. Soc.* 153, G846-G850 (2006).
16. L. Balamuth, Ultrasonic assistance to conventional metal removal, *Ultrasonics* 4, 125–130 (1966).
17. E. Kinsler and A. R. Frey, *Fundamentals of Acoustics*, John Wiley & Sons, New York (1950).
18. J. R. Frederick, *Ultrasonic Engineering*, John Wiley & Sons, New York (1965).
19. L. H. Thompson and L.K. Doraiswamy, Sonochemistry: Science and engineering, *Ind. Eng Chem. Res.* 38, 1215–1249 (1999).
20. F.E. Fox and W. A. Wallace, Absorption of finite amplitude sound waves, *J. Acoust. Soc. Am.* 26, 994–1006 (1954).

21. T. G. Leighton, Acoustic bubble detection – I: The detection of stable gas bodies, *Environmental Eng.*, 7, 9–16 (September 1994).
22. P. Boudjouk, Synthesis with ultrasonic waves, *J. Chem. Educ.*, 63, 427–429 (1986).
23. A. E. Crawford, *Ultrasonic Engineering*, Academic Press, New York (1995).
24. S. B. Awad, Ultrasonic cavitations and precision cleaning, *Precision Cleaning*, 12–17, (November 1996).
25. M. Pedzy, Higher-frequency and multiple-frequency ultrasonic systems, in *Handbook for Critical Cleaning*, B. Kanegsberg and E. Kanegsburg, (Eds.), CRC Press, Boca Raton, FL, 227–232 (2001).
26. D. Weber and M. Walter Ultrasonic transducer, *US Patent 05,200,666* (1993).
27. K. R. Gopi and S.B. Awad, Ultrasonic cleaning with two frequencies, in: *Handbook for Critical Cleaning*, B. Kanegsberg and E. Kanegsberg, (Eds.), 2<sup>nd</sup> edition, 241–246, CRC Press, Boca Raton, FL (2011).
28. M. O'Donoghue, The ultrasonic cleaning process, *Microcontamination*, 2, 62–67 (1984).
29. S. B. Awad, Determination of residual particles on surfaces. An updated method for particle extraction using ultrasonics in, *Particles on Surfaces 9: Detection, Adhesion and Removal*, K. L. Mittal (Ed.), pp. 1–8 CRC Press, Boca Raton, FL (2006).
30. B. Haase, Surface condition and nitriding, *HTM J. Heat Treatment. Mater*, 63, 104–114 (2008).
31. S. S. Seelig, The chemical aspects of cleaning, *Precision cleaning*, 33 (March 1995).
32. S. B. Awad, Aqueous ultrasonic cleaning and corrosion protection of steel components, *Metal Finishing* 102, 56–61 (September 2004).
33. B. Kanegsberg, Aqueous cleaning for high value processes, *A2C2 Magazine*, 25 (September 1999).
34. K. S. Suslick, P. F. Schubert, and J. W. Goodale, The chemical uses of ultrasonics in homogeneous systems, *J Am Chem Soc* 103, 7342 - 7344 (1981).
35. D. Ensminger, *Ultrasonics: Data, Equations, and their Practical Uses*, CRC Press, Boca Raton, FL, 328–358 (2009).
36. R. A. Bowling, A theoretical review of particle adhesion, in: *Particles on Surfaces 1: Detection, Adhesion and Removal*, K.L. Mittal (Ed.), Plenum Press, New York, 129–142 (1988).
37. M. B. Ranade, Adhesion and removal of fine particles on surfaces, *Aerosol Sci. Technol.*, 7, 161–176 (1987).
38. S. B. Awad, Ultrasonic aqueous cleaning and particle removal of disk drive components, *Datatech*, 59–63 (March 1999).
39. K. L. Mittal, Surface contamination concepts and concerns, *Precision Cleaning*, 17–22 (September 1995).
40. A. A. Busnaina, G. W. Gale and I. I. Kashkoush, Ultrasonic and megasonic theory and experimentation, *Precision Cleaning*, 13 -19 (April 1994).



# Megasonic Cleaning for Particle Removal

Manish Keswani\*, Rajesh Balachandran, and Pierre Deymier

*Department of Materials Science and Engineering,  
University of Arizona, Tucson, AZ*

---

## Abstract

This chapter covers fundamental aspects of megasonic cleaning with special emphasis on acoustic cavitation and streaming. The first part of the chapter focuses on various forms of cavitation (stable and transient) and streaming (Eckart, Schlichting, and Rayleigh) and their physical effects in liquids including microstreaming, shock waves, and liquid microjets. A review of studies by several researchers on the role of various sound field and solution parameters on particle removal and feature damage during megasonic cleaning is provided in the second part of the chapter. The importance of understanding the cleaning mechanisms and optimization of process variables in achieving damage-free and effective megasonic cleaning process is also highlighted.

**Keywords:** Megasonic cleaning, silicon wafer, particle removal, acoustic streaming, acoustic cavitation

## 6.1 Introduction

The field of acoustics has grown significantly over the last several decades due to increasing use of sound energy in a variety of technological areas including medical imaging, detection/non-destructive testing, chemical processing, sonolysis (wastewater treatment) and cleaning. The cleaning industry employs sound energy in a wide range of frequency and intensity depending on the application. Typically, moderate intensity-ultrasonic

---

\*Corresponding author: manishk@email.arizona.edu

frequencies (20–150 kHz) are employed for cleaning of jewelry, lenses and optical parts, surgical instruments, etc.; high intensity-ultrasonic frequencies are used for sonochemical processes and wastewater treatment; and low intensity-megasonic frequencies (0.5–3 MHz) are employed for cleaning of electronic devices. The choice of megasonic frequencies for cleaning of silicon devices in semiconductor industry is based on lower cavitation and higher streaming forces at these frequencies that allows effective removal of sub-micrometer size particulate contaminants without causing any damage to delicate features. These frequencies would not, however, be suitable for cleaning of hard and robust materials used in industrial parts where size of particulate contaminants is much larger than a micrometer. There are some general guidelines that have been provided on selection of sound frequency for removal of different types of contaminants from various surfaces [1]. For example, upper range of ultrasonic frequencies (100–200 kHz) have been found to be effective in degreasing using volatile solvents where the cavitation is milder due to high vapor pressure, low viscosity and low surface tension of these solvents. The decontamination of metal surfaces is recommended using a cleaning step with frequency in the range of 40–100 kHz followed by use of 60–200 kHz frequency in the rinse step. In the case of plastics, low to medium range ultrasonic frequencies (30–70 kHz) are preferred due to absorption of sound wave and its attenuation. The cleaning of silicon devices requires use of megasonic frequencies generating milder cavitation to avoid damage to fragile features while achieving effective removal of sub-micrometer sized particles from patterned wafer and mask surfaces.

### 6.1.1 Wafer Cleaning

Semiconductor devices are the foundation of electronics industry, which is the largest industry in the world. The unique properties of semiconductor materials have allowed development of a wide range of ingenious devices that have dramatically changed our lives. With the ever-growing need to improve the performance of electronic devices, there has been a continuous effort to reduce the size of these individual components and increase the chip size. This allows more components to be integrated on a chip, thus significantly enhancing the functioning of the integrated systems and keeping the cost low at the same time. In the 1970's, Gordon Moore, Intel cofounder, described an important trend in the history of computer hardware that the number of transistors on a chip would double every two years without accounting for an increase in the chip size [2]. This trend has been preserved over the years and has led to continuous improvement in



the computing power and development of high-tech devices. One of the drivers behind this growth is the evolution of wafer cleaning technology that has maintained the contamination and defectivity levels within the required specifications.

Wafer cleaning is an important step in fabrication of very large scale integration (VLSI) and ultra large scale integration (ULSI) silicon circuits in order to maintain their reliability and efficient performance. It is estimated that about fifty percent of yield losses in the integrated circuit (IC) industry are due to particle contamination [3]. A continuous effort to improve this yield has led to not only an increase in the number of cleaning steps but also an imposition of more critical requirements by the International Technology Roadmap for Semiconductors (ITRS) on the tolerable size and number of contaminant particles on the front and back side of wafer surfaces. The ITRS dictates that by 2015, the killer defect density, critical particle diameter and count must not exceed  $0.006 \text{ \#/cm}^2$ , 11.3 nm and 34.2  $\text{\#/wafer}$  respectively for the front surface of a 450 mm wafer [4]. Several wafer cleaning techniques incorporating solution chemistries have evolved over time to meet the particle contamination challenge. These include 1) immersion cleaning, 2) centrifugal spinning/spraying, 3) brush scrubbing, 4) high-pressure fluid jet cleaning, and 5) megasonic cleaning (immersion and single wafer). Of these, megasonic cleaning is one of the commonly used techniques in practice today for the removal of particulate contaminants from wafer and mask surfaces.

Current technologies are based on the development of environmentally-benign chemistries and techniques that will require minimal chemical usage and disposal in order to achieve the desired cleaning. Hydrogen peroxide based wet chemistries are still the common form of cleaning techniques used for removal of organic, metallic and particulate contaminants from wafer surfaces. However, its implementation has changed over the years from immersion cleaning to centrifugal spray cleaning, megasonic cleaning, centrifugal spin cleaning and other methods.

Wet cleaning methods employ liquid based chemistries such as hydrofluoric acid (HF) solutions, sulfuric acid-peroxide mixtures (SPM), alkaline and acidic peroxide solutions (standard clean-1 (SC-1) and standard clean (SC-2) solutions) and sulfuric acid-ozone mixtures (SOM). The role of each of these chemical systems in removal of contaminants from wafers is very unique, which has been of great advantage to the wafer cleaning community. In most cases, the particle removal by these chemistries is carried out by etching of the underlying substrate. The maximum allowed silicon or oxide loss per cleaning step in current and near-future generation technology nodes, as indicated by ITRS, should not exceed  $0.1 \text{ \AA}$ . Under

such conditions, use of dilute chemistries or alternative non-reactive chemicals becomes the obvious choice. Unfortunately, this puts a restriction on the cleaning efficiencies that can be achieved by employing these chemistries alone. Therefore, various external sources of energy such as acoustic (megasonic) energy are used in conjunction with dilute chemistries for removal of contaminants.

A typical cleaning sequence of these chemistries used for wafer cleaning is shown in Figure 6.1. Mixtures of 98 % sulfuric acid and 30 % hydrogen peroxide, also known as Piranha, at temperatures of 120–150 °C are used for removal of organic contaminants from the wafer surface due to the strong oxidizing power of  $\text{HSO}_5^-$  and  $\text{H}_3\text{O}_2^+$ , formed during the reaction between  $\text{H}_2\text{O}_2$  and  $\text{H}_2\text{SO}_4$  [5,6,7,8]. Hydrofluoric acid (HF) solutions etch the silicon dioxide ( $\text{SiO}_2$ ) films (R6.1) formed during Piranha cleaning step and assist in removal of particulate contamination from wafer surfaces. SC-1 cleaning involves using mixtures of ammonium hydroxide (29 %), hydrogen peroxide (30 %) and water in the ratios from  $1\text{NH}_4\text{OH}:1\text{H}_2\text{O}_2:100\text{H}_2\text{O}$  to  $1\text{NH}_4\text{OH}:1\text{H}_2\text{O}_2:500\text{H}_2\text{O}$  at 70–80 °C. The pH of this solution is close to 11. Hydroperoxyl anions formed from dissociation of hydrogen peroxide at alkaline pH of SC-1 oxidize silicon and ammonium hydroxide etches it as per reactions R6.2 and R6.3, respectively [9]. This continuous oxidation and etching aids in removal of particles from

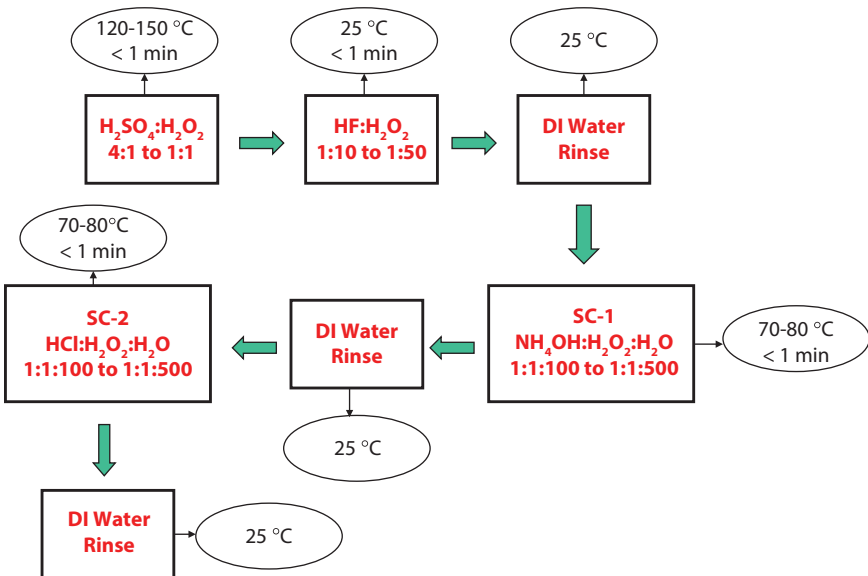
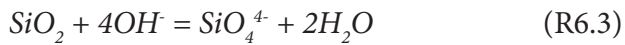
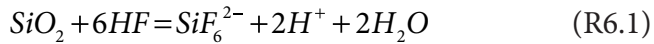


Figure 6.1 Wafer cleaning sequence typically used in semiconductor fabrication.

wafer surfaces. The SC-1 solution is also found to be useful in complexing metal ions such as  $\text{Ag}^+$  and  $\text{Cu}^{2+}$  and in the dissolution of metals (silver, copper, chromium, cobalt, etc.). The SC-2 cleaning solution consists of a mixture of hydrochloric acid (37 %), hydrogen peroxide (30 %) and water in a ratio of  $1\text{HCl}:1\text{H}_2\text{O}_2:100\text{H}_2\text{O}$  to  $1\text{HCl}:1\text{H}_2\text{O}_2:500\text{H}_2\text{O}$  at 70–80 °C. The pH of this solution is less than 1. Metal ions such as  $\text{Fe}^{3+}$ ,  $\text{Al}^{3+}$ ,  $\text{Zn}^{2+}$  and  $\text{Mg}^{2+}$  hydrolyze in the SC-1 solution and form insoluble metal hydroxides that are not removed. Hence, SC-2 solution is used since it can dissolve any metal as metal ion due to the acidic nature of the solution.



## 6.2 Principles of Megasonic Cleaning

In megasonic cleaning, sound waves with a frequency of 1 MHz or larger are directed from the transducer(s) either parallel or perpendicular to the wafers that are immersed in the cleaning liquid. The transducers are made up of piezoelectric materials that possess the ability to convert electrical energy into mechanical energy when high-frequency AC voltage, between 500 and 2000 kHz, is applied causing the transducer material to rapidly change dimension or vibrate. The resonant mass of the transducer transmits these vibrations into the liquid, producing acoustic waves in the cleaning fluid. Cleaning is achieved through proper choice of chemical solutions at desired temperatures, transducer power density and frequency of the acoustic field. The acoustic frequency plays an important role in determining the acoustic boundary layer thickness, which is typically much smaller than the hydrodynamic boundary layer and affects the particle removal. The acoustic boundary layer thickness ( $\delta$ ) depends on fluid kinematic viscosity ( $\nu$ ) and angular acoustic frequency ( $\omega$ ) and is given by equation 6.1.

$$\delta = \left( \frac{2\nu}{\omega} \right)^{1/2} \quad (6.1)$$

As seen from Figure 6.2, at 1 MHz, the acoustic boundary layer thickness in water is  $\sim 1 \mu\text{m}$  and increases with decrease in acoustic frequency. For a liquid such as glycerol with a much higher kinematic viscosity of

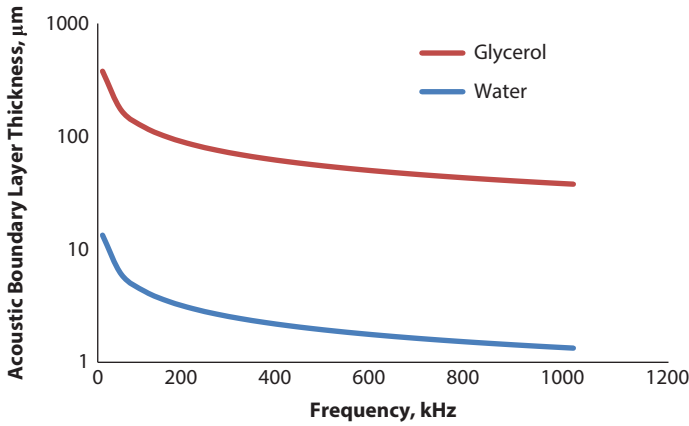


**Figure 6.2** Acoustic boundary layer thickness as a function of frequency for water and glycerol at 25°C.

about 714 mm<sup>2</sup>/s [10], the acoustic boundary layer thickness at 1 MHz is about 50 μm.

By comparison, the turbulent hydrodynamic boundary layer (BL) thickness in water at the center of a 450 mm wafer for a free stream velocity as high as 10 m/s is ~ 4400 μm (calculated using equation (6.2) [11]). Thus, a particle in an acoustic field is likely to experience higher drag than in a hydrodynamic flow for the same microstreaming or hydrodynamic flow velocity, respectively.

$$\text{Hydrodynamic BL}_{\text{Turbulent}} = 0.16 \left( \frac{\nu}{Ux} \right)^{\frac{1}{3}} x \quad (6.2)$$

where  $\nu$  = kinematic viscosity of liquid (m<sup>2</sup>/s),  $x$  = distance from leading edge to center of a 450 mm wafer (m), and  $U$  = free stream velocity (m/s)

### 6.2.1 Acoustic Streaming

Acoustic streaming refers to time independent motion of fluid due to the loss of acoustic momentum caused by viscous attenuation and wave interactions with solid boundaries. Particle removal in megasonic cleaning relies on reduction in boundary layer thickness at the solid-fluid interface that is achieved by means of three types of streaming, namely Eckart, Schlichting and Rayleigh which are classified according to scale of the patterns formed. It is a well known fact that liquid velocities in an acoustic field may not

simply be sinusoidal even though the motions of sound sources essentially are sinusoidal [12]. Patterns of steady vortices or time independent circulations of fluid were first observed by Faraday [13]. Rayleigh did the first theoretical analysis of such phenomena and deduced the flow patterns [14,15]. He found that a time independent component of velocity exists in addition to the oscillating component which can be obtained by solving the Navier-Stokes equation governing the flow. This occurs because of small drifts in the position of fluid elements during each acoustic cycle, caused by an attenuation of the wave in a viscous medium [16]. These flows occur either in a non-uniform sound field or near a solid boundary immersed in fluid irradiated with sound field or near the oscillating sound source itself. The flow velocity increases with sound intensity but is always smaller than the maximum fluid element velocity due to primary sound wave [17].

### 6.2.1.1 Eckart Streaming

Eckart streaming, which occurs outside the boundary layer, is a bulk flow of fluid and is characterized by vortices on the scale of the flow field and only affects the hydrodynamic boundary layer [18]. It reduces the diffusion boundary layer thickness and thus increases the chemical reactivity at the surface. Figure 6.3 shows the schematic of a typical Eckart streaming velocity profile in a megasonic tank. The maximum velocity occurs at the center of the transducer and approaches zero close to the wall. Further, the streaming velocity increases with sound field intensity or transducer power density.

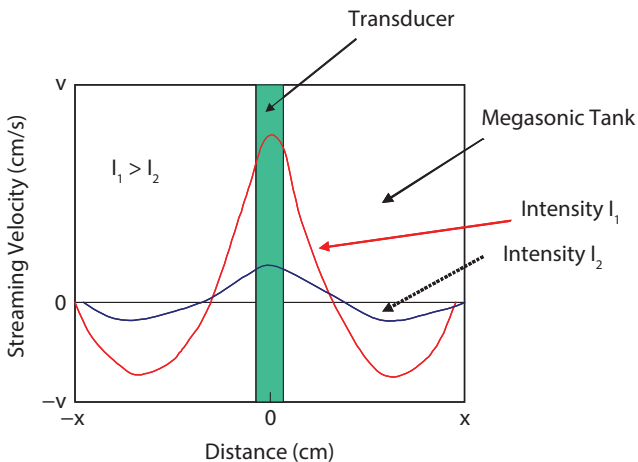


**Figure 6.3** Schematic of Eckart streaming velocity profile in a megasonic cleaning tank.

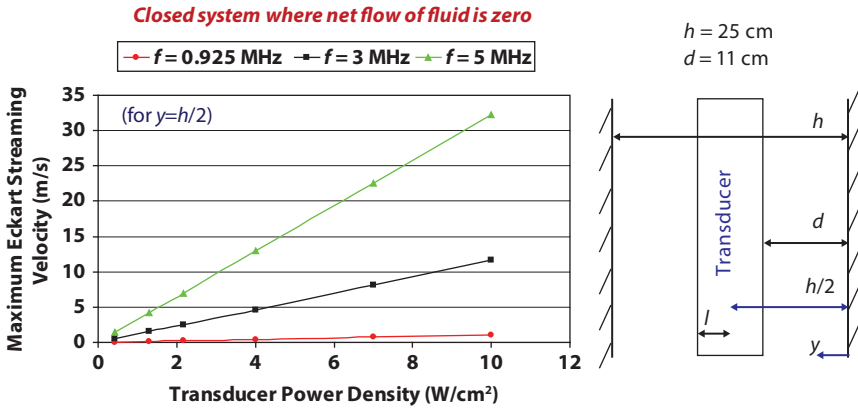


**Figure 6.4** Maximum Eckart streaming velocity at different transducer power densities and sound wave frequencies,  $f$ , for a closed channel, where ‘ $h$ ’ is the distance between the walls of the closed channel, ‘ $d$ ’ is the distance between the edge of the transducer and the channel wall, ‘ $l$ ’ is half the width of the transducer, ‘ $y$ ’ is the variable distance from the channel wall, and  $y = h/2$  corresponds to the center of the transducer at which the Eckart streaming velocity is calculated.

The Eckart streaming velocity is proportional to the product of the square of the acoustic frequency and transducer power density and ratio of bulk to shear viscosity of the fluid. In Figure 6.4, maximum Eckart streaming velocity [19,20] in water is plotted as a function of transducer power density for three different megasonic frequencies of 1, 3 and 5 MHz. These calculations are performed for a closed system where the net flow of liquid in the megasonic tank is zero. Clearly, the Eckart streaming velocity increases linearly with transducer power density and as the square of the sound frequency. At 1 MHz frequency, the Eckart streaming velocity at  $0.5 \text{ W/cm}^2$  is  $\sim 0.05 \text{ m/s}$  and increases to  $\sim 1.0 \text{ m/s}$  at  $10 \text{ W/cm}^2$ . At higher megasonic frequency of 3 MHz, the streaming velocity increases to  $\sim 10 \text{ m/s}$  at  $10 \text{ W/cm}^2$ . The streaming forces can cause high viscous stresses and large velocity gradients in the boundary layer for the removal of contaminants from the substrate.

### 6.2.1.2 Schlichting Streaming and Rayleigh Streaming

Schlichting streaming (boundary layer streaming) results from attenuation due to continuity of the acoustic displacement field at the solid – viscous fluid interface [21]. It is a vortex flow inside the viscous layer resulting from interactions with a solid boundary. The length scale of vortices is much smaller than the acoustic wavelength and is typically about twice the

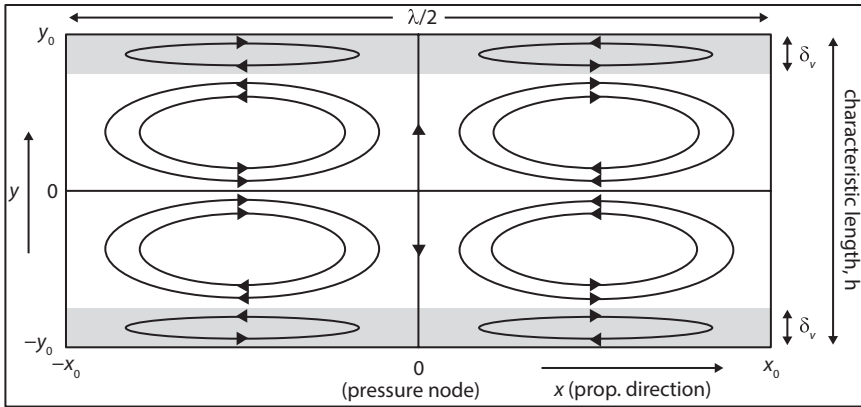


**Figure 6.5** Schlichting streaming and Rayleigh streaming [23,24], Reprinted from *Lab on a Chip*, M. Wiklund, R. Green and M. Ohlin, *Acoustofluidics 14: Applications of acoustic streaming in microfluidic devices*, pp. 2438–2451, copyright (2012) with permission from RSC Publishing, Adapted from M.F. Hamilton, Y. A. Ilinskii, E. A. Zabolotskaya, *Acoustic streaming generated by standing waves in two-dimensional channels of arbitrary width*, *J. Acoust. Soc. Am.*, 113, 1, pp. 153–160 (2003).

acoustic boundary layer thickness [22]. Rayleigh streaming, which occurs outside the boundary layer, produces vortices that are of the scale of the acoustic wavelength [23,24]. Steady viscous stresses are exerted on the boundaries where these types of rotational motions occur, and these stresses may contribute significantly to removal of contaminants from surfaces. A schematic of Schlichting streaming and Rayleigh streaming is shown in Figure 6.5. A standing wave parallel to the solid surfaces and propagating in the  $x$ -direction consisting of spatially fixed pressure nodes and antinodes is formed. The Schlichting streaming flow occurs within the viscous boundary layer (gray region) which then generates counter rotating streaming vortices or Rayleigh streaming outside the viscous boundary layer.

## 6.2.2 Acoustic Cavitation

Cavitation may be defined as stimulated bubble (or cavity) activity in a liquid [25]. When the bubble activity is induced by acoustic waves, it is referred to as acoustic cavitation. This bubble activity is known to produce chemical and physical effects such as acoustic streaming, shock waves, fluid jet formation, sonoluminescence, chemical reactions, radiation forces, and erosion. In turn, these effects drive applications and processes such as ultrasonic and megasonic cleaning, sonochemistry, sonolysis,

medical diagnostic imaging, drug delivery, lithotripsy etc. In order to form a bubble in a liquid, a reduction in liquid pressure is required, which can be achieved by passing a sound wave through a medium. The tensile strength of pure water at 25 °C is about 1000 atm. This means that sound wave pressure amplitude of at least 1000 atm is required to initiate cavitation in water, assuming no other nuclei are present [26,27]. However, cavitation is observed in liquids with pressure amplitudes as low as 1 atm, which suggests the pre-existence of nuclei within the liquid. Thus, the threshold pressure for inception of bubbles in liquid can be significantly lower than the theoretically predicted values depending on several factors including gas trapped in crevices or cracks of solid particles, organic skins around bubbles, partially wetted particulate contaminants, and others.

#### 6.2.2.1 *Stable Cavitation*

Two types of cavities, stable and transient, form when the fluid is subjected to an oscillating pressure field [28]. Stable cavitation has been investigated in detail by Coakley and Nyborg [29]. Stable cavitation, acting as a secondary sound source and leading to microstreaming, entails oscillations of bubbles about an equilibrium size over many acoustic cycles. Acoustic microstreaming occurs due to emission of the sound waves from the oscillating bubbles, especially resonating bubbles, generating rapid currents in localized regions. Microstreaming behavior was first observed by Kolb and Nyborg in 1956 [30]. The movement of carmine red (indicator particle) in water was monitored using a low power microscope under acoustic frequencies of about 5–10 kHz. It was noticed that in the absence of dissolved gas in water and at pressure amplitudes of about 0.1 atm, there was no movement of the carmine red particles, while in the presence of dissolved gas, the movement was very chaotic. This chaotic movement was attributed to the movement generated by the vibration of the bubble (microstreaming). At lower pressure amplitudes, orderly vortex motions were observed. The presence of microstreaming was further justified by the same authors while investigating the degradation of an organism, *Parmecium Caudatum*. It was observed that after exposure to pressure amplitude of about 0.1 atm in the presence of dissolved gas, the organisms were destroyed after 10 min, while they remained intact when exposed to sound field in the absence of dissolved gas. The destruction was attributed to the bombardment of the organisms with the walls of the container or among each other due to the microstreaming forces generated.



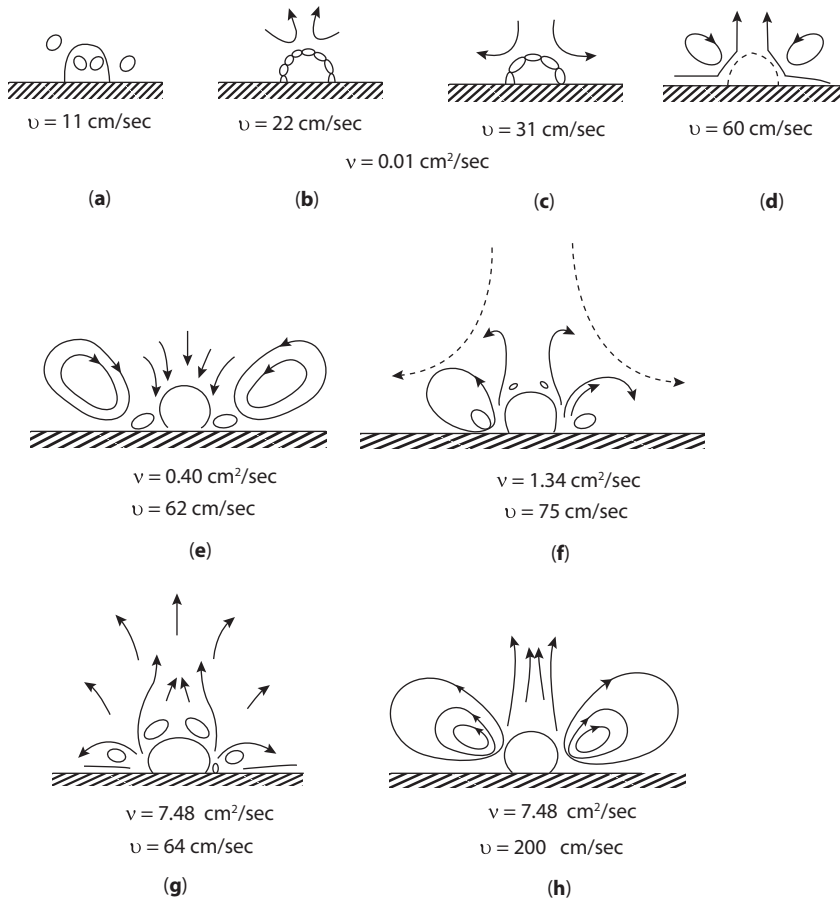


**Figure 6.6** Sequence of microstreaming patterns at different bubble surface velocities [31], Reprinted from *The Journal of the Acoustical Society of America*, 31 (1), S. Elder, Cavitation Microstreaming, pp. 54–64, copyright (1959) with permission from ASA Publishing.

Vibration of bubbles close to the solid boundary leads to several stages of streaming as illustrated in Figure 6.6. A stable mode of bubble vibration is observed when bubble surface velocity is close to 11 cm/s causing microstreaming near the top of the bubble [31]. A reversal in streaming occurs at a bubble surface velocity of 31 cm/s followed by chaotic surface agitation at 60 cm/s. At this bubble surface velocity, transformation from stable mode occurs and the bubble is surrounded by a large vortex ring [31]. Microstreaming can be very useful in transporting the particles from the viscous boundary to the bulk of the solution.

### 6.2.2.2 *Transient Cavitation*

The second form of cavitation termed as transient cavitation is characterized by large bubble size variations and eventual bubble collapse (typically in less than a few cycles), which can be quite violent. This violent collapse, accompanied by extremely high temperature and pressure conditions, often leads to the formation of shock waves with or without the formation of microjets depending on whether the bubble collapse occurs in the vicinity or away from the solid boundary. It is known that during collapse of bubbles, temperatures of the order of 4500 K can be reached, which results in formation of active radicals such as  $\text{OH}^\bullet$ ,  $\text{H}^\bullet$ ,  $\text{HO}_2^\bullet$ ,  $\text{O}_2^{\bullet-}$  etc. [32,33]. Both shock waves and microjets can cause dislodgment of particles from surfaces.

#### 6.2.2.2.1 Shock Wave and Fluid Jet Formation

Bubbles driven into activity by acoustic waves act as sources of pressure variation and fluid motion [25]. For example, bubbles driven at a resonance frequency entail high fluid velocity causing enhanced heat, mass and momentum transfer. These high fluid velocities occur at cavitation sites, the most common forms of which include contaminants on the surfaces. This situation is very advantageous for removal of particulates or other contaminants from the surfaces. Whether it be large scale cleaning using ultrasonics or cleaning of fine structures using megasonics, the type of cavitation must produce high velocities for creating necessary drag forces on the particles without powerful inertial cavitation which might cause damage to the features on the surface. To lower the destructive effect of cavitation, a solvent with higher vapor pressure may be added which provides a cushioning effect to the collapsing cavity and softens its impact. Similarly, addition of gas to the liquid in optimum amount reduces the impact of cavitation.

Ohl *et al.* have shown that the dynamics of bubble collapse depends on the distance of separation between the solid boundary and the bubble center [34]. When this distance is three times or greater the radius of the bubble, the bubble stays spherical during its collapse and shock waves are emitted [35]. If the distance is lower than three times the bubble radius, asymmetrical collapse of the bubble occurs resulting in a fluid jet formation. Shock waves are emitted in this case also, but are less violent.

Flynn suggests that during transient cavitation, the bubble implodes and rebounds with extreme pressures [36]. We know that the speed of sound is an increasing function of liquid pressure. This leads to a significant increase in sound speed during collapse and eventual formation of a shock wave.

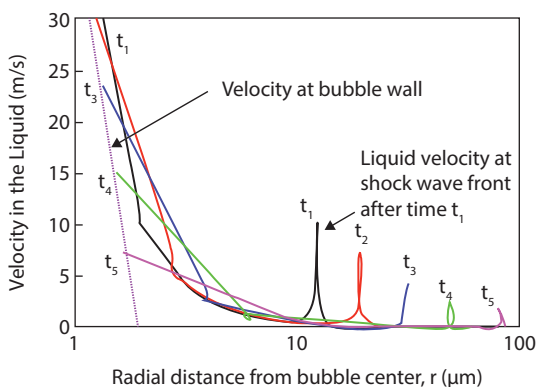


**Figure 6.7** Liquid velocity as a function of distance from bubble center after specified elapsed time [37], Reprinted from *Ultrasonics Sonochemistry*, 15 (4), V. Minsier and J. Proost, Shock wave emission upon spherical bubble collapse during cavitation induced megasonic surface cleaning, pp. 598–604, copyright (2008) with permission from Elsevier.

Minsier and Proost illustrated that a physical discontinuity occurs between the liquid pressure and velocity during bubble collapse, suggesting the presence of a shock wave [37]. It was demonstrated using numerical computations that rebound of the liquid after bubble collapse results in spikes in liquid velocity at a few radial distances from the bubble center. These spikes correspond to the liquid velocity at the shock wave front as shown in Figure 6.7. One can notice the decrease in spikes or shock wave front velocity over time.

The effect of solution parameters on liquid velocity at the shock wave front is critical in cavitation induced cleaning of surfaces. A high liquid velocity at shock wave front can clean but can also damage the surface. Therefore, tuning of solution conditions to optimize the velocity of liquid at shock wave front is necessary. Cavitation process variables such as initial bubble radius, sound source pressure amplitude and solution surface tension have been investigated for their effect on liquid velocity at the shock wave front. The calculations were performed for water and the results are displayed in Figures 6.8 and 6.9. It was observed that the liquid velocity at the shock front increases with acoustic pressure and goes through a maximum as a function of the initial radius of the bubble. The trend is similar to that observed for maximum velocity at the bubble wall, the latter values being much higher in magnitude (of the order of 1000–6000 m/s depending on the solution conditions). In the case of effect of surface tension, the liquid velocity at the shock front decreases with increasing surface

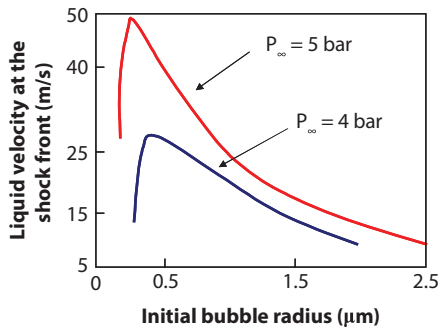


**Figure 6.8** Effect of source pressure amplitude ( $P_{\infty}$ ) and initial bubble radius on liquid velocity at shock wave front [37], Reprinted from *Ultrasonics Sonochemistry*, 15 (4), V. Minsier and J. Proost, Shock wave emission upon spherical bubble collapse during cavitation induced megasonic surface cleaning, pp. 598–604, copyright (2008) with permission from Elsevier

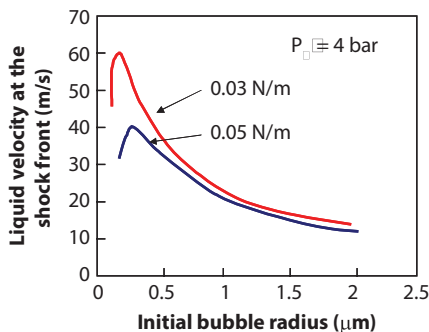


**Figure 6.9** Effect of liquid surface tension and initial bubble radius on liquid velocity at shock wave front at a source pressure amplitude of 4 bar [37], Reprinted from *Ultrasonics Sonochemistry*, 15 (4), V. Minsier and J. Proost, Shock wave emission upon spherical bubble collapse during cavitation induced megasonic surface cleaning, pp. 598–604, copyright (2008) with permission from Elsevier.

tension. This was attributed to the fact that the maximum bubble velocity decreases with an increase in surface tension due to the lower maximum radius of the bubble attained during expansion in liquid with higher surface tension.

Plesset had indicated that the stresses produced by rebound during collapse of a spherical bubble fall off rapidly with distance and hence may not have a significant impact on damage to surfaces observed during cleaning [38]. Kornfeld and Suvorov [39] proposed that liquid jets are formed during

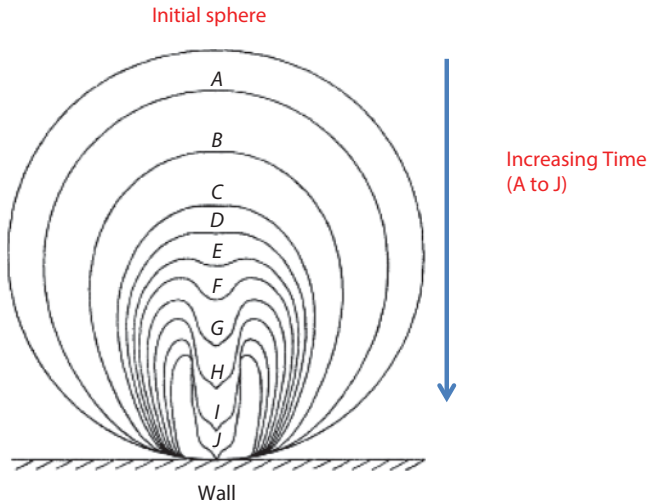


**Figure 6.10** Collapse of a spherical bubble initially in contact with a solid boundary [40], Reprinted from *The Journal of Fluid Mechanics*, 47 (2), M. Plesset and R. Chapman, Collapse of an initially spherical vapor cavity in the neighborhood of a solid boundary, pp. 283–290, copyright (1971) with permission from Cambridge University Press.

bubble collapse close to a solid boundary. These bubbles start their collapse as spheres followed by elongation in the direction normal to the wall and then form an inward moving jet on the side of the bubble opposite the wall.

Plesset and Chapman used a numerical method for collapse of vaporous bubbles lacking spherical symmetry and obtained the jet velocities for two cases: a bubble initially in contact with a solid boundary and a bubble initially at a distance half its radius from the boundary at the nearest point [40]. The jet velocities of 130 m/s and 170 m/s were obtained respectively for the two cases. The shapes of the bubbles and jet formations during the collapse for the two cases are shown in Figures 6.10 and 6.11.

Keswani *et al.* used high time resolution cyclic voltammetry and chronoamperometry techniques to characterize transient cavitation in megasonic ( $\sim 1$  MHz) irradiated aqueous solutions containing additives such as dissolved gases (Ar, N<sub>2</sub> or CO<sub>2</sub>) or non-ionic surfactants (Triton X<sup>®</sup>-100 or NCW<sup>®</sup>-1002) [41,42]. Their results revealed that dissolved Ar and non-ionic surfactants increase the intensity of transient cavity collapses while dissolved CO<sub>2</sub> significantly reduces it. An example of cyclic voltammetry (CV) plots for experiments conducted using a 25  $\mu\text{m}$  platinum working electrode in solutions containing 50 mM potassium ferricyanide and saturated with Ar or CO<sub>2</sub> is shown in Figure 6.12. The current ‘peaks’ (or

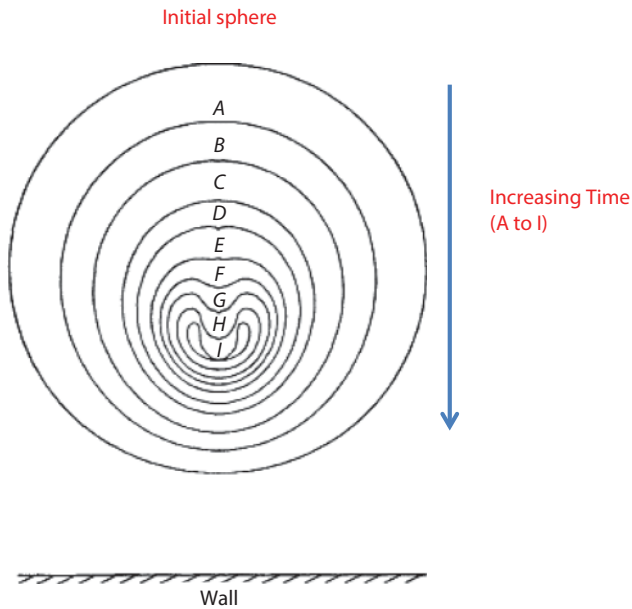


**Figure 6.11** Collapse of a spherical bubble initially at a distance half its radius from a solid boundary [40], Reprinted from *The Journal of Fluid Mechanics*, 47 (2), M. Plesset and R. Chapman, Collapse of an initially spherical vapor cavity in the neighborhood of a solid boundary, pp. 283–290, copyright (1971) with permission from Cambridge University Press.

actually inverse peaks) observed in CV plots for Ar saturated solutions exposed to  $\sim 1$  MHz acoustic energy were attributed to diffusion of ferricyanide resulting from its accumulation by advection at the end of a transient cavity collapse. These peaks were not observed in CV of  $\text{CO}_2$  saturated solutions suggesting absence of transient cavitation in these solutions. The authors also developed a diffusion based mathematical model that correlates the size of transient bubbles prior to collapse and intensity of bubble collapse to the magnitude and the rise and fall time of current peaks.

The effect of acoustic frequency, acoustic pulse width, and degassing of DI water on pressure threshold amplitude to initiate cavitation as measured using a hydrophone was illustrated by Gouk *et al* [43]. The pressure threshold in air saturated DI water was found to decrease significantly (about 4 times) with increase in acoustic pulse width from  $\sim 0.5$  to 12 ms at acoustic frequencies of 0.98 and 1.76 MHz. The degassing of the DI water also had a dramatic effect on increasing the threshold. The threshold increased slightly with increasing the frequency from 0.78 to 1.76 MHz.

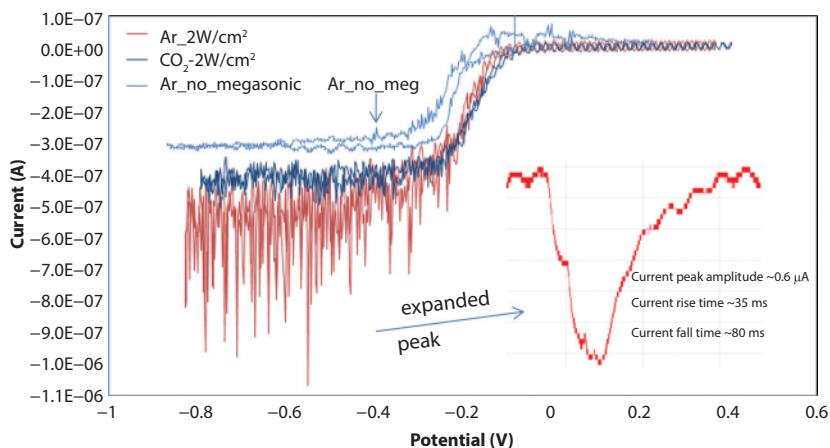


**Figure 6.12** Effect of dissolved gases ( $\text{CO}_2$  and Ar) in 50 mM  $\text{K}_3\text{Fe}(\text{CN})_6$  and 0.1 M KCl solution on current-voltage behavior ( $\sim 1$  MHz sound frequency and  $2.0 \text{ W/cm}^2$  power density,  $25 \mu\text{m}$  Pt working electrode and  $500 \mu\text{m}$  Pt counter and reference electrodes, scan rate =  $0.05 \text{ V/s}$ ) [41], Reprinted from *Microelectronic Engineering*, 102, M. Keswani, S. Raghavan and P. Deymier, Characterization of transient cavitation in gas sparged solutions exposed to megasonic field using cyclic voltammetry, pp. 91–97, copyright (2013) with permission from Elsevier.

### 6.3 Particle Removal Mechanisms During Megasonic Cleaning

Although several mechanisms have been known to occur in megasonic cleaning of surfaces, the actual cleaning mechanism has been a topic of debate for many years. Olim estimated that the acoustic pressure force, which acts parallel to the surface due to the pressure gradient in the direction of sound wave propagation, cannot remove particles smaller than 350 nm. It was suggested that removal of these particles in megasonic cleaning requires additional cleaning mechanisms [44].

Ferrell and Crum highlighted two mechanisms by which wafer cleaning can be achieved, one by direct interaction of the sound wave with the particle adhered to the wafer and the other due to cavitation [45]. It was suggested that the propagation of the sound wave generates a periodic movement of the fluid element which will cause displacement of the particle. If the particle is displaced sufficiently away from the surface, it may get detached. However, simple calculations show that the fluid element in water at  $\sim 1$  MHz of sound frequency is displaced only a few angstroms from its equilibrium position at a transducer power density of  $\sim 1$  to  $2 \text{ W/cm}^2$  and is unlikely to cause particle removal [46].

Shwartzman *et al.* claimed that the time for cavity formation in megasonic cleaning was too short ( $1.25 \mu\text{s}$ ) and that rocking action due to sound waves, rather than cavitation, was the primary cleaning mechanism [47]. Deymier *et al.* showed that the acoustic pressure force due to the scattering of acoustic wave by a particle adhered to the wafer surface is negligible and therefore unlikely to generate a significant pressure field to cause removal of particle from the surface [48]. Kim *et al.* [49] determined that particle removal in the presence of a megasonic field was brought about by the interfacial and pressure gradient forces generated by microbubbles present in the vicinity of adhered particles. Their studies were performed on both blanket and patterned Si wafers contaminated with fluorescent polystyrene latex (PSL) particles of  $\sim 0.7$  and  $1 \mu\text{m}$  in diameter in the presence of  $0.95 \text{ MHz}$  acoustic field. They showed that acoustic pressure gradient does not primarily remove particles but acts as a secondary factor. However, after numerous discrepancies, two major cleaning mechanisms, namely acoustic cavitation and streaming, have evolved to become widely accepted mechanisms for removal of particles during megasonic cleaning.

McQueen considered the usefulness of acoustic streaming in reducing the boundary layer thickness based on his work on removal of nanoparticles from surfaces [50,51]. Deymier *et al.* investigated the effect of second-order sound fields such as Schlichting streaming on removal of particles in megasonic cleaning [52]. They treated the solid as an isotropic elastic medium and water as a viscous fluid. It was shown that the normal component (perpendicular to the wafer surface) of the removal force resulting from the second-order acoustic field was too small to remove the sub-micrometer sized particles. However, they predicted that the parallel component of the streaming force can exert significant drag on the particle and remove it through a rolling mechanism.

Gale and Busnaina explained the roles of cavitation and acoustic streaming in megasonic cleaning [18]. They suggested that stable cavitation results in strong microstreaming currents close to the wafer surface that can induce cleaning. Acoustic microstreaming occurs due to the large stable oscillations of the gaseous cavities which, in turn, causes the rapid movement of the surrounding liquid in the same pattern as the bubble wall. These gaseous cavities can either nucleate on a solid surface or pre-exist in the liquid solution. If asymmetry in the bubble oscillations occurs, say due to the presence of a boundary of a particle or a surface, intense microstreaming patterns develop causing significant shear stresses along the boundary. In addition to stable cavitation, shock waves and liquid jet formation occurs due to cavity collapse, which can cause particle detachment. The detached



particle is then carried away from the wafer surface by streaming forces, due to strong currents and boundary layer thinning.

Microjet formation is often observed where inertially controlled oscillating bubbles with large displacement amplitudes become unstable following an asymmetry in the flow field around them. This causes one wall of the bubble to collapse faster than the other, thereby forming a liquid jet that can attain supersonic velocity and impact the boundary that caused asymmetry in the first place. If the boundary happens to be a particle surface, it can get dislodged from the surface as a result of this impact. This form of cavitation is believed to be the primary mechanism for removal of particulate contaminants from surfaces during cleaning in a megasonic field. When the same effect is present in ultrasonic cleaning of surfaces, damage of the surface can occur in addition to removal of particles due to higher impact velocities of microjets.

Busnaina *et al.* considered three different mechanisms that may contribute to particle removal: lifting, sliding, or rolling [11]. Zhang *et al.* proposed that particles will be removed if the drag force ( $F_D$ ), lift force ( $F_L$ ) and the adhesion force ( $F_a$ ) satisfy the following condition with  $C_F$  being the coefficient of friction [53]:

$$F_D \geq C_F (F_a - F_L) \quad (6.3)$$

In a megasonic field, the lift force is normally very small and can be neglected compared to the adhesion force [54]. The van der Waals force, which is the dominant adhesion force, is given by

$$F_a = \frac{A_{123}R}{6H_0^2} \quad (6.4)$$

where  $F_a$  is the adhesion force (van der Waals) between a solid flat surface and a spherical particle in a liquid medium,  $A_{123}$  is the Hamaker constant for particle 1 and substrate 2 with medium 3 in between,  $R$  is the radius of particle and  $H_0$  is the distance between particle and solid surface.

The removal of a particle by rolling can occur when the ratio of the hydrodynamic rolling moment to the adhesion resisting moment,  $RM$  (Eq. 5), is much larger than 1 [55]. The rolling mechanism with different parameters is shown in Figure 6.13.

$$RM = \frac{F_D (1.399R - \delta)}{F_a a} \quad (6.5)$$

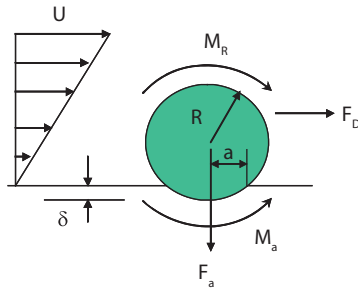


**Figure 6.13** The different forces involved in a rolling removal mechanism [62], where,  $M_a$ ,  $M_R$  are the adhesion and rolling moments, respectively and  $F_D$  is the drag force, Reprinted from *Microelectronic Engineering*, 87, P. Karimi, T. Kim, J. Aceros, J. Park and A.A Busnaina, The removal of nanoparticles from sub-micron trenches using megasonics, pp. 1665–1668, copyright (2010) with permission from Elsevier.

## 6.4 Types of Megasonic Systems

There are three most common types of megasonic cleaning systems that exist in market today, namely, immersion type, single wafer spray type, and single wafer with radial transducer (MegPie<sup>®</sup>, Prosys Inc., Campbell, CA). The immersion cleaning systems can be direct or indirect type. In direct type of megasonic system, sound energy is directly transmitted into the cleaning fluid as the transducer resonator surface is in direct contact with the fluid. In indirect megasonic system, the resonator is in contact with degassed DI water through which the sound wave is transmitted first before reaching the cleaning fluid. Figure 6.14 shows schematics of a typical direct and indirect immersion megasonic cleaning systems.

The advantage with indirect megasonic system is that resonator does not come in contact with the cleaning chemistry, which improves its durability and lifetime. However, the main drawback with indirect megasonic cleaning system is that sound energy losses can occur at the solid boundary that separates the DI water from the cleaning fluid. Attempts have been made to understand the effect of angle of incidence of sound waves at the solid boundary on the transmission characteristics [56].

In single wafer spray megasonic cleaning system, sound wave is propagated through a cleaning liquid that is sprayed from a nozzle onto a rotating wafer surface (Figure 6.15(a)). The spray nozzle moves from the center of the wafer to the edge at different speeds to allow for uniform distribution of sound energy across the radius of the wafer.

The MegPie<sup>®</sup> is a spin cleaning tool with a radial transducer for wet cleaning of single wafers (Figure 6.15 (b)) under megasonic conditions.

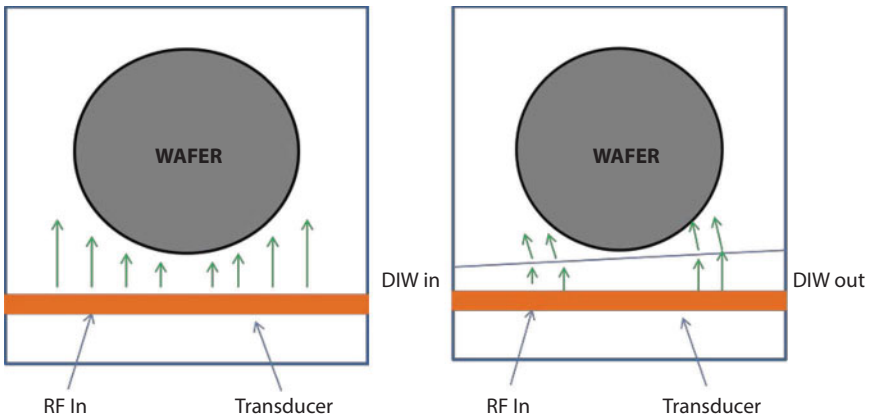


**Figure 6.14** Schematics of direct (left) and indirect (right) immersion megasonic cleaning systems.

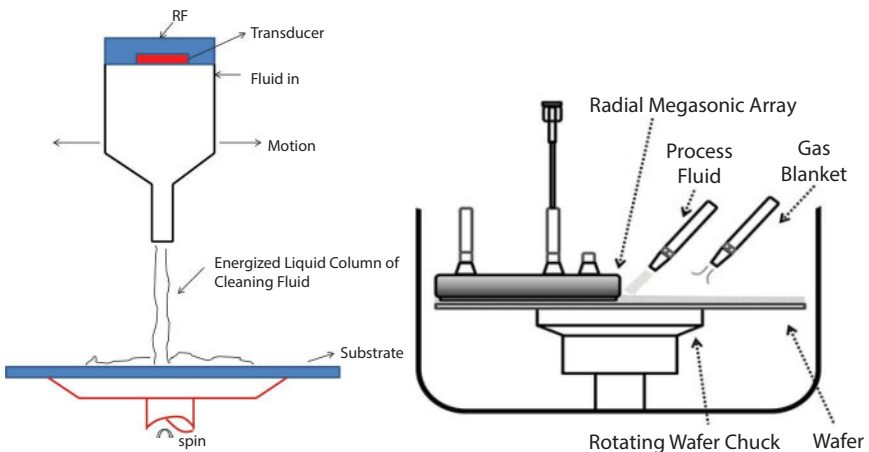


**Figure 6.15** Schematics of spray megasonic (left) and MegPie® (right) cleaning tools [65], Reprinted from *ECS Transactions*, 41 (5), S. Kumari, M. Keswani, S. Singh, M. Beck, E. Liebscher, L. Q. Toan and S. Raghavan, Effect of dissolved  $\text{CO}_2$  in de-ionized water in reducing wafer damage during megasonic cleaning in MegPie, pp. 93–99, copyright (2011) with permission from ECS-The Electrochemical Society.

The radial transducer (area  $32.3 \text{ cm}^2$ ) is designed to apply uniform acoustic field to a rotating substrate (typically 0 - 60 rpm) at a frequency of 0.925 MHz. Acoustic power density can be generated in the range of 0.15 to  $2.94 \text{ W/cm}^2$ . The rotating chuck is designed to hold single wafer at a time. Cleaning solutions are dispensed on top of the rotating wafer

at an appropriate flow rate such that a continuous liquid film (meniscus) is formed between the rotating wafer and the transducer. In recent years, single wafer tools have become the choice of cleaning tools and have slowly replaced immersion tools.

## 6.5 Particle Removal and Feature Damage in Megasonic Cleaning

Considerable work has been done to understand the particle removal mechanisms in megasonic cleaning using different solution chemistries. Bakhtari *et al.* studied the removal of polystyrene latex (PSL) nano-particles from silicon wafers in SC-1 and DI water solutions at 0.760 MHz [57]. The proposed cleaning mechanism was based on acoustic streaming for dislodging the particles and double layer repulsive force for preventing re-deposition of the particles. Lifting, sliding and rolling of the particles resulting from a higher ratio of drag force moment to adhesion force moment has been shown to be useful in megasonic cleaning of substrates [11]. Gale and Busnaina concluded that the particles get removed from the wafer surface due to microstreaming but are transferred to the bulk solution away from the wafer by means of other streaming flows [18].

In another megasonic cleaning study by Busnaina and Gale the removal of PSL and silica particles of different sizes was investigated at 0.862 MHz at 150 W in SC-1 (1NH<sub>4</sub>OH:1H<sub>2</sub>O<sub>2</sub>:5DI) solution as a function of time. The cleaning time for complete removal of particles smaller than 300 nm from the wafer surface was found to be 20 min or longer [58]. Such long cleaning times can cause excessive loss of wafer surface due to continuous oxidation and etching in SC-1 solution. The use of DI water instead of SC-1 eliminates the problem of silicon/oxide loss but requires much higher transducer intensity to achieve a comparable level of cleaning. Keswani *et al.* conducted investigations on the feasibility of removal of positively charged aminated silica particles (~400 nm) from silicon wafers with chemical oxide in near neutral (pH ~ 6) KCl solutions of different ionic strengths (1  $\mu$ M to 1 M) irradiated with megasonic waves at ~ 1 MHz [59]. As can be seen from Figure 6.16, the particle removal efficiency (PRE) increases with KCl concentration (ionic strength) and transducer power density and much lower power densities were required at higher KCl concentration for a comparable level of cleaning. In DI water alone at 0.43 W/cm<sup>2</sup>, the PRE was lower than 10 %. When KCl solution was used at same power density, the PRE increased from 20 to 95 % with increase in ionic strength (or KCl concentration) from 1  $\mu$ M to 0.5 M. Similar trends were observed

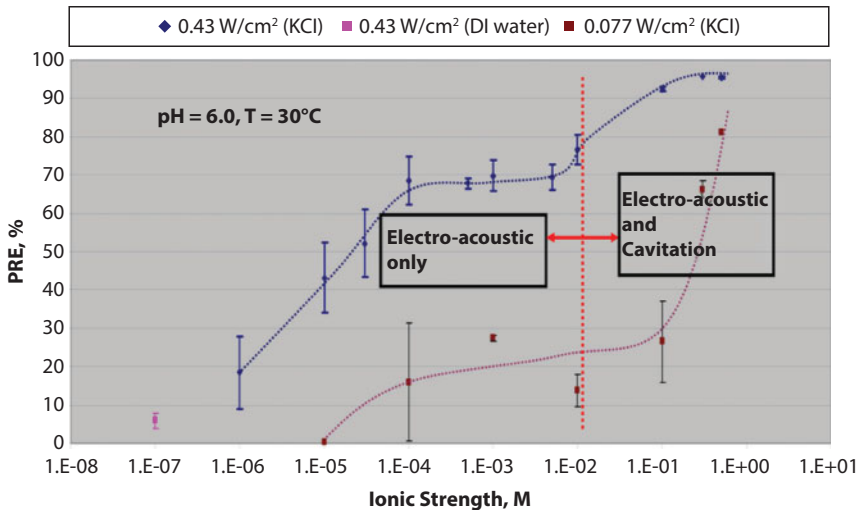


**Figure 6.16** Effect of ionic strength on removal of aminated silica particles from silicon wafers immersed in KCl solution subjected to megasonic field [59], Reprinted from *Microelectronic Engineering*, 86 (2), M. Keswani, S. Raghavan, P. Deymier and S. Verhaverbeke, Megasonic cleaning of wafers in electrolyte solutions: Possible role of electro-acoustic and cavitation effects, pp. 132–139, copyright (2009) with permission from Elsevier.

at lower power density of  $0.077 \text{ W/cm}^2$ . Theoretical computations showed that removal forces due to electro-acoustic effects generated in acoustically irradiated electrolyte solutions were comparable to van der Waals adhesion forces under certain conditions and were likely responsible for significant enhancement of particle removal efficiencies. The work illustrated that benign electrolytes at near-neutral pH can be used to achieve enhanced cleaning of wafers at much lower megasonic power densities where feature damage may be absent.

The removal of particles from patterned wafers is much more challenging than that from blanket wafers [60]. In a study comparing removal efficiency of 330 nm silica particles from blanket silicon wafers and wafers with  $1 \mu\text{m}$  wide by  $2.2 \mu\text{m}$  deep silicon trenches, it was observed that particle removal was significantly lower for patterned wafers under megasonic conditions of 0.85 MHz frequency and  $3.7 \text{ W/cm}^2$  power density. Other studies have revealed that removal of particles attached to the trench side-walls or deposited at the bottom of the trench is far more difficult than removal from top of the trench [61]. The effect of trench width on particle removal efficiency as a function of transducer power density and cleaning times at 0.76 MHz of sound frequency was illustrated by Karimi *et al* [62].

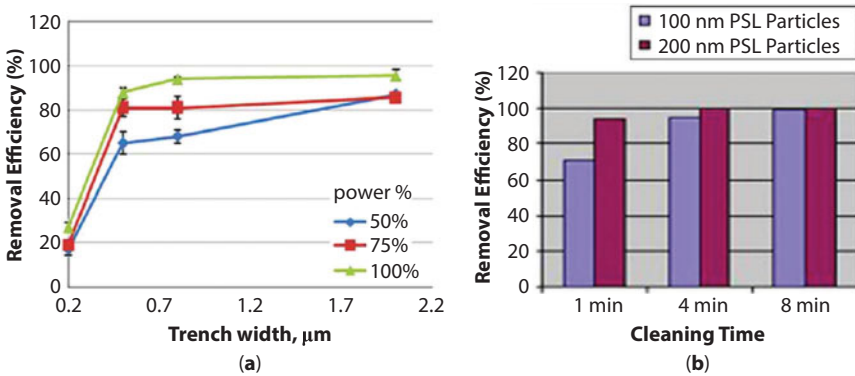


**Figure 6.17** Particle removal efficiency of polystyrene latex particles as a function of (a) trench width (100 nm particles, 4 min cleaning time) and (b) cleaning time (100% power, 2  $\mu\text{m}$  trench width [62], Reprinted from *Microelectronic Engineering*, 87 (9), P. Karimi, T. Kim, J. Aceros, J. Park, A. A. Busnaina, The removal of nanoparticles from sub-micron trenches using megasonics, pp. 1665–1668, copyright (2010) with permission from Elsevier.

It was shown, as illustrated in Figure 6.17(a), that for 4 min of cleaning time at 7.75 W/cm<sup>2</sup>, the removal efficiency of 100 nm polystyrene latex fluorescent particles reduced from ~ 95 to 25 % as the trench width decreased from 2 to 0.2  $\mu\text{m}$  for aspect ratio of 1 and percent power of 100 %. At lower percent powers, the PRE reduced for all widths of the trench. The cleaning studies conducted at higher cleaning time of 8 min at 100 % megasonic power revealed that particle removal efficiency for 100 nm particles was more sensitive to power density than to cleaning time. Figure 6.17(b) shows comparison of particle removal efficiencies of 100 and 200 nm particles from 2  $\mu\text{m}$  wide trenches at 100 % megasonic power as a function of cleaning time. Clearly, the removal of smaller 100 nm particles is more difficult than larger 200 nm particles as larger particles experience higher drag for the same streaming velocity. It is apparent from these studies that by using high levels of megasonic power density and long cleaning times, significant particle removal can be achieved for patterned surfaces. Unfortunately, higher megasonic power also results in more intense transient cavitation, a phenomenon known to cause damage to fragile features [63].

The effect of megasonic power density on damage to single crystalline silicon fins of varying widths (30–80 nm) and lengths (10–100  $\mu\text{m}$ ) was investigated by Muralidharan *et al.* [64]. It was shown that as the power density increased from 0.43 to 2.2 W/cm<sup>2</sup> at ~ 1 MHz of sound frequency, the defect density increased from 0 to 165 #/mm<sup>2</sup> in air saturated DI water. Additionally, thin and long lines were found to be more susceptible to

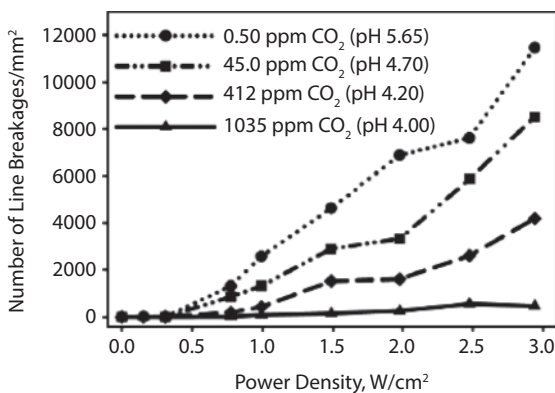


**Figure 6.18** Effect of concentration of dissolved carbon dioxide in DI water and megasonic power density on damage to high k-metal gate structures consisting of 2 mm long and 36 nm wide array of lines separated by 523 nm [65], Reprinted from *ECS Transactions*, 41 (5), S. Kumari, M. Keswani, S. Singh, M. Beck, E. Liescher, L. Q. Toan and S. Raghavan, Effect of dissolved CO<sub>2</sub> in de-ionized water in reducing wafer damage during megasonic cleaning in MegPie, pp. 93–99, copyright (2011) with permission from ECS-The Electrochemical Society.

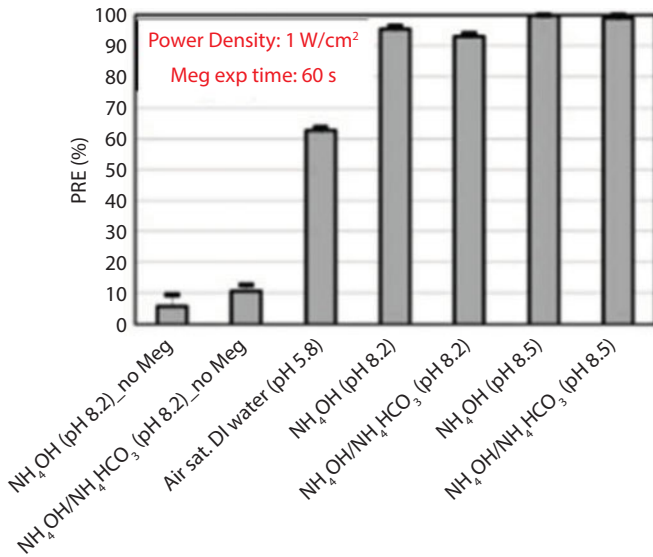
damage than thick and short lines. Kumari *et al.* conducted a detailed and systematic study on damage to high-k metal gate test structures (consisting of HfO<sub>2</sub>/AlO, TiN and Si layers) with 2 mm long and 36 nm wide array of lines in air or CO<sub>2</sub> containing DI water for a range of transducer power densities (0–3 W/cm<sup>2</sup>) at 0.93 MHz of megasonic frequency [65]. The study revealed that breakage of lines was a strong function of power density and type of gas dissolved. As demonstrated in Figure 6.18, the number density of line breakages increases from zero to more than 10000 #/mm<sup>2</sup> with increase in power density from 0 to 3 W/cm<sup>2</sup> in air saturated solutions containing 0.5 ppm of dissolved CO<sub>2</sub>. The defect density decreased progressively with increase in the concentration of dissolved CO<sub>2</sub>. In CO<sub>2</sub> saturated solution, the defect density was lower than 500 #/mm<sup>2</sup> at all investigated power densities.

Other studies have directed their efforts in optimizing the megasonic process for maximum cleaning performance and lowest damage by controlling the amount and type of dissolved gas in the cleaning solution and modulating the power density [66,67]. One such study reports that DI water containing dissolved H<sub>2</sub> exhibits significantly improved PRE but simultaneously creates more defects on patterned substrates [66]. Kumari *et al.*, identified a novel way of suppressing pattern damage and enhancing megasonic particle removal efficiency by using chemical systems such as

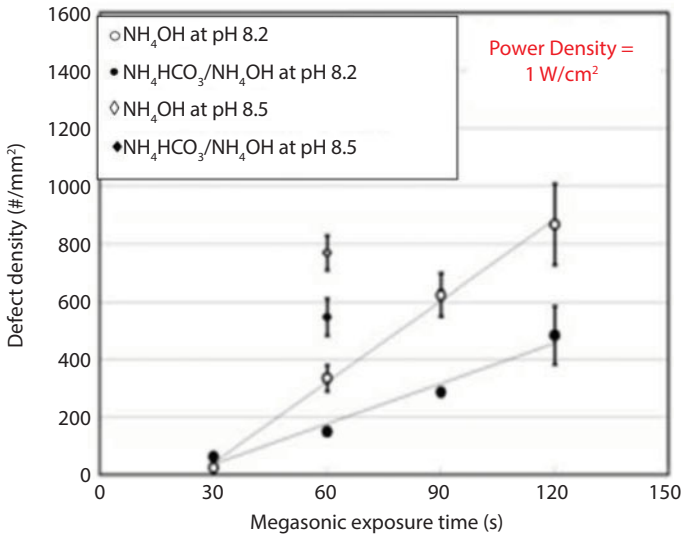
$\text{NH}_4\text{HCO}_3/\text{NH}_4\text{OH}$  that release dissolved  $\text{CO}_2$  to inhibit damaging transient cavitation at slightly alkaline pH of the solution required to achieve effective particle removal [68]. This work was continued by Han *et al.*, [69], who further developed the process by optimization of solution variables such as pH and cleaning time at  $\sim 1$  MHz and  $1.0$  W/cm<sup>2</sup> of power density for cleaning of patterned wafers (consisting of thin high  $k$ - metal lines) contaminated with  $\sim 200$  nm silicon dioxide particles. Figure 6.19(a) shows particle removal efficiency in two different solutions namely  $\text{NH}_4\text{OH}$  and  $\text{NH}_4\text{HCO}_3(0.5 \text{ M})/\text{NH}_4\text{OH}$  at two different pHs of 8.2 and 8.5 in the presence and absence of megasonic fields. The authors reported that both  $\text{NH}_4\text{OH}$  and  $\text{NH}_4\text{HCO}_3/\text{NH}_4\text{OH}$  solutions exhibited comparable and high cleaning efficiencies at both pHs. However, damage studies conducted under similar megasonic conditions as a function of time revealed that defect density was lower in  $\text{NH}_4\text{HCO}_3/\text{NH}_4\text{OH}$  solutions compared to  $\text{NH}_4\text{OH}$  solutions as can be seen from Figure 6.19(b). It should be noted that any increase of pH of  $\text{NH}_4\text{HCO}_3(0.5 \text{ M})/\text{NH}_4\text{OH}$  solutions would have yielded lower concentrations of  $\text{CO}_2(\text{aq.})$  which would have reduced the damage suppressing capacity of  $\text{CO}_2(\text{aq.})$ . One of the disadvantages of this process is that it requires significant concentration of  $\text{NH}_4\text{HCO}_3$  to generate necessary concentration of  $\text{CO}_2(\text{aq.})$  for damage reduction and relies on etching for particle removal.

Another study by Hagimoto *et al.* indicated that greater the concentration of dissolved gases such as  $\text{N}_2$  and  $\text{O}_2$ , higher is the particle removal under megasonic conditions [70]. Experiments were performed on silicon substrates with polysilicon gate structures ( $<90\text{nm}$  thick). The substrates were contaminated with SiN particles and subjected to megasonic cleaning in ammonia-peroxide mixtures (APM). It can be clearly seen from Figure 6.20 (a) that as the concentrations of  $\text{N}_2$  and  $\text{O}_2$  increase from 2 ppm and 5 ppm to 16 ppm and 20 ppm, respectively, there is a simultaneous increase in particle removal. However, in the case of dissolved  $\text{CO}_2$  as the concentrations of dissolved  $\text{CO}_2$  increased from 50 ppm to 300 ppm, the PRE remained almost constant. The effect of higher concentrations of dissolved  $\text{N}_2$  and  $\text{O}_2$  in improving PRE was attributed to movement of water molecules due to microbubbling effect of dissolved gases. A contrasting behavior was observed in the presence of dissolved  $\text{CO}_2$  owing to the fact that  $\text{CO}_2$  readily reacts with water to form  $\text{HCO}_3^-$  or  $\text{CO}_3^{2-}$  ions, thereby it does not activate the movement of water molecules. Damage studies at two different megasonic powers indicated (results shown in Figure 6.21(a)) that almost no damage (# of pattern collapses) was observed in solutions containing dissolved  $\text{N}_2$  and  $\text{O}_2$  at lower power of 200 W while significant damage was observed with dissolved  $\text{CO}_2$  under similar megasonic conditions.





(a)



(b)

**Figure 6.19** Particle removal efficiency (a) and defect density (b) for patterned samples (high-k-metal lines) contaminated with 200 nm silicon dioxide particles at megasonic conditions of ~ 1 MHz and 1.0 W/cm<sup>2</sup> [69].

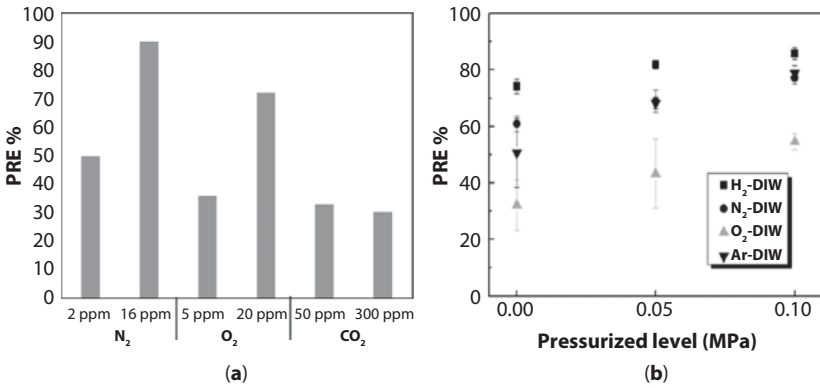


**Figure 6.20** Particle removal efficiency as a function of dissolved gases in (a) APM mixture [70] and (b) pressurized DI water [66], <sup>[a]</sup> Adapted from IEEE, Y. Hagimoto, K. Asada, H. Iwamoto, The effective damage-free megasonic cleaning using N<sub>2</sub> dissolved APM, pp. 215–218 (2005), <sup>[b]</sup> Reprinted from *ECS Transactions*, 41 (5), B-K. Kang, M-S. Kim, S-H. Lee, H-S. Sohn and J-G. Park, Effect of acoustic cavitation on dissolved gases and their characterization during megasonic cleaning, pp. 101–107, copyright (2011) with permission from ECS-The Electrochemical Society.

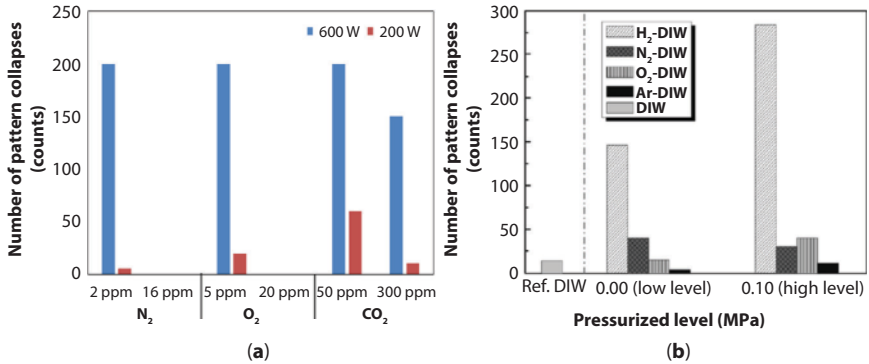


**Figure 6.21** Damage as a function of dissolved gases for substrates in (a) APM mixture [70] and (b) pressurized DI water [66], <sup>[a]</sup> Adapted from IEEE, Y. Hagimoto, K. Asada, H. Iwamoto, The effective damage-free megasonic cleaning using N<sub>2</sub> dissolved APM, pp. 215–218 (2005), <sup>[b]</sup> Reprinted from *ECS Transactions*, 41 (5), B-K. Kang, M-S. Kim, S-H. Lee, H-S. Sohn and J-G. Park, Effect of acoustic cavitation on dissolved gases and their characterization during megasonic cleaning, pp. 101–107, copyright (2011) with permission from ECS-The Electrochemical Society.

Increasing the megasonic power to 600 W significantly increased the number of pattern collapses for all gases.

Another study [66] reported investigations of particle removal from 200mm p-type (100) silicon substrate contaminated with  $\text{Si}_3\text{N}_4$  particles (0.1–10  $\mu\text{m}$ ) in DI water gasified with different gases ( $\text{H}_2$ ,  $\text{N}_2$ ,  $\text{O}_2$  and Ar). Pattern collapse studies were conducted on  $\text{SiO}_2$ /polysilicon/ $\text{SiO}_2$  gate stacks (60–120 nm) and photoresist lines (150–300 nm). The transducer frequency was 0.83 MHz and power was maintained at 70% of the peak value. Figure 6.20 (b) indicates that as the partial pressure of the dissolved gas ( $\text{H}_2$ ,  $\text{O}_2$ ,  $\text{N}_2$  and Ar) increases from a low level to 0.1 MPa, the PRE also increases. Highest PRE was observed for dissolved  $\text{H}_2$  gas at a partial pressure of 0.1 MPa, which was attributed to the greater diffusivity of  $\text{H}_2$ . On the other hand, although Ar has the highest solubility amongst these gases, it yields the lowest PRE owing to its cushioning effect.

Damage studies (Figure 6.21 (b)) revealed that dissolved  $\text{H}_2$  gas caused the maximum damage even at low levels, while, the opposite was observed with Ar dissolved DI water. Again, high damage in  $\text{H}_2$  dissolved DI water was attributed to the higher intensity of transient cavitation of  $\text{H}_2$  bubbles due to greater diffusivity of hydrogen.

Transducer variables such as power, frequency, duty cycle and pulse duration have been of great interest in determining efficient conditions for particle removal. Detailed cavitation studies have been conducted by Hauptmann and coworkers [71,72,73] to improve understanding of bubble behavior which affects particle removal. They noted that at  $\sim 1$  MHz, for a given duty cycle of 25%, by varying the pulse duration (PD) from 10 ms to 1 s, there is an optimal value of PD ( $\sim 300$  ms) for which a maximum in cleaning efficiency occurs [71]. It was suggested that for a fixed pulse duration and duty cycle, there exists a bubble size (probably largest) that generates a maximum particle removal force (upon collapse). The authors conducted cleaning studies using 300mm silicon wafers in  $\text{O}_2$  saturated ultrapure water (UPW). The transducer frequency, power density and duty cycle were maintained at 980 kHz, 0.5  $\text{W}/\text{cm}^2$  and 25%, respectively. It can be seen from Figure 6.22 that as the pulse duration increases, the PRE initially increases and reaches a maximum at about 250–300 ms and decreases with further increase in PD. The variability in PRE with respect to pulse duration was attributed to different size distributions in bubbles.

Shende *et al.* [74] performed a study on the effect of transducer frequency and type of chemistry on the acoustic energy and damage. Substrates used for the study were photomasks with aspect ratio of 1:1 to 1.8:1. Four different transducer frequencies (1, 2, 3 and 4 MHz) were employed. The chemistries used were  $\text{CO}_2$  containing DI water,  $\text{H}_2$  containing DI water,  $\text{NH}_4\text{OH}$ -DI

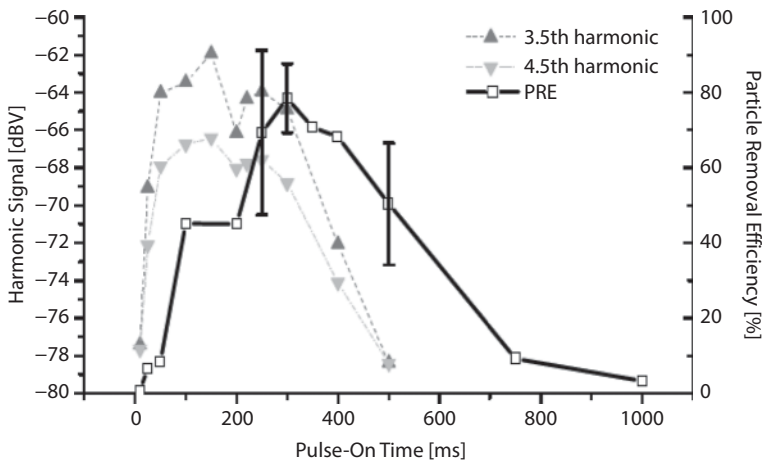


**Figure 6.22** Particle removal efficiency and sound (harmonic) signal as a function of pulse duration (PD), duty cycle = 25%, power density = 0.5 W/cm<sup>2</sup> and acoustic frequency = 980 kHz [71], Reprinted from *AIP Conference Proceedings*, 1433 (1), M. Hauptmann, H. Struyf, P. Mertens, M. Heyns, S. De Gendt, C. Glorieux and S. Brems, The importance of control over bubble size distribution in pulsed megasonic cleaning, pp. 299–303, copyright (2012) with permission from AIP Publishing LLC.

water and SC-1 solution. It can be seen, from Figure 6.23 (a), that for samples treated with CO<sub>2</sub> containing DI water, the acoustic energy increases with decreasing frequency. A similar trend was seen for other chemistries. This increase in cavitation with decreasing frequency could possibly mean that cavitation is more intense at lower frequencies. Figure 6.23 (b) indicates that at a particular transducer frequency of 3 MHz, the acoustic energies for NH<sub>4</sub>OH-DI water, SC-1-DI water and CO<sub>2</sub>-DI water were almost similar while that for H<sub>2</sub>-DI water was lower than the others.

Figure 6.23 (c) and (d) show that at transducer frequencies of 3 and 4 MHz, the damage counts are highest for a medium concentration of dissolved H<sub>2</sub>. This observation is in contrast to the results obtained from acoustic energy experiments. The acoustic energy plots show a moderate acoustic energy for medium dissolved concentration of H<sub>2</sub>. It is to be noted that the damage counts observed for other concentrations of H<sub>2</sub> were lower in the case of 4 MHz in comparison to that at 3 MHz. Also, in the study it was concluded that the sonoluminescence signal was higher at lower frequencies which was in agreement with the acoustic energy studies.

Considerable amount of research has been done on the effect of megasonic field in cleaning of EUV masks [75,76,77,78]. These studies have investigated the effects of various factors such as type and flow rate of cleaning

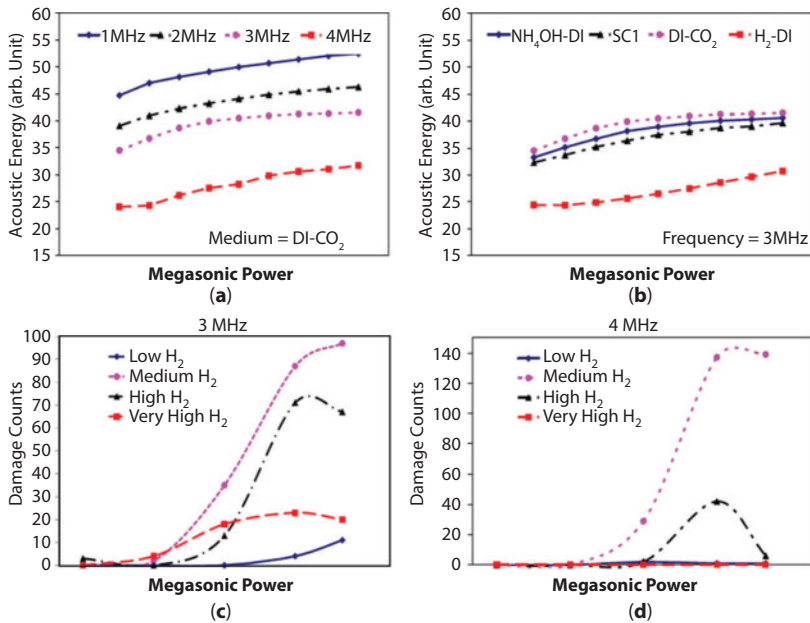


**Figure 6.23** Acoustic energy as function of applied megasonic power at (a) different transducer frequencies for substrates in DI- CO<sub>2</sub>, (b) different chemistries at constant transducer frequency of 3 MHz. Damage counts as a function of megasonic power for H<sub>2</sub>- DI water solutions with different concentrations of H<sub>2</sub> for transducer frequency of (c) 3 MHz and (d) 4 MHz [74], H. Shende, S. Singh, J. Baugh, R. Mann, U. Dietze and P. Dress, Megasonic cleaning: Possible solutions for 22nm node and beyond, Photomask Technology 2011, W. Maurer and F. E. Abboud, Editors, Proc. SPIE 8166, 816614 (2011), Copyright 2011 Society of Photo-Optical Instrumentation Engineers.

solution, concentration and nature of dissolved gases, acoustic frequency, proximity of transducer to cleaning surface, substrate rotation speed, and type of sound source (MegPie® and horn type) on particle removal and damage. Particle removal efficiencies have been reported to increase with substrate rotation speed (100–500 rpm) and decrease with increase in megasonic frequency (3 and 4 MHz) [78]. Interestingly, transducer geometry plays an important role in generation of defects (pits), which have been reported to be lower in number when MegPie® tool is used due to the uniformity in the sound field. As for dissolved gases, increasing the concentrations of dissolved gases such as O<sub>2</sub>, N<sub>2</sub> and CO<sub>2</sub>, has shown to increase the number of pits suggesting that there is an optimal concentration of gases that results in lower number of defects [77]. Single and multiple/batch wafer cleaning processes have also been pursued by researchers, primarily to determine a more efficient method for particle removal [79]. For a

fixed power density (0.35 or 0.7 W/cm<sup>2</sup>) and cleaning time (30, 60, 120 or 300 s), it has been observed that for Si<sub>3</sub>N<sub>4</sub> or SiO<sub>2</sub> particles (greater than 60 nm in size), single wafer cleaning processes provide higher PRE compared to batch/multiple wafer cleaning processes [79]. Overall, the studies have highlighted the importance of optimizing the sound field, and solution and tool variables in development of a megasonic cleaning process that can offer good cleaning performance with no damage.

## 6.6 Summary

A comprehensive understanding of the acoustic field effects such as streaming and cavitation is essential for identifying particle removal mechanisms that play an important role in megasonic cleaning. The successful development of a damage-free and effective megasonic cleaning process requires a careful optimization of various sound field and solution parameters including acoustic frequency, power density, pulse time and duty cycle, solution chemistry, and dissolved gases, which directly affect the cavitation and streaming phenomena. This book chapter covers in detail both fundamental and practical aspects of megasonic cleaning technology with the intention that the readers will be able to advance their knowledge in acoustic field and apply it for solving megasonic cleaning problems in industry.

## References

1. S. Awad, Particle removal with ultrasonics and megasonics, in: *Particles on Surfaces 7: Detection, Adhesion and Removal*, K. L. Mittal (Ed.), pp. 341–354, CRC Press, Boca Raton, FL (2002)
2. G. Moore, Progress in digital integrated electronics, Technical Digest, *International Electron Devices Meeting*, IEEE, pp. 11–13 (1975)
3. W. Kern, The evolution of silicon wafer cleaning technology, *J. Electrochem. Soc.*, 137, 1887–1892 (1990)
4. ITRS, The International Technology Roadmap for Semiconductors, <http://www.itrs.net/> (2012)
5. H. Abe, H. Iwamoto, T. Toshima, T. Iino, and G. Gale, Novel photoresist stripping using ozone/vaporized water mixture, *IEEE Trans., Semicond. Manuf.* 16, 401–408 (2003)
6. H. Tomita, M. Sato, S. Nadahara, and T. Saitoh, Photoresist stripping using novel sulfuric/ozone process, in: Proc. IEEE International Semiconductor Manufacturing Symposium, pp. 199–202 (2001)

7. S. Raghavan and M. Keswani, Thermal and chemical characteristics of SPM systems for resist stripping applications, in: Proc. SEMICON STS II, pp. 223–227(2008)
8. A. Ermakov, I. Larin, Y. Kozlov, and A. Purmal, The thermodynamic characteristics of hydrogen peroxide in  $H_2SO_4$ - $H_2O$  solutions, *Russian J. Phys. Chem.* 80, 1895–1901 (2006)
9. D. Sinha, Evaluation of etch behavior and importance of surface quality of doped silicon wafer in wet cleaning process, *ECS Trans.*, 6, 621–628 (2007)
10. P. N. Shankar and M. Kumar, Experimental determination of the kinematic viscosity of glycerol-water mixtures, *Proc. Royal Soc. London, Series A*, 444, 573–581 (1994)
11. A. Busnaina, H. Lin, and N. Moumen, Surface cleaning mechanisms and future cleaning requirements, in: Proc. IEEE/SEMI Advanced Semiconductor Manufacturing Conference, pp. 328–333 (2000)
12. W. Nyborg, Acoustic streaming, in: *Physical Acoustics*, Vol. 2, Part B, W. P. Mason (Ed.), Academic Press, New York (1965)
13. M. Faraday, On a peculiar class of acoustical figures; and on certain forms assumed by groups of particles upon vibrating elastic surfaces, *Philos. Trans. R. Soc. Lond.*, 121, 299–340 (1831)
14. L. Rayleigh, On the circulation of air observed in KUNDT'S tubes, and on some allied acoustical problems, *Philos. Trans. R. Soc. Lond.*, 175, 1–21 (1884)
15. L. Rayleigh, *Theory of Sound*, Dover Publications, New York (1945)
16. C. Lee and T. Wang, Outer acoustic streaming, *J. Acoust. Soc. Am.* 88, 2367–2375 (1990)
17. L. Rozenberg, *High Intensity Ultrasonic Fields*, Plenum Press, New York (1971)
18. G. Gale and A. Busnaina, Roles of cavitation and acoustic streaming in megasonic cleaning, *Particulate Sci. Technol.* 17, 229 – 238 (1999)
19. W. Nyborg, Acoustic streaming due to attenuated plane waves, *J. Acoust. Soc. Am.* 25, 68–75 (1953)
20. D. Zhang, Fundamental study of megasonic cleaning, Ph.D. Thesis, University of Minnesota (1993)
21. H. Schlichting and K. Gersten, *Boundary Layer Theory*, 8th Edition, Springer-Verlag (2001)
22. L. Kuznetsova and W. Coakley, Applications of ultrasound streaming and radiation force in biosensors, *Biosens. Bioelectron.* 22, 1567–1577 (2007)
23. M. Wiklund, R. Green, and M. Ohlin, Acoustofluidics 14: Applications of acoustic streaming in microfluidic devices, *Lab Chip*, 12, 2438–2451 (2012)
24. M.F. Hamilton, Y. A. Ilinskii, and E. A. Zabolotskaya, Acoustic streaming generated by standing waves in two-dimensional channels of arbitrary width, *J. Acoust. Soc. Am.*, 113, 153–160 (2003)
25. R. Apfel, Sonic effervescence: A tutorial on acoustic cavitation, *J. Acoust. Soc. Am.* 101, 1227–1237 (1997)
26. M. Volmer and A. Weber, Nuclei formation in supersaturated states, *Z. Phys. Chem.*, 119, 277–301 (1926)

27. W. Doring, Die überhitzungsgrenze und zerreifestigkeit von flussigkeiten, *Z. Phys. Chem.*, 36, 371–386 (1937)
28. F. R. Young, *Cavitation*, McGraw-Hill, London (1989)
29. W. Coakley and W. Nyborg, Cavitation, dynamics of gas bubbles; applications, in: *Ultrasound: Its Applications in Medicine and Biology*, F. Fry (Ed.), p. 109, Elsevier (1978)
30. J. Kolb and W.L. Nyborg, Small-scale acoustic streaming in liquids, *J. Acoust. Soc. Am.* 28, 1237–1242 (1956)
31. S. Elder, Cavitation microstreaming, *J. Acoust. Soc. Am.* 31, 54–64 (1959)
32. Y. Didenko, W. McNamara III, and K. Suslick, Hot spot conditions during cavitation in water, *J. Am. Chem. Soc.*, 121, 5817–5818 (1999)
33. M. Kohno, T. Mokudai, T. Ozawa, and Y. Niwano, Free radical formation from sonolysis of water in the presence of different gases, *J. Clin. Biochem. Nutr.*, 49, 96–101 (2011)
34. C. Ohl, T. Kurz, R. Geisler, O. Lindau, and W. Lauterborn, Bubble dynamics, shock waves and sonoluminescence, *Philos. Trans. R. Soc. London A* 357, 269–294 (1999)
35. A. Philip and W. Lauterborn, Cavitation erosion by single laser produced bubbles, *J. Fluid Mech.*, 361, 75–116 (1998)
36. H. Flynn, Physics of acoustic cavitation in liquid, in: *Physical Acoustics*, vol 1B, W. Mason (Ed.), p. 85, Academic Press, New York (1964)
37. V. Minsier and J. Proost, Shock wave emission upon spherical bubble collapse during cavitation induced megasonic surface cleaning, *Ultrason. Sonochem.*, 15, 598–604 (2007)
38. M. Plesset, Shock waves from cavitation collapse, *Phil. Trans. R. Soc. London*, 260, 241–244 (1966)
39. M. Kornfeld and L. Suvorov, On the destructive action of cavitation. *J. Appl. Phys.* 15, 495–506 (1944)
40. M. Plesset and R. Chapman, Collapse of an initially spherical vapor cavity in the neighbourhood of a solid boundary, *J. Fluid Mech.* 47, 283–290 (1971)
41. M. Keswani, S. Raghavan, and P. Deymier, Characterization of transient cavitation in gas sparged solutions exposed to megasonic field using cyclic voltammetry, *Microelectron. Eng.*, 102, 91–97 (2013)
42. M. Keswani, S. Raghavan, and P. Deymier, Effect of non-ionic surfactants on transient cavitation in a megasonic field, *Ultrason. Sonochem.*, 20, 603–609 (2013)
43. R. Gouk, D. Kittelson, T. Kuehn, and Y. Wu, Measurements and modeling of megasonic cleaning, in: *Particles on Surfaces 5&6: Detection, Adhesion and Removal*, K.L. Mittal (Ed.), pp. 191–201, CRC Press, Boca Raton, FL (1999)
44. M. Olim, A theoretical evaluation of megasonic cleaning for submicron particles, *J. Electrochem. Soc.*, 144, 3657–3659 (1997)
45. G. Ferrell and L. Crum, A novel cavitation probe design and some preliminary measurements of its application to megasonic cleaning, *J. Acoust. Soc. Am.*, 112, 1196–1201 (2002)



46. L. Kinsler and A. Frey, *Fundamentals of Acoustics*, 2nd edition, Wiley Publications (1962)
47. S. Shwartzman, A. Mayer, and W. Kern, Megasonic particle removal from solid state wafers, *RCA Review*, 46, 81–105 (1985)
48. P. Deymier, A. Khelif, D. Rouhani, J. Vasseur, and S. Raghavan, Theoretical calculation of the acoustic force on a patterned silicon wafer during megasonic cleaning, *J. Appl. Phys.*, 88, 2423–2429 (2000)
49. W. Kim, T-H. Kim, J. Choi, and H-Y. Kim, Mechanism of particle removal by megasonic waves, *Appl. Phys. Letters*, 94, 081908, 1–3 (2010)
50. D. McQueen, Frequency dependence of ultrasonic cleaning, *Ultrasonics*, 24, 273–280 (1986)
51. D. McQueen, Ultrasonically enhanced chemical dissociation from solid surfaces with application to cleaning electronic circuit boards, *Ultrasonics*, 28, 422–427 (1990)
52. P. Deymier, J. Vasseur, A. Khelif, D. Rouhani, L. Dobrzynski, and S. Raghavan, Streaming and removal forces due to the second-order sound field during megasonic cleaning of silicon wafers, *J. Appl. Phys.*, 88, 6821–6835 (2000)
53. F. Zhang, A. Busnaina, and G. Ahmadi, Particle adhesion and removal in chemical mechanical polishing (CMP) and post-CMP cleaning, *J. Electrochem. Soc.*, 146, 2665–2669 (1999)
54. G. W. Gale, B.K. Kirkpatrick, and F. W. Kern Jr., Surface preparation, in: *Handbook of Semiconductor Manufacturing Technology*, R. Doering and Y. Nishi (Eds.), pp. 2–30, CRC Press, Boca Raton, FL (2007)
55. F. Zhang, A. Busnaina, M. Fury, and S. Wang, The removal of deformed submicron particles from silicon wafers by spin rinse and megasonics, *J. Electronic Mater.*, 29, 199–204 (2000)
56. H. Hatano and S. Kanai, High-frequency ultrasonic cleaning tank utilizing oblique incidence, *IEEE Trans. Ultrasonics, Ferroelectrics and Frequency Control*, 43, 531–535 (1996)
57. K. Bakhtari, R. Guldiken, P. Makaram, A. Busnaina, and J. Park, Experimental and numerical investigation of nanoparticle removal using acoustic streaming and the effect of time, *J. Electrochem. Soc.*, 153, G846-G850 (2006)
58. A. Busnaina and G. Gale, Ultrasonic and megasonic particle removal, in: *Proceedings of Precision Cleaning Conference*, pp. 347–360 (1995)
59. M. Keswani, S. Raghavan, P. Deymier, and S. Verhaverbeke, Megasonic cleaning of wafers in electrolyte solutions: Possible role of electro-acoustic and cavitation effects, *Microelectron. Eng.*, 86, 132–139 (2009)
60. K. Wostyn, V. Quenette, G. Vereecke, and P. Mertens, The removal of silica particles from micron wide trenches by megasonic cleaning, *Solid State Phenomena*, 134, 221–224 (2008)
61. O. Guldiken, K. Bakhtari, A. Busnaina, and J. Park, Metrology and removal of nanoparticles from 500 micron deep trenches, *Solid State Phenomena*, 103–104, 137–140 (2005)

62. P. Karimi, T. Kim, J. Aceros, J. Park, and A. Busnaina, The removal of nanoparticles from sub-micron trenches using megasonics, *Microelectron. Eng.*, 87, 1665–1668 (2010)
63. V. Kapila, P. A. Deymier, H. Shende, V. Pandit, S. Raghavan, and F. O. Eschbach, Megasonic cleaning, cavitation and substrate damage: An atomistic approach, *Proc. SPIE*, 6283, 628324/1–12 (2006)
64. K. Muralidharan, M. Keswani, H. Shende, P. Deymier, S. Raghavan, F. Eschbach, and A. Sengupta, Experimental and simulation investigations of acoustic cavitation in megasonic cleaning, *Proc. SPIE*, , 6517, 65171E-1/12 (2007)
65. S. Kumari, M. Keswani, S. Singh, M. Beck, E. Liebscher, L. Toan, and S. Raghavan, Effect of dissolved CO<sub>2</sub> in deionized water in reducing wafer damage during megasonic cleaning in MegPie, *ECS Trans.*, 41, 93–99 (2011)
66. B. Kang, M. Kim, S. Lee, H. Sohn, and J. Park, Effect of acoustic cavitation on dissolved gases and their characterization during megasonic cleaning, *ECS Trans.*, 41, 101–107 (2011)
67. S. Lee, B. Kang, M. Kim, J. Lim, J. Jeong, and J. Park, Optimization of DIO<sub>3</sub> with megasonic cleaning of Ru capped EUVL mask for effective carbon contaminant removal, *ECS Trans.*, 41, 131–138 (2011)
68. S. Kumari, M. Keswani, S. Singh, M. Beck, E. Liebscher, and S. Raghavan, Enhanced megasonic processing of wafers in MegPie® using carbonated ammonium hydroxide solutions, *Microelectron. Eng.*, 114, 148–153 (2014)
69. Z. Han, M. Keswani, and S. Raghavan, Megasonic cleaning of blanket and patterned samples in carbonated ammonia solutions for enhanced particle removal and reduced feature damage, *IEEE Trans. Semicond. Manuf.*, 26, 400–405 (2013)
70. Y. Hagimoto, K. Asada, and H. Iwamoto, The effective damage-free megasonic cleaning using N<sub>2</sub> dissolved APM, in: *Proc. IEEE International Symposium on Semiconductor Manufacturing*, 215–218 (2005)
71. M. Hauptmann, H. Struyf, P. Mertens, M. Heyns, S. De Gendt, C. Glorieux, and S. Brems, The importance of control over bubble size distribution in pulsed megasonic cleaning, *AIP Conf. Proc.*, 1433, 299–303 (2012)
72. S. Brems, M. Hauptmann, E. Camerotto, A. Pacco, H. Struyf, P. Mertens, C. Gottschalk, and S. De Gendt, The influence of dissolved carbon dioxide on cavitation intensity in ultrasound cleaning systems, *Japanese J. Appl. Phys.*, 52 066602, 1–7 (2013)
73. M. Hauptmann, H. Struyf, S. De Gendt, C. Glorieux, and S. Brems, Evaluation and interpretation of bubble size distributions in pulsed megasonic fields, *J. Appl. Phys.*, 113, 184902, 1–16 (2013)
74. H. Shende, S. Singh, J. Baugh, R. Mann, U. Dietze, and P. Dress, Megasonic cleaning: Possible solutions for 22nm node and beyond, *Proc. SPIE*, 8166, 816614, 1–10 (2011)
75. M. House, A. Rastegar, D. Dussault, and E. Liebscher, Improving megasonic exposure uniformity for EUV mask substrate cleaning, *ECS Trans.*, 41, 123–139 (2011)

76. A. Rastegar, A. House, and A. J. Kadaksham, Cleaning challenges of EUV mask substrates, blanks and patterned masks, *ECS Trans.*, 41, 139–146 (2011)
77. H. Kurtuldu, A. Rastegar, and M. House, Study of the durability of the Ru-capped MoSi multilayer surface under megasonic cleaning, *Proc. SPIE*, 8522, 85221Q, 1–8 (2012)
78. J. Yoon, H-S. Lee, H. Kim, H. Oh, J. Choi, P. Chung, I. Shin, and C. Jeon, New paradigm for effective particle removal cleaning of EUV mask, *Proc. SPIE*, 8441, 84410X, 1–9 (2012)
79. K. Suzuki, Y. Imazeki, K. Han, S. Okano, J. Soejima, and Y. Koike, Application of novel ultrasonic cleaning equipment that uses the waveguide mode for the single-wafer cleaning process, *Japanese J. Appl. Phys.*, 50, 05EC10, 1–5 (2011)



# High Speed Air Jet Removal of Particles from Solid Surfaces

Kuniaki Gotoh

*Department of Chemistry and Biotechnology,  
Okayama University, Okayama, Japan*

---

## Abstract

The method for removal of solid particulate contaminants using high speed impinging air jet is discussed with particular attention to the effects of operating conditions on the removal efficiency. The operating conditions described here are air pressure in the jet nozzle, distance between nozzle tip and the surface on which particles are adhered, jet impinging angle, humidity of removal environment, and scan speed of the nozzle. The effect of the surface material is also described.

It was shown that the effects of the air pressure and the distance could be evaluated from the dynamic pressure of air jet which can be estimated from analytical equations. It was also shown that the removal efficiency was significantly affected by the humidity in the environment of particle removal and reached a peak at a certain humidity (=optimum humidity). The optimum humidity depended on the surface material. In addition, two methods for enhancing the removal efficiency, pulsed jet method and vibrating jet method, are presented.

**Keywords:** Air jet, impinging air jet, resuspension, dynamic pressure, impinging angle, humidity, surface material, pulsed jet, vibrating jet, particle removal

## 7.1 Introduction

Surface cleaning using high speed air jet can be applied for the removal of solid particulate contaminants adhered on a solid surface. The procedure is simple. Air jet generated by a nozzle is applied to the surface on which particulate contaminants are adhered, and the air blows off the particulate contaminants. However, the mechanism of removal of particles is not well understood.

---

*E-mail:* [gotoh@okayama-u.ac.jp](mailto:gotoh@okayama-u.ac.jp)

---

K.L. Mittal and Ravi Jaiswal (eds.) Particle Adhesion and Removal, (281–312)  
2015 © Scrivener Publishing LLC

The phenomenon causing the removal by an air jet is called resuspension. The resuspension phenomenon has been studied as one of the phenomena relating to a particle-laden pipe flow in a chemical process. Many experimental and theoretical studies have been reported (these are well summarized by Ziskind *et al.* [1] and Gradon [2]). It is expected easily that the adhesion force between the particle and the solid surface and the force induced by the fluid such as lift force [3,4,5] are related to resuspension. One of the simplest models assumes that particles are resuspended when the force induced by the flow exceeds the adhesion force [6]. According to this model, a particle having smaller adhesion force than the force induced by the flow should be resuspended at once. However, it is well known that the number of resuspended particles gradually increases with time, even if the flow is steady state [7,8,9]. Thus, another model assuming that the flow fluctuation dictates the magnitude of the force induced by the flow is proposed. As the cause for fluctuation, bursting motion of fluid particles in the vicinity of the surface [10,11] or the velocity fluctuation caused by the turbulence [12,13,14,15] is assumed. However, the bursting motion or the flow fluctuation in the turbulence has not been understood well. Thus, intensity of the bursting motion or of the flow fluctuation cannot be predicted. Accordingly, the model of the resuspension phenomenon has not been established yet.

As the resuspension phenomenon, which is a fundamental phenomenon in air jet removal, has not fully understood yet, the removal efficiency by this method cannot be estimated theoretically. Therefore, the empirical knowledge on the air jet removal is important for the estimation of the removal efficiency. On the other hand, air jet is well investigated and analyzed theoretically [16]. As shown in this chapter, some results of removal experiments can be correlated by the characteristics of air jet predicted by theoretical equations of air jet. Therefore, in this chapter, fundamental characteristics of the air jet are summarized first. Following this, the results and discussions from several studies are summarized. Many of the results shown in this chapter had been included in a previous paper [17]. In the current chapter, these results have been supplemented with newly obtained data with particular attention to the effects of operating conditions on the removal efficiency. In addition, new methods to enhance air jet removal efficiency are introduced.

## 7.2 Fundamental Characteristics of the Air Jet

Before showing the removal efficiency, the characteristics of the air jet are summarized in this section. In a two-dimensional air jet shown in

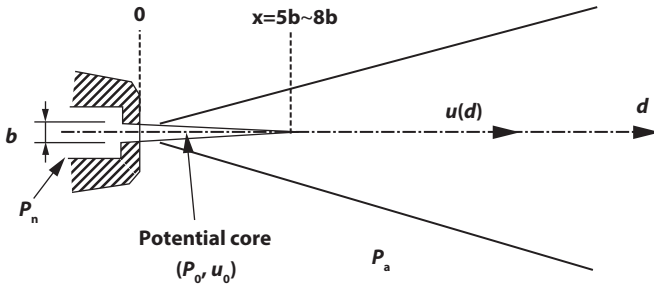


Figure 7.1 Schematic diagram of air jet.

Figure 7.1, there is the region in which the air velocity  $u_0$  and static pressure  $P_0$  are constant. This region is called the potential core. The length of the potential core is within  $d = 5b \sim 8b$  ( $b =$  nozzle gap) from the nozzle tip [16]. The air velocity,  $u_0$  can be estimated from thermodynamic equations as discussed below.

Here, we assume that the flow in the nozzle is a nonadiabatic nonisothermal flow. The relation between gas pressure,  $p$  and gas volume,  $v$  in the nonadiabatic nonisothermal flow can be approximated by

$$p v^n = \text{const.} \tag{7.1}$$

The flow or process expressed by the above equation is called polytropic process and the index,  $n$  is called polytropic index [18]. When polytropic index,  $n$  is unity, the process is an isothermal process. When  $n$  is equal to heat capacity ratio,  $\kappa$  ( $=C_p/C_v$ ,  $C_p =$  specific heat capacity at constant pressure,  $C_v =$  specific heat capacity at constant volume), the process is an adiabatic process.

When the flow in the nozzle is a polytropic process, the air velocity at the nozzle tip  $u_0$  is given by the following equation [19,20].

$$u_0 = \sqrt{\frac{2g\kappa}{\kappa-1} \frac{P_0}{\rho_0} \left\{ 1 - \left( \frac{P_n}{P_0} \right)^{(n-1)/n} \right\}} \tag{7.2}$$

Here,  $P_n$  is the air pressure in a nozzle,  $P_0$  is the air pressure at the nozzle tip, and  $\rho_0$  is mass density of air at the nozzle tip.  $g$  is the gravitational acceleration ( $=9.81 \text{ m/s}^2$ ) and  $n$  is polytropic index. The heat capacity ratio,  $\kappa$  of air is 1.4 [19]. The polytropic index,  $n$  can be estimated from the definition of the velocity coefficient,  $\phi$  representing nozzle characteristics.

$$\phi = \sqrt{\left\{ 1 - \left( \frac{P_n}{P_0} \right)^{(n-1)/n} \right\} \left\{ 1 - \left( \frac{P_n}{P_0} \right)^{(\kappa-1)/\kappa} \right\}^{-1}} \tag{7.3}$$

It is known that the coefficient,  $\phi$  for the nozzle having a well finished wall is in the range of 0.95~0.975 [20].

When the nozzle pressure,  $P_n$  reaches a critical pressure,  $P_{nc}$  calculated by the following equation, the air attains the maximum velocity [19].

$$\frac{P_{nc}}{P_a} = \left( \frac{2}{n+1} \right)^{-n/(n-1)} \tag{7.4}$$

When the nozzle pressure exceeds the critical pressure,  $P_{nc}$ , the air pressure,  $P_0$  at the nozzle tip is larger than the ambient air pressure,  $P_a$ , i.e.,

$$P_0 = P_n \left( \frac{2}{n+1} \right)^{n/(n-1)} \tag{7.5}$$

The high-pressure air spouted from the nozzle tip expands in the potential core region. As the momentum is conserved during the expansion, the air velocity  $u_0$  after the expansion can be expressed as follows [19,20].

$$u_0 = \sqrt{\frac{P_0}{P_a} u_0'^2 + \frac{(P_0' - P_a)}{\rho_a}} \tag{7.6}$$

$u_0'$ : air velocity at the critical pressure ( $P_n = P_{nc}$ )

$\rho_a$ : mass density of air at atmospheric pressure

On the other hand, it is known that the air velocity in a fully developed region of a free jet is proportional to  $d^{1/2}$  [16]. Assuming that the imaginary origin of the jet is on the nozzle tip, the air velocity  $u(d)$  at distance  $d$  can be expressed by

$$u(d) = \sqrt{\frac{K_u}{d}} u_0 \tag{7.7}$$

$K_u$ : proportionality constant

Figure 7.2 shows a slit-type air jet nozzle [21,22]. The nozzle has a nozzle gap  $b = 0.25\text{mm}$ . Therefore, it is estimated that the length of the potential



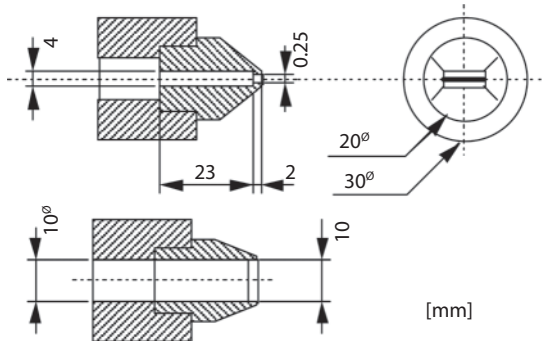


Figure 7.2 Slit-type air jet nozzle. Cross-sectional side-view (figure on left-side on top), top-view (figure on left-side on bottom) and the view from nozzle tip (right side). Unit of length is [mm].

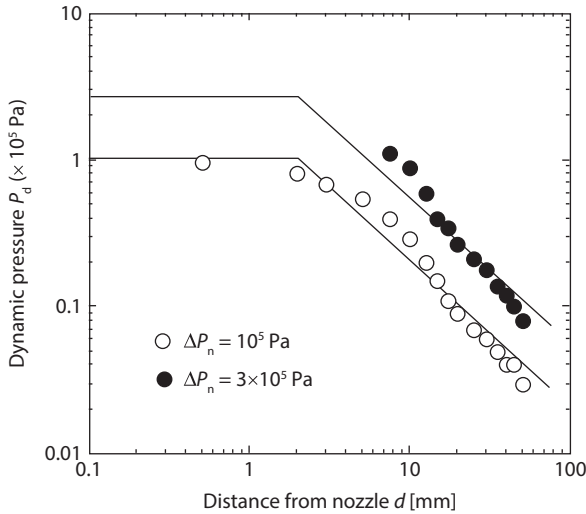


Figure 7.3 Dynamic pressure  $P_d$  as a function of distance from nozzle  $d$ . White and black symbols designate experimental data obtained by nozzle pressures  $\Delta P_n = 10^5$  and  $3 \times 10^5$ , respectively. Solid lines are calculated values from eqs.(7.2)–(7.7).

core is  $d = 2.0\text{mm} (=8b)$ . At this point, the air velocity  $u(d)$  is equal to  $u_0$ . Thus, the constant,  $K_u$  is determined as  $2.0 \times 10^{-3}$ . By substituting  $K_u$  into eq.(7.7), the air velocity under various operating conditions can be estimated. Figure 7.3 shows a comparison between the estimated dynamic pressure,  $P_d (= \rho_a u(d)^2 / 2)$  and the measured data [22]. In the calculation, the velocity coefficient,  $\phi$  was assumed to be 0.975. The lines almost fit the

data. This means that the velocity distribution of the air jet used in this study can be estimated by the equations for the polytropic process and the free jet. It should be noted that the constant,  $\phi$  represents nozzle characteristics. This means that different values should be adopted for different shapes of the nozzle.

### 7.3 Fundamentals of Air Jet Particle Removal

#### 7.3.1 Definition of Parameters and Removal Efficiency [21, 22]

Figure 7.4 shows a typical apparatus for particle removal using the high speed air jet. The air fed by a compressor usually contains water mist, which is separated before passing through a pressure regulator and to the jet nozzle. When the air jet nozzle shown in Figure 7.2 is used, the flow through the conduit in the nozzle is suddenly reduced near the nozzle outlet and the pressure drop caused by the flow contraction is the highest in the air jet system. The pressure drop at the nozzle tip  $\Delta P_n (=P_n - P_a, P_n$ : air pressure in the nozzle,  $P_a$ : ambient air pressure), therefore, is almost the same as that set by using the pressure regulator. The pressure drop  $\Delta P_n$  is one of the main operating conditions.

Figure 7.5 shows the configuration of the nozzle and the surface on which the particles are deposited. The geometric parameters for the removal are the impinging angle  $\theta$  between the nozzle centerline and the surface, and the distance  $d$  between the nozzle tip and the point O on the surface where the nozzle centerline crosses the surface. In the following sections, the effect of these parameters on the removal efficiency is described.

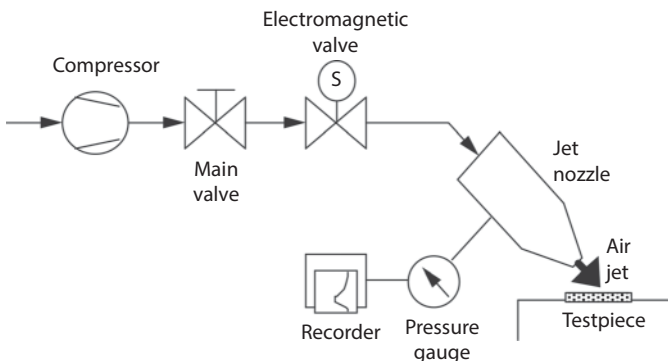


**Figure 7.4** Typical apparatus setup for particle removal using high speed air jet.

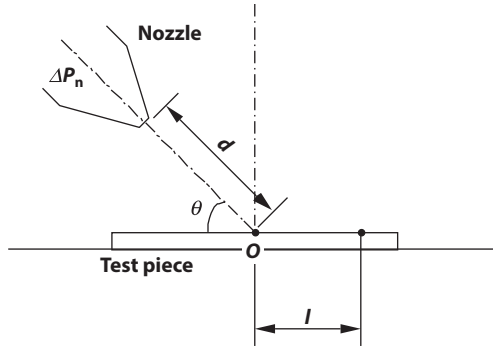


Figure 7.5 Geometric parameters for the nozzle and the surface (testpiece).

The data shown in this chapter were obtained from the experiments using mono-dispersed standard latex particles (styrene / divinylbenzene) as test particles and borosilicate glass as a standard surface. The test particles were once dispersed into static air and then deposited by gravitational sedimentation. After the deposition, testpiece was dried for 100hr in a desiccator. In all experiments, the testpiece was transferred to a controlled environment, and the removal experiment was conducted after leaving the testpiece in the environment for 2 min or longer. The reason for this experimental procedure setting is explained in section 7.3.5.

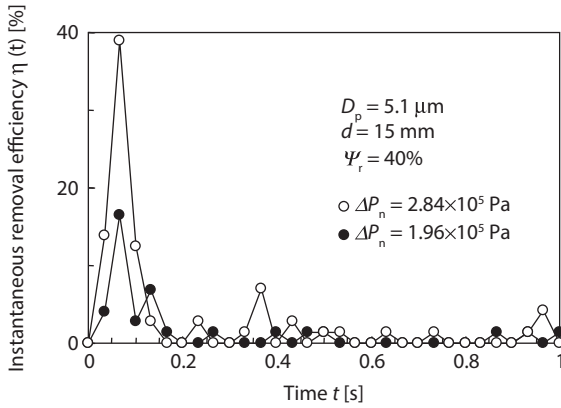
As described above, it is well known that the resuspension flux changes with time [7,8,9]. The removal efficiency obtained by the air jet also changes with time as shown in Figure 7.6. In the Figure, the authors defined two removal efficiencies, i.e., instantaneous removal efficiency  $\eta(t)$  and integrated removal efficiency  $\Sigma\eta(t)$  as follows.

$$\eta(t) = \left( \sigma_p(t + \Delta t) - \sigma_p(t) \right) / \sigma_{p0} \tag{7.8}$$

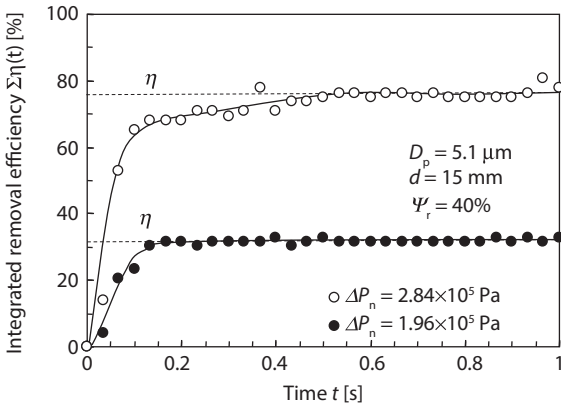
$$\Sigma\eta(t) = \left( \sigma_p(t) - \sigma_{p0} \right) / \sigma_{p0} \tag{7.9}$$

Here,  $\sigma_p(t)$  is the number density of deposited particles on the surface at time  $t$ ,  $\sigma_{p0}$  is the initial number density.

In some cases, the final removal efficiency was reached within 150ms after the jet start. In other cases, after a quick initial change (first step removal), the integrated removal efficiency further increased with jet exposure time and finally reached saturation after typical times of 1 second. The removal efficiencies during steps 1 and 2 depend on the air jet condition. The mechanism of removal in each step is under investigation. Therefore,



(a) Instantaneous removal efficiency



(b) Integrated removal efficiency

**Figure 7.6** Removal efficiency as a function of time  $t$ .  $\Delta P_n$  is pressure drop at nozzle tip,  $D_p$  is particle diameter tested,  $d$  is the nozzle distance and  $\Psi_r$  is humidity at removal. Saturated removal efficiency expressed by dotted line is defined as removal efficiency  $\eta$ .

in this chapter the focus will be on the saturated removal efficiency. The saturated removal efficiency is simply defined as the removal efficiency  $\eta$ .

### 7.3.2 Effect of Pressure Drop $\Delta P_n$ and Distance $d$ on Removal Efficiency $\eta$ [22]

Figure 7.7 shows the removal efficiency  $\eta$  of various particles as a function of the pressure drop  $\Delta P_n$  at the nozzle tip. The removal efficiency increases with the pressure drop. When the distance  $d$  is longer, higher pressure is required to achieve the same removal efficiency. In order to evaluate the

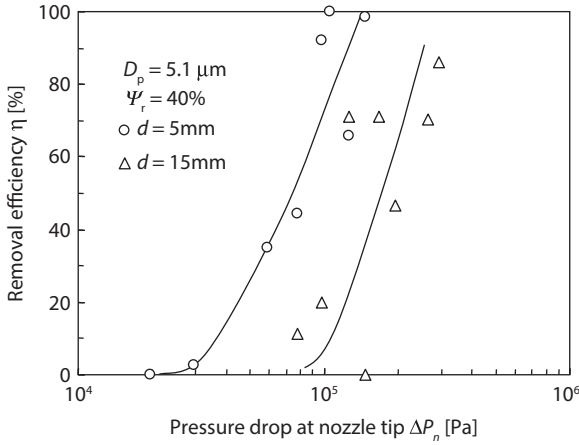


**Figure 7.7** Removal efficiency as a function of pressure drop  $\Delta P_n$ .  $D_p$  is particle diameter tested,  $d$  is the nozzle distance and  $\psi_r$  is humidity at removal.

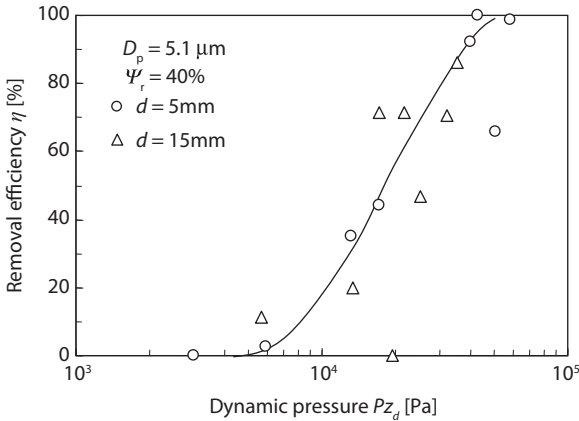


**Figure 7.8** Removal efficiency as a function of dynamic pressure  $P_d$ .  $D_p$  is particle diameter tested,  $d$  is nozzle distance and  $\psi_r$  is humidity at removal.

difference caused by the distance, the dynamic pressure at distance  $d$  was used as a representative value of the energy of the air jet. Figure 7.8 shows the removal efficiency as a function of the dynamic pressure  $P_d$ . Here, the air velocity at distance  $d$  was estimated by eq. (7.7). The removal efficiency is well correlated with the dynamic pressure and is independent of the distance and pressure drop. Using this Figure, removal efficiency for other distances can be estimated.

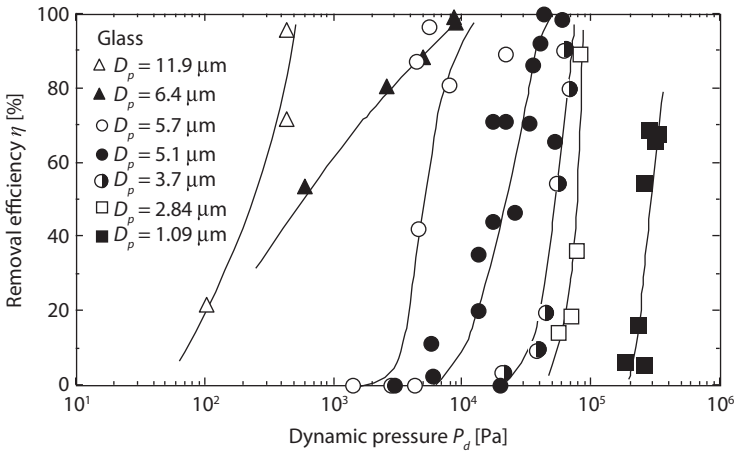


**Figure 7.9** Removal efficiency curve for each particle size,  $D_p$  obtained from Glass substrate.

Figure 7.9 shows the performance curve for various particles obtained by the nozzle shown in Figure 7.2. It is obvious that smaller particle requires higher dynamic pressure. The curve for a particle with  $D_p = 6.4\mu\text{m}$  shows a slower increase in removal efficiency than other particles, which may be because particles with  $D_p = 6.4\mu\text{m}$  have a relatively wide size distribution than the other particles. This fact implies that the performance curve depends both on the nozzle and on the particle size distribution.

### 7.3.3 Effect of Impinging Angle $\theta$ [21, 23]

Figure 7.10-a shows the removal efficiency for an impinging angle ( $\theta$ ) of  $45^\circ$  as a function of the distance  $l$  from the impinging point  $O$ . The other parameters are the nozzle pressure  $\Delta P_n = 10^5\text{Pa}$ , the distance  $d = 10\text{ mm}$ , and the duration of the jet  $t = 10\text{ seconds}$ . The data denoted by run No. 1, 2, and 3 showed wide scatter. However, near the impinging point  $O$  ( $l = 0$ ), removal efficiency  $\eta$  is high and repeatability of the experiment is good. The efficiency  $\eta$  upstream of the point  $O$  ( $-10\text{mm} < l < 0$ ) decreases sharply, and the particle detachment by the jet is unstable for the region  $l < -15\text{mm}$ . In the downstream location, the efficiency  $\eta$  is higher than that found in the upstream location. However, the region showing high removal efficiency is restricted only to a small part around the jet impinging point ( $l < 3\text{mm}$ ). Particle removal by the jet again shows wide variability for the region  $l > 3\text{mm}$ . For larger impinging angle, the trend of the data was similar to that obtained here for  $\theta = 45^\circ$ .

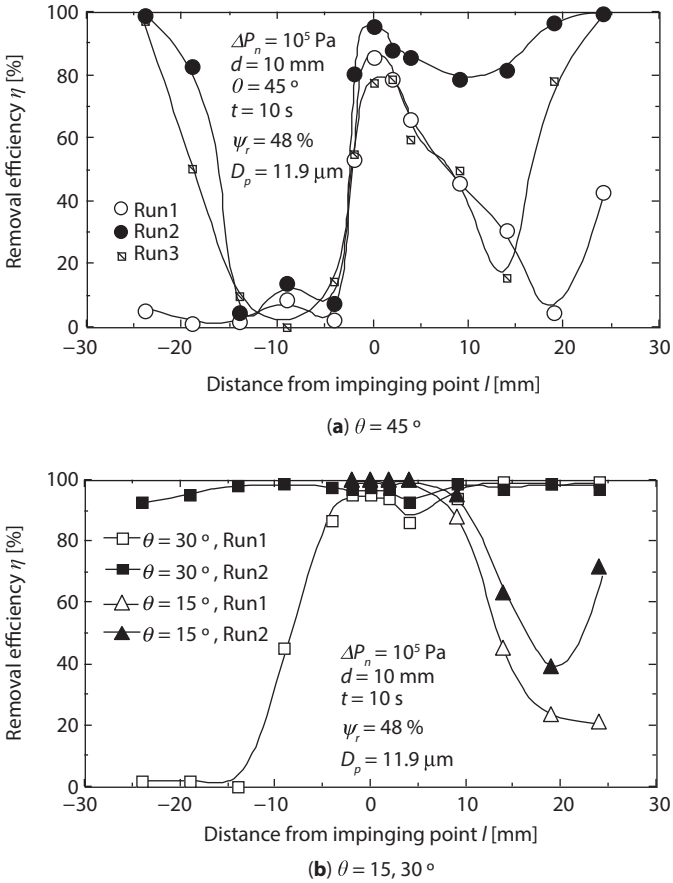


**Figure 7.10** Effect of impinging angle  $\theta$  on removal efficiency. All experiments shown here were carried out under the conditions of pressure drop  $\Delta P_n = 10^5$  Pa, nozzle distance  $d = 10$  mm, jet duration time  $t = 5$  s, humidity at removal  $\psi_r = 48\%$  and particle size  $D_p = 11.9 \mu\text{m}$ .

Figure 7.10-b shows the removal efficiency  $\eta$  obtained by setting the impinging angle  $\theta = 30$  and  $15^\circ$ . The high efficiency region around the jet impinging point is wider than that for  $\theta = 45^\circ$  shown in Fig.7.10-a. Furthermore, the data for  $\theta = 30^\circ$  show a relatively low-efficiency region between  $5\text{mm} < l < 10\text{mm}$ . The high-efficiency region of  $l < 5\text{mm}$  can be attributed to the direct jet impingement as in the case of  $\theta = 45^\circ$ . The reason for the high removal efficiency found in the region of  $l > 10\text{mm}$  will be discussed later. As for the high-efficiency region around the jet impinging point, the region for  $\theta = 15^\circ$  covers up to about  $l = 10\text{mm}$  and is wider than that for  $\theta = 30^\circ$ .

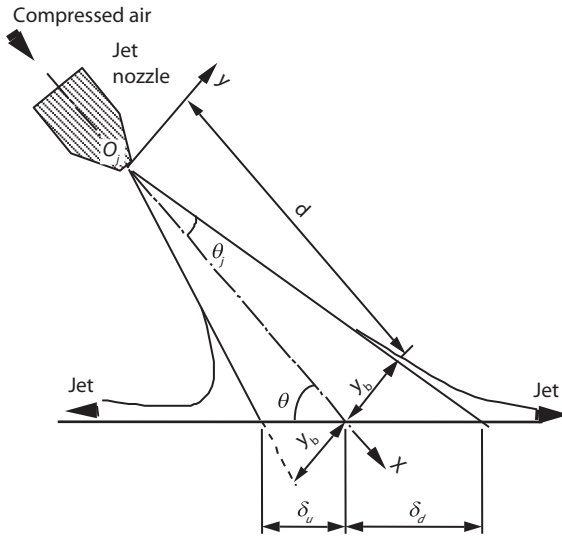


Figure 7.11 Schematic diagram of impinging air jet.

Now, we will discuss the jet characteristics in order to identify the reason for data variability and to define the rule for determining the high-efficiency region. Figure 7.11 schematically shows the jet impinging on a flat wall, where  $x, y$  coordinates are set as shown in the figure and the jet origin is represented by  $\theta_j$ . As discussed in Section 7.2, the impinging point  $d = 10\text{mm}$  is in the fully developed region of the jet. The effective jet width  $y$  is obtained by Tollmien's equation [16];

$$\phi_j = \frac{y}{K_j x} = 2.4 \tag{7.10}$$

The above equation gives the outer boundary of the two-dimensional jet where the  $x$ -component of the flow velocity becomes zero. The empirical constant  $K_j$  has a value between 0.09 and 0.12 [16]. Here we will assume  $K_j = 0.1$  as the average. Then the effective jet width  $y$  is represented by

$$y = 0.24 x \tag{7.11}$$

If we assume that the tip of the nozzle along the centerline is the origin of the jet, the impinging point is given by  $x = d$  and the effective jet width  $y_b$  is given by

$$y_b = 0.24 d \tag{7.12}$$



In Figure 7.10,  $d = 10\text{mm}$  and, therefore,  $y_b$  is 2.4mm. The angle of spreading of the jet  $\theta_j$  is determined to be  $13.5^\circ$  since  $\tan\theta_j$  is 0.24(= 2.4mm/10mm). The jet expanding width on the flat surface is calculated by the following equations for the upstream and the downstream locations, respectively:

$$\delta_u = d \sin \theta \left\{ \tan \left( \frac{\pi}{2} - \theta \right) - \tan \left( \frac{\pi}{2} - \theta - \theta_j \right) \right\} \quad (7.13)$$

$$\delta_d = d \sin \theta \left\{ \tan \left( \frac{\pi}{2} - \theta + \theta_j \right) - \tan \left( \frac{\pi}{2} - \theta \right) \right\} \quad (7.14)$$

The jet expanding widths calculated by Eqs.(13) and (14) are given below:

$$\text{for } \theta = 45^\circ; \delta_u = 2.73 \text{ mm}, \delta_d = 4.47 \text{ mm}$$

$$\text{for } \theta = 30^\circ; \delta_u = 3.39 \text{ mm}, \delta_d = 8.22 \text{ mm}$$

$$\text{for } \theta = 15^\circ; \delta_u = 4.89 \text{ mm}, \delta_d = 89.2 \text{ mm}$$

The high-efficiency region in Figure 7.10 satisfies the relation  $\delta_u < \delta < \delta_d$ . Outside this region, the removal efficiency decreases or becomes unstable. The instability may be caused by the turning over and/or separation of the jet from the flat surface. The high efficiency for  $\theta = 30^\circ$  and  $l > 10\text{mm}$  is exceptional, because the flow did not separate from the surface in this case. In this sense, it can be stated that  $\theta = 30^\circ$  is the optimum jet angle for detaching small particles from a flat surface without flow separation.

Figure 7.12 shows the removal efficiency around the impinging point as a function of dynamic pressure  $P_d$  for two different particle sizes. When the impinging angle  $\theta$  is more than  $30^\circ$ , the  $\theta$  does not affect the efficiency for both particle sizes. However, lower impinging angle  $\theta$  requires higher dynamic pressure to obtain the same efficiency. In the removal process, not only the removal area discussed above, but also the high efficiency is important. When the angle is higher than  $45^\circ$ , the removal area decreases with increasing the angle, although the efficiency is not affected by the angle. When the angle is smaller than  $45^\circ$ , the efficiency decreases with decreasing the angle, although the removal area increases. Because of both these effects,  $45^\circ$  is the optimum for obtaining a wide removal area with high removal efficiency. However, Ziskind *et al.* [24] reported that the removal efficiency decreases with the angle over  $45^\circ$  and it shows a peak at angle  $30^\circ$ . The effect of the angle seems to depend on the nozzle shape.

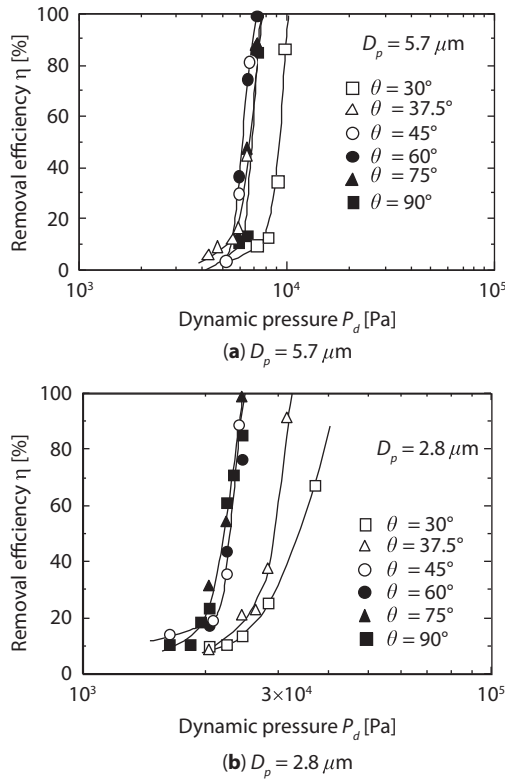


**Figure 7.12** Effect of impinging angle,  $\theta$ , on removal efficiency for particle size,  $D_p$ ,  $5.7\mu\text{m}$  (top) and  $2.8\mu\text{m}$  (bottom).

### 7.3.4 Effect of Scan Speed of Air Jet

The fundamental investigations described in previous sections were carried out by means of fixed nozzle and fixed target. However, the jet nozzle or the removal target is scanned in the industrial application of the air jet removal. Therefore, we aimed to elucidate how the scan speed of the target flat plate affects the removal efficiency [25].

As shown in Figure 7.13, removal efficiency under constant air pressure decreased with increase of the scan speed  $v_s$  of the target plate. Here, the direction of the target scanning has no effect. With increasing the scan speed, the residence time  $t'$  in the effective jet length in which the adhered particles can be removed is decreased. The effective length can be estimated by equation for the stable removal range for a fixed target as  $d_u + d_d$  by equations (13), (14). Thus, the scan speed  $v_s$  was converted to the residence time  $t'$ .

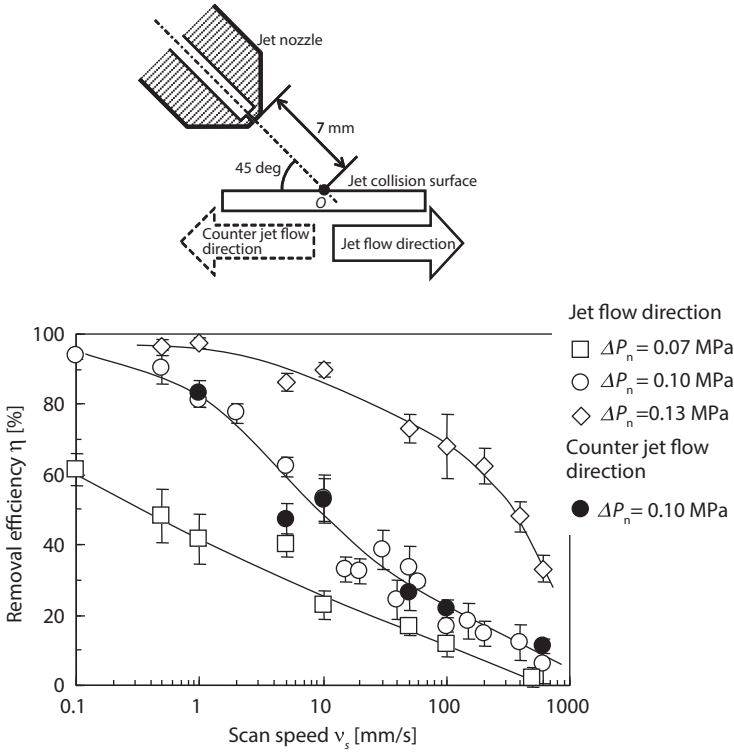


**Figure 7.13** Effect of scan speed on removal efficiency. Top figure shows geometric parameters and scan direction of the surface. Parameter in bottom figure is pressure drop,  $\Delta P_n$ .

$$t' = (\delta_u + \delta_d) / v_s \tag{7.15}$$

The trend of the converted removal efficiencies was almost the same as the cumulative removal efficiency  $\eta(t)$  from a fixed target as shown in Figure 7.14. This implies that the decrease of the removal efficiency with increase of the scan speed was mainly caused by the decrease of the residence time in the impinging air jet.

### 7.3.5 Other Parameters Affecting the Removal Efficiency [23,26]

When we consider the industrial process required for the removal of particulate contaminants, the process can be divided into three stages, namely, contamination, transfer from the contaminated zone to the removal apparatus, and removal of the contaminants. This means that there are three environments in the industrial process. Thus, we have investigated the effects of the humidity at the deposition of particles and the time to transfer

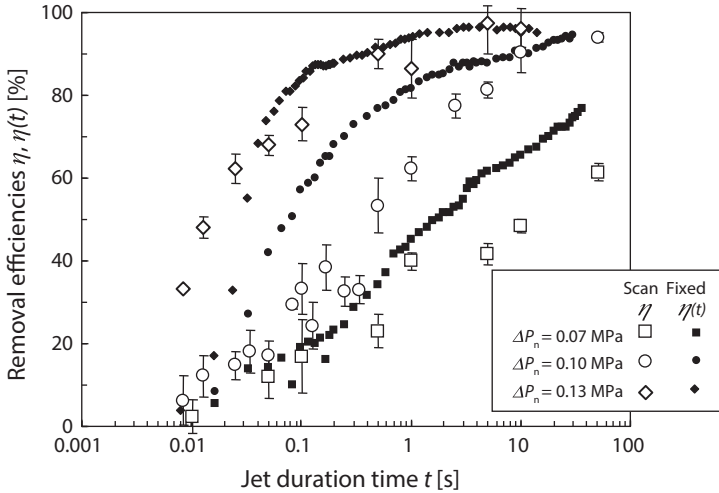


**Figure 7.14** Comparison of removal efficiencies obtained by scan jet  $\eta$  and fixed jet  $\eta(t)$  under the conditions of pressure drop  $\Delta P_n = 0.07, 0.10$  and  $0.13$  MPa.

particles [23]. Here, the humidity of the transfer environment was kept constant and very low (=15%) using a desiccator. In addition, the transfer time was taken as the drying time  $t_d$  in desiccator.

Figure 7.15 shows the results of the removal experiment by varying the drying time in the desiccator and taking the humidity  $\Psi_d$  at deposition of particles as a variable parameter. The humidity  $\Psi_r$  at removal was constant at 59%. As it can be found in Figure 7.15 that (1) the removal efficiency decreased as the drying time increased for the case when the deposition took place at a humidity no higher than the humidity  $\Psi_r$  at removal; (2) the removal efficiency increased at the beginning, and decreased after the maximum efficiency was achieved at a certain drying time for the case when the deposition took place at a humidity no lower than that at removal; and (3) the removal efficiency was not affected by the humidity  $\Psi_d$  at deposition after 80 hr of drying. As a result, it is supposed that the removal efficiency is higher immediately after deposition of particles for the case when the particle is deposited at a relatively low humidity, and after drying them to a certain level, for the case when the particles are deposited at a high humidity.

In order to avoid this effect, longer than 80hr of drying time was needed. This is the reason why the testpiece was dried for 100hr. It was also confirmed by other experiments that the removal efficiency is not affected by the residence time in the removal environment if the time is longer than 1 min.

Figure 7.16 shows the result of removal experiment conducted by varying the humidity  $\Psi_r$  in the removal environment. The surfaces  $\Psi$  used in these

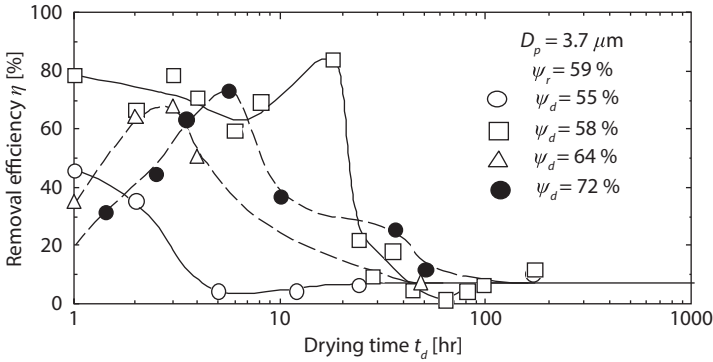


**Figure 7.15** Effect of humidity at deposition,  $\psi_d$ , and drying time,  $t_d$ , on removal efficiency for particle size,  $D_p$ ,  $3.7\mu\text{m}$  and humidity at removal,  $\psi_r$ , 59%.

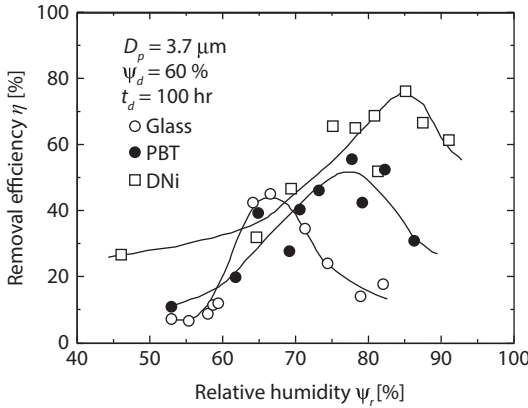


**Figure 7.16** Removal efficiency as a function of relative humidity,  $\psi_r$ , in the removal environment for particle size,  $D_p$ ,  $3.7\mu\text{m}$ , humidity at deposition,  $\psi_d$ , 60% and drying time,  $t_d$ , 100 hr. Tested substrates are Glass, Poly(butylene terephthalate) (PBT) and Double nickel coated iron (DNi).

experiments are borosilicate glass, poly(butylene terephthalate) (PBT) and double nickel coated iron (DNi). For all surfaces, the removal efficiency is low at a low humidity, and rapidly increases as the humidity is increased. When the humidity  $\psi_r$  during removal is 67% for glass plate, the maximum efficiency is achieved, and it decreases for higher humidity. From the Figure, it is clear that the removal efficiency can be increased by adjusting the humidity  $\psi_r$  in the removal environment. Here, the humidity that achieves the maximum removal efficiency is defined as the optimum humidity  $\psi_{opt}$ .

Since the conditions of jet impingement are unchanged, the particle removing force provided by the air jet is considered to be constant.

Therefore, it is assumed that the removal efficiency depends on the humidity because water molecules on a particle and surface may have an effect on the adhesion force between the particle and the solid surface. When the humidity is low and the effect of the water molecules is absent, the van der Waals force is the dominant adhesion force. The force can be approximated by the value in vacuum, and represents an adhesion force higher than that in the presence of water molecules. It is well known that the liquid bridging force increases with the humidity, when a liquid bridge is formed between a particle and a surface at high humidity. Thus, it is considered that the removal efficiency reduced mainly with increase in the van der Waals force at a low humidity, whereas it is reduced with the increase of liquid bridge force at high humidity. The maximum removal efficiency is attained at a humidity at which the liquid bridge is not formed.

As shown in Figure 7.16, the optimum humidity  $\Psi_{opt}$  and the maximum efficiency depend on the surface material. The optimum humidity  $\Psi_{opt}$  for various surface materials listed in Table 7.1 is shown in Figure 7.17.

**Table 7.1** Substrates tested for particle removal [26]

	Height of asperities		Peak count	
	Average	Standard deviation	Average	Standard deviation
	$R_a$ [ $\mu\text{m}$ ]	$\sigma_r$ [ $\mu\text{m}$ ]	$P_c$ [ $\mu\text{m}^{-1}$ ]	$\sigma_p$ [ $\mu\text{m}^{-1}$ ]
<b>Metals</b>				
Double nickel coated iron (DNi)	0.513	0.19	0.44	0.12
Nickel coated iron (Ni)	0.46	0.23	0.23	0.083
Zinc coated iron (Zn)	0.062	0.015	1.13	0.35
<b>Plastics</b>				
Polycarbonate (PC)	0	0	0	0
Poly(butylene terephthalate) (PBT)	0.1	0.024	0.67	0.19
Thermotropic liquid crystal polymer (TLCP)	0.086	0.026	0.63	0.19
Polyphenylene sulfide (PPS)	0.067	0.021	0.73	0.24
<b>Glass</b>				
Borosilicate glass (Glass)	0	0	0	0

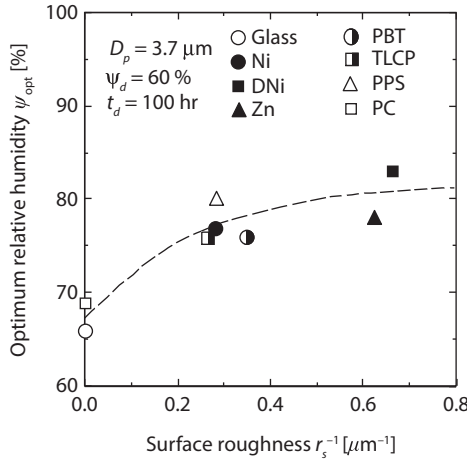


**Figure 7.17** Optimum relative humidity,  $\psi_{opt}$ , for highest removal efficiency obtained from various substrates listed in Table 7.1 as a function of inverse of surface roughness,  $r_s^{-1}$  for particle size,  $D_p$ ,  $3.7 \mu\text{m}$ , humidity at deposition,  $\psi_d$ , 60% and drying time,  $t_d$ , 100 hr.

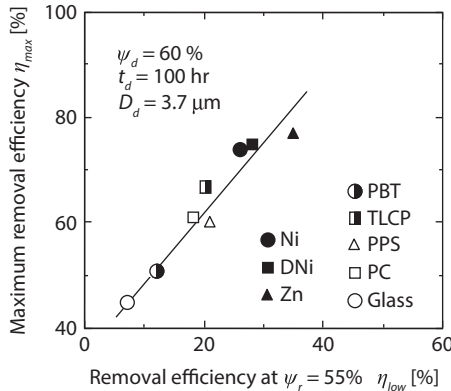


**Figure 7.18** Correlation between maximum removal efficiency,  $\eta_{max}$ , and removal efficiency,  $\eta_{low}$ , obtained at the humidity in the removal environment,  $\psi_r$ , 55% for particle size,  $D_p$ ,  $3.7 \mu\text{m}$ , humidity at deposition,  $\psi_d$ , 60% and drying time,  $t_d$ , 100 hr.

Some materials used in the experiments have micrometer size asperities. The average height  $R_a$  and peak count  $P_c$  in unit length of the asperities are listed in the table. If the asperity is assumed to be a part of a sphere, the radius of the sphere is calculated by means of the average height  $R_a$  and the peak count  $P_c$ . The surface roughness  $r_s$  is represented by the radius. The optimum humidity  $\Psi_{opt}$  is well correlated to the surface roughness  $r_s$ .

On the other hand, as shown in Figure 7.18, the maximum removal efficiency has a strong correlation with the removal efficiency at  $\Psi_r=55\%$

at which the liquid bridge does not exist. This implies that the adhesion force at the optimum humidity is dominated by the van der Waals force. Thus, the difference in the maximum removal efficiencies between surface materials must be attributed to the surface properties such as Hamaker's constant, surface roughness and stiffness of the surface material. Phares *et al.* [27] studied the effect of surface material properties and particle size on removal, and carried out the theoretical analysis in which the surface properties were taken into consideration.

## 7.4 New Methods Using Air Jet

### 7.4.1 Pulsed-jet Method

One of the methods enhancing the efficiency of air jet removal is a pulsed air jet method. The conditions reported in the literature are summarized in Table 7.2. Masuda *et al.* [21] reported that the pulsed air jet did not significantly enhance particle removal. In contrast, Otani *et al.* [28] found that the removal efficiency increased with increase in the number of pulsed jets.

**Table 7.2** Experimental conditions for pulsed jet particle removal from the literature

	Masuda <i>et al.</i> [21]	Otani <i>et al.</i> [28]	Ziskind <i>et al.</i> [24]
Nozzle exit shape	Rectangular	Rectangular	Circular
Surface material	Glass	Glass, Silicon	Glass, Silicon
Particle material	Styrene/ divinylbenzene	Polystyrene latex	Alumina silicate
Particle diameter [ $\mu\text{m}$ ]	1.09–11.9	0.25–1.1	2.0–5.0
Distance from nozzle [mm]	3.0–25.0	6	30
Impinging angle [deg]	15–45	30	20–50
Duration of pulse [s]	1	1	0.0078–0.0047
Pulse interval [s]	1	3	0.0078–0.0047
Frequency [Hz]	0.5	0.25	64–107



Ziskind *et al.* [24] also found that there is a marked enhancement in the removal efficiency at a certain frequency, below and above this frequency the removal efficiency is lower. The differences in the results may be attributed to the differences in the nozzle shape and the geometric parameters for the nozzle and surface.

Figure 7.19 shows comparison of removal efficiencies obtained by a pulsed jet and a normal jet generated by two types of jet nozzles [29]. In case of Nozzle B and a particle with  $D_p = 4.7 \mu\text{m}$ , there is no difference in the

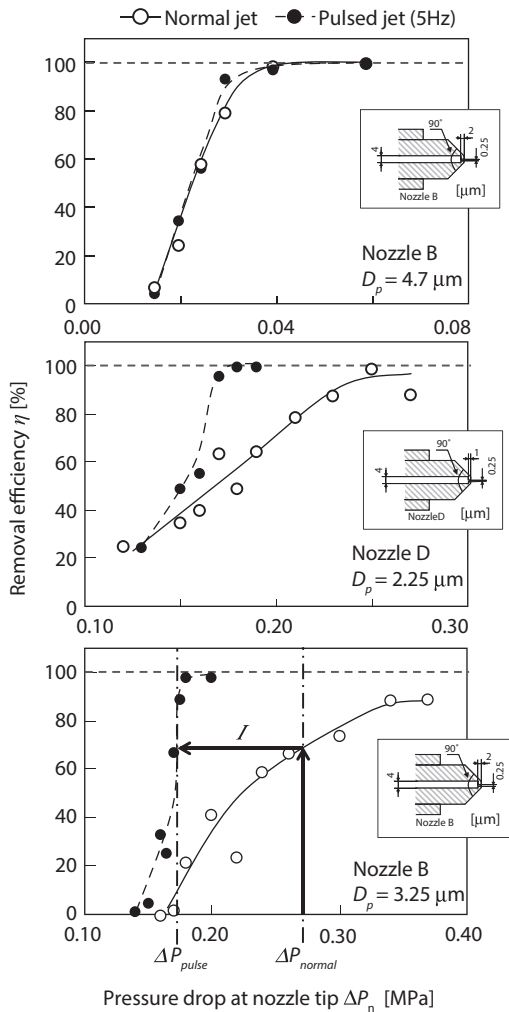


**Figure 7.19** Comparison of removal efficiencies obtained by pulsed jet and normal jet for particle size,  $D_p$ , 4.7  $\mu\text{m}$  (top), 2.25  $\mu\text{m}$  (middle), and 3.25  $\mu\text{m}$  (bottom).

removal efficiencies obtained by the pulsed jet and the normal jet. While, when they were applied to a particle with  $D_p=3.25\mu\text{m}$  the removal efficiency obtained by the pulsed jet is higher than that obtained by the normal jet. In case of Nozzle D and a particle with  $D_p=2.25\mu\text{m}$ , the pulsed jet enhanced the removal efficiency.

Here, we defined the index  $I$  of removal efficiency improvement by pulsed jet as the difference in the nozzle pressures giving the same removal efficiencies. The index  $I$  is shown in Figure 7.20 as a function of the nozzle pressure in normal jet  $\Delta P_{\text{normal}}$ . The index  $I$  increased from a certain nozzle pressure. The pressure at which the index  $I$  starts to increase is independent of the nozzle shape and tested particle diameter. The pressure is almost the same as the critical pressure  $P_{nc}$  (see Eq.(7.4)) in which the air jet speed at the nozzle tip reaches the sonic speed. In other words, the improvement in removal efficiency by pulsed air appears only when the nozzle pressure is more than the critical pressure  $P_{nc}$ .

When the nozzle pressure is set above the critical pressure, the improvement is the maximum at a certain pulse frequency (=optimum frequency) as shown in Figure 7.21. Measurement of the dynamic pressure at the surface of flat plate revealed that the air pressure never falls to zero when the pulse frequency is high, as shown in Figure 7.22. Here, we defined an index

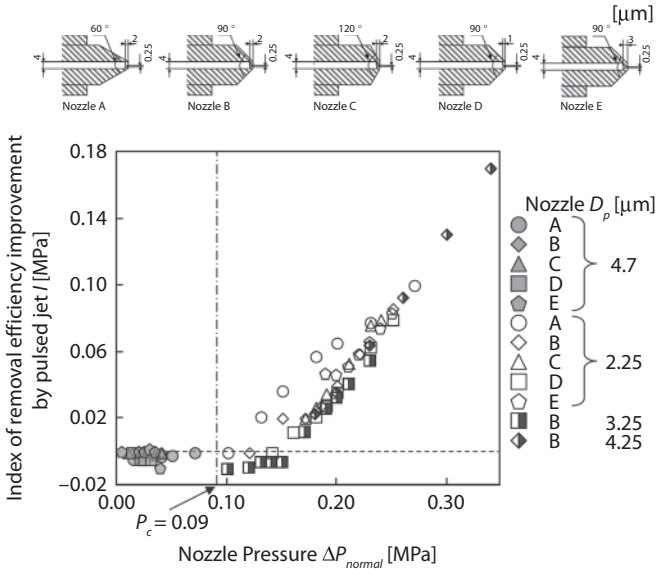


**Figure 7.20** Index  $I$  of removal efficiency improvement by pulsed jet as a function of nozzle pressure for normal jet obtained from particle sizes,  $D_p$ , 2.25, 3.25 and 4.7  $\mu\text{m}$ .

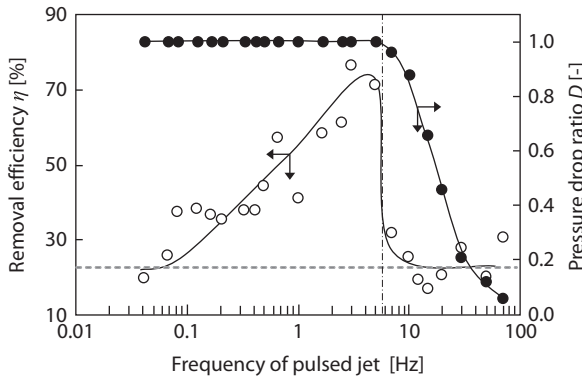


**Figure 7.21** Pressure drop ratio,  $D$ , and removal efficiency as a function of frequency of pulsed jet.

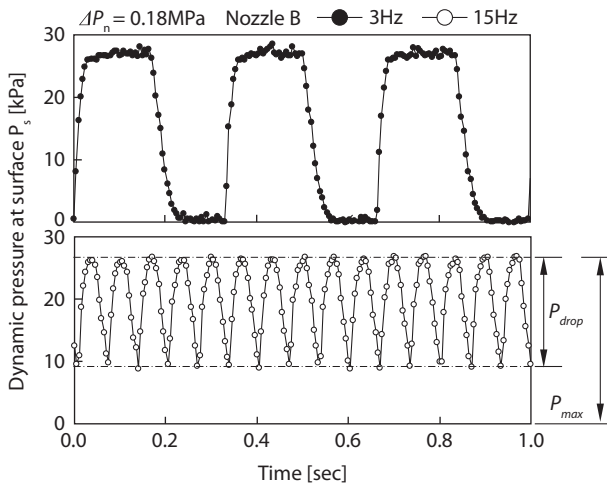


**Figure 7.22** Dynamic pressure at surface,  $P_s$ , as a function of time. Nozzle used is Nozzle B shown in Fig. 7.19 with nozzle pressure 0.19 MPa. Top and bottom figures are the results of the frequency of pulsed jet 3 and 15Hz, respectively.

$D$  representing the air pressure change at the flat plate as a ratio of the pressure drop  $P_{drop}$  between the maximum and the minimum pressures to the maximum pressure  $P_{max}$ . The pressure drop ratio  $D$  decreases drastically in the higher frequency range than at the optimum frequency. This implies that the pulse effect appears when each air jet acts independently at the surface where particles are adhered.

Ziskind *et al.* [24] explained that the repeated air jet brings the flow field near the surface to its initial state, and the velocity inside the boundary

layer becomes high once again. Therefore, the force acting on the particles is at its maximum value every time for each pulsed jet. This implies that the average force for the jet duration time increases with frequency, while the impulse of the jet decreases with increase of frequency. Thus, the optimum frequency is achieved. This explanation is on the assumption that the pulses are independent. If the pulse is affected by the flow induced by the former pulse, the pulsed air jet may have almost the same effect as the continuous normal jet.

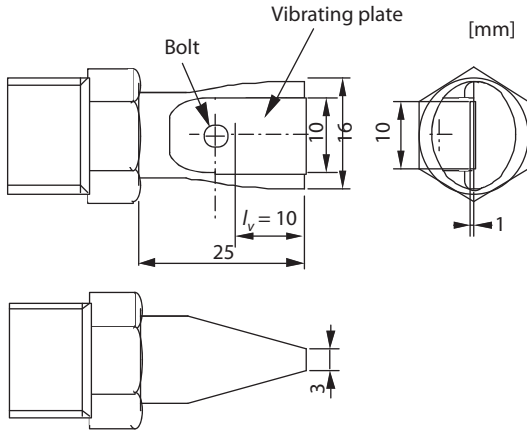
One of the other methods using consecutive air jets is the removal by impinging shock waves studied by Smedley *et al.* [30]. The shock waves are generated in an open-ended shock tube, thus producing ultrasonic velocity pulses with large time intervals. These focus on the removal length in the direction aligned with the long axis of the removal area where it is circular (=normal impingement) or elliptic shape (=inclined impingement). The length increases with the number of shock waves.. This fact means the number of jets enhances the removal.

Watano and coworkers [31, 32] proposed a new removal method based on pulsed air jet. They built a corona discharge neutralizer into the jet nozzle. It was shown that the removal efficiencies of 10–30 $\mu\text{m}$  particles of cornstarch and talc adhered on a gelatin film were enhanced by the corona discharge. The results imply that elimination of an electrostatic force is effective for enhancement of removal efficiency.

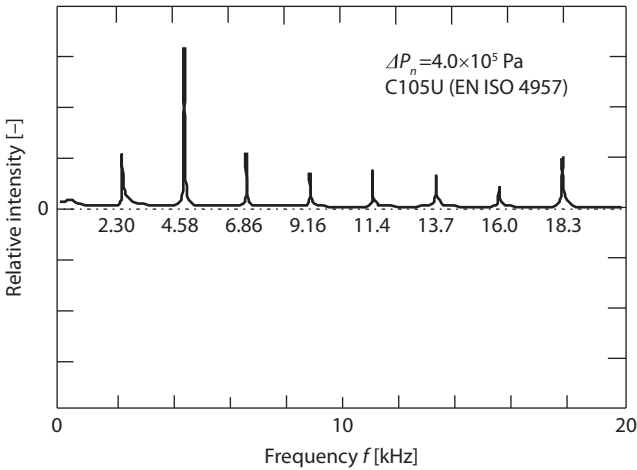
#### 7.4.2 Vibrating Air Jet Method [33]

Figure 7.23 shows the newly designed vibrating type air jet nozzle. It has a vibrating metal plate at the tip. Compressed air introduced into the nozzle causes vibration of the metal plate and generates a vibrating air jet. The width of the nozzle tip is 10mm and the effective vibrating length  $l_v$  of the plate is 10mm. The plate is fixed with a bolt, and the plate can be replaced with a different plate. In this experiment, carbon tool steel C105U (EN ISO4958) or quenched C105U was used as the vibrating plate. The thickness of plate is 0.2mm for both materials.

The vibration of the air jet has an audible frequency. As shown in Figure 7.24, the vibration generated by the nozzle consists of a fundamental frequency (i.e., the lowest frequency) and the harmonics. Here, we have defined the frequency having the highest intensity as the representative frequency  $f$  of the vibration. The frequency  $f$  changes with the compressed air pressure  $\Delta P_n$ . When the pressure  $\Delta P_n$  is below  $2.0 \times 10^5 \text{Pa}$ , no clear vibration but a Gaussian noise is obtained. When  $\Delta P_n$  is over  $4.0 \times 10^5 \text{Pa}$ , the air jet has no vibration. Therefore, for the vibrating nozzle, the applied nozzle



**Figure 7.23** Vibrating air jet nozzle. Top-view (figure on left-side on top), side-view (figure on left-side of bottom) and the view from nozzle tip (right side). Unit of length is [mm].



**Figure 7.24** Spectrum of vibrating air jet obtained by vibrating plate of C105U (EN ISO 4957) with nozzle pressure,  $\Delta P_n$ ,  $4 \times 10^5$  Pa.

pressure was  $2.0\text{--}4.0 \times 10^5$  Pa. The frequency values for minimum and maximum nozzle pressures are listed in Table 7.3.

Figure 7.25 shows experimental results of the vibration air jet removal for particles with  $D_p = 1.09 \mu\text{m}$  at various nozzle pressures. Although it was almost impossible for the standard nozzle to remove these particles under any nozzle pressure tested with  $d = 10$  mm, a removal efficiency of 76% was achieved by the vibrating air jet under the same operating conditions. The

**Table 7.3** Vibration frequencies of air jet obtained by vibrating air jet nozzle with nozzle pressure  $\Delta P_n$ . Vibrating plate materials used are C105U (EN ISO 4957) and C105U with quenching [33]

$\Delta P_n$ [Pa]	$2.3 \times 10^5$	$4.0 \times 10^5$
C105U [kHz]	2.48	4.58
C105U with quenching [kHz]	2.53	4.78

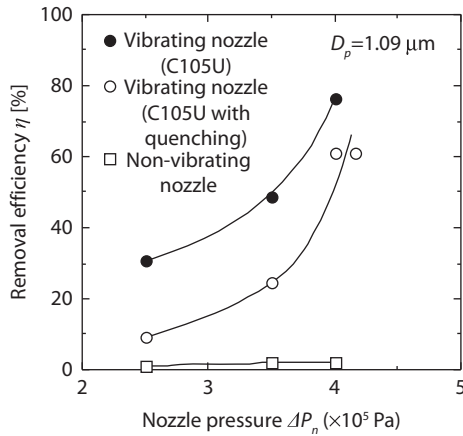


**Figure 7.25** Comparison of removal efficiencies between vibrating and non-vibrating nozzles for particle size,  $D_p$ , 1.09  $\mu\text{m}$ . Vibrating plate materials used are C105U (EN ISO 4957) and C105U with quenching.

results show that the vibrating air jet is more effective than the standard air jet. However, the effects of frequency  $f$  and nozzle pressure  $\Delta P_n$  on the efficiency are very complex [34]. The optimum vibration of air jet has not been established yet.

When we compare the results of a vibrating jet to a pulsed jet it is found that the frequency of vibrating jet is higher than the optimum frequency of the pulsed jet. In case of the pulsed jet, the pulsed air jet has almost the same effect as continuous normal jet when the frequency of the pulse exceeds the optimum frequency. Therefore, the high frequency vibration may have different enhancement mechanism of removal from the pulsed jet.

In case of the pulsed jet, renewal of the flow field near the surface was pointed out as the cause for the enhancement of removal efficiency [24]. In other words, un-steady state of air flow at the start of each air jet is key factor for the enhancement. On the other hand, the vibrating jet is not a jet consisting of independent jets, i.e., it is a kind of continuous jet with strong

fluctuation compared to a normal jet. Therefore, it can be expected that flow fluctuation control must be a key factor for achieving a high removal efficiency. The flow fluctuation can be controlled not only by the special nozzle shown in Figure 7.23 but also by the sound generated by an acoustic speaker. Maynard and Marshall [35] developed a novel jet nozzle which generates a vortex flow. Fuhrmann *et al.* [36] set four acoustic speakers on the nozzle in order to add the vibration of an air jet. When 1.90, 3.16 or 4.43 kHz acoustic vibrations were added to the air jet, an enhanced removal area was observed. The results show the possibility of flow fluctuation control for enhancement of removal efficiency by acoustic vibration which is one of the easiest ways to control the frequency of the vibration.

## 7.5 Summary and Prospect

In this chapter, we have summarized the empirical knowledge on particle removal using a high speed air jet. The removal efficiency obtained by an air jet can be correlated with the dynamic pressure which can be estimated from analytical equations and is independent of the distance and pressure drop. The high efficiency region around the jet impinging point can be estimated by assuming a free jet. The effect of scan speed of the nozzle can be converted to jet duration time by means of the estimated width of the high efficiency region and the scan speed. These calculated values from analytical equations are time-averaged characteristics of the jet. From these facts, it can be said that the effect of the operating conditions of an air jet on the removal efficiency can be estimated by time-averaged jet characteristics of the air jet. It should be noted, however, that these correlations were obtained when the same nozzle was used.

A pulsed air jet enhances removal of particles when the nozzle pressure exceeds the critical pressure. As one of the causes of the enhancement, renewal of the flow field near the surface was pointed out [24]. In addition, the expansion of high-pressure air spouted from the nozzle tip may affect the enhancement of removal efficiency because the enhancement appears only when the nozzle pressure exceeds the critical pressure. One of the possible causes of the enhancement of removal efficiency must be a strong fluctuation generated by intermittent expansions of the air. As expected from the model of resuspension phenomenon described in Section 7.1, the flow fluctuation may dictate the magnitude of the resuspension force induced by the flow.

One of the methods for adding a flow fluctuation to an air jet is the use of vibrating type air jet nozzle. As shown in Section 7.4.2, a high frequency

vibrating air jet is effective for the enhancement of removal efficiency and 76% removal of  $1.09\mu\text{m}$  particles on a glass plate was achieved. Fuhrmann *et al.* [36] also showed that an acoustic vibration generated by acoustic speakers can enhance removal efficiency. From these facts, it can be expected that flow fluctuation control must be a key parameter for achieving a high removal efficiency.

On the other hand, when particle size become small, the resistance force from the fluid flow also becomes small. This implies that a minimum limit of removable particle size by air flow must exist. It is expected, however, that a high speed air jet with strong fluctuation can be employed for precise removal of solid particles of sub-micrometer size if the flow fluctuation is controlled properly by optimizing the nozzle shape or by adding equipment generating the fluctuation because the removal results for sub-micrometer particles by a pulsed jet had been already reported and particles with  $D_p=1\mu\text{m}$  can be removed by vibrating air jet with high efficiency.

## List of Symbols

$b$	nozzle gap	[m]
$C_p$	specific heat capacity at constant pressure	[J/kg·K]
$C_v$	specific heat capacity at constant volume	[J/kg·K]
$D_p$	particle diameter	[m]
$d$	distance between nozzle tip and surface	[m]
$f$	frequency of vibrating air jet	[Hz]
$g$	gravitational acceleration (=9.81)	[m/s <sup>2</sup> ]
$K_u$	proportionality constant in eq.(7.7)	[m]
$K_j$	constant in eq.(7.10)	[m]
$l$	distance from jet impinging point	[m]
$l_v$	effective length of vibrating plate	[m]
$n$	polytropic index	[-]
$p$	gas pressure	[Pa]
$P_0$	static pressure in potential core of air jet	[Pa]
$P_0'$	air pressure at the nozzle tip when the nozzle pressure exceeds $P_{nc}$	[Pa]
$P_a$	pressure of ambient air	[Pa]
$P_d$	dynamic pressure of air jet	[Pa]
$P_c$	peak count of asperities on surface	[m <sup>-1</sup> ]
$P_n$	air pressure in nozzle	[Pa]
$P_{nc}$	critical pressure in nozzle	[Pa]
$P_s$	dynamic pressure at surface	[Pa]



$R_a$	average height of asperities on surface	[m]
$r_s^{-1}$	surface roughness (=inverse of the radius of curvature of asperities)	[m <sup>-1</sup> ]
$t$	jet duration time	[s]
$t_d$	drying time	[s]
$u_0$	air velocity in the potential core of air jet	[m/s]
$u(d)$	air velocity at the distance, $d$	[m/s]
$v$	volume of gas	[m <sup>3</sup> ]
$v_s$	scan speed of jet nozzle	[m/s]
$W$	width of nozzle	[m]
$y_b$	effective jet width	[m]
$\Delta P_n$	pressure drop at nozzle tip	[Pa]
$\delta_u$	jet expansion width (=virtual impinging width of jet on surface) for upstream	[m]
$\delta_d$	jet expansion width for downstream	[m]
$\eta$	removal efficiency	[-]
$\eta_{\max}$	maximum removal efficiency	[-]
$\eta(t)$	instantaneous removal efficiency	[-]
$\kappa$	heat capacity ratio	[-]
$\rho_a$	mass density of air at atmospheric air pressure	[kg/m <sup>3</sup> ]
$\theta$	jet impinging angle	[deg]
$\theta_j$	angle of spreading of air jet	[deg]
$\Sigma \eta(t)$	integral removal efficiency	[-]
$\sigma_p$	standard deviation of peak count $P_c$	[m <sup>-1</sup> ]
$\sigma_{p0}$	initial number density of deposited particles	[m <sup>-2</sup> ]
$\sigma_p(t)$	number density of remaining particles on the surface at time $t$	[m <sup>-2</sup> ]
$\sigma_r$	standard deviation of height of asperities $R_a$	[m]
$\phi$	velocity coefficient	[-]
$\Psi_d$	relative humidity at deposition environment	[-]
$\Psi_{opt}$	relative humidity for achieving the maximum removal efficiency	[-]
$\Psi_r$	relative humidity of removal environment	[-]

## References

1. G. Ziskind, M. Fichman and C. Gutfinger, Resuspension of particulates from surfaces to turbulent flows –Review and analysis, *J. Aerosol Sci.*, 26, 613–644 (1995)

2. L.Gradon, Resuspension of particles from surfaces: Technological, environmental and pharmaceutical aspects, *Adv. Powder Technol.*, 20, 17–28 (2009)
3. M.E. O'Neill, A sphere in contact with a plane wall in a slow linear shear flow, *Chem. Eng. Sci.*, 23, 1293–1298 (1968)
4. S.L. Goren, The normal force exerted by creeping flow on a small sphere touching a plane, *J. Fluid Mech.*, 41, 619–625 (1970)
5. D. Leighton and A. Acrivos, The lift on a small sphere touching a plane in the presence of a simple shear flow, *J. Appl. Math. Phys.*, 36 174–178 (1985)
6. M. Phillips, A force balance model for particle entrainment into a fluid stream, *J. Phys. D: Appl. Phys.*, 13, 221–233 (1980)
7. H.Y. Wen and G. Kasper, On the kinetics of particle reentrainment from surfaces, *J. Aerosol Sci.*, 20, 483–498 (1989)
8. D. Hall and J. Reed, The time dependence of the resuspension of particles, *J. Aerosol Sci.*, 20, 839–842 (1989)
9. D.A. Braaten, K.T. Paw U and R.H. Shaw, Particle resuspension in a turbulent boundary layer – Observed and modeled, *J. Aerosol Sci.*, 21, 613–628 (1990)
10. J.W. Cleaver and B. Yates, Mechanism of detachment of colloidal particles from a flat substrate in a turbulent flow, *J. Colloid Interface Sci.*, 44, 464–474 (1973)
11. J.W. Cleaver and B. Yates, The effect of re-entrainment on particle deposition, *Chem. Eng. Sci.*, 31, 147–151 (1976)
12. M.W. Reeks, J. Reed and D. Hall, On the resuspension of small particles by a turbulent flow, *J. Phys. D: Appl. Phys.*, 21, 574–589 (1988)
13. M.W. Reeks and D. Hall, Deposition and resuspension of gas-borne particles in recirculating turbulent flows, *J. Fluid Eng.*, 110, 165–171 (1988)
14. P. Vainshtein, G. Ziskind, M. Fichman and C. Gutfinger, Kinetic model of particle resuspension by drag force, *Phys. Rev. Letters*, 78, 551–554 (1997)
15. G. Ziskind, M. Fichman and C. Gutfinger, Adhesion moment model for estimating particle detachment from a surface, *J. Aerosol Sci.*, 28, 623–634 (1997)
16. N. Rajaratnam, *Turbulent Jet*, pp.1–26, Elsevier Science Publishing Co. (1976)
17. K. Gotoh, Removal of micrometer-size particles from solid surfaces by impinging air jet, in : *Particles on Surfaces 9: Detection, Adhesion and Removal*, K.L. Mittal (Ed.), pp. 329–355, CRC Press, Boca Raton, FL (2006)
18. Y.A. Cengel and M.A. Boles (Translated in Japanese by T. Asami, Y. Hosokawa and K. Momose), *Thermodynamics*, Ohmsha, Tokyo, Japan (1997)
19. S.W. Churchill, Compressible flows, in: *Handbook of Fluids in Motion*, N.P. Cheremisinoff and R. Gupta (Eds.) Chapter 8, pp.211–221, Ann Arbor Science Publishers, Ann Arbor, MI (1983)
20. Nihon Kikai Gakkai (Ed), *Kikai Kagaku Binran, 6th-edition*, pp.11–69, Nihon Kikai Gakkai, Tokyo, Japan (1977)
21. H. Masuda, K. Gotoh, H. Fukada and Y. Banba, The removal of particles from flat surfaces using a high-speed air jet, *Adv. Powder Technol.*, 5, 205–217 (1994)

22. K. Gotoh, M. Kida and H. Masuda, Effect of particle diameter on removal of surface particles using high speed air jet, *Kagaku Kogaku Ronbunshu* 20, 693–700 (1994)
23. K. Gotoh, S. Takebe, H. Masuda and Y. Banba, The effect of humidity on the removal of fine particles on a solid surface using high-speed air jet, *KONA*, 13, 191–203 (1995)
24. G. Ziskind, L.P. Yarin, S. Peles and C. Gutfunger, Experimental investigation of particle removal from surfaces by pulsed air jet, *Aerosol Sci. Technol.*, 36, 652–659 (2002)
25. M. Okazaki, R. Kusumura, M. Yoshida, J. Oshitani and K. Gotoh, Effect of target plate scanning on the removal of adhered particles by a high- speed air jet, *J. Soc. Powder Technol., Japan*, 45, 690–696 (2008) (in Japanese)
26. K. Gotoh, S. Takebe and H. Masuda, Effect of surface material on particle removal using high speed air jet, *Kagaku Kogaku Ronbunshu*, 20, 685–691 (1994) (in Japanese)
27. D.J. Phares, G.T. Smedley and R.C. Flagan, Effect of particle size and material properties on aerodynamic resuspension from surfaces, *J. Aerosol Sci.*, 31, 1335–1353 (2000)
28. Y. Otani, N. Namiki and H. Emi, Removal of fine particles from smooth flat surfaces by consecutive pulse air jets, *Aerosol Sci. Technol.*, 23, 665–673 (1995)
29. M. Okazaki, M. Yoshida, J. Oshitani and K. Gotoh, Effect of pulsed air jet on the air jet removal of adhered single particles, *J. Soc. Powder Technol., Japan*, 45, 297–304 (2008) (in Japanese)
30. G.T. Smedley, D.J. Phares and R.C. Flagan, Entrainment of fine particles from surfaces by impinging shock waves, *Experiments in Fluids*, 26, 116–125 (1999)
31. S. Watano, T. Hamashita and T. Suzuki, Removal of fine powders from film surface. I. Effect of electrostatic force on the removal efficiency, *Chem. Pharm. Bull.*, 50, 1258–1261 (2002)
32. S. Watano, T. Okamoto and T. Suzuki, Removal of fine powders from film surface. II. Effect of operating parameters on the removal efficiency, *Chem. Pharm. Bull.*, 50, 1262–1264 (2002)
33. K. Gotoh, K. Karube, H. Masuda and Y. Banba, High-efficiency removal of fine particles deposited on a solid surface, *Adv. Powder Technol.*, 7, 219–232 (1996)
34. K. Gotoh, K. Takahashi and H. Masuda, Removal of single particles adhered on a flat surface by vibrating air jet, *J. Aerosol Res., Japan*, 13, 133–141 (1998) (in Japanese)
35. A.B. Maynard and J.S. Marshall, Particle removal from a surface by a bounded vortex flow, *Int. J. Heat Fluid Flow*, 32, 901–914 (2011)
36. A. Fuhrmann, J.S. Marshall and J. Wu, Effect of acoustic levitation force on aerodynamic particle removal from a surface, *Appl. Acoustics*, 74, 535–543 (2013)



# Droplet Spray Technique for Particle Removal

James T. Snow<sup>1\*</sup>, Masanobu Sato<sup>2</sup> and Takayoshi Tanaka<sup>2</sup>

<sup>1</sup>*DNS Electronics, 2315 Luna Road, Carrollton, TX,*  
<sup>2</sup>*Screen Semiconductor Solutions Co., Ltd., Shiga, Japan*

---

## Abstract

Particle removal from semiconductor surfaces without damage to sensitive structures and loss of substrate is required for maximum device performance and yield. While many techniques are available, the use of an atomized droplet or dual-fluid spray for damage-free particle removal has proven to be one of the more effective strategies. The forces created upon droplet impact can be utilized to enable this cleaning method to be applied for the cleaning of semiconductor wafers. Spray nozzle design has progressed to permit the separate control of droplet size and velocity, which is essential for cleaning three-dimensional structures without damage.

**Keywords:** Particle removal, particle removal efficiency, PRE, wafer cleaning, dual-fluid spray, atomized spray, droplet spray, droplet impact, cleaning process window, wet cleaning

## 8.1 Introduction

It has been reported that the production of semiconductor logic devices is expected to require ~1500 processing steps at the 14-nm technology node as shown in Figure 8.1, with surface preparation using wet cleaning accounting for ~10% of the total number of steps [1]. The removal of surface contaminants, especially particles, is essential to properly prepare the wafer surface for subsequent processes.

---

\*Corresponding author: jim.snow@dnse.com

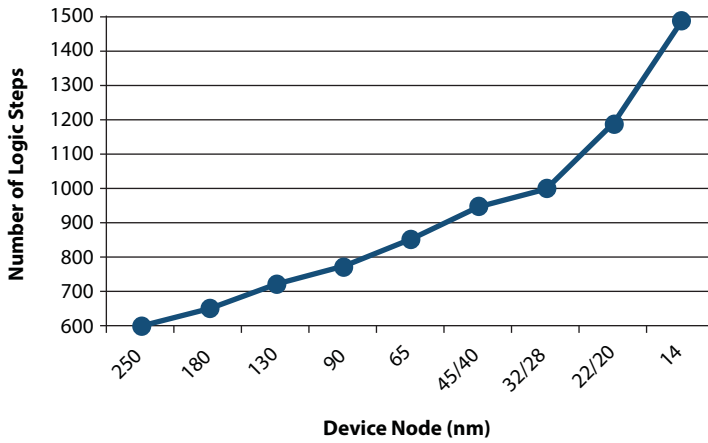


**Figure 8.1** Trend in number of logic process steps relative to device node.

The International Technology Roadmap for Semiconductors (ITRS) [2] provides guidelines for the successful manufacture of semiconductor devices. Particles with a diameter larger than the specified critical particle diameter, i.e. half of the Metal 1 half-pitch dimension, need to be removed in order to prevent device failure. For devices in 2014 with 18-nm gate length (26-nm Metal 1  $\frac{1}{2}$ -pitch), the critical particle diameter is 13 nm as shown in Table 8.1. This diameter further shrinks to 9.0 nm for 12.8-nm gate length in 2018. The numbers of these sized particles are limited to 12 and 34 particles for 300- and 450-mm wafers, respectively. Removal of these critical-sized particles must be done with essentially zero material loss ( $<0.1 \text{ \AA}$ ) and without damaging any fragile device features. A variety of techniques have been documented in the literature for particle removal [3]. In this chapter, which is modified and updated from previously published material [4], atomized droplet or dual-fluid spray cleaning is presented as it provides a good method for damage-free particle removal.

## 8.2 Droplet Impact Phenomena

Dual-fluid spray cleaning is a technique where liquid droplets are generated from a nozzle and propelled to a substrate surface with the resulting impact and subsequent effects generating sufficient energy for wafer cleaning, i.e. particle removal. The phenomena of a liquid droplet impacting a surface have been well documented in the literature. Results from single

**Table 8.1** ITRS Front End Surface Preparation Roadmap for Critical Particle Size and Number\*

Year of Production	2013	2014	2015	2016	2017	2018
DRAM ½ pitch (nm) (contacted)	28.0	26.0	24.0	22.0	20.0	18.0
MPU/ASIC M1 ½ pitch (nm) (contacted)	40	32	32	38.3	25.3	22.5
MPU physical gate length (nm)	20	18	17	15.3	14.0	12.8
Wafer diameter (mm)	300	300	450	450	450	450
Critical particle diameter (nm)	14	13	12	10.5	10	9.0
Critical particle count (#/wafer)	20.16	11.69	31.15	33.33	54.72	33.77
Critical particle count >28 nm (#/wafer)	5	2.5	5.7	4.7	7.0	3.5
Si and oxide loss (Å) / LDD step	0.1	0.1	0.1	0.1	0.1	0.1

\*The data in this table have been extracted from Table FEP10 – Front End Surface Preparation Technology Requirements in reference 2

droplets impacting solid, dry surfaces [5–11], malleable surfaces [12,13], droplets impacting a liquid film on a solid surface [14], and droplet impact on both solid and liquid surfaces [15–17] have been reported.

### 8.2.1 Impact on Solid Surface

When a liquid droplet first impacts a solid surface, it deforms and the liquid within the droplet becomes denser at the base adjacent to the substrate surface. While the liquid in the droplet bordering the solid surface is extremely compressed, the remainder of the fluid in the droplet is undisturbed. These two different liquid regions, compressed and uncompressed, are divided by a shock wave front which spreads into the bulk liquid as shown in Figure 8.2 [7]. The density and compressibility of the liquid, as well as the droplet's impact velocity and radius are all critical parameters.

The shock wave pressure generated after impact is largest at the contact edge to the substrate surface and lowest at the center. The pressure produced depends on the nature of the target surface, i.e. a more malleable surface can absorb the energy from the droplet and diminish the resultant force [14]. The shock wave velocity can be assumed to be equal to  $C_0$  for most liquids at low impact velocities.

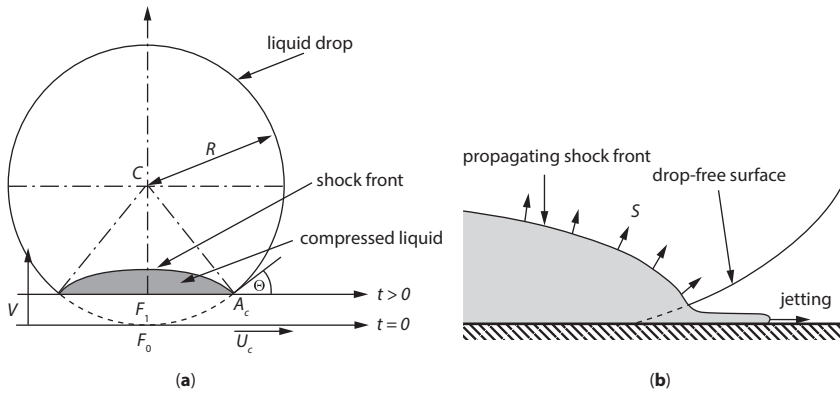


**Figure 8.2** Impact of liquid drop showing formation of shock front (a) and subsequent start of sideways liquid jetting (b).

Initial studies of a single droplet contacting an inelastic surface employed the waterhammer theory to provide an impact pressure  $P$  given by Equation (8.1):

$$P = \rho_o C_o V_o, \quad (8.1)$$

where  $P$  is the generated pressure,  $\rho_o$  is the liquid density,  $C_o$  is the sonic speed in the liquid and  $V_o$  is the impact velocity. This one-dimensional approach assumed that a planar shock wave moved through the liquid at a constant speed  $C_o$ , which was shown by subsequent researchers to be erroneous, i.e. the velocity is not constant and the shape of the shock wave is hemispherical. While Equation (8.1) can be used to calculate the pressure at the moment of impact, it is inadequate to express the maximum pressure generated.

Subsequent researchers utilized a two-dimensional model to provide a better estimate of the resulting pressures in the impact velocity range of 45–450 m/s [5]. The calculated pressure at the moment of first impact was similar to the result from the one-dimensional approach; however, when the contact angle  $\Theta$  in Figure 8.2 reached half the critical angle (the radius of the shock wave when it separates from the impacted substrate), the pressure increased rapidly until approximately three times the waterhammer pressure.

The shock wave front is initially pinned to the contacting surface upon impact; however, after a few nanoseconds, the shock wave front separates from the contact edge and forms a sideways jet of liquid as shown in Figure 2b. The velocity of this formed jet can be 2–5 times larger than the



initial impact velocity. During this same time, an expansion wave moves into the liquid droplet, which might result in cavitation.

### 8.2.2 Crown Formation

Droplet impact on a thin liquid layer can have similar characteristics as impact on an uneven solid surface [18]. In both cases, a crown-like formation is created like that shown in Figure 8.3 [19]. In the case of impact on a liquid film, the crown takes a longer time to form and the height is larger. This occurs since additional liquid is incorporated into the wall of the crown from a small cavity formed in the target liquid film. The velocity of the base of the crown is about one order of magnitude larger than the initial impact velocity. This cavity and crown wall subsequently collapse to create a liquid jet, termed a Rayleigh jet, which sprouts from the middle of the prior impacted area. The height of the Rayleigh jet depends on the initial impact energy.

In the case of droplet impact on a very smooth, hard surface, a crown does not form and the liquid merely spreads across the surface. If the droplet impact frequency is sufficiently high, the liquid layer surface will not recover before the arrival of subsequent drops, which affects their impact characteristics.



**Figure 8.3** Crown formation from droplet impacting a liquid surface.

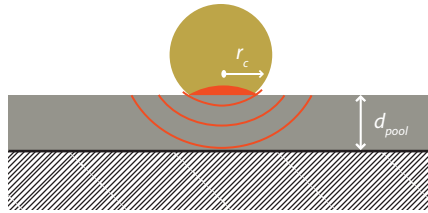


Figure 8.4 Droplet impact on liquid layer and shock wave propagation.

### 8.2.3 Impact on Liquid Film

If the shock wave has to cross a liquid film to reach a hard surface underneath as shown in Figure 8.4, the pressure on the solid surface is different compared to the case when exposed [20].

Assuming that the droplet contact radius  $r_c$  is small ( $\sim 1 \mu\text{m}$ ) compared to the liquid layer thickness  $d_{\text{pool}}$  and keeping the thickness of the shock wave and depth of liquid layer both constant, the shock wave pressure generated at the substrate surface is provided by Equation (8.2).

$$P_{\text{surface}} = \frac{3p_{\text{wh}}\pi r_c^2}{4\pi d_{\text{pool}}^2} = \frac{3\rho s v^3 d^2}{8c^2 d_{\text{pool}}^2} \quad (8.2)$$

where  $p_{\text{wh}}$  is the waterhammer pressure,  $\rho$  is the liquid density,  $d$  is the diameter of the droplet,  $s$  is the velocity of the droplet,  $v$  is the velocity of the shock wave and  $c$  is the speed of sound [21].

As shown in Equation (8.2), the pressure upon impact now also depends on the radius of the droplet and the liquid layer thickness. The series of shock wave curves formed from droplet impact on a surface coated with a 10- $\mu\text{m}$  liquid film at different velocities are shown in Figure 8.5. Wostyn, *et al.* [20] also calculated the resulting dynamic pressures on the solid surface taking into account the effects of crown formation.

## 8.3 Cleaning Process Window

It is evident that droplets of varying sizes and velocities will generate different pressures upon impact. The force required for damage-free particle removal must be carefully selected as shown in Figure 8.6 [22]. If the distribution of the particle removal force is not tightly controlled, some particles will not be removed and/or some damage may occur. This potential damage issue has been exacerbated by the introduction of new three-dimensional architectures, e.g. FinFETs, which are more sensitive than planar devices.

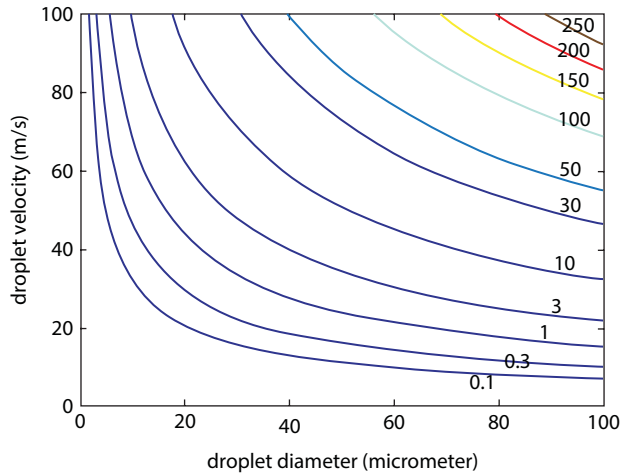


**Figure 8.5** Shock wave pressure curves (in bar) from impact of droplets with varying diameters and velocities on a liquid film coating a solid surface.

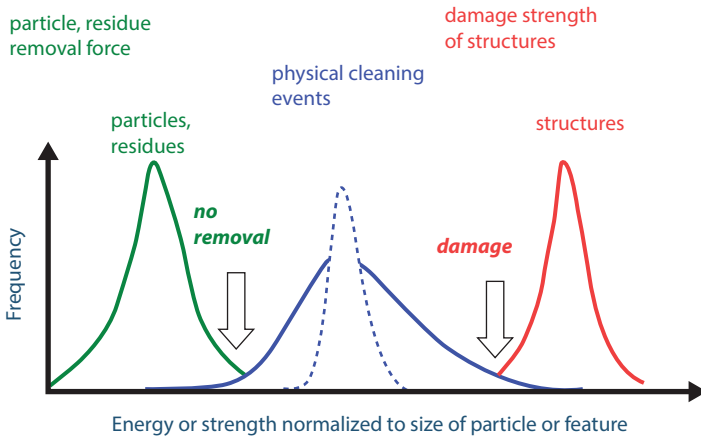


**Figure 8.6** Idealized cleaning process window depicting optimized cleaning force distribution (dotted line) located between particle adhesion and structural integrity force distributions.

### 8.3.1 Theoretical Studies

The forces required to remove a particle or damage a semiconductor structure have been reported [23–30]. Tardif and coworkers [23,24] contrasted the forces required for removal of particles against those that could damage structures, either deposited on the wafer or patterned from the substrate. As shown in Figure 8.7, the shock wave force needed to remove critical

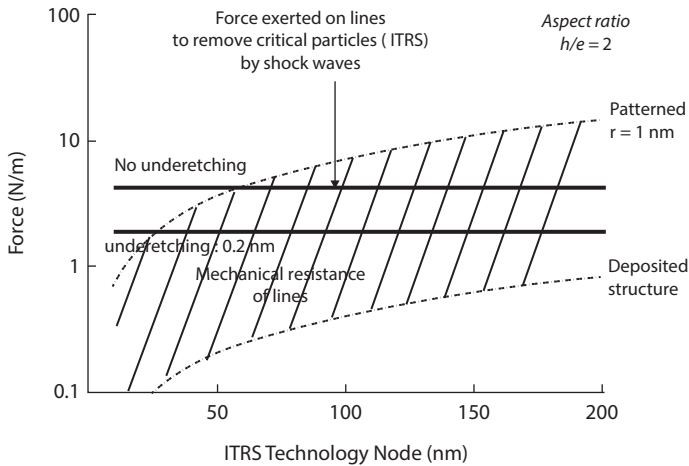


**Figure 8.7** Comparison of the shock wave drag force for removal of critical-sized particles (with and without slight underetching) vs. the mechanical strengths of patterned (upper dotted line) and deposited (lower dotted line) structures. Reproduced by permission of ECS - The Electrochemical Society.

particles can damage patterned structures at <50nm technology node. It was concluded that a high-velocity spray process for particle removal had to be carefully optimized in order not to damage device structures.

Numerical simulation has likewise been employed to examine removal of 30–100 nm particles by 66- and 100- $\mu\text{m}$  sized deionized water (DIW) droplets delivered by a dual-fluid spray [26]. The mechanisms for particle removal were limited to lift-off and drag forces. For particles <50 nm in size, the removal force was similar for both droplet sizes. For particles >50 nm, the larger-sized droplet provided a greater removal force. Dual-fluid spray cleaning was deemed capable for removal of 30–100-nm sized particles.

## 8.3.2 Experimental Studies

### 8.3.2.1 AFM Investigations

Several studies have used atomic force microscopy (AFM) to measure the forces necessary to remove particles [27] or to damage Si-based structures [28–30] from silicon wafer surfaces. The removal force for silicon oxide ( $\text{SiO}_2$ ) particles varied from  $\sim 15$  nN for particles aged for two days at 0% RH up to  $\sim 500$  nN for particles aged for 15 days at 100% RH. The higher removal force for the latter particles was attributed to formation of a water meniscus with the wafer surface.

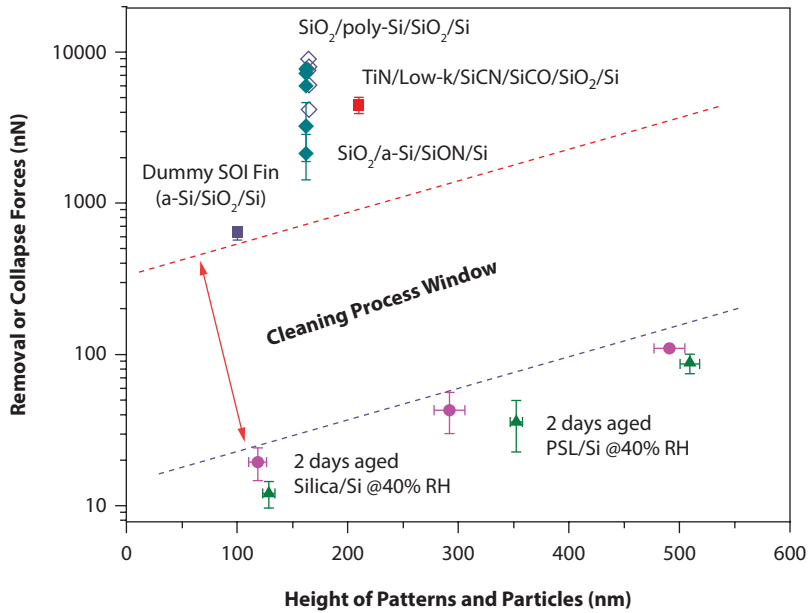


**Figure 8.8** Cleaning process window exists between observed less energy required for particle removal (lower region) vs. larger forces necessary to break lines and damage structures (upper region). Figure provided courtesy of Tae-Gon Kim and used with permission.

The forces required to damage silicon (both amorphous and poly) lines of varying lengths and widths, as well as Fin structures have likewise been quantified using the AFM technique. Among the Fin structures, those constructed from amorphous silicon required less force to cause damage ( $\sim 600$  nN) compared to ones constructed from poly- or crystalline silicon. Fins with a higher aspect ratio were also more easily damaged. The forces to damage dummy gate stacks were larger, i.e. in the range of 2–9  $\mu\text{N}$ . The AFM results were used to demonstrate that a non-damaging particle removal process window still theoretically exists as shown in Figure 8.8; however, the apparent smaller force needed to remove smaller particles does not consider boundary layer effects.

### 8.3.2.2 Droplet Energy Density Approach

A different understanding of a cleaning process window was generated through evaluating the results of cleaning experiments and developing the concept of droplet energy density. An initial study examined the damage to photoresist lines with two different droplet diameters [31]. The observed effect of droplet size on damage events could not be explained by kinetic

energy of the droplet alone, but was explained from the droplet energy density,  $E_d$ , which is the ratio of the kinetic energy to the projected impact area,  $A$ , at the moment of impact as shown in Equation (8.3).

$$E_d = \frac{E_k}{A} = \frac{\frac{\pi \rho d^3 v^3}{4}}{\frac{\pi d^2}{4}} = \frac{\rho d v^2}{3} \quad (8.3)$$

where  $E_k$  is the droplet kinetic energy,  $d$  is the droplet diameter,  $v$  is the droplet velocity and  $\rho$  is the density of liquid.

The relationship between the number of damage sites and the droplet energy density could be graphically represented as shown in Figure 8.9.

The condition when the number of damage sites equaled one is the damage threshold energy,  $E_{th}$ , and was expressed as shown in Equation (8.4).

$$E_{th} = \frac{\rho d v^2}{3}, \text{ therefore } v = \sqrt{\frac{3E_{th}}{\rho d}} \quad (8.4)$$

This was graphically depicted as a curve separating a damage-free zone from a damage-potential zone, as shown in Figure 8.10.

If droplet energy is less than the threshold to cause damage, it is located within the damage-free zone. However, if the value is more than  $E_{th}$ , it is located in the zone above the threshold curve and is capable of causing damage. The same approach was used in a subsequent paper to evaluate 78-nm

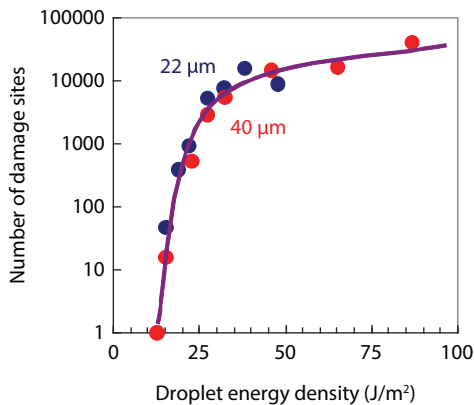


**Figure 8.9** Correlation of damage with droplet energy density from droplets of 22- and 40- $\mu\text{m}$  diameters.

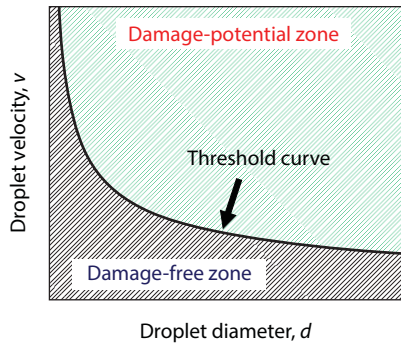


**Figure 8.10** Threshold energy curve separating damage-free and damage-potential zones.

$\text{SiO}_2$  particle removal and contrasted with damage potential of poly-Si gate structures [32]. The strengths of the gate structures and particle adhesion forces were measured using the AFM technique. In this latter study, the threshold energy density  $E_{th}$  for particle removal was determined to be  $\sim 4 \text{ J/m}^2$ , which was smaller than the pattern damage threshold value of  $\sim 12 \text{ J/m}^2$ .

In addition, the maximum pressure generated by impact of droplets of varying sizes and velocities on a  $10\text{-}\mu\text{m}$  water layer on solid substrate was then calculated to elucidate the relationship between the droplet impact pressure and droplet energy density. The results showed that the maximum pressure at droplet impact was equivalent to droplet energy density as shown in Equation (8.5).

$$P \approx E_d = \frac{\rho d V^2}{3} \quad (8.5)$$

A new representation of a cleaning process window was depicted as shown in Figure 8.11. The upper curve represented the threshold for pattern damage, the lower curve for particle removal, and the gap between the two curves was the cleaning process window for particle removal without pattern damage. Plotted in this graph were the measured droplet sizes and velocities generated by two different nozzle designs, a dual-fluid nozzle and advanced spray nozzle, which will be discussed in more detail in Section 8.4. As seen, the droplets from the dual-fluid spray nozzle had a much wider distribution with many droplets residing outside the process window, i.e.  $\sim 60\%$  were located below the particle removal threshold curve and  $\sim 3\%$  were in the damage-potential zone. In contrast, all droplets from the advanced spray nozzle were situated inside the process window. This result showed that the droplet size and velocity of the advanced spray droplets were well controlled and this technique provided a better method for particle removal without damage.

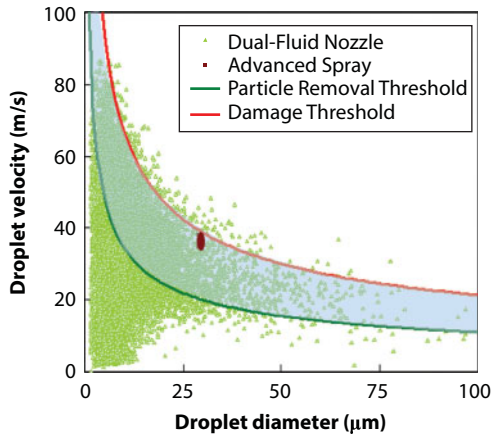


**Figure 8.11** Threshold curves for particle removal and pattern damage with dual-fluid spray and advanced spray nozzles. Reproduced by permission of ECS - The Electrochemical Society.

## 8.4 Droplet Spray Technique for Semiconductor Wafer Cleaning

### 8.4.1 Initial Studies

One of the first reports of using a droplet spray for damage-free removal of sub-micrometer sized particles from semiconductor wafers was in 1998 [33]. The water droplets had a diameter of 10  $\mu\text{m}$  and were accelerated to the wafer surface with speeds varying between 50 – 330 m/s. Additional details were subsequently disclosed [34,35]. The use of a supersonic jet cleaning machine for particle removal [36] was followed by a study comparing a dual-fluid spray technique with roll and disk-type brush scrubbing methods [37]. Particle removal using the aerosol was attributed to the high impingement pressure of the water droplets and the resulting side jet of liquid.

The particle removal efficiency (PRE) of  $\text{SiO}_2$  or silicon nitride ( $\text{Si}_3\text{N}_4$ ) particles using three different cleaning chemistries, i.e. ozonated ( $\text{O}_3$ ) water, diluted HF (dHF), and ammonia-peroxide mixture (APM), employing a spray nozzle (Soft Spray) was disclosed by other researchers [38]. The cleaning sequence had a hot APM dispense followed by dual-fluid spray cleaning. Complete removal of  $\text{SiO}_2$  particles was achieved regardless of chemistry; however, if the spray step was omitted, particle removal was negligible. The impact of the cleaning chemistries on removal of nitride



particles was pronounced, e.g. use of APM as the fluid in the spray nozzle provided >98% PRE of >60-nm  $\text{Si}_3\text{N}_4$  particles. The improvement in PRE was attributed to better zeta-potential control. Several papers on particle removal using droplet spray cleaning were subsequently published by other authors [39–43].

The benefit of incorporating an APM step prior to dual-fluid spray cleaning was likewise confirmed by other researchers; a 2X improvement in the PRE of  $\text{SiO}_2$  particles was demonstrated [39]. Three different cleaning techniques, i.e. nitrogen cryogenic, megasonic and single wafer spray cleaning, were evaluated for damage-free particle removal using blanket wafers contaminated with >65-nm  $\text{Si}_3\text{N}_4$  particles and silicon fins patterned on silicon-on-insulator (SOI) wafers [40]. 95% PRE was achieved without damage using the spray cleaning technique. The importance of droplet size and velocity distributions was detailed by Xu, *et al.* [41]. Outlier droplets were most likely responsible for observed damage and therefore proper nozzle design was critical to provide droplets of uniform size and velocity.

## 8.4.2 Droplet Distribution Optimization

### 8.4.2.1 Effects of Nozzle Design

The aerosol droplets from the dual-fluid spray cleaning technique are created by mixing a liquid and gas in a nozzle. In the Soft Spray nozzle depicted in Figure 8.12a [44,45], the liquid is introduced through a side

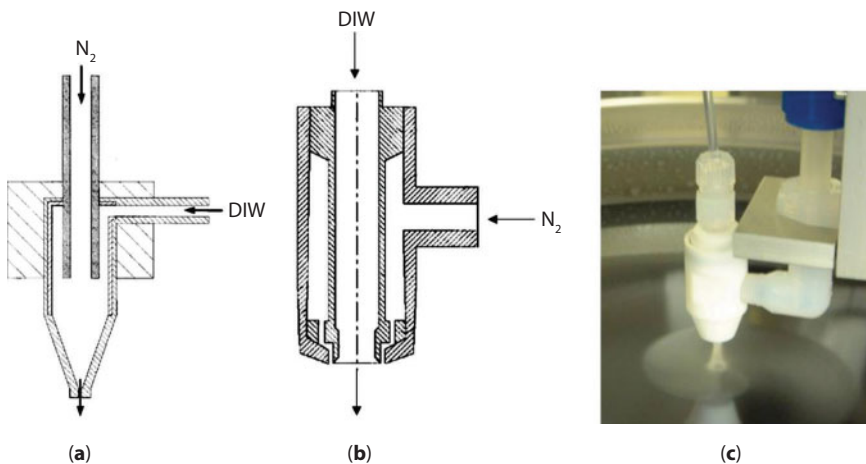


**Figure 8.12** Schematic drawings of dual-fluid Soft Spray (a) and Nanospray (b) nozzles with actual picture of Nanospray nozzle (c).

inlet port and gas through upper inlet. The aerosol is formed in an atomizing zone, gets accelerated by the inlet gas and exits at the bottom port. In another nozzle design, the Nanospray nozzles shown in Figures 12b,c, the liquid is introduced at the top of the nozzle and gas at the side. The shape and dimensions of the nozzle influence the size and velocity distributions of the formed aerosol droplets.

The resulting spray exiting the Nanospray nozzle was conical in shape as shown in Figure 8.13b; the Soft Spray delivered a more columnar-shaped spray as shown in Figure 8.13a.

Aerosol droplet size and velocity distributions were likewise influenced by nozzle design. Figure 8.14 shows the diameter and velocity of individual droplets captured by high-speed photography and sized. Inspection of the large droplet distribution generated at similar PRE level revealed that those

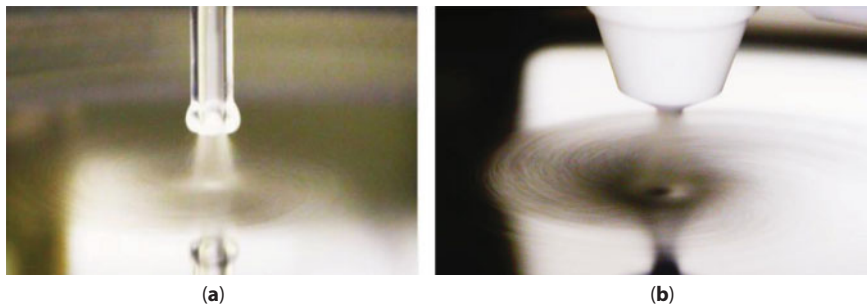


**Figure 8.13** Aerosol sprays exiting Soft Spray (a) and Nanospray (b) nozzles.

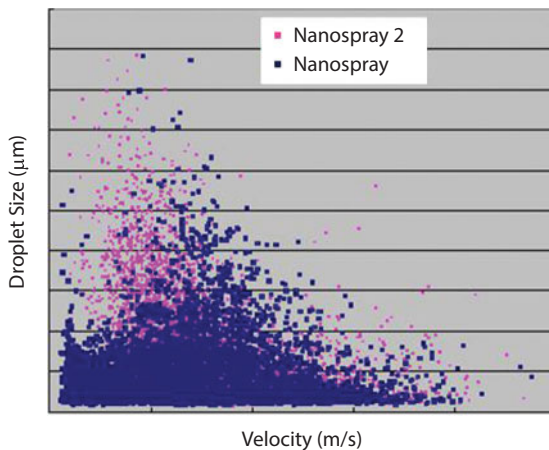


**Figure 8.14** Droplet size and velocity distributions from two aerosol nozzles at similar PRE conditions.

exiting the Nanospray2 nozzle had a lower peak velocity than Nanospray and, therefore, less propensity to cause damage.

#### 8.4.2.2 Effects of Fluid Flow Rates

Disregarding the effect on potential substrate damage, an increase in particle removal efficiency could be achieved by increasing the velocity and thus energy of the aerosol droplets to the substrate surface. With the traditional spray nozzle design, increased spray droplet energy was achieved by increased inlet gas flow.

Figure 8.15 shows the effect of gas flow rate increase on the resulting velocity and distribution. The peak velocity centered at 5 m/s at inlet gas flow rate of 20 L/min increased by an order of magnitude to 50 m/s when the gas flow rate was changed to 70 L/min. The velocity distributions were observed to be much tighter at the lower gas flow rates.

A change in the gas flow rate also affected the size distribution of the formed droplets as shown in Figure 8.16. On reducing the  $N_2$  flow rate, the resulting velocity decreased but the droplets showed a wider diameter distribution with more outlier droplets of larger diameter at lower velocities.

Depending on nozzle design, the inlet liquid flow rate could also affect the resulting droplets, albeit to a lesser extent than gas flow rate. Figure 8.17 shows the effect on removal efficiency of 100-nm Si particles from two different nozzles. At gas flow rates  $>60$  L/min, both the Soft Spray and

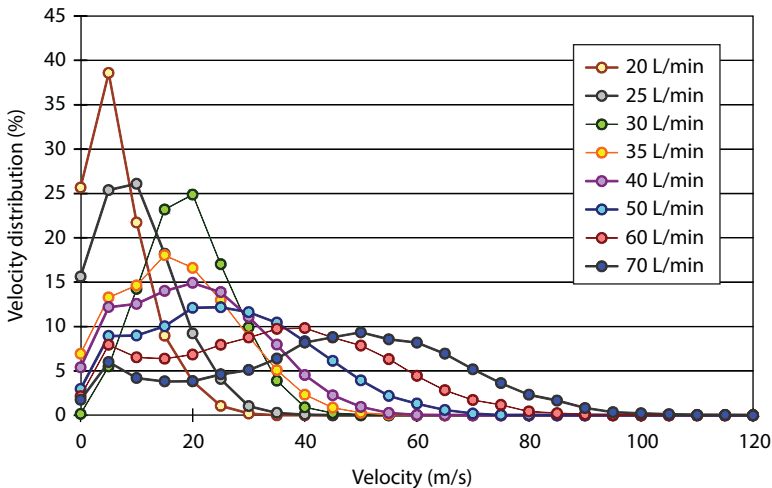


**Figure 8.15** Velocity distribution of dual-fluid spray droplets at varying inlet gas flow rates.

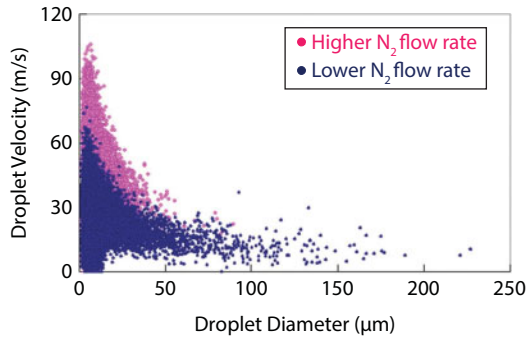


**Figure 8.16** Effect of  $N_2$  flow rate on droplet diameter and velocity distributions for a dual-fluid nozzle.

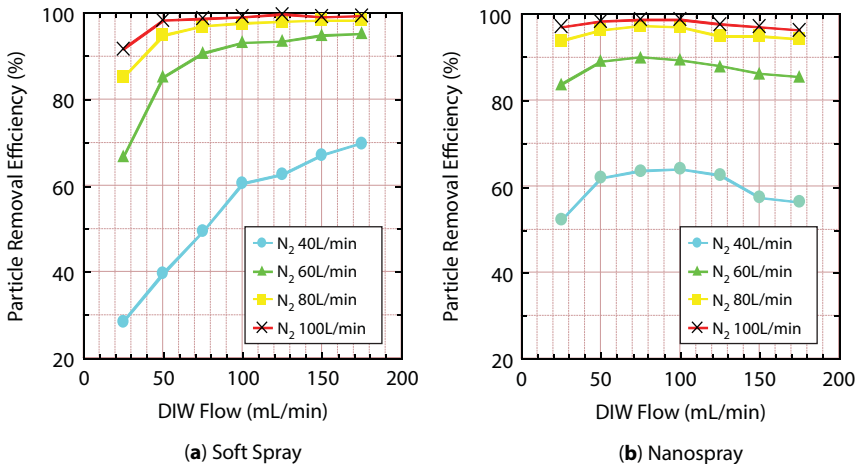


**Figure 8.17** Effect of DIW and  $N_2$  flow rates on PRE of 100-nm Si particles with (a) Soft Spray and (b) Nanospray dual-fluid nozzles.

Nanospray nozzles showed good removal of Si particles. However, compared to the Soft Spray nozzle, the Nanospray nozzle showed a relatively broad process window within the evaluated DIW flow rate range. At lower DIW flow rates, the PRE was more influenced by the liquid flow rate in the Soft Spray nozzle.

As devices became more complex with the continued shrinking of structural elements and introduction of three-dimensional topographies, the need to precisely control the droplet energy became mandatory. Great advances had been made in tightening the size and velocity distributions of aerosol droplets from the traditional dual-fluid spray nozzles, but

production of large outlier droplets, which could damage these sensitive structures, could not be eliminated. Generation of a carefully controlled distribution of smaller droplets at lower velocities was needed; however, the design of the traditional aerosol nozzle had an inherent flaw: droplet size could not be varied without affecting droplet velocity. A lower inlet gas flow rate decreased the droplet velocity, but created larger droplets which subsequently caused more damage. A new nozzle design was required to alleviate the influence of fluid flow rate on droplet size.

### 8.4.3 Advanced Spray

A new nozzle was introduced in 2010 which used a piezoelectric element to eject droplets with  $\pm 5\%$  (3  $\sigma$ ) size nonuniformity as contrasted to the large size variation from a traditional dual-fluid nozzle as shown in Figures 8.18 and 8.19 [46,47].

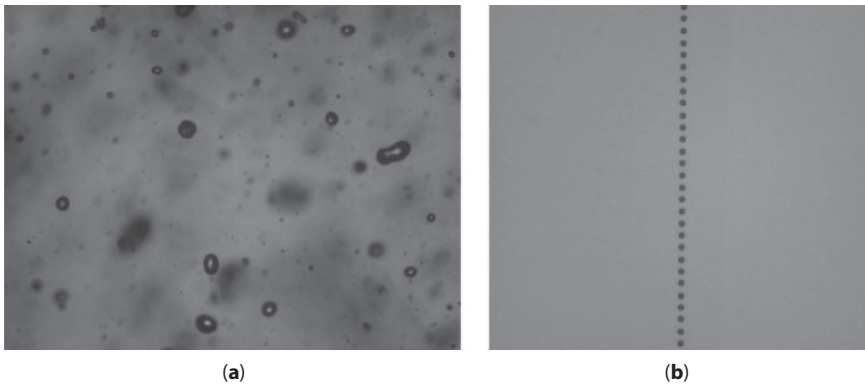


**Figure 8.18** High-speed camera images of droplets from dual-fluid (a) and advanced (b) spray nozzles.

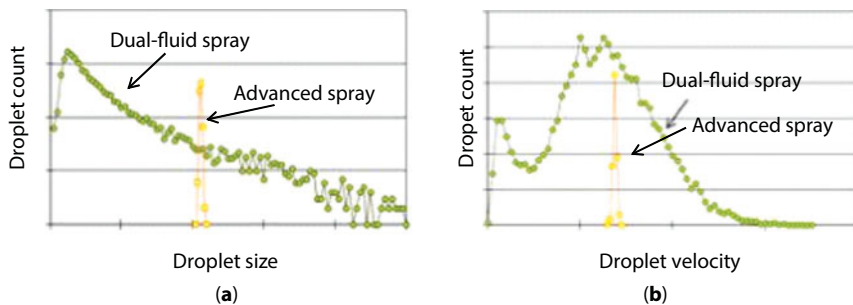


**Figure 8.19** Droplet size (a) and velocity distributions (b) for dual-fluid and advanced sprays.

In addition, another large improvement with the advanced spray nozzle was that droplet size and velocity could be adjusted separately without affecting the value or distribution of the other. Figure 8.20 shows the impact of varying the inlet DIW flow rates and the resulting velocity of the exiting droplets at a fixed droplet diameter.

The improvement compared to a traditional dual-fluid spray nozzle for small particle removal without damage to 37-nm device structures was reported as shown in Figure 8.21 [48].

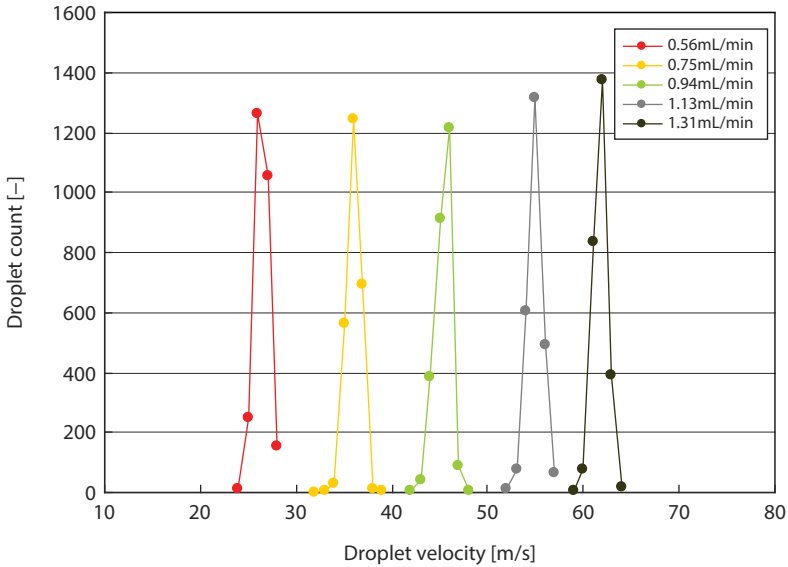


**Figure 8.20** Droplet velocity curves from advanced spray nozzle at varying inlet liquid flow rates.

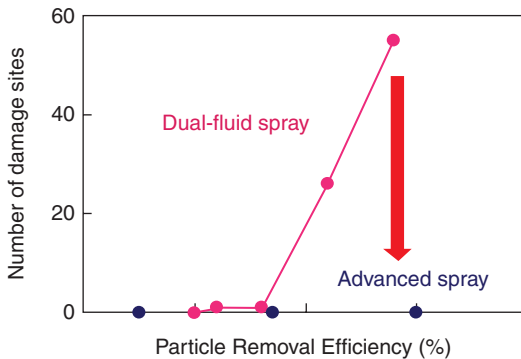


**Figure 8.21** Performance benefit of an advanced spray nozzle compared to traditional dual-fluid spray nozzle for small particle removal without damage.

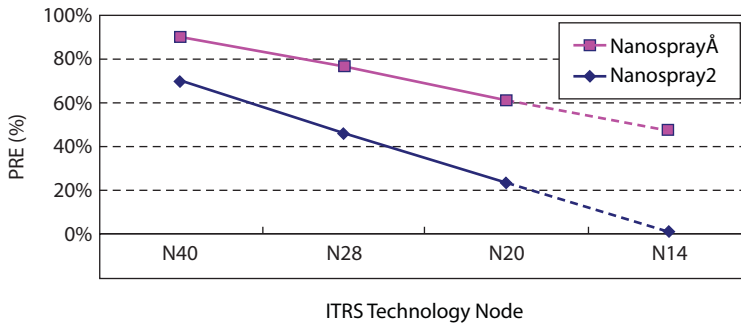


**Figure 8.22** The PRE performance of dual-fluid (Nanospray2) and advanced spray (NanosprayÅ) nozzles for removal of >45-nm sized PSL spheres.

A subsequent study reported on the PRE and damage threshold performances with 2Xnm technology node devices using the traditional dual-fluid and advanced spray nozzles [49]. Using spray settings that would not cause damage, the PRE performance for removal of >45-nm polystyrene latex (PSL) spheres between the two nozzles is shown in Figure 8.22. The PRE using the advanced spray nozzle was 40% higher than the conventional dual-fluid nozzle. It was estimated that with 1X nm devices, the conventional dual-fluid spray nozzle would no longer be an effective technique for damage-free particle removal.

## 8.5 Summary

The utilization of the forces created from the droplet impact phenomena from droplet spray cleaning has proven to be one of the more effective techniques for particle removal without damage in semiconductor wafer cleaning processing. The further improvement in droplet size and velocity distributions control from the development and introduction of the advanced NanosprayÅ nozzle will extend this technique to future, more-sensitive devices.

## References

1. S. Han, Challenges as we move through the materials era, Proc. SEMATECH Surface Preparation and Cleaning Conference, Austin, Texas (2013).
2. International Technology Roadmap for Semiconductors, 2013 Update. SEMATECH, Albany, NY (2013).

3. (a) K. L. Mittal (Ed.) *Particles on Surfaces 1, 2 & 3: Detection, Adhesion and Removal*, Plenum Press, New York (1988, 1989 & 1991).  
(b) K. L. Mittal (Ed.) *Particles on Surfaces: Detection, Adhesion and Removal*, Marcel Dekker, New York (1995).  
(c) K. L. Mittal (Ed.) *Particles on Surfaces 5 & 6: Detection, Adhesion and Removal*, CRC Press, Boca Rotan, FL (1999). (d) K. L. Mittal (Ed.) *Particles on Surfaces 7, 8 & 9: Detection, Adhesion and Removal*, CRC Press, Boca Raton, FL (2002, 2003 & 2006).
4. J. T. Snow, M. Sato and T. Tanaka, Dual-fluid spray cleaning technique for particle removal, in: *Developments in Surface Contamination and Cleaning, Vol. 6*, R. Kohli and K. L. Mittal (Eds.) pp. 107–138, Elsevier, Oxford, UK (2013).
5. F. J. Heymann, High-speed impact between a liquid drop and a solid surface, *J. Appl. Phys.* 40, 5113 (1969).
6. K. K. Haller, Y. Ventikos, D. Poulikakos and P. Monkewitz, Computational study of high-speed liquid droplet impact, *J. Appl. Phys.* 92, 2821 (2002).
7. K. K. Haller, Y. Ventikos, and D. Poulikakos, Wave structure in the contact line region during high speed droplet impact on a surface: Solution of the Riemann problem for the stiffened gas equation of state, *J. Appl. Phys.*, 93, 3090 (2003).
8. H.-Y. Kim, S.-Y. Park and K. Min, Imaging the high-speed impact of micro-drop on solid surface, *Rev. Sci. Instrum.* 74, 4930 (2003).
9. P. A. Lin and A. Ortega, The influence of surface tension and equilibrium contact angle on the spreading and receding of water droplets impacting a solid surface, *Proc. 13th IEEE ITherm Conference*, 1379 (2012).
10. S. Chandra and C. T. Avedisian, On the collision of a droplet with a solid surface, *Proc. R. Soc. Lond. A*, 432, 13 (1991).
11. M. Bussmann, S. Chandra and J. Mostaghimi, Modeling the splash of a droplet impacting a solid surface, *Phys. Fluids*, 12, 3121 (2000).
12. K. K. Haller, D. Poulikakos, Y. Ventikos and P. Monkewitz, Shock wave formation in droplet impact on a rigid surface: Lateral liquid motion and multiple wave structure in the contact line region, *J. Fluid Mech.* 490, 1 (2003).
13. J. E. Field, J. P. Dear and J. E. Ogren, The effects of target compliance on liquid drop impact, *J. Appl. Phys.* 65, 533 (1989).
14. T. Sanada, K. Ando and T. Colonius, Effects of target compliance on a high-speed droplet impact, *Solid State Phenom.* 187, 137 (2012).
15. F. H. Harlow and J. P. Shannon, Distortion of a splashing liquid drop, *Science* 157, 547 (1967).
16. F. H. Harlow and J. P. Shannon, The splash of a liquid drop, *J. Appl. Phys.* 38, 3855 (1967).
17. M. Rein, Phenomena of liquid drop impact on solid and liquid surfaces, *Fluid Dynamics Res.* 12, 61 (1993).
18. Z. Levin and P. V. Hobbs, Splashing of water drops on solid and wetted surfaces: Hydrodynamics and charge separation, *Phil. Trans. Royal Soc. Lond. A* 269, 555 (1971).



19. Randy Heisch, Untitled Photo, Reprinted with permission, URL [http://photo.net/photodb/photo?photo\\_id=7209027](http://photo.net/photodb/photo?photo_id=7209027).
20. K. Wostyn, M. Wada, K. Sano, M. Andreas, R. Janssens, T. Bearda, L. Leunissen and P. Mertens, Spray systems for cleaning during semiconductor manufacturing, Proc. 22nd European Conference on Liquid Atomization and Spray Systems, Como Lake, Italy (2008).
21. There is also an additional factor of  $\frac{1}{2}$  not included in the original citation, since the water hammer pressure upon impact on water is half of the value compared to the impact on a solid. K. Wostyn, personal communication (2012).
22. P. W. Mertens, G. Vereecke, R. Vos, S. Arnauts, F. Barbagini, T. Bearda, S. Degendt, C. Demaco, A. Eitoku, M. Frank, W. Fyen, L. Hall, D. Hellin, F. Holsteys, E. Kesters, M. Claes, K. Kim, K. Kenis, H. Kraus, R. Hoyer, T. Q. Le, M. Lux, K.-T. Lee, M. Kocsis, T. Kotani, S. Malhouitre, A. Muscat, B. Onsia, S. Garaud, J. Rip, K. Sano, S. Sioncke, J. Snow, J. Van Hoeymissen, K. Wostyn, K. Xu, V. Parachiev and M. Heyns, Roadblocks and critical aspects of cleaning for sub-65nm technologies, Proc. 2006 International Symposium on VLSI Technology, Systems and Applications, Hsinchu, Taiwan, pp. 123–126 (2006).
23. F. Tardif, A. Danel and O. Raccurt, Understanding of wet and alternative particle removal processes in microelectronics: Theoretical capabilities and limitations, Proc. 6th Symposium on Diagnostics and Yield: Advanced Silicon Devices and Technologies for ULSI Era, Warsaw, Poland (2003).
24. F. Tardif, O. Raccurt, J. C. Barbé, F. de Crécy, P. Besson and A. Danel, Mechanical resistance of fine microstructures related to particle cleaning mechanisms, Proc. 8<sup>th</sup> International Symposium on Cleaning Technology in Semiconductor Device Manufacturing, Electrochemical Society, Pennington, NJ, pp 153–160 (2003).
25. N. Hirano, K. Takayama, J. Falcovitz, T. Kataoka, K. Shimada and E. Ando, Microscopic analysis of particle removal by gas/liquid mixture high-speed flow, Solid State Phenom. 65–66, 207 (1999).
26. Z. Sun and R. Han, Numerical studies on nano-particle removal with microdroplet spray, Proc. of the 1st IEEE International Conference on Nano/Micro Engineered and Molecular Systems, Zhuhai, China, pp 303–305 (2006).
27. T.-G. Kim, K. Wostyn, T. Bearda, J.-G. Park, P. W. Mertens and M. Heyns, Investigation of physical cleaning process window by atomic force microscope, ECS Trans. 25(5), pp 203–210 (2009).
28. T.-G. Kim, K. Wostyn, P. W. Mertens, A. A. Busnaina and J.-G. Park, Collapse behavior and forces of multistack nanolines, Nanotechnology 21, 1 (2010).
29. A. Pacco, T.-G. Kim and P. W. Mertens, Correlation of collapse forces determined by lateral force AFM with damage generation due to physical cleaning processes, Electrochem and Solid State Lett. 14, H380 (2011).
30. T.-G. Kim, A. Pacco, K. Wostyn, S. Brems, X. Xu, H. Struyf, K. Arstila, B. Vandeveld, J.-G. Park, S. DeGendt, P. W. Mertens and M. Heyns, Effects of

- interfacial strength and dimension of structures on physical cleaning window, *Solid State Phenom.* 195, 123 (2013).
31. T. Tanaka, M. Sato, M. Kobayashi and H. Shirakawa, Development of a novel advanced spray technology based on investigation of droplet energy and pattern damage, *Solid State Phenom.* 187, 153 (2012).
  32. M. Sato, K. Sotoku, K. Yamaguchi, T. Tanaka, M. Kobayashi and S. Nadahara, Analysis on threshold energy of particle removal in spray cleaning technology, *Proc. 12th International Symposium on Cleaning Technology in Semiconductor Device Manufacturing*, Electrochemical Society, Pennington, NJ, pp 75–82 (2011).
  33. I. Kanno, N. Yokoi and K. Sato, Wafer cleaning by water and gas mixture with high velocity, *Proc. 5th International Symposium on Cleaning Technology in Semiconductor Device Manufacturing*, Electrochemical Society, Pennington, NJ, pp 54–61 (1998).
  34. I. Kanno, Wafer cleaning apparatus, U.S. Patent 5,873,380 (1999).
  35. I. Kanno, M. Tada and M. Ogawa, Two-fluid cleaning jet nozzle and cleaning apparatus, and method utilizing the same, U.S. Patent 5,918,817 (1999).
  36. K. Kitagawa, K. Shimada, K. Nishizaki, Y. Tatehara, T. Yoneda and E. Andou, Removal of micro-particles by supersonic jet cleaning machine, *Proc. 58th Autumn Meeting of the Japan Society of Applied Physics and Related Societies*, p. 842 (1997).
  37. Y. Tatehara, K. Kitagawa, K. Shimada and E. Ando, Wafer backside cleaning by twin-fluid flow cleaning, *Solid State Phenom.* 65–66, 183–186 (1999).
  38. A. Eitoku, J. Snow, R. Vos, M. Sato, S. Hirae, K. Nakajima, M. Nonomura, M. Imai, P. W. Mertens and M. M. Heyns, Removal of small (<100-nm) particles and metal contamination in single-wafer cleaning tool, *Solid State Phenom.* 92, 157–160 (2003).
  39. Y. Hirota, I. Kanno, K. Fujiwara, H. Nagayasu and S. Shimose, Damage-free wafer cleaning by water and gas mixture jet, *Proc. IEEE International Symposium on Semiconductor Manufacturing*, pp 219–222 (2005).
  40. J. M. Lauerhaas, R. Cleavelin, W. Xiong, K. Mochizuki, B. Clappin and T. Schulz, Damage-free cleaning and inspection of advanced multiple-gate FETs, *Solid State Technol.* 48 (March 2008).
  41. K. Xu, S. Pichler, K. Wostyn, G. Cado, C. Springer, G. Gale, M. Dalmer, P. W. Mertens, T. Bearda, E. Gaulhofer and D. Podlesnik, Removal of nano-particles by aerosol spray: Effect of droplet size and velocity on cleaning performance, *Solid State Phenom.* 145–146, 31 (2009).
  42. S. Verhaverbeke, R. Gouk, E. Porras, A. Ko, R. Endo, B. Brown and J. T. C. Lee, An investigation of the critical parameters of an atomized, accelerated liquid spray to remove particles, *ECS Trans.*, 1 (3), 127 (2005).
  43. S. Verhaverbeke, R. Gouk, E. Porras, A. Ko and R. Endo, Using mixed-fluid jet bombardment for advanced particle removal, *Solid State Technol.* 47 (March 2006).

44. K. Nakajima, M. Sato, H. Sugimoto, A. Hashizume and H. Tsujikawa, Substrate cleaning apparatus and substrate cleaning method, US Patent 7,314,529 B2 (2008).
45. K. Nakajima, M. Sato, H. Sugimoto, A. Hashizume and H. Tsujikawa, Substrate cleaning apparatus and substrate cleaning method, US Patent 7,422,641 B2 (2008).
46. Dainippon Screen Manufacturing Co., Ltd., Kyoto, Japan, Establishment of World's First Cleaning Technology for Ultra Miniaturization, URL <http://www.screen.co.jp/press/pdf/NR101012E.pdf>.
47. M. Sato, Substrate cleaning method and substrate cleaning apparatus, U.S. Patent Application Publication US2011/0031326 A1 (2011).
48. J. Snow and S. Nadahara, Advanced particle removal techniques for <20nm device node, Proc. SEMATECH Surface Preparation and Cleaning Conference, Austin, TX (2012).
49. Y.-H. C. Chien, M. Yeh, S. Ku, C. M. Yang, C. C. Chen, S. M. Jang, K. Izumoto, K. Sotoku, T. Tanaka, M. Sato, H. Shirakawa and M. Tanaka, Physical cleaning enhancement using advanced spray with uniform droplet control, Solid State Phenom. 195, 195 (2013).



# Laser-Induced High-Pressure Micro-Spray Process for Nanoscale Particle Removal

Daehwan Ahn, Changho Seo and Dongsik Kim\*

*POSTECH, Department of Mechanical Engineering, Pohang, Republic of Korea*

---

## Abstract

The beginning part of this chapter summarizes the importance of nanoscale contamination control in semiconductor industry and provides a brief review of various physical cleaning methods to remove nanoscale particles from solid surfaces, including laser cleaning, cryogenic aerosol cleaning, ultrasonic cleaning, and spray cleaning. The rest of the chapter introduces a recently developed opto-hydrodynamic surface cleaning technique to remove nanoscale particles as small as  $\sim 10$  nm. The process utilizes a laser-generated high-speed spray jet containing atomized liquid droplets. In the process cycle, optical breakdown of a micro liquid droplet with pulsed laser produces a high-speed micro jet with atomized droplets. The mechanisms of spray jet generation in laser-induced breakdown of a droplet as well as those of particle removal by spray jets are summarized with discussion on the potential of the technique.

**Keywords:** Laser-induced breakdown; nanoparticle removal; opto-hydrodynamic processing; spray cleaning

## 9.1 Introduction

### 9.1.1 Nanoscale Contamination Control

Effective contamination control has long been one of the key requirements in the semiconductor industry and, particularly, removal of nanoscale particles from surfaces will be increasingly important in nanoscale device fabrication processes. In VLSI (Very Large Scale Integration) fabrication, elimination of

---

\*Corresponding author: [dskim87@postech.ac.kr](mailto:dskim87@postech.ac.kr)

particles is a critical factor that determines the performance of a device and yield of a fabrication process. Cleaning is generally required before and after major steps of semiconductor fabrication, such as photo-lithography, etching, deposition, etc. Accordingly, approximately 30–40 % of semiconductor fabrication processes are cleaning steps. Furthermore, decrease in line widths requires multiple cleaning cycles, increasing the number of cleaning steps. According to the ITRS (International Technology Roadmap for Semiconductors), the half pitch size will reach 18 ~25 nm in DRAM and flash memory [1], which means that cleaning technique capable of removing ~ 10 nm particles needs to be developed to remove the ‘killer particles.’

The adhesion between a particle and a surface is determined by various factors, including van der Waals forces, electrostatic forces, capillary forces, chemical bonds and magnetic attraction. While the adhesion forces decrease linearly with decreasing particle size, the cleaning forces generally decrease in proportion to the square of the size. Therefore, hydrodynamic cleaning mechanisms become ineffective when the particle size becomes small [2]. In the case of nanoscale particles, cleaning methods using inertia or electrical force also become ineffective because of small mass and low electric-charging efficiency.

### 9.1.2 Review of Physical Cleaning Methods

Chemical wet cleaning methods using solvents and deionized water have been most popular in semiconductor cleaning since 1970s [3]. The methods, however, have problems, such as high maintenance cost, a large footprint, difficulty in equipment clustering, a big environmental load, inapplicability to Cu and low-k materials. Various physical cleaning methods capable of removing nanoscale contaminants have thus been developed, overcoming the above-mentioned problems.

Ultrasonic and megasonic cleaning methods use hydrodynamic drag and lift forces induced by cavitation and unsteady flow around a particle [4,5]. When high-frequency sound waves are used in megasonic cleaning, thin boundary layers are formed on the surface and the effect of acoustic streaming along with cavitation produces the cleaning force. It has been reported that cleaning solutions such APM (Ammonium Peroxide Mixture) enhance the cleaning efficiency by reducing the adhesion force. The strong acoustic pressure in megasonic cleaning can cause damages to the pattern, which becomes a serious issue when higher frequencies are used for eliminating nanoscale particles. Development of efficient processes to dry the cleaning solution is also a challenging issue related to megasonic cleaning.

Cryogenic cleaning is a dry cleaning method using impact of sprayed cryogenic particles [6]. CO<sub>2</sub> and Ar are often employed as a cryogenic source. When a high-pressure gas is ejected through a nozzle at a cryogenic temperature, dry ice or aerosols are formed as the thermodynamic state changes. This physical cleaning process is environment friendly in the sense that dry ice or aerosols do not leave any residue on the surface. Recently, effective removal of 10 nm particles has been reported [7]. The cryogenic cleaning process requires relatively complicated equipment to maintain cryogenic and vacuum conditions. Also, dry ice or aerosol can cause mechanical damage to the surface.

Various cleaning processes using lasers have been proposed as laser-based techniques have several unique advantages including environmental soundness, non-contact nature, flexibility and capability of selective-area cleaning [8–11]. In dry laser cleaning (DLC), direct illumination of a laser beam induces photochemical/photothermal ablation and/or photoacoustic excitation of the particles on the surface to detach the particles [9,10]. In the case organic contaminants, ultraviolet (UV) pulses are especially effective for decomposing the particles by photochemical reaction [11]. Some studies indicated that DLC processes for nanoscale particle removal can cause damages to the surface because of the near-field effect, i.e., due to generation of high-intensity hot spots underneath the particles. When the particle is inorganic, DLC is generally ineffective for submicrometer or smaller particles.

In steam laser cleaning (SLC) [12–14], a thin liquid film is deposited before laser pulse irradiation. The laser pulse then induces phase explosion of the liquid and the exploding bubbles exert cleaning force to particles [13]. SLC is a semi-dry cleaning process in the sense that the liquid film is completely removed during the process. SLC can generate much higher cleaning power than DLC but the pressure waves from the bubbles can also be a source of surface damage.

In laser shock cleaning (LSC) [15–19], optical breakdown of the ambient gas around the surface to be cleaned generates hot laser-induced plasma (LIP) in the ambient gas. Expansion of the plasma then produces a high-intensity shockwave which impinges onto the surface and removes the particles from the surface by aerodynamic drag. As the surface is not directly exposed to the laser beam in LSC, the chance of surface damage is relatively slim. As a dry cleaning process, LSC can remove submicrometer particles when a high-power pulsed laser is used. Some studies reported removal of ~100 nm particles using LSC [16,19]. However, the process cannot remove ~10 nm particles because the thermal radiation from the laser-induced plasma tends to cause thermal damage as the cleaning power, i.e., the shock intensity, is increased [20,21].

High-speed liquid jets generated by ejecting pressurized liquid through properly designed nozzles are widely used in various engineering applications [22–29]. The high-speed jet can cut, erode, or remove various materials without thermal side effect and can thus be employed in surface cleaning. High-pressure water jet cleaning is employed in pipe inside cleaning, paint stripping, and rust removal [22]. In semiconductor industry, liquid jet-based cleaning methods are also being developed for removal of photoresists, coatings, particles, etc. Processes using high-speed jet impingement are generally considered inadequate for nanoscale particle removal because of bulk usage of water, lack of cleaning power, and high chance of surface damage. Recently, pulsed liquid jet cleaning methods and spray jet cleaning processes using gas-liquid mixtures have been studied to overcome the problems.

In pulsed liquid jet cleaning, a liquid jet is broken up into a series of liquid slugs and they collide with the surface periodically to remove the contaminant [23]. Mechanical impact much higher than that generated by continuous jet is produced at the collision site due to the water hammer pressure. The impact stress generated by periodic collision weakens the particle-surface adhesion. Oscillating mechanical valves or ultrasonic vibration modules are used to produce the pulsed liquid jet. In dual-spray cleaning using two-fluid mixed fluid jet [24–27], both pressurized gas and liquid pass through the ejecting nozzle, which breaks up the liquid jet and generates atomized droplets. The gas flow accelerates the droplets and collides with the contaminants on the surface. Removal of submicrometer particles, e.g., 130 nm PSL (Polystyrene Latex) particles [25], was reported by a dual spray process. The dual-spray cleaning process is a physical cleaning process which does not use a chemical solvent and the droplet speed and size can be easily controlled by varying the gas pressure and flow rate. However, surface erosion by cavitation can be induced by the spray and nanoscale particles cannot be removed effectively because the achievable droplet speed is not sufficient.

## 9.2 Concept of Droplet Opto-Hydrodynamic Cleaning (DOC)

There have been attempts to generate micro liquid jets using lasers. Methods to generate small-volume pulsed liquid jets were developed based on the optical breakdown of liquid [28,29] and the methods were applied to drug delivery and micro dissection. In LILJ (Laser-Induced Liquid Jet) generation, optical cavitation produces an expanding bubble in a liquid



chamber to discharge a micro jet through a nozzle. The LILJ speed is on the order of 100 m/s, which is significantly smaller than that of commercially used high-speed water jet. The speed is also less than the level required for nanoscale particle removal.

In this chapter, a newly developed opto-hydrodynamic cleaning method using high-speed pulsed microjet (spray) from micro droplets [30–33] will be described in detail. Laser-induced breakdown (LIB) of a small droplet followed by hydrodynamic phenomena is employed in the technique to achieve droplet speeds over 1000 m/s. In the spray cleaning process, use of liquid makes it possible to generate substantially larger drag forces than those produced in such dry cleaning processes as LSC and van der Waals adhesion forces are much lower in liquid medium than in the air medium. It has been reported that sub-100 nm particles can be removed by using the impingement of sub-100  $\mu\text{m}$  liquid droplets moving at the speed of 100 m/s [24,25]. Nevertheless, simple estimation of the drag force indicates that removal of particles as small as 10 nm requires a much higher speed of the droplets, which means that conventional spray cleaning techniques cannot be a solution for  $\sim 10$  nm scale contamination control. Figure 9.1 shows that the droplet speed required to overcome the van der Waals adhesion force approaches  $\sim 1000$  m/s in the case of alumina particles on a Si wafer. In the figure, the order of magnitude of the drag force  $F_D$  has been estimated by  $F_D \sim \rho_L d^2 V^2$ , where  $\rho_L$ ,  $d$ , and  $V$  are liquid density, particle

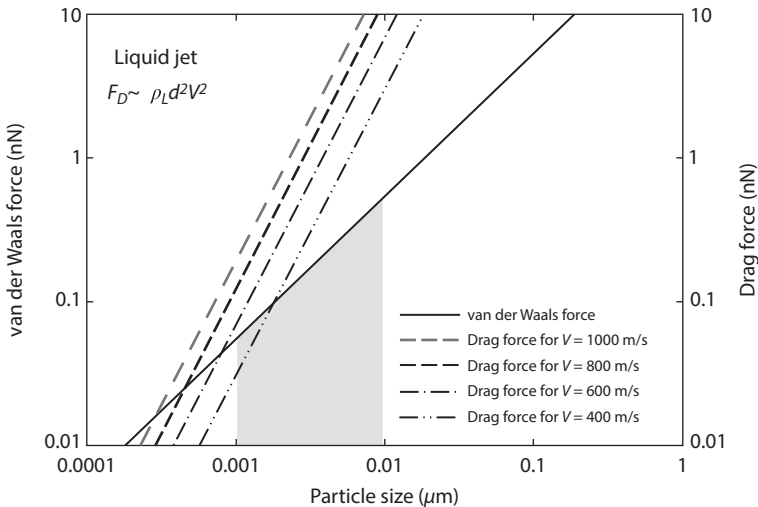


**Figure 9.1** van der Waals force on an alumina particle on a Si wafer and magnitudes of hydrodynamic drag exerted on the particle exposed to water flow at different speeds.

diameter and droplet speed, respectively. It is noted that the flow speed in the vicinity of a small particle on a surface is substantially lower than the jet/droplet speed measured away from the surface because the small particle is positioned deep in the boundary layer.

When an intense laser pulse is focused inside or on a droplet as shown in Figure 9.2, optical breakdown generates laser-induced plasma (LIP) with high temperature and high pressure. Expansion of the LIP breaks up the droplet, forming forward/backward jets and/or splash as well as shock waves in the ambient gas surrounding the droplet. Previous studies showed that the hydrodynamics can be controlled by adjusting the plasma intensity and location (laser intensity  $E$  and relative position of the droplet  $s$  in Figure 9.2). The laser-induced hydrodynamic phenomena (pulsed micro liquid jet from a droplet and/or spray jet composed of atomized droplets smaller than the original droplet) occurring in optical breakdown of a liquid droplet can be used for various applications as the jet/spray has several unique characteristics. Because the jet/spray speed is large enough to erode most surfaces without any additive, it can remove film-type contaminants, thin films, surface layers, etc. from a solid substrate. The high speed of the

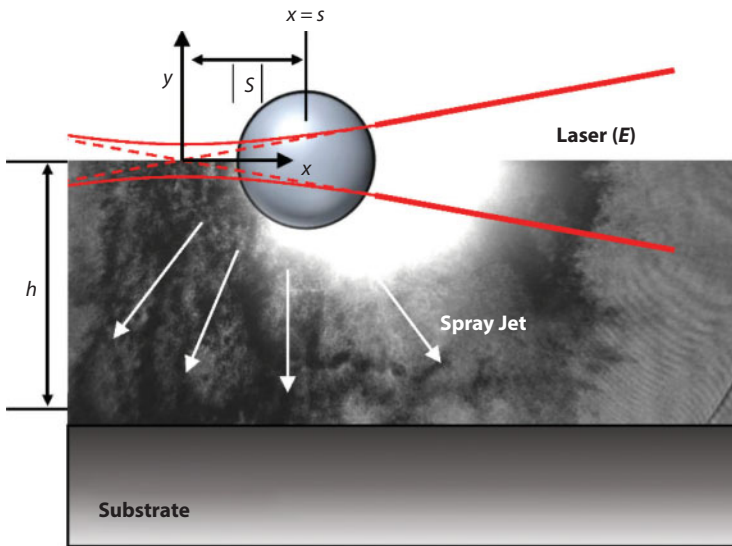


**Figure 9.2** Laser induced optical breakdown in liquid droplet. ( $s$ : position of the droplet relative to the laser focus,  $E$ : incident laser energy,  $h$ : gap distance between a droplet and surface).

spray jet makes it possible to remove nanoscale particles from a surface. As shown in Figure 9.1, removal of  $\sim 10$  nm particles requires a liquid spray with a speed over several hundred m/s. Another important advantage of employing a small droplet to generate a spray jet composed of smaller droplets for surface cleaning is that the process consumes only a minuscule amount of water because of the small (feed) droplet size, less than  $\sim 100$   $\mu\text{m}$ . The spray frequency and droplet size can be adjusted to completely dry the surface without any separate drying process, i.e., by natural evaporation of the thin-film water only. Similarly to the steam laser cleaning process, in this sense, the spray cleaning process can be classified as semi-dry.

### 9.3 Micro-Spray Generation by LIB

If a laser pulse with an irradiance over the LIB threshold is focused on a droplet, plasma is formed and heated by the inverse bremsstrahlung mechanism. The plasma temperature and pressure reach 6,000–15,000 K and 20–60 kbar, respectively [34]. The laser induced plasma (LIP) expands, forming a cavitation bubble, and generates a flow field inside the droplet. Depending on the flow structure, various types of jets, splash, droplets, vapor plume, etc. are ejected from the surface of the droplet. The LIB thresholds of liquids are generally smaller than those of gases. In the case of water, experimentally observed LIB threshold is approximately 10  $\text{GW}/\text{cm}^2$  [35–39]. The value is smaller than the theoretically calculated threshold by a factor of 10 ~ 100, which is due to the impurities contained in water. Table 9.1 display the LIB thresholds of various liquids and gases.

**Table 9.1** Experimental irradiance threshold ( $I_{th}$ ) for optical breakdown using ns laser pulse.

Medium	Wavelength (nm)	Pulse width (ns)	Beam dia. ( $\mu\text{m}$ )	$I_{th}$ ( $10^{10} \text{ W}/\text{cm}^2$ )	Reference
Air	1064	150–200	270	10–100	[35]
Air	532	20	15	8	[36]
Water	1064	7	71	2.1	[37]
Water	1064	7	22	1.82	[37]
Water	532	3	26	0.9	[38]
Water	532	6	5.3	2.9	[39]

Because the LIB threshold of water is lower than that of air, LIB starts on or inside a droplet at low irradiances. When the laser irradiance exceeds the air breakdown threshold before reaching the droplet, LIB begins from air in the upstream of the laser beam. The location and intensity of LIB, which are the most important factors that determine the hydrodynamics, are determined by the laser pulse energy  $E$ , focal length of the laser beam, and the position of the droplet relative to the focal point ( $s$  in Figure 9.2).

## 9.4 Mechanisms of Particle Removal by Laser-Induced Spray Jet

When a liquid jet is ejected in the form of a spray, micrometer and nanometer-sized atomized droplets collide with the particles on a surface. Hydrodynamic drag force generates two different mechanical effects explained below. If the drag force exceeds the adhesion force, the particles are removed from the surface [25,26,40,41].

First, the jetting effect by radial flow is generated when a spherical droplet with a speed above  $\sim 500$  m/s collides with a surface (Figure 9.3(a)). Because the incident velocity is close to or over the speed of sound, the liquid in the droplet cannot escape easily in the lateral direction in the early stage of collision. Therefore, a strongly compressed liquid zone is formed in the contact region, enveloped by a shock front. The collision exerts impact pressure to the surface and produces a large density/pressure gradient near

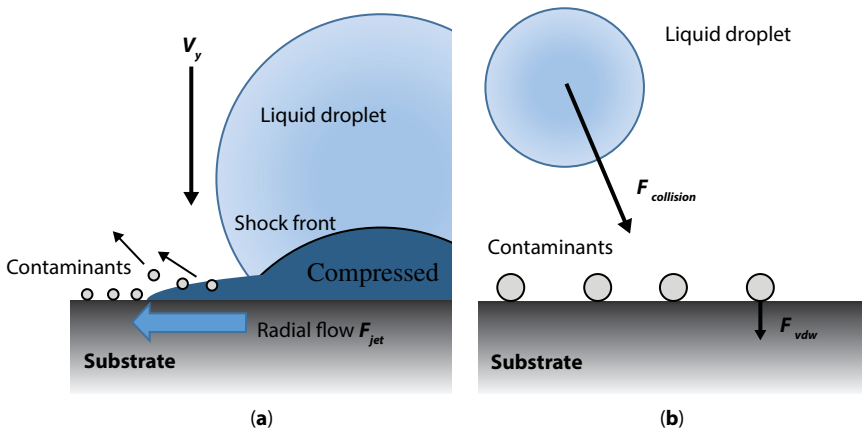


**Figure 9.3** Model for removing particle from a surface by (a) radial flow (b) impinging droplet.

the free surface. The large gradient breaks up the droplet along the contact edge and produces radial flow. The impact pressure generated by collision of a droplet with a surface can be estimated by

$$P_{impact} = \frac{1}{2} \frac{0.41 \rho_L C_L V}{1 + 5.9 (\rho_L C_L / \rho_s C_s)} \quad (9.1)$$

( $\rho_L$ : density of liquid,  $C_L$ : Sound velocity in the liquid,  $\rho_s$ : density of substrate,  $C_s$ : Sound velocity in the substrate,  $V$ : Velocity of liquid droplet) [25]. The drag force acting on a particle by the radial flow is then obtained by

$$F_{jet} = C_{d1} \left( \frac{\pi d^2}{4} \right) P_{impact} \quad (9.2)$$

( $C_{d1}$ : drag coefficient of the radial flow,  $d$ : diameter of particle).

Secondly, particles that collide with an impinging droplet experience a hydrodynamic drag by the flow passing around them (Figure 9.3(b)). The drag force produced by this collisional effect can be estimated by

$$F_{collision} = \frac{1}{2} \pi C_{d2} \rho_L d^2 V^2 \quad (9.3)$$

( $C_{d2}$ : drag coefficient for the impinging flow).

## 9.5 Generation of Micro-Spray Jet

### 9.5.1 Experimental Setup

Figure 9.4 shows an example of spray jet generation. A Q-switched Nd:YAG laser (full width at half maximum FWHM = 6 ns) was employed as a laser source. A homemade droplet generator using a piezoelectric dispenser was built to eject water droplet of sizes up to several hundred  $\mu\text{m}$ . A pulse delay generator was used to synchronize between the droplet ejection and the laser pulse firing. An optical droplet sensing system composed of a HeNe laser and a photodiode was also employed to precisely target a droplet with a laser pulse. The opto-hydrodynamic phenomena, including laser induced jet/droplet ejection, atomization and shockwave formation and propagation, were visualized by laser flash shadowgraphy. In the visualization technique, a  $\text{N}_2$ -pumped dye laser was used to obtain time-resolved shadowgraph images.

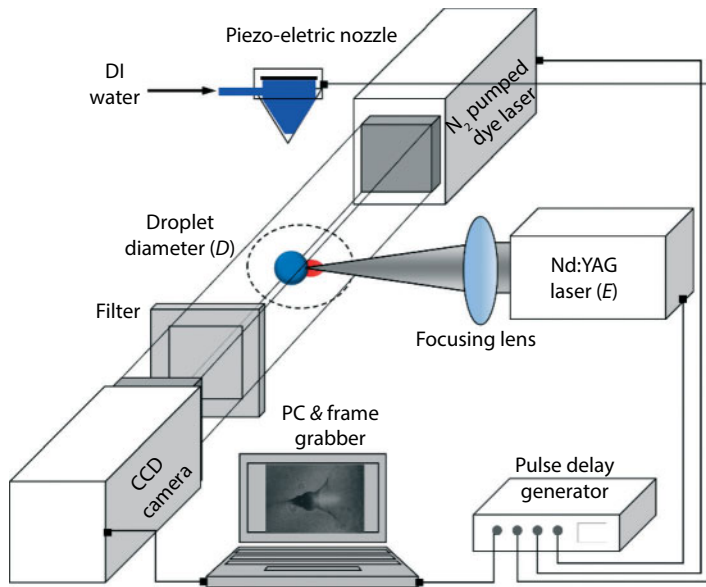


Figure 9.4 Experimental setup for the DOC and in situ shadowgraphic visualization.

## 9.5.2 Hydrodynamic Phenomena

### 9.5.2.1 Effect of Incident Laser Energy ( $E$ )

The dynamics of micro liquid jet formation was analyzed based on the time-resolved shadowgraph images. The overall hydrodynamics of the laser-generated micro liquid jet from a  $400\ \mu\text{m}$  liquid droplet, i.e., formation, propagation, divergence and breakup of the jet, was analyzed by time-resolved shadowgraphy at  $s = 0$  and  $s = 1\ \text{mm}$ .

Once a droplet was struck by a laser pulse at  $s = 0$ , LIB of the droplet generated a forward liquid jet on the shadow side of the droplet (the forward jet) and a splash on the irradiated side (Figure 9.5). The forward jet broke up into small droplets after propagating forward. When the laser pulse energy  $E$  was smaller than a critical value, the effect of air breakdown was negligible and the jet speed increased with  $E$ . At high  $E$ , a tightly focused laser pulse (beam spot size:  $10\text{--}20\ \mu\text{m}$ ) induced strong air breakdown in the illuminated side of the droplet (right side in Figure 9.2). The air plasma absorbed a substantial portion of  $E$  before reaching the droplet, which led to decrease in speed of the laser-induced jet. Accordingly, there was an optimum pulse energy  $E$  that maximized the jet speed. At  $s = 0$ ,

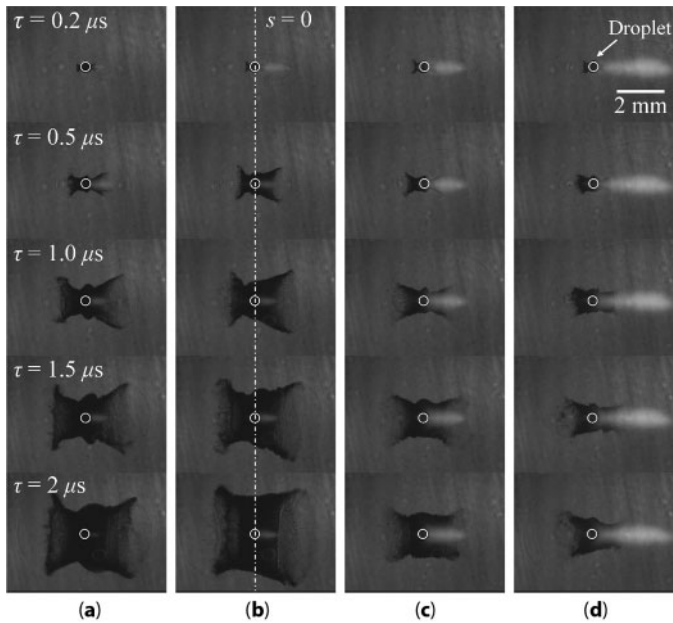


**Figure 9.5** Behavior of laser-induced micro liquid jets as a function of incident laser energy (a)  $E = 33$  mJ, (b)  $E = 60$  mJ, (c)  $E = 100$  mJ, and (d)  $E = 400$  mJ (relative position of the droplet  $s = 0$ , droplet diameter  $D = 400$   $\mu\text{m}$ ,  $\tau$ : time after laser pulse firing).

a relatively thick and diverging jet with a diameter similar to that of the droplet was produced in the initial stage (Figures 9.5(a)–5(d)), regardless of  $E$ . The jet broke up into small droplets after propagating forward. The jet diverged with an initial angle up to  $25^\circ$ , and the angle increased with distance from the droplet.

At  $s = 1$  mm, effects of  $E$  can be shown more clearly. Increasing the incident laser energy  $E$  shifted the center of the laser-induced plasma to the laser irradiation side. A relatively low laser energy ( $E = 33$  mJ) produced a liquid jet with a large divergent angle. The liquid jet was ejected from the shadow side of the droplet with no splash from the irradiated side (Figure 9.6(a)). A relatively high laser energy ( $E = 60$ – $100$  mJ), on the contrary, generated radially spreading liquid jets from the entire droplet surface (Figures 6(b) and 6(c)). At  $E = 400$  mJ, the air breakdown, i.e., laser energy absorption by the air plasma, caused reduction of the jet speed (Figure 9.6(d)). The position of LIP relative to a droplet governs the hydrodynamics of laser-generated liquid jet and maximum speed of liquid jet is produced by the high intensity of LIP positioned in the center of the droplet.

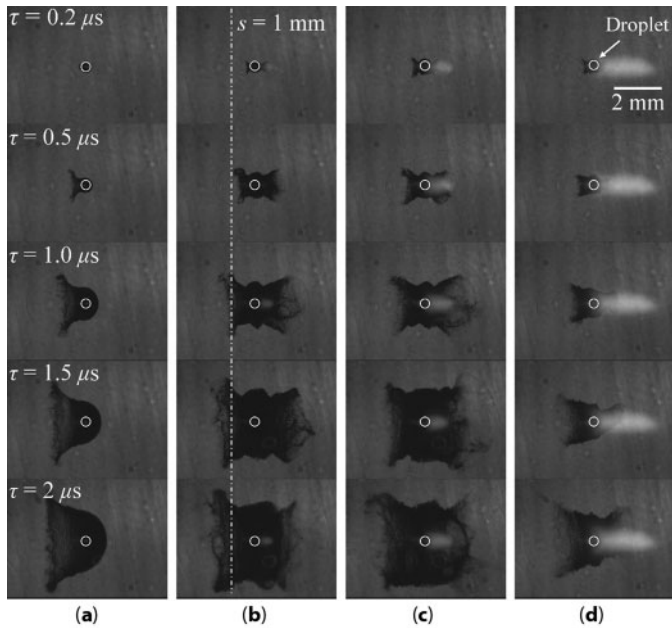


**Figure 9.6** Behavior of laser-induced micro liquid jets as a function of incident laser energy (a)  $E = 33$  mJ, (b)  $E = 60$  mJ, (c)  $E = 100$  mJ, and (d)  $E = 400$  mJ (relative position of the droplet  $s = 1$  mm, droplet diameter  $D = 400$   $\mu\text{m}$ ,  $\tau$  : time after laser pulse firing).

### 9.5.2.2 Effect of Droplet Position ( $s$ )

The divergence and speed of the laser-generated liquid jet were found to be most sensitively dependent on the position of the droplet relative to the laser focus ( $s$ ). Shadowgraph images with  $s$  values varying from the positive to the negative were captured, and simple ray-tracing calculations were performed to reveal the mechanism for forming various types of liquid jets, by estimating the formation of LIP (Figure 9.7).

For positive values of  $s$ , i.e., when the droplet was placed ahead of the laser beam focus, a diverging forward jet was obtained (Figure 9.7(a)). When  $E$  (and laser beam intensity  $I$ ) was high enough to induce a plasma from the illuminated surface of the droplet, a large portion of the droplet exploded, forming a diverging forward jet and a back splash. When  $E$  was small, e.g.  $E = 33$  mJ, the refracted laser beam, as shown in a ray-tracing illustration, was focused at a location close to the shadow side of the droplet, and expansion of the plasma from the point induced a conical-shaped highly diverging jet (Figure 9.7(a)). The plasma generation on the shadow side of the droplet was also confirmed by shock wave formation during the



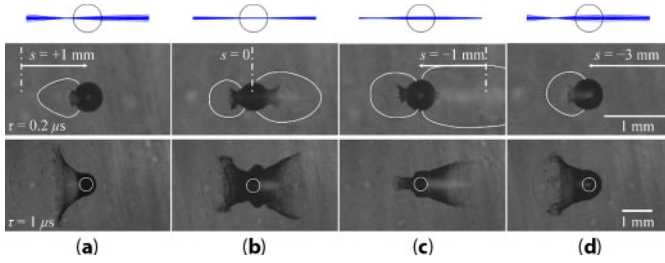


**Figure 9.7** Shadowgraph images and ray-tracing results at (a) relative position of the droplet  $s = 1$  mm, (b)  $s = 0$ , (c)  $s = -1$  mm, and (d)  $s = -3$  mm, showing the  $s$  dependence for generating a micro liquid jet (droplet diameter  $D = 400 \mu\text{m}$ ,  $E = 33$  mJ),  $\tau$ : time after laser pulse firing.

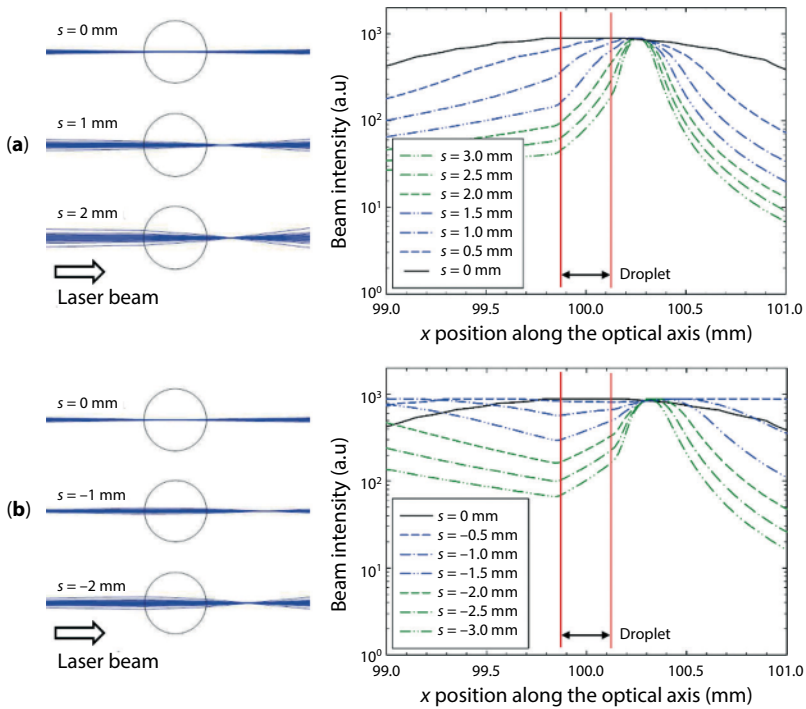


**Figure 9.8** Beam intensity distribution along the optical axis for the exterior/interior region of the droplet (droplet diameter  $D = 300 \mu\text{m}$ ); (a)  $s > 0$  and (b)  $s < 0$  ( $s$ : relative position of the droplet).

initial stage (e.g., see the shadowgraph image  $0.2 \mu\text{s}$  after laser pulse firing in Figure 9.7(a)). In Figure 9.8(a), beam intensity distributions on the interior and exterior of the droplet were calculated using the ray-tracing results by varying the  $s$  value in the positive region. With increasing the

$s$  value, the beam intensity gradient along the optical axis increased. This means that the beam intensity in the shadow side region was large enough to induce optical breakdown of water. Consequently, diverging liquid jets were emitted from the shadow side surface. The overall timescale of jet ejection, i.e., the pulse width of the jet, ranged from 1 to 10  $\mu\text{s}$  and the average jet speed was estimated from a moving distance during 1  $\mu\text{s}$ , and varied around 1000 m/s depending on  $s$  and  $E$ . For fixed  $E = 33$  mJ, the maximum jet speed of approximately 1300 m/s was obtained for  $s > 0$ , with a relatively large divergence angle of  $\sim 40^\circ$ .

For negative values of  $s$  ( $s = -1$  mm), i.e., when the droplet was placed behind the laser beam focus, a relatively thin converging or collimated liquid jet formed on the shadow side of the droplet (Figure 9.7(c)). In this case, the backward splash was conical and had a wide divergence angle. The laser beam, whose intensity was weakened by LIB of air, was distributed inside the droplet narrowly and initiated plasma generation close to its shadow surface. When the plasma expanded, the small amount of liquid close to the shadow surface of the droplet was pushed in the forward direction and formed a thin forward jet. In Figure 9.8(b), beam intensity distributions across the droplet are displayed. The beam intensity has a relatively uniform distribution compared with  $s > 0$  cases. After ignition of the LIP at the shadow side of the droplet, the LIP propagated rapidly to the illuminated side because of a gradual distribution of the beam intensity, resulting in narrow and widely-distributed LIP in the droplet. At an optimized  $s$  value ( $< 0$ ), nearly collimated liquid jets could be produced. When the position of a droplet became more negative ( $s = -3$  mm), the conditions necessary to generate a diverging forward jet, similar to those for positive  $s$ , were generated (Figure 9.7(d)). In this case, the beam intensity distribution is steeper than for cases of  $s \approx 0$  (Figure 8(b)) and the jet was ejected only from the shadow side of the droplet as in case of  $s > 0$ .

The jet speed varied around 1000 m/s depending on  $s$  and  $E$ . Generally, laser-generated liquid jet has the maximum speed when a high intensity LIP is located on the droplet such as at  $s > 0$ . Figure 9.9 shows the dependence of the liquid jet speed on  $E$  and  $s$ . The speed depends on these two parameters because these two parameters determine the location and intensity of the LIP. At fixed  $s = 3.5$  mm, laser energy of  $E = 300$  mJ was an optimum and produced  $x$ -directional liquid jet of  $\sim 1200$  m/s with  $\sim 40^\circ$  diverging angle (Figure 9.9(a)). It is notable that the jet speed decreased slightly with  $E$  for  $E > 300$  mJ because the divergence angle increased. At a fixed value of  $E$ , as mentioned above, dynamics (jet speed and divergence angle) depended strongly on  $s$  (Figure 9.9(b)). Jet speed and divergence angle varied from 500 to 1400 m/s and from  $7^\circ$  to  $45^\circ$ , respectively. Consequently, relatively high-speed liquid

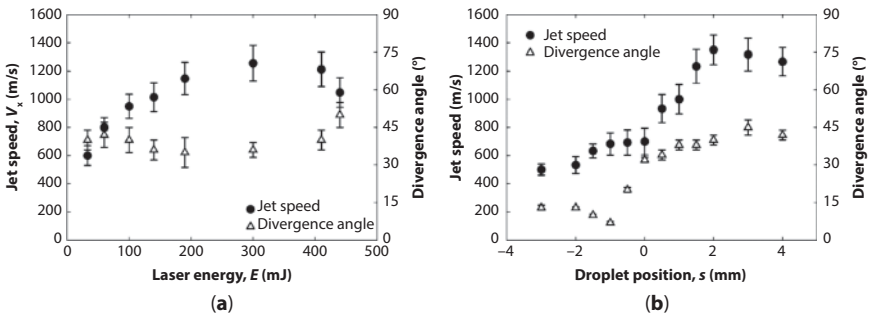


**Figure 9.9** Jet speed and divergence angle as function of (a) incident laser energy  $E$  at  $s = 3.5$  mm and (b) the position of the droplet relative to the laser focus  $s$  with  $E = 100$  mJ.

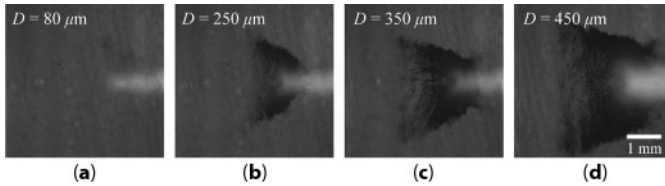


**Figure 9.10** Shadowgraph images of laser-generated liquid jets for different droplet diameters  $D$ ; (a) 80, (b) 250, (c) 350, and (d) 450  $\mu\text{m}$  (time after laser pulse firing  $\tau = 2 \mu\text{s}$ , relative position of the droplet  $s = 1$  mm, incident laser energy  $E = 400$  mJ).

jets with large divergence angle, which are suitable for surface cleaning applications, are produced with  $s > 0$ . On the contrary, converging liquid jets suitable for micromachining are produced with  $s \approx -1$  mm.

### 9.5.2.3 Effect of Droplet Size ( $D$ )

The effect of  $D$  was not critical in determining the overall jet dynamics (Figure 9.10). When producing liquid jets from droplets of  $D = 250$ , 350, and 450  $\mu\text{m}$ , jet speed in each case was varied slightly but divergence feature was similar. Beam intensity distributions along the normalized coordinate are also similar even when varying the droplet sizes as 200, 300, and 400  $\mu\text{m}$  (Figure 9.11). It is noted that a spatial distribution of the beam intensity governs the droplet opto-hydrodynamic phenomena. However, when  $D$  fell below a critical value for a given  $E$ , the droplet exploded completely, ejecting a uniformly distributed vapor plume (Figure 9.10(a)). Consequently, the optimal condition for highest jet speed is that  $s$  is set to be positive and the droplet size is larger than the critical value for complete explosion for a given  $E$ .

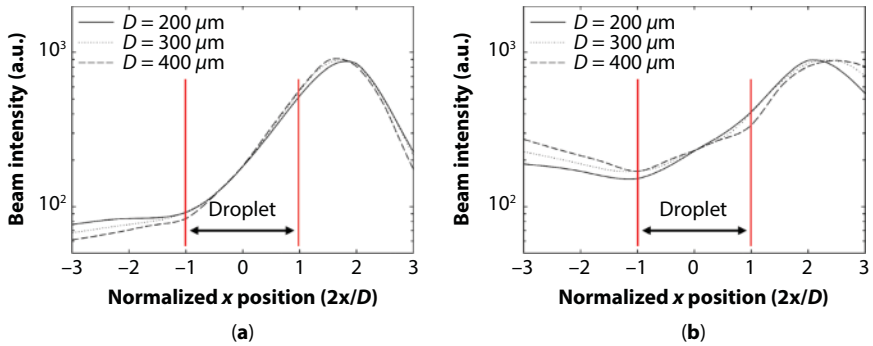


**Figure 9.11** Beam intensity distribution along the normalized  $x$  position for various diameters  $D$  of the droplet at (a)  $s = 2$  mm and (b)  $s = -2$  mm ( $s$ : relative position of the droplet).

## 9.6 Nanoscale Particle Removal

### 9.6.1 Experimental Setup

The performance of the droplet opto-hydrodynamic cleaning (DOC) technique was tested for particles as small as 10 nm [31,33]. In the experiment, cleaning samples were prepared using 20 ~ 300 nm-sized polystyrene latex (PSL) particles and 10 ~ 50 nm-sized alumina ( $\text{Al}_2\text{O}_3$ ) particles. The particles were suspended in de-ionized (DI) water and dispersed for 24 hours with magnetic stirring followed by 30 minutes of ultrasonic agitation. Both spin-coating and dip-coating methods were employed to deposit the particles on silicon wafers. The sample was then dried for 12 hours before the cleaning test. For surface analysis, optical microscopy, field emission scanning electron microscopy (FE-SEM) and atomic force microscopy (AFM) were used.

### 9.6.2 Optimization of Micro-Spray Jet

The opto-hydrodynamics was analyzed and optimized for cleaning experiments (to maximize the jet speed and divergence angle). Figure 9.12(a) shows the  $E$  dependence of the opto-hydrodynamics. Increasing the laser energy shifted the center of the laser-induced plasma (LIP) to the laser irradiation side. At a relatively low laser energy (e.g.,  $E = 30$  mJ), a liquid jet with a relatively large divergence angle was emitted from the shadow side of the droplet surface. A high laser energy (e.g.,  $E = 200$  mJ) generated a

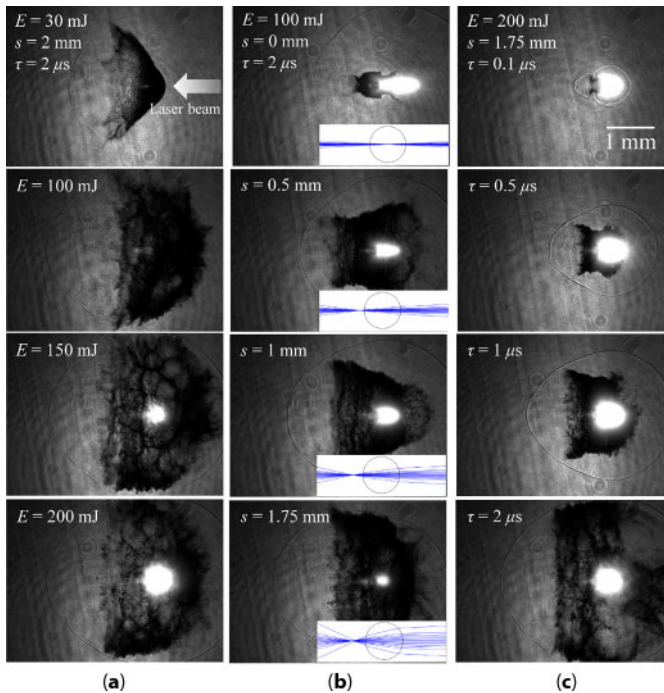


**Figure 9.12** Shadowgraph images for varying (a) incident laser energy  $E$ , (b) relative position of the droplet  $s$ , and (c) time after laser pulse firing  $\tau$ .

radially spreading spray liquid jet. As explained earlier, the opto-hydrodynamic phenomena were highly sensitive to the relative position of the droplet ( $s$ ). As  $s$  increased, the center of the LIP moved to the shadow side of the droplet. Accordingly, liquid jets with a narrow divergence angle,  $s = 0$ , or a wide divergence angle,  $s = 1.75$  mm, could be produced (Figure 9.12(b)). An optimal cleaning process was developed by optimizing the position  $s$  to produce a uniformly spreading high-speed liquid jet. The jet dynamics under these conditions ( $s = 1.75$  mm) was visualized, as shown in Figure 9.2(c). The liquid jet generated at  $E = 200$  mJ and  $s = 1.75$  mm propagated a distance greater than 2 mm for 2  $\mu$ s. As the jet spread out, it was broken up into a number of micrometer-sized atomized droplets because of the flow instability. The density of the atomized droplets in the spray jet decreased with the jet propagation distance because the jet spread out radially (Fig 9.12(c)).

Movement along the  $y$ -direction, which corresponded to the transition time, was measured using shadowgraph images over the interval

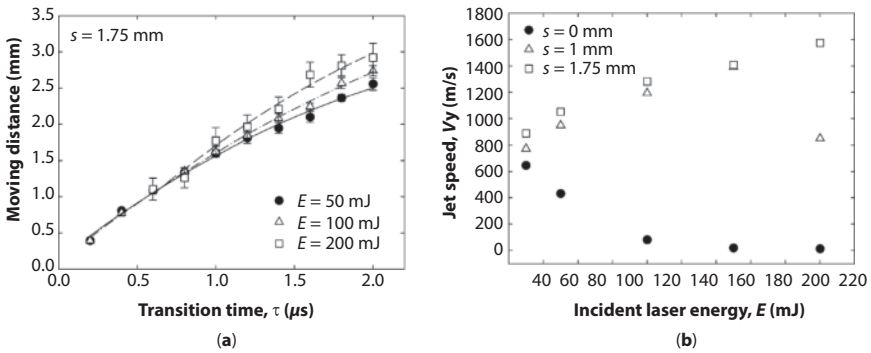


**Figure 9.13** (a)  $y$ -Directional movement of a liquid jet ( $s = 1.75$  mm) and (b) jet speed of the liquid jet as a function of the incident laser energy  $E$  at 1 mm from the center of the droplet.

$\tau = 0.2\text{--}2$   $\mu\text{s}$  (Figure 9.13(a)). The jet speed after moving 1 mm from the center of the droplet was calculated from the moving distance with a least-squares curve fit (Figure 9.13(b)). The jet speed was fully coupled to the process parameters  $E$  and  $s$ . For the case of  $s = 0$ , as shown in Figure 9.12(b), mainly  $x$ -directional moving jet was produced at  $E = 100$  mJ. In this case, the  $y$ -directional jet speed ( $V_y$ ) was maximized at the lowest laser energy ( $E = 30$  mJ), near the breakdown threshold energy of the droplet, as air breakdown occurred in the illuminated side of the droplet when  $E$  became larger than the optical breakdown threshold of air for  $E \geq 30$  mJ in the present case. LIP in the ambient air absorbed a substantial portion of the pulse energy and the plasma intensity in the droplet decreased with  $E$ . For the case of  $s = 1.75$  mm,  $V_y$  of the liquid jet was proportional to the incident laser energy, reaching a maximum value of 1600 m/s (Figure 13(b)).  $V_y$  of the liquid jet for the case of  $s = 1$  mm was also proportional to the incident laser energy over the range of 30–150 mJ. Over this laser energy range,  $V_y$  decreased because the center of the LIP moved toward the laser irradiation side and the laser energy was lost due to air breakdown.

The spray jet generated at  $E = 200$  mJ and  $s = 1.75$  mm propagated radially (Figure 9.14). In initial stage of the LIB, shockwave propagated ahead of the laser-generated liquid jet, but the speed of shockwave decreased rapidly and liquid jet caught up with the shockwave front in 2  $\mu\text{s}$  (Figure 9.14(f)). Accordingly, in the DOC process with  $h = 1$  mm, the airborne shockwave impacts the contaminant before the atomized droplets in the jet strike the particles.

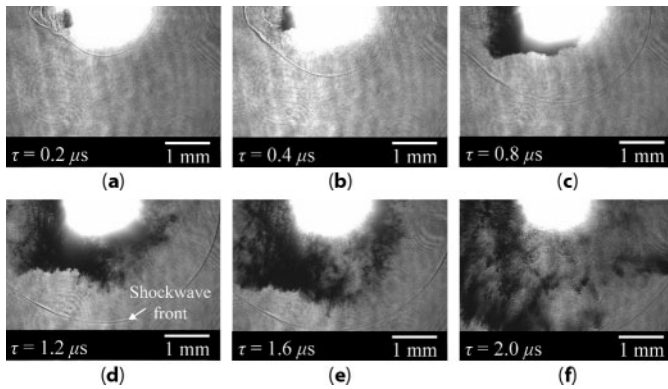


**Figure 9.14** Shadowgraph images of radially spreading liquid jet for varying transition time  $\tau$ ; (a) 0.2, (b) 0.4, (c) 0.8, (d) 1.2, (e) 1.6, and (f) 2.0  $\mu\text{s}$  (relative position of the droplet  $s = 1.75$  mm, incident laser energy  $E = 200$  mJ).

### 9.6.3 Effect of Process Parameters

The effects of the process parameters on the particle removal efficiency were determined by varying the incident laser energy ( $E$ ), the relative position of the droplet ( $s$ ), the gap distance between the droplet and the surface ( $h$ ), and the pulse number ( $R$ ), as shown in Figures 9.15 and 9.16. The largest 300 nm PSL particles were used in these parametric studies for the ease of particle counting. Optical microscope images of the contaminated surfaces of the silicon wafer samples before and after the cleaning process were captured to quantify the cleaning performance by calculating the particle removal efficiency (PRE),

$$\text{PRE} = \frac{n_b - n_p - n_0}{n_b - n_0} \times 100(\%) \quad (9.4)$$

where  $n_b$  is the number of particles after particle deposition,  $n_p$  the number of particles after cleaning and  $n_0$  the number of initially existing particles before particle deposition.

The 300 nm PSL particles were perfectly removed by impingement of a 1300 m/s jet at  $E = 100$  mJ,  $s = 1.75$  mm,  $h = 1$  mm, and  $R = 10$  (Figure 9.15(d)). Moreover, the impingement of a 900 m/s jet at  $E = 30$  mJ removed 300 nm particles with a 95 % efficiency (Figure 9.16(a)). As  $s$  decreased to 0 or  $-1$  mm, the  $y$ -directional speed of the liquid jet reached a minimum and the cleaning efficiency decreased because only

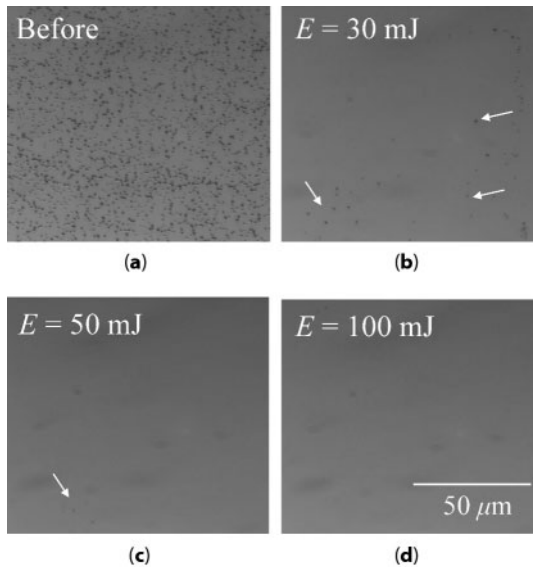


**Figure 9.15** Optical microscope images of Si wafer surface; (a) before cleaning, (b) after cleaning with pulse energy  $E = 30$  mJ, (c)  $E = 50$  mJ, and (d)  $E = 100$  mJ (relative position of the droplet  $s = 1.75$  mm, gap distance  $h = 1$  mm, pulse number  $R = 10$ ).

the airborne shock wave from the LIP affected the removal of particles (Figure 9.16(b)). The performances of conventional laser shock cleaning (LSC) processes decrease as the gap distance between the center of an LIP and the contaminated surface increases. The PRE of the DOC process also decreased with  $h$  because the speed of the radially spreading jet as well as the density of the atomized droplets decrease with the propagation distance (Figure 9.16(c)). The cleaning efficiency decreased to 70% at  $h = 2$  mm, even for a jet speed exceeding 1000 m/s. Liquid jets with radially spreading over long distances could not effectively remove contaminants. The optimal conditions for nanoparticle removal,  $V_y \geq 1000$  m/s and  $h \leq 1$  mm, removed 300 nm PSL particles above a 95% efficiency using only 5 pulses (Figure 9.16(d)).

The droplet opto-hydrodynamic process with  $s = 0$  performed much better than the conventional LSC method, even though the  $y$ -directional speed of the liquid jet was minimized. The shock wave intensity previously limited the performances of LSC processes. Amplifying the laser-induced airborne shock wave via the breakdown of a liquid column/droplet increased the cleaning efficiency [30]. Similarly, the droplet increased the shock wave intensity substantially in the opto-hydrodynamic process and



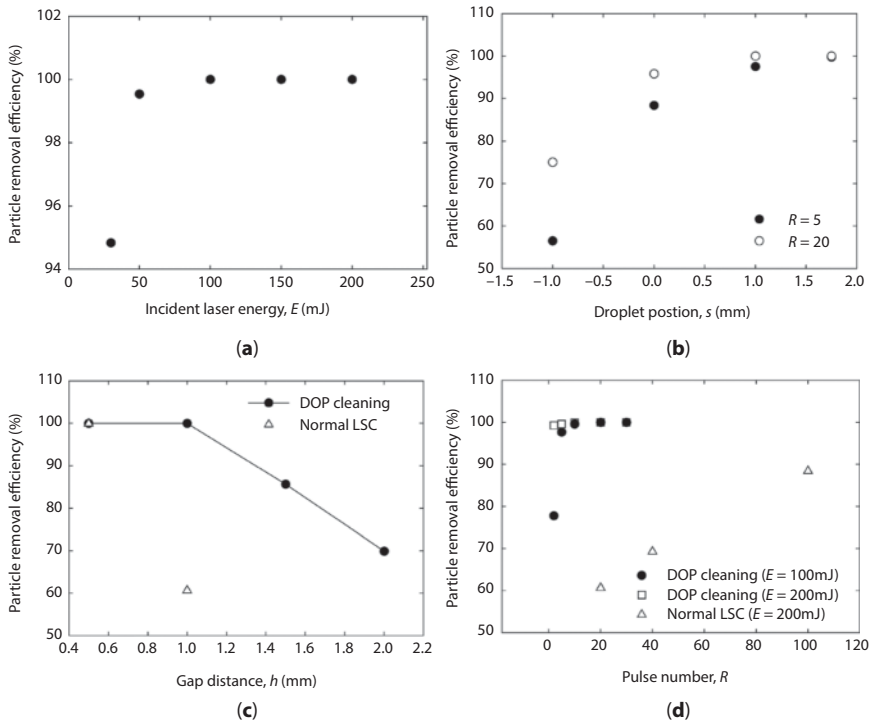
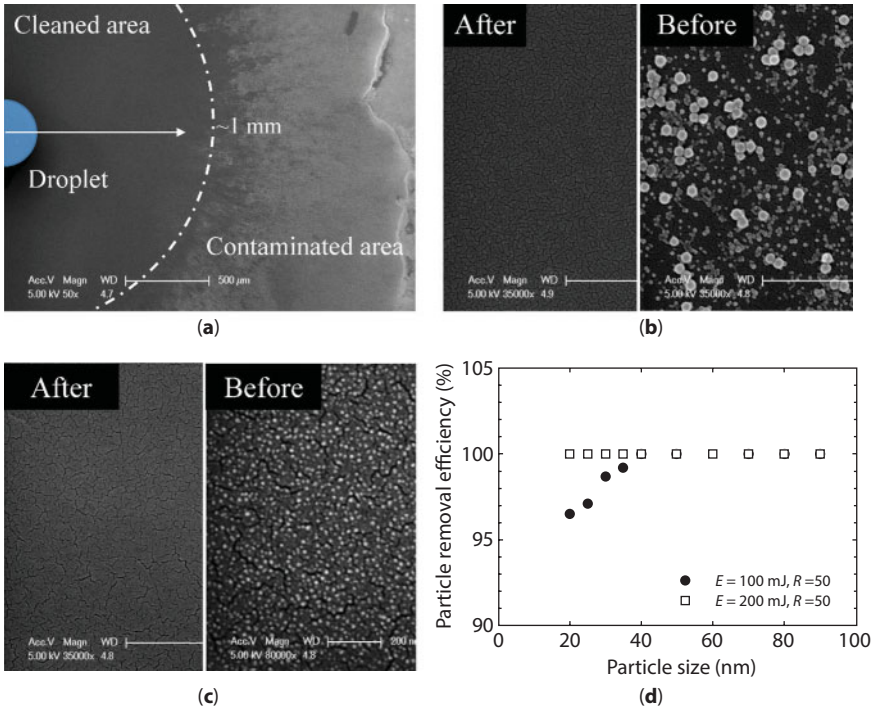


Figure 9.16 Particle removal efficiency (300 nm PSL) as a function of the process parameters; (a) as a function of  $E$  ( $s = 1.75$  mm,  $h = 1$  mm, and  $R = 10$ ), (b) as a function of  $s$  ( $E = 200$  mJ,  $h = 1$  mm), (c) as a function of  $h$  ( $E = 200$  mJ,  $s = 1.75$  mm,  $R = 20$ ), and (d) as a function of  $R$  ( $s = 1.75$  mm,  $h = 1$  mm).

nanoparticles were removed via both the impingement of a high-speed liquid jet and the force of the enhanced shock wave from the droplet. Nevertheless, the impingement and subsequent surface flows of high-speed liquid jet, consisted of droplets a few micrometers in size, played a principal role in detaching the nanoparticles from the surface because the density, i.e., the drag force, of water is greater than that of air by three orders of magnitude.

#### 9.6.4 Sub-100 nm Particle Cleaning

The limits of the cleaning performance were tested by attempting to clean Si wafers contaminated with sub-100 nm particles, including 20–90 nm PSL particles and  $\text{Al}_2\text{O}_3$  particles less than 50 nm in diameter. Confirming that the estimated hydrodynamic drag force exerted on a 10 nm particle is



**Figure 9.17** SEM images of (a) the cleaned area and the contaminated surfaces; (b) before and after removal of 30–90 nm PSL particles, and (c) before and after cleaning the 20 nm PSL particles at incident laser energy  $E = 200 \text{ mJ}$ , gap distance  $h = 1 \text{ mm}$ , relative position of the droplet  $s = 1.75 \text{ mm}$ , pulse number  $R = 50$ , and (d) particle removal efficiency as a function of the PSL particle size.

on the order of  $10^{-8}$ – $10^{-7} \text{ N}$  at 1000 m/s whereas the van der Waals adhesion force is on the order of  $10^{-9} \text{ N}$  [7], the particles could be removed by the hydrodynamic drag exerted by the 1000 m/s liquid jet. As shown in Figure 9.17(a), the radially spreading high-speed liquid jet was effective over a radius of 1 mm from the center of the droplet. PSL particles 20–90 nm in diameter were completely removed by multiple 1600 m/s liquid jets obtained under optimized conditions:  $E = 200 \text{ mJ}$ ,  $s = 1.75 \text{ mm}$ ,  $h = 1 \text{ mm}$ , and  $R = 50$ . As the jet speed decreased to 1300 m/s at  $E = 100 \text{ mJ}$ , PSL particles above 40 nm in diameter were completely removed, whereas smaller PSL particles 20–40 nm in size were removed with a 95 % removal efficiency (Figure 9.17(d)).

$\text{Al}_2\text{O}_3$  particles less than 50 nm in diameter were more adhesive than PSL particles of the same size [42]. The removal of  $\text{Al}_2\text{O}_3$  particles required more cleaning cycles with 1600 m/s liquid jets (Figure 9.18). It was shown

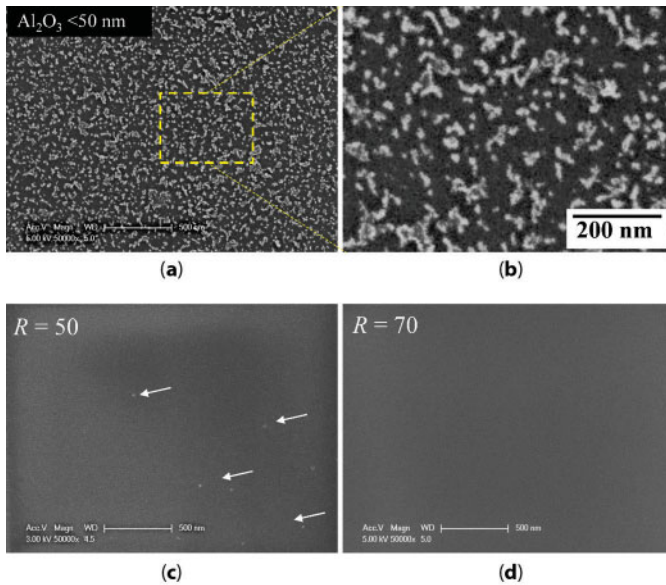


**Figure 9.18** SEM images of surfaces contaminated with 10–50 nm  $\text{Al}_2\text{O}_3$  particles; (a) before cleaning, (b) enlarged for showing the deposition of 10 nm particles, (c) after removing the 10–50 nm particles at incident laser energy  $E = 200 \text{ mJ}$ , relative position of the droplet  $s = 1.75 \text{ mm}$ , pulse number  $R = 50$ , and (d) after cleaning with  $E = 200 \text{ mJ}$ ,  $s = 1.75 \text{ mm}$ ,  $R = 70$ .

that some  $\text{Al}_2\text{O}_3$  particles less than 10 nm in diameter existed in the samples, but most of the particles were in the range of 10–50 nm in diameter (Figures 9.18(a) and 9.18(b)). Figure 9.18(c) shows that some particles, indicated with dashed lines, remained in place even after 50 iterations of jet impingement. Increasing the number of jet impingements to  $R = 70$  removed all  $\text{Al}_2\text{O}_3$  particles smaller than 50 nm over an approximately 1 mm diameter region relative to the center of the droplet (Figure 9.18(d)). These results were confirmed by tapping-mode AFM, and no particles were found on the surface after cleaning (Figure 9.19). These results show that the DOC technique is an effective physical cleaning tool for nanoscale contamination control, especially removal of particles as small as 10 nm. In comparison with the recently developed  $\text{CO}_2$  aerosol cleaning process [7], which also removed 10 nm particles from Si surfaces successfully, the DOC process is simple and cost effective because it does not require complex cryogenic/vacuum equipment. An obvious drawback of DOC is that it is not a completely dry process although only a minuscule amount of water is used in the process.

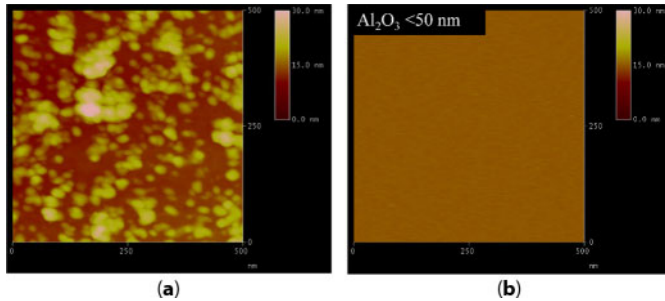


**Figure 9.19** AFM images of surfaces contaminated with  $\text{Al}_2\text{O}_3$  particles smaller than 50 nm (a) before cleaning and (b) after cleaning (incident laser energy  $E = 200$  mJ, relative position of the droplet  $s = 1.75$  mm, pulse number  $R = 70$ ).

## 9.7 Summary

As control of nanoscale contamination has been of crucial importance in various industrial sectors including semiconductor and microelectronics, intensive efforts are exerted to develop powerful cleaning technology. Especially, development of an effective physical cleaning method that can remove particles as small as 10 nm from a solid surface has become a key issue. In this chapter, a recently developed cleaning process, entitled DOC (Droplet Opto-hydrodynamic Cleaning), is described in detail. The opto-hydrodynamic process of micro-liquid jet generation using optical breakdown of a micro droplet has been optimized and tested for the removal of 20 ~ 300 nm PSL nanoparticles and 10 ~ 50 nm alumina ( $\text{Al}_2\text{O}_3$ ) particles. A radially spreading spray jet was obtained by controlling the incident laser energy and the position of the droplet relative to the focal point, and speed reached a maximum of ~1600 m/s. The direct impingement of the atomized droplet in the spray and the resultant surface flows provided the primary forces for removing 10 nm particles. The airborne shock wave developed cleaning process could completely remove 20 nm PSL and 10 nm alumina particles from the Si surface. Consequently, the laser-induced spray cleaning technique has a strong potential in nanoscale particle removal as a “semi-dry” process.

## References

1. International Technology Roadmap for Semiconductors (ITRS), <http://www.itrs.net/Links/2012ITRS/Home2012.htm> (2012).
2. W. Kern (Ed.) *Handbook of Semiconductor Wafer Cleaning Technology: Science, Technology, and Applications*, Noyes Publications, Park Ridge, NJ (1993).

3. K. L. Mittal (Ed. ) *Particles on Surfaces 8 : Detection, Adhesion and Removal*, CRC Press, Boca Raton, FL (2003).
4. K. L. Mittal (Ed. ) *Particles on Surfaces 9 : Detection, Adhesion and Removal*, CRC Press, Boca Raton, FL (2006).
5. G. Vereecke, F. Holsteyns, S. Arnauts, S. Beckx, P. Jaenen, K. Kenis, M. Lismont, M. Lux, R. Vos, J. Snow, and P. W. Mertens, .Evaluation of megasonic cleaning for sub-90 nm technologies. *Solid State Phenom.* 103–104, 141 (2005).
6. R. Sherman, .Carbon dioxide snow cleaning. *Particulate Sci. Technol.* 25, 37 (2007).
7. I. Kim, K. Hwang, and J.-W. Lee, .Removal of 10-nm contaminant particles from Si wafers using CO<sub>2</sub> bullet particles. *Nanoscale Res. Lett.* 7, 211 (2012).
8. A. C. Tam, W. P. Leung, W. Zapka, and W. Ziemlich, . Laser-cleaning techniques for removal of surface particulates. *J. Appl. Phys.* 71, 3515 (1992).
9. X. Wu, E. Sacher and M. Meunier, .The modeling of excimer laser particle removal from hydrophilic silicon surfaces. *J. Appl. Phys.* 87, 3618 (2000).
10. D. Grojo, A. Cros, Ph. Delaporte and M. Sentis, .Experimental investigation of ablation mechanisms involved in dry laser cleaning. *Appl. Surf. Sci.* 253, 8309 (2007).
11. H. Park, C. P. Grigoropoulos, W. P. Leung and A. C. Tam, .A practical excimer laser-based cleaning tool for removal of surface contaminants. *IEEE Trans. Component Packaging A* 17, 631 (1994).
12. W. Zapka, A. C. Tam, G. Ayers, and W. Ziemlich, .Liquid film enhanced laser cleaning. *Microelectron. Eng.* 17, 473 (1992).
13. A. C. Tam, H. Park, P. Costas and C. P. Grigoropoulos, .Laser cleaning of surface contaminants. *Appl. Surf. Sci.* 127–129, 721 (1998).
14. M. Mosbacher, V. Dobler, J. Boneberg, and P. Leiderer, .Universal threshold for the steam laser cleaning of submicron spherical particles from silicon. *Appl. Phys. A* 70, 669 (2000).
15. J. Lee and K. Watkins, .Removal of small particles on silicon wafer by laser-induced airborne plasma shock waves. *J. Appl. Phys.* 89, 6496 (2001).
16. I. Varghese and C. Cetinkaya, .Non-contact removal of 60-nm latex particles from silicon wafers with laser-induced plasma. *J. Adhesion Sci. Technol.* 18, 795 (2004).
17. B. Oh, J.-W. Lee, J.-M. Lee and D. Kim, .Numerical simulation of laser shock cleaning process for micro-scale particle removal. *J. Adhesion Sci. Technol.* 22, 635 (2008).
18. D. Jang, J. Lee, J.-M. Lee and D. Kim, .Visualization of particle trajectories in the laser shock cleaning process. *Appl. Phys. A* 93, 147 (2008).
19. X. Y. Wang, R. K. Kang, W. J. Xu, D. M. Guo, and J. Wang, .Laser cleaning of fine particles on Si-wafers, AIP Conference Proc. 1315, p. 1588 (2010).
20. M. Mosbacher, H. J. Munzer, J. Zimmermann, J. Solis, J. Boneberg, and P. Leiderer, .Optical field enhancement effects in laser-assisted particle removal. *Appl. Phys. A* 72, 41 (2001).

21. D. Jang, J.-H. Oh, J.-M. Lee, and D. Kim, .Enhanced efficiency of laser shock cleaning process by geometrical confinement of laser-induced plasma. *J. Appl. Phys.* 106, 014913 (2009).
22. A. Guha, R. M. Barron and R. Balachandar, .An experimental and numerical study of water jet cleaning process. *J. Mater. Process. Technol.* 211, 610 (2011).
23. N. Findanis and M. Southam, .Control and management of particulate emissions using improved reverse pulse-jet cleaning systems. *Procedia Eng.* 49, 228 (2012).
24. T. Yoneda, H. Hoko, E. Hoshino, T. Ogawa, S. Okazaki, Y. Isobe, T. Matsumoto, and T. Mizoguchi, .Evaluation of cleaning techniques for EUVL mask by using a highly sensitive particle detection system. *Microelectron. Eng.* 61–62, 213 (2002).
25. Y. Seike, K. Miyachi, T. Shibata, Y. Kobayashi, S. Kurokawa, and T. Doi, .Silicon wafer cleaning using new liquid aerosol with controlled droplet velocity and size by rotary atomizer method. *Jpn. J. Appl. Phys.* 49, 066701 (2010).
26. J. T. Snow, M. Sato and T. Tanaka, Dual-fluid spray cleaning technique for particle removal, in *Developments in Surface Contamination and Cleaning*, Vol. 6, R. Kohli and K. L. Mittal (Eds.) pp. 107–138 Elsevier, Oxford, UK (2013).
27. J. Thietje, Semiconductor wafer cleaning system, US Patent 5,468,302 (1995).
28. A. Nakagawa, T. Hirano, M. Komatsu M. Sato, H. Uenohara, H. Ohyama, Y. Kusaka, R. Shirane, K. Takayama and T. Yoshimoto, .Holmium: YAG laser-induced liquid jet knife: Possible novel method for dissection. *Laser Surg. Med.* 31, 129 (2002).
29. H. Jang, M. Park, F. V. Sirotkin and J. Yoh, .Laser-induced microjet: Wavelength and pulse duration effects on bubble and jet generation for drug injection. *Appl. Phys. B* 10, 00340 (2013).
30. D. Jang, J.-G. Park, and D. Kim, .Enhancement of airborne shock wave by laser-induced breakdown of liquid column in laser shock cleaning. *J. Appl. Phys.* 109, 073101 (2011).
31. D. Ahn, D. Jang, T.-Y. Choi and D. Kim, .Surface processing technique based on opto-hydrodynamic phenomena occurring in laser-induced breakdown of a microdroplet. *Appl. Phys. Lett.* 100, 104104 (2012).
32. D. Ahn, C. Seo and D. Kim, .Removal of metals and ceramics by combined effects of micro liquid jet and laser pulse. *J. Appl. Phys.* 112, 124916 (2012).
33. D. Ahn, J. Ha and D. Kim, .Development of an opto-hydrodynamic process to remove nanoparticles from solid surfaces. *Appl. Surf. Sci.* 265, 630 (2013).
34. P. K. Kennedy, D. X. Hammer and B. A. Rockwell, .Laser-induced breakdown in aqueous media. *Prog. Quantum Electron.* 21, 155 (1997).
35. D. E. Lencioni, .Laser-induced air breakdown for 1.06- $\mu\text{m}$  radiation. *Appl. Phys. Lett.* 25, 15 (1974).
36. J. H. Eickmans, W.-F. Hsieh and R. K. Chang, .Laser-induced explosion of  $\text{H}_2\text{O}$  droplets: Spatially resolved spectra. *Opt. Lett.* 12, 22 (1987).

37. F. Docchio, C. A. Sacchi and J. Marshall, .Experimental investigation of optical breakdown thresholds in ocular media under single pulse irradiation with different pulse durations. *Lasers Ophthalmol.* 1, 83 (1986).
38. P. K. Kennedy, S. A. Boppart, D. X. Hammer, B. A. Rockwell, G. D. Noojin and W. P. Roach, .First -order model for computation of laser- induced breakdown thresholds in ocular and aqueous media: Part II -comparison to experiment. *IEEE J. Quantum Electronics* 31, 2250 (1995).
39. A. Vogel, K. Nahen, D. Theisen and J. Noack, .Plasma formation in water by picosecond and nanosecond Nd: YAG laser pulses. I. Optical breakdown at threshold and superthreshold irradiance. *IEEE J. Selected Topics Quantum Electron.* 2, 847 (1996).
40. K. K. Haller, Y. Ventikos and D. Poulikakos, .Computational study of high-speed liquid droplet impact. *J. Appl. Phys.* 92, 2821 (2002).
41. A. S. Grinspan and R. Gnanamoorthy, .Impact force of low velocity liquid droplets measured using piezoelectric PVDF film. *Colloids Surfaces A* 356, 162 (2010).
42. M. B. Ranade, .Adhesion and removal of fine particles on surfaces. *Aerosol Sci. Technol.* 7, 161 (1987).





# Wiper-Based Cleaning of Particles from Surfaces

Brad Lyon and Jay Postlewaite\*

*Texwipe, An ITW Company, Kernersville, NC, USA*

---

## Abstract

Wiper-based cleaning of surfaces is one of the most effective methods to physically remove surface contamination such as particles from cleanroom processes and environments in a controlled manner. Other methods of particle cleaning are available like poly(vinyl alcohol) (PVA) brushing of surfaces, carbon dioxide snow blasting of surfaces, and acoustic energy cleaning. However, these methods are not transferable to typical cleanroom surfaces, which require frequent cleaning to protect the process and product. The wiper's particle and fiber contamination characteristics are affected by the raw material type, fabric construction, and edge type. Procedures to assess a wiper's particle and fiber contamination levels are described. The decision in selecting a wiper uses this information in conjunction with an understanding of how and where the wiper will be used in the process or critical or controlled environment. The technique for using a wiper properly is presented. The mechanism for particle removal by using a wiper is proposed. This mechanism includes the interaction of the wiper at the filament level with the particle adhering to the surface. As the filament pushes against the particle, the forces causing the particle to adhere to the surface decrease as the particle begins to establish adhesion forces with the wiper filament. The wiper-based cleaning efficiency was measured on three different types of surfaces. It was found that the cleaning efficiency was highest for larger particle size ranges and decreased as the particle size range decreased. The use of pre-wetted wipers for cleaning yielded higher cleaning efficiencies than the use of dry wipers.

---

\*Corresponding author: [jpostlewaite@texwipe.com](mailto:jpostlewaite@texwipe.com)

**Keywords:** Wiper, Wiper-based cleaning, surface cleaning, particle and fiber contamination removal, and surface particle removal

## 10.1 Introduction

Technological advances in the high-end microelectronics, semiconductor chip and disk drive, life science, medical device, biologics, and pharmaceutical areas require the use of extremely clean environments in which to manufacture products. Cleanrooms are constructed to maintain extremely clean process areas to reduce the environmental impact to the manufacturing process. In the life science industries, environmental cleanliness is essential to minimize the safety risk of the product to the patient receiving the medication or medical device. As pharmaceutical active ingredients get more potent, the risk from cross-contamination becomes more important for the patient. Also, these potent products require that the manufacturing personnel are protected from the product. Because of these issues, manufacturers spend significant resources to construct and maintain cleanroom environments which require complex air handling and monitoring systems. These systems are required to maintain the airborne contamination levels at the ISO class level desired and specified for optimum operation.

While knowing the airborne contamination level status of the cleanroom is critical to minimize the risks to the patient and cleanroom personnel, it is not sufficient for a continuing operation. As a cleanroom is used, personnel, equipment, materials and consumables enter and leave the cleanroom. To maintain acceptable contamination levels in a cleanroom, operational controls, procedures and protocols must be set up and validated to ensure that surfaces, equipment, instrumentation, and, most importantly, people do not inadvertently contribute contaminants to the cleanroom environment. Added contaminant burden risks the product or personnel.

### 10.1.1 Why Wipe?

To keep the cleanroom environment in operational condition, contamination must be removed from the more critical areas in the cleanroom to minimize contamination risk. Physical methods include vacuuming, blowing compressed gas, irrigating with a liquid, ultra- and megasonics, and wiping. Cleaning surfaces by wiping is one of the most effective methods to physically remove contamination. While other methods may be used, they tend to have side effects that may further compromise the environmental contamination in the room with some actually scattering contamination throughout the cleanroom. Wiping is most effective because it serves

to physically capture and hold contaminants in place, without spreading them further. A variety of surfaces need to be wiped that have various shapes, sizes and materials and are in cleanrooms that are certified to be operational at various ISO classes.

### 10.1.2 Particle Cleanliness

It is important to remove particle contamination from surfaces for several reasons. Particles may damage the process equipment or product through surface effects like corrosion and scratching or cause short-circuiting. A particle may actually be a microbe or be a food source and encourage microbial growth. They may attract other contaminants, may be a safety risk to workers or patients as fine particles of high potency active pharmaceutical ingredients, or promote damage to optical surfaces in imaging equipment.

A number of techniques have been used for particle removal from a variety of surfaces [1,2,3]. Examples of removing particles from surfaces include, but are not limited to, the use of a poly(vinyl alcohol) (PVA) brush for surfaces, carbon dioxide (CO<sub>2</sub>) snow to clean equipment and parts, acoustics for cleaning of surfaces of parts, and wipers for removing particles and other contaminants from surfaces. Particles and other contaminants must be removed from the process, equipment, environment, and the product. If not, the product yield or environment may be adversely impacted.

#### 10.1.2.1 PVA Brush for Cleaning Silicon Wafers

Particles on a wafer surface will interfere with the next stage in microchip manufacturing. Examples of interferences are a metal particle, which allows conduction between two circuit traces, or a particle that contains ions, which may chemically modify the wafer surface properties and interfere with the next process step. Removing surface particles and chemical contamination is an integral part of the microelectronic wafer manufacturing process. An example of a slurry-chemical solution combination is found in this patent [4]. The wafers are placed in a device that spins the wafer about its central axis and many wafers are then spun around in a great circle. When the polishing step is completed, the slurry and chemical solution must be removed from the wafer without altering the wafer surface.

A typical wafer cleaning process is using a PVA brush and a water-based cleaning solution. The spinning PVA brush with a water solution flowing from the inside out to the brush surface rubs against the wafer surface to remove the particle contamination from the wafer surface [5]. The particles

are suspended in the solution and are washed away by the water flow. Additives in the water phase modify the zeta potential between the wafer surface and the water phase to increase the repelling forces between the wafer surface, water phase, and brush. The particles are removed from the wafer surface without re-deposition or lodging on the PVA brush and are removed with the water flow from the system. A processed wafer is left particle free ready for the next manufacturing step.

The advantage of this cleaning system is its effectiveness in removing the slurry and other particles from the wafer surface. However, this effective cleaning system is not readily adaptable for cleaning typical worksurfaces found throughout a cleanroom environment.

#### 10.1.2.2 *Carbon Dioxide (CO<sub>2</sub>) Snow Cleaning*

Another system for cleaning surfaces is the use of CO<sub>2</sub> snow. This method can be used on a variety of surfaces including electronic devices. As the device progresses through the manufacturing process, particles and other contaminants require removal from a surface in preparation for the next fabrication step. Carbon dioxide snow cleaning may be used to get into congested areas that other cleaning methods or chemicals cannot.

Carbon dioxide snow uses thermal, mechanical, and the sublimation processes to clean a surface [6]. The snow itself has a temperature around  $-78^{\circ}\text{C}$ . This low temperature freezes the contamination on the surface causing it to contract faster than the surface below it. This loosens the particles from the surface allowing the mechanical process to start. The loose particle is impinged with snow particles that force it off the surface. After being warmed by the surface, the carbon dioxide snow sublimates. During the phase change, expansion occurs, and the loose contaminants are carried away in the gas from the surface. If this process is performed in a water-free environment, the surface is left clean and dry.

The advantage of this process is that it can be used on a variety of surfaces from small, intricate circuit boards to large, flat surfaces. The disadvantage is that the cleaning must be in a contained environment, or the contamination will spread into the air or onto other adjacent surfaces.

#### 10.1.2.3 *Acoustic Cleaning*

Another system for cleaning surfaces is the use of acoustics, ultrasonics and megasonics. This method can be used on a variety of hard surfaces such as metals or plastics making it an excellent cleaning method for silicon wafers [7], optics, electronic equipment, hard disk drive platens, pharmaceutical equipment, and medical devices. Sonic cleaning may be used

on finished components that are compatible with the liquid and are resistant to damage from the acoustic energy.

Sonic cleaning uses the energy from sound waves in a liquid medium with frequencies above human hearing range (>20 kHz). These waves are formed when an alternating voltage is applied to a piezoelectric crystal. The varying voltage causes the crystal to expand and contract. When this crystal is affixed to a metal container or submerged in a liquid medium, the vibrating crystal causes acoustic pressure waves in the liquid medium. The liquid medium is usually water with surfactants added to reduce the surface tension, but it can be other liquids. As the ultrasonic pressure wave travels through the liquid, cavitation bubbles are generated when the pressure in the liquid falls below its vapor pressure. Depending on conditions in the liquid, a bubble can collapse violently. During this collapse or implosion, the surrounding liquid rushes in to fill the void. This rapid flow causes intense shock waves that may be used for cleaning and streaming of the liquid. If these shock waves occur near a particle-contaminated surface, particles may be dislodged from the surface. If the surface is too delicate, surface damage may occur. The streaming liquid moves the particles into the liquid phase away from the surface.

The advantage of using acoustical cleaning is that it can be used on a variety of surfaces from small, intricate surfaces to large, flat surfaces as long as the piece can be submerged into a liquid-containing vessel. The disadvantage is the part to be cleaned must be resistant to the liquid phase solution and the acoustic energy. This cleaning method is difficult to transfer to surfaces found in a production cleanroom unless they are moveable and can be submerged into the cleaning vessel.

#### 10.1.2.4 *Wiper-Based Cleaning*

Wiper-based cleaning is performed (simply) by holding a wiper in a hand and moving the wiper on the surface with firm, overlapping strokes. Because of the physical characteristics of a wiper, its size, shape and how it is used, wiper-based cleaning has distinct advantages over other methods. Wiper-based cleaning is not suitable for all cleaning situations, e.g., a hole in an intricate device. Below is a list of advantages for using wiper-based cleaning to remove surface particles over other cleaning methods:

- Focused cleaning – wipers may be used to clean one surface without contaminating another adjacent surface. Other cleaning methods may impact or further contaminate adjacent surfaces or the entire cleanroom.

- Removed contamination is collected into the wiper. The contaminated wiper and the contained contaminants are easily removed from the cleanroom.
  - Disposal – The method of wiper disposal is controlled by the type and level of contaminants.
  - Reusable – Not recommended, but some wipers may be reused after they undergo a cleaning process.
- A wiper may clean a variety of surfaces both soft and hard. Examples of these surfaces include, but are not limited to:
  - Soft surfaces
    - Notebook covers
    - Outer packaging in preparation for transferring objects into the cleanroom.
    - Furniture, e.g., cleanroom chairs
  - Hard surfaces
    - Walls, floors, windows, and doors
    - Mechanical tools, e.g., hammers
    - Process equipment
    - Other furniture pieces, e.g., tables and carts
- Hard to clean areas can be accessed through the use of a swab, which may be viewed as a small wiper on a handle.
- Wiper selection is dependent on the application or need. The physical and contamination characteristics are dependent upon the construction and composition of the wiper.
- Liquid management - A wiper may be used in spill control, excess liquid application, e. g., allow a liquid to cover a hard-to-remove contaminant to aid in its removal, and cleaning and disinfecting solutions application as long as the solutions are compatible with the wiper material and the surface being cleaned.
- Surface protector – The wiper may serve as a worksurface that may protect the object’s surface from the worksurface, i.e., the object is less contaminated than the worksurface, or protect the worksurface from the object, i.e., the object is more contaminated than the worksurface.
  - Reduce damage to susceptible surfaces. A wiper material may be chosen to prevent or reduce damage to the worksurface.

- Wipers are consumables. No capital investment is required. No on-going mechanical maintenance routine is required like for equipment.
- Wipers are relatively small in size and have a minimal storage requirement.

## 10.2 Basic Mechanism of Wiping for Cleaning of Particles and Other Contaminants

As a cleanroom is used, particles are shed from anything that can enter the cleanroom environment: personnel and equipment or process activity. These particles begin to adhere to all cleanroom surfaces and require removal to maintain the cleanliness level of the cleanroom and to mitigate process or product failures.

### 10.2.1 Why Wiping Works

To understand why wiping is effective in removing contamination from a surface requires the understanding of how contamination adheres to surfaces. The adhesion forces that particles experience are a combination of chemical and physical forces. For a discussion of adhesion forces between contaminant particles and surfaces, the reader should refer to the review by Bowling [8] and by Ranade [9] and are also summarized below. These forces must be overcome to remove particles from surfaces for cleaning to occur. Typical forces are the van der Waals, electrostatic, and capillary forces.

#### 10.2.1.1 *van der Waals (vdW) Forces*

The van der Waals forces [10] are intermolecular forces that arise from the spontaneously changing electron density of molecules. As the electron density changes, there is a formation of an instantaneous dipole moment in the molecule. This dipole moment in one molecule affects the electron clouds of surrounding molecules which may induce dipole moments in them. The dipole moments, because of their orientation, create an attractive force.

The vdW forces increase as particles deform because of increased contact area with the surface. A spherical particle with a diameter of 5  $\mu\text{m}$  has a vdW attraction force of  $7 \times 10^{-7}$  Newton (N). If the particle deforms 1%,

the van der Waals force due to deformation alone is  $1.74 \times 10^{-6}$  N. The total van der Waals force is the sum of these, which, for this example, is  $2.44 \times 10^{-6}$  N. This increase implies that if deformable particles are present, cleaning should be done as soon as possible after the surface is contaminated.

### 10.2.1.2 Electrostatic Forces

Two types of electrostatic forces may be present for particle adhesion to a surface. The first is caused by excess charge on the surface of the substrate. This force is caused by the attraction of charges distributed over the substrate and particle.

As the particle gets smaller, the electrostatic adhesion forces increase. Spinning a silicon wafer disk at  $10^6$  rotations per minute will not remove a  $1 \mu\text{m}$  sized particle. For small particles, adhesion forces range from  $10^{-10}$  to  $10^{-3}$  N, which, for a  $1 \mu\text{m}$  diameter particle, yields a force per unit area in the range from 127 to  $1.27 \times 10^9$  Pa ( $\text{N}/\text{m}^2$ ).

The other electrostatic force is contact potential induced electrical double layer forces. Ranade [9] has a good diagram depicting the distribution of charges and forces around a particle. Two materials in contact with each other will experience a small voltage difference due to electrons moving from one surface to the other until equilibrium is reached. The range of voltage difference is zero to 0.5 volts. At 0.5 V, the force for a  $1 \mu\text{m}$  diameter particle is  $1 \times 10^{-8}$  N.

Another point of view about the mitigation of the electrostatic force effect is given by Reid *et al.* [11] who state that if there is an electrostatic interaction between the surface and contaminant, a wetted wiper effectively neutralizes the electrostatic effect since even pure water is ionized at a low level [12]. Reid *et al.* also state that water that has been in contact with air has even more ions due the absorption of carbon dioxide from the surrounding environment forming the carbonate and bicarbonate ions in solution.

In summary, in a quick comparison of the van der Waals and electrostatic adhesion forces exerted on a particle, the van der Waals forces predominate over the electrostatic forces for very small particles.

### 10.2.1.3 Capillary Forces

Particles also experience the capillary force, which causes an adhesion force between the solid particle and the substrate. This force is a function of the particle radius and the surface tension of the liquid. For a particle with a  $1 \mu\text{m}$  diameter, the force is  $4.6 \times 10^{-7}$  N, which translates to a pressure of  $5.86 \times 10^5$  Pa ( $\text{N}/\text{m}^2$ ).



### 10.2.2 Wiping Mechanisms for Particle Removal

The following mechanism is proposed for removing a particle from a substrate surface when using a wiper for cleaning. In order for a particle to be removed, the adhesion forces between the particle and substrate surface must be overcome by the forces available from the wiper and its motion. The combined adhesion forces represented by  $F_{AD}$  and described above are the van der Waals, electrostatic and capillary forces. Figure 10.1 depicts the various forces available for acting on a particle as a wiper is moving across the surface during cleaning.

When a pre-wetted wiper is used, other forces become available (Figure 10.1b). The drag force,  $F_{Drag}$ , becomes available from the liquid interacting with the particle. The net buoyancy force,  $F_{Bn}$ , arrow indicates the reduction of the particle's weight due to presence of the liquid. The capillary force,  $F_{Capillary}$ , indicated by an upward directed arrow is used to show that if this force was present in  $F_{AD}$  originally, it is cancelled due to the excess liquid that has flowed between the substrate surface and adhered particle. If this force was not present originally, this arrow indicates that the force is not present. In either case,  $F_{Capillary}$  is not present, which reduces the adhesion between the particle and substrate. This makes the removal of particles during cleaning easier. In addition, the vdW force during wet-wiping will be smaller than in the dry-wiping as the presence of liquid medium screens the electromagnetic interactions and hence lowers the

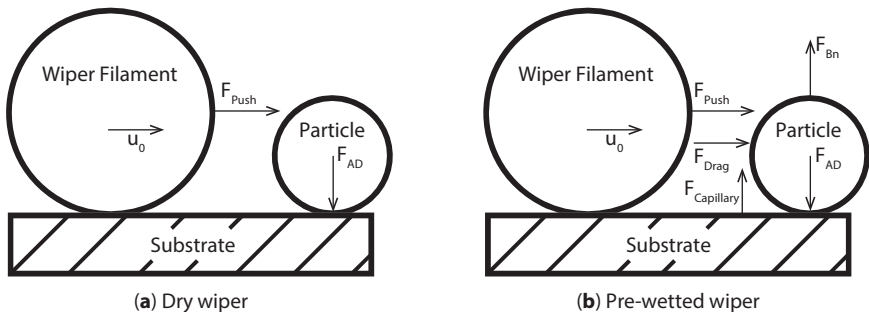


**Figure 10.1** Figure 10.1 a is a diagram of the forces acting on a particle adhered to a substrate surface as a moving dry wiper filament is acting on the particle during the cleaning process. Figure 10.1 b is a diagram of the forces acting on a particle adhered to a substrate surface as a moving pre-wetted wiper filament is acting on the particle during the cleaning process.  $F_{AD}$  is the force resulting from all the forces acting to keep a particle adhered to the substrate surface. A filament from a wiper is moving with a velocity,  $u_0$ , across the surface.  $F_{Push}$  is the force from a wiper filament striking the particle. When cleaning with a dry wiper, the only force available to remove an adhered particle is  $F_{Push}$ .

Hamaker constant. This is another factor which makes the wet-wiping easier and efficient over the dry-wiping.

### 10.2.2.1 Push Force

No matter how a wiper is constructed, on a microscopic level, the wiper is reduced to a series of polymer filaments. As a wiper is used to clean a substrate surface, these filaments press and move against the surface as the wiper is moved. Wiping, a physical process, exerts approximately 690 kPa (100 psi) pressure on the surface [13]. The main force available from a wiper for removing a particle is the force from a filament in the wiper pushing against the particle,  $F_{push}$ . This force is modeled as an impulse force like that of a bat hitting a ball with the bat representing a wiper filament and the ball representing the particle. This force is defined below.

$$F_{Push} = \frac{m_p(u_0 - v_0)}{\Delta t}$$

Where,

- $F_{push}$  is the force available to push the particle from the substrate,
- $m_p$  is the mass of the particle adhered to the substrate,
- $u_0$  is the velocity of the wiper filament on the substrate,
- $v_0$  is the initial velocity of the particle which is taken to be zero, and
- $\Delta t$ , the duration of the force acting on the particle.

The duration of this interaction,  $\Delta t$ , is no longer than the particle diameter divided by the velocity of the wiper motion,  $u_0$ .

### 10.2.2.2 Drag Force

When a pre-wetted wiper is used, other forces become available. These forces are the liquid drag force [14],  $F_{drag}$ , on the particle, a net buoyancy force,  $F_{Bn}$ , which depends on the particle and liquid densities, and the capillary force,  $F_{Capillary}$ , resulting from the use of a liquid. These forces are defined below.

$$F_{drag} = \frac{C_D \rho_{liquid} u_0^2 A_p}{2g_c}$$

Where,

- $F_{drag}$  is the drag force resulting from the liquid interacting with the particle,
- $C_D$  is the dimensionless drag coefficient,
- $\rho_{liquid}$  is the liquid density,

$u_0$  is the liquid velocity,  
 $A_p$  is the projected particle area, and  
 $g_c$  is the Newton's law mass to force conversion factor.

As the pre-wetted wiper is moved across the substrate, the motion of the wiper pushes a liquid front with density,  $\rho_{liquid}$ , ahead of the filament. This liquid front flows across the particle on the surface at a velocity of  $u_0$  acting on the apparent area,  $A_p$ , of the exposed particle. The flowing liquid creates a shear drag force that is essentially parallel to the wiper motion which acts on the particle. A film of liquid remains on the substrate after the wiper has passed across the substrate surface.

### 10.2.2.3 Net Buoyancy Force

Another force that is available when a pre-wetted wiper is used is the net buoyancy force,  $F_{Bn}$ .

$$F_{Bn} = g m_{particle} \left( \frac{\rho_{particle} - \rho_{liquid}}{\rho_{particle}} \right)$$

Where,

$F_{Bn}$  is the net buoyancy force,  
 $g$  is the acceleration due to gravity,  
 $m_{particle}$  is the particle mass,  
 $\rho_{particle}$  is the particle density, and  
 $\rho_{liquid}$  is the liquid density.

Depending on the relative densities of the liquid and the particle, this force may lift the particle if the liquid density,  $\rho_{liquid}$ , is greater than the particle density,  $\rho_{particle}$ . In any case, the weight of the particle is reduced because of the liquid and particle density difference.

### 10.2.2.4 Capillary Force

The final force that is available if a pre-wetted wiper is used is the capillary force,  $F_{Capillary}$ . This new force may modify the capillary force already established between the substrate and the particle. If the surface tension of the pre-wetting solution is less than the liquid participating in the creation of the adhesion between the particle and substrate, the adhesion force is reduced. If the surface tension of the liquid is the greater, then the adhesion force is increased. If the liquid surface tension is the same, there is no change in the adhesion force,  $F_{AD}$ , between the particle and the substrate.

If enough liquid is present, the capillary force is removed making the particle easier to remove from the surface during cleaning.

$$F_{\text{Capillary}} = 2\pi\gamma d$$

Where,

$F_{\text{Capillary}}$  is the capillary force,

$\gamma$  is the surface tension of the liquid used to pre-wet the wiper, and

$d$  is the diameter of the particle.

Of the many forces that exist which may bind particles to the surface, Reference [15] highlights the importance of the capillary force. Severing or even lowering this force is critical to the removal of particles. Breaking the capillary force between the contaminant particle and the surface is best achieved by using a liquid such as water, other solvents such as an alcohol, or other cleaning agents. Therefore, wetted wipers are more effective in

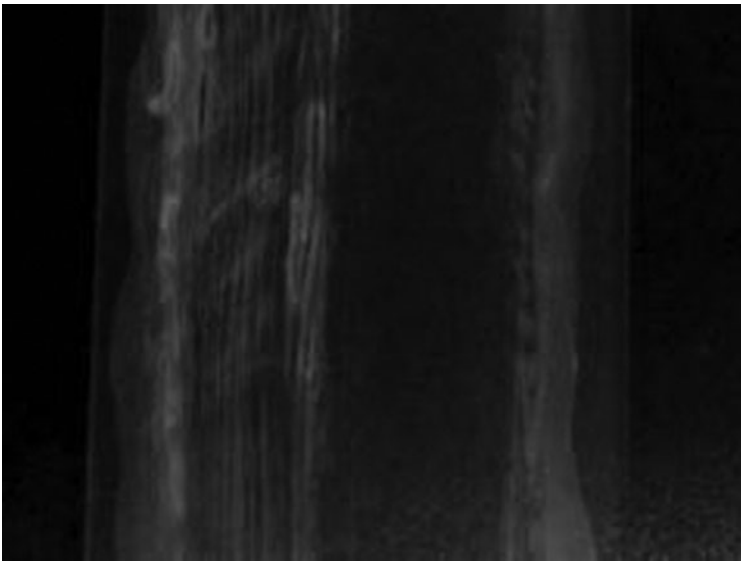


**Figure 10.2** This photograph shows the effect of using a dry and wetted wiper in removing particles from a surface. Two drops of Nanosphere™ Size Standard 600 nm (Catalog Number 3600A from ThermoScientific) solution were applied to a glass microscope slide surface and allowed to dry. An area of a wiper was wetted with deionized water. Using a gloved finger, the wiper was swiped down the length of the microscope slide. The dry part of the wiper on the left hand side was not able to remove all of the particles as shown by the series of vertical lines. The wetted wiper area, nearly centered in the photograph, shows the particles neatly removed. The white streaks on the far left and the far right hand sides are the unaffected particle layers.

removing contaminants than dry wipers. See Figure 10.2 below for a more typical demonstration of the effect of using a wetted wiper compared to a dry wiper for particle removal from a surface.

The 600 nm (0.6  $\mu\text{m}$ ) particles are not visible to the naked eye. Particles larger than 40  $\mu\text{m}$  are visible [16]. However, a collection of small particles may become visible because of particle aggregation creating the appearance and effect of larger particles. These larger particles are more easily removed from the surface. The surfactant that suspends and prevents the small particles from associating in solution is now deposited between the particle surfaces during drying. As the wetted wiper passes over the particle clumps, the surfactant dissolves into the liquid reducing the capillary force between the particles and possibly between the particles and the surface due to reduction of surface tension. This facilitates the removal of visible particles from the surface.

#### 10.2.2.5 Particle Removal Process Summary

As the filament from the wiper approaches the particle adhered to the substrate surface, the forces that are available for adhesion to the substrate surface become available for the particle to adhere to the filament surface. An additional force for removing the particle is  $F_{push}$  which helps move the particle on the surface. When the adhesion forces between the particle and substrate surface become less than the adhesion forces between the particle and the wiper filament, the particle is removed from the substrate surface and moves to the filament surface in the wiper.

Because the adhesion forces on a particle are strong, not every encounter between the wiper filament and particle will remove the particle from the surface. However, a wiper has many filaments and after repeated encounters, particles are removed from the surface. Once the particle is removed from the surface, it becomes attached to the filament surface and may be entrained or entangled into the wiper for permanent removal from the substrate surface. The surface particulate contamination level is reduced. The particles are trapped onto the wiper and do not spread from the substrate surface of interest to another surface.

In summary, the proposed mode of particle removal is a wiper filament interacting with a particle. The forces that aid the particle's adhesion to the substrate surface start to transfer to the filament surface as the filament interacts with the particle. The particle breaks free from the surface when the forces that enable the particle to adhere to the surface are less than the forces being created between the particle and the filament. To clean a surface with a wiper, the contaminant must have a greater attraction for the wiper than the surface being cleaned.

The liquid in a pre-wetted wiper may cause other forces that may act on the particle. If enough liquid is present, the capillary force will be eliminated allowing for easier particle removal during cleaning.

Different sizes of wipers are particularly suited for a given surface or contamination challenge. Swabs, which have a small wiper area, are effective for cleaning small and difficult-to-reach areas. Mops, which are large wipers, are designed to clean large surfaces like walls. The different sized wipers allow effective cleaning at different scales.

### 10.2.3 Contamination Types

Particulate matter in large and small sizes, various chemicals, acids, bases, salts and organic material, any material in both solid and liquid form used in the manufacturing process, all non-volatile residues (NVRs), and microbes are examples of surface contaminants that may be commonly present and need to be removed from a cleanroom. Very little of these contaminants is visible; however, they can destroy a process or product. While some macro-sized residues like fibers or spills may be visible to the naked eye, cleanroom contamination is typically concerned with micro-sized residues with sizes ranging from below  $0.1\ \mu\text{m}$  to about  $100\ \mu\text{m}$ .

Even with the superior air handling and filtration offered by proper cleanroom construction, surfaces can be contaminated with a variety of different residues and materials that differ physically and chemically. This is demonstrated in Figure 10.3.

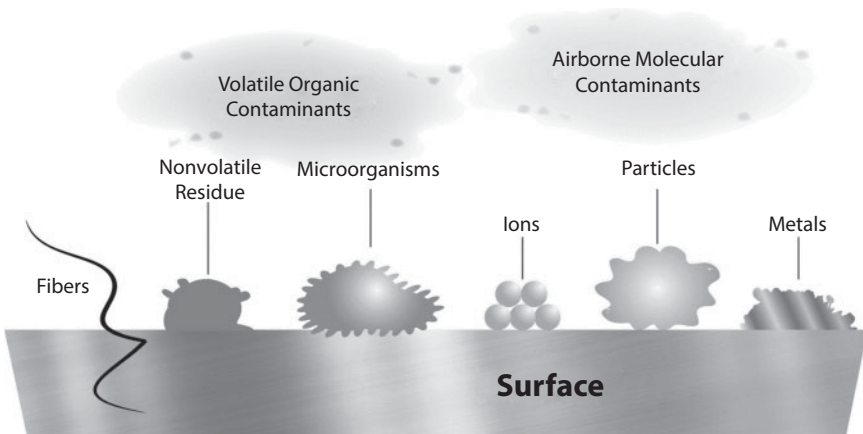


**Figure 10.3** Artist illustration of different kinds of surface contaminants.

The risk caused by these contaminants is not only that they exist in a cleanroom environment potentially impacting the product's integrity, but they also may migrate to other locations in the cleanroom. To reduce this risk, the contamination must be promptly, frequently and periodically removed. In fact, wiping is the best method for contaminant removal since other methods increase the potential of undesirable contaminant migration. To protect product integrity, most cleanroom operations document specific cleaning procedures, tools and frequencies as part of their Quality Assurance systems to ensure that product integrity will not be compromised.

### 10.3 Various Types of Wipers

As cleanroom and manufacturing needs have become more exacting, cleanroom wipers and evaluation methods have advanced as well. The construction of the fabric for cleanroom wipers can be broken down into four distinct groups: knit, microdenier, woven, and non-woven. These categories are traditional textile classes. The construction of the wiper's edge impacts its particle and fiber contamination characteristics. The edge types are classified as cut-edge, sealed-edge, and sealed-border.

Before discussing the details of wiper construction methods, a glossary of terms and definitions is provided below as a reference to characterize and describe wiper performance attributes. This reference material may help in deciding which wiper is needed for a particular use or application in a cleanroom.

#### Glossary of Terms

- Particles / fibers contamination level – One attribute for evaluating wiper performance. Not all wipers have the same particle and fiber contamination characteristics. Different environments and processes can tolerate different levels of particles and fibers from wipers without causing harm to the product.
- Ions – These are generally more important in microelectronics, semiconductor, and aerospace applications.
- NVR (non-volatile residue) – An important consideration if a wiper is used with a solvent which may leach residue and it remains as a contaminant on the wiped surface.
- Sorption characteristics – This property is related to how fast and how much liquid a wiper will hold.

- Chemical resistance / interaction – An attribute that reflects how a wiper’s fabric will interact with the chemicals to which it is exposed. Exposing a wiper to a chemical where it lacks resistance may cause it to break down and generate contamination.
- Raw material components – The components of a wiper which may impact cleanliness, cost, overall performance and chemical interactions.
- Metals – Metals on the surface or integrated into the filaments that can be extracted from the wiper and remain as a contaminant. They may interrupt chip circuitry or cause allergic reactions.
- Leave behind – Any residues or particles remaining after wiping a surface. It may or may not be visible to the naked eye.
- Extractable – A substance that may be extracted through the use of mechanical or chemical force and may be considered a contaminant.
- ESD – Electro Static Dissipative material has the ability to dissipate charge slowly so as not to cause damage to a charge or discharge-sensitive product. ESD is also known as Electro Static Discharge.
- Abrasion characteristic – An attribute related to a wiper’s ability to create particle or fiber contamination when used with rough surfaces.
- Outgassing - The release of a gas or vapor that was dissolved, trapped, frozen or absorbed in the wiper. Outgassing is of particular concern when trying to maintain a clean, high-vacuum environment or in critical environments where airborne molecular contamination (AMC) is a concern.
- Microbes – Generally thought of as a contaminant in life science industry. They may have a negative impact if a microbe is transferred on or into a product that ultimately is placed inside the body. Microbes may also be considered as a contaminant particle in other industries.

Common textile terms and definitions related to cleanroom wipers:

- Yarn: A generic term for a continuous strand of textile fibers or filaments in a form suitable for knitting, weaving, or otherwise entangling to form a textile fabric.



- **Filament:** A fiber of an indefinite length such as found naturally in silk. Manufactured polymers are extruded into filaments that are converted into filament yarn.
- **Filament yarn:** A yarn composed of many continuous filaments.
- **Ply:** The number of single yarns twisted together to form a plied yarn.
- **Knit:** A method of manufacturing a textile fabric by interconnecting loops of yarn.
- **Woven fabric (weaving):** A method of manufacturing a textile by interlacing two yarns to cross each other at right angles. The yarn that runs the length of the fabric is called the warp, and the yarn across the fabric is the weft or filling.
- **Nonwoven fabric:** An assembly of textile fibers held together by mechanical interlocking as a random web. The web may be held together by fusing (thermoplastic fibers), bonding with a chemical additive, or hydro-entangling, where high pressure water jets are used to entangle the web materials.
- **Microdenier:** Filaments that weigh less than one gram per 9000 meters.

### 10.3.1 Fabric Construction

The construction of the fabric for cleanroom wipers can be broken down into four distinct groups: knit, microdenier, woven, and non-woven. The fabric construction can affect the particle and fiber contamination characteristics of wipers.

#### 10.3.1.1 *Knit Wipers*

Critical clean environments require the cleanest wiper for use in and maintenance of a cleanroom. Knit materials are the cleanest wipers available on the market. Knit material is comprised of interlocking loops of yarn [17]. Polyester is the best commercially available polymer used to make the yarn; however, nylon is also available. Though nylon wipers are still in use, polyester has replaced this polymer because of its cleaner properties, lower extractable levels, fewer generated particles and fibers, better chemical resistance profile, and better value for use as a raw material.

Forming fabrics through the knitting process is more favorable for developing new wipers with different properties. Knitting machines can be changed to a new knit pattern relatively easily and quickly. Short lengths of

fabric may be made for testing its physical and contamination characteristics and processing ability.

The ability to vary the knit pattern allows changes to be made to the wiper's physical properties. If a wiper will experience rough surfaces during its use, a tight fabric structure with minimal stretch is best. The yarn will less likely snag and break and generate particles and fibers. If the wiper will be used in an environment requiring frequent spill control, a looser knit provides a greater sorption capacity. Varying the type of yarn for a different hand or feel may modify the moisture management characteristic. This same property may translate into different wiper performance characteristics.

For wipers like any other product, there is a balance of properties. Improving or increasing one performance characteristic usually adversely impacts at least one other performance characteristic. Knit fabric design is limited by the imagination of the fabric designer, the process capabilities of the manufacturer, and the final cost of the fabric.

#### 10.3.1.2 *Microdenier or Microfiber Wipers*

Microfiber materials have been available commercially for many years, but were not used in controlled environments until recently. They are made from synthetic materials because the diameter of the filament is very small, one to ten micrometers in diameter [18]. Because of the difficulty in cleaning the fabric, no interest was found in the controlled environment community. Microdenier fabrics have the ability to clean smooth surfaces, e.g., glass or polished stainless steel, without the use of water or isopropyl alcohol because of the increased surface area of the yarn. This positive attribute, unfortunately, is accompanied by the negative attribute of the filaments being fragile and easily broken because of their small diameter. When a filament in a yarn breaks, fibers and particles are released.

Since the 1990s, microfiber fabrics have been used as mops and cloths for wiping surfaces for their microbial cleaning efficiency in the health care industry [19]. It was found that the microfiber material removed microbes better compared to wipers commonly used in the food service and health care industries on hard surfaces that included micro-fissures where bacteria may dwell. Methicillin Resistant *Staphylococcus aureus* (MRSA) and *Clostridium difficile* were the bacteria tested. When the microdenier fabric was wetted with deionized water, it was able to remove almost one hundred percent of the microbes. Microdenier yarns give a superior wiping characteristic, but the yarn itself has a higher cost due to its manufacturing process which impacts the final wiper cost.

### 10.3.1.3 Woven Fabric Wipers

The first wiper specifically made for cleanroom applications was a cotton twill produced by the Texwipe Company in 1964. Woven fabric is constructed from two interlaced yarns that are perpendicular to each other. Figure 10.4 shows common patterns found in woven fabrics.

Woven materials are more expensive to make. The yarn itself requires many preparation steps before it can be used. The process itself is relatively slow. This investment in time and effort increases the fabric cost. Like a knit material, many fabric designs are available, but the designs are generally limited by the type of weaving machine.

Some of the attributes of woven materials are that they have minimal stretch and are denser than a knit. The density makes the wiper more abrasion resistant, but may limit the sorption capacity of the wiper. Also, because of the higher density, the fabric is harder to clean for making wipers suitable for a controlled environment.

### 10.3.1.4 Nonwoven Fabric Wipers

Knitted and woven fabrics have a defined and distinct pattern that bonds the fabric together. In contrast, nonwoven materials have a random pattern

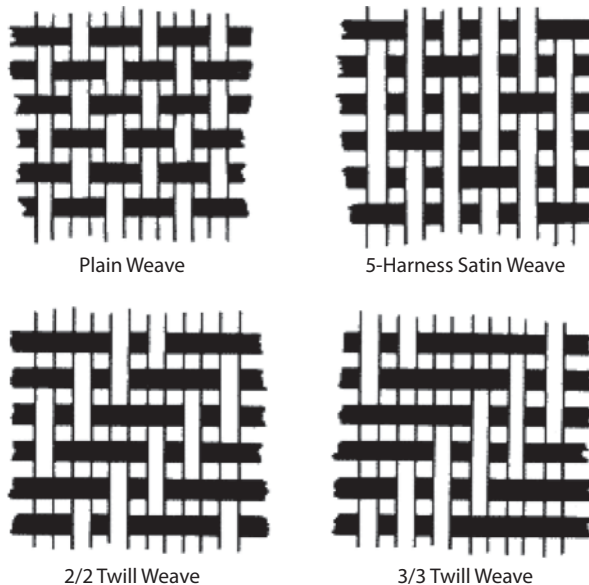


**Figure 10.4** Common patterns found in woven materials showing the perpendicular, interlaced yarns.

that mechanically stabilizes the fabric as illustrated in the scanning electron microscope micrograph Figure 10.5. The nonwovens are not like other textile materials made of filaments and fibers, not yarns. The high-volume, high-speed production process allows a cost advantage, but it is offset by the design and construction. Due to these constraints, nonwoven materials generally lack the cleanliness needed for cleanrooms (ISO Class 4 or cleaner). Because of the construction, the fabric cannot be further processed to improve its cleanliness since the fabric will unravel in the washing process unlike knitted and woven fabrics.

Nonwoven wipers can be made from different types of materials including, but not limited to, cellulosics (rayon, tissue, etc.) and polymers (poly(ethylene terephthalate) (polyester), polypropylene, etc.). Each material gives different performance and contamination properties. Most nonwovens contain some sort of cellulose. When cellulose is used as the base material, the wiper may now more easily remove spills, have enhanced sorptive capacity, and may wipe a surface dry like a paper towel used at

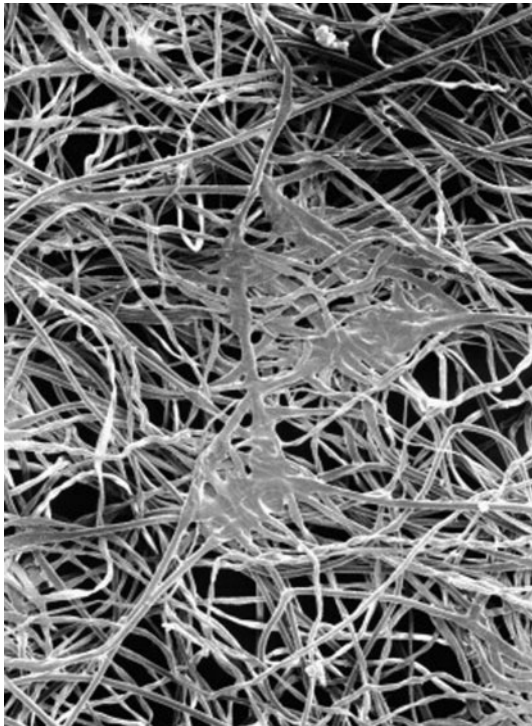


**Figure 10.5** SEM micrograph of a hydro-entangled nonwoven illustrates the random fiber pattern of the construction.

**Table 10.1** Data showing the impact on a wiper's  $>0.5 \mu\text{m}$  particle and  $>100 \mu\text{m}$  fiber contamination characteristics by the raw material type and construction.

Raw material type	Construction	Edge type	$>0.5 \mu\text{m}$ particles, ( $\times 10^6$ Particles/ $\text{m}^2$ )	$>100 \mu\text{m}$ fibers, (Fibers/ $\text{m}^2$ )
Polyester	Knit	Cut	8.4	2,000
Nylon	Knit	Cut	15	2,000
Cotton	Woven	Cut	38	46,000
55% Cellulose / 45% Polyester	Hydro-entangled	Cut	72	55,000

home. Polypropylene can be made by a spun-bond process, where the polymer beads are extruded into fibers that are converted into a fabric web. The advantage of this process is that a continuous filament is made with minimal process aids which may reduce the contamination level of the wiper. However, these wipers are not as clean as laundered polyester wipers.

The data compiled in Table 10.1 indicate the impact of the raw material type used to make a wiper. Wipers made from natural materials like cellulose and cotton shed more fibers. The wipers made from man-made raw materials like nylon and polyester are cleaner shedding fewer fibers. The wiper construction impacts the greater than  $0.5 \mu\text{m}$  particle-size contamination characteristic. The edge type also impacts the particle and fiber contamination characteristics and here it is consistent for comparison purposes.

### 10.3.2 Edge Type

Not all laundry-processed polyester wipers are made the same. In selecting a cleanroom wiper for use in any kind of cleanroom application, it is important to understand the impact of the wiper's edge on the particle and fiber contamination characteristics. Even though the edge is a small fraction of the wiper, the edge type affects the particle contamination characteristic, which changes the suitability of a wiper for cleaning process or product surfaces.

The edge type also impacts the cost of the wiper. The end user needs to balance the cost of the wiper with the cost impact on the product or process. A wiper with higher contaminant levels can be used in a cleaner environment or process depending on how the wiper is introduced and used

in the environment. The contrary is also true. If the process or product is negatively impacted by how the wiper is used even though the process is not in a clean environment, then a cleaner wiper should be selected. The choice of wiper type is more determined by process or product impact than the actual cost of the wiper.

There are three basic types of wiper perimeters: cut-edge, sealed-edge, and sealed-border. There are other types, e.g., where the edge of the wiper is folded under and sewn, but these wipers are not as common.

### 10.3.2.1 *Cut-Edge*

Rolls of fabric are unwound and layered onto a lay-up table in preparation for cutting. The depth of the lay-up will depend on many factors including the construction material and the length of the knife used to cut the layers. A pattern is generated and laid over the layers to guide the operator in cutting the wipers.

The type of knife used to cut the fabric impacts the final particle contamination characteristic. A smooth, sharp, reciprocating knife is used to make the wipers. Other blades are available, but the smooth edge minimizes small particle and fiber generation.

The cut-edge wiper (Figure 10.6, left wiper corner) has unbound fibers at the edge that surround the wiper. Even though proper wiping technique

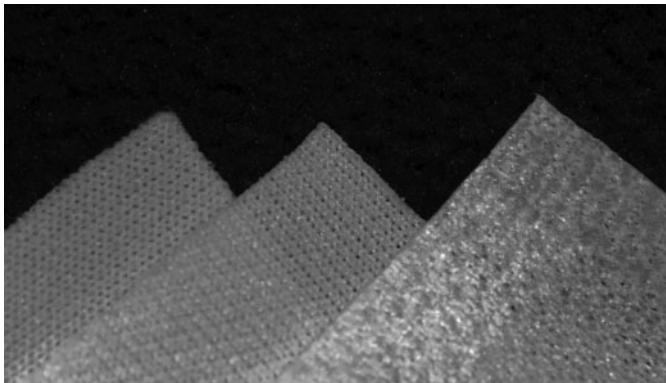


**Figure 10.6** The photograph above displays the corners of three common wiper edge types. All three of these wipers are made from continuous filament polyester yarn. The wiper corner on the left is a cut-edge wiper. Notice the loose loops of the knit pattern on the edges. Loose fibers can be seen near the tip of the corner. The middle corner of fabric has a sealed-edge. Notice that the edge looks smoother with slightly fused loops that are occasionally joined, but are always melted to seal the edge. The rightmost corner is a sealed-border wiper. Approximately one-quarter of an inch of the wiper is fused to create the border. The edge is smooth with no visible loops.

reduces or prevents most of the edge from contacting the surface, the particles and fibers generated at the edge can still contaminate the wiper.

### 10.3.2.2 Sealed-Edge

The sealed-edge (Figure 10.6, center wiper corner) is formed through two different processes. The first is through the use of a “hot knife” and pressure. The hot knife is a thermally heated rotary knife. As the fabric is passed against the knife, the edge is melted and crushed creating two pieces and the wiper edges are formed. Wipers formed through this process are also known as “Hot Cut” wipers.

The other method of forming sealed-edge wipers is by using a laser. The laser melts the polyester yarn while ablating a thin sliver of fabric which separates the edges and forms the wiper. In Figure 10.6, the middle corner, which is a laser cut wiper, demonstrates the sealed-edge. It has a finished look with no loops or fibers showing.

### 10.3.2.3 Sealed-Border

The sealed-border (Figure 10.6, right wiper corner) is formed through the use of an ultrasonic horn and anvil setup. As the material passes through the set-up, the yarns are melted and fused together. After the fusion process, the borders are slit to form wiper edges [20].

The products presented in Table 10.2 are all polyester knits that are washed and dried through a conventional laundry process. As the border becomes more substantial, the contamination levels from particles and fibers decrease.

Figure 10.7 shows a relationship between the fiber and small particle generation and the method used to form the wipers by different manufacturing methods. The different wiper forming processes generally fall into three categories. The “Cut-Edge” manufacturing process generates small particles while fibers shed from the rough edge. The “Sealed-Edge”

**Table 10.2** Data showing the impact of a wiper’s edge type on the particle and fiber contamination characteristics.

Product	Edge type	>0.5 $\mu\text{m}$ particles, ( $\times 10^6$ Particles/ $\text{m}^2$ )	>100 $\mu\text{m}$ fibers, (Fibers/ $\text{m}^2$ )
1	Cut-Edge	8.4	2,000
2	Sealed-Edge	3.5	600
3	Sealed-Border	2.9	100

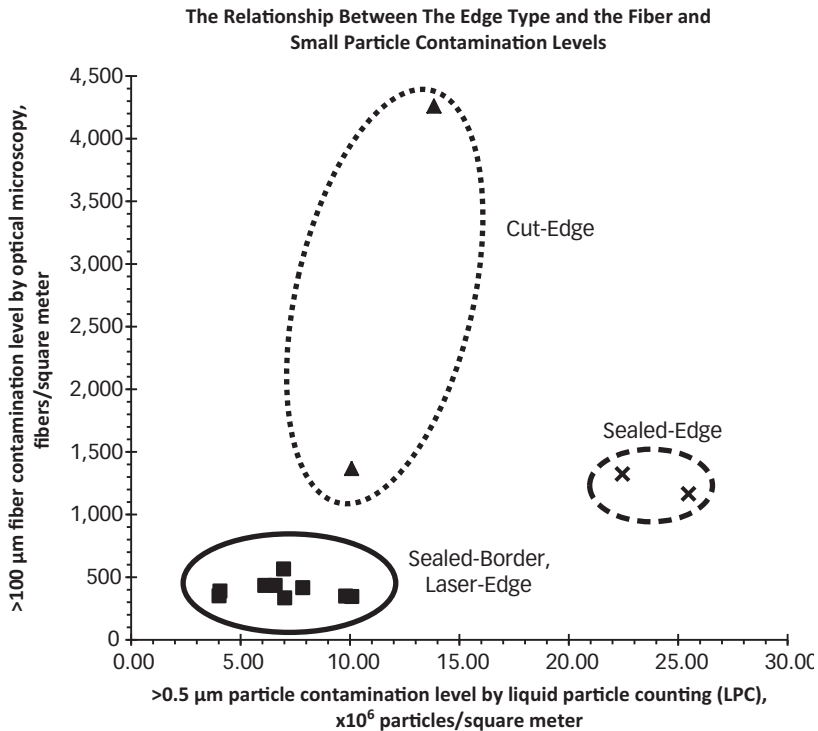


**Figure 10.7** A scatter chart is shown comparing the IEST-RP-CC004.3, Section 6, >100 μm optical microscopy analysis test results to the IEST-RP-CC004.3, Section 6, biaxial shake, >0.5 μm LPC (liquid particle counting) analysis test results for wipers manufactured by different edge types. A “Cut-Edge” wiper is formed through the use of a sharp knife to cut the fabric. A “Sealed-Edge” wiper is made by cutting the wiper with thermally heated rotary knife. “Sealed-Border, Laser-Edge” wipers are formed by melting a small width of the wiper edge either by ultrasonics or by a laser as described in the text.

manufacturing process generates small particles through the knife crushing the yarn in the fabric, but the thermal energy melts the ends of the fabric yarns. The “Sealed-Border, Laser-Edge” manufacturing process melts the polymer yarn producing only a few small particles and seals the edges of the wiper to create the sealed-border.

### 10.3.3 Selecting a Cleanroom Wiper

Selecting a cleanroom wiper requires an understanding of how and where it will be used in the cleanroom environment or process area. Other factors to consider are the impact of the wiper on the background environment and the nature of the residues to be removed. As stated before, cleaning a



**Table 10.3** Guidelines for the selection of the optimal wiper fabric and edge type for a given cleanroom class.

Cleanroom Class	Optimal Fabric and Edge Type	Comments
ISO Class 3 - 4	Polyester knit, sealed-border or sealed-edge	These wipers have the lowest particle, fiber, NVR, and ion levels. These wipers are processed through edge sealing, laundering, and cleanroom bagging.
ISO Class 4 - 5	Polyester knit, cut-edge	These wipers have lower particle, fiber, NVR, and ion levels. Particle and fiber levels are higher than in sealed border or sealed edge wipers. These wipers undergo cutting, laundering, and cleanroom bagging.
ISO Class 5 - 7	Non-woven materials, cut-edge	These wipers can be used in areas in which only moderate levels of contamination control are required. The wipers are processed by cutting and bagging in a controlled environment.
> ISO Class 7	Composite materials, cut-edge	These wipers can be used in processes or environments where some particle control is needed. The wipers are processed by cutting and bagging in a controlled environment. Typically, these wipers have a high absorbency characteristic.
	Cotton, cut-edge on fabric diagonal	These wipers are used where heat resistance and slight abrasion resistance are desired. These wipers are processed by cutting on the fabric diagonal to prevent edge fraying and unraveling and bagging in a controlled environment.

surface to reduce the particle contamination level requires that the wiper is wetted at least with water, if not a solvent, that further reduces the surface tension and adhesion forces between the particle and surface.

Table 10.3 represents a guide for selecting a cleanroom wiper for a range of cleanroom classes. The recommendations below are based on the physical and contamination characteristics of the wiper and historical usage patterns. The actual use activity is not represented in the table, but the

activity may affect the choice of wiper. Caution must be used when selecting multiple types of wipers to be employed in the same or adjacent process areas. A wrong wiper, because it is close by or has a particular favorable physical characteristic, may be used in the wrong area of the cleanroom or wrong part of the process and adversely impact the environment, process, or product yield. Typically, one wiper is suggested for use for all cleaning activities in a particular cleanroom, if possible. If more than one wiper type is needed, then some segregation technique, such as bag color-coding, is recommended.

It should be noted that there is no recognized test, procedure or recommended practice that can be performed to determine the correct wiper for a particular cleanroom, process or activity. The final choice rests with the user in this determination. Typically, the decision is based on the wiper physical and contamination characteristics and its cost, i.e., the wiper characteristics and environment, process, or product yield costs.

## **10.4 Proper Ways to Carry Out Wiping or How to Use Wipers Properly**

### **10.4.1 The Purpose of Wiping**

The purpose of wiping is to reduce, control, and maintain the contamination level in a cleanroom. The wiper serves as the vehicle to remove the contamination from the wiped surface and transfer it to the wiper. After the contaminated wiper is removed from the cleanroom, the overall cleanroom contamination level is reduced.

A dry wiper is used to contain and remove spilled material. Spilled material is defined as a liquid, a powdered solid, or solid material such as a broken vial or slurry. It is important that the wiper is compatible with the contaminant being removed. Using a nylon wiper to clean an acid solution may result in wiper dissolution as it is used, thereby spreading organic contamination (dissolved nylon) over the surface. Large broken pieces or large amounts of spilled solids need to be reduced in volume before using a wiper, for example, using a HEPA filtered vacuum cleaner. Once the spilled material is reduced in volume to a level that is not visible to the naked eye, a wetted wiper is used to further reduce the contamination level at that location.

Wetted wipers are used on dry surfaces to reduce the contamination level through movement and capillary force reduction to move the contaminant from the surface to the wiper. The technique used in wiping a surface is critical. Improper technique will spread contamination over the

surface. Proper technique reduces the contamination on the surface and, ultimately, in the cleanroom as a whole.

Wiping the surfaces in a cleanroom should follow a prescribed protocol that is designed to minimize the spread of contamination on the specific surface being cleaned and also the cleanroom as a whole. The protocol starts with cleaning from clean areas to dirty areas. The process area and its immediate surroundings should be the cleanest area in the cleanroom. The entrance to the cleanroom with its exposure to the outside environment is the dirtiest area. With a good cleanroom design, this entrance would be on the opposite wall furthest from the process area. Considering this design, cleaning should start nearest or in the process area and proceed to the entrance. With good laminar airflow, areas toward the ceiling are cleaner than the surface of the floor. So, the cleaning protocol would generally be written such that cleaning would start at the upper walls at the back of the cleanroom and finishing at the entrance floor.

Part of the protocol defines how wiping is performed. Most wipers are large enough to have multiple surfaces available for cleaning. These surfaces are generated typically by quarter-folding the wiper. The process of quarter folding is demonstrated in Figure 10.8a-c. As the wiper is folded, new surfaces are formed. Being able to control the edges is an added benefit. The quarter-folding allows one to use more of the wiper surface. Once a wiper quarter-fold surface is used, the wiper is carefully refolded to generate a new, clean wiper surface. The contaminated surface is enclosed preventing the spread of contamination from the wiper back to the surface.

After the wiper is quarter-folded, hold the wiper as shown in Figure 10.9. When the wiper is held correctly, the cut corners will be pointing up

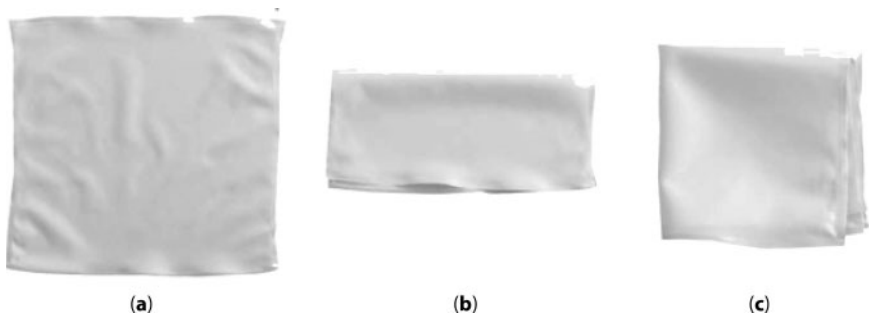


**Figure 10.8a-c.** Demonstration of how a wiper is folded in mid-air to deliver the quarter-folded wiping surface. The wiper in Figure 10.8a is held in the middle by the edges on opposing sides. The wiper is flipped resulting in the wiper shape shown in Figure 10.8b. The wiper is grabbed by the opposing edges again and flipped forming a quarter-folded wiper as shown in Figure 10.8c.

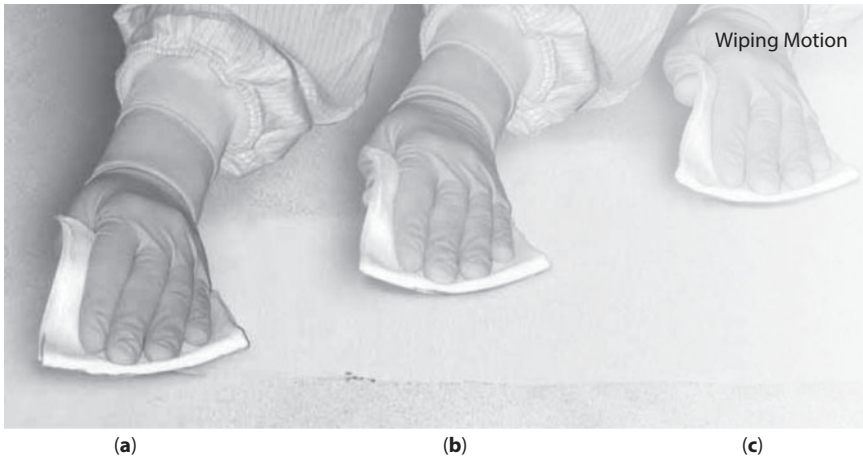


**Figure 10.9a–c.** Demonstration of how the wiping motion is actually performed on a contaminated surface using firm, overlapping strokes. Figure 10.9a shows the first stroke that is almost complete. Figure 10.9b illustrates what the next path would be. The path is parallel to and overlapping with the first stroke. Figure 10.9c repeats the previous stroke to reinforce that parallel, overlapping strokes are necessary for satisfactory surface cleaning.

between the thumb and forefinger. The cut edges, not the folded edges, of the wiper will be parallel to the forefinger. The cut edges will not contact the surface during use. The two edges formed by folding the wiper will contact the surface. The wiping motion starts with the wiper held above the surface to be wiped. The arm is stretched out to the beginning of the wiping stroke. To start the stroke, bring the wiper to the surface with the fingers closed and the hand slightly arched to keep the cut edges off the surface as shown in Figure 10.9. With consistent pressure from the palm and fingers, glide the wiper across the surface. Pick up the wiper, refold, and continue with the next parallel stroke overlapping with the previous one by about 25%. Whenever the wiper appears to be visibly contaminated, refold the wiper to form a clean surface. Repeat this last stroke. The parallel, overlapping strokes ensure that the whole surface is contacted and cleaned. Figure 10.9 shows how to hold the wiper and how to wipe with parallel, overlapping strokes.

The stroke length is determined by the initial condition of the surface to be cleaned. If the surface starts relatively clean, longer strokes may be used. If the surface is heavily contaminated, e.g., from a spill, the strokes will be short. In general, the stroke length is dictated by what is required to maintain the classification of the cleanroom and should be part of the cleaning protocol.

Different surfaces are cleaned using the same principles. Instead of using a wiper with a hand, mops with covers are used for large surfaces. The mop replaces the hand and mop covers are essentially large wipers. The mop's long handle allows the wall near the ceiling to be reached. Another type of surface is found in isolators, which have unique cleaning needs. The surfaces are relatively small, but are out-of-reach for most users. In this instance, an isolator cleaning tool is used. It is a small device with a short handle that allows accessibility to most surfaces in the isolator and has a small head for more intricate motions. For corners, edges and channels, a swab may be used to clean these hard-to-reach surfaces. The same wiping techniques apply again since the swab head is made of cleanroom wiper material, but on a smaller scale.

### 10.4.2 Wiping Methods

The control or removal of a spill, the removal of surface contaminants, or the application of a cleaning solution are all ways of cleaning through wiping. Wipers come in different types. The choice of wiper raw material type depends on the controlled environment classification, the application, e.g., a high particle-shedding wiper could be used in an ISO Class 1 environment because of the wiper characteristics fit the use requirements best and has minimal impact on the product yield.

Dry wipers, in general, are used as a worksurface or a protective covering, for spill control and removal, and for cleaning solution application. Different wiper types are designed to meet the needs of these categories.

#### 10.4.2.1 *Worksurface or Protective Covering*

Some objects used in a process are fragile and need to be protected from the worksurface. A wiper is placed on the worksurface as a buffer between the fragile object and hard worksurface. The wiper's cleanliness and thickness as well as its density are characteristics to be considered depending on the process. A wiper can be used to protect an object as part of its packaging during transport or after final assembly and cleaning.

#### 10.4.2.2 *Spill Control and Removal*

Sorption capacity, the amount of liquid a wiper can hold, is the critical characteristic for spill control and removal. High-capacity wipers are used to clean spills. The high capacity characteristic can be built into the wiper through the use of natural fibers, fabric design, or chemistry. This type of

wiper allows the spill to wick into the material quickly and not leave a thin liquid layer that may trail a wiper during use.

Synthetic wipers may leave a liquid trail. The liquid absorbs between multiple filaments that make up the yarn. Synthetic wipers do not absorb liquids as fast and do not have as much capacity as wipers made from natural materials. Most importantly, the cleanroom classification and the actual process environment must be considered for which type of wiper to use, natural materials like cellulose with its improved wiping characteristics or a synthetic like polyester with its generally lower particle- and fiber-shedding characteristics.

The wiper properties and process needs must be balanced. The surface to be wiped needs to be considered as well as the ISO class of the work environment. If the surface has texture or abrasiveness, a wiper which can withstand the surface condition must be used. These wipers may have less sorptive capacity, but shed fewer particles. Wipers with higher capacities may shed more particles because of their construction or raw material type.

#### *10.4.2.3 Solution Application and/or Removal*

While most wiper applications are focused on controlling and removing spilled material, sometimes a solution covering a surface is required. As an example, in the life science industry, solutions like cleaning agents, disinfectants, or other specialty solutions can be poured and dispersed across the entire worksurface with a dry wiper. Afterwards, another dry wiper is used to remove the solution from the surface as one would do when controlling a spill. The wiper characteristics that are important to this application are its cleanliness, abrasion resistance, sorptive capacity, and chemical compatibility. When applying a disinfectant, enough volume of the solution must be left behind so as to keep the entire surface wet for the contact time for disinfectant efficacy. If the solution dries, it may be difficult to remove, which can change the desired wiper characteristics. Another example is the application and removal of wax from a car. A sponge is used to apply the wax while it is wet with the sponge being a reservoir for the wetness and the wax solution. After the wax dries on the surface, a soft, clean cloth is used to remove the dried material from the surface. The cloth used to remove the wax must be able to withstand the forces encountered while buffing the surface.

#### *10.4.2.4 Cleaning*

Since many physical forces may hinder the capture and removal of contaminants, dry wipers, with the possible exception of microdenier wipers because of the yarn construction, are rarely used to clean a surface. There

are applications where a dry wiper is used to burnish a surface. The dry wiper material may be dispensed from a continuous roll and indexed to bring fresh material for the next surface to be processed.

Because dry wipers are likely to push around and spread surface contamination through electrostatic forces being stronger between the contaminant and the surface than between the contaminant and the wiper, one often avoids their use. Microdenier wipers may be an exception to this because of their yarn construction. The microdenier filaments used in forming the yarn have greater surface area and may be able to capture and remove bacteria from a surface [19].

A dampened or pre-wetted wiper is the preferred approach for removing contamination since the wetting solution has the ability to reduce electrostatic forces and also decrease or eliminate the capillary force. The wiper provides a channel for particle trapping and removal once it is released from the surface. Once the particle is trapped, the particle is less likely to redeposit elsewhere.

The level of wiper wetness is a critical characteristic for surface cleaning. The optimum range is defined by the type of wiper, the solution wetting the wiper, and the application. Extreme wetness levels are easy to envision. With no wetting, i.e., a dry wiper, the contaminants are pushed around and not entrapped into the wiper. At the other extreme, where the wiper is saturated or over-saturated, the contaminants are released from the surface, get entrained in the solution, but not trapped into the wiper surface, and are possibly delivered onto adjacent areas. At the proper level of wiper wetness, the wiper will leave a thin layer of solution behind that will evaporate. Using a squirt bottle to deliver a solution to the wiper surface will give inconsistent wetness across the wiper surface, from wiper to wiper, and user to user. A manufactured pre-wetted wiper will be consistently wet across the wiper surface and consistently wet from wiper to wiper.

### **10.4.3 Introductory Training Example for Wiper-Based Particle Cleaning**

The removal of sugar-free, colored drink crystals from an aluminum foil surface may be used for wiper use training. The benefits of this technique are that the drink powder is visible, and the wiping effectiveness can be quickly assessed.

In preparation for the training, an aluminum foil sheet is affixed to a surface to protect it from being stained. Colored drink powder is sprinkled lightly and evenly on the foil. The first step in the training is to ask the trainees to wipe as they do at home. Their typical technique is using a circular

motion which results in the drink powder being spread unevenly across the aluminum foil. The next step is to show how to wipe using parallel, overlapping stroke and a single layer wiper across the aluminum foil surface. This results in a lower level of drink powder spread unevenly across the surface. However, if the used wiper surface is examined, a distinct hand pattern is observed. The next step is to correct the uneven color pattern created by the hand when wiping. The technique for quarter folding a wiper is demonstrated. How multiple layers of fabric will distribute the hand pressure more evenly on the surface is also discussed. The contaminated surface is wiped again using the quarter-folded wiper. The aluminum foil surface is examined for the powdered drink contamination pattern, and the wiper is evaluated for the hand pattern from wiping. The aluminum foil surface may still have an uneven distribution of the drink powder. The used wiper should show a more diffuse hand pattern from the colored drink powder on its surface than the previous step. Finally, a pre-wetted wiper is quarter folded and used to wipe the aluminum foil surface. The surface should be visibly clean, and the color pattern from the colored powder should be diffuse. The result of using this technique and wiper is a diffuse hand pattern in the wiper and a clean aluminum foil surface.

## **10.5 Characterization of Wipers**

Before continuing further, an evaluation of a range of performance characteristics including fabric construction, material and micro-structure, wiper edge type, sorption capacity and rate, bioburden, ions, metals and non-volatile residues (NVRs), and particulate burden of various wiper sizes should be performed since these wiper characteristics can impact the quality of a cleanroom. One or more of these properties are important to reduce the impact on the controlled environment, product or process. The determination of which of these properties is important is mostly made by the personnel responsible for the condition and output of the cleanroom. Unfortunately, no test can designate a wiper for a specific cleanroom ISO class.

### **10.5.1 Methods to Assess Wiper Particle and Fiber Contamination Levels**

The performance and contamination characteristic of the wiper is measured through testing. A consistent set of common test protocols can be found in IEST-RP-CC004.3, "Evaluating Wiping Material Used in Cleanrooms and Other Controlled Environments" [21]. The recommended practice (RP)



describes the different types of tests used to measure the contamination levels related to wiper cleanliness. The three major types of contaminations described are particles and fibers, ions, and non-volatile extractable matter. The procedures for the enumeration of small particles and fibers are summarized below.

#### 10.5.1.1 Particle and Fiber Extraction Procedures

Testing for wiper cleanliness uses some type of motion to release particles and fibers from the wiper material. The orbital and biaxial shaker motions are used to suspend the extracted particles and fibers in the extraction medium. The orbital shaker motion lies in the horizontal plane. Water is added to a photographic tray that is placed on the orbital motion shaker. The orbital motion generates a gentle wave in the water that sluices over the wiper. This relatively gentle motion is used to remove releasable particles and fibers, i.e., particles that are resting on the surface of the wiper.

The biaxial shaker motion is generated in two planes, side-to-side and up-and-down and in a more aggressive motion. The container must be sealed to ensure that the water remains in the container. The water motion agitates the wiper in the liquid, i.e., the wiper rubs against itself, the wall, etc. This motion is used to quantify generated and releasable particles and fibers. The number of particles and fibers from a wiper that has undergone biaxial shaking is typically higher than from wipers that have undergone orbital shaking.

When the extraction is performed in an orbital shaker, different liquids can be used to aid in the release and suspension of the particles and fibers. The data presented for fiber values use a dilute solution of an octylphenol ethoxylate (TRITON® X-100 from Dow Chemical) as the extraction liquid.

##### 10.5.1.1.1 Orbital Shaker for Fiber Enumeration

The following procedure is implemented to prepare a sample for enumerating the fiber level on a wiper. In an ISO 5 (Class 100) or cleaner particle hood, 500 milliliters of deionized water is added to a well-rinsed photographic tray. Twenty-five milliliters of a 0.1% stock solution of the TRITON® X-100 surfactant is added. The tray is agitated on the orbital shaker for one minute to mix. The shaker is stopped and a test wiper is gently placed into the water. The tray is shaken for five minutes. At the end of this period, the wiper is removed and measured to determine its area. The extract water is filtered through a filter with a 0.4 µm average pore size. The filter is dried and viewed under an optical microscope (40X magnification works well). The best image for viewing fibers is generated by having the light enter the viewing field from a grazing angle, approximately 15° above the horizontal. The total number of fibers are counted and divided by the

area of the wiper extracted to give the reported results with unit of fiber per square meter (fibers/m<sup>2</sup>).

A more detailed explanation of this extraction and measurement method is presented in ASTM Standard E2090, "Standard Test Method for Size-Differentiated Counting of Particles and Fibers Released from Clean Room Wipers Using Optical and Scanning Electron Microscopy" [22].

#### 10.5.1.1.2 Biaxial Shaker for >0.5 $\mu\text{m}$ LPC Particle Enumeration

For the >0.5  $\mu\text{m}$  LPC data reported in this chapter, the wipers were extracted using the biaxial shaker and the particles were enumerated by a >0.5  $\mu\text{m}$  liquid particle counter (LPC). Wipers were extracted using only deionized water. Since an LPC operates on light scattering phenomenon, using a surfactant would generate bubbles which may interfere with the particle counting.

In an ISO 5 (Class 100) or cleaner particle hood, 600 milliliters of deionized water is added to a two-liter Erlenmeyer flask. The wiper is added to the flask. The flask is sealed with a cleaned aluminum foil lid and placed into the biaxial shaker. The wiper and water are shaken for five minutes. At the end of five minutes, the extract water is decanted into a clean beaker. The water is sampled and analyzed by a liquid particle counter. The cumulative number of particles at 0.5  $\mu\text{m}$  and larger is used for calculating the number of particles. The wiper is removed and its area measured. The number of particles in the extract is divided by this area to give the reported results in units of particles per square meter (particles/m<sup>2</sup>). A more detailed explanation of this extraction and measurement method is presented in IEST-RP-CC004.3, "Evaluating Wiping Material Used in Cleanrooms and Other Controlled Environments" [21].

The theory behind liquid particle counting is the scattering of light by small, spherical particles. The original light scattering by small particles theory can be found in [23] and in [24]. In essence, the theory states that the light scattering from a small particle is a function of index of refraction of the medium (water) and of the particle, the diameter of the particle, the angle of detection, and whether or not the particle absorbs at the incident wavelength. Particle Measuring Systems' article [25] and book [26] review the particle light scattering theory, give examples, and show applications.

## 10.6 Results Obtained Using Wiping

Cleaning is an important part of a maintenance program for a cleanroom or process. Although cleaning is a common activity, everybody does not

understand the value of cleaning using a wiper. In the cleanroom or as part of the manufacturing process, many types of surfaces are cleaned. Data will be presented showing the removal efficiency of particles from a surface by using a wiper.

The substrates that were chosen for these data do not have perfectly smooth surfaces as one finds, for example, on a cleaned silicon wafer after the chemical mechanical planarization process. In contrast, these surfaces have been in use for some time, so they will have some imperfections. However, no obvious scratches were visible on the surfaces used in the data collected below.

The particle contamination level of a surface was measured in a defined area before and after cleaning with a dry or pre-wetted wiper using a Dryden Engineering Model Q III<sup>®</sup> Surface Particle Detector. The Q III particle detector system injects air across the substrate surface under the probe which lifts releasable particles from the surface. This particle-contaminated air is swept into the air particle detector where the particles are sized and counted. The system has the ability to detect a range of particle sizes 0.3  $\mu\text{m}$  and larger. Five sizes were preset, 0.3, 0.5, 1, 5, and 10  $\mu\text{m}$ , and these were used in this experiment. Through calibration, the system determines the contamination level of the surface through the use of the air flow rate through the particle detector, the probe surface contact area, and the number of particles counted. The values for each channel are cumulative and are expressed in particles per square centimeter.

### 10.6.1 Test Method

A surface was selected for measuring the particle contamination level. A length of two feet was marked on the surface. Sufficient width was marked to allow for two separate passes of a wiper and another approximately six inches between these areas. After these sections were marked, a Dryden Engineering Model Q III Surface Particle Detector probe was scanned along the substrate surface in the center section three times. The values for each particle size range following each scan were recorded after each surface scan. These sets of three values represented the initial contamination level. A dry wiper was quarter-folded in preparation for use. The same was performed with a pre-wetted wiper. Using proper wiping technique and holding a dry wiper in the left hand and a pre-wetted wiper in the right hand, the surfaces were wiped from back to front once (shaded areas in Figure 10.10). The particle contamination level was measured for the left side where the dry wiper was used. The right side was allowed to

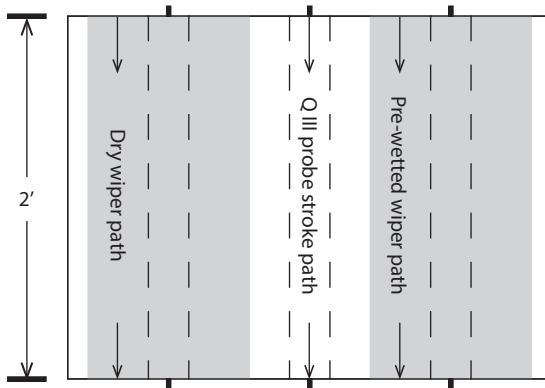


**Figure 10.10** Experimental setup for collecting surface particle contamination under different conditions. Three regions are denoted in the figure. The center white region is where the initial particle contamination level is measured. The Q III probe will sample the area between the dashed lines labeled as “Q III probe stroke path.” The shaded regions represent the areas where the dry or pre-wetted wipers pass to clean the surface. The left area is designated for the dry wiper, and the right side is designated for the pre-wetted wiper. The Q III probe passes between the dashed lines in each region three times when measuring the particle contamination level. The length of the test area is two feet. The width of each wiped area is approximately eight inches.

dry visibly with an additional one-minute delay before the particle contamination level was measured. Figure 10.10 shows the different areas referred to in the test method.

The percent cleaning efficiency for the region cleaned by the dry wiper is calculated by summing the three values for the dry region and dividing this value by the sum of the initial contamination level values and multiplying by 100% for each particle size range. The same operations are performed to determine the pre-wetted wiper cleaning efficiency by inserting the pre-wetted wiper values sum instead of the dry wiper region values sum.

### 10.6.2 Experimental Setup

Two areas (shaded) with approximately eight inch width were marked on either side of an approximate six-inch clear area (white). The center of this six-inch area was where initial surface contamination level was measured. A mark was placed in the center of each of the areas, top and bottom, to serve as a guide for the Q III probe stroke path for measuring the particle contamination level after a single pass of a dry or pre-wetted wiper in the shaded areas of Figure 10.10.

### 10.6.3 Data Collection

The Q III probe was passed three times along the same path in the center of the marked area to measure the initial surface contamination level. These values were summed. A dry wiper and a 70% isopropanol / 30% deionized water pre-wetted wiper were quarter-folded as described above. Using the wiping technique described previously, a single pass was made in the eight-inch area. The left area was used for the dry wiper. The right area was used for the pre-wetted wiper. The contamination level for each area was measured by passing the Q III probe three times over the same path marked in the center of each area. The area cleaned by the pre-wetted wiper was allowed to dry. Measurements were taken one minute after the entire area was visibly dry.

The wipers used for these experiments were critically cleaned wipers that are available as a dry wiper and also as a wiper pre-wetted with 70% isopropanol / 30% deionized water.

### 10.6.4 Results

Three substrate types were measured representing common worksurfaces in the industries that employ controlled and classified environments. The substrates used were high-density polyethylene to represent plastic surfaces, an epoxy surface commonly found in laboratories, and a stainless steel surface. The cleaning efficiencies resulting from using dry and pre-wetted wipers on a high-density polyethylene substrate at three particle contamination levels are compiled in Table 10.4.

**Table 10.4** Dry and Pre-Wetted Wiper Cleaning Efficiency Results by Particle Size on a High-Density Polyethylene Substrate at Three Relative Contamination Levels

High Contamination Level	Contamination Level, Particles/cm <sup>2</sup>			Cleaning Efficiency, %	
	Particle Size Range, $\mu\text{m}$	Initial	Post Dry Wiper	Post Pre-Wetted Wiper	Dry Wiper
>0.3	410.1	55.5	20.6	86.5	95.0
>0.5	312.1	17.1	9.0	94.5	97.1
>1	170.5	3.8	3.0	97.8	98.2
>5	41.7	0.5	0.8	98.8	98.1
>10	31.7	0.5	0.7	98.4	97.8

Middle Contamination Level	Contamination Level, Particles/cm <sup>2</sup>			Cleaning Efficiency, %	
	Initial	Post Dry Wiper	Post Pre-Wetted Wiper	Dry Wiper	Pre-Wetted Wiper
>0.3	242.9	23.6	23.2	90.3	90.4
>0.5	190.9	11.8	9.9	93.8	94.8
>1	102.9	4.5	3.2	95.6	96.9
>5	23.5	1.0	0.8	95.7	96.6
>10	17.1	0.7	0.5	95.9	97.1

Low Contamination Level	Contamination Level, Particles/cm <sup>2</sup>			Cleaning Efficiency, %	
	Initial	Post Dry Wiper	Post Pre-Wetted Wiper	Dry Wiper	Pre-Wetted Wiper
>0.3	114.6	19.9	20.2	82.6	82.4
>0.5	86.7	9.1	10.3	89.5	88.1
>1	45.2	3.6	2.8	92.0	93.8
>5	12.1	1.1	0.4	90.9	96.7
>10	10.1	0.8	0.3	92.1	97.0

The high-density polyethylene surface was located in a packaging area where cardboard boxes are used. The area is controlled, but not classified. Personnel are required to wear only hairnets and gloves in this area.

The cleaning efficiencies resulting from using dry and pre-wetted wipers on an epoxy-based substrate at three particle contamination levels are compiled in Table 10.5.

The epoxy-based substrate was located in a packaging area where cardboard boxes are used. The area is controlled, but not classified. Personnel are required to wear only hairnets and gloves in this area.

The cleaning efficiencies resulting from using dry and pre-wetted wipers on a stainless steel substrate at three particle contamination levels are compiled in Table 10.6.

**Table 10.5** Dry and Pre-Wetted Wiper Cleaning Efficiency Results by Particle Size on an Epoxy-based Substrate at Three Relative Contamination Levels

High Contamination Level	Contamination Level, Particles/cm <sup>2</sup>			Cleaning Efficiency, %	
	Initial	Post Dry Wiper	Post Pre-Wetted Wiper	Dry Wiper	Pre-Wetted Wiper
Particle Size Range, $\mu\text{m}$					
>0.3	915.5	52.2	43.0	94.3	95.3
>0.5	829.6	32.2	28.7	96.1	96.5
>1	573.2	18.7	10.7	96.7	98.1
>5	182.7	0.4	0.2	99.8	99.9
>10	146	0.2	0.1	99.9	99.9

Middle Contamination Level	Contamination Level, Particles/cm <sup>2</sup>			Cleaning Efficiency, %	
	Initial	Post Dry Wiper	Post Pre-Wetted Wiper	Dry Wiper	Pre-Wetted Wiper
Particle Size Range, $\mu\text{m}$					
>0.3	423.4	29.3	24.7	93.1	94.2
>0.5	348.4	20.4	12.0	94.1	96.6
>1	208.3	9.8	3.8	95.3	98.2
>5	70.2	1	0.3	98.6	99.6
>10	57.5	0.3	0.3	99.5	99.5

Low Contamination Level	Contamination Level, Particles/cm <sup>2</sup>			Cleaning Efficiency, %	
	Initial	Post Dry Wiper	Post Pre-Wetted Wiper	Dry Wiper	Pre-Wetted Wiper
Particle Size Range, $\mu\text{m}$					
>0.3	81.1	27.8	25.4	65.7	68.7
>0.5	63.2	12.6	12.3	80.1	80.5
>1	38.8	3.7	3.2	90.5	91.8
>5	13.4	0.4	0.1	97.0	99.3
>10	9.6	0.4	0.1	95.8	99.0

**Table 10.6** Dry and Pre-Wetted Wiper Cleaning Efficiency Results by Particle Size on a Stainless Steel Substrate at Three Relative Contamination Levels

High Contamination Level	Contamination Level, Particles/cm <sup>2</sup>			Cleaning Efficiency, %	
	Initial	Post Dry Wiper	Post Pre-Wetted Wiper	Dry Wiper	Pre-Wetted Wiper
Particle Size Range, $\mu\text{m}$					
>0.3	30.4	7.7	0.1	74.7	99.7
>0.5	14.9	4.3	0.0	71.1	100
>1	2.9	0.6	0.0	79.3	100
>5	0.3	0	0.0	100	100
>10	0.2	0	0.0	100	100

Middle Contamination Level	Contamination Level, Particles/cm <sup>2</sup>			Cleaning Efficiency, %	
	Initial	Post Dry Wiper	Post Pre-Wetted Wiper	Dry Wiper	Pre-Wetted Wiper
Particle Size Range, $\mu\text{m}$					
>0.3	7.6	1.2	0.2	84.2	97.4
>0.5	6.1	1	0.1	83.6	98.4
>1	3.1	0.5	0.0	83.9	100
>5	1	0	0.0	100	100
>10	1	0	0.0	100	100

Low Contamination Level	Contamination Level, Particles/cm <sup>2</sup>			Cleaning Efficiency, %	
	Initial	Post Dry Wiper	Post Pre-Wetted Wiper	Dry Wiper	Pre-Wetted Wiper
Particle Size Range, $\mu\text{m}$					
>0.3	4.1	0	0.2	100	95.1
>0.5	3.6	0	0.1	100	97.2
>1	1.7	0	0.0	100	100
>5	0.4	0	0.0	100	100
>10	0.3	0	0.0	100	100



The stainless steel surface was located in a controlled area where a manufactured product undergoes its final cleaning and packaging steps. Product enters and exits this area by a cleanroom pass-through window. No cardboard boxes are used in this area. Cleaning activities include daily surface wipe downs of the walls and all worksurfaces. Personnel are required to wear hairnets, masks, smocks, shoe covers and gloves in this area.

### **10.6.5 Comments**

The cleaning efficiency approaches 100% at higher surface contamination levels on all surface types studied. Larger particles are easier to remove as shown by the increasing cleaning efficiencies as was predicted [8, 9].

It should be noted that the process for these measurements of the surface contamination level values were generated from particles that were released from the surface and entrained for counting in high velocity air.

## **10.7 Future Directions**

### **10.7.1 Nanotechnology**

As cleanrooms use nanotechnology or manufacturing components containing nano-sized components (such as the line widths found in the leading edge semiconductor technology), new types of wipers are needed. The contamination profile of the wiper material will also be important. Any particles shed by the wiper will contain the same constituents as the wiper. Presently, the semiconductor technology companies are focusing their efforts on line widths in the 14 – 22 nm range, approximately 50 atoms across. Because of the narrow line widths, quantum effects may be significant. Particles whose diameter is much larger than these line widths may distort the electronic signals passing through the point of contact. Wiper material and cleaning capability must be able to meet this challenging environment. Wiper material of construction must change from the current relatively cleaner polyester to another polymer such as poly(vinylidene fluoride) or poly(tetrafluoroethylene) (Teflon®). However, these polymers are expensive and difficult to form into fabric for wiper construction. Since these materials are not readily available, the cost to manufacture will be expensive.

### **10.7.2 Microfiber Technology**

In the biotechnology and injectable drug segments of the Life Sciences industry, aseptic cleanrooms are used for manufacturing complex

pharmaceuticals derived from microbes grown in a broth or by dissolving small molecules in solution to be ready for injection. In these cleanrooms, larger particles, e.g., greater than 5  $\mu\text{m}$ , and microbes are critical sources of contamination. Sterile wipers are used for removing particles and microbes and also for applying and removing disinfectants from surfaces. Microfiber aids in the removal of these contaminants, especially microbes.

Microfiber fabrics are produced through two processes. One process forms more smaller-than-normal diameter filaments made from a single polyester polymer. The benefit of this process is that the final wiper has the same chemical resistance as a normal polyester wiper. The disadvantage of this process is that filaments are more prone to break during processing, which may produce particles and fibers. Another manufacturing process co-extrudes two polymers, such as nylon and polyester. The yarn is extruded as larger filaments allowing easier yarn processing. After the yarn is knitted or woven into a fabric, it is chemically treated to remove the nylon. The filament's shape changes from circular to textured, e.g., a star pattern, with a high surface area. The benefit of this process is the ease of fabric manufacturing using a stronger yarn. The disadvantage is the chemical treatment process never removes all the nylon from the fabric. This leads to increased particle shedding and poorer chemical resistance than pure polyester. Using either microdenier manufacturing process yields yarn with increased surface area of the filaments. The same physical characteristics that give microfiber wipers the ability to clean surfaces make it difficult to manufacture suitably clean wipers. The future of microfiber wiper products depends on finding manufacturing processes that can clean these wipers to meet the needs of the industry.

## 10.8 Summary

Wiper-based cleaning is used throughout the controlled-area industries. This method is the most efficient for contamination removal from large areas in a controlled fashion. The contaminating particles are removed for the process or environmental surface and transferred to the wiper. The contaminated wiper is removed from the area taking the particle contamination with it.

Different methods for removing particles were briefly discussed. These methods have their own advantages and disadvantages and were developed for a specific type of surface or a specific surface configuration. While these methods work well for their intended use, they are not flexible enough to remove particles from a variety of surfaces and shapes and to prevent the loosened particle contamination from spreading. A hand and a wiper have

the advantage of being able to wipe a surface irrespective of the orientation or type. The particle contamination is removed from the surface and trapped into the wiper. Typically, a hand and a wiper are used for most horizontal surfaces. If the surface is vertical, e.g., walls, the wiper is attached to a mop head and handle for reaching from the floor to the ceiling.

The adhesion of particles to surfaces is the result of many forces acting together. The strongest force is the van der Waals force where interactions between the electron densities of molecules in the particle and surface create an attractive force. Electrostatic and capillary forces also induce attraction between the contaminating particle and the surface. Overcoming these forces is required to clean a surface. The proposed mechanism is primarily a wiper filament impacting a particle adhered to a surface, especially when cleaning with a dry wiper. Once the particle is released from the surface, it becomes attracted and attached to the wiper filament. The mechanism is the same when using a pre-wetted wiper; however, there is liquid that can act to reduce or eliminate the capillary force between the particle and the surface. Again, once the particle is released from the surface, it becomes attracted and attached to the wiper filament. The result is a cleaner surface with the contaminating particles contained in the wiper.

Cleaning is a tedious and time-consuming process; however, it is an extremely important task since it impacts the environment, process and product yield. Deciding which wiper to select for cleaning is a not a simple task. The physical and contamination characteristics of a wiper must be compared to the needs of the environment, process and product, and the contaminants and surfaces to be cleaned. Reliably measuring the particle contamination level, one aspect of the contamination characteristics of a wiper, is difficult. However, extracting particles from a wiper using a liquid medium is repeatable. The resulting medium contaminated with particles can be assayed for the particle level, and, through some calculations, the particle contamination level of the wiper can be determined. Even after this determination, the cleanest (lowest number of particles) wiper may not be suitable for the intended use. A wiper is more than its particle contamination level. The other physical characteristics also affect the cleaning performance. Cost must also be considered as part of the wiper selection process. All of these aspects of the wiper are used in the selection process to determine which wiper is best for cleaning the environmental and process surfaces to achieve acceptable product yields.

Measurements of the cleaning efficiency for several types of surfaces were made. It was observed that the cleaning efficiency of a pre-wetted wiper was generally higher than that of a dry wiper. The increased cleaning efficiency is due to the reduction or elimination of the capillary force acting between the particle and the surface.

## References

1. K.L. Mittal (Ed.), *Particles on Surfaces 8: Detection, Adhesion and Removal*, CRC Press, Boca Raton, FL (2003).
2. K.L. Mittal (Ed.), *Particles on Surfaces 9: Detection, Adhesion and Removal*, CRC Press, Boca Raton, FL (2006).
3. J. Postlewaite, B. Lyon, and S. Kalelkar, Cleanroom wipers for removal of surface contamination, in: *Developments in Surface Contamination and Cleaning*, Vol. 5, R. Kohli and K.L. Mittal (Eds.), pp. 123–163, Elsevier, Oxford, UK (2013).
4. T.K. Kim, S.Y. Kim, H.J. Kim, and K.H. Suh, CMP slurry composition and a method for planarizing semiconductor device using the same, US Patent 7029509 assigned to Dongbuanam Semiconductor, Inc. (Apr 18, 2006).
5. D. Hynes, I. Malik, J. Zhang, and R. Emami, Brush scrubbing emerges as future wafer-cleaning technology, *Solid State Technol.*, 40 (7), 209–214 (1997).
6. D. Jackson, CO<sub>2</sub> composite cleaning critical for photonic devices, *Photonics Spectra*, 47 (6), 52–53 (2013).
7. F. Zhang, A.A. Busnaina, M.A. Fury, and S-Q Wang, The removal of deformed submicron particles from silicon wafers by spin rinse and megasonics, *J. Electronic Mater.*, 29, 199–204 (2000).
8. R.A. Bowling, A theoretical review of particle adhesion, in: *Particles on Surfaces 1: Detection, Adhesion, and Removal*, K.L. Mittal (Ed.), pp. 129–142, Plenum Press, New York (1988).
9. M.B. Ranade, Adhesion and removal of fine particle on surfaces, *Aerosol Sci. Technol.*, 7, 161–176 (1987).
10. C.E. Mortimer, *Chemistry: A Conceptual Approach*, 4<sup>th</sup> edition, p. 136, Van Nostrand Reinhold Company, New York (1979).
11. R.C. Reid, J.M. Prausnitz, and B.E. Poling, *The Properties of Gases & Liquids*, 4th ed., McGraw-Hill, Boston (1987).
12. D.R. Lide, (Ed.), *CRC Handbook of Chemistry and Physics*, 72th ed., CRC Press, Boca Raton, FL (1991).
13. H. Siegeman, *Wiping Surfaces Clean*, Vicon Publishing, Inc., Amherst, NH (2004).
14. W.L. McCabe and J.C. Smith, *Unit Operations of Chemical Engineering*, 2nd ed., p.163, McGraw-Hill Book Co., New York (1967).
15. Cleanroom housekeeping: Operating and monitoring procedures, IEST-RP-CC018.4 (2007).
16. Y. Wong, How small can the naked eye see?, *Focus Science and Technology*, <http://sciencefocus.com/qa/how-small-can-naked-eye-see> (2010).
17. Y. Igarashi and Y. Ito, Double-knit fabric having non-run and stretchability characteristics and method and apparatus for knitting the same, US Patent 5463881 assigned to Precision Fukuhara Works, Ltd. (November 7, 1995).
18. A.W. Koester, New developments in microdenier fibers and fabrics, a report from Oregon State University Extension Service, Corvallis, OR (1992).

19. M.W.D. Wren, M.S.M. Rollins, A. Jeanes, T.J. Hall, P.G. Coën, and V.A. Gant, Removing bacteria from hospital surfaces: A laboratory comparison of ultra-microfibre and standard cloths, *Hospital Infection*, 70, 265–271 (2008).
20. S.J. Paley, C.A. Eberhardt, and E. Paley, Wipers for cleanroom use, US Patent 4888229 assigned to The Texwipe Company (December 19, 1989).
21. Evaluating wiping materials used in cleanrooms and other controlled environments, IEST-RP-CC004.3 (2004).
22. Standard test method for size-differentiated counting of particles and fibers released from cleanroom wipers using optical and scanning electron microscopy, ASTM E2090–00 (2012).
23. G. Mie, Beiträge zur Optik trüber Medien, speziell kolloidaler Metallösungen, Leipzig, *Annals Phys.* 330, 377–445 (1908).
24. D.W. Hahn, University of Florida, Gainesville, Florida, Light Scattering Theory, <http://plaza.ufl.edu/dwhahn/Rayleigh%20and%20Mie%20Light%20Scattering.pdf> (2009).
25. Particle Measuring Systems, Boulder, Colorado, Basic Guide to Particle Counters and Particle Counting, [http://www.pmeasuring.com/wrap/filesApp/BasicGuide/file\\_1/ver\\_1317144880/basicguide.pdf](http://www.pmeasuring.com/wrap/filesApp/BasicGuide/file_1/ver_1317144880/basicguide.pdf) (2011).
26. E. Terrell, J. Gromala, and D. Beal, *Understanding Liquid Particle Counters*, Particle Measuring Systems, Boulder, CO (2006).



# Application of Strippable Coatings for Removal of Particulate Contaminants

Rajiv Kohli

*The Aerospace Corporation, NASA Johnson Space Center, Houston, TX*

---

## Abstract

The use of strippable coatings is a low-cost, effective method for removal of particle contaminants from the surface of high quality parts and to protect the cleaned parts from surface damage. The coating is applied to the surface by spraying, rolling or brushing. The coating is allowed to cure and then removed by peeling. A wide variety of solvent- and water-based strippable coatings are available for precision cleaning of surfaces and for protecting surfaces that have been cleaned. The coating formulations are designed to entrain the particle contaminants by physical or chemical means. This chapter provides an overview of the types of strippable coatings and their properties, and discusses some of the applications of these coatings for removal of particle contaminants on a variety of surfaces. One successful application has been removal of dust and debris from precision optical surfaces, such as coated lenses and mirrors. Other applications include decontamination of surfaces by removal of hazardous and radioactive contaminants.

**Keywords:** Strippable coatings, decontamination, mirrors, telescopes, optics, radioactive decontamination, collodion, particles

## 11.1 Introduction

Peelable strippable coatings are used to remove microsize contaminants from high quality surfaces such as glass and optics, as well as metals, ceramics and polymers and to protect the cleaned parts from surface damage. One successful application has been removal of dust and debris from

---

*E-mail:* rajiv.kohli@aero.org

---

K.L. Mittal and Ravi Jaiswal (eds.) Particle Adhesion and Removal, (411–452)  
2015 © Scrivener Publishing LLC

precision optical surfaces, such as coated lenses and mirrors. For such cleaning applications, the coating must also mechanically or chemically trap the surface contaminants, and it must easily release from the surface after it has dried. The coating can be applied by simply pouring it over the surface to be cleaned. After drying (5 minutes to 4 hours at room temperature in air), the coating is removed by peeling. Contaminant particles (20 to 30  $\mu\text{m}$ ) on the surface can be completely removed. This is a low-cost, effective method for cleaning and protecting high quality surfaces. However, care has to be taken to ensure that the coating itself does not leave any residue on the surface. The strippable coating can be effectively applied to all solid surfaces for particle removal, regardless of the roughness of the surface.

This chapter is an update of a previous overview of strippable coatings and their application to removal of surface contaminants [1]. The primary emphasis in this chapter will be on coatings for removal of particle contaminants with examples of recent applications.

## 11.2 Coating Description

Typically, strippable coatings contain non-volatile components comprising about 41–71% and volatile components comprising about 29–59% by weight of the coating composition. The non-volatile components consist of a resin which is incorporated into a solvent or aqueous carrier, together with wetting agents and defoamers. The mixture is dispersed by means of additives to produce a stable polymeric emulsion or dispersion, which can be easily applied by spraying, brushing or rolling. The solvent and the water in the carrier evaporate upon application of the coating and leave behind a clear coating. A combination of release aids and plasticizers incorporated into the composition allows the coating to maintain its cohesiveness when it is subsequently peeled off. The dried coating itself acts as a barrier to protect the release agents. Many coating formulations applied to metal test panels and dried at 120°C for 30 minutes form a film which is mechanically strippable even more than a year after application [2].

### 11.2.1 Coating Properties

The desirable properties of a strippable coating are listed below.

- The coating cures at low temperatures.
- It is fast drying or curing.



- It has low viscosity for air assisted spray application.
- The coating material has excellent water and acid resistance at temperatures to 100°C.
- It must have excellent adhesion to most surfaces including metals, ceramics, concrete and other materials, but it must be peelable from the surface.
- It should have the ability to lock in the surface contaminants.
- The coating leaves no residue after removal from the applied surface.
- The coating has excellent cohesion. When pulled, it stretches and peels off in large sheets.
- It does not exhibit any sag.
- The coating retains its flexibility and does not become brittle with age.
- The coating is easily applied by spray, brush, or roller.
- The coating should be nonflammable.
- It should meet United States EPA (Environmental Protection Agency) and OSHA (Occupational Safety and Health Administration) requirements for low solvent emission and safety in the workplace.

### 11.3 Types of Strippable Coatings

There are two primary types of strippable coatings in commercial use. These are either solvent-based coatings or they are water-based coatings. Due to concerns for the environment, the use of water-based coatings is finding increasing application. Other coating formulations have been developed for special applications.

#### 11.3.1 Solvent-Based Coatings

One of the most common solvent-based strippable coatings that has proven to be very effective in precision cleaning of optical components is collodion.

##### 11.3.1.1 *Collodion*

Collodion is a nitrocellulose, ethyl alcohol, and ether solution that has been around since its discovery in 1846 [3, 4]. However, it was not until 1848 that collodion became a highly desirable commercial commodity

when John Maynard created collodion as a liquid bandage for surgical application, which would harden on skin, seal the wound, and provide a protective covering [5]. Its structure and properties have been extensively investigated [1].

Collodion in which there is a great excess of ether forms a very tough film upon evaporation. The film left by collodion containing a large quantity of alcohol is soft and easily torn; but in hot climates the presence of an excess of alcohol is an advantage, as it prevents the rapid evaporation of the ether.

Collodion has a wide range of uses in industry including applications in the manufacture of photographic film, in fibers, in lacquers, and in engraving and lithography. Collodion is also widely used for manipulating and removing small particles (0.5  $\mu\text{m}$  and larger) in preparation for microanalysis [6,7]. Celloidin, a form of collodion, is a pure type of pyroxylin used to embed specimens which will be examined under a microscope [8,9]. Collodion membranes have been used extensively in medical and biological applications [10], while composite membranes with a fluorocarbon polymer, such as Nafion, have also been used for desalination of water [11].

From its first discovery, collodion has been available in many different grades and compositions [12–14]. Normal or plain collodion is a solution of pyroxylin in a mixture of ether and alcohol. For cleaning applications, only Collodion USP should be used. This grade of collodion is a mixture of cellulose nitrate (3–7 wt %) in an ethyl ether (65–75 wt %) and ethanol (20–30 wt %) solution [15].

### 11.3.1.2 *Other Solvent-Based Coatings*

Carbicote 946 (Carbit Paint Company, Chicago, IL) [16] is a white solvent-based booth coating which protects spray booth surfaces from the overspray of paints and coatings applied within the spray booth. The coating applies easily by spray, brush, or roller and forms a continuous film membrane, which acts as a barrier between the wet paint overspray and the clean metal spray booth surface. It is a temporary coating designed to be stripped during booth maintenance. The product dries quickly; after 15 minutes it can be handled and it is hard in 30 minutes for a typical thickness of 0.05 mm. Drying times will be extended by high humidity, cold temperatures, and increased film thickness. The thickness can be built quite rapidly with minimum sagging and running. Typical coverage is 4 m<sup>2</sup> per liter at 0.05 mm dry thickness.

Discoat 4210 (General Chemical Corporation, Brighton, MI) is a clear, solvent-based, water-resistant coating for protection of optical media such

as compact discs and video discs from scratching and marring during manufacturing process [17]. It is stabilized against brittleness and is not softened or penetrated by most water-based compounds. It can be applied by spinning or dipping and it does not leave a residue. The coating is impregnated with transparent blue dye for easy visual inspection as well as identification and is non-staining and stable to 100°C. Discoat 4210 offers some real performance advantages, especially its ability to remove water stains and moisture related defects. Moisture related defects, as measured by loss of electrical signal read-back of nickel electroforms, are reduced by as much as 50%. This is significant since an optical nickel electroform can cost between \$50 and \$75 to produce.

### 11.3.2 Water-Based Coatings

Several water-based coatings have been developed and are available commercially.

#### 11.3.2.1 *Opticlean*®

Opticlean® (Photonic Cleaning Technologies, Platteville, WI) is a molecular polymer cleaning system [18, 19]. It was developed to clean and protect silicon wafers during manufacturing. The solvents used to hold the polymer in solution are acetone, ethanol and ethyl acetate. As the polymer cures it shrinks and absorbs any contamination on the part surface into the polymer molecule. This includes particulates as well as fingerprints, grease, oil and atmospheric pollution. When the cured film is peeled away, the polymer removes all the adsorbed contaminants with it leaving a molecularly clean surface (Figure 11.1). The polymer is hydrophilic and can be softened with the application of a touch of water. In many industrial applications the polymer is left on for long periods of time, sometimes for many months. The Opticlean® cured film is rugged and slightly pliable, giving it good protection against fingerprints, atmospheric contamination and any other minor hazards. The film can be removed just as easily after two weeks as after two minutes.

This type of coating is difficult to see as it forms a thin uniform layer. The “D” test shows the effect very well. By cleaning a “D” shaped section on one half of the lens, it is easy to see how much contamination has been removed from the surface by the coating.

The high cost of Opticlean® can be a deterrent to more common use of the coating for cleaning lenses. However, so little is used to clean camera lenses that one standard package can clean both the front and back



**Figure 11.1** A protected aluminum mirror before and after cleaning with Opticlean®. Courtesy of Photonic Cleaning Technologies, Platteville, WI.

elements of more than 12 typical standard lenses. This compares favorably to the cost of conventional cleaning methods. Furthermore, Opticlean® is non-abrasive and leaves a perfectly clean surface, which is the best way to clean mirrors and lenses without removal from the mounts. Lens mounts are not normally plastic and are unlikely to be damaged in any way by the polymer.

#### 11.3.2.2 CARBICOTE®

CARBICOTE® is a water-based strippable coating that can be easily removed from many surfaces [20]. It is commonly used as safe peel-off protection for spray booth walls, lights, and windows. The coating is available as a reflective or a transparent coating. The coating offers several advantages. It is easy to apply by spray, brush, or roller. It dries quickly, forming a removable barrier in minutes. The coating has excellent cohesion and peels off in large sheets. It adheres well to most surfaces including stainless steel and it does not become brittle with age. The coating is freeze-thaw stable with a built-in safety factor that protects it from accidental freezing.

#### 11.3.2.3 Universal Photonics Coatings

Several coatings are offered by Universal Photonics, Hicksville, NY [21]. The Strippable Black Coating is a fully strippable material which leaves no residue or film whatsoever and will, in fact, pick up foreign particles that

are removed when the coating is stripped off. It is well suited for cleaning mirrors. The Peelable Blue Coating removes easily with cellophane tape or rinsing in hot water and is suitable for plastic or glass lenses and mirrors. This product will remove dust and loose particles on the surface of the mirror, but it will not remove spots or stains caused by liquid or moisture on the surface. The Ultra Red Stripcoat is a transparent, brushable or sprayable coating that prevents marring of bright metal and optical surfaces from dirt and dust. It is soluble in toluene or methyl ethyl ketone. These coatings are available in liquid form or in aerosol spray cans and may be easily peeled off after use. They dry to the touch in 15 to 20 minutes and one can of the coating will cover approximately  $0.19 \text{ m}^2$  surface area or approximately  $5.4 \text{ m}^2$  per liter.

#### 11.3.2.4 *CorShield® VpCI™*

CorShield® VpCI™ Strippable Coating (Cortec Corporation, St. Paul, MN) is a water-based, non-flammable, environmentally friendly temporary coating that can be easily removed without the use of paint strippers or cleaners [22]. It does not leave residual contamination on stripping. The unique combination of water-based acrylic polymers, vapor phase corrosion inhibitors and a thixotropic thickener provides excellent barrier, surface and corrosion protection. Designed for use as a fast-drying, temporary coating for parts and equipment, this product is resistant to sagging and running. It can be applied by spraying, brushing, rolling or dipping. The clear coating can be tinted in a variety of custom colors. The coating can be used in one or two coats. Two coats should be applied on porous surfaces and for medium to long-term outdoor protection. To achieve good strippability, the recommended thickness per coat should not be less than 0.05 mm.

#### 11.3.2.5 *Adhesive Coatings*

ARclean® and ARclear® (Adhesives Research Inc, Glen Rock, PA) [23] are acid-free, electronically clean (meets particle cleanliness requirements), low-outgassing acrylic adhesive products for controlling chemical contamination in the hard disk drive industry and the assembly of touch screens, flat panel displays, and liquid crystal display (LCD) screens. They have low extractable ions and offer resistance to environmental aging. The products minimize corrosion and reduce fogging and potential oxidation of oxide surfaces or conductive circuitry in touch-screen devices. These products eliminate contamination and minimize labor costs associated with adhesive residue during rework.

### 11.3.3 Coatings for Removal of Radioactive Contamination

#### 11.3.3.1 ALARA 1146™ Strippable Coating

ALARA 1146™ Strippable Coating (Carboline Company, St. Louis, MO) is a single component, water-borne vinyl coating that contains no solvents or toxic materials [24]. It has a solids content of  $41\% \pm 2\%$  by volume and volatile organic content of 14 g/l. The coating migrates into microvoids on the surface to contact contaminants. It attracts and mechanically binds the surface contaminants into the polymer matrix. Drying times are approximately 18 hours for handling and foot traffic and 24 hours for removal by peeling. These times are based on recommended dry film thickness per coat of 0.5–0.75 mm at 28°C and 75% relative humidity. Strippability is thickness dependent. Low film thicknesses make it difficult to remove the coating. Coating thicknesses above the recommended maximum result in slower drying times. Removal of the film decontaminates the surface and produces a solid waste. ALARA 1146 can achieve decontamination factors of 30 to 100 depending on the substrate.

#### 11.3.3.2 Stripcoat TLC Free™

Stripcoat TLC Free™ (Bartlett Services, Inc., Plymouth, MA) is a non-hazardous, non-toxic solution designed as a simple, cost effective method for safely removing and preventing the spread of radioactive contamination [25]. It can be used for nuclear reactor cavity, area or equipment decontamination, including glove boxes and hot cells. The coating can also be used as a barrier to prevent areas and equipment from becoming contaminated during maintenance activities, or as a covering to contain contamination. For decontamination purposes, the coating is applied and allowed to cure. Surface contaminants are mechanically and chemically entrapped in the coating. When the cured coating is removed, the surface contaminants are removed with the coating, yielding a solid waste product that is fully approved for disposal at low-level radioactive waste facilities or by incineration. 30 m<sup>2</sup> of coated surface generates approximately 0.03 m<sup>3</sup> of uncompacted radioactive waste. Depending on the substrate, decontamination factors (DFs)<sup>1</sup> of several hundred can be achieved with Stripcoat.

---

<sup>1</sup> DF is a measure of the effectiveness of a decontamination process. It is the ratio of the original radioactivity to the remaining activity after decontamination.

### 11.3.3.3 DeconGel™

DeconGel™ (Cellular Bioengineering, Inc., Honolulu, HI) is a one component, water-based, broad application peelable decontamination hydrogel that lifts, binds and encapsulates surface contaminants into the rehydratable matrix [26]. Safe and user friendly, DeconGel™ can be used for radiological and non-radiological decontamination, including radioisotopes, particulates, and heavy metals, as well as water-soluble and insoluble organic compounds (including tritiated compounds). The product can be easily applied to a wide variety of horizontal, vertical and inverted metallic and non-metallic surfaces (Figure 11.2). It is already in broad use at many industrial and nuclear sites. Further testing has shown the efficacy of variations of this gel against chemical and biological contamination including spore-forming organisms, raising the possibility of its use as a single chemical, biological and nuclear decontamination agent.

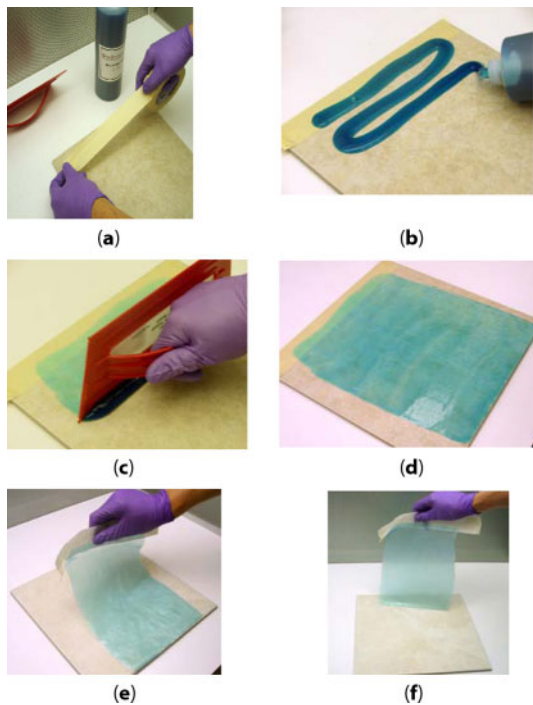


**Figure 11.2** Application of DeconGel™ coating on flat surfaces. (a) One end of the contaminated area is taped. (b) The coating is applied to the tape and the contaminated area. (c) and (d) The coating is spread by a trowel held at 90° to the surface to cover the contaminated area. (e) and (f) Once the coating has dried, it is peeled off using the taped end. *Courtesy of Cellular Bioengineering Inc., Honolulu, HI.*

#### 11.3.3.4 *InstaCote CC Strip and CC Wet*

Contamination Control Strippable (CC Strip) and Contamination Control Wet (CC Wet) coatings from InstaCote Inc, Erie, MI are used in a dual-step process to decontaminate surfaces contaminated with plutonium and uranium [27, 28]. Both materials are water-based, non-toxic, and non-hazardous, and can be applied by spraying or brushing. The material sets in less than about 1 hour and is substantially unaffected by exposure to radiation. CC Wet is the first step in controlling removable contamination. CC Strip is then applied over CC Wet. CC Strip causes the CC Wet to be rehydrated and absorbed by the CC Strip. The contamination originally captured by the CC Wet is now removable with the CC Strip. CC Wet contains a UV sensitive dye that allows feedback to the applicator during application. After CC Wet has cured, an ultraviolet light will insure verification of coverage to all surfaces. DFs as high as 100 can be achieved using CC Strip in plutonium glove boxes.

#### 11.3.3.5 *Capture Coating*

Encapsulation Technologies (Encapsulation Technologies, Los Angeles, CA) has developed a patented process to eliminate airborne radioactivity and fix contamination in place remotely without the need for people or equipment to enter the process area [29]. The process employs a Passive Aerosol Generator (PAG) which creates an aerosol by submerging parabolic shaped piezoelectric ultrasonic transducers in the solution of the capture coating. Capture coatings consist of a water-based polyurethane suspended in a two-part organic solution. They are formulated for various applications, from tacky, glycerin-based coatings that allow the application of a strippable coating for convenient disposal of the surface contaminants, to formulations with special adhesion promoters to enable the capture coating to more easily form on difficult hard surfaces. Using ultrasonic technology creates an aerosol that has the same chemical properties as the liquid coating. The droplet size (mean size  $\sim 2 \mu\text{m}$ ) is such that the coating material assumes the properties of a gas, making it possible to slowly and evenly coat inaccessible areas and crevices. The aerosol droplets formed have the same chemical properties as the liquid. The droplet size of the aerosol is controlled by varying the frequency of the transducers. The aerosol or „fog“ is introduced into the process area where it condenses on surfaces. The small organic molecules begin to coalesce and encapsulate the contaminants in place. The small aerosol droplet size allows the capture coating to effectively „scrub“ airborne contaminants from the air.



#### 11.3.3.6 *Isotron Radblock™*

Isotron Radblock™ (Isotron Corporation, Seattle, WA) is a fixative system using a rubber-based coating that attracts and binds particulate contamination through adhesive bonding or ionic radionuclides through chemical bonding or ionic exchange [30–32]. It is applied by a variety of brush, roll or spray equipments. Upon curing, the coating mechanically and chemically traps contaminants and can be peeled to remove contamination in a solid waste form. The coating provides theoretical coverage of approximately 3 m<sup>2</sup> surface area and the recommended optimal coating thickness is 0.5–1.0 mm.

#### 11.3.3.7 *Smart Coatings*

Polymeric smart coatings have been developed that are capable of both detecting and removing hazardous nuclear contaminants [33, 34]. The coatings are commonly based on polymers and copolymers in a water base modified through the use of organic or inorganic additives as plasticizers, chelating agents, and indicators. A typical example of such a smart coating is SensorCoat developed by Los Alamos National Laboratory for the detection and removal of both uranium and plutonium from contaminated surfaces [35]. This coating consists of a blend of a low viscosity, partially hydrolyzed poly(vinyl alcohol) and poly(vinyl pyrrolidone) in water. The coating also contains a glycerin plasticizer (4% to 12%), a chelating masking agent, and a colorimetric indicator. The coating exhibits color changes from orange to purple for uranium and orange to red for plutonium. Tests on uranium-contaminated surfaces (Al, Ni, stainless steel and painted cement) showed DFs from 490 to 1540, illustrating the effectiveness of this coating. The coating was less effective on plutonium-contaminated stainless steel where a DF of only 146 was achieved.

#### 11.3.3.8 *Electro-Decontamination System*

A decontamination system has been proposed that combines the advantages of strippable coatings and electrochemical stripping to remove both smearable and fixed radioactive contaminants [36]. The method consists in applying a gel-like strippable coating to a contaminated surface of the object and passing an electrical current through the applied gel which will drive the contaminants into the coating material. The applied coating is cured and removed by peeling. This system can remove both fixed and smearable contaminants from large stationary surfaces, regardless of orientation, by capturing the contaminants in the gel, and preventing

uncontrolled transport of the radioactive materials to other locations. The cured gel contains the radioactive materials in a solid form that can be handled by existing radioactive waste handling processes. The system is suitable for use in tight and confined spaces, such as under glove boxes, inside tanks and vessels, or in overhead ceiling spaces and pipe chases. This electrochemical strippable coating system is available commercially as the ElectroDecon™ system with the electroactive strippable coating, RedOxy Peel™ [37].

Several other coatings and pastes for removal of radioactive contamination have been developed and successfully demonstrated in a number of decontamination applications [1].

### 11.3.4 Hazardous Materials Cleaning

#### 11.3.4.1 *HaloShield® Coatings*

HaloShield® (HaloSource Inc, Bothell, WA) coatings are being developed as strippable barriers and reactive coatings for the U.S. Department of Defense (DoD) and U.S. Department of Homeland Security (DHS) [38–43]. These coatings are based on patented technology that binds chlorine molecules to virtually any textile, hard surface or paint, thereby extending chlorine's efficacy for the life of the material (Figure 11.3). Research shows that 99.99 percent of odor-causing bacteria are killed in 30 seconds to an hour after they come in contact with a surface or textile.

#### 11.3.4.2 *Coatings for Removal of Beryllium*

For solid beryllium remediation, the common preferred method is to wash, soak or rinse the contaminated area with aminophenyl methylene diphosphoric acid (APMDP) and collect the washes for disposal. This is ideal for machine tools or work surfaces, but not practical for larger environmental areas such as fields or roads. Several more appropriate methods have been proposed that use a gel, foam or strippable coating containing APMDP that could be pulled away from the surface by hand, by mechanical means, or by vacuum [44]. The cleaned solid or liquid material can be recycled.

### 11.3.5 UV Curable Coatings

In ultraviolet (UV) curing, a reactive, low viscosity and usually solvent free coating material is applied to the substrate and then polymerized by exposure to UV-light [17]. The UV curing mechanism involves chemical reactions of polymerization of di-functional and poly-functional compounds

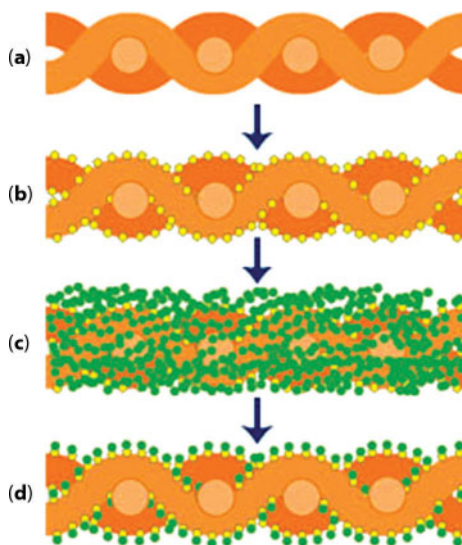


**Figure 11.3** Principle of HaloShield® technology. (a) Untreated fiber. (b) The fiber surface is treated with HaloShield® N-halamine technology. (c) The treated fiber is washed in chlorine bleach. (d) The chlorine molecules are bound by the HaloShield® coating and are anchored to the fiber. *Courtesy of HaloSource Inc., Bothell, WA.*

in the formulation, resulting in cross linking of the cured films. UV curable peelable coatings are one-component systems which typically consist of oligomeric acrylates, acrylic monomers, reactive diluents, photoinitiators, additives and modifiers. The main types of acrylic oligomers used are: epoxy acrylates, polyester acrylates and polyurethane acrylates. These oligomers provide the basic functional properties of the resulting coating. Photoinitiators are a very important component of coating composition, which initiate the polymerization (curing) process when the coating composition is exposed to UV light at a certain wavelength. Different additives can be used to enhance coating properties such as wetting, surface leveling, flow rate, and color. Modifiers can increase durability (impact and crack resistance) of the UV peelable coatings.

Through careful raw material selection, UV curable coatings formulators can more easily manipulate physical properties, such as chemical and weather resistance as well as mechanical properties, such as tensile strength and elongation. Controlling these properties can lead to customized peelable coatings that meet specific performance criteria for each application. The properties of UV cured peelable coatings are often superior to those of other systems.

In addition to performance benefits, UV-curable strippable coatings provide several processing advantages over traditional solvent-borne or aqueous-based technologies.

- Since UV curable coatings contain no solvents, volatile organic compound (VOC) emissions are in compliance with U.S. EPA regulations.
- UV curable, peelable coatings cure (air dry) much faster than solvent-borne/water-borne counterparts. In fact, curing takes only a few seconds, which makes UV curable coatings particularly economical by decreasing application (masking) times and increasing production cycles (profitability).
- Very little heat is applied to the substrate.
- Curing is not dependent on temperature or humidity conditions of the environment.
- Superior film properties (thermosetting, mechanical, and chemical properties) can be achieved.
- The coatings exhibit good cost/performance ratios.
- The application of these coatings requires minimal capital investment.
- Coating dispersion can be automated.
- The coating may be applied by dipping, spraying, screen printing or pad printing.
- These coatings are worker and environmentally friendly.

Probably the most widely used UV cured protective coating is the peelable type coating. UV curing, which cures the film in a few seconds, provides durable and cross-linked films with sufficient adhesion for surface protection of objects during handling, storage, transportation, and in manufacturing operations such as machining, acid stripping, and solvent cleaning. UV curable peelable coatings are easily removed manually or with the help of a non-abrasive tool. Typically, removal of the coating starts by lifting up the edge and then peeling off the complete coating in one piece rather than in fragments. The peeled coating is basically cross-linked plastic and non-hazardous film which can be disposed of according to local regulations for waste plastic materials. These films exhibit elastic properties at room temperature and several films are available that retain their elastic properties at temperatures above 100°C [45–48].

These water-based and solvent-based peelable optical media protective coatings are used for silicon wafers, glass, photomasks, magnetic media

platter, and optical media discs. The coatings are fast drying peelable coatings to protect optical media temporarily from scratching and marring during industrial processing or in material handling and long term storage.

### 11.3.5.1 Adhesive Tape

An adhesive tape can be used to remove sub-micrometer particles from silicon wafers [49–52]. Typically, the tape has a carrier film (polypropylene) and an adhesive layer (acrylic-based adhesive) which is applied to the polished wafer surface. UV radiation is used for curing which breaks down the adhesive layer. Since the cohesive strength of the adhesive layer is greater than the adhesion force between the contaminant particles and adhesive layer, the particles are removed when the tape is peeled off (Figure 11.4). One commercially available tape from Nitto Denko Corporation (Toyohashi, Aichi, Japan) contains a microcapsule foaming agent in the adhesive which is activated when a certain temperature is reached during UV curing [53]. The heat energy is converted to mechanical energy for adhesive release. The foam adhesive is nearly three times as effective in removing contaminant particles as is conventional tape that contains non-foam adhesive [54].

One disadvantage of conventional adhesive tape is that it leaves residual contamination on the wafer or other substrate when the tape is removed [53,55]. However, cleanroom-compatible tapes used for cleaning and protection of surfaces contain very low amounts of additives of low cohesive strength [53,54]. Any adhesive residue remaining on the wafer surface can be removed by rinsing the wafer in a solvent.

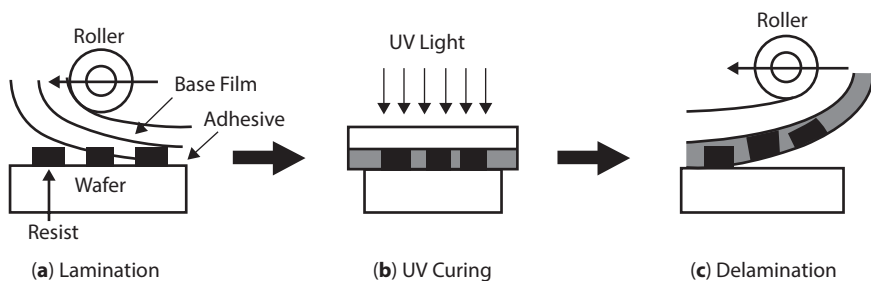


**Figure 11.4** Process flow for removal of resist from a wafer surface using adhesive tape. (a) The initial lamination step in which the tape is applied to the wafer on a heated stage. (b) UV radiation exposure to cure the adhesive. (c) The delamination step in which the tape with the resist peeled off the wafer surface [52].

## 11.4 Issues with Strippable Coatings

There are several issues with strippable coatings that need to be considered for their use in surface cleaning [56]. These coatings require surface preparation similar to conventional coatings to achieve optimum results. Contaminants, such as grease and oil in large concentration, result in poor adhesion to the surface, while dirt and paint affect the release of the film from the surface due to increased porosity on the surface. The coating tends to cling to the irregular surface, loses its coherence, and breaks off in pieces when peeled.

Trace amounts of residual adhesive may remain on the surface after stripping the coating. The residue can be characterized by available techniques [57–60]. For highly sensitive components, this residue may not be acceptable and must be removed.

The thickness of the applied film is also of concern, particularly for low-weight solids coatings. If the film is applied without sufficient thickness, it will tend to strip poorly from the surface. The application of additional film material helps the film to release properly. Films with high-weight solids do not exhibit this poor release characteristic.

Water-based strippable coatings should not be excessively stirred or agitated which can cause bubbling. These air bubbles create irregularities, such as craters and depressions, in the surface of the dried film, which can result in poor cleaning of high quality surfaces. Water-based coatings that are not freeze-thaw stable are also affected by freezing conditions. They tend to lose their adhesion and release properties when frozen and thawed.

Most strippable coatings soften when exposed to strong solvents such as acetone and methyl ethyl ketone, making them difficult to remove. However, this problem can be remedied by building sufficient thickness of coating to prevent the solvent from penetrating the coating before it evaporates. Alternatively, a solvent-resistant strippable coating can be used. Water-based coatings with excellent cohesion are available that resist solvent penetration and strip very well.

If used for removal of hazardous and radioactive contaminants, strippable coatings can also generate hazardous or radioactive mixed wastes that must be disposed. The regulations for disposal of such wastes are stringent and the costs to meet the regulations can be very high.

Some drawbacks to using strippable coatings for decontamination in urban populated areas are cost (\$50 to \$200/m<sup>2</sup>) and multiple applications (typically three applications) for maximum decontamination are required [61]. The time required to remove the coating can be extensive. In addition, the DFs may not be adequate in highly contaminated areas, particularly on concrete.

The environmental impact of strippable coatings is less than competing decontamination technologies. A recent Life Cycle Assessment (LCA) of strippable coating compared with a competing baseline steam vacuum cleaning technology confirmed better environmental performance (impact on human health, ecosystem quality and resources expended for production and waste disposal) of strippable coatings in all phases of application of these technologies [62]. The LCA assessment was extended to include a simplified economic analysis which showed strippable coatings to be five times more cost effective than the baseline steam vacuum cleaning technology due to the need for disposal of much larger volumes of waste generated by steam vacuum cleaning [63,64]. In effect, the waste disposal phase becomes the most important LCA discriminator between these technologies.

## 11.5 Precision Cleaning Applications

The use of strippable coatings for precision and other cleaning applications is discussed in the following sections using examples from different industries and applications.

### 11.5.1 Optical Surfaces

Modern optical instruments have very sophisticated high quality antireflection coated optics surfaces that sometimes require cleaning [65,66]. Dry cleaning systems for optical applications require wiping the lens surface with the risk of scratching if there are any small hard particles of contamination on the surface. Wet cleaning systems leave a residual smear. This smear acts as a surface layer, effectively softening the focus and contrast of the image.

#### 11.5.1.1 *Cleaning Optics with Collodion*

The technique for cleaning optical mirrors with collodion was first reported in 1953 [67]. The collodion was poured over the mirror surface, allowed to dry and peeled off. As shown in Figure 5, cleaning with collodion increased the reflectance, although the maximum reflectance was achieved only after cleaning multiple times. Even for a fresh aluminum surface that had been protected in a closed drawer, the reflectance increased from 14% after 8 weeks to 33% after cleaning 6 times with collodion.

Subsequently, collodion was also used to successfully clean aluminum mirrors without removing them from their mounts [68]. However, the

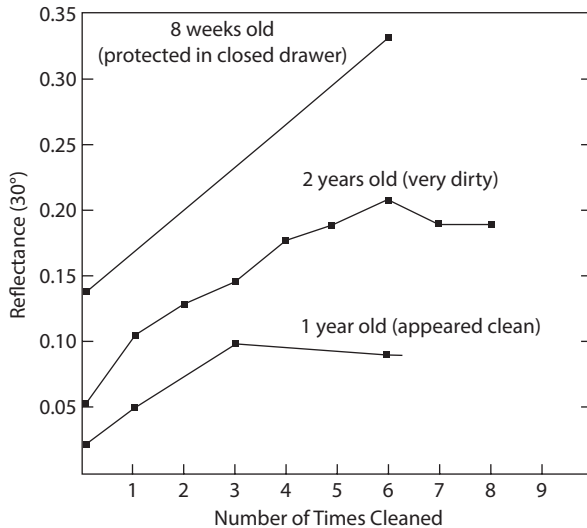


**Figure 11.5** Effect of collodion cleaning on the reflectance of 2 polished aluminum samples in the wavelength range 1140 to 1190 Å. The upper curve is for a sample 2 years old that was kept unwrapped in a drawer. The lower curve is for a sample 1 year-old that had been kept wrapped in cotton [67].

widespread use of collodion to clean mirrors and other high quality optical surfaces was established in 1964 with two methods for cleaning mirrors that had been removed from the instrument and for cleaning mirrors remaining in the instrument [69]. A mirror that had been exposed to the atmosphere for 6 months was cleaned on one half of the surface with a solution of distilled water and methanol and the other half with collodion. The results showed that the side cleaned with collodion was returned to almost its original reflectance, while the other half showed a coarse surface appearance with heavy scattering. In addition, fresh fingerprints also could be easily removed. Surfaces cleaned by this method have perhaps 10 times less residual contaminants as compared to a methanol-distilled water cleaned surface. Improvements to this cleaning procedure were proposed in 1970 and included the addition of multiple layers of cheesecloth embedded in the collodion layers. This allowed the collodion to seep through and form a solid seal of cheesecloth and collodion over the entire mirror surface. The cheesecloth also aided in peeling the dry collodion from the mirror [70].

A variety of coated mirrors have been successfully cleaned with collodion without damage to or degradation of the coatings, including  $\text{MgF}_2$ -coated aluminum mirrors and evaporated rhenium films [1].



Experiments with collodion to clean large primary mirrors have shown promising results, but there have been objections on safety grounds [71]. Examples of successful cleaning applications include the 0.58-meter Alvan Clark objective at the Charles E. Daniel Observatory in Greenville, South Carolina [72]; cleaning of the 0.76 meter telescope of the Manastash Ridge Observatory at the University of Washington [72]; and the 0.6 meter telescope at the University of California Los Angeles [73].

Recently, collodion has been very successfully used to remove particle contamination from the surface of high quality multilayer-coated optics and even uncoated transparent 'superpolished' fused quartz substrates [74]. The scattering losses of the cleaned substrates were nearly constant at the lowest scattering losses of the substrate before cleaning. A previous investigation measuring substrates before and after the cleaning process showed no influence on the lowest scatter losses. Thus, the cleaning process removes particles without degradation of the surface.

Collodion cleaning has been suggested to maintain consistent reflecting qualities of the surface of variety of semitransparent materials used as a light reflection standard [75]. These materials include quartz, IR glass, AgCl, ZnS, AsS, Si and Ge.

#### *11.5.1.2 Cleaning Laser Windows*

Custom lasers often require Brewster windows free of films and particles. Even in operation laser windows show small numbers of particles on the surface. The collodion method of window preparation was found to be best suited for their application at the University of California Berkeley [76]. The final step in the window preparation protocol which yielded laser quality windows consisted of coating the optical surfaces of the Brewster windows with collodion and then peeling away the resulting film. The coating was allowed to dry for 30–60 seconds and then peeled off. Fine contaminant particles were bound in the collodion layer and removed with it.

The collodion method of particle removal was used in the late 1970's to bond clean, thinned Si wafers to low sodium glass for solar cell research. This process was originally termed field-assisted bonding and is now known as anodic bonding. The collodion method could be applicable to eliminating particles on microelectromechanical systems.

#### *11.5.1.3 Cleaning Guidelines*

In using collodion for cleaning, these guidelines should be followed. The general cleaning procedure is outlined on the Antique Telescope Society website [72].

1. Only USP collodion should be used. Flexible collodion should not be used.
2. Collodion should be applied by simply pouring, spraying, or laying it on with a camel's hair brush.
3. If the mirror or lens is in its cell, it may be necessary to make a dam of masking tape, cardboard or other material to prevent the collodion from seeping between the glass and the cell. If applied with a brush in thin coats, the dam may not be necessary. Any collodion that manages to creep under the tape will form a hard, thick layer which will have to be cleaned by dissolving in acetone.
4. Adding a layer of cheesecloth or surgical gauze while the collodion is still wet will make it easier and simpler to peel off the coating in a single sheet when dried. For small optics, the gauze may not be necessary or desirable. A second coat of collodion should be applied over the cheesecloth.
5. After application, the collodion should be allowed to dry before removal. Generally, telltale signs that it is ready for removal are slight shrinkage, and curling or lifting of the leading edges. At this stage, it can be simply peeled off slowly and carefully in a single sheet, if possible. If patches remain, they can be mopped up carefully with a masking tape.
6. Collodion is extremely flammable and emits ether in concentrations high enough to cause dizziness and eye irritation. All work should be performed in a well ventilated area with no possible ignition sources anywhere in the area. Also, gloves may be desirable for some applications.

The cleaning steps are illustrated below for cleaning a small mirror (Figure 11.6).

On small to mid-sized mirrors, collodion is very effective in removing surface contaminants. Another advantage is that the optics can be cleaned in their holder without the need for removing them. One disadvantage is that collodion tends to part and leave small residual fragments on the surface. These fragments can be removed with a masking or an adhesive tape. However, collodion generally adheres more efficiently to modern anti-reflection coatings than to uncoated glass, which could result in removal of the coating [66]. The possibility of damaging the lens or mirror coating had been noted on cleaning with collodion if it pulled off a part of the coating, as happened previously with both mirrors and coated lenses [77]. This technique was not recommended for the general cleaning of optics.



**Figure 11.6** Cleaning a small mirror with collodion. (a) Visibly contaminated mirror. (b) The mirror is coated with collodion. (c) Cheesecloth is placed on the mirror to hold the collodion film together when it is peeled. (d) The edges of the collodion film lift up when the film is dry. (e) The cheesecloth and collodion coating are peeled off, leaving a clean mirror surface [72].

A similar experience was reported at the National Optical Astronomy Observatories (Tucson, Arizona) in which the collodion coating appeared to trap water under the aluminum mirror coating which can cause flaking of the coating from the substrate [78].

#### 11.5.1.4 *Non-Collodion Cleaning of Optics*

A very early application of the use of an adhesive strippable coating for removing particles from optical surfaces in high-powered laser systems was carried out in 1978 [79]. A coating from 3M Company was tested for its efficiency in removing  $5\ \mu\text{m}$  alumina particles uniformly distributed on the surface of flat optical surfaces and polished metal surfaces. The removal efficiency for these particles was 95–98% and the lowest achieved particle concentration was  $500\ \text{particles}/\text{cm}^2$ .

Two commercially available non-collodion strippable coatings from Universal Photonics were tested for their efficacy in removing dust and

debris from an optical surface [80]. In addition, the tests were designed to determine if the coating itself left any contamination on the surface and to determine the ease of application and removal of the coating. The optical parts included surface mirrors and glass flats with various thin-film coatings (anti-reflective (AR), tin oxide, or indium tin oxide), as well as blank glass plates for comparison. The coatings were applied by simply pouring the coating formulation over the surface at a slow rate to achieve a thick layer. The coatings were dried at room temperature for 24 hours and then easily removed in one piece by pulling a strip of adhesive duct tape attached to the dry coating. Both coatings were capable of removing dust particles from the surface, but one of the materials left a visible film on the sample. Interferometry measurements on the thin-film coated samples and the blank plates did not show any evidence of a residual film after removal of the strippable material. The coating materials could also be used to form a uniform layer on concave or convex parts, by either rotating the part or by a barrier to prevent the material from flowing over the edges.

An aerosol spray of polymer base (polyurethane) dissolved in solvent has been used for cleaning the 1-meter primary mirror of the Royal Greenwich Observatory telescope in La Palma, Spain. When sprayed onto a dusty or greasy mirror, the solvent lifts the dirt from the coated surface and suspends it in the polymer film. The contamination is removed when the film is peeled off. Provided the coating has not been attacked chemically, the original performance of the mirror should be restored [71].

The peelable blue coating from Universal Photonics was used to successfully clean several small mirrors [81]. The coating was applied by spraying on the surface of the mirror. The coating dried quickly, leaving a soft, pliable blue membrane on the mirror. It came off easily in a sheet, taking the dust and grime with it from the face of the mirror. There was no apparent residue and the mirrors were clean (Figure 11.7).

A polymer-based strippable coating has been used to protect and clean the contamination from vacuum pads used to lift the 6.5 m and 8.4 m mirrors after polishing and to install them in the telescope [82]. The pad was placed on polished glass and a vacuum applied several times. The neoprene pad material left contamination that was visibly apparent but was easily cleaned. After the glass was silver coated, the pad was placed on the silver mirrored glass surface coated with the strippable coating. When the strippable coating was removed, absolutely no damage to the mirror coating was observed.

The Opticlean® coating is used to clean almost every optical surface available. Laser gyro mirrors are perhaps the most perfect surface made by man. Flatness of 1/10 wave or better is achieved regularly, along with

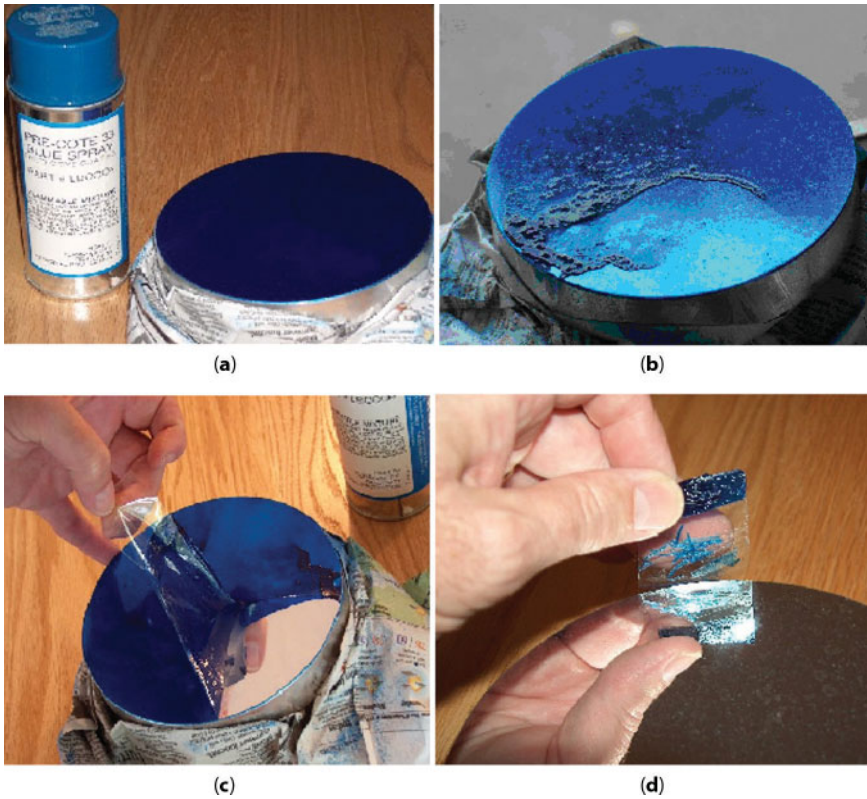


**Figure 11.7** Sequence of steps for cleaning an optical mirror with peelable blue coating. (a) The mount is wrapped to protect it from the coating. The coating is applied by spraying a thick layer on the surface. (b) The coating is starting to dry. (c) The dried coating is removed by peeling. The mirror surface is clean. (d) Any remaining coating around the bevel is removed with fresh tape [81].

parallelism of  $0.762\ \mu\text{m}$  over a 230 mm substrate. Parts with angular tolerances better than 3 arc-minutes are provided to customers with NIST traceable certificates accurate to within 5 arc-seconds for the optical angle. Opticlean<sup>®</sup> is the cleaning method of choice for these mirrors. Many manufacturers of coated surfaces are now using Opticlean<sup>®</sup> as the cleaning system to prepare the surface for coating. This has been shown to be equal to or better than the automated ultrasonic chlorofluorocarbon (CFC) based system commonly used to produce the level of cleanliness needed for this application.

Cleaning large first surface mirrors (in which the reflective surface is above a backing) has also been successfully performed with Opticlean<sup>®</sup> Spray Polymer Solution [18,19]. Spray application of Opticlean<sup>®</sup> polymer

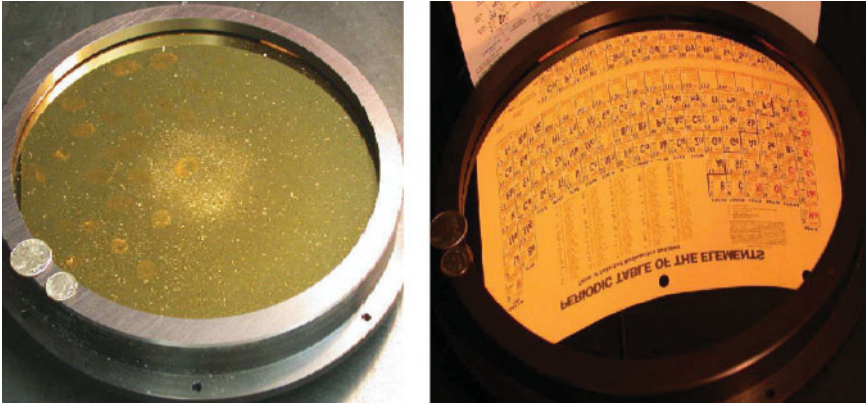


Figure 11.8 A large 1-meter unprotected gold first surface mirror before cleaning (left photograph) and after cleaning (right photograph) with Opticlean®. Courtesy of Photonic Cleaning Technologies, Platteville, WI.

using manual pumps or pressure sprayers allows complete coverage of any size optic surface using a completely touch-free process (Figure 11.8). No wipes or brushes are required, thus eliminating any danger of scratching the surface.

Examples of large, unprotected mirrors cleaned with Opticlean® include mirrors at the W. M. Keck Observatory in Hawaii (1.8 meter diameter hexagonal mirrors), the La Silla Paranal Observatory (0.875 to 3.6 meter diameter mirrors) in La Silla, Chile, and the LuLin Observatory (76-cm diameter honeycomb mirror) in Taiwan. Other applications include several military optics depots with responsibility for cleanliness of telescope mirrors from 20 cm to 3.6 m diameter.

#### 11.5.1.5 Cleaning Silicon Wafers

Opticlean® can remove 1  $\mu\text{m}$  to 5  $\mu\text{m}$  diameter particles as well as contamination remaining from previous drag wipe cleaning on a used silicon wafer [83,84]. In addition, no residue that produced scattering was found on a fresh silicon wafer when Opticlean® was applied and then stripped off. The total integrated scattering technique used for the measurements could measure scattering levels of He-Ne laser light as low as a few ppm, corresponding to an rms (root mean square) surface roughness of  $<1 \text{ \AA}$ .

#### 11.5.1.6 Cleaning Phase Masks

Traditional methods for cleaning phase masks are time consuming and require hazardous chemicals. Opticlean® simplifies cleaning phase masks.

If the contaminants are only particulates the application amount may be as little as 1 ml for an area of 22.5 cm<sup>2</sup>; but if there are oils or fingerprints on the surface, 1 ml may be required for 13 cm<sup>2</sup> surface area. The coating is safe on fused silica, glasses of all kinds, and crystals.

#### 11.5.1.7 *Cleaning Stampers for Compact Discs*

A novel, improved method for cleaning high precision optical components has been reported by removing smudges, oil, dust, saliva, and other contaminants from cleaning molds utilized in the production of compact discs [85]. The method involves applying a curable coating to an optical or optical forming surface which has been contaminated with undesirable foreign matter, allowing the coating to dry to form a resilient dried film, and then removing the dried film together with the undesirable foreign debris which has contaminated the optical surface. The curable coating is formed from an aqueous polyurethane emulsion. It also includes a butyl cellulose (2-butoxy ethanol) solvent and a trace amount of surfactant/thickener as wetting agent and for viscosity control. The use of a dual solvent system (water and butyl cellulose) is advantageous since these solvents are mutually soluble and have the ability to dissolve a variety of solutes which may be present as foreign debris on the surface being decontaminated. The method allows foreign debris to be removed with a very high degree of reliability and completeness and the stampers are restored to like new condition.

### 11.5.2 Other Applications

Collodion film is a very popular sample preparation medium. It is conveniently available on a microscope slide and can be reconstituted instantly (made lightly viscous) with a single drop of amyl acetate [6,7]. Small drops of the reconstituted sample on the end of a tungsten needle are used for isolating, characterizing and preparing small particles for further analysis. The reconstituted sample will remain lightly viscous for up to 15 minutes. The slide can be reused many times and stored indefinitely (Figure 11.9).

This extraction replication technique is especially useful when the surface is rough and soft at the same time. The collodion film will separate the particles lightly held in crevices without removing any of the substrate. Particles can also be collected directly on collodion films for subsequent analysis [86,87].

Opticlean® has been used to collect the residual slurry debris from polishing the surface of meta-phosphate laser glass to study the effects of the

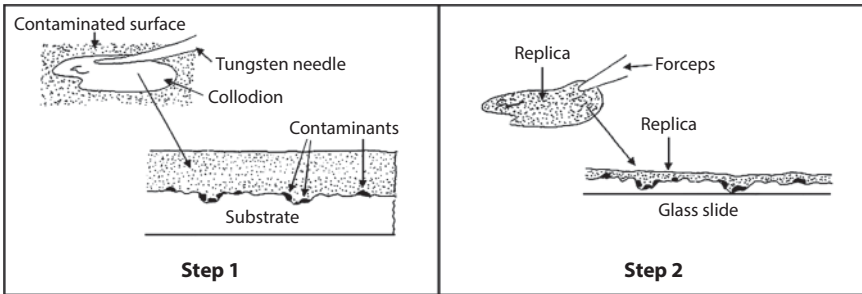


**Figure 11.9** Collodion extraction replication technique for particle sample preparation. (a) In step 1, the collodion solution is spread over a small area of the contaminated surface. (b) The dry collodion film with the particles is pulled off the substrate in step 2 and placed, particle side down, on a glass slide for analysis [6, 7].

slurry on the surface topography of the glass [88]. This was done by applying Opticlean® on the surface of full-size samples. The coating was peeled off and portions of the coating were treated in aqua regia to analyze the solution by ICP-MS (Inductively Coupled Plasma Mass Spectrometry) for cerium polishing residue. The coating was effective in collecting all the residue from the surface.

Strippable coatings and gels have been proposed as swipe material, especially for recovery of the encapsulated contaminants given the high removal factors (>90%) of these materials [89]. These coatings have the potential for making swipe measurements a more realistically quantitative determination of removable surface activity with detection limits that may be lower than current practice can achieve. This is a relatively new application, but preliminary results have been encouraging.

Other unusual cleaning applications have been described previously [1].

### 11.5.3 Non-Optical Cleaning Applications

Strippable coatings are increasingly employed in non-optical cleaning applications, such as radioactive decontamination and other hazardous contaminant removal. Some examples of these applications are described below.

#### 11.5.3.1 Radioactive Decontamination

The conventional coating treatment method for decontaminating radioactively contaminated components is to apply a pre-vulcanized rubber latex compound to the surface, allow it to dry, and then pull it off the surface to



remove the contaminants. Unfortunately, the conventional method suffers from several drawbacks. The latex compound can take days to dry and can thus prolong the shutdown time. The latex compound is also sometimes difficult to pull off the surface after it dries. Furthermore, the latex compound is not totally effective in removing the contaminants and reducing radioactive exposure to an industry accepted level. Recently, the latex rubber coating has been modified by incorporating a complexing alkali detergent and a fine pumice in the latex solution to enhance its decontaminating efficiency [90]. DFs of 100–200 were achieved with the modified coating when the coating was used to remove fission product contaminants from a variety of substrates, including stainless steel, aluminum, copper, painted wood and plastic.

The disadvantages of the latex rubber coating treatments for radioactive surface decontamination can be overcome by improved strippable coatings [91–96]. However, strippable coatings are not very effective in removing contaminants that have seeped below the surface of the part.

Reactor cavity decontamination at the Nine Mile Point Nuclear Station in Oswego, New York was performed using the Isotron coating Isolock 300 [97]. The application and removal of the coating required a total of 148 hours to complete. Radiological surveys performed after the removal of the coating indicated contamination levels of 10,000 dpm/100 cm<sup>2</sup> and 50,000 dpm/100 cm<sup>2</sup> (dpm = disintegrations per minute) on the walls and floors, respectively. The cavity decontamination was completed with 65 man-mSv of exposure, a reduction of approximately 38% as compared to the previous outage. This was attributed to an increase in worker efficiency due to a decline in the protective clothing and respiratory protection required to perform the work. The calculated dose equivalent to the skin as a result of these contaminations was down from 312 mSv to 120 mSv.

At the Savannah River Site (SRS), approximately 264 m<sup>2</sup> of the wall and floor areas of a fuel fabrication facility were decontaminated with ALARA 1146™ strippable coating [98–101]. This area was contaminated with highly enriched uranium and designated a high contamination area. The intent was to remove enough of the loose radioactive material to drive transferable contamination levels below the free release limits. The coatings were sprayed onto painted and unpainted carbon steel and concrete surfaces in the process area of the facility. The results showed that the strippable coating was effective in removing contamination from all surfaces that were tested. For the surfaces that had the highest contamination levels, DFs up to 7.2 for alpha activity and up to 3.9 for beta-gamma activity were achieved. The DF was lower for the less contaminated surfaces, as would be expected.

The Capture Coating has been used in conjunction with InstaCote CC Strip [28] in a two-step process that removes the plutonium contamination from the air by the aerosolized Capture Coating and then seals it in place on the floor or walls of a room or other surfaces with InstaCote. At the Rocky Flats plant in Golden, Colorado, implementation of this process reduced the contamination in a room containing plutonium nitrate solution processing tanks from more than 90,000 derived air concentrations (DACs), a measure for plutonium particles in the air, to less than 100 DAC. For this unique application, the Capture Coating was modified by adding a blue fluorescent tracer that is visible in UV light ("black light"). This helps in tracking potentially contaminated fog residues that may adhere to worker clothing and equipment. Capture Coating and InstaCote, either together or separately, have been used to decontaminate a range of items at the Rocky Flats plant from tanks to glove boxes, to ventilation ducts, process piping, and other highly contaminated rooms, as well as at other sites [29,102].

Recently, the EPA evaluated Stripcoat TLC Free™ and Isotron coatings for their ability to remove Cs-137 isotope from concrete surfaces [103,104]. The coatings were applied with a paint sprayer to concrete coupons (Type I and II Portland cements) contaminated with Cs-137 (Figure 11.10).

The treated surfaces were allowed to cure overnight into a solid coating and the coating was then removed from the concrete surface. Isotron binds radiological material through chemical and physical interactions when it is cured. Stripcoat TLC Free™ binds radiological material only through physical interaction between the radiological material and the cured coating. Table 11.1 compares the operational factors involved in using these strip-pable coatings [103,104].

The decontamination efficacy calculated for each of the contaminated coupons is expressed in terms of percent removal (%R). For Stripcoat TLC Free™, the overall average %R for both 7-day and 30-day tests was  $32.0 \pm 9.9$ . For Isotron, the overall average %R for both 7-day and 30-day tests was  $76.2 \pm 7.4$ . The removal rate of Isotron will likely depend on the characteristics of the surface being decontaminated as some scraping is required for removal. The Stripcoat TLC Free™ can be applied to irregular surfaces and easily removed from across the borders of the coupons.

Film coating combined with electrolysis methods has been used to decontaminate equipment contaminated with uranium [105]. The strip-pable film consisted of polyaniline doped with  $\text{SO}_4^{2-}/\text{TiO}_2$  superacid that replaced the more commonly used HCl to increase the conductivity of the film. The decontamination methods evaluated were as follows.

**Stripcoat Coating**

Preparation

Application

Removal

**Isotron Coating**

Preparation

Application

Removal

**Figure 11.10** Application of commercial strippable coatings for removal of radioactive contaminants from a concrete surface. The upper series of pictures show the preparation, application and removal of Stripcoat TLC™ Free coating from the surface. The lower series of pictures show the preparation, application and removal of Isotron coating from the surface [103,104].

- Coating the contaminated metal surface with the film and peeling off the dried film.
- Coating the surface with the film and electrolyzing in a phosphoric acid solution. The film was peeled off the dried metal surface after electrolysis and analyzed
- The contaminated metal surface was coated with the film and electrolyzed in a dry medium. The film was peeled off after electrolysis and analyzed.

Decontamination efficiencies from 73% to 98% were achieved with the best results obtained from dry electrolysis in the third method.

Six different coatings (water-based (two), ethanol-based, silicone-based, latex, and polymer composite) were evaluated for decontaminating typical materials used in urban environments, including concrete, road base asphalt, mild steel for buildings and structures, and sandstone paving [106]. The contaminants included Cs-137, U-238 (yellowcake), and Sr-85. The results showed removal efficiencies between 30% and 50%. The ease of decontamination was yellowcake followed by Cs-137 and Sr-85.

**Table 11.1** Strippable Coating Operational Factors

Factors	Stripcoat TLC Free™	Isotron
<b>Application and removal</b>	Application: 12 m <sup>2</sup> /hour Removal: 4.9 m <sup>2</sup> /hour	Application: 4.6 m <sup>2</sup> /hour Removal: 1.6 m <sup>2</sup> /hour
<b>Ease of use on irregular surfaces</b>	Elastic coating readily peels off surface	Some scraping might be required
<b>Labor requirements</b>	No specialized training	No specialized training
<b>Utility requirements</b>	If sprayer used, 110 V; otherwise none	If sprayer used, 110 V; otherwise none
<b>Portability</b>	Portable	Portable
<b>Secondary waste</b>	Solid waste production: ~0.26 kg/m <sup>2</sup> Solid waste density: ~0.145 g/cm <sup>3</sup>	Solid waste production: ~0.5 kg/m <sup>2</sup> Solid waste density: ~0.188 g/cm <sup>3</sup>
<b>Surface damage</b>	Minimal, only loose particles removed	Minimal, only loose particles removed
<b>Preparation and cleanup</b>	Product used "as is"; pump rinsed with mineral spirits between applications to avoid clogging	Product requires mixing; pump rinsed with water between applications
<b>Cost</b>	\$16.66/m <sup>2</sup> for one application	\$58.84/m <sup>2</sup> for one application

DeconGel™ has been evaluated on a variety of materials (concrete, carbon steel, stainless steel, Plexiglas, painted concrete, porcelain tile (with and without grout), granite (with grout), vinyl composite tile) and surfaces (smooth, rough, painted, porous) for its efficacy to remove radionuclides. In general, the gel was poured onto the surface of the contaminated coupons and allowed to dry overnight. It was easy to peel off the coating from all the coupons, the most difficult being concrete. The coatings were all removed in a single sheet. None of the coatings fractured during removal. Testing on samples contaminated with isotopes Cs-137, Co-60, Eu-154, Np-237, U-238, Pu-238, Pu-239 and Pu-241, Am-241, I-125 and I-131, Tc-99, Tl-201, C-14 and tritium has shown removal efficiencies ranging from 82% to as high as 100% [107–112]. Lower values were attributed to particular material and surface chemistry combinations, as well as 90%

humidity conditions, damp porous concrete, and incomplete cure time, illustrating the importance of these factors when planning any decontamination procedure. A second gel application performed two months later on the same test coupons gave results that were as good as or better than first application results with an average removal efficiency of 87% and a median of 99%. The results indicated that the majority of contamination removed by the gel with high DFs was not simply loose particulate, but fixed in the surface.

A novel process has been developed in which an aqueous biopolymer solution is used to coat a contaminated metal surface (such as steel), solubilize the heavy metals from the surface, and bind the heavy metals into the biopolymer [113]. The biopolymer coating containing the immobilized hazardous metal contaminants can be stripped as a viscous film, as a dry powder, or by washing. The soluble polysaccharide (SPS) fraction of biopolymers, produced by the cyanobacterium *Nostoc muscorum* strain HPDP22, was tested for sorption properties with regard to barium, cadmium, iron, copper, and uranium. The results showed that the biopolymer removes > 80% of the fixed uranium (VI) from contaminated steel coupons.

Several strippable coatings were evaluated for efficiency and cost-effectiveness for removal of cesium isotopes deposited on soil and grass from radioactive fallout from nuclear accidents such as Chernobyl [114]. A modified poly(vinyl alcohol) coating, a commercial lignin coating (available as calcium lignosulfonate), and a liquid plastic coating "Liquid Envelope" (Cufadan A/S, Copenhagen, Denmark) were tested on small (0.03 m<sup>3</sup>) soil core samples from the Chernobyl area. All three coatings removed 94–95% of the cesium from the bare soil samples, while the lignin coating could remove nearly 72 % cesium from a cut grassed surface. No other coatings were tested on the grass samples. A comparison of the total cost of decontamination (materials, equipment, labor, and waste management) showed that Liquid Envelope was nearly 3 to 4 times higher than the other 2 coatings.

#### 11.5.3.2 *Non-Radioactive Decontamination Applications*

Many surfaces exposed to the environment are continuously being contaminated by undesirable deposits, such as soot, grease, dust, traffic pollution, and other contaminants. Furthermore, accidental spills can make stains that can be extremely difficult or even impossible to remove. Cleaning such contaminated surfaces generally requires strong alkaline solutions or organic solvents which cause health hazards and are not environmentally friendly. Masking procedures are often difficult to perform on

curved or irregular surfaces. Recently, a process has been developed for facilitating the removal of undesired contamination from a surface that overcomes these disadvantages [115]. A solution containing a polysaccharide and a solvent is applied to the contaminated surface and the solution is allowed to dry to form a solid polysaccharide film. The polysaccharide can be selected from the groups consisting of celluloses and derivatives, starch and starch derivatives, plant gums, capsular microbial polysaccharides, pectins, inulins, and algal polysaccharides. The solid polysaccharide is capable of redissolving or swelling in water or other liquids. The swollen or dissolved layer can be removed by any suitable technique, carrying the contaminants with the film. To achieve maximum mechanical strength of the coating about 5–20% by weight of plasticizer is usually added to the solution. Although dry polysaccharide films are hard and brittle due to the multiplicity of hydrogen bonding sites, under normal conditions water is always present, making the films soft and pliant. The polysaccharide films have been applied to contaminated concrete, galvanized steel and other surfaces. After removal of the dried film, no contamination was visible.

Stripcoat TLC Free™ was used to successfully decontaminate three floor areas of the Tokamak Fusion Test Reactor at Princeton University that were contaminated with lead dust [116]. A thick coating was applied to the floor and after approximately 24 hours the coating was peeled and the floor was sampled. The results were below the release guidelines.

ALARA™ 1146 and Stripcoat TLC Free™ coatings were evaluated for removal of mercury contamination on metals (Al, Cu, carbon steel and stainless steel) and tile and grout samples [117]. Removal efficiencies ranged from ~35% to 95% for ALARA™ 1146 and from ~5% to ~68% for Stripcoat TLC Free™. Decontamination with strippable coating is also a very simple and fast process. Since mercury binds sulfur strongly, sulfur modified coating materials may be a good alternative. However, such coatings are not commercially available. Surface pretreatment before applying the coating may also improve the mercury removal efficiency.

The effect of APMDP acid on BeO debris has been investigated in the Contained Firing Facility at Lawrence Livermore National Laboratory to prove the effectiveness of the chelator on environmental samples, and to prove that chelation could in fact dissolve and bind beryllium oxide [44, 118]. Varying concentrations of APMDP acid chelator (adjusted to pH 7) were added to vials containing BeO debris and left to stand for 3 days, with manual shaking performed for 2 minutes for each vial, twice a day. Samples were then filtered through a 0.2 µm membrane and filtrates were analyzed by ICP-MS. The results clearly demonstrated a linear concentration profile, indicating that APMDP acid dissolves insoluble BeO fines and binds beryllium.

An alternative method has been proposed for decontaminating porous materials [119]. In this method, a polyphosphazine-based polymer coating is applied to the surface of the contaminated porous material. The surface of the porous material is irradiated with a beam of coherent electromagnetic radiation with a wavelength in the range that does not cause ablation of the structure. Irradiation of the surface causes the contaminants within the cracks and pores to redistribute towards the surface of the structure. The contaminants are physically or chemically bound to the coating and are removed when the cured coating is peeled off the surface.

## 11.6 Summary

Peelable strippable coatings are a low-cost effective method for precision cleaning of surfaces, in which the coating is applied to the surface by spraying, rolling or brushing. The coating is allowed to cure and then removed by peeling. A wide variety of solvent- and water-based strippable coatings are available for precision cleaning of surfaces and for protecting surfaces that have been cleaned. The coating formulations are designed to entrain the particle contaminants by physical or chemical means. When the coating is peeled, the contaminants are carried with the coating. The types of surfaces cleaned include coated and uncoated optical lenses and mirrors, silicon wafers, metals, plastics and concrete. The contaminants that have been successfully removed include dust, hydrocarbon films, radioactive materials, beryllium and other hazardous materials.

## Disclaimer

Mention of commercial products in this chapter is for information only and does not imply recommendation or endorsement by The Aerospace Corporation. All trademarks, service marks, and trade names are the property of their respective owners.

## References

1. R. Kohli, *Strippable Coatings for Removal of Surface Contaminants*, in: *Developments in Surface Contamination and Cleaning: Particle Deposition, Control and Removal*, R. Kohli and K. L. Mittal (Eds.), Vol. 2, pp. 177–224, Elsevier, Oxford, UK (2010).
2. G. W. Grogan and R. H. Boyd, *Aqueous Based, Strippable Coating Composition and Method*, U.S. Patent 5,143,949 (1992).

3. M. R. Fisch, *Liquid Crystals, Laptops and Life*, World Scientific Publishing, Singapore (2004).
4. J. J. Meister, *Polymer Modification: Principles, Techniques, and Applications*, CRC Press, Boca Raton, FL (2000).
5. J. P. Maynard, Communication to the Boston Society for Medical Improvement, Boston, MA, March 1848. See *The New York Medical Journal*, Volume IV, page 390 (1867) and *The Annual Cyclopaedia and Register of Important Events of the Year 1898*, page 558, D. Appleton & Co., New York, NY (1899).
6. A. S. Teetsov, Unique Preparation Techniques for Nanogram Samples, in: *Practical Guide to Infrared Microspectroscopy*, H. J. Humecki (Ed.), CRC Press, Boca Raton, FL (1995).
7. A. S. Teetsov, Uses for Flexible Collodion in the Analysis of Small Particles, White Paper, McCrone Associates, Westmont, IL (2004).
8. R. Jagels, Celloidin Embedding Under Alternating Pressure and Vacuum, *Trans. Amer. Microsc. Soc.* 87, 263 (1968).
9. *Dorland's Illustrated Medical Dictionary*, 31<sup>st</sup> Edition, Saunders Imprint, Elsevier, UK (2007).
10. S. L. Bigelow and A. Gemberling, Collodion Membranes, *J. Membrane Sci.* 100, 57 (1995).
11. A. Yamauchi and A. M. El Sayed, New Approach to a Collodion Membrane Composite via Fluorocarbon Polymer (Nafion) Blending in Terms of a Diffusion Coefficient of Redox Substances and Transport Properties, *Desalination* 192, 364 (2006).
12. F. A. Castle and C. Rice (Eds.), Collodion Combinations, *American Druggist* 13, 5 (1884).
13. H. W. North, *Cooley's Cyclopaedia of Practical Receipts*, 7<sup>th</sup> Edition, Volume 1, J&A Churchill, London, UK (1892).
14. *The Columbia Encyclopedia*, 6<sup>th</sup> Edition, Columbia University Press, New York, NY (2009).
15. Collodion USP, Material Safety Data Sheet (2001).
16. Carbicote 946 White Booth Coating, Product Data Sheet, Carbit Paint Company, Chicago, IL. [www.carbit.com](http://www.carbit.com).
17. UV Curable Peelable Coatings, General Chemical Corporation, Brighton, MI. <http://www.strippablecoating.com/OpticalMedia.aspx>.
18. P. Jackson, Große Spiegel reinigen und schützen, *Photonik*, pp. 64–67 (May 2007).
19. OPTICLEAN First Contact Cleaning Coating, Dantronix Research, Platteville, WI. <http://www.dantronix.com>.
20. Carbicote® Strippable Coatings, Carbit Paint Company, Chicago, IL. [www.carbit.com](http://www.carbit.com).
21. Universal Photonics, Hicksville, NY. <http://www.universalphotonics.com>.
22. CorShield® VpCI® Strippable Coating, Cortec Corporation, St. Paul, MN. <http://www.cortecvci.com>.



23. Adhesives Research, Inc, Glen Rock, PA. <http://www.adhesivesresearch.com>.
24. ALARA 1146 Strippable Coating, Product Data Sheet, Carboline Company, St. Louis, MO. <http://www.carboline.com>.
25. Stripcoat TLC Free™, Product Data Sheet, Bartlett Services, Inc., Plymouth, MA. <http://www.bartlettinc.com>.
26. DeconGel™, Decontamination Solutions for Chemical, Biological and Radioactive Threats, Cellular Bioengineering, Inc., Honolulu, HI. <http://www.decongell.com>.
27. T. J. Nachtman and J. H. Hull, Method for Containing or Removing Contaminants from a Substrate, U.S. Patent 5,763,734 (1998).
28. Contamination Control Strippable (CC Strip) Coating, Product Data Sheet, InstaCote Inc., Erie, MI. <http://instacote.com/products.htm>.
29. Capture Coating, Product Data Sheet, Encapsulation Technologies, Los Angeles, CA. <http://www.fogging.com>.
30. H. L. Lomansey, In-Situ Polymeric Membrane for Cavity Sealing and Mitigating Transport of Liquid Hazardous Materials Based on Aqueous Epoxy-Rubber Alloys, U.S. Patent 5,091,447 (1992).
31. J. Shelton, Polymer Technologies for Lockdown and Removal of Radioactive Contamination, Proc. United States Special Operations Command (USSOCOM) Chemical, Biological, Radiological, and Nuclear (CBRN) Conference & Exhibition, Tampa, FL (2005). [www.dtic.mil/ndia/2005ussocom/wednesday/shelton.pdf](http://www.dtic.mil/ndia/2005ussocom/wednesday/shelton.pdf).
32. Isotron Radbloc, Product Data Sheet, Isotron Corporation, Seattle, WA. <http://www.isotron.net>.
33. H. N. Gray and D. E. Bergbreiter, Applications of Polymeric Smart Materials to Environmental Problems, *Environ. Health Perspect.* 105 (Suppl. 1), 55 (1997).
34. W. Feng, S. H. Patel, M-Y. Young, J. L. Zunino III and M. Xanthos, Smart Polymeric Coatings - Recent Advances, *Adv. Polym. Technol.* 26, 1 (2007).
35. P. LaFrate, Jr., J. Elliott, D. Siddoway and M. Valasquez, Decontamination and Size Reduction of Plutonium Contaminated Process Exhaust Ductwork and Glove Boxes, Report LA-UR-97-254, Los Alamos National Laboratory, Los Alamos, NM (1996).
36. B. D. Veatch, Z. Ibrisagic, A. K. Kimball and T. E. Broderick, Electro-Decontamination of Contaminated Surfaces, International Patent WO/2007/001263 (2007).
37. ElectroDecon™, The Electrochemical Strippable Coating System, ADA Technologies, Inc, Littleton, CO. <http://www.adatech.com/>.
38. J. F. Williams and U. Cho, Antimicrobial Functions for Synthetic Fibers: Recent Developments, *AATCC Review* 5, 17 (2005).
39. J. F. Williams, J. C. Suess, M. M. Cooper, J. I. Santiago, T-Y. Chen, C. D. Mackenzie and C. Fleiger, Antimicrobial Functionality of Healthcare Textiles: Current Needs, Options, and Characterization of N-halamine-Based Finishes, *Res. J. Textiles Apparel* 10, 1 (2006).

40. L. Quian, T. Y. Chen, G. Sun and J. F. Williams, Durable and Regenerable Antimicrobial Textiles: Thermal Stability of Halamine Structures, *AATCC Review* 6, 55 (2006).
41. J. Liang, Y. Chen, K. Barnes R. Wu, S. D. Worley and T.-S. Huang, N-halamine/quat Siloxane Copolymers for Use in Biocidal Coatings, *Biomaterials* 27, 2495 (2006).
42. G. Sun and S. D. Worley, Halamine Chemistry and its Application in Biocidal Textiles and Polymers, in: *Modified Fibers with Medical and Specialty Applications*, J. V. Edwards, G. Buschle-Diller and S. C. Goheen (Eds.), Chap. 6, pp. 81–89, Springer Verlag, New York, NY (2006).
43. HaloSource, Inc, Bothell, WA. <http://www.halosource.com>.
44. M. Sutton, S. R. Burastero, J. Perkins, M. L. Chiarappa-Zucca and B. D. Andresen, Alpha-Aminobenzyl-Alpha,Alpha,-Diphosphoric Acid Selective Chelation of Beryllium, U.S. Patent Application 20070254827 (2007).
45. M. Gotoh, S. Kobayashi and K. Kawabata, Pressure Sensitive Adhesive Composition and Pressure Sensitive Adhesive Tape or Sheet Making Use of the Same, U.S. Patent 5,286,781 (1994).
46. J. G. Southwick, K. S. Kiibler and J. R. Erickson, Non-Aqueous Solvent Free Process for Making UV Curable Adhesives and Sealants from Epoxidized Monohydroxylated Diene Polymers, U.S. Patent 5,776,998 (1998).
47. J. R. Erickson and J. Crivello, Non-Aqueous Solvent Free Process for Making UV Curable Adhesives and Sealants from Epoxidized Monohydroxylated Diene Polymers (III), U.S. Patent 5,837,749 (1998).
48. J. R. Erickson and D. R. Hansen, Formulation for Strippable Adhesive and Coating Films and High Performance Adhesives, U.S. Patent 6,541,553 (2003).
49. R. Sugino and H. Mori, Removing Particles from Silicon Wafer Surfaces with Adhesive Tape, *MICRO* 14, 43 (April 1996).
50. T. Kubozono, Y. Moroshi, Y. Ohta, H. Shimodan and N. Moriuchi, A New Process for Resist Removal after Photolithography Process Using Adhesive Tape, *Proc. SPIE* 2724, 677–689 (1996).
51. C. C. Lee, Method for Removing Sub-Micron Particles from a Semiconductor Wafer Surface by Exposing the Wafer Surface to Clean Room Adhesive Tape Material, U.S. Patent 5,690,749 (1997).
52. Y. Terada, E. Toyoda, M. Namikawa, A. Maekawa and T. Tokunaga, A Novel Method for Resist Removal after Etching of the Organic SOG Layer with the Use of Adhesive Tape, *Proc. IEEE Int. Symp. Semiconductor Manufacturing*, pp. 295–298, IEEE, Piscataway, NJ (1999).
53. K. Sano, Future Evolution of Pressure Sensitive Adhesive Tapes, Nitto Technical Report 38, 11 (December 2000).
54. High performance Dust Preventive Adhesive Roll Cleaner SDR/ELEP-F Series, Product Information, Nitto Denko Corporation, Toyohashi, Japan. <http://www.nitto.com/productc/datasheet/process/011>.
55. P. Lazzeri, G. Franco, M. Garozzo, C. Gerardi, E. Iacob, A. Lo Faro, A. Privitera, L. Vanzetti and M. Bersani, TOF-SIMS Study of Adhesive Residuals

- on Device Contact Pads after Wafer Taping and Backgrinding, *Appl. Surf. Sci.* 203–204, 445 (2003).
56. D. L. Westerman, Strippable Coatings, *Metal Finishing* 98, 155 (June 2000).
  57. D. Y. Song, F. S. Zhang, H. A. Macleod, and M. R. Jacobson, Study of Surface Contamination by Surface Plasmons, *Proc. SPIE* 678, 211–218 (1986).
  58. R.-H. R. Wang, An Optical Probe of Thin Film and Surface Contamination Based on Surface Plasmon Resonance, Ph.D. Dissertation, University of Arizona, Tucson, AZ (1990).
  59. R. Kohli, Methods for Monitoring and Measuring Cleanliness of Surfaces, in: *Developments in Surface Contamination and Cleaning: Detection, Characterization, and Analysis of Contaminants*, R. Kohli and K. L. Mittal (Eds.), Vol. 4, pp. 107–178, Elsevier, Oxford, UK (2012).
  60. R. Kohli, Developments in Imaging and Analysis Techniques for Micro- and Nanosize Particles and Surface Features, in: *Developments in Surface Contamination and Cleaning. Detection, Characterization, and Analysis of Contaminants*, R. Kohli and K. L. Mittal (Eds.), Vol. 4, pp. 215–306, Elsevier, Oxford, UK (2012).
  61. J. Heiser and T. Sullivan, Decontamination Technologies Task 3. Urban Remediation and Response Project Prepared for New York City Department of Health and Mental Hygiene, Report BNL-82389–2009, Brookhaven National Laboratory, Upton, NY (2009).
  62. F. Cumo, L. de Santoli and G. Guidi, LCA of Strippable Coatings and of Principal Competing Technology used in Nuclear Decommissioning, *Chem. Eng. Trans.* 7, 601 (2005).
  63. Radioactive Waste Management and Advanced Nuclear Fuel Cycle Technologies, Progress Report 2006, FPN Radwaste Division, ENEA, Rome-Frascati, Italy (2006).
  64. G. Guidi, F. Cumo and L. de Santoli, LCA of Strippable Coatings and of Steam Vacuum Technology Used for Nuclear Plants Decontamination, *Clean Technol. Environ. Policy*, Published online DOI: 10.1007/s10098–009–0208–5 (March 24, 2009).
  65. M. B. Pepin, *Care of Astronomical Telescopes and Accessories: A Manual for the Astronomical Observer and Amateur Telescope Maker*, Springer, London, UK (2004).
  66. J. Cipriano, Cleaning Modern Antireflection-Coated Optics with Collodion, *Cloudy Nights Telescope Reviews* (November 2005). [http://216.92.113.163/item.php?item\\_id=1304](http://216.92.113.163/item.php?item_id=1304).
  67. J. D. Purcell, Reflectance Measurements from 1140Å to 1190Å by a Simple Open Air Method, *J. Opt. Soc. Am.* 43, 1166 (1953).
  68. W. I. Kaye, Far Ultraviolet Spectroscopy. 1. Modification of the Beckman DK Spectrophotometer for Automatic Transmittance Recording in the Region 1700–2000 Å, *Appl. Spectroscopy* 15, 89 (1961).
  69. J. B. McDaniel, Collodion Technique of Mirror Cleaning, *Appl. Opt.* 3, 152 (1964).

70. J. B. Tyndall, Collodion Technique of Mirror Cleaning, Report LAR-10675, NASA Langley Research Center, Langley, VA (1970). See also Brief 70–10463, NASA Tech Briefs (August 1970).
71. J. R. Powell and D. M. Jackson, Cleaning of Optical Components, RGO/La Palma Technical Note No. 2, Royal Greenwich Observatory, Greenwich, London, UK (June 1984).
72. R. Ariail, The Artistry of Telescope Restoration - A Professional Method for Cleaning Optics, *J. Antique Telescope Soc.* 6, 1008 (1995). See also Antique Telescope Society website: <http://www.webari.com/oldscope> (2009).
73. F. Henriquez, Cleaning the Optics. The UCLA 24-Inch Telescope (October 2006). [http://frank.bol.ucla.edu/24inch.html#Cleaning\\_the\\_optics](http://frank.bol.ucla.edu/24inch.html#Cleaning_the_optics).
74. O. Kienzle, J. Staub and T. Tschudi, Description of an Integrated Scatter Instrument for Measuring Scatter Losses of ‘Superpolished’ Optical Surfaces, *Measurement Sci. Technol.* 5, 747 (1994).
75. C. E. Miller, Standard Reflective Device, U.S. Patent 4,346,996 (1982).
76. R. M. Hamilton, Fast, Cost Effective Particle Removal for Anodic Bonding, University of California Berkeley, Berkeley, CA (October 1995). <http://mail.mems-exchange.org/pipermail/mems-talk/1995-October/000212.html>.
77. T. M. Back, Cleaning Telescope Optics, NightTimes, Lake County Astronomical Society, Ingleside, IL (April 2004). <http://www.bpccs.com/lcas/Articles/cleanoptics.htm>.
78. W. D. Kimura, G. H. Kim and B. Balick, Comparison of Laser and CO<sub>2</sub> Snow Cleaning of Astronomical Mirror Samples, *Proc. SPIE* 2199, 1164–1171 (1994).
79. I. F. Stowers and H. G. Patton, Cleaning Optical Surfaces, *Proc. SPIE* 140, 16–31 (1978).
80. J. Fine and J. B. Pernick, Use of Strippable Coatings to Protect and Clean Optical Surfaces, *Appl. Opt.* 26, 3172 (1987).
81. W. Prewitt, How to Remove Dust from Your Mirror without Scratching. [http://www.astrocaver.com/blue\\_clean.html](http://www.astrocaver.com/blue_clean.html).
82. W. Davison, D. Ketelsen, R. Cordova, J. Williams, W. Omann and W. Kindred, Vacuum Lifting Equipment to Handle Polished Mirrors, Technical Memo UA-93–09, Large Binocular Telescope Project, University of Arizona, Tempe, AZ (1993).
83. J. M. Bennett, L. Mattsson, M. P. Keane and L. Karlsson, Test of Strip Coating Materials for Protecting Optics, *Appl. Opt.* 28, 1018 (1989).
84. J. M. Bennett and D. Rönnow, Test of Opticlean Strip Coating Material for Removing Surface Contamination, *Appl. Opt.* 39, 2737 (2000).
85. T. K. Moynagh, Cleaning Method for High Precision Molding Components, U.S. Patent 5,810,941 (1998).
86. K. Okada and K. Kai, Atmospheric Mineral Particles Collected at Qira in the Taklamakan Desert, China, *Atmos. Env.* 38, 6927 (2004).
87. Air Particle Analyzer. QCM Cascade Particle Impactor, Technical Note, California Measurements, Inc., Sierra Madre, CA (2009).

88. T. I. Suratwala, P. E. Miller, P. R. Ehrmann and R. A. Steele, Polishing Slurry Induced Surface Haze on Phosphate Laser Glasses, *J. Noncryst. Solids* 351, 2091 (2004).
89. J. Griggs and K. Hall, A Performance-Based Approach to the Use of Swipe Samples in Response to a Radiological or Nuclear Incident, Report EPA 600/R-11/122, U. S. Environmental Protection Agency, Cincinnati, OH (2011).
90. B. W. Ariss and C. R. Thomas, The Use of Coatings to Facilitate Decontamination, in: *Proc. 1<sup>st</sup> Intl. Symp. on Decontamination of Nuclear Installations*, H. J. Blythe, A. Catherall, A. Cook and H. Well (Eds.), pp. 55–64, Cambridge University Press, Cambridge, UK (1967).
91. A. D. Turner, G. Worrall and J. T. Dalton, A Survey of Strippable and Tie-Down Coatings for Use in the Decommissioning of Alpha-Active Facilities, Report AERE-R-12474, United Kingdom Atomic Energy Authority, Harwell Laboratory, Oxfordshire, UK (1987).
92. H. Weichselgartner, Decontamination with Pasty Pickling Agents Forming a Strippable Coating, Report EUR 13498, Commission of the European Communities, Luxembourg (1991).
93. Decommissioning Handbook, DOE/EM-0142P, Office of Environmental Restoration, U.S. Department of Energy, Washington, D. C. (1994).
94. IAEA Technical Report Series, State of the Art for Decontamination and Dismantling of Nuclear Facilities, TRS No. 395, International Atomic Energy Agency, Vienna, Austria (1999).
95. J. L. Tripp, R. H. Demmer and R. L. Merservey, Decontamination, in: *Hazardous and Radioactive Waste Treatment Technologies Handbook*, C. H. Oh (Ed.), Chapter 8, CRC Press, Boca Raton, FL (2001).
96. EPA Technology Reference Guide for Radiologically Contaminated Surfaces, EPA-402-R-06-003, U.S. Environmental Protection Agency, Washington, D.C. (2006).
97. C. Laney, Decontamination of Reactor Cavity using Isolock-300, ALARA Note #8, Brookhaven National Laboratory, Brookhaven, NY (2005).
98. J. W. Lee, M. Ahlen, M. Bruns, V. Fricke, C. May, J. Pickett, and S. Salaymeh, Application of New and Innovative Technologies on the 321-M Fuel Fabrication Facility Large Scale Demonstration and Deployment Project, Report WSRC-MS-98-00122, Office of Science and Technology, U. S. Department of Energy, Savannah River, SC (1998).
99. M. A. Ebadian, Assessment of Strippable Coatings for Decontamination and Decommissioning, Report DE-FG21-95EW55094-32, Florida International University, Miami, FL (1998).
100. V. Fricke, S. Madaris and C. May, ALARA™ Strippable Coating, Report WSRC-TR-99-00458, Office of Science and Technology, U. S. Department of Energy, Savannah River, SC (1999).
101. ALARA™ 1146 Strippable Coating, Summary Report DOE/EM-0533, Deactivation and Decommissioning Focus Area, Office of Science and Technology, U. S. Department of Energy, Savannah River, SC (2000).

102. J. McFee, E. Stallings, M. Romero and K. Barbour, Improved Technologies for Decontamination of Crated Large Metal Objects, in: WM'02, Proc. Waste Management Conference 2002, R. Post (Ed.), Waste Management Society, Phoenix, AZ (2002).
103. R. R. James, Z. J. Willenberg, R. V. Fox and J. Drake, Bartlett Services Inc. Stripcoat TLC Free™ Radiological Decontamination Strippable Coating, Technology Evaluation Report EPA/600/R-08/099, U. S. Environmental Protection Agency, Cincinnati, OH (September 2008).
104. R. R. James, Z. J. Willenberg, R. V. Fox and J. Drake, Isotron Corp. Orion™ Radiological Decontamination Strippable Coating, Technology Evaluation Report EPA/600/R-08/100, U. S. Environmental Protection Agency, Cincinnati, OH (September 2008).
105. H.-L. Yin, Z.-Y. Tan, Y.-T. Liao and Yi.-J. Feng, Application of  $\text{SO}_4^{2-}/\text{TiO}_2$  Solid Supercap in Decontaminating Radioactive Pollutants, *J. Environ. Radioactivity* 87, 227 (2006).
106. A. Parkinson, T. Evans, D. Hill, and M. Colella, An Empirical Assessment of Post-Incident Radiological Decontamination Techniques, in: Report on the 2007 Workshop on Decontamination, Cleanup, and Associated Issues for Sites Contaminated with Chemical, Biological, or Radiological Materials, S. Dun (Ed.), Report EPA/600/R-08/059, pp. 180–183 (May 2008).
107. K. C. Holt, Testing for Radiological Decontamination Strippable Coating for Cellular Bioengineering, Inc. (Cs-137, Pu-239, Am-241), Letter Reports, Sandia National Laboratories, Albuquerque, NM (October 2007 and December 2007).
108. K. J. Walter, A. E. Draine and T. E. Johnson, Decontamination of a Fume Hood Contaminated with Tritiated Thymidine, Paper THAM-C.4, Proc. 52<sup>nd</sup> Ann. Mtg. Health Physics Society, Portland, OR (2007).
109. J. D. VanHorne-Sealy, Evaluating the Efficiency of Decon Gel 1101 for Removal of Cs-137, Co-60, and Eu-154 on Common Commercial Construction Materials, M.S. Thesis, Oregon State University, Corvallis, OR (May 2008).
110. M. Sutton, R. P. Fischer, M. M. Thoet, M. P. O'Neill and G. J. Edgington, Plutonium Decontamination Using CBI Decon Gel 1101 in Highly Contaminated and Unique Areas at LLNL, Report LLNL-TR-404723, Lawrence Livermore National Laboratory, Livermore, CA (June 2008).
111. A. E. Draine, T. E. Johnson, M. P. O'Neill, G. J. Edgington and K. J. Walter, Decontamination of Medical isotopes from Hard Surfaces Using Peelable Polymer-Based Decontamination Agents, Proc. 53<sup>rd</sup> Ann. Mtg. Health Physics Society, Philadelphia, PA (2008).
112. A. E. Draine, Decontamination of Medical Radioisotopes from Hard Surfaces Using Peelable Polymer-Based Decontamination Agents, M.S. Thesis, Colorado State University, Fort Collins, CO (March 2009).
113. B. H. Davison, T. Kuritz, K. P. Vercruyse and C. K. McKeown, Green Biopolymers for Improved Decontamination of Metals from Surfaces:

- Sorptive Characterization and Coating Properties, Final Report, Project Number: EMSP 64907, Oak Ridge National Laboratory, Oak Ridge TN (2002).
114. K. G. Andersson and J. Roed, Removal of Radioactive Fallout from Surface of Soil and Grassed Surfaces Using Peelable Coatings, *J. Environ. Radioactivity* 22, 197 (1994).
  115. S. Svensson, Contamination Removal Process, U.S. Patent 5,017,237 (1991).
  116. M. E. Lumia and C. A. Gentile, Industrial Hygiene Concerns During the Decontamination and Decommissioning of the Tokamak Fusion Test Reactor, Report PPPL-3647, Princeton Plasma Physics Laboratory, Princeton University, Princeton, NJ (2002).
  117. M. A. Ebadian, M. Allen, Y. Cai and J. F. McGahan, Mercury Contaminated Material Decontamination Methods: Investigation and Assessment, Report HCET-2000-D053-002-04, Florida International University, Miami, FL (2001).
  118. M. Sutton, B. Andresen, S. R. Burastero, M. L. Chiarappa-Zucca, S. Chinn, P. Coronado, A. E. Gash, J. Perkins, A. Sawvel and S. C. Szechenyi, Modern Chemistry Techniques Applied to Metal Behavior and Chelation in Medical and Environmental Systems, Final Report UCRL-TR-209476, Lawrence Livermore National Laboratory, Livermore, CA (2005).
  119. R. V. Fox, R. Avci and G. S. Groenewold, Decontamination Materials, Methods for Removing Contaminant Matter from a Porous Material, and Systems and Strippable Coatings for Decontaminating Structures that Include Porous Material, U.S. Patent Application 200702400733 (2007).





# Cryo-aerosol Cleaning of Particles from Surfaces

Souvik Banerjee

Senior Manager, Flextronics, Milpitas, CA, USA

---

## Abstract

Cryo-aerosol cleaning has been used as a dry cleaning technique in electronics manufacturing for more than two decades. It has primarily been used to remove particulate contamination from surfaces. There are two distinct gas chemistries, equipment sets, and methodologies in this cleaning process: Carbon dioxide gas based and argon or nitrogen or their mixture. This chapter describes the history of both these cryo-aerosol cleaning methods, the physics of the aerosol formation and the cleaning process. There are several factors that need to be controlled to obtain desired cleaning performance. The chapter gives an overview of these factors and discusses cleaning data on semiconductor wafers, photomasks, and other surfaces. The author has concluded the chapter with his insights into how this cleaning technology, currently used in only some niche areas, can be broadened to encompass other cleaning applications.

**Keywords:** Cleaning, particles, residues, cryo-aerosol, cryogenic, semiconductor, photomasks, nozzle, gas

## 12.1 Introduction

Cleaning is an important and integral part of most manufacturing processes. In some cases such as in metal fabrication it takes the simple form of degreasing with organic solvents. However, in other cases such as in electronics manufacturing or in healthcare, precision cleaning or

---

*E-mail:* [mitasouvik@sbcglobal.net](mailto:mitasouvik@sbcglobal.net)

---

K.L. Mittal and Ravi Jaiswal (eds.) Particle Adhesion and Removal, (453–476)  
2015 © Scrivener Publishing LLC

surface conditioning faces several challenges. Not only the precision cleaning technique has to remove different contaminants such as homogeneous (film residues) and inhomogeneous (particles) from the surface but it must do so by preserving the integrity of fragile features and being highly selective to the underlying substrate to which the particles adhere.

The most common cleaning method has been to use organic or inorganic chemicals dissolved in de-ionized (DI) water aided by physical forces of removal from brushes, ultrasonics, or megasonics. The chemicals remove the contaminants by either dissolving them, without affecting the substrate to which the contaminant adheres, or by providing electrostatic repulsive forces originating from zeta potential between the particles and the surface. The physical forces of removal, such as the brush or sonication, aid in the cleaning process by reducing the fluid boundary layer on the surface and by providing physical force of removal on the contaminants. Thus a combination of physical and chemical cleaning mechanisms has been successfully employed over many decades to remove contaminants of various types from surfaces.

In precision cleaning applications as in electronics manufacturing, there is a growing need for removal of nanometer size particles. According to the International Technology Roadmap for Semiconductors (ITRS) in 2013 the critical defect size in integrated circuit manufacturing process was 14 nm and for photomask it was 25 nm [1]. The removal of nanometer size particles is very challenging and is further made difficult by the constraint on the substrate material loss during the removal process. Since aqueous cleaning removes particles partly by chemical etching at the interface between the contaminant particle and the underlying substrate, certain amount of substrate loss occurs during the cleaning process. Specifically, the ITRS Front End of Line (FEOL) roadmap states that less than 1 Å of SiO<sub>2</sub> and polysilicon substrate may be lost per cleaning step for the 65-nm technology node. The allowable substrate material loss decreases to less than 0.4 Å per cleaning step at 45-nm node and below [1,2]. Thus the need for achieving low material loss during aqueous cleaning has hampered the cleaning performance of nanometer sized particles.

This has given rise to other cleaning processes such as dry cleaning to complement wet cleaning. One such cleaning method is cryogenic aerosol cleaning which could be used either with carbon dioxide (CO<sub>2</sub>) or combination of argon and nitrogen (Ar/N<sub>2</sub>) gases. In this chapter both types of cryoaerosol processes are discussed and the results are presented to give the reader insights into this dry cleaning technique.

## 12.2 History of Cryoaerosol Cleaning

Carbon dioxide aerosol cleaning was introduced first, followed by Ar/N<sub>2</sub> aerosol cleaning. In 1986 Prof. Stuart Hoenig of the University of Arizona published a paper on solid CO<sub>2</sub> dry ice cleaning [3]. In this paper he explains the limitations to remove submicrometer particles due to fluid boundary layer effect in aqueous cleaning, as described in the previous section. The slow expansion of liquid CO<sub>2</sub> through an orifice results in hard pellets of solid CO<sub>2</sub>, "much like hail". The pellets were used to blast off contaminants from surfaces without scratching or otherwise causing damage. This cleaning method was described as dry ice cleaning by Hoenig. One of the earlier applications of this cleaning technique was the removal of paint from aircraft by Lockheed.

In 1990, Layden and Wadlow [4] reported a modification of this cleaning technique in which CO<sub>2</sub> in gas phase was made to expand through a nozzle. The high velocity aerosol jet created by the converging/diverging nozzle is directed towards the substrate to be cleaned. Details of the cleaning mechanism will be discussed in sections 12.3.1 and 12.4. The authors reported cleaning of 2" diameter silicon wafer challenged with zinc orthosilicate particles to a concentration of 538,000 particles per cm<sup>2</sup>. Although the particle size was not reported in the paper, cleaning efficiency of 99.9% was obtained by this method. Effective removal of organic residues was also demonstrated with CO<sub>2</sub> aerosol cleaning with the removal of human skin oil and silicone grease as measured with x-ray photoelectron spectroscopy (XPS). Degassing of ion source components was also demonstrated to be better with this cleaning method compared to solvent cleaning and, consequently, showed shorter vacuum pump down time of the ion source following the cleaning procedure.

Sherman and colleagues [5–8] described the use of CO<sub>2</sub> snow cleaning for removing hydrocarbon residues from a variety of surfaces such as metals (Al and Cu), semiconductors (Si and InP wafers), and insulators (ceramics, glass plates, laser optics, and polymers) in surface analysis applications. These papers explain that two separate mechanisms are at work in CO<sub>2</sub> snow cleaning, a collision based approach for particulate removal and solvation based for organic residues. Both these methods will be explained in section 12.4.

In 1991 the Ar/N<sub>2</sub> cryoaerosol process was introduced after being developed at Air Products and Chemicals and IBM [9,10]. The technique has since been used primarily for cleaning flat surfaces such as silicon wafers in integrated circuit (IC) manufacturing. McDermott and Butterbaugh [9] describe different process steps in IC manufacturing where Ar/N<sub>2</sub> aerosol

cleaning can be used. These include pre- and post- deposition of metals and dielectrics (both PVD and CVD processes), post-etch residue removal after metal, polysilicon, and dielectric film etches, and residue removal after photoresist ashing. The authors also describe back-end IC manufacturing processes such as cleaning after electrical test probe contact of the metallic pads of the completed chip. Particulate contamination left on the probe after contact is removed by this aerosol cleaning method. Section 6 describes the results obtained with both CO<sub>2</sub> and Ar/N<sub>2</sub> aerosol cleaning techniques.

The history of cryoaerosol cleaning from 1986 has been discussed in this section. Both CO<sub>2</sub> and Ar/N<sub>2</sub> aerosol cleaning methods have been investigated and shown to be successful in a broad range of cleaning applications such as silicon wafers, photomasks, optical mirrors and lenses, magnetic disk drives, and many others. Both techniques have evolved significantly since their adoption by the industry to overcome process issues from surface cooling during cleaning process, potential damage to fine structures on the surface being cleaned, and contamination from the gas source.

A successful cleaning process must, therefore, have a controlled environment in which processing of the substrate is done. In the subsequent sections mature CO<sub>2</sub> and Ar/N<sub>2</sub> cleaning systems implemented in the industry for routine use in component manufacturing will be discussed along with their application results.

### 12.3 Thermodynamics of Cryoaerosol Processes

The triple point of cryogenic fluids is an important parameter governing the formation of cryoaerosols. Table 12.1 gives the triple point pressure and temperature of some of the gases which have been used in cryogenic cleaning. At the triple point, all three states of matter (solid, liquid and gas) co-exist with each other in equilibrium.

Gibbs phase rule, Equation (12.1), describes the number of degrees of freedom for a given system at equilibrium.

$$F = C - P + 2 \quad (12.1)$$

where F is the number of degrees of freedom, C the number of components in the system, and P is the number of phases in the system. The degrees of freedom represent the number of variables such as pressure, temperature, and composition which can be varied over a finite range without changing the number of phases of the system. Thus for pure CO<sub>2</sub> (C = 1) to exist in equilibrium in all of its three states of matter simultaneously (P = 3), Gibbs

**Table 12.1** Pressure and Temperature at Triple Point of Select Gases

Gas	Triple Point Pressure (atm)	Triple Point Temperature (°C)
Nitrogen (N <sub>2</sub> )	0.12	-210.0
Oxygen (O <sub>2</sub> )	1.44E-3	-218.8
Hydrogen (H <sub>2</sub> )	0.07	-259.4
Neon (Ne)	0.49	-248.6
Argon (Ar)	0.68	-189.4
Krypton (Kr)	0.72	-157.4
Xenon (Xe)	0.80	-111.8
Methane (CH <sub>4</sub> )	0.12	-182.5
Carbon dioxide (CO <sub>2</sub> )	5.11	-56.6

equation indicates that the number of degrees of freedom is 0 ( $F=0$ ). In other words, there is only one temperature and pressure condition, known as the triple point, at which CO<sub>2</sub> can coexist as solid, liquid and gas. At all other temperatures and pressure conditions, one of the three phases will evaporate, condense, melt, freeze, or sublime resulting in the fluid existing in either a single- or two-phase equilibrium state. On the other hand, a single phase of solid, liquid, or gas of this mono-component system is defined by a combination of pressure and temperature. An equilibrium condition of any of these two phases of this system is described by only pressure or temperature but not by both.

For a two-component system such as Ar/N<sub>2</sub> cryoaerosol, the phase diagram is more complicated than for a single phase system. In such a case where  $C=2$  and  $P=1$ , the number of intensive variables  $F$  is 3 from equation (12.1). This implies that a given phase of a two-component system is defined by three parameters: pressure, temperature, and mole fraction of each component. This will be further illustrated in section 12.3.2.

### 12.3.1 Thermodynamics of CO<sub>2</sub> Aerosol Process

Figure 12.1 is the pressure-temperature (P-T) diagram showing the conditions at which CO<sub>2</sub> can exist in single phase or coexist in equilibrium in multiple phases. The critical point denotes the P-T condition above

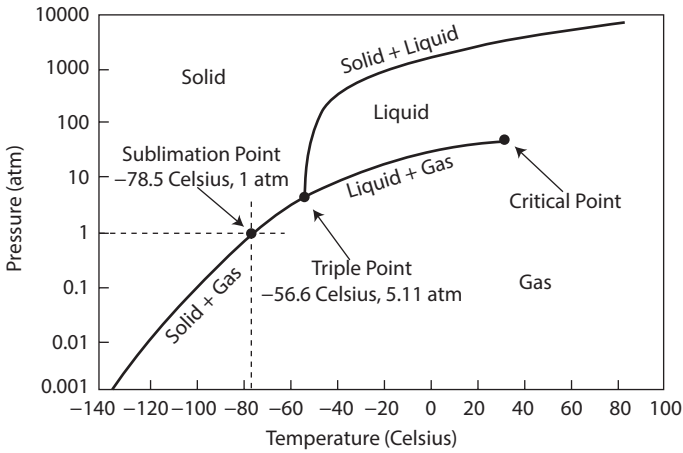


**Figure 12.1** Pressure-Temperature diagram of CO<sub>2</sub>

which CO<sub>2</sub> has properties of both liquid and gas, this region is known as the supercritical CO<sub>2</sub> region. The triple point denotes the combination of pressure and temperature at which it can exist in equilibrium in all three phases, solid, liquid, and gas, as discussed in section 12.3. The gas used in CO<sub>2</sub> cryoaerosol cleaning is stored in a cylinder at pressure of 57.8 atmospheres (5.9 MPa) and temperature of about 20°C (ambient or room temperature). The figure shows that at the cylinder pressure and temperature conditions, CO<sub>2</sub> exists in equilibrium in liquid and gas phases.

During the cleaning process liquid CO<sub>2</sub> is drawn from the cylinder into a specially designed nozzle. The fluid expands through the orifice of the nozzle [11] undergoing an adiabatic expansion accompanied by Joule-Thomson cooling, resulting in pressure and temperature drop of the liquid CO<sub>2</sub>. The cleaning chamber is kept at atmospheric pressure. The reduction in pressure and temperature of the liquid CO<sub>2</sub> results in formation of solid CO<sub>2</sub> particles (frozen) dispersed in gas-phase CO<sub>2</sub> or an aerosol which exits out of the nozzle. The aerosol stream consisting of frozen CO<sub>2</sub>, also called “snow”, is responsible for cleaning, the mechanism of which will be described in section 12.4.

The P-T graph of Figure 12.1 helps us understand changes the CO<sub>2</sub> fluid undergoes during its transition from liquid to cryogenic aerosol. It does not however explain how the starting phase of the CO<sub>2</sub> (whether it is liquid or gas) entering the nozzle has an effect on the fraction of solid particles in the aerosol composition formed by the nozzle. This is explained by the pressure-enthalpy (P-E) diagram of the three phases of CO<sub>2</sub> [2,11,12] shown in Figure 12.2. From the P-T diagram of Figure 12.1, one can see

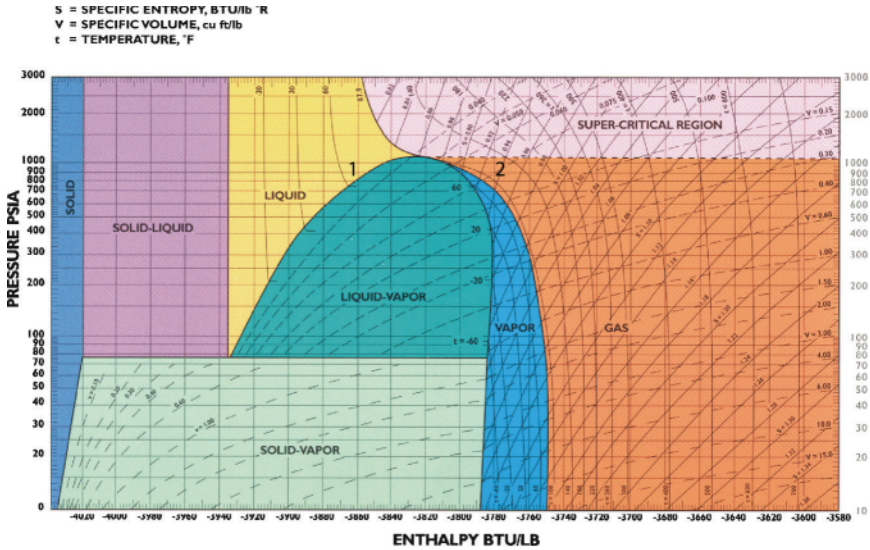


Figure 12.2 Pressure-Enthalpy diagram of CO<sub>2</sub>

that at a cylinder pressure of 5.9 MPa and ambient temperature of about 20°C, CO<sub>2</sub> can exist in equilibrium between liquid and vapor phases. Two examples of cryogenic aerosol formation are shown in Figure 12.2, one in which the starting phase of CO<sub>2</sub> is liquid and the other in which it is gas.

If the starting phase of CO<sub>2</sub> is liquid at 5.9 MPa, the corresponding point in Figure 12.2 is shown as Point 1. It is at the border of the liquid and liquid-vapor regions. Thus starting from phase Point 1, as CO<sub>2</sub> expands through the nozzle, in an adiabatic and isenthalpic (constant enthalpy) manner, some of the liquid initially gets converted to vapor. Further, as the pressure decreases below 0.5 MPa, the phase point crosses the boundary between liquid/vapor and solid/vapor regions during which a portion of the liquid freezes into cryogenic particles while the remainder turns into vapor. The resulting percentage of solid in the aerosol starting from liquid CO<sub>2</sub> is around 40%.

On the other hand, if the starting phase of CO<sub>2</sub> flowing into the nozzle is gas, the corresponding point on the P-E diagram is denoted by Phase Point 2. The CO<sub>2</sub> gas is shown to be in equilibrium with liquid as it is on the border of the liquid-vapor and vapor regions. As the expansion through the nozzle takes place, some portion of the vapor condenses to liquid as the phase point crosses into the liquid/vapor region. On further expansion to less than 0.5 MPa, the phase point crosses the solid/vapor boundary. In this case a portion of the liquid freezes into solid while the remaining

undergoes phase change into vapor. The percentage of solid in the aerosol starting from gas phase  $\text{CO}_2$  is less than 10%.

The pressure-enthalpy diagram of Figure 12.2 therefore demonstrates that the  $\text{CO}_2$  aerosol composition and mechanism of formation is strongly dependent on the starting phase of the fluid. The ability to control the aerial density of the frozen solid particles in the aerosol plume (i.e., greater fraction of the solids starting from liquid  $\text{CO}_2$  and less from gas) has significant process advantages in non-damaging surface cleaning and will be further discussed in section 12.5.

### 12.3.2 Thermodynamics of Ar/ $\text{N}_2$ Cryogenic Aerosol System

The Ar/ $\text{N}_2$  aerosol system is slightly different from the  $\text{CO}_2$  system. The fundamental concept of a fluid forming an aerosol by expansion through a nozzle is the same for both systems. However, the comparatively lower triple point temperatures of Ar and  $\text{N}_2$ , shown in Table 12.1, compared to  $\text{CO}_2$ , make the two systems sufficiently different.

The Ar gas or a mixture of Ar/ $\text{N}_2$  is first extracted from the cylinder at 0.76 MPa and ambient temperature of about  $20^\circ\text{C}$ . The gas is converted into the liquid phase by pre-cooling achieved by passing through liquid nitrogen. The pre-cooled Ar or Ar/ $\text{N}_2$  mixture exiting out of the liquid nitrogen Dewar at  $-172^\circ\text{C}$  and 0.53 MPa, exists in equilibrium between its liquid and gas phases as shown on the pressure-temperature phase diagram, Figure 12.3. The liquid/gas mixture is then delivered to the process chamber maintained at sub-atmospheric pressure. The fluid mixture enters the chamber through a specially designed nozzle where it expands to form

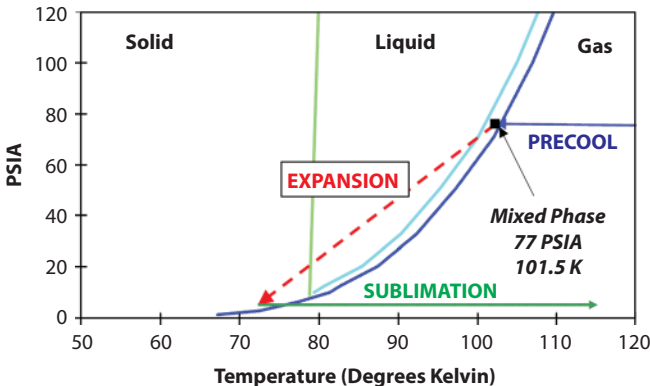


Figure 12.3 Pressure-temperature diagram of Ar/ $\text{N}_2$  system.



aerosol of liquid droplets dispersed in the gas phase. As the aerosol exits out of the nozzle and into the sub-atmospheric pressure chamber, the liquid droplets freeze during the expansion process through evaporative cooling, thereby generating the cryogenic aerosol inside the process chamber [13]. The phase path during the expansion of the liquid droplets is shown by the dotted arrow in Figure 12.3.

## 12.4 Cleaning Mechanism

This section describes the basic mechanism of cleaning using cryogenic aerosol. Banerjee and colleagues [2], Hinds [14], and Bowling [15] discuss detailed mechanisms of particle removal including various forces of particle-substrate adhesion during cleaning process. Particulate contamination is removed primarily by momentum transfer aided by the drag of gas flow over the surface. The aerosol comprised of frozen solid particles entrained in a gas stream coming out of a nozzle is directed at the contaminants on the surface of the substrate as shown in Figure 12.4. The frozen particles of  $\text{CO}_2$  or  $\text{Ar}/\text{N}_2$  collide with the contaminant particle thereby imparting force to it through momentum transfer. If the force imparted to the contaminant particle is greater than the force of adhesion between the contaminant particle and substrate, the particle on the surface dislodges. The gaseous component of the aerosol then drags the particles away from the surface. A purge gas such as  $\text{N}_2$  flowing parallel to the surface is used as a curtain to keep the particles from re-depositing on the surface from which it was removed.

Sherman and colleagues [5–8] also describe removal of organic residues from the surface of substrates by  $\text{CO}_2$  aerosol cleaning. It is achieved due to the effective solvent properties of liquid carbon dioxide for dissolving

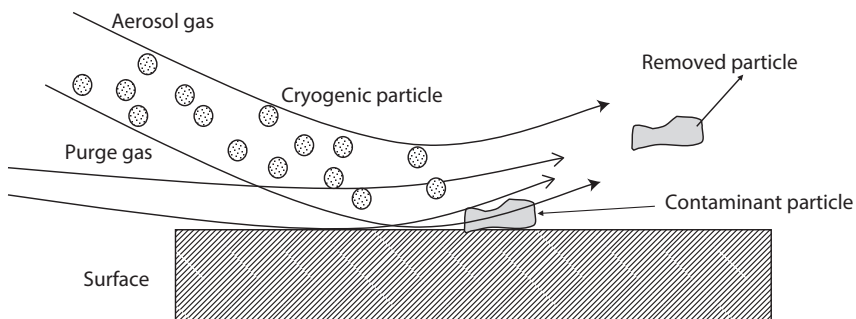


**Figure 12.4** Schematic of particle removal in cryogenic aerosol cleaning process.

organic residues and non-polar contaminants. Liquid  $\text{CO}_2$  is formed at the interface of the aerosol particle and the substrate during impact of the snow particle on the substrate. The pressure on the  $\text{CO}_2$  particle at the contact point depresses the freezing point of the solid particle so that a thin layer of liquid  $\text{CO}_2$  is formed. It is this liquid film which is responsible for dissolution of organic contaminants.

## 12.5 Factors Affecting Cleaning Performance

There are several factors affecting the performance of cryoaerosol cleaning. The simple systems in the past [6] consisted of a nozzle, an on/off device such as a hand-held gun, and the hose or tubing to connect the cleaning equipment to a carbon dioxide source, i.e., a cylinder as shown in Figure 12.5. Such systems do not give optimized cleaning performance in precision cleaning application. Subsections 12.5.1–12.5.5 provides an overview of the key cleaning parameters needed to be properly controlled and the methods of controlling them for obtaining optimized cleaning



Figure 12.5 Hand-held  $\text{CO}_2$  cryoaerosol cleaning gun [6]

performance. The commercial  $\text{CO}_2$  and  $\text{Ar}/\text{N}_2$  cleaning systems for use in component manufacturing all employ effective control of each of these factors.

### 12.5.1 Moisture Control

In both  $\text{CO}_2$  and  $\text{Ar}/\text{N}_2$  aerosol cleaning systems, the expansion of the fluid through the nozzle causes a significant drop in temperature. The temperature drop will cause moisture in the system or in the gas to condense onto the substrate during the cleaning process. The condensed moisture in the interstitial space between the particle and substrate creates a capillary effect, increasing the force of adhesion between the contaminant particle and the substrate [2,14,15]. The increase in the force of adhesion will make it difficult to remove the particle thereby resulting in an undesirable cleaning performance. Thus for optimized cleaning performance the humidity in the environment and the moisture in the gas must be controlled.

The humidity inside the cleaning system is lowered by purging the cleaning chamber. Substrates are inserted into the cleaning chamber through a slot using standard automated handling systems. The chamber is continuously purged with dry  $\text{N}_2$  or clean dry air (CDA). The flow of purge gas is kept on during the entire time the substrate is inside the cleaning chamber. Figure 12.6 shows the  $\text{Ar}/\text{N}_2$  cryoaerosol semiconductor wafer cleaning chamber and the gas delivery system. The purge gas flow, shown by the arrow inside the chamber, is directed over the wafer surface to create a laminar flow pattern. The gas flow not only keeps the chamber dry but also helps to carry away the contaminant particles removed from the surface.

The cleaning gas also needs to be dried prior to introduction into the cleaning chamber. Section 12.5.5 shows the contamination levels, including moisture needed to obtain good cleaning performance particularly for removing sub-micrometer particulate contamination.

### 12.5.2 Control of Electrostatic Charging

Another important consideration in cryoaerosol cleaning is the control of electrostatic charging during the process. The dry environment needed to achieve good particle removal performance, mentioned in section 12.5.1, can result in the substrate getting electrostatically charged [16]. The charging occurs by a process known as triboelectrification [17] due to high velocity flow of dry gas over an insulating substrate such as silicon wafer or glass. The electric field on the charged surface, when exceeding 3 MV/m, results in an electrostatic discharge in air. The energy liberated during the

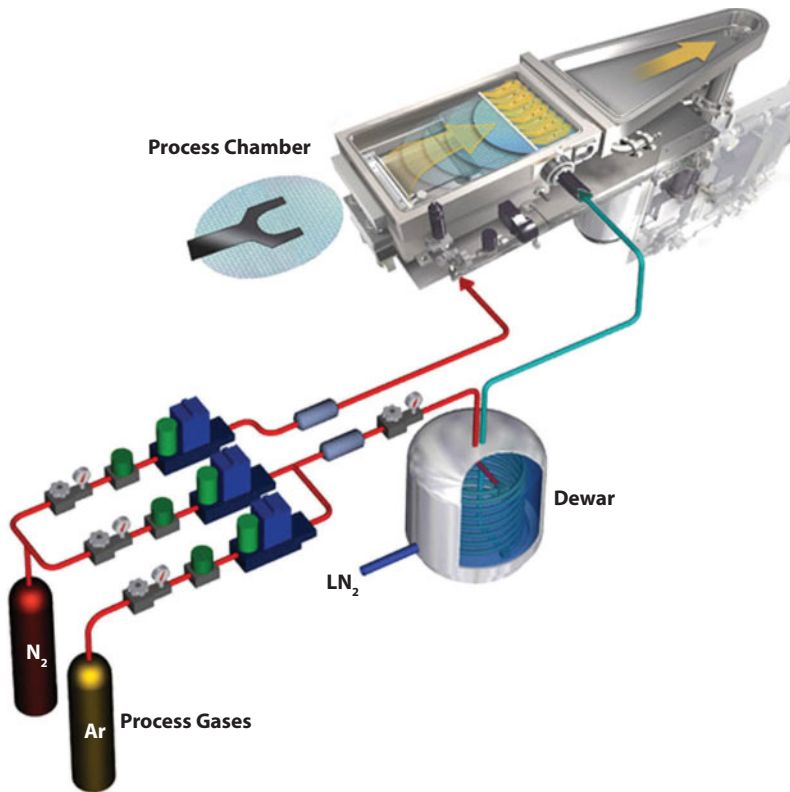


**Figure 12.6** 3D model of the Ar/N<sub>2</sub> cryoaerosol cleaning chamber and gas delivery system.

discharge can cause damage to ultra-fine surface features such as commonly seen in many electronic devices. Besides causing feature damage, the charging of the substrate can also attract particles to it, thereby contaminating the cleaned surface.

Controlling the surface electrostatic charge is, therefore, very critical to successful cleaning process. The charge control can be achieved by such means as +ve and -ve corona bars, and alpha particle emitting radioactive source such as Po-210. These devices generate ions of both polarities. The ions thus formed neutralize residual charge on the substrate thereby preventing any electrostatic charge build-up and subsequent discharge and damage. It is also important to keep the substrate properly grounded to provide a path for any accumulated charge to flow to ground in a controlled manner. Electrical grounding can only be possible with conductive substrates. For insulating substrates, the charge dissipation means have to

rely on corona bars and radioactive sources. References [16–19] describe these various methods of electrostatic charge control in aerosol cleaning systems.

### 12.5.3 Airflow Management

In section 5.1 the importance of purge air flow to create a dry environment for obtaining proper cleaning performance was described. The purge gas was also seen to remove the particles from the surface of the substrate during the cleaning process thereby preventing re-deposition on the cleaned surface. The purging process forms a curtain of laminar gas flow over the surface, the velocity and direction of which helps to carry away the particles removed and shields the cleaning surface from re-deposition of the particles. The particles removed are made to flow through a High Efficiency Particulate Air (HEPA) filter in the exhaust line of the system, where they get trapped [16–20].

Figure 12.7 shows the inside of an Ar/N<sub>2</sub> aerosol cleaning chamber with a semiconductor wafer as the substrate to be cleaned. A broad nozzle with multiple aerosol plumes exiting from it is swept over the substrate at a controlled speed. The width of the nozzle is large enough to cover the entire wafer surface. Nitrogen purge gas is flown over the surface of the wafer in a laminar flow pattern during the cleaning process. The purge gas flow “sweeps” away the particles released from the wafer during cleaning, carrying them away from the substrate to prevent re-contamination. The performances of CO<sub>2</sub> and Ar/N<sub>2</sub> aerosol cleaning systems discussed in section 6 have all been obtained with automated systems employing such airflow management.

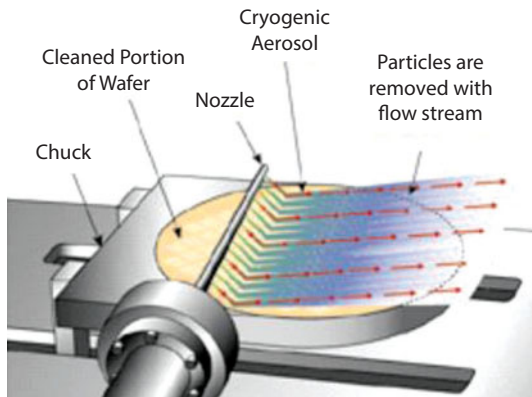


Figure 12.7 Controlled air flow in the cleaning chamber.

### 12.5.4 Aerosol Particle Size Control

Banerjee *et al.* [2] describe in detail the various forces of adhesion between particles and surface and the physics of momentum transfer of the aerosol particles for effective removal of surface contaminants. They also describe the effect of cryoaerosol particle size on the momentum transferred to the contaminant particles.

In certain cleaning applications where the substrate has delicate features, such as in MEMS and microelectronics, feature damage can be caused by the force imparted to them during the cleaning process. In such cases, it is imperative to control the cryogenic particle size distribution for effective removal of sub-micrometer particles without causing damage.

Theoretical calculations [21–23] showed that small cryoaerosol particles have sufficient force for removal of sub-micrometer contaminant particles and without the damaging aspect of cleaning process. Figure 12.8 shows the velocity and size distributions of CO<sub>2</sub> cryoaerosol particles obtained with specially designed nozzles to control pattern damage during cleaning.

The velocity and size of the aerosol particles shown in Figure 12.8 have been measured using Phase Doppler Anemometry the schematic of which is shown in Figure 12.9 and the picture of the actual system in Figure 12.10. The aerosol is made to flow through a sensing volume created by two intersecting beams of laser shifted slightly in frequency by the Bragg cell [24,25].

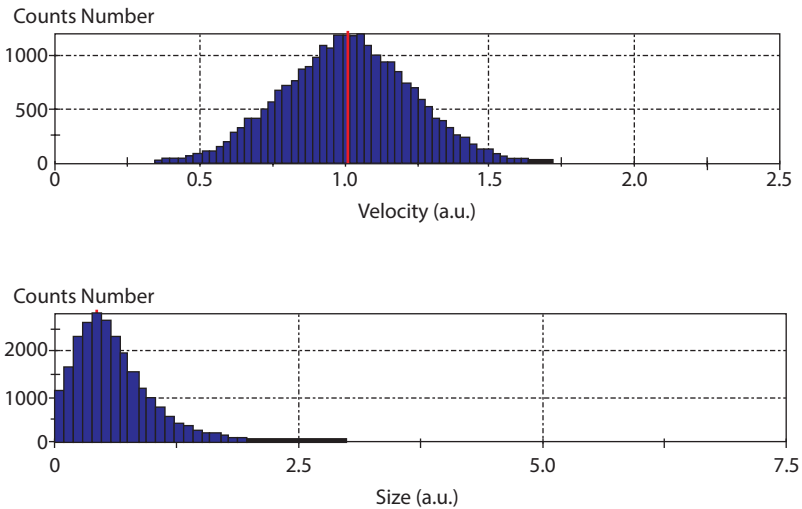


**Figure 12.8** Controlled distributions of aerosol particle velocity and size required for damage-free cleaning in microelectronics applications [23,24].

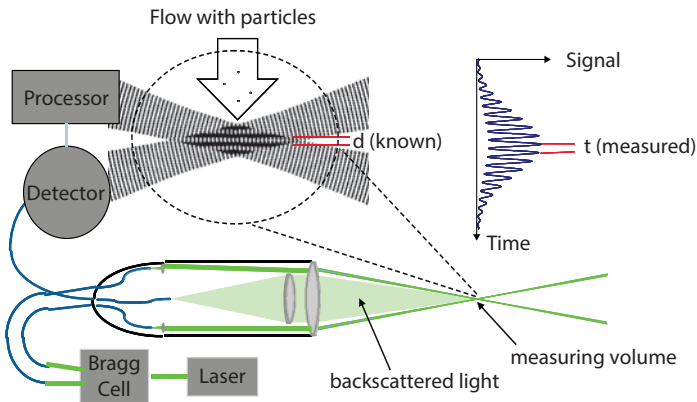


**Figure 12.9** Schematic of the Phase Doppler Anemometry to measure cryoaerosol particle size and velocity.

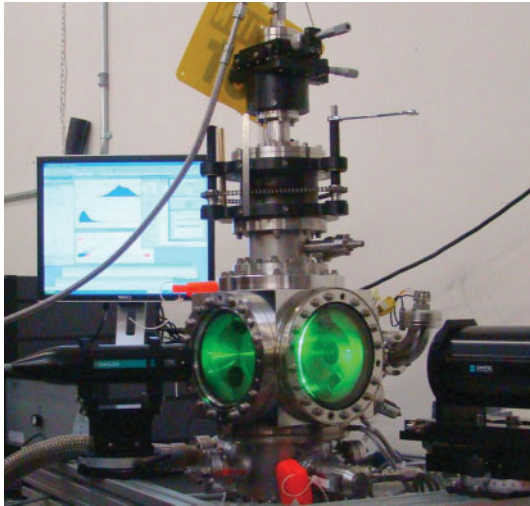


**Figure 12.10** Phase Doppler Anemometry setup to simultaneously measure cryoaerosol particle size and velocity.

The backscattered light from the sensing volume is measured by a photo-detector and the signal analyzed to provide information on aerosol particle velocity and size which is shown in Figure 12.8. Nozzles can be designed using this kind of measurement technique to provide controlled cryoaerosol particles which will have sufficient momentum to remove sub-micrometer particles but without the damaging aspect on sensitive features.

### 12.5.5 Gas Purity

The purity of gases used in cleaning has a profound influence on particle removal performance. High molecular weight organics also called non-volatile organic residues (NVORs) and other contaminants such as metallic particles in the  $\text{CO}_2$ , Ar or  $\text{N}_2$  gases can precipitate on the surface of the substrate being cleaned. These contaminants can get carried from inside the gas cylinder by the cleaning fluid and subsequently partition out of the fluid phase during its expansion through the nozzle. The contaminants can then condense onto the substrate in the form of particles.

Johnson *et al.* patent [26] describes a system for removing these contaminants. The NVORs are effectively removed by combusting the hydrocarbons in a catalytic converter in presence of an oxidant at an elevated temperature. The oxidant can be either oxygen or air. If the  $\text{CO}_2$  already has sufficient oxygen content then the oxidant addition step can be eliminated. The NVORs in the presence of oxygen and catalyst in the temperature range of 150 to 288 °C oxidize to  $\text{CO}_2$  and water vapor resulting in a gas purity which has <10 ppb of the heavy organics. Additional purification stages using coalescing filters and adsorber beds are employed to remove particles and moisture from the  $\text{CO}_2$  stream. Figure 12.11 shows measurements using gas chromatography followed by mass spectrometry (GC-MS) of purified  $\text{CO}_2$ . There are two curves overlaid on top of each other as indicated. The curve representing the  $\text{CO}_2$  which did not go through the

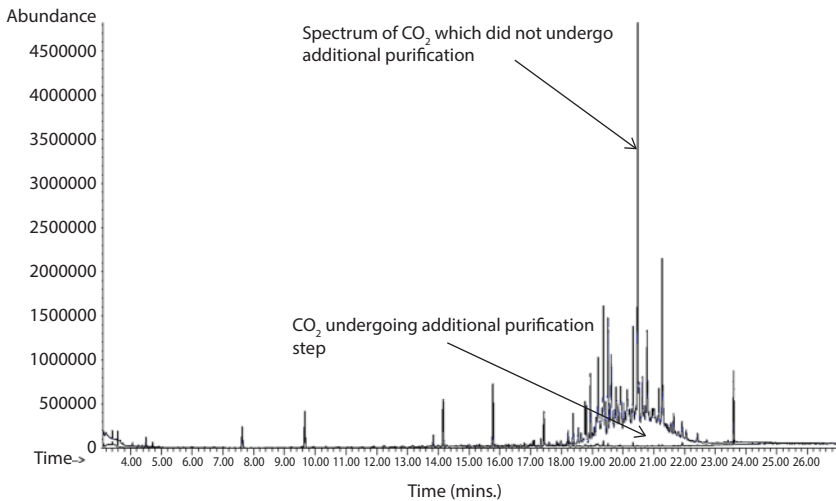


**Figure 12.11** Comparison of GC-MS analyses of  $\text{CO}_2$  undergoing additional purification step through example of a system described in [26] compared to  $\text{CO}_2$  which did not go through the purifier.



**Table 12.2** Impurities in commercially available CO<sub>2</sub> used in cleaning

Impurity	Upper Specification Limit
Oxygen	2 ppm
Nitrogen	5 ppm
Hydrogen	0.1 ppm
Carbon monoxide	0.1 ppm
Moisture	0.5 ppm
Total Hydrocarbons as CH <sub>4</sub>	2 ppm
Total Extractable Halocarbons as CCl <sub>4</sub>	100ppb

purifier had several isolated peaks throughout the retention time period as well as a broad contamination peak over the retention time period of 18–23 minutes. The second curve representing the CO<sub>2</sub> which underwent purification did not show any of the contaminant peaks.

Besides the hydrocarbons, moisture in the gas is another key impurity as described in section 12.5.1. Table 12.2 gives the concentrations of various impurities in a commercially available CO<sub>2</sub> gas used in cryogenic cleaning by integrated device manufacturers.

## 12.6 Results Obtained by Cryoaerosol Cleaning

In sections 12.1 and 12.2 it was shown that cryoaerosol technique could be used in precision cleaning for removal of particulate contamination from a wide variety of substrates. In this section specific examples of cleaning in integrated circuit fabrication and photomask manufacturing [2,24,25,27,28], are discussed.

Figure 12.12 shows particle removal efficiency of CO<sub>2</sub> cryogenic aerosol cleaning process. Bare Si wafers were seeded with colloidal silica slurry particles used in Chemical Mechanical Planarization (CMP) to planarize films after deposition in IC manufacturing. The wafers were prepared by dipping them in a dilute slurry mixture, then rinsing with deionized water. They were subsequently dried and the number of slurry particles on the wafers at 0.12μm and above were measured with SP1, a laser light scattering instrument from KLA Tencor. The particle seeded wafers were then exposed to the CO<sub>2</sub> cryogenic cleaning process from Eco-Snow Systems.

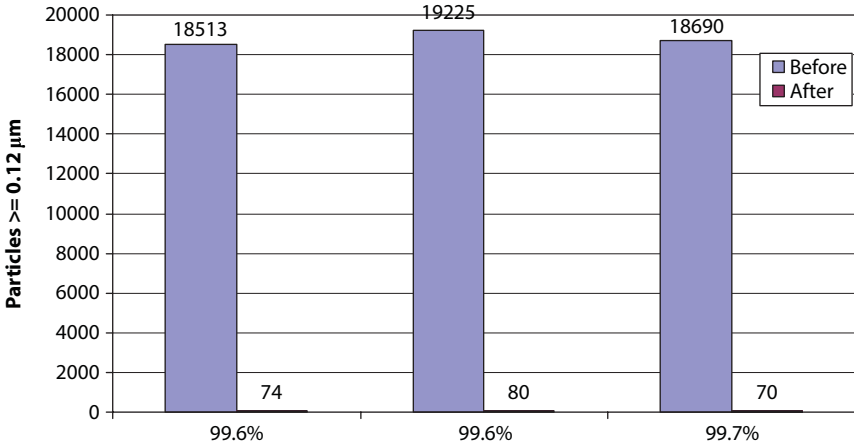


**Figure 12.12** Removal efficiency (%) of silica slurry particles using CO<sub>2</sub> cryogenic cleaning. The before and after bars denote the number of particles at 0.12 μm and greater left on the wafers prior to cryogenic cleaning and after, respectively.

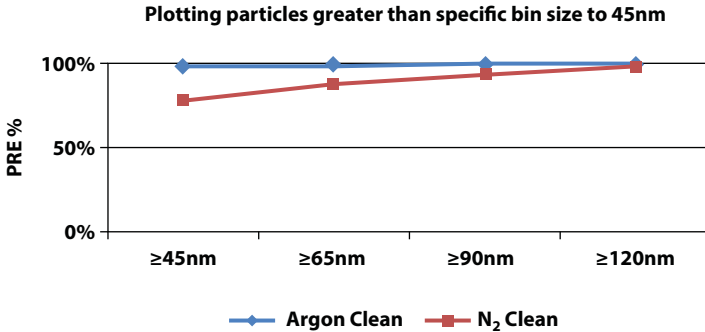


**Figure 12.13** Comparison of particle removal efficiency (PRE) using pure argon and nitrogen gases in the aerosol cleaning system shown in Figure 12.6.

The number of particles left on the wafer after the cleaning was again determined using SP1.

The Figure shows the 120 nm particles and larger before and after CO<sub>2</sub> cryogenic cleaning [2] achieving greater than 99% removal efficiency in this example. Kim *et al.* [27] describe the removal of even smaller size particles of 10 nm diameter using this cleaning method.

Figure 12.13 shows particle removal results with Argon and Nitrogen aerosol cleaning for particles 45 nm and above. This cleaning method can use the gases Ar and N<sub>2</sub> separately or in some combination of each other to

give good cleaning performance. The figure compares the results of cleaning obtained with Ar and N<sub>2</sub> separately. The Ar aerosol has higher cleaning efficiency compared to N<sub>2</sub> aerosol for particles smaller than 100 nm size but both show greater than 99% removal efficiency for larger particles.

Thus the two cryoaerosol cleaning systems described in this chapter, where one system uses CO<sub>2</sub> and the other uses pure Ar or N<sub>2</sub> or a combination of Ar and N<sub>2</sub>, demonstrate excellent particle removal performance. These experiments were performed in the commercially available systems with proper system control and gas purification methods described in section 12.5.

In section 12.5.4 the importance of cleaning without damaging sensitive features on substrates was discussed. It is especially important in integrated device manufacturing process where nanometer scale features are fabricated. To ensure non-damaging cleaning, the need for measuring and controlling the aerosol particle size was considered to be important. Figures 12.14 and 12.15 demonstrate the effectiveness of cryoaerosol cleaning without damage.

Figure 12.14 shows the results of cleaning high aspect ratio structures used in BEOL processes with CO<sub>2</sub> cryogenic aerosol. The trenches formed in an MSQ (methyl-silsesquioxane) low- $\kappa$  film after etch was subjected to a CO<sub>2</sub> cryogenic cleaning procedure. The post-cleaning SEM micrograph

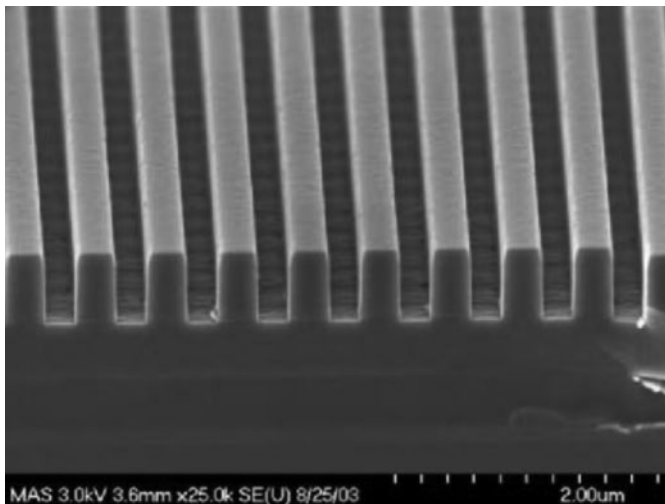


**Figure 12.14** SEM micrograph of trench structures in low- $\kappa$  dielectric carbon doped oxide film after CO<sub>2</sub> cryogenic cleaning, showing particle removal without damage to the trenches.

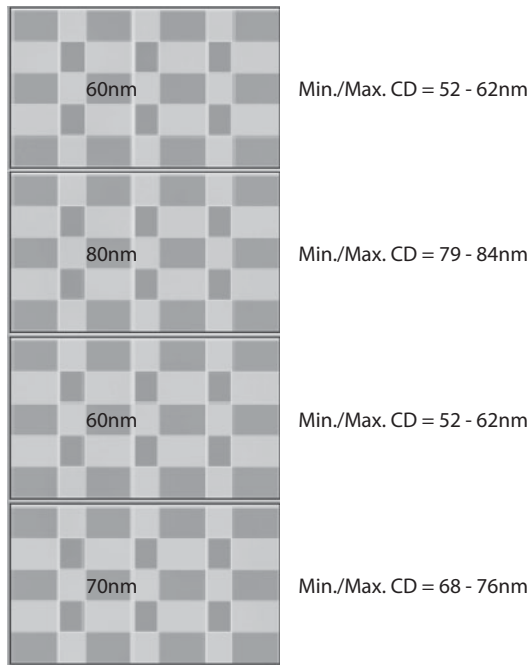


**Figure 12.15** Non-damaging CO<sub>2</sub> cryoaerosol cleaning of four SRAFs with minimum critical dimensions (CD) varying from 52nm to 79 nm and maximum CD from 62 nm to 84 nm on photomasks.

shows effective particle removal from the surface without damage to the trenches discussed by Banerjee *et al.* [2].

Cryoaerosol cleaning can also be non-damaging to less than 100 nm Sub Resolution Assist Feature (SRAF) in photomasks [24,25]. Pattern transfer in lithography works best for moderate to dense patterns on masks but suffers for isolated features. The SRAFs are fabricated on the masks around isolated patterns to diffract light like dense patterns would, but are small enough themselves to not be printed on the wafer. Figure 12.15 shows successful CO<sub>2</sub> cryoaerosol cleaning of nearly 3:1 aspect ratio SRAFs without damaging them.

It has been reported by Van der Donck and colleagues [28] that masks for extreme UV lithography (EUV) do not have pellicle protection. Such masks are highly susceptible to particulate contamination which in turn would print defects on the wafer during exposure. Their work demonstrated that EUV masks challenged with 50 nm polystyrene latex (PSL) particles and 30–100 nm SiO<sub>2</sub> particles can be successfully cleaned by CO<sub>2</sub> cryoaerosol cleaning. Particle removal efficiency of 60–70% was obtained

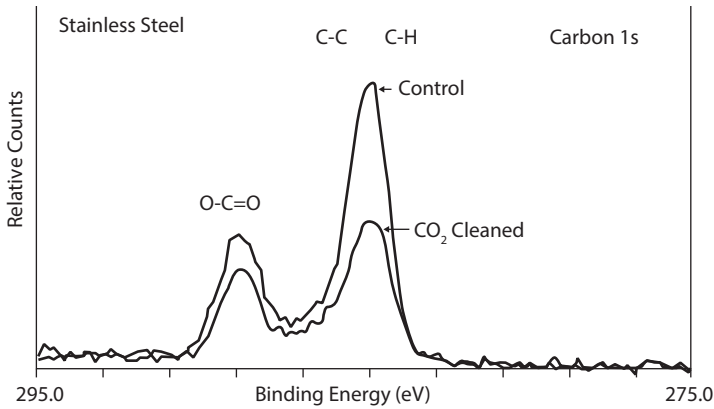


**Figure 12.16** XPS spectra showing the carbon 1s peaks before and after CO<sub>2</sub> aerosol cleaning [6].

for the PSL particles while nearly complete removal was seen for the SiO<sub>2</sub> particles from both the flat areas as well as the trench structures on the EUV masks.

Figures 12.12–12.15 show the effectiveness of particulate or inhomogeneous contaminant removal without damaging nanometer size features on the substrates. It has also been shown in literature that cryoaerosol cleaning is effective in removing homogeneous contaminants of organic residues from substrates. Sherman and Adams [6] have shown that CO<sub>2</sub> cryoaerosol cleaning can remove organic residues from a wide variety of substrates such as metals, ceramics, glass for optics, and silicon wafers. Figure 12.16 shows that the carbon 1s peaks of C-C, C-H, and O-C=O moieties decrease after cleaning. The amount of organic reduction was found to be 27% on 316L stainless steel substrates as shown in the overlaid spectrum of the control substrate which did not undergo cleaning and the CO<sub>2</sub> cleaned substrates. The authors conclude that besides the hydrocarbon residue removal, the decrease in the O-C=O peak indicates possible removal of microscopic corrosion and electropolishing residues from substrates as well.

## 12.7 Summary and Prospects

Cryogenic aerosol cleaning is a dry method which has been in existence for more than three decades as a form of precision cleaning. There are two types of cryogenic aerosol cleaning commercially available, a CO<sub>2</sub> based

and Ar/N<sub>2</sub> based. Both have certain advantages over aqueous cleaning as they do not require drying after the cleaning process. This is especially desirable for substrates which are negatively impacted by the presence of liquid in contact with them. The contaminant removal is primarily by physical method of momentum transfer and hence does not etch or oxidize surfaces as seen in conventional wet cleaning. It has been shown to effectively remove particulate as well as organic films without damage to small features as seen in microelectronics manufacturing. This cleaning method addresses a number of challenges with conventional wet and plasma cleaning in integrated device manufacturing and is an integral part of the ITRS roadmap for advanced cleaning.

However, this cleaning method has not been adopted as widely as aqueous cleaning in spite of its effectiveness and demonstrated advantages. It is still used in niche applications. The primary reason being its reliance on physical contaminant removal mechanism and does not have chemical means such as with dissolved chemistries and surfactants as in wet cleaning methods. The sole reliance on physical forces of particle removal from surfaces severely restricts its efficiency to remove wide variety of contaminants adhered to the underlying surface not only by physical bonds but also by chemical bonds of adhesion. Hence, in order to make this cleaning method widely applicable, it should be combined with other approaches as described in US patents by Banerjee and Chung [21,22]. By combining the cryogenic aerosol dry cleaning with other forms of cleaning, a very powerful surface cleaning approach can be developed which will be effective in removing homogeneous and inhomogeneous contaminants without causing damage in a wide variety of manufacturing processes.

## References

1. Semiconductor Industry Association, *International Technology Roadmap for Semiconductors* (ITRS), San Jose, CA (2013).
2. S. Banerjee, R. F. Reidy and L. B. R. Mauer, Cryogenic aerosols and supercritical fluid cleaning, in: *Handbook of Silicon Wafer Cleaning Technology*, K. Reinhardt and W. Kern (Eds.), pp429–478, William Andrew, Norwich, NY (2008).
3. S. A. Hoenig. Cleaning surfaces with dry ice. *Compressed Air Magazine*. 22–25, (August 1986).
4. L. Layden and D. Wadlow. High velocity carbon dioxide snow for cleaning vacuum system surface. *J. Vac. Sci. Technol.* **A8**, 3881–3883 (1990).
5. R. Sherman, J. Grob and W. Whitlock. Dry surface cleaning using CO<sub>2</sub> snow. *J. Vac. Sci. Technol.* **B9**, 1970- 1977 (1991).

6. R. Sherman and P. Adams. Carbon dioxide snow cleaning – The next generation of cleaning. *Proceedings of Precision Cleaning Conference*, 271–300 (1995).
7. R. Sherman. Carbon dioxide snow cleaning. *Particulate Sci. Technol.* **25**, 37–57 (2007)
8. R. Sherman. Carbon dioxide snow cleaning, in: *Developments in Surface Contamination and Cleaning: Fundamentals and Applied Aspects*, R. Kohli and K. L. Mittal (Eds.), pp. 987–1012, William Andrew, Norwich, NY (2008)
9. W. T. McDermott and J. W. Butterbaugh. Cleaning using argon/nitrogen cryogenic aerosols, in: *Developments in Surface Contamination and Cleaning: Fundamentals and Applied Aspects*, R. Kohli and K. L. Mittal (Eds.), pp. 951–986, William Andrew, Norwich, NY (2008)
10. W. T. McDermott, R.C. Ockovic, J.J. Wu and R.J. Miller. Removing sub-micron surface particles using a cryogenic Argon aerosol technique. *Microcontamination*, 33–36 (Sept. 1991).
11. L. N. Cajar and F. S. Manning, *Thermodynamic Properties and Reduced Correlations for Gases, Section 15, Carbon Dioxide*, Gulf Publishing Company, Houston (1967)
12. Discussions with Dr. Shuen-Cheng Huang of BOC Group, Murray Hill, New Jersey
13. J. W. Butterbaugh, S. Loper, and G. P. Thomes, Enhancing yield through argon/nitrogen cryokinetic aerosol cleaning after via processing. *MICRO*, 33 (June 1999)
14. W. Hinds, *Aerosol Technology*, John Wiley & Sons, New York (1982)
15. R. A. Bowling, A theoretical review of particle adhesion, in: *Particles on Surfaces I: Detection Adhesion and Removal*. K. L. Mittal (Ed.), pp. 129–142, Plenum Press, New York (1988).
16. C. W. Bowers, Electrostatic discharge properties of static sensitive devices cleaned with carbon dioxide spray, US Patent 5,837,064, assigned to Eco-Snow Systems Inc. (1998).
17. S. Matsusaka, Control of particle tribocharging. *KONA Powder and Particle Journal* **29**, 27–38 (2011)
18. W. V. Brandt and C. W. Bowers, Apparatus for cleaning and testing precision components of hard drives and the like, US Patent 5,989,355, assigned to Eco-Snow Systems Inc. (1997)
19. W. K-Schmidt and J. R. Markle, Environment control apparatus, US Patent 5,316,560, assigned to Hughes Aircraft Co. (1993)
20. J. M. Lauerhaas, J. F. Weygand, and G. P. Thomes, in: Proc. IEEE/SEMI Advanced Semiconductor Manufacturing Conference, Munich, Germany, 11–16 (2005).
21. S. Banerjee and H. F. Chung, Liquid-assisted cryogenic cleaning, US Patent 7,056,391, assigned to BOC Inc. (2006).
22. S. Banerjee and H. F. Chung, Vapor-assisted cryogenic cleaning, US Patent, 6,949,145 assigned to BOC Inc. (2005).

23. S. Banerjee, Parametric study of CO<sub>2</sub> cryoaerosol particles for effective non-damaging clean, in: Proc. Sematech Surface Cleaning Conference, Austin, TX, (2008).
24. I. Varghese, C. Bowers, Rodriguez and M. Balooch, Advances in CO<sub>2</sub> cryogenic technology for photomask post AFM repair, in: Proc. Sematech 6<sup>th</sup> Annual Mask Cleaning Workshop, Monterey, CA, (2009).
25. I. Varghese, M. Balooch and C. Bowers, CO<sub>2</sub> cryogenic aerosol technology application for photomask cleaning, in: Proc. Sematech 7<sup>th</sup> Annual Mask Cleaning Workshop, Monterey, CA, (2010).
26. M. C. Johnson, C. J. Heim and J. F. Billingham, Method for moving contaminants from gases, US Patent 6,962,629, assigned to Praxair Inc. (2005).
27. I. Kim, K. Hwang and J. W. Lee, Removal of 10-nm contaminant particles from Si wafers using CO<sub>2</sub> bullet particles, in: *Nanoscale Res. Letters* 7, 211 (2012)
28. J. C. J. Van der Donck, R. Schmits, R. E. V. Vilet, and T. G. T. M. Bastien, Removal of sub-100-nm particles from structured substrates with CO<sub>2</sub> snow, in: *Particles on Surfaces 9: Detection Adhesion and removal*. K. L. Mittal (Ed), pp. 291–302, CRC Press, Boca Raton, FL. (2006).



# Supercritical Carbon Dioxide Cleaning: Relevance to Particle Removal

Rajiv Kohli

*The Aerospace Corporation, NASA Johnson Space Center, Houston, TX*

---

## Abstract

Supercritical carbon dioxide (SCCO<sub>2</sub>) is an established precision cleaning technique with application in many different industries. The gas-like viscosity and the liquid-like density of CO<sub>2</sub> are the key characteristics that allow the process to be tuned to the application. In addition, the very low surface tension of SCCO<sub>2</sub> ensures high wettability and makes it very attractive for precision cleaning applications, particularly for intricate parts with complex geometries. The cleaning process is operated at near-ambient temperatures. Although the operating pressures for SCCO<sub>2</sub> cleaning are high, this can be compensated for by operating for longer cleaning cycles. SCCO<sub>2</sub> cleaning is a batch process. Applications range from cleaning and drying of micro and nanostructures such as carbon nanotubes; terminal sterilization of microbial organisms and food pasteurization; cleaning of metal surfaces, glass, optical elements, silicon wafers, and polymers; precision cleaning and drying of parts with complex geometries and tight spaces; sterilization of medical equipment; garment cleaning; pesticide mitigation in museum collections; and decontamination.

**Keywords:** Supercritical CO<sub>2</sub> (SCCO<sub>2</sub>); Hansen solubility parameters; carbon nanotubes; precision cleaning techniques; solvent; tunable density; gas-like viscosity; liquid-like density; surface tension; particles

## 13.1 Introduction

For many well-known reasons, conventional precision cleaning techniques for removal of particle contaminants are largely centered on aqueous and solvent cleaning. These cleaning techniques have several serious

---

*E-mail:* rajiv.kohli@aero.org

---

K.L. Mittal and Ravi Jaiswal (eds.) Particle Adhesion and Removal, (477–518)  
2015 © Scrivener Publishing LLC

limitations, including non-removal of sub- $\mu\text{m}$  particles, involved processing, and expensive disposal of toxic solvent-waste matrices. In the search for alternate cleaning techniques, carbon dioxide ( $\text{CO}_2$ ) in its different states has been found to be an effective medium for cleaning in a wide variety of industries for many years. It is inexpensive, naturally abundant, relatively inert towards reactive compounds, non-toxic, non-flammable, and it can be easily recycled, making  $\text{CO}_2$  highly desirable as an alternate substance to chlorinated solvents, hydrochlorofluorocarbons (HCFCs), trichloroethane and other ozone-depleting solvents for precision cleaning [1–22].

$\text{CO}_2$  gas can be used for cleaning by blowing it at high velocity over the contaminated substrate, but this method is only effective for particles larger than about  $50\ \mu\text{m}$  [7]. Solid  $\text{CO}_2$ , in the form of dry ice pellets, is well established for gross cleaning applications such as paint removal on aircraft, nuclear and asbestos decontamination, and cleaning and restoration of historical monuments [21,22].  $\text{CO}_2$  snow cleaning, which employs a less-dense form of dry ice, is a gentle precision cleaning technique that can remove particles in the 30 to 40 nanometer range, as well as thin films of organic contaminants ( $< 10\ \text{nm}$  thick) [18,19,23]. The liquid state of  $\text{CO}_2$  exhibits attractive physical properties that are increasingly being exploited for surface contaminant removal. Liquid  $\text{CO}_2$  cleaning involves immersion in a cleaning vessel with agitation to increase the effectiveness of the removal process [24]. Supercritical  $\text{CO}_2$  ( $\text{SCCO}_2$ ) has both gas-like transport properties and liquid-like solvent properties which makes it more flexible than the other states for contaminant removal, although the process must be operated at very high pressures. This chapter is focused on the application of  $\text{SCCO}_2$  for removal of surface contaminants.

## 13.2 Surface Cleanliness Levels

Surface contamination can be in many forms and may be present in a variety of states on the surface. The most common categories of contaminants are given below.

- Particles such as dust, metals, ceramics, glass, and plastics in the sub- $\mu\text{m}$  to macro size range
- Thin film or molecular contamination that can be organic (hydrocarbons) or inorganic (acids gases, bases)
- Cationic (such as  $\text{Na}^+$  and  $\text{K}^+$ ) and anionic (such as  $\text{Cl}^-$ ,  $\text{F}^-$ ,  $\text{SO}_3^-$ ,  $\text{BO}_3^{3-}$  and  $\text{PO}_4^{3-}$ ) contamination
- Microbial contamination (bacteria, fungi, algae).

Other contaminant categories include metals, toxic and hazardous chemicals, radioactive materials, and biological substances, that are identified for surfaces employed in specific industries, such as semiconductor, metals processing, chemical production, nuclear industry, pharmaceutical manufacture, and food processing, handling, and delivery. Common contamination sources can include machining oils and greases, hydraulic and cleaning fluids, adhesives, waxes, human contamination, and particulates. In addition, a whole host of other chemical contaminants from a variety of sources may also soil a surface. Typical cleaning specifications are based on the amount of specific or characteristic contaminant remaining on the surface after it has been cleaned.

Space agencies worldwide specify surface precision cleanliness levels for space hardware by particle size (in the  $\mu\text{m}$  size range) and number of particles, as well by film contamination represented by nonvolatile residue (NVR) [25,26]. The cleanliness levels are based on contamination levels established in industry standard IEST-STD-CC1246D for particles from Level 1 to Level 1000 and for NVR from Level AA5 ( $10\text{ ng}/0.1\text{m}^2$ ) to Level J ( $25\text{ mg}/0.1\text{m}^2$ ) [27]. Table 13.1 lists the allowable cleanliness levels<sup>1</sup>.

In many other commercial applications, the precision cleanliness level is defined as an organic contaminant level less than  $10\ \mu\text{g}$  of contaminant per  $\text{cm}^2$ , although many applications are setting the requirement at less than  $1\ \mu\text{g}/\text{cm}^2$  [27]. These cleanliness levels are either very desirable or are required by the function of parts such as machined parts, electronic assemblies, optical and laser components, precision mechanical parts, and computer parts.

### 13.3 Dense Phase Fluids<sup>2</sup>

Critical phenomena and the supercritical phase were first discovered in 1822 [29,30]. Above a critical temperature, the distinction between the liquid phase and the gas phase disappears, resulting in a single supercritical fluid phase. The term critical point was coined in 1869 from experiments

---

<sup>1</sup> The cleanliness levels have been revised or redesignated in revision E of this standard [28]. The maximum allowable number of particles for each particle size range has been rounded in revision E, while the NVR designation levels have been replaced with a single letter R followed by the maximum allowable mass of NVR. For example, former NVR level J has the new designation R25; level A/2 is now R5E-1; and level AA5 is now R1E-5. However, this revision has not yet been officially adopted by the space agencies.

<sup>2</sup> Throughout this chapter fluid refers to the liquid phase.

**Table 13.1** Product surface cleanliness levels for commercial and non-commercial applications [27]

Cleanliness Level	Particulate Level		NVR level	
	Particle size $\mu\text{m}$	Maximum allowable count per 0.1 m <sup>2</sup> /or 0.1 L of gas or liquid	Level	Quantity mass/0.1 m <sup>2</sup> or mass/ 0.1 L
1	1	1	AA5	10 ng
5	1	2.8	AA4.7	20 ng
	2	2.3	AA4.3	50 ng
	5	1	AA4	100 ng
10	1	8.4	AA3.7	200 ng
	2	6.9	AA3.3	500 ng
	5	2.9	AA3	1 $\mu\text{g}$
	10	1	AA2.7	2 $\mu\text{g}$
25	2	53.1	AA2.3	5 $\mu\text{g}$
	5	22.7	A/100	10 $\mu\text{g}$
	15	13.3	A/50	20 $\mu\text{g}$
	25	1	A/20	50 $\mu\text{g}$
50	5	166	A/10	100 $\mu\text{g}$
	15	24.6	A/5	200 $\mu\text{g}$
	25	7.2	A/2	500 $\mu\text{g}$
	50	1	A	1 mg
100	5	1780	B	2 mg
	15	264	C	3 mg
	25	78.4	D	4 mg
	50	10.7	E	5 mg
	100	1	F	7 mg

Cleanliness Level	Particulate Level		NVR level	
	Particle size $\mu\text{m}$	Maximum allowable count per 0.1 m <sup>2</sup> /or 0.1 L of gas or liquid	Level	Quantity mass/0.1 m <sup>2</sup> or mass/ 0.1 L
200	15	4180	G	10 mg
	25	1230	H	15 mg
	50	169	J	25 mg
	100	15.8		
	200	1		
300	25	7450		
	50	1020		
	100	95		
	250	2.2		
	300	1		
500	50	11800		
	100	1090		
	250	26.3		
	500	1		
750	50	95800		
	100	8910		
	250	213		
	500	8.1		
	750	1		
1000	100	42600		
	250	1020		
	500	38.7		
	750	4.7		
	1000	1		

**Table 13.2** Comparison of physicochemical properties of a typical organic fluid in the liquid, gas, and supercritical fluid states

State	Diffusivity (cm <sup>2</sup> /s)	Viscosity (mPa·s)	Density (kg/m <sup>3</sup> )
Liquid	<10 <sup>-5</sup>	1	1000
Supercritical fluid	10 <sup>-2</sup> – 10 <sup>-3</sup>	10 <sup>-2</sup>	300
Gas	0.1	10 <sup>-2</sup>	1

performed on CO<sub>2</sub> [31]. The measured values of 304.05 K for the critical temperature and 7.40 MPa for the critical pressure in those experiments are in remarkable agreement with the presently accepted values of 304.2 K and 7.38 MPa [32,33]. The strong solvating power of supercritical fluids for solids was first demonstrated in 1880 [34,35]. The attractiveness of supercritical fluids as solvents stems from their unique combination of liquid-like and gas-like properties. Table 13.2 compares the diffusivity, viscosity and density of a typical organic fluid in the liquid, gas, and supercritical fluid state. The properties of the supercritical phase are intermediate between the gas phase and the liquid phase, with the diffusivity and viscosity similar to the transport properties of gases, but the density is similar to that of a liquid.

### 13.3.1 Supercritical Carbon Dioxide

Of the many different supercritical fluids available for precision cleaning (Table 13.3), SCCO<sub>2</sub> is the most widely preferred solvent [1,4]. When CO<sub>2</sub> is compressed, it acquires increasingly liquid-like densities. Depending on the pressure and temperature, CO<sub>2</sub> is obtained as the liquid or as a supercritical fluid. On the pressure-temperature phase diagram for CO<sub>2</sub> (Figure 13.1), the liquid phase exists above the triple point (0.52 MPa, 216.75 K) and the supercritical phase exists above the critical point (7.38 MPa, 304.2 K). CO<sub>2</sub> has no permanent dipole moment, but it has a strong quadrupole moment which affects its physical properties, including the high critical pressure of CO<sub>2</sub> [40–44].

#### 13.3.1.1 Physical and Transport Properties

Small changes in the temperature or pressure near the critical point result in large changes in density, as seen in Figure 13.2 for CO<sub>2</sub> [45–48]. Since the solvating power of a fluid is generally related to its density, this gives SCCO<sub>2</sub> its strong solvating powers.

Table 13.3 Critical properties of various solvents\*

Solvent	Mol Wt g/ mol	T <sub>c</sub> K	P <sub>c</sub> MPa	V <sub>c</sub> cm <sup>3</sup> /mole	ρ <sub>c</sub> kg/m <sup>3</sup>	Z <sub>c</sub>	η mPa.s	σ mN/m
Acetone (C <sub>3</sub> H <sub>6</sub> O)	58.08	508.1	4.70	209	0.278	0.232	0.3311	23.70
Ammonia (NH <sub>3</sub> )	17.031	405.65	11.28	72.5	235	0.241	0.0098	0.234
Argon (Ar)	39.948	150.86	4.898	74.9	537.7	0.292	0.0211	0.0122
Carbon Dioxide (CO <sub>2</sub> )	44.01	304.2	7.38	93.9	0.469	0.274	0.0137	0.05
Ethane (C <sub>2</sub> H <sub>6</sub> )	30.07	305.3	4.889	148.3	0.203	0.285	0.00855	21.16
Ethanol (C <sub>2</sub> H <sub>5</sub> OH)	46.069	513.9	6.14	167.1	0.276	0.240	1.095	22.39
Ethylene (C <sub>2</sub> H <sub>4</sub> )	28.054	282.6	5.076	130.4	0.215	0.280	0.00951	18.1
Methane (CH <sub>4</sub> )	16.043	190.5	4.596	99.2	0.162	0.288	0.01028	17.78
Methanol (CH <sub>3</sub> OH)	32.04	512.6	8.09	118.0	0.272	0.224	0.59	22.50
Propane (C <sub>3</sub> H <sub>8</sub> )	44.096	369.8	4.25	203.0	0.217	0.281	0.11	0.26
Propylene (C <sub>3</sub> H <sub>6</sub> )	42.081	365.57	4.63	0.188	0.232	0.286	0.09	0.000189
Sulfur Hexafluoride (SF <sub>6</sub> )	146.054	318.6	3.759	198.8	6.27	0.282	0.0141	0.29
Water (H <sub>2</sub> O)	18.015	647.13	21.94	57.1	0.322	0.235	18.0	0.72
Xenon (Xe)	131.293(6)	289.77	5.841	0.1194	1.11	0.291	0.0211	28.27
Trichlorofluoromethane (R11)**	137.7	471.1	4.38	247.8	554.24	0.279	0.42	0.22

V<sub>c</sub> = critical volume; ρ<sub>c</sub> = critical density; Z<sub>c</sub> = critical compressibility ratio; η = viscosity; σ = surface tension

\*The data in this table have been compiled from references 36–39, manufacturer data sheets, and data available from various websites.

\*\*Due to concerns about its ozone-depleting potential, the consumption of trichlorofluoromethane (R11) is stopped. It is replaced by alternative chlorinated solvents such as dichlorotrifluoroethane (R123).

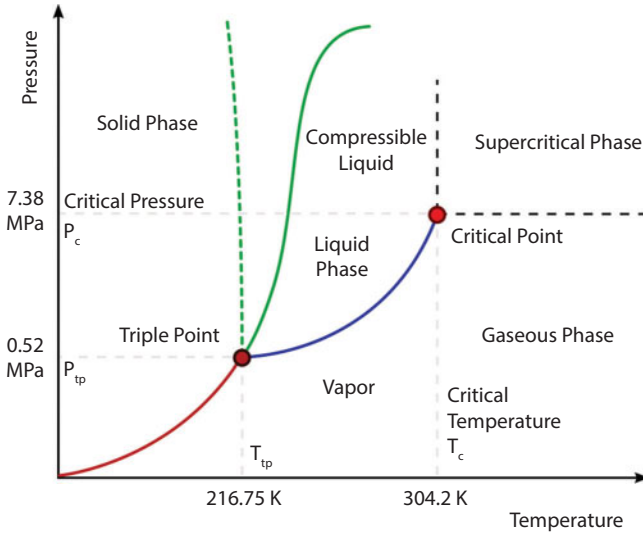


**Figure 13.1** Pressure-temperature phase diagram for  $\text{CO}_2$ .  $P_c$  is the critical pressure;  $P_{tp}$  is the pressure at the triple point;  $T_c$  is the critical temperature;  $T_{tp}$  is the temperature at the triple point [36–39].

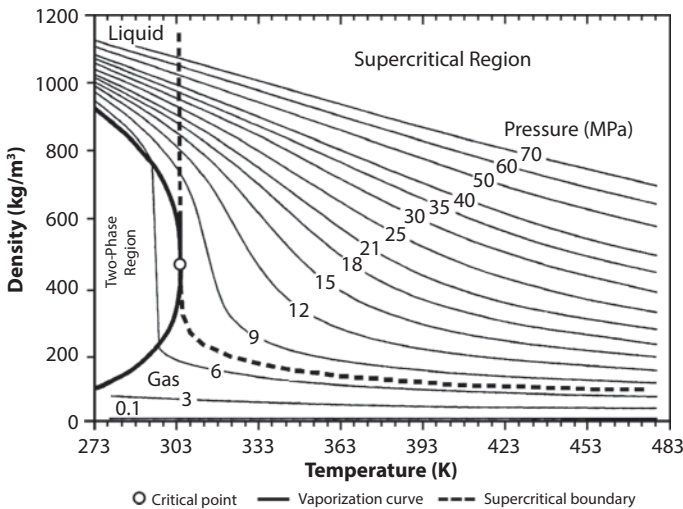


**Figure 13.2.** Variation of density of  $\text{CO}_2$  as a function of temperature at different pressures.



Thus, the tunable density, and therefore the tunability of solvent power, which can be varied from gas to liquid via a simple change of pressure at constant temperature, and the solvation effects at the densities in the vicinity of the critical point provide the most attractive attributes of supercritical fluids for surface contaminant removal. However, as the temperature is raised, the change becomes more pronounced only at higher pressures. This makes it difficult to control the density near the critical temperature, and, consequently, control of processes in the critical region is difficult.

The transport properties of  $\text{CO}_2$  are also important to its application as a dense phase fluid. The gas-like viscosity enables it to effectively penetrate fine scale structures such as high aspect ratio vias, through-holes, small pores and cervices, and clean components with complex geometries and tight spaces. The viscosity rises with pressure similarly to the density, however, the effect is less pronounced (Figure 13.3) [47,51–54]. In general, the viscosity is an order of magnitude lower than the viscosity of typical organic solvents [36]. The self-diffusivity of  $\text{CO}_2$  in the vicinity of the critical point is approximately  $5 \times 10^{-4} \text{ cm}^2/\text{s}$ , which is nearly 2 orders of magnitude larger than the diffusivity of solutes in normal liquids [1]. Many organic solutes too have significantly higher diffusion coefficients in  $\text{SCCO}_2$ , although the diffusion coefficients drop off in the critical region and are nearly zero at the critical point [55]. This has the advantage of faster transport and shorter process times during supercritical removal of contaminants. Finally, the very low surface tension of  $\text{SCCO}_2$  (Table 13.3)

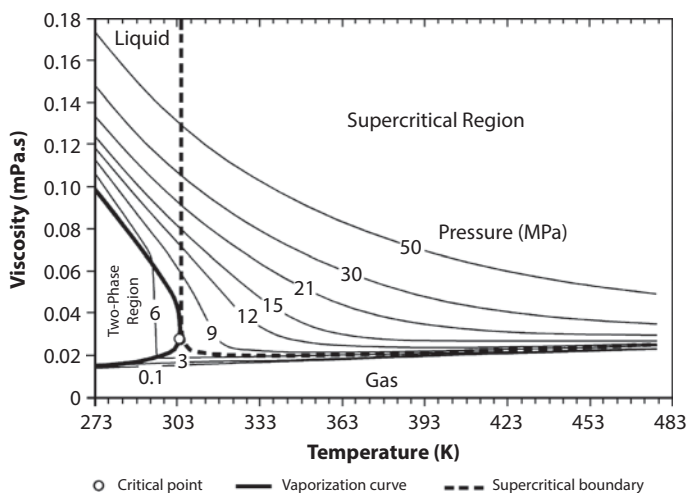


**Figure 13.3.** Variation of viscosity of  $\text{CO}_2$  as a function of temperature at different pressures.

provides for excellent wettability of components with complex geometries that make it very attractive in the dense phase for commercial precision cleaning applications.

### 13.3.1.2 Pressure-Enthalpy Diagram

The phase diagram does not aid in understanding the contaminant removal process; instead, the  $\text{CO}_2$  pressure - enthalpy diagram in Figure 13.4 provides insight into the phase changes that occur [18]. The features include the same three phases along with the regions of pressure and enthalpy where these phases co-exist. These regions are the phase boundaries in the phase diagram (Figure 13.1). In using this diagram, it is imperative to understand that the expansion of  $\text{CO}_2$  through an orifice is ideally a constant enthalpy process. Therefore, as the pressure drops in an orifice, the pressure decreases vertically along a constant enthalpy line.

A  $\text{CO}_2$  source such as a cylinder at room temperature filled with liquid  $\text{CO}_2$  has a gas pressure of about 5.5 MPa (55 bar) above the liquid. The enthalpies available to the cylinder contents are those values in the liquid-gas two-phase region at about 5.5 MPa (55 bar), at points labeled “A” for the gaseous  $\text{CO}_2$  and “B” for liquid  $\text{CO}_2$ . As the gas or liquid enters an orifice, the pressure drops from these two points with constant enthalpy values (under ideal conditions) into the two-phase liquid-gas region. With

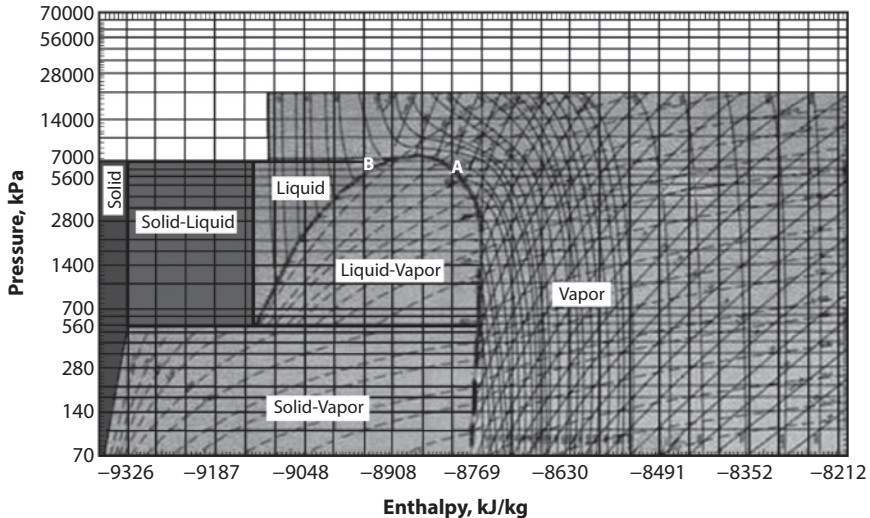


Figure 13.4. Pressure-enthalpy diagram for  $\text{CO}_2$  [18].

a gas fed source (starting from point A) as the pressure drops in the orifice, liquid droplets nucleate and the percentage of liquid increases. At the interface between the liquid–gas and gas–solid regions (about 0.53 MPa or 5.3 bar), all the liquid converts to solid yielding about 6% dry ice. With a liquid fed source (starting at point B), as the pressure drops in the orifice, gas bubbles form and the percentage of gas increases until the gas–solid boundary is reached. The remaining liquid is transformed into solid yielding about 45% dry ice. This diagram gives us information on the initial and final states and the phase changes that occur during cleaning.

### 13.3.1.3 Solubility Considerations

SCCO<sub>2</sub> is an excellent solvent for non-polar, low molecular weight organic compounds, such as greases, oils, lubricants and fingerprints [1,4]. It is this ability to dissolve organic compounds which underlies its commercial applications. On the other hand, hydrophilic compounds, such as inorganic salts and metal ions, do not dissolve. This has been attributed to the large quadrupole moment and the weak van der Waals forces in CO<sub>2</sub> [56,57]. Extensive compilations of the solubility of organic compounds in SCCO<sub>2</sub> can be found in [58–61].

The solubility behavior in binary mixtures of CO<sub>2</sub> and a co-solvent can be considered in terms of the contributions of the individual forces to the total energy of vaporization,  $E$ . Thus,

$$E = E_d + E_p + E_h \quad (13.1)$$

where  $E_d$ ,  $E_p$  and  $E_h$  are the energy contributions due to dispersion forces, polar interactions (dipole-dipole forces), and hydrogen bonding, respectively [62].

The Hildebrand solubility parameter,  $\delta$ , is  $(E/V)^{1/2}$  and Eq. 13.1 becomes

$$\delta^2 = \delta_d^2 + \delta_p^2 + \delta_h^2 \quad (13.2)$$

where  $\delta_d$ ,  $\delta_p$  and  $\delta_h$  are the Hansen solubility parameters for the dispersion, polar and hydrogen bonding interactions, respectively [62,63], and  $V$  is the molar volume. This approach considers the solubility in terms of the inter-molecular forces of the solvents which have unique molecular structures and exhibit unique solubility behavior. Thus, the Hansen solubility parameters are of significant value in predicting the solubility behavior of co-solvents.

For co-solvents such as methanol, ethanol, propanol, acetone, ethylene glycol and water, the values for  $\delta_d$  do not differ significantly from the values

for SCCO<sub>2</sub>. By contrast, the polar and hydrogen bonding Hansen parameters,  $\delta_p$  and  $\delta_h$ , are considerably higher than the values for SCCO<sub>2</sub> [62]. This would suggest that there is a lack of miscibility in these binary mixtures. In the liquid state, these co-solvents have high polarities and they form self-associates. Also, these compounds can hydrogen bond with their own molecules in CO<sub>2</sub>, leading to reduced dipole moment and polarity of the binary mixture. The reduced polarity of the co-solvent component due to self-association leads to better matching of the polarity with SCCO<sub>2</sub> and high miscibility, as has been observed in the CO<sub>2</sub>-alcohol binary and ternary systems [64–66]. In fact, it is possible to form and maintain a single phase at high pressures over the entire composition range [65].

The large quadrupole moment of CO<sub>2</sub> affects the value of  $\delta$ , which reduces the non-polar  $\delta_d$  for ionic compounds. For example, at pressures above 20 MPa, the value of  $\delta$  for CO<sub>2</sub> is higher than the value for ethane, yet CO<sub>2</sub> is incapable of dissolving an ionic surfactant with a hydrocarbon tail, such as AOT (sodium bis(2-ethylhexyl) sulfosuccinate) [66], which readily dissolves in ethane. Nearly 20% of the  $\delta$  value can be attributed to the quadrupole moment, which reduces  $\delta_d$  considerably below the value for ethane.

Several techniques have been proposed for correlations or predictions of the solubilities of solid solutes in SCCO<sub>2</sub> using density-based empirical equations, equations of state (EOS), or solution models [61,68–79]. These models require parameter optimization by fitting available experimental data for the systems under consideration, and also critical properties and sublimation pressures for solutes for the EOS models. Thus, these models are applicable only to systems for which sufficient solubility data are available. A newly developed activity coefficient model is a more general approach which does not require data fitting [80]. In general, the percentage of predicted values versus experimental data for solutes containing only C, H, and O atoms is higher as compared with solutes containing other atoms such as N, S, Cl and F.

Until recently, the lack of solubility of hydrophilic solutes in CO<sub>2</sub> has been a serious limitation to widespread use of SCCO<sub>2</sub> for removing polar inorganic contaminants and particles in precision cleaning applications. This limitation is increasingly being overcome by new developments to incorporate co-solvents, such as low molecular weight alcohols and acetone in SCCO<sub>2</sub> to increase the solvent strength. For example, the addition of only 2 mol percent of tri-*n*-butyl phosphate to CO<sub>2</sub> increases the solubility of hydroquinone by a factor of 250 [37]. Surfactants and water too have been added to SCCO<sub>2</sub> to form microemulsions and dendritic micelles, as well as chelating fluorinated ligands [39,81–91]. These molecules can dissolve inorganic solutes and ionic species.

A novel application is to incorporate fluoropolymers in  $\text{SCCO}_2$  for cleaning and protection of historical stone buildings and monuments [92].

### 13.4 Principles of Supercritical $\text{CO}_2$ Cleaning

$\text{SCCO}_2$  exhibits strong solvent power for dissolving nonpolar organic compounds. Organic contaminants most often encountered in industrial applications consist of non-polar compounds as films or as particles. Thin films are removed easily by dissolution either in pure  $\text{CO}_2$  or in a mixture with a co-solvent. Organic particles too can be removed because  $\text{CO}_2$  will help loosen the particles on the surface. For highly polar contaminants, the solubility can be enhanced by adding a suitable co-solvent in an amount sufficient to maintain the supercritical phase at the system operating conditions (temperature and pressure). The discussion and calculations presented in the previous section can help define the solubility and phase equilibria and the process operating conditions for removal of contaminants.

In many precision cleaning applications, the contaminants are present as non-organic particles. These particles adhere to the surface by strong van der Waals, electrostatic or capillary forces [10]. It is necessary to penetrate the boundary layer and also to overcome the adhesion force by an applied drag force to remove these particles. In an  $\text{SCCO}_2$  system for cleaning applications, the critical drag force is achieved by turbulent flow. Based on theoretical considerations, in order to remove  $0.1\text{-}\mu\text{m}$  size particles, a stream velocity of approximately  $200\text{ cm/s}$  at  $375\text{ K}$  is required with  $\text{SCCO}_2$ , as compared with air which requires a velocity greater than  $1000\text{ cm/s}$  (Figure 13.5) [93, 94]. Other considerations that are important to removal of contaminants are the chemistry of the system and the operating

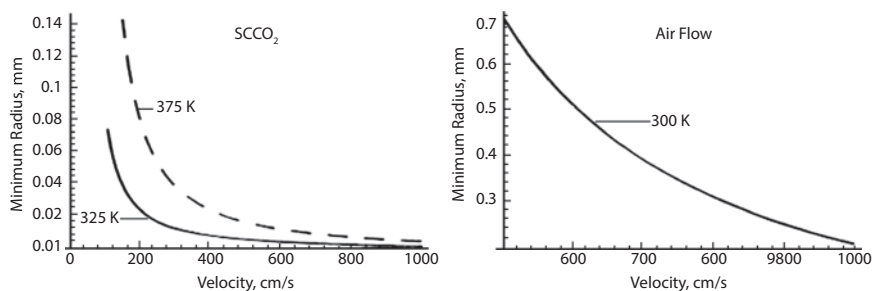


**Figure 13.5** Minimum particle size removed as a function of stream velocity by a)  $\text{SCCO}_2$  at  $30\text{ MPa}$ ; and b) air flow at  $0.1\text{ MPa}$  (1 atmosphere) [93, 94].

temperature and pressure. These parameters are optimized for the specific cleaning application being considered [6,95,96].

### 13.4.1 Cleaning Systems

The basic technology of the  $\text{SCCO}_2$  cleaning process is similar to liquid  $\text{CO}_2$  cleaning technology [97–124]. In fact, many of the cleaning systems can use either liquid  $\text{CO}_2$  or  $\text{SCCO}_2$ . Figure 13.6 shows a typical schematic of the process. The component to be cleaned is placed in the cleaning chamber, which is filled with  $\text{SCCO}_2$ . The  $\text{CO}_2$  dissolves the contaminants and it flows to the separation chamber where the fluid is subjected to a pressure and temperature change (pressure is reduced and the carbon dioxide vaporizes). As that occurs, the solubility of the contaminant in the carbon dioxide decreases, causing the contaminant to separate from the bulk fluid. Once all the  $\text{CO}_2$  is evacuated from the separator, the concentrated contaminant is usually in form of an oily or tar-like liquid residue that is simply drained from the separator. The residue can be recovered, recycled, or reused, if suitable; or the residue can be disposed as a sole component of the waste stream. No solvents, wastewater, or other contaminants are present to increase the volume of waste disposed. Co-solvents or other additives (surfactants, dispersants, and chelating agents) are added as needed. In order to get  $\text{SCCO}_2$  and co-solvent or additive to mix, it is

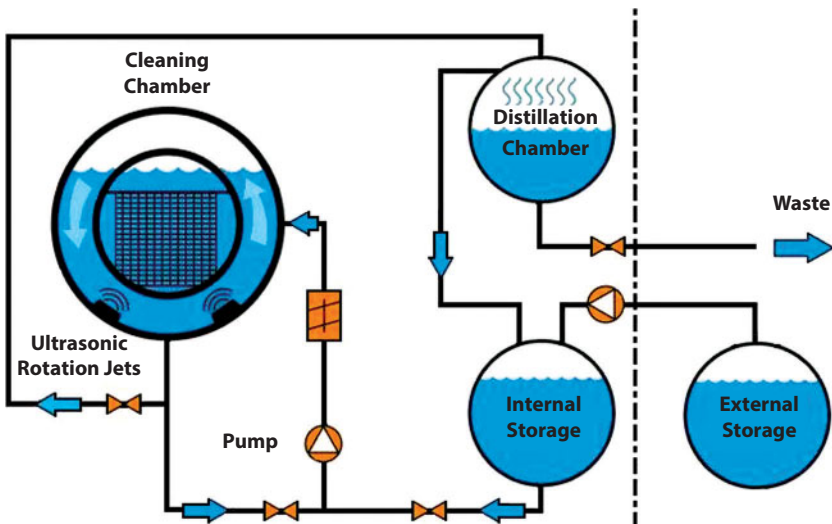


Figure 13.6 Typical  $\text{SCCO}_2$  cleaning process [120].



Figure 13.7 Modular commercial SCCO<sub>2</sub> cleaning system with 1 (left figure), 3 (middle figure), and 5 (right figure) cleaning modules [123]. Courtesy of eCO<sub>2</sub>, Switzerland.

often necessary to inject the co-solvent or additive into a flowing stream of SCCO<sub>2</sub> as it enters the chamber.

Process temperatures generally range from 308 K to 440 K. The operating pressures are in the range of 10 MPa to 17 MPa, although the cleaning chamber is often designed to operate at pressures as high as 30 MPa for SCCO<sub>2</sub> cleaning operations, resulting in significantly greater equipment weights and footprints. Agitation by mechanical or other means (ultrasonic transducers or magnetic stirring) enhances the effectiveness of the cleaning process [118,120]. The cleaning systems are designed as modular units in which additional modules can be added for increased capacity (Figure 13.7). Figure 13.8 shows examples of commercial SCCO<sub>2</sub> cleaning systems.

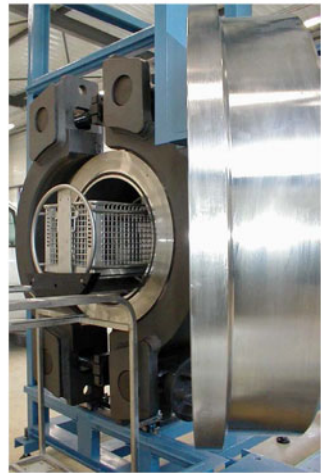
Many polymers absorb significant amounts of gases and vapors when exposed at high pressures [1,125]. In particular, CO<sub>2</sub> absorption can induce plasticization, swelling, and a decrease in the glass transition temperature significantly below that observed at atmospheric pressure [126–132]. This effect can be utilized to achieve effective polymer-based photoresist removal. Lowering the glass transition temperature of the polymer softens it, thereby enhancing penetration and diffusion of SCCO<sub>2</sub> to the polymer/substrate interface. By suddenly releasing the pressure, a rapid volume change occurs that ruptures the polymer from the substrate [133]. A small amount of co-solvent enhances the solubility of the polymer and the chemical interactions at the polymer/substrate interface, which promotes photoresist removal.

### 13.4.2 Costs

Commercial SCCO<sub>2</sub> cleaning systems are expensive, but operating and waste disposal costs are usually low [13,95,134–144]. The installed costs can range from less than \$100,000 for small-capacity (1 liter volume) equipment to



(a)



(b)

**Figure 13.8** Examples of commercial SCCO<sub>2</sub> cleaning systems. (a) Dürr-EcoCO<sub>2</sub> [124]; (b) Unitech-Annemasse [120]. *Courtesy of Dürr-EcoClean, Germany and Unitech-Annemasse, France.*

several hundred thousand dollars for large-capacity (30 liter volume) equipment. The cost of the equipment increases considerably with size, and also depends on the complexity of the controls and other components, and the degree of automation required. For large parts it may be more cost effective to install lower-pressure-rated equipment and operate the cleaning system in supercritical mode for longer times at lower pressure. The systems are operated in batch mode. Interlocks for continuous operation between high



and ambient pressure are too expensive to be justified. Recovery and recycling of the  $\text{CO}_2$  will add 15 to 25%. If the contaminant is readily soluble in liquid  $\text{CO}_2$ , the system can be rated for lower pressure  $\text{LCO}_2$  (at 5–6 MPa) operation as an alternative to  $\text{SCCO}_2$  which can reduce the equipment cost by 10 to 15%.

Operating costs are generally low. Power costs are minimal (~2.5 kWh for a 120-liter system) because cleaning cycles are short and there is no heat input into the process. The cost of supplying beverage-grade liquid  $\text{CO}_2$  to the system is quite small (~\$1.3 to \$1.5 per kg), although high purity supercritical grade  $\text{CO}_2$  is considerably more expensive [143,144]. Typically,  $\text{CO}_2$  consumption per cleaning cycle is approximately 0.8 kg for a 120-liter system. Maintenance costs for the equipment range between 5–7% per year.

Waste disposal costs for  $\text{SCCO}_2$  cleaning are lower than competing cleaning technologies since the waste residue is 100% contaminant. And if the contaminant can be recovered, recycled, or reclaimed, there is no cost associated with disposal of waste.

For contaminants that are readily soluble in  $\text{SCCO}_2$ , the costs for cleaning are competitive with aqueous or solvent cleaning technologies. In one example,  $\text{SCCO}_2$  processes developed for preparing polymeric materials have successfully replaced solvent and thermal vacuum extraction processes for military and commercial spacecraft applications.  $\text{SCCO}_2$  proved to be much faster, less costly, more effective and cleaner than solvent processes [145]. For sterilization of heat-sensitive materials and devices, dense-phase  $\text{CO}_2$  has been shown to have significantly lower cost per unit (cubic foot or load) than conventional sterilization with ethylene oxide, and comparable costs with hydrogen peroxide gas plasma sterilization [141].

## 13.5 Advantages and Disadvantages of Supercritical $\text{CO}_2$ Cleaning

$\text{SCCO}_2$  has become an established process for removal of surface contaminants. The advantages and disadvantages of the process are discussed in the following subsections.

### 13.5.1 Advantages

1.  $\text{SCCO}_2$  has very low surface tension with excellent wettability, which makes it very attractive for cleaning intricate parts, or parts with deep crevices, tiny holes, or very tight tolerances.

2. CO<sub>2</sub> has a supercritical temperature near ambient temperatures which is a significant advantage for cleaning temperature-sensitive parts.
3. The low viscosity of SCCO<sub>2</sub> results in very high Reynolds numbers for flowing CO<sub>2</sub>. Such turbulent flow is an advantage in particle removal applications.
4. The liquid-like high density of CO<sub>2</sub> in the dense phase gives it very high solvation power for many low molecular weight organic compounds and many common fluorinated solvents. High purity co-solvents, surfactants (anionic, cationic, and nonionic), dispersants, and chelating compounds are readily available to broaden the range of cleaning applications for dense phase CO<sub>2</sub>.
5. CO<sub>2</sub> is non-toxic with a high threshold limit value (TLV) of 5000 ppm as compared with common organic solvents such as acetone (750 ppm) and chloroform (10 ppm).
6. CO<sub>2</sub> is nonflammable, which is a significant safety advantage in cleaning.
7. SCCO<sub>2</sub> is compatible with virtually all metals. High-density cross-linked polymers are not affected by SCCO<sub>2</sub>, but low crystallinity amorphous polymers are susceptible to plasticization and resulting brittleness of the component.
8. For most cleaning applications, the degree of cleanliness is equal to or better than conventional aqueous or solvent cleaning processes.
9. A further advantage of SCCO<sub>2</sub> cleaning in the medical industry is the ability to remediate bacterial contamination by sterilization. Sterilization by SCCO<sub>2</sub> is a technologically and economically viable alternative to conventional processes.
10. SCCO<sub>2</sub> cleaning is typically performed in closed-loop systems, designed to maximize recycling of the carbon dioxide. For challenging applications such as particle removal, the addition of agitation can significantly enhance the cleaning effectiveness, as well as reduce the time required for cleaning.
11. The cleaning process times are relatively short, typically 15 to 30 minutes per batch, which leads to reduced process operating costs.
12. Completely dry and clean parts are obtained at room temperature. No supplemental drying is needed which

reduces the amount of energy, water, and time required for processing.

13. CO<sub>2</sub> is plentiful, inexpensive and recyclable, making the solvent consumption cost an insignificant contributor to the overall cleaning process costs.
14. The process operating costs are low.
15. Energy consumption is generally low since there is no heat input to the process. Energy is required to operate the pumps to perform cleaning.
16. Contaminants are the sole waste. Hence, the waste disposal costs are low. In fact, waste disposal costs may be eliminated if the contaminants can be recovered, reclaimed or recycled.
17. This is a non-corrosive, environmentally-friendly process. No hazardous wastes and emissions are generated.

### 13.5.2 Disadvantages

1. The low dielectric constant of CO<sub>2</sub> makes it difficult to dissolve polar compounds.
2. The process is ineffective in removing hydrophilic (polar molecules) contaminants, inorganic contaminants, and large bulk particles and other debris. Particle removal can be enhanced with mechanical or sonic (ultrasonic or megasonic) agitation, but that increases the capital costs. Co-solvents and other additives are available to remove these kinds of contaminants; however, the process costs are correspondingly high.
3. SCCO<sub>2</sub> cleaning is a batch process. The high costs of interlocks between high pressure and ambient pressure required for continuous operation are not justified.
4. The installed costs of SCCO<sub>2</sub> cleaning equipment are very high due to the need for expensive high pressure equipment. The equipment costs can be reduced by operating at lower pressures and longer cycle times.
5. The high operating pressures of SCCO<sub>2</sub> cleaning requires robust heavy cleaning chambers that scale with the capacity. In addition, peripheral equipment for storage, distillation, and recovery of the CO<sub>2</sub> necessitates equipment with a large footprint.

6. The extremely high pressures at which SCCO<sub>2</sub> cleaning takes place makes it unsuitable for cleaning components containing gas or evacuated spaces because they could implode or deform during the cleaning cycle. Delicate critical parts can also be damaged by the high operating pressures.
7. Process complexity is high especially if the chemistry has to be tailored for unknown contaminants. This also requires high level of technical skill.
8. A major concern with SCCO<sub>2</sub> cleaning processes is the safety risk of high operating pressures. Equipment must be properly maintained to prevent overpressure or failure of the high-pressure components in the cleaning system.
9. Although CO<sub>2</sub> is non-toxic and non-flammable, it can displace oxygen and cause asphyxiation if leakage occurs in closed, occupied spaces. CO<sub>2</sub> monitoring may be required.

## 13.6 Applications

SCCO<sub>2</sub> has been employed for a wide range of precision and commercial cleaning applications including metal surfaces, glass, optical elements, Si wafers, polymers, parts with complex geometries and tight spaces, terminal sterilization of medical equipment and microbially contaminated surfaces, garment cleaning, pesticide mitigation in museum collections, soil decontamination, and decontamination of radioactively contaminated surfaces. SCCO<sub>2</sub> has been successfully used with additives (co-solvents, surfactants, dispersants, and chelating agents) to remove a wide variety of contaminants [1,2,4,6–17,20,24,146–176]. The types of contaminants removed include greases, lubricants, silicone oils, machining oils, flux residue, trace metals, photoresist containing plasticizers, outgassing compounds, printing ink, adhesives, and small particles. Addition of a small amount of a polar co-solvent, such as ethanol or propanol, can significantly enhance the removal of small particles. As an example, the cleaning efficiency for fabrics contaminated with clay particles (<10 μm diameter) is two to three times greater with the addition of the co-solvent compared with cleaning without a co-solvent (20 to 30% vs. approximately 10%) [163,164]. The co-solvent tends to adsorb on the surface to increase the particle-surface distance and decrease the attractive adhesion force. Even nanoparticles may be dislodged from the surface by use of appropriate co-solvents and surfactants.

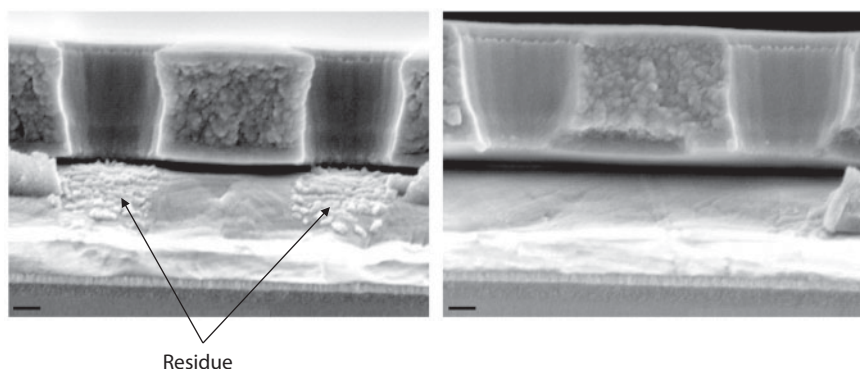


**Figure 13.9** Example of removal of post-etch residue from a silicon wafer with  $\text{SCCO}_2$ . The scale bars are 100 nm [160].

Photoresist stripping and cleaning was one of the first applications of  $\text{SCCO}_2$  in integrated circuit processing. Figure 13.9 shows a typical example of removal of post-etching contaminant residue removed with  $\text{SCCO}_2$  [160].

The results of  $\text{SCCO}_2$  cleaning generally show high degree of cleanliness with contaminant removal efficiencies better than 90%. One advantage of  $\text{SCCO}_2$  for precision cleaning is that the process leaves no residues, since it evaporates completely when depressurized. The cleaned surfaces will usually meet the commonly established precision cleanliness level of  $1 \mu\text{g}/\text{cm}^2$  of the contaminant on the surface.

Many of the applications mentioned above have been reviewed previously [1,2,4,6–17,20,24,146–175]. Some recent less common and innovative examples of  $\text{SCCO}_2$  cleaning applications are discussed below.

### 13.6.1 Cleaning Spacecraft Components and Planetary Protection

Traditional cleaning methods are not very effective in removing live and dead microorganisms and hydrophilic biomolecules from spacecraft piece parts of slightly complicated geometry, such as tubing and loosely fitted nuts and bolts. These microorganisms are relevant to life detection on outer planets, as well as to planetary protection. A  $\text{SCCO}_2$  precision cleaning system has been developed for removing organic and particulate contaminants from spacecraft components [176]. The parts to be cleaned are secured in an inner basket and can be rotated up to 1,400 rpm by a magnetic drive. The fluid flows within the vessel generate tangential forces on

the surfaces of the parts, enhancing the cleaning effectiveness and shortening the soaking time. During the flushing cycle, the pump subsystem delivers fresh  $\text{CO}_2$  into the cleaning vessel at a constant flow rate between 0.01 and 200 mL/min. Both temperature and pressure are strictly controlled during decompression to prevent bubbles from being generated in the cleaning vessel that could stir up the contaminants that sank to the bottom by gravity. The results using this new cleaning system demonstrated that both  $\text{SCCO}_2$  and  $\text{SCCO}_2$  with 5% water as a co-solvent can achieve cleanliness levels of 0.01 mg/cm<sup>2</sup> or less for contaminants of a wide range of hydrophobicities. The latter composition is representative of the Martian environment which consists of 95%  $\text{CO}_2$ .

### 13.6.2 Cleaning of Printing Rollers

A recent application of  $\text{SCCO}_2$  has been to clean rollers used in the printing and packaging industry [177]. These engraved rollers contain large numbers of microscopic cells (5 to 100  $\mu\text{m}$  diameter) that carry inks or adhesives to the film substrate and are very difficult to clean due to the size and the depth of the cells on the roller surface. Conventional cleaning methods include manual brush cleaning, ultrasonic chemical cleaning, high pressure washing, blasting with fluid or dry media, and vapor injection. These cleaning methods can be expensive and time consuming; require complex maintenance of the cleaning system; employ harsh caustic and toxic chemicals; and often do not provide adequate cleaning of the rollers. The proposed new cleaning technique is based on the use of N-methyl pyrrolidone (NMP), which has high solubility for polyurethane adhesives, and  $\text{CO}_2$ . The presence of  $\text{SCCO}_2$  lowers the critical point of the cleaning solution to 10 MPa at 313 K, thus providing processing conditions that are technologically favorable. Nearly complete removal of the dried red ink (polychlorovinyl resin) residue from the microscopic cells has been obtained after cleaning in 80% (NMP)- $\text{CO}_2$  mixture at 313K and 15 MPa (Figure 13.10). Cleaning is ineffective at low (10%) NMP concentrations, but increases with NMP concentration.

### 13.6.3 Carbon Nanotubes

Carbon nanotubes (CNTs) are increasingly being used as electron field emitters for field emission displays. For this application the CNTs must be free of contamination and adsorbed moisture that often result from the manufacturing process. This contamination degrades the field emission characteristics of the CNTs. A novel method has been developed to

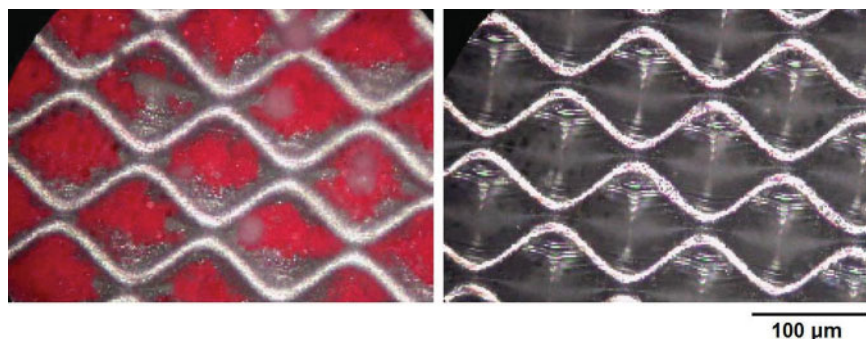


**Figure 13.10** Optical microscope images of the cells of an engraved roller after cleaning for 60 minutes with a supercritical solution of 10% NMP + CO<sub>2</sub> (left figure) and 80% NMP + CO<sub>2</sub> (right figure) at 15 MPa and 313 K. The dried red ink residue is nearly completely removed with mixture composition of 80% NMP [177].

enhance the emission characteristics of CNTs by treating them for 5 minutes at 327 K with SCCO<sub>2</sub> + 5 volume % isopropyl alcohol as co-solvent [178, 179]. This treatment was sufficient to remove the adsorbed moisture as was evident from the stability of the emission current of the SCCO<sub>2</sub> + co-solvent treated CNTs. By comparison, the emission performance of the CNTs treated with pure SCCO<sub>2</sub> was significantly degraded.

### 13.6.4 Soil Cleaning with Ionic Liquids and SCCO<sub>2</sub>

A novel application of dense phase CO<sub>2</sub> is to employ SCCO<sub>2</sub> with ionic liquids (ILs) serially to clean contaminated soils [180–182]. The IL is used to dissolve soil contaminants under ambient conditions and SCCO<sub>2</sub> is used to recover the contaminants from the IL extracts. The efficacy of the process has been demonstrated by extracting naphthalene from soil by 1-*n*-butyl-3-methylimidazolium hexafluorophosphate [bmim][PF<sub>6</sub>] ionic liquid. The amount of naphthalene remaining in the soil was below the allowable contamination limit. Subsequently, SCCO<sub>2</sub> was used to recover the naphthalene dissolved in the IL. At 313 K and 14 MPa, naphthalene recovery was nearly 84% for an extraction time of 4 hours. A process flowsheet has been developed for IL extraction of contaminated soils and continuous SCCO<sub>2</sub> extraction of the contaminants from IL extracts for recovery and reuse of the IL.

### 13.6.5 Conservation of Historical Art Objects and Structures

Several applications of dense phase CO<sub>2</sub> have been developed for cleaning of historical art objects and structures [183–188]. Museum collections

often use organic and inorganic pesticides containing toxic metals such as arsenic and mercury for conservation and protection of the art objects. Unfortunately, this often resulted in contamination of the indoor air from the dust settling on the treated surfaces of the objects. In other cases, fragile textiles of historic value that may have also been damaged must be cleaned to preserve their fiber structure and value. Other materials needing remediation include waterlogged paper and wood, fluoropolymer coated stone, and various fabrics such as silk, wool and leather. Surface cleaning will not remove the hazardous chemicals embedded in the matrix. The use of  $\text{SCCO}_2$  has been successfully demonstrated for cleaning various objects. Treatment times are generally just a few minutes to extract the contaminants from artifacts without damaging fragile materials and without leaving a residue. Not surprisingly, removal efficiencies of 80 to 95% have been achieved for organic pesticides, but inorganic or polar compounds are not removed to a sufficient extent. In the case of silk textiles, the fibers and the textile structure were not physically damaged and there was no loss of material by  $\text{SCCO}_2$  + isopropanol + water -assisted cleaning (Figure 13.11). Extraction effectiveness is improved with a co-solvent such as water, isopropanol or acetone. Detailed knowledge about the properties of the different materials (contaminants and objects) is necessary in order to prevent any possible damage to objects sensitive to  $\text{SCCO}_2$ .

### 13.6.6 Sterilization

In the health and food sectors, the risk of transmission of diseases due to contamination is a subject of growing concern. As an example, viral and bacterial contamination of implants and allograft tissue, widely used

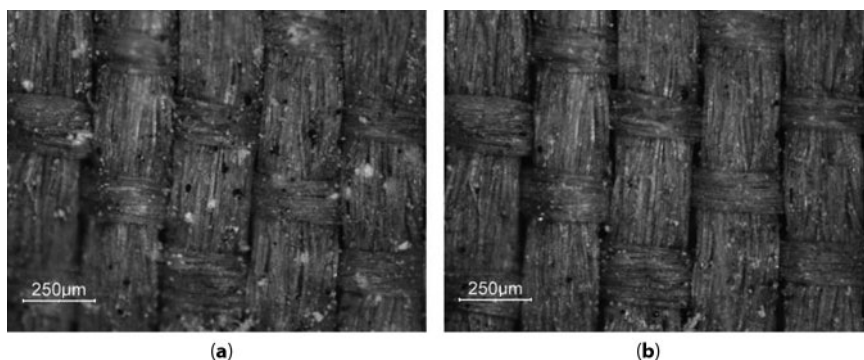


**Figure 13.11.** Removal of contaminant particles on an antique silk textile (a) before and (b) after cleaning with  $\text{SCCO}_2$  + isopropanol + water [185].



by transplant surgeons for orthopedic (joint replacement), trauma, and cancer (surgical reconstruction) procedures, can have disastrous consequences for the patient and are a major concern [189]. Similarly, safe contamination-free liquid foods and beverages are critical to human health [190]. Efforts to minimize disease transmission have generally included donor screening, bioburden assessment, and aseptic handling, as well as sterilization before, during and after processing [191–210]. Terminal sterilization refers to a sterility assurance level (SAL<sub>6</sub>) of  $10^{-6}$  (SAL<sub>6</sub> is considered the standard for medical devices [211]) and describes the process that ensures that the medical devices and implants are sterile at the point of use.

Common sterilization methods include: steam autoclaving; dry heat; sterilizing gaseous (for example, ethylene oxide, chlorine dioxide, hydrogen peroxide) or liquid (such as glutaraldehyde, hydrogen peroxide, formaldehyde) chemicals; gamma, X-ray or electron beam irradiation; and UV-ozone treatment. All of these methods have certain drawbacks and limitations and cannot be applied to many materials and substances that are temperature sensitive or reactive with other forms of sterilization. For example, achieving terminal sterilization with these methods frequently compromises the osteogenic and biomechanical properties of the allograft. A novel approach to sterilization, with emphases on reducing the process temperature and minimizing contamination, is based on dense phase CO<sub>2</sub> technology [192, 196–210]. The process involves exposure of the item to SCCO<sub>2</sub> with additives such as hydrogen peroxide or peracetic acid, at temperatures in the range 313 K to 333 K and pressures from 5 to 30 MPa. Treatment times can range from 5 minutes to 6 hours to achieve SAL<sub>6</sub>, depending on the microorganism. Clinically relevant gram-positive and gram-negative vegetative bacteria can be deactivated in single step, but the treatment efficacy increases rapidly with temperature. Rapid pressurization/depressurization cycles also have a very positive effect on sterilization efficacy due to membrane disruption and cell lysis. Bacterial spores can also be sterilized with CO<sub>2</sub>-based processes.

SCCO<sub>2</sub> can penetrate and sterilize delicate products and materials, such as allograft tissue and engineered tissues including skin, ligament, tendon and bone, without damage to the structural or chemical integrity of the products. The very low surface tension of SCCO<sub>2</sub> facilitates penetration into the interior of the tissue, thereby allowing inactivation of embedded pathogens. Other biological sterilization applications include: inactivation of viruses; elimination of endotoxins and pyrogens; production of sterile immunogenic preparations; medical implants and devices; sterilization of active and inactive pharmaceutical ingredients; and pest control (killing of insect eggs and larva).

Recently, attention has been focused on food pasteurization and sterilization using SCCO<sub>2</sub> [190, 205–208]. Microorganisms are destroyed and enzymes can be inactivated in liquids, such as juices for example, by continuously flowing SCCO<sub>2</sub> along flow paths. Contact between the flows can be achieved with counter-current columns, vessel agitation (stirring or mixing), or with a membrane containing minute pores at which the flows contact each other in a non-dispersive manner. The process does not adversely affect properties of the liquid, such as taste, aroma and nutritional content.

### 13.6.7 Monitoring of SCCO<sub>2</sub> Precision Cleaning Processes with the Quartz Crystal Microbalance

SCCO<sub>2</sub> cleaning has mostly used ultraviolet fluorescence detection for in-situ monitoring of the cleaning process, although other techniques such as ellipsometry and gravimetric techniques have also been used [212, 213]. However, these techniques do not provide sufficient sensitivity required for precision cleaning requirements, or they are complicated to use, or they require long equilibrium times in high pressure environments. Quartz crystal microbalances (QCMs) have a sensitivity of 10<sup>-9</sup>g and can be used for accurate in situ monitoring of SCCO<sub>2</sub> cleaning processes [213–217]. One application of the QCM monitoring method involves partial or complete removal of a film or coating from the QCM surface by SCCO<sub>2</sub> using precision cleanliness criteria defined in Table 13.1. The thickness and the amount of CO<sub>2</sub> dissolved in a surface polymer film can affect the QCM response, although the QCM is applicable for films up to ~1 μm thickness. Another application is to sample the SCCO<sub>2</sub> fluid following the cleaning cycle into a QCM measurement chamber at a pressure at which SCCO<sub>2</sub> is converted to a gas. The contaminants in the sample stream deposit on the QCM and the mass change can be monitored during the cleaning process. The QCM is also capable of monitoring the mass changes in SCCO<sub>2</sub> drying of MEMS structures.

## 13.7 Summary and Conclusions

Dense-phase CO<sub>2</sub> in its supercritical state is an established precision cleaning technique with application in many different industries. The gas-like viscosity and the liquid-like density of CO<sub>2</sub> are key characteristics that allow the process to be tuned to the application. In addition, the very low surface tension of CO<sub>2</sub> in the dense-phase ensures high wettability and

makes it very attractive for precision cleaning applications, particularly for intricate parts with complex geometries. The cleaning process is operated at near-ambient temperatures. Although the operating pressures for SCCO<sub>2</sub> cleaning are high, this can be compensated for by operating at lower pressures in the liquid phase and for longer cleaning cycles. SCCO<sub>2</sub> is a batch processes. Applications range from cleaning and drying of micro and nanostructures such as carbon nanotubes, terminal sterilization of microbial organisms and food pasteurization, cleaning of metal surfaces, glass, optical elements, silicon wafers, and polymers, precision cleaning and drying of parts with complex geometries and tight spaces, sterilization of medical equipment, garment cleaning, pesticide mitigation in museum collections, and soil and surface decontamination.

## Acknowledgement

The author would like to thank the staff at the STI Library at the Johnson Space Center for help with locating obscure reference articles.

## Disclaimer

Mention of commercial products in this chapter is for information only and does not imply recommendation or endorsement by The Aerospace Corporation. All trademarks, service marks, and trade names are the property of their respective owners.

## References

1. M. A. McHugh and V. J. Krukonis, *Supercritical Fluid Extraction*, 2<sup>nd</sup> Edition, Elsevier, Oxford, UK (1994).
2. L. J. Snowden-Swan, *Supercritical Carbon Dioxide Cleaning Market Assessment and Commercialization/Deployment Plan*, Report PNL-10044, Pacific Northwest Laboratory, Richland, WA (1994).
3. *Cleaner Technologies Substitutes Assessment: Professional Fabricare Processes*. Chapter 11.1 Liquid Carbon Dioxide Process, Report EPA 744-B-98-001, U.S. Environmental Protection Agency, Washington, D.C. (1998).
4. J. McHardy and S.P. Sawan (Eds.), *Supercritical Fluid Cleaning: Fundamentals, Technology and Applications*, Noyes Publications, Westwood, NJ (1998).
5. B. Carver and D. Jackson, *Liquid CO<sub>2</sub> Immersion Cleaning*, *Products Finishing Magazine* (June 1999).

6. R. Kohli, Co-Solvents in Supercritical Fluids for Enhanced Effectiveness in Particle Removal, in: *Particles on Surfaces 5&6: Detection, Adhesion and Removal*, K. L. Mittal (Ed.), pp. 135–147, VSP, Utrecht, The Netherlands (1999).
7. R. Kohli, Precision Cleaning and Processing in Industrial Applications, in: *Particles on Surfaces 5&6: Detection, Adhesion and Removal*, K. L. Mittal (Ed.), pp. 117–133, VSP, Utrecht, The Netherlands (1999).
8. A. A. Clifford and J. R. Williams (Eds.), *Supercritical Fluid Methods and Protocols. Methods in Biotechnology, Volume 13*, Humana Press, Totowa, NJ (2000).
9. M. Perrut, Supercritical Fluid Applications: Industrial Development and Economic Issues, *Ind. Eng. Chem. Res.* 39, 4531 (2000).
10. R. Kohli, Adhesion of Small Particles and Innovative Methods for Their Removal, in: *Particles on Surfaces 7: Detection, Adhesion and Removal*, K. L. Mittal (Ed.), pp. 113–149, VSP, Utrecht, The Netherlands (2002).
11. G. L. Weibel and C. K. Ober, An Overview of Supercritical CO<sub>2</sub> Applications in Microelectronics Processing, *Microelectron. Eng.* 65, 145 (2003).
12. J. W. King and L. L. Williams, Utilization of Critical Fluids in Processing Semiconductors and Their Related Materials, *Curr. Opin. Solid State Mater. Sci.* 7, 413 (2003).
13. R. J. Lempert, P. Norling, C. Pernin, S. Resetar, and S. Mahnovski, Next Generation Environmental Technologies. Benefits and Barriers, Appendix A1. Supercritical or Liquid CO<sub>2</sub> as Solvent, Rand Monograph Report MR-1682-OSTP, Rand Corporation, Santa Monica, CA (2003). [www.rand.org](http://www.rand.org).
14. DoD Joint Service Pollution Prevention Opportunity Handbook, Supercritical Fluid Cleaning as a Solvent Alternative, Section 11–4, Department of Defense, Naval Facilities Engineering Service Center (NFESC), Port Hueneme, CA (2004).
15. M. J. Meziani, P. Pathak, and Y.-P. Sun, Supercritical Carbon Dioxide in Semiconductor Cleaning, in: *Handbook of Semiconductor Manufacturing Technology*, 2<sup>nd</sup> Edition, Y. Nishi and R. Doering (Eds.), pp. 6–1 to 6–28, Taylor & Francis Group, Oxford, UK (2007).
16. G. Levitin and D. W. Hess, Elevated Pressure CO<sub>2</sub> –Based Fluids Containing Polar Co-Solvents for Cleaning in Microelectronic Device Fabrication, in: I. Johansson and P. Somasundaran (Eds.), *Handbook for Cleaning/Decontamination of Surfaces*, pp. 539–571, Elsevier, Oxford, UK (2007).
17. S. Banerjee, R. F. Reidy, and L. B. Rothman, Cryogenic Aerosols and Supercritical Fluid Cleaning, in: *Handbook of Silicon Wafer Cleaning Technology*, 2<sup>nd</sup> Edition, K. A. Reinhardt and W. Kern (Eds.), pp. 429–478, William Andrew Publishing, Norwich, NY (2008).
18. R. Sherman, Carbon Dioxide Snow Cleaning, in: *Developments in Surface Contamination and Cleaning. Fundamentals and Applied Aspects*, R. Kohli and K. L. Mittal (Eds.), pp. 987–1012, William Andrew Publishing, Norwich, NY (2008).

19. R. Sherman, Cleaning with Carbon Dioxide Snow, in: *Handbook for Critical Cleaning. Cleaning Agents and Systems*, 2<sup>nd</sup> Edition, B. Kanegsberg and E. Kanegsberg (Eds.), Vol. 1, pp. 397–410, CRC Press, Boca Raton, FL (2011).
20. W. M. Nelson, Cleaning with Dense-Phase CO<sub>2</sub>: Liquid CO<sub>2</sub>, Supercritical CO<sub>2</sub>, and CO<sub>2</sub> Snow, in: *Handbook for Critical Cleaning. Cleaning Agents and Systems*, 2<sup>nd</sup> Edition, B. Kanegsberg and E. Kanegsberg (Eds.), pp. 453–476, Vol. 1, pp. 411–423, CRC Press, Boca Raton, FL (2011).
21. Dry Ice Cleaning Solutions, Artimpex N.V., Ghent, Belgium (2012). [www.cryonomic.com](http://www.cryonomic.com).
22. Dry Ice Blasting, Cold Jet, Loveland, OH (2012). [www.coldjet.com](http://www.coldjet.com).
23. S. Banerjee, Cryoaerosol Cleaning of Particles from Surfaces, in: *Particle Adhesion and Removal*, K. L. Mittal and R. Jaiswal (Eds.), pp. 453–476, Wiley-Scrivener, Beverly, MA (2015).
24. R. Kohli, Surface Contamination Removal Using Dense Phase Fluids: Liquid and Supercritical Carbon Dioxide, in: *Developments in Surface Contamination and Cleaning: Contaminant Removal and Monitoring*, Vol. 5, R. Kohli and K. L. Mittal (Eds.), pp. 1–55, Elsevier, Oxford, UK (2013).
25. NASA JSC Contamination Control Requirements Manual, JPR 5322.1 (2009).
26. Space Product Assurance - Cleanliness and Contamination Control, ECSS-Q-70-01B (2008).
27. Product Cleanliness Levels and Contamination Control Program, IEST-STD-CC1246D (2002).
28. Product Cleanliness Levels – Applications, Requirements, and Determination, IEST-STD-CC1246E (2013).
29. C. Cagniard de la Tour, Exposé de quelques résultats obtenu par l'action combinée de la chaleur et de la compression sur certains liquides, tels que l'eau, l'alcool, l'éther sulfurique et l'essence de pétrole rectifiée, *Annales Chim. Phys.* 21, 127 (1822); Supplément, *ibid.*, p. 178.
30. C. Cagniard de la Tour, Nouvelle note sur les effets qu'on obtient par l'application simultanée de la chaleur et de la compression a certains liquides, *Annales Chim. Phys.* 22, 410 (1823).
31. T. Andrews, The Bakerian Lecture: On the Continuity of the Gaseous and Liquid States of Matter, *Philos. Trans. Royal Soc.* London 159, 575 (1869).
32. Carbon Dioxide, Report AIGA 068/10, Based on CGA G-6 7<sup>th</sup> Edition, Asia Industrial Gases Association, Singapore (2009).
33. Gas Encyclopedia, Air Liquide, Paris, France (2012). <http://encyclopedia.air-liquide.com/Encyclopedia.asp>.
34. J. B. Hannay and J. Hogarth, On the Solubility of Solids in Gases, *Proc. R. Soc. London* 30, 178 (1880).
35. J. B. Hannay, On the Solubility of Solids in Gases. II, *Proc. R. Soc. London* 30, 484 (1880).
36. B. E. Poling, J. M. Prausnitz, and J. P. O'Connell, *The Properties of Gases and Liquids*, 5<sup>th</sup> Edition, McGraw-Hill Professional, New York, NY (2000).

37. D. W. Green and R. H. Perry (Eds.), *Perry's Chemical Engineers' Handbook*, 8<sup>th</sup> Edition, McGraw-Hill Professional, New York, NY (2007).
38. W. M. Haynes (Ed.), *CRC Handbook of Chemistry and Physics*, 92<sup>nd</sup> Edition, CRC Press, Taylor and Francis Group, Boca Raton, FL (2011–2012). 93<sup>rd</sup> Edition (2012–2013).
39. Springer Materials The Landolt-Börnstein Database (2012). <http://www.springer.com/springermaterials>.
40. J. F. Kauffman, Quadrupolar Solvent Effects on Solvation and Reactivity of Solutes Dissolved in Supercritical CO<sub>2</sub>, *J. Phys. Chem. A* 105, 3433 (2001).
41. E. J. Beckman, Supercritical and Near-Critical CO<sub>2</sub> in Green Chemical Synthesis and Processing, *J. Supercrit. Fluids* 28, 121 (2004).
42. M. F. Kemmere, Supercritical Carbon Dioxide for Sustainable Polymer Processes, in: *Supercritical Carbon Dioxide: in Polymer Reaction Engineering*, M. F. Kemmere and T. Meyer (Eds.), pp. 1–14, Wiley-VCH, Weinheim, Germany (2005).
43. C. Reichardt and T. Welton, *Solvents and Solvent Effects in Organic Chemistry*, John Wiley & Sons, New York, NY (2011).
44. K. L. Stefanopoulos, Th. A. Steriotis, F. K. Katsaros, N. K. Kanellopoulos, A. C. Hannon, and J. D. F. Ramsay, Structural Study of Supercritical Carbon Dioxide Confined in Nanoporous Silica by In Situ Neutron Diffraction, *J. Phys. Conf. Series* 340, 012049 (2012).
45. R. Span and W. Wagner, A New Equation of State for Carbon Dioxide Covering the Fluid Region from the Triple-Point Temperature to 1100 K at Pressures up to 800 MPa, *J. Phys. Chem. Ref. Data* 25, 1509 (1996).
46. S. Bachu, Screening and Ranking Sedimentary Basins for Sequestration of CO<sub>2</sub> in Geological Media in Response to Climate Change, *Environ. Geol.* 44, 277 (2003).
47. B. Metz (Ed.), *Carbon Dioxide Capture and Storage. Annex I. Properties of CO<sub>2</sub> and Carbon-Based Fuels*, Cambridge University Press, Cambridge, UK (2005).
48. Z. Duan and Z. Zhang, Equation of State of the H<sub>2</sub>O, CO<sub>2</sub>, and H<sub>2</sub>O–CO<sub>2</sub> Systems up to 10 GPa and 2573.15 K: Molecular Dynamics Simulations with Ab Initio Potential Surface, *Geochim. Cosmochim. Acta* 70, 2311 (2006).
49. D. L. McCollum and J. M. Ogden, Techno-Economic Models for Carbon Dioxide Compression, Transport, and Storage & Correlations for Estimating Carbon Dioxide Density and Viscosity, Report UCD-ITS-RR-06-14, University of California Davis, Davis, CA (2006).
50. Equation of State Prediction of Carbon Dioxide Properties, Technical Note KCP-GNS-FAS-DRP-0001, Kingsnorth Carbon Capture & Storage Project, Department of Energy and Climate Change, London, UK (2010). <http://www.decc.gov.uk/assets/decc/11/ccs/chapter6/6.23-equation-of-state-prediction-of-carbon-dioxide-properties.pdf>.
51. V. Vesovic, W. A. Wakeham, G. A. Olchowy, J. V. Sengers, J. T. R. Watson, and J. Millat, The Transport Properties of Carbon Dioxide, *J. Phys. Chem. Ref. Data* 19, 763 (1990).

52. N. B. Vargaftik, Y. K. Vinogradov, and V. S. Yargin, *Handbook of Physical Properties of Liquids and Gases : Pure Substances and Mixtures*, 3<sup>rd</sup> Edition, Begell House, Redding, CT (1996).
53. A. Fenghour, W. A. Wakeham, and V. Vesovic, The Viscosity of Carbon Dioxide, *J. Phys. Chem. Ref. Data* 27, 31 (1998).
54. Y. Tanaka, N. Yamachi, S. Matsumoto, S. Kaneko, S. Okabe, and M. Shibuya, Thermodynamic and Transport Properties of CO<sub>2</sub>, CO<sub>2</sub>-O<sub>2</sub>, and CO<sub>2</sub>-H<sub>2</sub> Mixtures at Temperatures of 300 to 30,000 K and Pressures of 0.1 to 10 MPa, *Electrical Engineering in Japan* 163, 18 (2008).
55. O. Suárez-Iglesias, I. Medina, C. Pizarro, and J. L. Bueno, On Predicting Self-Diffusion Coefficients in Fluids, *Fluid Phase Equilibria* 269, 80 (2008).
56. K. E. O'Shea, K. M. Kirmse, M. A. Fox, and K. P. Johnston, Polar and Hydrogen-Bonding Interactions in Supercritical Fluids. Effects on the Tautomeric Equilibrium of 4-(Phenylazo)-1-Naphthol, *J. Phys. Chem.* 95, 7863 (1991).
57. K. Harrison, J. Goveas, K. P. Johnston, and E. A. O'Rear III, Water-in-Carbon Dioxide Microemulsions with a Fluorocarbon-Hydrocarbon Hybrid Surfactant, *Langmuir* 10, 3536 (1994).
58. K. D. Bartle, A. A. Clifford, S. A. Jafar, and G. F. Shilstone, Solubilities of Solids and Liquids of Low Volatility in Supercritical Carbon Dioxide, *J. Phys. Chem. Ref. Data* 20, 713 (1991).
59. R. B. Gupta and J. J. Shim, *Solubility in Supercritical Carbon Dioxide*, CRC Press, Boca Raton, FL (2007).
60. S. A. Abdullah, *Solubility in Supercritical Carbon Dioxide*, M.S. Thesis, New Jersey Institute of Technology, Newark, NJ (2007).
61. M. Škerget, Z. Knez, and M. Knez-Hrnčič, Solubility of Solids in Sub- and Supercritical Fluids: A Review, *J. Chem. Eng. Data* 56, 694 (2011).
62. C. M. Hansen, *Hansen Solubility Parameters: A User's Handbook*, 2<sup>nd</sup> Edition, CRC Press, Boca Raton, FL (2007).
63. A. F. M. Barton, *CRC Handbook of Solubility Parameters and Other Cohesion Parameters*, 2<sup>nd</sup> Edition, CRC Press, Boca Raton, FL (1991).
64. Y. Koga, Y. Iwai, Y. Hata, M. Yamamoto, and Y. Arai, Influence of Cosolvent on Solubilities of Fatty Acids and Higher Alcohols in Supercritical Carbon Dioxide, *Fluid Phase Equil.* 125, 115 (1996).
65. T. S. Reighard, S. T. Lee, and S. V. Olesik, Determination of Methanol/CO<sub>2</sub> and Acetonitrile/CO<sub>2</sub> Vapor-Liquid Phase Equilibria Using a Variable-Volume View Cell, *Fluid Phase Equil.* 123, 215 (1996).
66. R. Yaginuma, T. Nakajima, H. Tanaka, and M. Kato, Volumetric Properties and Vapor-Liquid Equilibria for Carbon Dioxide + 1-Propanol System at 313.15 K, *Fluid Phase Equil.* 144, 203 (1998).
67. G. J. McFann, K. P. Johnston, and S. M. Howdle, Solubilization in Nonionic Reverse Micelles in Carbon Dioxide, *AIChE J.* 40, 543 (1994).
68. H.Y. Shin, K. Matsumoto, H. Higashi, Y. Iwai, and Y. Arai, Development of a Solution Model to Correlate Solubilities of Inorganic Compounds in Water Vapor under High Temperatures and Pressures, *J. Supercrit. Fluids* 21, 105 (2001).

69. M. Sauceau, J. J. Letourneau, D. Richon, and J. Fages, Enhanced Density-Based Models for Solid Compound Solubilities in Supercritical Carbon Dioxide with Cosolvents, *Fluid Phase Equilibria* 208, 99 (2003).
70. J. S. Cheng, Y. P. Tang, and Y. P. Chen, Calculation of Solid Solubility of Complex Molecules in Supercritical Carbon Dioxide Using a Solution Model Approach, *Mol. Simulation* 29, 749 (2003).
71. P. Coimbra, C.M.M. Duarte, and H.C. de Sousa, Cubic Equation-of-State Correlation of the Solubility of Some Anti-Inflammatory Drugs in Supercritical Carbon Dioxide, *Fluid Phase Equilibria* 239, 188 (2006).
72. M. Hojjati, Y. Yamini, M. Khajeh, and A. Vetanara, Solubility of Some Statin Drugs in Supercritical Carbon Dioxide and Representing the Solute Solubility Data with Several Density-Based Correlations, *J. Supercrit. Fluids* 41, 187 (2007).
73. C. S. Su and Y. P. Chen, Correlation for the Solubilities of Pharmaceutical Compounds in Supercritical Carbon Dioxide, *Fluid Phase Equilibria*, 254, 167 (2007).
74. Y. Shimoyama, M. Sonoda, K. Miyazaki, H. Higashi, Y. Iwai, and Y. Arai, Measurement of Solubilities for Rhodium Complexes and Phosphine Ligand in Supercritical Carbon Dioxide, *J. Supercrit. Fluids* 44, 266 (2008).
75. D. L. Sparks, R. Hernandez, and L. A. Estévez, Evaluation of Density-Based Models for the Solubility of Solids in Supercritical Carbon Dioxide and Formulation of a New Model, *Chem. Eng. Sci.* 63, 4292 (2008).
76. M. Shamsipur, J. Fasihi, A. Khanchi, Y. Yamini, A. Valinezhad, and H. Sharghi, Solubilities of Some 9,10-Anthraquinone Derivatives in Supercritical Carbon Dioxide: A Cubic Equation of State Correlation, *J. Supercrit. Fluids* 47, 154 (2008).
77. Y. Zhao, W. Liu, and Z. Wu, Solubility Model of Solid Solute in Supercritical Fluid Solvent Based on UNIFAC, *Ind. Eng. Chem. Res.* 49, 5952 (2010).
78. L. Vafajoo, M. Mirzajanzadeh, and F. Zabihi, Determining Correlations for Prediction of the Solubility Behavior of Ibuprofen in Supercritical Carbon Dioxide Utilizing Density-Based Models, *World Acad. Sci. Eng. Technol.* 49, 790 (2011).
79. A. Ajchariyapagorn, P. L. Douglas, S. Douglas, S. Pongamphai, and W. Teppaitoon, Prediction of Solubility of Solid Biomolecules in Supercritical Solvents Using Group Contribution Methods and Equations of State, *Am. J. Food Technol.* 3, 275 (2008).
80. Y. Shimoyama and Y. Iwai, Development of Activity Coefficient Model Based on COSMO Method for Prediction of Solubilities of Solid Solutes in Supercritical Carbon Dioxide, *J. Supercrit. Fluids* 50, 210 (2009).
81. J. B. McClain, D. E. Betts, D. A. Canelas, E. T. Samulski, J. M. DeSimone, J. D. Londono, H. D. Cochran, G. D. Wignall, D. Chillura-Martino, and R. Triolo, Design of Nonionic Surfactants for Supercritical Carbon Dioxide, *Science* 274, 2049 (1996).
82. T. S. Reighard and S. V. Olesik, Bridging the Gap Between Supercritical Fluid Extraction and Liquid Extraction Techniques: Alternative Approaches to



- the Extraction of Solid and Liquid Environmental Matrices, *Crit. Rev. Anal. Chem.* 26, 61 (1996).
83. M. J. Clarke, K. L. Harrison, K. P. Johnston, and S. M. Howdle, Water in Supercritical Carbon Dioxide Microemulsions: Spectroscopic Investigation of a New Environment for Aqueous Inorganic Chemistry, *J. Am. Chem. Soc.* 119, 6399 (1997).
  84. A. I. Cooper, J. D. Londono, G. D. Wignall, J. B. McClain, E. T. Samulski, J. S. Lin, A. Dobrynin, M. Rubinstein, A. L. C. Burke, J. M. J. Fréchet, and J. M. DeSimone, Extraction of a Hydrophilic Compound from Water into Liquid CO<sub>2</sub> Using Dendritic Surfactants, *Nature* 389, 368 (1997).
  85. C. H. Darwin and R. B. Lienhart, Surfactant Solutions Advance Liquid CO<sub>2</sub> Cleaning Potentials, *Precision Cleaning* 6, 28 (June 1998).
  86. C. Xu, D. W. Minsek, J. F. Roeder, M. B. Korzenski, and T. H. Baum, Supercritical Fluid Cleaning of Semiconductor Substrates, U.S. Patent Application 2008/0058238 (2007).
  87. C. Xu, D. W. Minsek, J. F. Roeder, and M. Healy, Treatment of Semiconductor Substrates Using Long-Chain Organothols or Long-Chain Acetates, U.S. Patent 7,326,673 (2008).
  88. J. F. Roeder, T. H. Baum, M. Healy, and C. Xu, Supercritical Fluid-Based Cleaning Compositions and Methods, U.S. Patent 7,485,611 (2009).
  89. J. Zhang and B. Han, Supercritical CO<sub>2</sub>-Continuous Microemulsions and Compressed CO<sub>2</sub>-Expanded Reverse Microemulsions, *J. Supercrit. Fluids* 47, 531 (2009).
  90. Y. Takebayashi, M. Sagisaka, K. Sue, S. Yoda, Y. Hakuta, and T. Furuya, Near-Infrared Spectroscopic Study of a Water-in-Supercritical CO<sub>2</sub> Microemulsion as a Function of the Water Content, *J. Phys. Chem. B* 115, 6111 (2011).
  91. M. Sagisaka, S. Iwama, S. Hasegawa, A. Yoshizawa, A. Mohamed, S. Cummings, S. E. Rogers, R. K. Heenan, and J. Eastoe, Super-Efficient Surfactant for Stabilizing Water-in-Carbon Dioxide Microemulsions, *Langmuir* 27, 5772 (2011).
  92. F. E. Hénon, M. Camaiti, A. L. C. Burke, R. G. Carbonell, J. M. DeSimone, and F. Piacenti, Supercritical CO<sub>2</sub> as a Solvent for Polymeric Stone Protective Materials, *J. Supercrit. Fluids* 15, 173 (1999).
  93. S. Bhattacharya and K. L. Mittal, Mechanics of Removing Glass Particulates from a Solid Surface, *Surf. Technol.* 7, 413 (1978).
  94. S. M. Chitanvis, C. W. Patterson, W. D. Spall, and K. E. Laintz, Dynamics of Particle Removal by Supercritical Carbon Dioxide, in: *Supercritical Fluid Cleaning: Fundamentals, Technology and Applications*, J. McHardy and S. P. Sawan (Eds.), pp. 70–86, Noyes Publications, Westwood, NJ (1998).
  95. R. Kohli, The Behavior of Co-Solvents in Supercritical Fluids for Enhanced Precision Cleaning Applications, Report BMI-110-1997, Battelle Memorial Institute, Columbus, OH (1996).
  96. Y. West, Precision Cleaning with Supercritical Carbon Dioxide, Proc. CleanTech 2000, pp. 433–438 Witter Publishing, Flemington, NJ, (2000).

97. D. P. Jackson and O. F. Buck, Cleaning Process Using Phase Shifting of Dense Phase Gases, U.S. Patent 5,013,366 (1991).
98. D. P. Jackson, Dense Phase Gas Photochemical Process for Substrate Treatment, U.S. Patent 5,068,040 (1991).
99. T. G. Dewees, F. M. Knafelc, J. D. Mitchell, R. G. Taylor, R. J. Iliff, D. T. Carty, J. R. Latham, and T. M. Lipton, Liquid/Supercritical Carbon Dioxide Dry Cleaning System, U.S. Patent 5,267,455 (1993).
100. R. J. Mielnik, J. A. Metalonis, R. K. Reber, L. R. Rosio, S. H. Shore, and C. W. Smith, Apparatus for Supercritical Cleaning, U.S. Patent 5,355,901 (1994).
101. C. W. Smith Jr, L. R. Rosio, S. H. Shore, and J. A. Karle, Precision Cleaning System, U.S. Patent 5,377,705 (1995).
102. P. M. Wetmore, V. J. Krukonis, and M. P. Coffey, Pressure Pulse Cleaning, U. S. Patent 5,514,220 (1996).
103. G. B. Jacobson, L. Williams, W. K. Hollis, J. C. Barton, and C. M. V. Taylor, SCORR - Supercritical Carbon Dioxide Resist Removal, Report LA-UR-01-6653, Los Alamos National Laboratory, Los Alamos, NM (1998).
104. M. Perrut and V. Perrut, Natural and Forced Convection in Precision Cleaning Autoclaves, in: Proc. 6<sup>th</sup> Mtg. Supercritical Fluids, Nottingham, UK, pp. 727-731 (1999).
105. L. Frazer, SCORR One for the Environment, Environ. Health Perspect. 109, A382 (2001).
106. B. Knutson, The Use of a Supercritical Carbon Dioxide-Based Solvent as a Cost Effective and Environmentally Sound Alternative to Current Photoresist Stripping Solvents, M.S. Thesis, University of Wisconsin-Stout, Menomonie, WI (2002).
107. L. B. Rothman, R. J. Robey, M. K. Ali, and D. J. Mount, Supercritical Fluid Process for Semiconductor Device Fabrication, Proc. IEEE/SEMI Advanced Semiconductor Manufacturing Conference, Boston, MA, pp. 372-375 (2002).
108. D. J. Mount, L. B. Rothman, R. J. Robey, and M. K. Ali, The Technology Behind Cleaning with Supercritical Fluids, *Solid State Technol.* 45, 103 (July 2002).
109. P. S. Malchesky, Sub-Critical Fluid Cleaning and Antimicrobial Decontamination System and Process, U.S. Patent 6,558,622 (2003).
110. J. P. DeYoung, J. B. McClain, and S. M. Gross, Methods for Removing Particles from Microelectronic Structures, U.S. Patent 6,613,157 (2003).
111. J. S. Jur, K. J. McCullough, W. M. Moreau, J. P. Simons, and C. J. Taft, Process for Cleaning a Workpiece Using Supercritical Carbon Dioxide, U.S. Patent 6,558,475 (2003).
112. G. Lumia, V. Achrad, Ch. Niemann, Ch. Bouscarle, and S. Sarrade, Supercritical CO<sub>2</sub> Cleaning: The DFD System: Dense Fluid Degreasing System, in: Proc. 6<sup>th</sup> Int. Symp. Supercrit. Fluids, Versailles, France (2003). <http://www.isasf.net/fileadmin/files/Docs/Versailles/Papers/Mc2.pdf>

113. M. Chandra, D. J. Mount, M. A. Costantini, H. D. Moritz, I. Jafri, J. Boyd, and R. M. Heathwaite, Supercritical Fluid Cleaning Process for Precision Surfaces, U.S. Patent 6,602,349 (2003).
114. M.B. Korzenski, C. Xu, and T.H. Baum, Supercritical Carbon Dioxide: The Next Generation Solvent for Semiconductor Wafer Cleaning Technology, in: Proc. 6<sup>th</sup> Int. Symp. Supercritical Fluids, Versailles, France, pp. 2049–2055 (2003). [www.isasf.net/fileadmin/files/Docs/Versailles/Papers/Mc1.pdf](http://www.isasf.net/fileadmin/files/Docs/Versailles/Papers/Mc1.pdf)
115. M. A. Biberger, F. P. Layman and T. R. Sutton, Apparatus for Supercritical Processing of Multiple Workpieces, U.S. Patent 6,748,960 (2004).
116. A. D. Preston, J. R. Turner, and C. Svoboda, Carbon Dioxide Dry Cleaning System, U.S. Patent 6,851,148 (2005).
117. D. P. Jackson, Precision Cleaning and Machining with Minimal Waste and Increased Profitability, *Process Cleaning Magazine* (July 2006).
118. W. T. McDermott, H. Subawalla, A. D. Johnson, and A. Schwarz, Processing of Semiconductor Components with Dense Processing Fluids and Ultrasonic Energy, U.S. Patent 7,267,727 (2007).
119. S. H. Kim, H. Yuvaraj, Y. T. Jeong, C. Park, S. W. Kim, and K. T. Lim, The Effect of Ultrasonic Agitation on the Stripping of Photoresist Using Supercritical CO<sub>2</sub> and Co-Solvent Formulation, *Microelectronic Eng.* 86, 171 (2009).
120. Technical File - DFD Supercritical CO<sub>2</sub> System, UNITECH ANNEMASSE, St Pierre-en-Faucigny, France (2010). <http://www.unitechannemasse.fr/co2.html>.
121. Phasex Corporation, Lawrence, MA (2012). <http://www.phasex4scf.com/>.
122. Critical Cleaning. Using Supercritical Fluids for Your Critical Cleaning Needs, Applied Separations, Allentown, PA (2012). [www.appliedseparations.com](http://www.appliedseparations.com).
123. Precision Cleaning, eCO<sub>2</sub> SA, Mezzovico, Switzerland (2012). <http://www.eco2.ch/>.
124. EcoCO<sub>2</sub> – Cleaning with CO<sub>2</sub>, Dürr Ecoclean GmbH, Filderstadt, Germany (2012). <http://www.durr-ecoclean.com/>.
125. Y. Kamiya, T. Hirose, K. Mizoguchi, and Y. Naito, Gravimetric Study of High-Pressure Sorption of Gases in Polymers, *J. Polym. Sci. Pt. B: Polym. Phys.* 24, 1525 (1986).
126. J. S. Chiou, J. W. Barlow, and D. R. Paul, Plasticization of Glassy Polymers by Carbon Dioxide, *J. Appl. Polym. Sci.* 30, 2633 (1985).
127. G. K. Fleming and W. J. Koros, Dilation of Polymers by Sorption of Carbon Dioxide at Elevated Pressures. 1. Silicone Rubber and Unconditioned Polycarbonate, *Macromolecules* 19, 2285 (1986).
128. R. G. Wissinger and M. E. Paulaitis, Swelling and Sorption in Polymer-Carbon Dioxide Mixtures at Elevated Pressures, *J. Polym. Sci. Pt. B: Polym. Phys.* 25, 2497 (1987).
129. G. K. Fleming and W. J. Koros, Dilation of Substituted Polycarbonates Caused by High Pressure Carbon Dioxide Sorption, *Polym. Sci., Polym. Phys. Ed.* 28, 1137 (1990).

130. A. R. Berens, G. S. Huvad, R. W. Korsmeyer, and F. W. Kunig, Application of Compressed Carbon Dioxide in the Incorporation of Additives into Polymers, *J. Appl. Polym. Sci.* 46, 231 (1992).
131. S. G. Kazarian, Polymer Processing with Supercritical Fluids, *Polym. Sci. Ser. C* 42, 78 (2000).
132. B. Bonavoglia, G. Storti, M. Morbidelli, A. Rajendran, and M. Mazzotti, Sorption and Swelling of Semicrystalline Polymers in Supercritical CO<sub>2</sub>, *J. Polym. Sci. B* 44, 1531 (2006).
133. J. C. Barton, Apparatus and Method for Providing Pulsed Fluids, U.S. Patent 6,085,762 (2000).
134. K. J. Heater, A. B. Parsons, and R. F. Olfenbittel, Evaluation of Supercritical Carbon Dioxide Technology to Reduce Solvent in Spray Coating Applications, EPA Document 600/R-94/043, U.S. Environmental Protection Agency, Cincinnati, OH (1994).
135. J. C. Barton, The Los Alamos Super Scrub™: Supercritical Carbon Dioxide System Utilities and Consumables Study, Report LA-12786, Los Alamos National Laboratory, Los Alamos, NM (1994).
136. P. Randall and D. Williams, Guide to Cleaner Technologies: Alternatives to Chlorinated Solvents for Cleaning and Degreasing, EPA, EPA/625/R-93/016 (February 1994).
137. I. J. Licis, Pollution Prevention Possibilities for Small and Medium-Sized Industries. Results of the WRITE Projects, EPA Document EPA/600/R-95/070, pp. 127–131, U.S. Environmental Protection Agency, Cincinnati, OH (1995).
138. C. W. Smith and G. Huse, Equipment Cost Considerations and Financial Analysis of Supercritical Fluid Processing, in: *Supercritical Fluid Cleaning: Fundamentals, Technology and Applications*, J. McHardy and S.P. Sawan (Eds.), pp. 245–266, Noyes Publications, Westwood, NJ (1998).
139. SCCO<sub>2</sub> Cleaning Economics, Pacific Northwest Pollution Prevention Resource Center, Richland, WA (1999). <http://www.pprc.org/pubs/techreviews/co2/co2econ.html>
140. R. Bergström and Ö. Ekengren, Evaluation of Carbon Dioxide Cleaning System, Report A20090, IVL Svenska Miljöinstitutet AB, Stockholm, Sweden (April 2000). [http://www.weatherlyinc.com/sok/download/IVL\\_eng.pdf](http://www.weatherlyinc.com/sok/download/IVL_eng.pdf)
141. M. A. Matthews, L. S. Warner, and H. Kaiser, Exploring the Feasibility of Using Dense-Phase Carbon Dioxide for Sterilization, Medical Device & Diagnostic Industry, Magazine, pp. 140–144 (May 2001).
142. CleanLogix, Eagan, MN (2012). <http://www.2cooltool.com/results.html>
143. Liquid CO<sub>2</sub> Technical Specification, Continental Carbonic Products Inc, Decatur, IL (2012). <http://www.continentalcarbonic.com/lco2>
144. Carbon Dioxide TechniPure Gas SFC Grade, Air Liquide America Specialty Gases, Plumsteadville, PA (2012). <http://www.alspecialtygases.com>
145. Enertia™ Centrifugal Immersion CO<sub>2</sub> Cleaning Systems, Cool Clean Technologies Inc., Eagan, MN (2012). <http://www.coolclean.com/v2011/Enertia.html>

146. R. A. Novak, W. J. Reightler, R. J. Robey, and R. E. Wildasin, Cleaning of Precision Components with Supercritical Carbon Dioxide, in: Proc. 1993 International CFC and Halon Alternatives Conference, Washington, D.C., pp. 541–547 (1993).
147. E. M. Russick, G. A. Poulter, C. L. J. Adkins, and N. R. Sorensen, Corrosive Effects of Supercritical Carbon Dioxide and Cosolvents on Metals, *J. Supercrit. Fluids* 9, 43 (1996).
148. J. A. Peters and K. James, Application of Near-Critical/Supercritical Solvent Cleaning Processes, Technical Note TN-102, Supercritical Fluids Technologies, Newark, DE (1996). <http://www.supercriticalfluids.com/wp-content/uploads/TN-102-Near-Critical-SF-Cleaning1.pdf>.
149. G. B. Jacobson, L. Williams, W. K. Hollis, J. Barton, and C. M. V. Taylor, SCORR - Supercritical Carbon Dioxide Resist Removal, Report LA-UR-01-6653, Los Alamos National Laboratory, Los Alamos, NM (1998).
150. J. B. Rubin, L. B. Davenhall, J. Barton, C. M. V. Taylor, and K. Tiefert, A Comparison of Chilled DI Water /Ozone and CO<sub>2</sub>-Based Supercritical Fluids as Replacements for Photoresist-Stripping Solvents, Proc. 23<sup>rd</sup> IEEE/CPMT Int. Electron Manuf. Technol. Symp. (1998).
151. J. B. Rubin, L. B. Davenhall, C. M. V. Taylor, L. D. Sivils, T. Pierce, and K. Tiefert, CO<sub>2</sub>-Based Supercritical Fluids as Replacements for Photoresist-Stripping Solvents, Report LA-UR-98-3855, Los Alamos National Laboratory, Los Alamos, NM (1998).
152. W. D. Spall and K. E. Laintz, A Survey on the Use of Supercritical Carbon Dioxide as a Cleaning Solvent, in: *Supercritical Fluid Cleaning: Fundamentals, Technology and Applications*, J. McHardy and S.P. Sawan (Eds.), pp. 162–194, Noyes Publications, Westwood, NJ (1998).
153. J. B. Rubin, L. D. Sivils, and A. A. Busnaina, Precision Cleaning of Semiconductor Surfaces Using Carbon Dioxide-Based Fluids, Report LA-UR-99-2370, Los Alamos National Laboratory, Los Alamos, NM (1999).
154. J. B. Rubin, L. B. Davenhall, C. M. V. Taylor, L. D. Sivils, and T. Pierce, Carbon Dioxide-Based Supercritical Fluids as IC Manufacturing Solvents, Proc. 1999 IEEE Int. Symp. Electronics and the Environment, Danvers, MA (1999).
155. M. Perrut and V. Perrut, Natural and Forced Convection in Precision Cleaning Autoclaves, in: Proc. 6<sup>th</sup> Mtg. Supercritical Fluids, pp. 727–731, Nottingham, UK (1999).
156. C. Devittori, P. Widmer, F. Nesi, and M. Prokic, Multifrequency Ultrasonic Actuators with Special Application to Ultrasonic Cleaning in Liquid and Supercritical CO<sub>2</sub>, Paper presented at Annual Symposium Ultrasonic Industry Association, Atlanta, GA (2001). [www.mpi-ultrasonics.com/cleaning-co2.html](http://www.mpi-ultrasonics.com/cleaning-co2.html)
157. N. Dahmen, V. Piottter, F. Hierl, and M. Roelse, Überkritische Fluide zur Behandlung und Herstellung komplexer Werkstoffe und

- Oberflächenstrukturen, Report FZKA 6585, Forschungszentrum Karlsruhe, Karlsruhe, Germany (2001).
158. L. L. Williams, Removal of Polymer Coating with Supercritical Carbon Dioxide, Ph.D. Thesis, Colorado State University, Fort Collins, CO (2001).
  159. L. B. Rothman, R. J. Robey, M. K. Ali, and D. J. Mount, Supercritical Fluid Process for Semiconductor Device Fabrication, Proc. IEEE/SEMI Advanced Semiconductor Manufacturing Conference, Boston, MA, pp. 372–375 (2002).
  160. L. B. Rothman, Supercritical CO<sub>2</sub> Tools & Applications for Semiconductor Processing, NSF/SRC Engineering Research Center for Environmentally Benign Semiconductor Manufacturing, Albany, New York (August 2003). [http://www.nsfstc.unc.edu/newsticker/ERCretreat03/Orals\\_August-22nd.pdf](http://www.nsfstc.unc.edu/newsticker/ERCretreat03/Orals_August-22nd.pdf).
  161. J. Schön, K. Buchmüller, N. Dahmen, P. Griesheimer, P. Scwab and H. Wilde, EMSIC Ein pfiffiges Verfahren zur Entölung von Metall- und Glas-Schleifschlämmen, Report FZKA 6799, Forschungszentrum Karlsruhe, Karlsruhe, Germany (2003).
  162. M. B. Korzenski, C. Xu and T. H. Baum, Supercritical Carbon Dioxide: The Next Generation Solvent for Semiconductor Wafer Cleaning Technology, in: Proc. 6<sup>th</sup> Int. Symp. Supercritical Fluids, Versailles, France, pp. 2049–2055 (2003). [www.isasf.net/fileadmin/files/Docs/Versailles/Papers/Mc1.pdf](http://www.isasf.net/fileadmin/files/Docs/Versailles/Papers/Mc1.pdf)
  163. M. J. E. van Roosmalen, Dry-Cleaning with High-Pressure Carbon Dioxide, Ph.D. Thesis, Technical University Delft, Delft, The Netherlands (2003).
  164. M. J. E. van Roosmalen, G. F. Woerlee, and G. J. Witkamp, Surfactants for Particulate Soil Removal in Dry-Cleaning with High-Pressure Carbon Dioxide, *J. Supercrit. Fluids* 30, 97 (2004).
  165. P. K. Sen, Precision Cleaning by Supercritical CO<sub>2</sub>, M.S. Thesis, Department of Chemical Engineering, Indian Institute of Technology, Bombay, India (2004).
  166. E. N. Hoggan, K. Wang, D. Flowers, J. M. DiSimone, and R. G. Carbonell, “Dry” Lithography Using Liquid and Supercritical Carbon Dioxide Based Chemistries and Processes”, IEEE Trans. Semiconductor Mfg. 17, 510 (2004).
  167. C. A. Jones III, A. Zweber, J. P. DeYoung, J. B. McClain, R. Carbonell, and J. M. DeSimone, Applications of “Dry” Processing in the Microelectronics Industry Using Carbon Dioxide, *Crit. Rev. Solid State Mater. Sci.* 29, 97 (2004).
  168. J.-L. Chen, Y.-S. Wang, H.-I. Kuo, and D.-Y. Shu, Stripping of Photoresist on Silicon Wafer by CO<sub>2</sub> Supercritical Fluid, *Talanta* 70, 414 (2006).
  169. S. Lambertz, Entwicklung eines kontinuierlichen Extraktionsverfahrens zur Reinigung von Kunststoffschmelzen mittels überkritischem Kohlendioxid, Ph.D. Thesis, Rheinisch-Westfälische Technische Hochschule, Aachen, Germany (2006).
  170. K. Saga and T. Hattori, Wafer Cleaning Using Supercritical CO<sub>2</sub> in Semiconductor and Nanoelectronic Device Fabrication, *Solid State Phenomena* 134, 97 (2008).

171. A. H. Romang and J. J. Watkins, Supercritical Fluids for the Fabrication of Semiconductor Devices: Emerging or Missed Opportunities?, *Chem. Rev.* 110, 459 (2010).
172. G. Brunner, Applications of Supercritical Fluids, *Annu. Rev. Chem. Biomol. Eng.* 1, 321 (2010).
173. G. Lumia, Ch. Bouscarle, and F. Charton, Carbon Dioxide: A Solution to Organic Solvent Substitution in Cleaning Processes, in: Proc. ICCDU XI 11<sup>th</sup> Int. Conf. on Carbon Dioxide Utilization, Dijon, France (June 2011).
174. M. Koh, J. Yoo, M. Ju, B. Joo, K. Park, H. K. Kim, H. D. Kim, and B. Fournel, Surface Decontamination of Radioactive Metal Wastes Using Acid-in-Supercritical CO<sub>2</sub> Emulsions, *Ind. Eng. Chem. Res.* 47, 278 (2008).
175. K. Park, J. Sung, M. Koh, H. D. Kim, and H. K. Kim, Decontamination of Radioactive Contaminants Using Liquid and Supercritical CO<sub>2</sub>, in: *Radioactive Waste*, R. A. Rahman (Ed.), InTech Publishing –Open Access Company, Rijeka, Croatia, ISBN: 978-953-51-0551-0 (2012). <http://www.intechopen.com/books/radioactivewaste/decontamination-of-radioactive-contaminants-using-liquid-supercritical-co2>.
176. Y. Lin, F. Zhong, D. C. Aveline, and M. S. Anderson, Supercritical CO<sub>2</sub> Cleaning System for Planetary Protection and Contamination Control Applications Cleaning Metal Substrates Using Liquid/Supercritical Fluid Carbon Dioxide, NASA Tech Briefs NPO-47414 (April 2012).
177. G. Della Porta, M.C. Volpe, and E. Reverchon, Supercritical Cleaning of Rollers for Printing and Packaging Industry, *J. Supercrit. Fluids* 37, 409 (2006).
178. P. T. Liu, C. T. Tsai, K. T. Kin, P. L. Chang, C. M. Chen, H. F. Cheng, and T. C. Chang, Effect of Supercritical Fluids on Field Emission from Carbon Nanotubes, Proc. IEEE Conference on Emerging Technologies - Nanoelectronics, pp. 383–387 (2006).
179. P. T. Liu, C. T. Tsai, T. C. Chang, K. T. Kin, P. L. Chang, C. M. Chen, and Y. C. Chen, Effects of Supercritical Fluids Activation on Carbon Nanotube Field Emitters, *IEEE Trans. Nanotechnol.* 6, 29 (2007).
180. S. Keskin, U. Akman, and O. Hortaçsu, Continuous Cleaning of Contaminated Soils Using Ionic Liquids and Supercritical CO<sub>2</sub>, Proc. 10<sup>th</sup> European Meeting on Supercritical Fluids: Reactions, Materials and Natural Products, Colmar, France (December 2005).
181. S. Keskin, D. Kayrak-Talay, U. Akman, and O. Hortaçsu, A Review of Ionic Liquids Towards Supercritical Fluid Applications, *J. Supercritical Fluids* 43, 150 (2007).
182. S. Keskin, U. Akman, and O. Hortaçsu, Soil Remediation via an Ionic Liquid and Supercritical CO<sub>2</sub>, *Chem. Eng. Proc.* 47, 1693 (2008).
183. B. Kaye, K. Morphet, and D. J. Cole-Hamilton, Supercritical Drying: A New Method for Conserving Waterlogged Archaeological Materials, *Stud. Conserv.* 45, 233 (2000).
184. E. Jelen, A. Weber, A. Unger, and M. Eisbein, Detox Cure for Art Treasures, *Pesticide Outlook* 14, 7 (2003).

185. M. Sousa, M. J. Melo, T. Casimiro, and A. Aguiar-Ricardo, The Art of CO<sub>2</sub> for Art Conservation: A Green Approach to Antique Textile Cleaning, *Green Chem.* 9, 943 (2007).
186. A. Unger, Decontamination of Pesticides from Wooden Art Objects with Supercritical Carbon Dioxide, Proceedings of COST IE0601 Meeting, Tervuren, Italy (June 2007). [http://ottimari.agr.unifi.it/~uzielli/Tervuren\\_proceedings/Unger.pdf](http://ottimari.agr.unifi.it/~uzielli/Tervuren_proceedings/Unger.pdf).
187. H. Tello and A. Unger, Liquid and Supercritical Carbon Dioxide as a Cleaning and Decontamination Agent for Ethnographic Materials and Objects, in: *Pesticide Mitigation in Museum Collections: Science in Conservation*, A. E. Charola and R. J. Koestler (Eds.), Proc. MCI Workshop Series. Smithsonian Contributions to Museum Conservation, pp. 35–50, Smithsonian Institution, Washington, D.C. (2010).
188. W. S. Zimmt, N. Odegaard, T. K. Moreno, R. A. Turner, M. R. Riley, B Xie, and A. J. Muscat, Pesticide Extraction Studies Using Supercritical Carbon Dioxide, in: A. E. Charola and R. J. Koestler (Eds.), *Pesticide Mitigation in Museum Collections: Science in Conservation*, Proc. MCI Workshop Series. Smithsonian Contributions to Museum Conservation, Smithsonian Institution, Washington, D.C., pp. 51–57 (2010).
189. S. Wang, C. Zinderman, R. Wise, and M. Braun, Infections and Human Tissue Transplants: Review of FDA MedWatch Reports 2001–2004, *Cell Tissue Bank* 8, 211 (2007).
190. H. Q. Zhang, G. V. Barbosa-Cánovas, V. M. Balasubramaniam, C. P. Dunne, D. F. Farkas, and J. T. C. Yuan (Eds.), *Nonthermal Processing Technologies for Food*, Wiley-Blackwell, West Sussex, UK (2011).
191. R. L. Morrisey and G.B. Phillips (Eds.), *Sterilization Technology: A Practical Guide for Manufacturers and Users of Health Care Products*, Van Nostrand Reinhold, New York, NY (1993).
192. N. Elvassore, S. Sartorello, S. Spilimbergo, and A. Bertucco, Micro-Organisms Inactivation by Supercritical CO<sub>2</sub> in a Semi-Continuous Process, in: M. Perrut and E. Reverchon (Eds.), Proc. 7<sup>th</sup> Meeting on Supercritical Fluids, pp. 773–778, Antibes, France (2000).
193. P. B. Webb, P. C. Marr, A. J. Parsons, H. S. Gidda, and S. M. Howdle, Dissolving Biomolecules and Modifying Biomedical Implants with Supercritical Carbon Dioxide, *Pure Appl. Chem.* 72, 1347 (2000).
194. J. Agalloco, J. Akers, and R. Madsen, Current Practices in the Validation of Aseptic Processing – 2001, PDA Technical Report #36, Parenteral Drug Association, Bethesda, MD (2002).
195. J. Agalloco, J. Akers, and R. Madsen, Aseptic Processing: A Review of Current Industry Practice, *Pharmaceutical Technol.* 126–150 (October 2004).
196. S. Spilimbergo and A. Bertucco, Non-Thermal Bacterial Inactivation with Dense CO<sub>2</sub>, *Biotechnol. Bioeng.* 84, 627 (2003).
197. A. Schmidt, K. Beermann, E. Bach, and E. Schollmeyer, Disinfection of Textile Materials Contaminated with *E. Coli* in Liquid Carbon Dioxide, *J. Cleaner Prodn.* 13, 881 (2005).



198. A. White, D. C. Burns, and T. W. Christensen, Effective Terminal Sterilization Using Supercritical Carbon Dioxide, *J. Biotechnol.* 123, 504 (2006).
199. T. W. Christensen, D. C. Burns, A. L. White, B. Ganem, and A. R. Eisenhut, Sterilization Methods and Apparatus which Employ Additive-Containing Supercritical Carbon Dioxide Sterilant, U.S. Patent 7,108,832 (2006).
200. J. Zhang, N. Dalal, C. Gleason, M. A. Matthews, L. N. Waller, K. Fox, A. Fox, M. J. Drews, M. LaBerge, and Y. H. An, On the Mechanisms of Deactivation of *Bacillus Atrophaeus* Spores Using Supercritical Carbon Dioxide, *J. Supercrit. Fluids* 38, 268 (2006).
201. J. Zhang, T. A. Davis., M. A. Matthews, M. J. Drews, M. LaBerge, and Y. H. An, Sterilization Using High-Pressure Carbon Dioxide-A Review, *J. Supercrit. Fluids* 38, 354, (2006).
202. A. Nichols, D. C. Burns, and R. Christopher, Studies on the Sterilization of Human Bone and Tendon Musculoskeletal Allograft Tissue Using Supercritical Carbon Dioxide, *J. Orthopaedics* 6, e9 (2009).
203. Q. Q. Qiu, P. Leamy, J. Brittingham, J. Pomerleau, N. Kabaria, and J. Connor, Inactivation of Bacterial Spores and Viruses in Biological Material Using Supercritical Carbon Dioxide with Sterilant, *J. Biomed. Mater. Res. B* 91, 572 (2009).
204. D. C. Burns, R. J. Humphrey, A. R. Eisenhut, and T. W. Christensen, Sterilization of Drugs Using a Supercritical Carbon Dioxide Sterilant, U.S. Patent 8,012,414 (2011).
205. M. Sims, Method and Membrane System for Sterilizing and Preserving Liquids Using Carbon Dioxide, U.S. Patent 6,331,272 (2001).
206. M. Sims, E. Estigarribia, and J. T. C. Yuan, Membrane Carbon Dioxide Sterilization of Liquid Foods: Scale Up of a Commercial Continuous Process, in: Proc. 6<sup>th</sup> Int. Symp. Supercrit. Fluids, Versailles, France (2003). <http://www.isasf.net/fileadmin/files/Docs/Versailles/Papers/Mc2.pdf>.
207. Y. Y. Bae, N. H. Kim, K. H. Kim, B. C. Kim, and M. S. Rhee, Supercritical Carbon Dioxide as a Potential Intervention for Ground Pork Decontamination, *J. Food Safety* 31, 48 (2011).
208. M. Perrut, Sterilization and Virus Inactivation by Supercritical Fluids (A Review), *J. Supercrit. Fluids* 66, 359 (2012).
209. A. Checinska, I. A. Fruth, T. L. Green, R. L. Crawford, and A. J. Paszczynski, Sterilization of Biological Pathogens Using Supercritical Fluid Carbon Dioxide Containing Water and Hydrogen Peroxide, *J. Microbiol. Methods* 87, 70 (2011).
210. Supercritical CO<sub>2</sub> Sterilization, NovaSterilis, Lansing, NY (2012). [www.novasterilis.com](http://www.novasterilis.com)
211. ORDB 510(K) Sterility Review Guidance, U.S. Food and Drug Administration, Washington, D.C. (1997). <http://www.fda.gov/MedicalDevices/DeviceRegulationandGuidance/GuidanceDocuments/ucm080211.htm>
212. K. M. Motyl, Cleaning Metal Substrates Using Liquid/Supercritical Fluid Carbon Dioxide, NASA Tech Briefs MFS-29611 (December 1990).

213. S. M. Sirard, P. F. Green, and K. P. Johnston, Spectroscopic Ellipsometry Investigation of the Swelling of Poly(dimethylsiloxane) Thin Films with High Pressure Carbon Dioxide, *J. Phys. Chem. B* 105, 766 (2001).
214. Y.-T. Wu and C. S. Grant, Microweighing in Supercritical Carbon Dioxide, in: *Dekker Encyclopedia of Nanoscience and Nanotechnology*, J. A. Schwarz, C. I. Contescu, and K. Putyera (Eds.), pp. 1977–1990, Marcel Dekker, New York, NY (2004).
215. E. S. Di Milia, D. A. Gleichauf, and T. E. Whiting, Supercritical Fluid Contamination Monitor, European Patent EP0555638 (1995).
216. Y. A. Hussain, Supercritical CO<sub>2</sub> Aided Processing of Thin Polymer Films Studied Using the Quartz Crystal Microbalance, Ph.D. Thesis, North Carolina State University, Raleigh, NC (2006).
217. Y. Hussain, Y.-T. Wu, P.-J. Ampaw, and C. S. Grant, Dissolution of Polymer Films in Supercritical Carbon Dioxide Using a Quartz Crystal Microbalance, *J. Supercrit. Fluids* 42, 255 (2007).

# The Use of Surfactants to Enhance Particle Removal from Surfaces

Brian Grady

*Director, Institute for Applied Surfactant Research, Conoco-DuPont Professor of Chemical Engineering, School of Chemical, Biological and Materials Engineering, University of Oklahoma, Norman, OK, USA*

---

## Abstract

This chapter describes the fundamental mechanisms of how surfactants enhance particle removal from solid surfaces. A critical discussion is presented as to how the structure of surfactants determines the physico-chemical characteristics important for particle removal. Of particular importance is surfactant adsorption on solid surfaces from water and this issue is discussed in some detail. Finally, studies that relate fundamental surfactant and solution characteristics to particle removal performance are discussed.

**Keywords:** Surfactant, particle removal, surfactant adsorption

## 14.1 Introduction

Particle removal from surfaces is extremely important in a variety of cleaning processes. In detergency, particle removal from fabric is a critical part of any activity that occurs in a washing machine. Particle removal from hard surfaces is also critically important in other applications; for example a particle that is adhered to a semiconductor surface can cause catastrophic failure of a component. Solid-solid interactions are obviously the key to particle removal and hence a short discussion appears in this chapter with an emphasis on those aspects relevant for surfactants. The use of surfactants is one way to reduce attractive forces between particles and surfaces and significantly enhance particle removal. Surfactants are molecules that have

---

*E-mail:* bpgrady@ou.edu

---

K.L. Mittal and Ravi Jaiswal (eds.) Particle Adhesion and Removal, (519–542)  
2015 © Scrivener Publishing LLC

both a hydrophobic and hydrophilic part which, in turn, causes a large variety of unique behaviors when these molecules are dissolved in water. Hence, a brief description of surfactants and their characteristics will be presented. One of these unique behaviors key to cleaning is surfactant adsorption, which is the mechanism by which particle adhesion is reduced because of adsorption on both the particle and the substrate. Hence, the fundamentals of surfactants and surfactant adsorption will be described in detail in this Chapter. Finally, the chapter will conclude with some examples of studies that have looked at the effects of surfactants on particulate removal.

This Chapter deals only with how surfactants enhance particle removal. Other aspects of the particle-removal process also enhance particle removal in situations where surfactants are used, but, since the mechanisms by which these characteristics operate are not affected significantly by the presence of surfactants, these characteristics will not be discussed in detail. Other mechanisms include hydrodynamic forces; however, since the addition of surfactants at typical levels for cleaning does not significantly change fluid rheological characteristics, there is no need to discuss these issues since the two issues are essentially independent. However, there is no question that hydrodynamic forces are often critically important to particle removal where surfactants are also used. Some surfactant-containing cleaners also contain particulates that act as abrasives to help particle removal; again surfactants do not significantly affect the mechanism of how abrasives work so abrasives will not be considered in this Chapter. Since surfactants generally adsorb on the surface of an abrasive, abrasive performance can change dramatically but this issue does not change the mechanism by which abrasives remove particulates. Temperature can have an effect on how well particulates are removed in systems that contain surfactants. However, temperature does not affect mechanisms by which surfactants remove particulates, so will not be discussed. Finally, water composition will be discussed only in the sense how water composition affects surfactant particular removal mechanisms. Other soluble components in water can have an extremely large effect on particle removal, but these components operate by mechanisms not directly related to how surfactants help particle removal (although surfactants can enhance or interfere with these mechanisms).

## 14.2 Solid-Solid Interactions

A quick examination of a number of different reference books on solids indicates that the terminology and approach to this subject vary widely,

which is likely related to the fact that we are still learning about solid-solid interactions today. Difficulties in measurement are one problem; but, as opposed to liquids, probably the fundamental reason for disagreements is that solid surfaces are inherently non-equilibrium since diffusion occurs over very long time scales. Hence, the reader of this Chapter should understand that the terminology used in this Chapter does not match the terminology found in all literature, although the author has tried to use the most widely-used terminology. Although this topic is covered in detail in Chapter 1 of this book, there are certain aspects that must be emphasized in order to understand how surfactants can influence particle adhesion to surfaces.

The surface energy (or surface free energy) is the fundamental quantity used to define the tendency of a solid surface to adhere to a second solid surface; it is fundamentally equivalent to the amount of work required to form a unit area of surface from the bulk (or half that value since two surfaces are formed from one bulk sample).<sup>1</sup> A higher surface energy means that a surface is more adhesive, i.e. it can more strongly stick to another surface. This adhesion force originates from molecule-molecule interactions (or more specifically electron cloud-electron cloud interactions). This type of force is different than the interlocking force that occurs when a liquid flows into a small pore and hardens to form a “ship-in-a-bottle” type of morphology. Since this Chapter is concerned with particle adhesion one might think that this latter type of force is unimportant; however, one of the most difficult stains to remove from clothing is animal-fat (grease) which hardens upon cooling. From a fundamental perspective this latter type of force is very difficult to model and describe since the details depend strongly on the surface morphology and no more will be said about this force. Further, surfactants will in general not be useful in breaking solids which is the necessary step required to remove interlocked solids. Clearly though for the first kind of force that depends on the surface energy, an understanding of molecular forces and interactions is necessary to understand how surfactants affect the adhesion of particles to surfaces.

---

<sup>1</sup> The surface energy has the same units as surface tension. Surface tension and surface energy are the same quantity for a liquid, but not for a solid. The surface tension is defined as the work required to stretch a liquid surface to make it larger, which is equivalent to the work or energy required to form a new surface for a liquid only. On a molecular level, a liquid's atoms can rearrange upon stretching the surface to form its appropriate equilibrium arrangement. However, stretching a surface is NOT the same as forming new surface for a solid. With a solid, the distance between atoms can change and the equilibrium atomic configuration at a surface will not be maintained and hence the stretching experiment is not the same as forming a new surface.

There are three types of intermolecular forces to be discussed: electrostatic forces, van der Waals forces, and repulsive forces due to electron cloud overlap. Two point charges  $q_1$  and  $q_2$  separated by a distance  $r$  have the force between them in a medium with dielectric constant  $\epsilon$  given by (with a positive force being attractive)

$$\text{Force} = -\frac{q_1 q_2}{4\pi\epsilon r^2} \quad (14.1)$$

This electrostatic force is by far the strongest between a particle and a surface (except that of electron sharing, e.g. covalent bonding, which is not relevant to particle removal from surfaces), which is why the adsorption of charged surfactants is so successful in removing particles. In other words, in a liquid medium in the absence of an interlocking force, the adsorption of charged surfactants will be able to reduce, eliminate or even reverse the electrostatic force between a particle and a surface if the surfactant is able to diffuse to the interface. Of course, pH plays a large role in charging effects as well, and very often pH and surfactant adsorption are used together to make the repulsive force of a charge-charge interaction as large as possible.

Van der Waals (vdW) forces arise from the fact that the electron cloud around an atom or molecule is not spherically symmetric, either permanently or in a temporal sense. In other words, the electrostatic force arises from the permanent removal of an electron(s) from an atom, while the vdW forces arise from their distribution in space around an atom. In the case where two species (atoms or molecules) have a permanent (in a temporal sense) non-spherically symmetric electron density distribution, then the force is termed dipole-dipole. In the simplest instance, the distribution can be represented as a dumbbell with a positive charge on one end and a negative charge on the other. For the case where two dumbbells are fixed in space, the force scales with  $1/r^4$  (in Equation 1, the force scales with  $1/r^2$ ). In the case where two dumbbells are freely rotating, the force scales with  $1/r^7$ . In the case where one of the species has a permanent dipole and the other a non-permanent dipole, the force also scales with  $1/r^7$ . Finally, in the case where there is no permanent dipole on either molecule, the force also scales with  $1/r^7$ . This latter situation is termed dispersion forces.

Repulsive forces arise from the fact that electron clouds will eventually overlap if two atoms are close enough to one another. Hence, the distance over which this force operates is extremely small but this force increases rapidly once the electron clouds begin to overlap. Combining this type of expression with the dispersion forces mentioned in the previous paragraph

gives the following expression for the force, called the Lennard-Jones expression, which has the following form:

$$Force = \frac{6A}{r^7} - \frac{12B}{r^{13}} \quad (14.2)$$

The constants  $A$  and  $B$  are called the Lennard-Jones constants. Because the distance-dependencies are the same, it is often assumed that all of the vdW terms are contained in the  $A$  term.

The Lennard-Jones potential can be used to calculate the surface free energy for a given material. Details of the derivation are beyond the scope of this text, see Pocius[1] for an outline of the derivation. An important incorrect assumption of this theory is that the density of atoms is the same throughout the material including at the surface; this assumption is generally not correct. With this (incorrect) assumption, the expression for the surface energy ( $\gamma$ ) becomes:

$$\gamma = \frac{\pi n^2 A}{32r_0^2} \quad (14.3)$$

Where  $n$  is the number of molecules on either side of the interface,  $A$  is the Lennard-Jones constant and  $r_0$  is the equilibrium distance between the two flat surfaces.

The above expression describes the case where a unit area of surface is created from the same solid, so in order to create two new surfaces from the a bulk material requires an energy  $2\gamma$ , in other words,  $2\gamma$  is the work (or energy) required on a per unit area basis to fracture a material. Since the world is never quite as simple as one would like, this very simple description holds only for an extremely limited number of materials because materials will absorb energy in a variety of ways when forming a new surface other than that which is required to form a new surface. In the case where we have one type of solid adhered to a second solid, the work of adhesion on a per unit area basis is given by

$$Work\ of\ Adhesion = \gamma_1 + \gamma_2 - \gamma_{12} \quad (14.4)$$

where  $\gamma_{12}$  is the interfacial energy of the two materials. From a molecular level perspective, the interfacial energy accounts for the fact that the interaction of atom from solid 1 with an atom of solid 2 may be different than the average interaction of an atom of solid 1 with an atom of solid 1 and an atom of solid 2 with an atom of solid 2. In general, the interactions of an atom of solid 1 with solid 1 is much stronger than 1 with 2, so  $\gamma_{12}$  is smaller

for a stronger interaction of atom 1 with 2. This simple equation, termed the Dupre equation, clearly demonstrates why higher surface energy materials tend to be more strongly adhered and more difficult to remove.

In terms of surfactants, if the surface is charged and the surfactant is of opposite charge, then the surfactant will be attracted to the surface because of this charge-charge interaction. Even without this charge-charge interaction, surfactants will generally adsorb to most surfaces because water does not wish to interact with the hydrophobic tails of the surfactants which, in turn, drives the hydrophobic tails to the surface. In fact, in this case the driving force for surfactant adsorption is entropic since spatial arrangements of water around a hydrophobic moiety are severely restricted and hence the entropy of the system is usually larger after adsorption even though the surfactant loses almost all of its entropy. To understand specifics of surfactant adsorption, it is first necessary to briefly introduce surfactants to the reader.

### 14.3 Introduction to Surfactants

Surfactants are molecules that have a hydrophobic part and a hydrophilic part and some common surfactants are shown in Figure 14.1. This definition for a surfactant is not sufficient, since linear alkyl alcohols have both hydrophobic and hydrophilic parts and most people would not consider these molecules to be surfactants. The definition of a surfactant is somewhat controversial; one very important book in the field [2] defines surfactants by their interfacial activity (and this is probably the most common definition for surfactants) and alcohols would fit this definition. The definition that this author prefers is the surface-active component must form a micelle at some finite concentration in order for the molecule to be considered a surfactant; this definition has the problem that in theory a surfactant in one liquid may not be in another. With this terminology, a micelle forms in water while an inverse or reverse micelle forms in oil; the reason for this definition will become clear below. A micelle is a term that may be unfamiliar to some readers, so a brief description of this type of molecular arrangement is given.

Micelles are structures that form because a molecule that has both a hydrophilic part and a hydrophobic part want the latter to be shielded from water. An inverse micelle forms because the former wants to be shielded from oil. Different geometrical structures can form; most commercial surfactants have a structure that favors spherical micelles, while cylindrical and lamellar structures are also possible as shown in Figure 14.2. Inverse



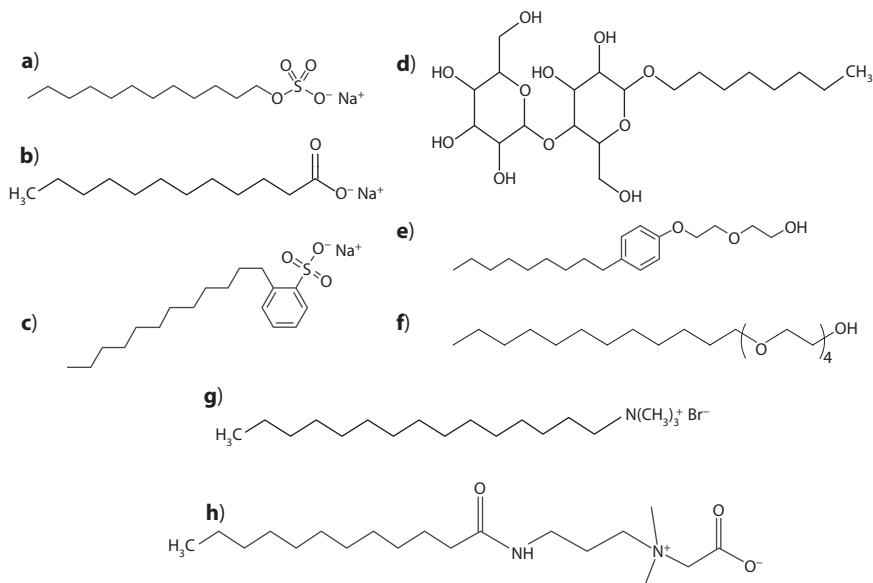


**Figure 14.1** Structures of some common surfactant families represented by an example of specific common molecules of those families. a–c) common anionic surfactants belonging to the family of alkyl sulfates (sodium dodecyl sulfate), alkyl carboxylates (soaps) (sodium dodecyl carboxylate) and benzene sulfonates (sodium dodecyl benzene sulfonate) respectively. d–f) common nonionic surfactants belonging to the family of alkyl polyglucosides, alkyl phenol ethoxylates (nonyl phenol ethoxylate) and alcohol ethoxylates, respectively. g) is a cationic surfactant belonging to the alkyl ammonium family (cetyl trimethylammonium bromide) while h) is a zwitterionic and belongs to the amidobetaine family. In all cases, common alkyl chain lengths are shown, although alkyl chain lengths will vary in length. The number of nonionic (e.g. glucoside or ethylene oxide) repeat units can also vary. For a more complete listing of different surfactants, see Ref [2].

micelles have the same type of structure, but the hydrophilic groups point inward towards the other molecules so as to be surrounded by moieties of its own type. The parameter that controls the geometrical structure is termed the packing factor, which is explained schematically in Figure 14.2. Surfactants in general fall into four different types as defined by the type of headgroup: anionic, cationic, nonionic and zwitterionic. The first two are self-explanatory, and a counterion of opposite charge is present to neutralize the charge (e.g. typically metal cations for anionic surfactants and halogen ions for cationic surfactants). Nonionic surfactants have headgroups without charge, while zwitterionic have both positive and negative charges on the same molecule. Another term, amphoteric, is often used; these

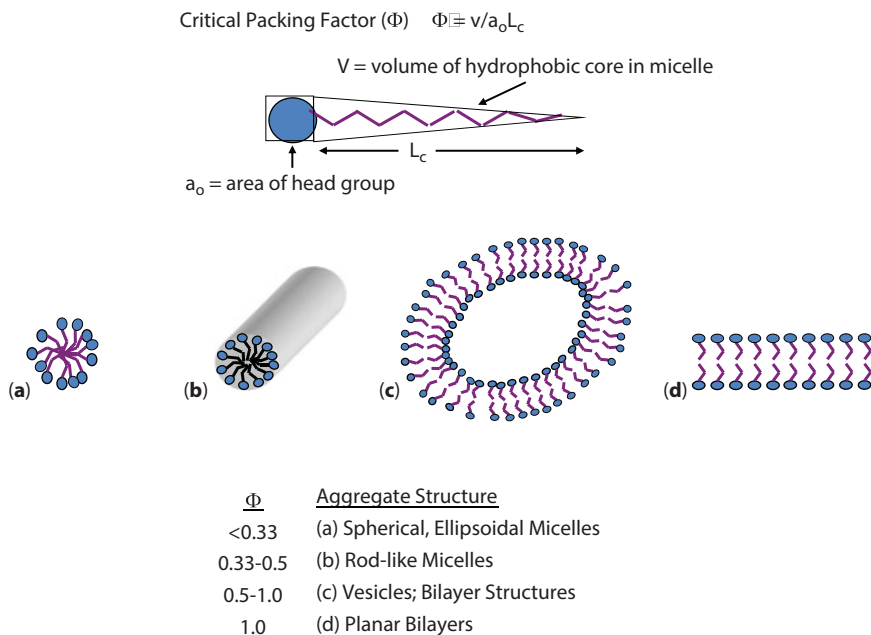


**Figure 14.2** Relationship between packing factor and different micelle structures.

surfactants have a charge that depends on pH. Amphoteric surfactants are a subset of zwitterionic surfactants; the difference is that in the latter no charge switching occurs because of the strength of the ionic groups.

As stated previously, micelles form because of the desire for the hydrophobic portion of the molecule to avoid contact with water molecules. The concentration at which micelles form is termed the critical micelle concentration (cmc), and is the most important thermodynamic parameter of a surfactant, at least in a commercial sense. Most properties of surfactants scale with the critical micelle concentration; for example, for a pure surfactant the surface tension reaches a minimum and does not change with more surfactant once the cmc is reached. Similarly, the chemical activity of the solution is almost constant once the cmc is reached. For this reason and others, micelles are considered as a separate phase although in a strict thermodynamic sense micelles are not a separate phase.

Measurement of the cmc is clearly critical for any surfactant or surfactant system. Surface tension is probably the most common method of measurement; the cmc is the concentration at which the surface tension reaches a constant value with added surfactant. Figure 14.3 shows a very commonly used Wilhelmy plate measurement that measures the force on the plate vs. distance and shows how the force changes because of a reduction in

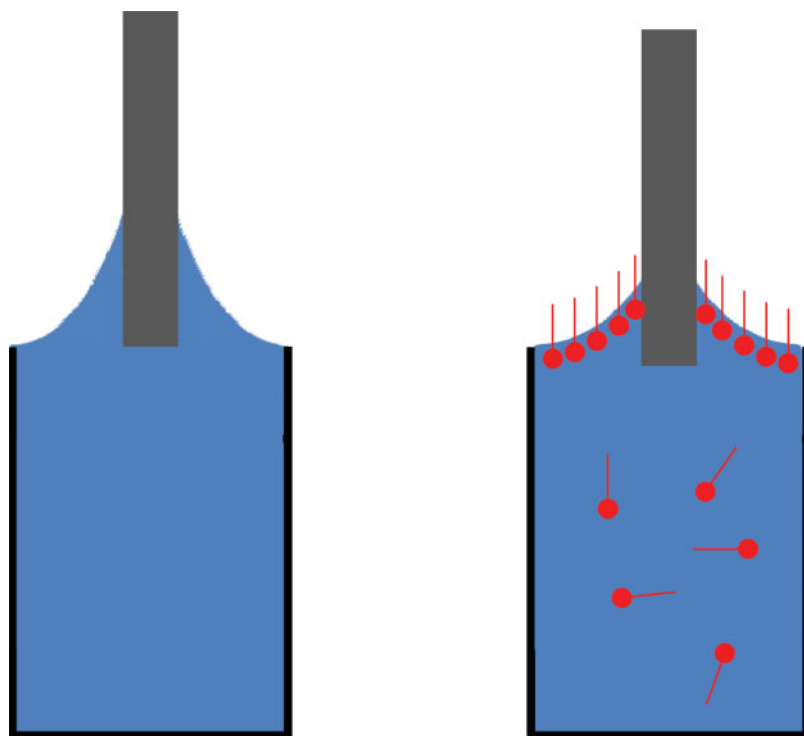


**Figure 14.3** Schematic of Wilhelmy plate measurement for surface tension without (left) and with (right) added surfactant.

surface tension. Other surface tension measurements, most commonly a drop shape analyzer, can also be used. Less commonly used measurements of the cmc rely on the ability to measure when individual surfactant molecules begin to aggregate in solution and include conductance (for ionic surfactants), NMR, light scattering, and fluorescence using a hydrophobic fluorescent probe. A more complete description of measurements used to determine the cmc are found in various tomes [3,4].

With this very simple introduction, to a first approximation design criteria for formulating a specific surfactant system in water can be discussed. Basically, the concentration of surfactant needs to be a few times the cmc unless for some application micelles are not desired. From an economic consideration assuming all raw material costs are the same, long hydrophobic chain lengths (or more generally high molecular weight hydrophobes) should be used because as the chain length increases, the cmc decreases. A rule of thumb is that the addition of two carbon atoms to an alkyl chain causes a factor of 10 decrease in the cmc and is similar to the well-known

Traube rule for surface tension. [5]. The perceptive reader will ask “what limits the hydrophobe chain length”, and the limitation is the ability of the hydrophile to make the hydrophobe soluble; in other words, at high enough hydrophobe content the molecule becomes insoluble in water. For ionic surfactants, as the concentration becomes too high a solid phase forms which for most surfactants is the pure (or mostly pure) crystal. The most common way to quantify this solubility is by the Krafft temperature (or Krafft point) which is the temperature at which the solubility becomes equivalent to the cmc. To maximize the chain length, typical Krafft points are between 10–20°C for most commercial ionic surfactants; nonionic surfactants have a different limit on the hydrophobic chain length described in the next paragraph. In general, raw material costs do not differ enough to offset the strong dependency of concentration on the cmc and hence for a given headgroup the most commercially important surfactant chain length is fairly standard and those standards are shown in Figure 14.1. The most commercially important nonionic surfactants have the property of adding more hydrophile (ethylene oxide or glucoside, see Figure 14.1) inexpensively, so the standard chain length depends on the number of hydrophile repeat units.

Nonionic surfactants in fact do not generally become insoluble at low temperature; rather they become insoluble at high temperature. Nonionic surfactants do not usually precipitate into pure crystals, rather they form surfactant-rich (coacervate) phases and surfactant-poor phases which in turn make a water solution turn cloudy. The cloud temperature (or cloud point) is the lowest temperature at which this separate phase will form. Formulation with the cloud point is not as simple as with the Krafft point; of course precipitation should be avoided at all costs in particle removal applications because the precipitate then will act as a particle itself (and these participates, also known as soap scum, are typically very hard to remove). Forming a separate phase with nonionic surfactants can be beneficial in some instances since the separate phase acts as a “natural” defoamer. Most often a typical nonionic surfactant used in laundry detergency has a cloud point between 40°C and 70°C.

If the formulation chemist only had the ability to vary chain length or hydrophile type, the design of surfactant formulations for particulate removal would be much simpler. With nonionic surfactants, it is possible to change the hydrophile length as well. Nonionic surfactants can have much lower cmc's than ionic surfactants, in other words the balance between solubility and hydrophobe mass results in a much lower cmc for nonionics while still maintaining sufficient solubility. Specifically, typical cmc's for water-soluble anionic surfactants are on the order of 1 millimolar while those for nonionics are typically 1–2 orders of magnitude lower. Since, as

implied previously, cleaning of particulates works best with charged surfactants, almost all surfactants used in any cleaning system, except in the cases where high foam is required, are mixtures of ionic and nonionic surfactants. Furthermore, because of price considerations (typical cationics are ~3 times more expensive than typical anionics), the ionic surfactant is usually anionic. Anionics are particularly common in particulate removal formulations; cationic surfactants are used only in specific applications because they tend to be better for skin and are harder to wash away than anionics, neither of which is a consideration for most particulate removal applications.

All of the structures drawn in Figure 14.1 have a hydrocarbon for the hydrophobic group. There are two examples of non-hydrocarbon based surfactants: fluorine- and siloxane-based surfactants. These surfactants have excellent properties in terms of having much lower cmc's than hydrocarbon-based surfactants without precipitating as well as much higher adsorption to interfaces. These surfactants are widely used in many specialty applications, but because of environmental and cost concerns have sales volumes orders of magnitude smaller than hydrocarbon-based surfactants. However, for very high value added products, use of fluorinated surfactants in particular can be very beneficial to cleaning and particle removal.

As stated previously, surfactants in cleaning applications are typically formulated to a concentration where the surfactant is a few times the cmc in solution. In terms of particulate removal, there is no increase in adsorption above the cmc, so using enough surfactant to be a few times the cmc is not necessary strictly speaking. However, since the surface area available for adsorption is almost never known (and hence the adsorbed amount is not known) and adsorbed surfactant is not present in solution in a thermodynamic sense, typically formulations are a few times the cmc. Another practical consequence as well is that when abrasives are used in a cleaning product, the amount of surfactant should be adjusted to account for adsorption by the abrasive. Furthermore, particle removal is often only part of the cleaning process; solubilization of hydrophobic oils does require the surfactant to be above the cmc. The characteristics of surfactant adsorption also influence this formulation, for example smaller species diffuse faster and hence adsorb in a shorter amount of time. The next section describes in detail the important characteristics of surfactant adsorption.

## 14.4 Surfactant Adsorption at Solid Surfaces

The fundamental measurement of adsorption is an adsorption isotherm, which plots adsorption on the y-axis and surfactant concentration on the

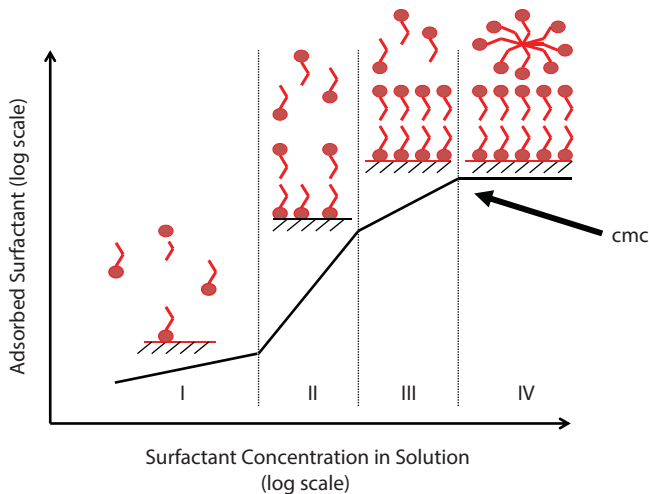


**Figure 14.4** Schematic representation of an adsorption isotherm showing the 4 regions of adsorption.

x-axis. A schematic of an ideal adsorption isotherm for a single surfactant is shown in Figure 14.4. Adsorption on the y-axis is ideally plotted as mass or moles of surfactant per unit surface area of solid; however since there are various methods to measure the surface area oftentimes per unit mass of solid is used. Many authors have made the mistake of using total amount of surfactant added in calculating concentration for the x-axis. In fact (surfactant added – surfactant adsorbed) must be used; in other words only the surfactant in solution after adsorption is plotted on the x-axis. The general shape of the isotherm is sigmoidal, which is the classical shape that indicates cooperativity during adsorption.

Four regions are shown in Figure 14.4 and each region from higher to lower concentration will be described. The transition between Region III and IV is attributed to the cmc; in Region 4 the concentration is above the cmc and the transition can be used to determine the cmc. The cmc is not necessarily the same as the cmc measured with no solid present. The cmc can shift with the introduction of a surface in surfactant mixtures because of preferential adsorption of a particular component, or in pure systems because most solids will release small amounts of molecules into solution which can change the cmc. To absolutely prove that the cmc shifted with the introduction of a solid is difficult, since solid particles interfere with most measurements of the cmc. In a thermodynamic sense, what this feature implies is that once micelles begin to form, the preferred environment for the next added surfactant molecule is in a micelle rather than at the

surface. However, and this may not be true in all cases but the author is not aware of a case where this is not true, this transition also roughly corresponds to a fully-packed surface. In other words, the surface becomes filled with surfactant at the same concentration where the thermodynamics becomes favorable for micelle formation. In fact, there is no reason why the surface could not be filled at a concentration above or below the cmc; again however this author is aware of no studies that have shown this behavior. Ellipsometry studies with pure surfactants and very clean surfaces have consistently found that the cmc occurs at the same concentration where the adsorption reaches a maximum[6].

The Region II-Region III transition represents a reduction in favorability for adsorption of surfactant. The simplest explanation for a transition between Regions II and III is that the surface charge reverses; in other words for adsorption of an anionic surfactant to a positively charged surface the surface is positively charged in Region II and negatively charged in Region III. However, this sort of transition is also observed in systems without oppositely-charged adsorption; another explanation is that the loss of free energy of adding another adsorbed molecule is less because of issues with surfactant-surface interactions. Although the transition is not limited to charged surfactants on oppositely charged surfaces, nonionic surfactants in general show much less of a Region II-Region III transition (in some cases to the point where it is not clear that such a transition exists).

The Region I-II transition represents a transition from where surfactant-surface interactions become the dominant driver for adsorption to where surfactant-surfactant interactions become the dominant driver. In other words, surfactant adsorption becomes dense enough in Region II in order for tail-tail interactions on neighboring surfactant molecules to become important (more precisely, water begins to be excluded from the immediate surroundings of hydrophobic tails). Region I is called the Henry's law region and in many isotherms is not measured because of the low concentrations involved. In this region, surfactants adsorb because of specific interactions with the surface.

A very rough quantification of Figure 14.4 is that the Region II-Region III transition occurs at a concentration at about half an order of magnitude below the Region III-Region IV transition and at an adsorption about half an order of magnitude below the maximum adsorption, while the Region I-II transition occurs at a concentration 1–2 orders of magnitude below the Region III-Region IV transition, and at an adsorption 1–2 orders of magnitude below the maximum adsorption.

In general, the area per molecule at saturated adsorption for a pure surfactant often does not differ substantially from that calculated from

adsorption at the air-water interface. When considered on a mass basis, maximum adsorption tends to be the same for many surfactants. In other words, if the y-axis is plotted on a surfactant mass basis and the x-axis is normalized to the cmc, adsorption isotherms tend not to be too different from one another. There are two significant differences between isotherms: the first occurs in Region I and is due to variations in the attractive forces between the head group and the surface since cooperative adsorption (e.g. tail-tail interactions) is unimportant in this regime. The second occurs in Regions II and III and tends to be very strongly dependent on the tail structure since it is the ability for tail-tail packing to be able to exclude water. Disrupting the regularity of the tail structure by branching for example is one way to significantly reduce surfactant adsorption since the entropy gain of water is not as large in these cases.

Measurement of adsorption can be done many different ways. With large surface area substrates, the so-called depletion method is used. A known amount of surfactant is weighed into a solution, solid is added and the concentration is measured. Typical equilibrium times are on the order of hours, so usually the samples are left to sit overnight. Some method is then used to quantify surfactant concentration in solution, most commonly liquid chromatography with an appropriate detector. One challenge is to make sure that the particulates do not interfere with the measurement which is one reason why chromatography is often used since any small particulates will be filtered out. Sometimes surface tension is used to quantify concentration with the assumption that the surface tension is a unique indicator of concentration which is a reasonable assumption if part of the solid does not dissolve in the solution. Another technique that works particularly well at low concentrations of surfactant (and hence low adsorption amounts) is calorimetry. With the latter, some standardization of the energy release upon adsorption of one molecule is necessary. With flat substrates, some sort of spectroscopic method that measures surface coverage on a molecularly-smooth (or almost molecularly smooth) substrate is used such as vibrational spectroscopy[7], quartz crystal microbalance studies[8], and most commonly ellipsometry[6]. The latter two have excellent time resolution so both can easily be adapted for kinetic studies. Because the amount of surfactant that is adsorbed is small with flat substrates, impurities can have a great effect on the measurement and one must be very careful to rigorously exclude impurities[9].

The structure of the adsorbed layers, although probably not an important consideration for particle-particle adhesion, is a fascinating subject and was the subject of a great number of studies in the late 1990's with the development of atomic force microscopy[10]. On molecularly smooth



surfaces such as mica or graphite, adsorbed surfactants at high surface coverage organize into one of six different morphologies, shown schematically in Figure 14.5. Other than whether the surface is hydrophilic or hydrophobic, the type of morphology is, to a first approximation, determined by the packing factor described in Figure 14.2. One misleading aspect about Figure 14.5 is that the organization of the individual surfactant molecules is not nearly as regular as Figure 14.5 suggests according to molecular dynamics simulations shown in Figure 14.6.

Since cmc is the key parameter in determining where the adsorption becomes constant with surfactant concentration, it is immediately clear

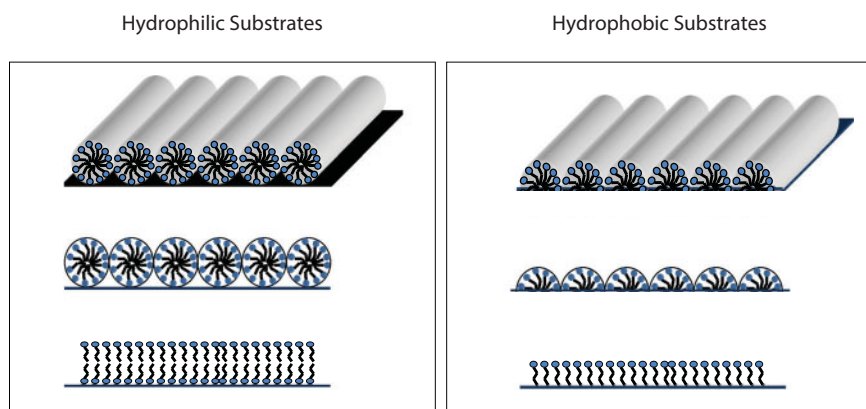


**Figure 14.5** Schematic representation of the six different morphologies possible at high surface coverages.

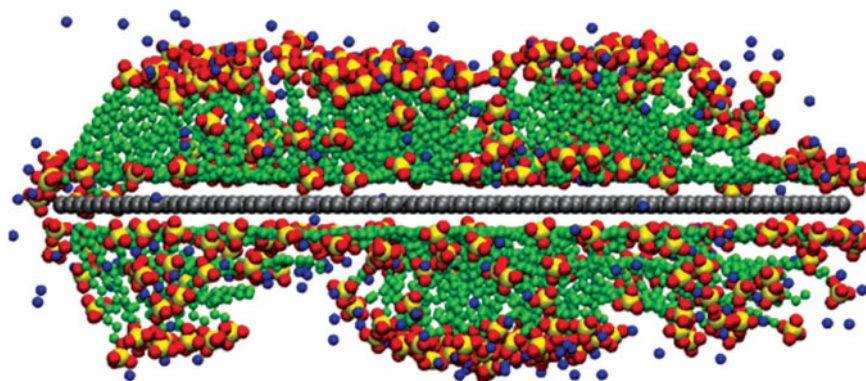


**Figure 14.6** Molecular dynamics simulations of sodium dodecyl sulfate on graphite with hemispherical structure (morphology in top right of Figure 14.5) sliced in the middle of a sphere showing the disordered nature of the morphology.

that a change that reduces the cmc in general will increase adsorption. For example, a longer hydrophobe length means that at a given concentration below the cmc of the smaller surfactant the molecule with the longer hydrophobe length will have higher adsorption. However as stated earlier, above the cmc of both surfactants with the y-axis plotted with a mass basis of surfactant, the adsorptions will be very similar. Since for a smaller surfactant this equivalence means more molecules and hence more charges, it may be beneficial to use a smaller surfactant for more charged surfaces. The addition of salt to a charged surfactant (e.g. anionic or cationic) tends to reduce headgroup-headgroup repulsion effects which in turn reduce the cmc since these repulsive effects oppose the formation of micelles; and hence tend to increase adsorption at higher surfactant concentrations. Of course, particle-particle charge-charge interactions also decrease at higher salt concentrations. At lower surfactant concentrations, in the case of an oppositely charged surface, the addition of salt decreases adsorption while in the case of a similarly charged surface the addition of salt will increase adsorption. The effect of temperature is very difficult to predict based on first principles; in general entropy dominates temperature effects, but the effect of temperature on the structure of water is very complicated by itself because of the strong dependence of hydrogen bonding on temperature. For nonionic surfactants, increasing temperature tends to increase adsorption for the same reason that a cloud point will eventually occur[11], while for ionic surfactants adsorption has been found to decrease with increasing temperature[12].

Since as stated earlier, surfactant mixtures are used in most commercial formulations for economic reasons (e.g. lower cmc), it is appropriate to consider the behavior of surfactant mixtures with respect to adsorption. From a molecular perspective, one reason that cmc's generally are smaller for mixtures than for the pure components is because unfavorable headgroup-headgroup interactions are reduced; also of course entropy of the micelle is higher with mixed micelles. A similar effect occurs with adsorption. In cases where only one surfactant adsorbs and the other does not, then mixing the two leads to a decrease in adsorption of the first and increase in adsorption of the second. A fundamental interesting question that has not been resolved is whether the composition of the adsorbed layer matches that of the micelle. From a particulate removal perspective, since electrostatic forces are typically the most important driving force in assisting in particulate removal the addition of nonionic surfactant to the adsorbed surfactant layer reduces the charge and hence the force of interparticle removal. As mixtures have more components, which is the standard situation for many commercial materials, adsorption becomes less

cooperative and the classical four-region isotherm becomes more like a two-region isotherm with a Henry's law-type region followed by a plateau at the cmc.

## 14.5 Surfactants and Particulate Removal

The number of refereed publications that have examined the effect of surfactants on particle removal is much smaller than the importance of this subject to various industrial processes. Figure 14.7 shows an excellent example of the expected behavior caused by the addition of ionic surfactant into a system where the two solid surfaces are of opposite charge or at least one of the two surfaces are uncharged[13]; a similar system with similar graphs can be found in [14,15]. Alumina is one of the few solids that is typically positively charged, and the graph qualitatively looks very similar to an adsorption isotherm, except of course the graph is flipped. In the specific case shown in this Figure, not enough information is given to know whether the amount of surfactant adsorbed is negligible, although the concentration where the maximum removal efficiency starts to occur is at the same concentration as the cmc within the error of the experiment. The same qualitative type of behavior is seen whether the surfactant is added to the particles before deposition of the particle, or after when the

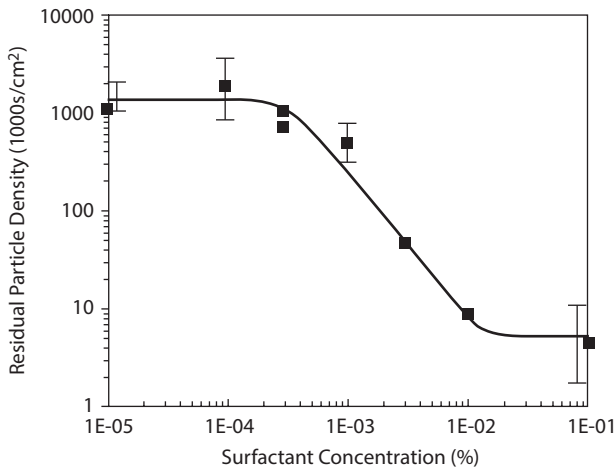


**Figure 14.7** Comparison of residual particle density (represented by the y-axis) as a function of cetyl pyridinium chloride (CPC) concentration following polishing of quartz glass with 0.7  $\mu\text{m}$  diameter alumina particles. The cmc of CPC in water is 0.04 wt. %. Figure duplicated from Ref [13] and used with permission.

particles have already been deposited[13]. Further, using very limited data the “Traube” rule was followed, that is a 2-carbon increase in chain caused particle removal curves to overlay if shifted an order of magnitude[15]. On a more fundamental basis, one publication using AFM showed that the force required to remove a single particulate was lessened by about a factor of 2 with the addition of surfactant[16]. The effect of surfactant on sonication, which is often used to enhance particulate removal processes, is not only to reduce the adhesion force but the reduction in surface tension due to the introduction of surfactant can change the characteristics of the sonication process[17]. This finding is not inconsistent with the statement earlier about surfactants not changing hydrodynamics; sonication involves the formation of gas bubbles, e.g. interfaces, and surfactants will alter the behavior of interfaces dramatically. A rather involved study comparing the different aspects of what surfactants do (e.g. reduce interfacial tension, increase particle-particle repulsive forces) concluded that like charged surfactants improve particle removal primarily by electrostatic repulsion between the particle and the substrate[18,19].

In the case where the two surfaces are of like charge and the surfactant is of opposite charge, the qualitative explanation concerning charge reversal given previously suggests that at a certain surfactant concentration, particle removal will be minimized. In other words, adding surfactant to reach this concentration is counterproductive to particle removal. As stated earlier, cationic surfactants tend to be more difficult to remove than anionic surfactants; the reason for this is that most surfaces tend to be negatively charged. So, as shown in Figure 14.8, the addition of the cationic surfactant cetyl trimethylammonium bromide (CTAB) below the cmc causes a depression in particulate removal which is recovered upon the addition of further surfactant[20]. The cmc of CTAB is 1 mM, so in fact the choice of this concentration as the “high” level was inappropriate since the actual concentration in solution may have been below the cmc because of surfactant adsorption. However, the authors did show via contact angle measurements that the surface was hydrophobic at 0.1 mM of added CTAB and hydrophilic at 1 mM of added CTAB.

Nonionic surfactants have been shown to be less effective in particulate detergency (which is not quite the same as particulate removal because any surfactant that remains with the substrate will negatively affect detergency and is irrelevant for particulate removal) than anionic surfactant but more effective than cationic surfactant. [18,19]. Cationic surfactant was thought to be the most ineffective due to unrinsed surfactant on the negatively charged polyester and cotton fabrics. The introduction of nonionic surfactants actually changed significantly the charge on hydrophobic particles

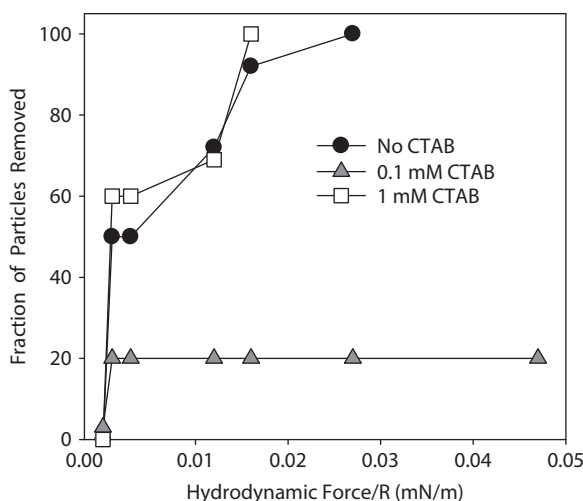


**Figure 14.8** Effect of cetyl trimethylammonium bromide (CTAB) concentration on the removal of 10  $\mu\text{m}$  hydrophilic glass particles from a hydrophilic glass substrate. The cmc of CTAB is 1 mM. Data adapted from Ref [20]. The x-axis shows the hydrodynamic removal force normalized by dividing by the particle radius to give a quantitative assessment of the relative removal force.

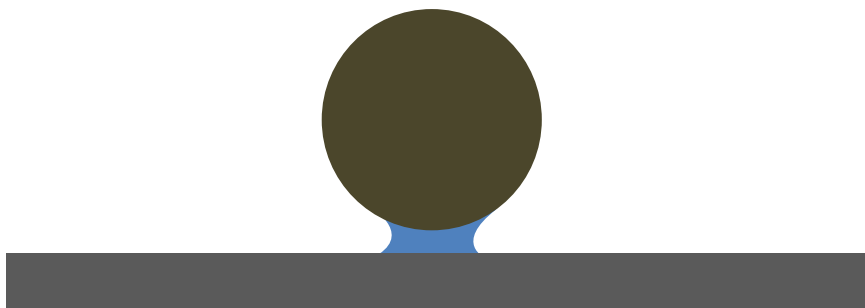
as measured by the zeta potential which seems counterintuitive but which was explained by change in the water bound to hydrophilic ethylene oxide groups which can shift the measurement volume (i.e. the measurement volume becomes closer to the particle). In terms of nonionic surfactant, the authors concluded that charge and steric effects (e.g. the ethylene oxide groups would rather be surrounded by water than by each other) both play a role in improving detergency.

Table 14.1 compiles the characteristics of surfactants and how they affect particle removal. However, a number of questions are not completely answered. As one example, what is the effect, if any, of particle size and shape on the ability of surfactants to improve particle removal. Two studies have suggested that larger particles are less affected by the addition of surfactant than smaller particles [19,21]. One of the aforementioned studies on particle removal did show significant differences in removal efficiency depending on the type of fabric used; the authors attributed this difference to surface roughness. How surface roughness affects surfactant adsorption and particulate removal are other questions that have not been explored significantly.

One other situation where surfactants are used to remove particles from surfaces can occur and the mechanism is completely different than what has been described in this Chapter up to this point. In some cases, for example

Table 14.1 Relationship between Surfactant Characteristics and Particle Removal

Surfactant Characteristic	How to Control With Change in Surfactant Structure	How Affects Particle Removal
Critical micelle concentration (cmc)	Increase surfactant hydrophobe chain length or reduce hydrophile size. Also adding nonionic to ionic surfactant, or ionic to nonionic surfactant solution will depress the cmc	Cmc determines how much surfactant is required in solution for effectiveness
Adsorption on solid surface	If surface is charged, then use oppositely charged surfactant. Control with cmc; as surfactant concentration increases adsorption increases until cmc is reached at which point no more adsorption occurs.	For ionic surfactants, same charge can build up on particle and solid surface aiding in particle removal via charge repulsion. For nonionic surfactants, excluded volume interactions can be obtained although these are not as effective as charge-charge interactions.
Precipitation or phase separation temperature	Branching of hydrophobe or introduction of aromaticity reduces tendency to precipitate, certain head groups have a higher likelihood of precipitating (carboxylates are a particular issue) and multivalent cations drive precipitation in anionic surfactants	If surfactant precipitates, you now have a second particle that must be removed.



**Figure 14.9** Schematic of how a non-water soluble liquid can be involved in the adhesion of a particle to a substrate. Note that the substrate does not need to be flat as drawn; in fact a rough surface where the liquid wets the surface is better able to “hold” liquid because of the capillary force involved with the liquid trapped in the rough depressions (e.g. pores).

where a water-insoluble liquid is used first for cleaning and then followed by an aqueous solution containing surfactant, the solid may be attached to the surface not through a solid-solid interaction, but rather through a solid-liquid interaction (actually two interactions) as represented in Figure 14.9. The magnitude of the force, termed the capillary force, can be quite high because the film is usually quite thin. Expressions for various geometries are given elsewhere[22]. In this case, the ability of the surfactant to remove the particles does not only depend on the surfactant’s ability to wet the surface of the solid. Instead, the surfactant’s ability to alter the three-phase contact line between the solid and the two liquids, as well as the reduction of interfacial tension between the water and the water-insoluble liquid are the relevant mechanisms. The latter is particularly important because with a reduction in interfacial tension the water is able to solubilize the liquid and hence remove the liquid from between the two surfaces.

## 14.6 Prospects

Surfactants are in general the most environmentally-friendly way to assist mechanical action in particle removal and are expected to be used far into the future. Environmental and sustainability concerns are expected to become more important in the future, so the exact chemical nature of the surfactants used in this application will likely be altered, but the mechanisms will still be the same. A reasonable understanding of the mechanism of particle removal is understood; although finer aspects such as the effect of surface roughness and particle size/shape still need further study.

## 14.7 Summary

Surfactants are used to enhance particle removal from a solid surface and work primarily on a mechanism that involves adsorption of the surfactant at both interfaces, and then charge repulsion helps the particle to be more easily removed from the surface via mechanical/hydrodynamic action, or in some cases the charge repulsion is enough to cause spontaneous removal. The amount of surfactant required to achieve maximal effect is given by the critical micelle concentration; addition of additional surfactant once the critical micelle concentration is reached after adsorption occurs will not improve separation of the particle from the surface. However, because of the unknown amount of adsorption by the solid surface, the amount of surfactant used is typically a few times the cmc. For economic and other reasons, normally anionic surfactants are used although for economic reasons sometimes mixtures of anionic and non-ionic surfactants are used in particle-removal applications. Normally, surfactants are used as part of a system that also involves mechanical action to aid in particle removal.

## Acknowledgements

The authors would like to thank the sponsors of the Institute of Applied Surfactant Research: CESI Chemical, Church & Dwight, Clorox, Conoco Phillips, Ecolab, GlaxoSmithKline, Halliburton Services, Huntsman, InVia-WestVaco, Novus, Phillips 66, Procter and Gamble, Sasol, S.C. Johnson, and Shell Chemical.

## References

1. A. V. Pocius *Adhesion and Adhesives Technology: An Introduction*; first edition, Hanser Gardner, Cincinnati, OH (2002).
2. M. J. Rosen *Surfactants and Interfacial Phenomena*, third edition, John Wiley & Sons, Hoboken, New Jersey (2004).
3. J. C. Berg *An Introduction to Interfaces and Colloids: The Bridge to Nanoscience*, first edition, World Scientific Publishing, Hackensack, New Jersey (2010).
4. A. W. Adamson and A. P. Gast *Physical Chemistry of Surfaces*, sixth edition, Wiley-Interscience, New York (1997).
5. I. Traube, The physical properties of elements from the standpoints of van der Waals equation of states, *Z Anorg. Chem.*, 34, 413–426 (1903).



6. F. Tiberg, J. Brinck and L. Grant, Adsorption and surface-induced self-assembly of surfactants at the solid-aqueous interface, *Curr. Opin. Colloid Interface Sci.*, 4, 411–419 (1999).
7. P. L. Hayes, A. R. Keeley and F. M. Geiger, Structure of the cetyltrimethylammonium surfactant at fused silica/aqueous interfaces studied by vibrational sum frequency generation, *J. Phys. Chem. B*, 114, 4495–4502 (2010).
8. C. Gutig, B. P. Grady and A. Striolo, Experimental studies on the adsorption of two surfactants on solid-aqueous interfaces: Adsorption isotherms and kinetics, *Langmuir*, 24, 4806–4816 (2008).
9. S. B. Velegol, B. D. Fleming, S. Biggs, E. J. Wanless and R. D. Tilton, Counterion effects on hexadecyltrimethylammonium surfactant adsorption and self-assembly on silica, *Langmuir*, 16, 2548–2556 (2000).
10. G. G. Warr, Surfactant adsorbed layer structure at solid/solution interfaces: Impact and implications of AFM imaging studies, *Curr. Opin. Colloid Interface Sci.*, 5, 88–94 (2000).
11. O. Dietsch, A. Eltekov, H. Bock, K. E. Gubbins and G. H. Findenegg, Crossover from normal to inverse temperature dependence in the adsorption of non-ionic surfactants at hydrophilic surfaces and pore walls, *J. Phys. Chem. C*, 111, 16045–16054 (2007).
12. M. Alkan, M. Karadas, M. Dogan and O. Demirbas, Zeta potentials of perlite samples in various electrolyte and surfactant media, *Colloids Surfaces A*, 259, 155–166 (2005).
13. M. L. Free and D. O. Shah The role of cetyl pyridinium chloride in reducing adhesion forces between alumina particles and quartz surfaces, in: *Particles on Surfaces 5&6: Detection, Adhesion and Removal*, K. L. Mittal (Ed.), pp. 95–106, CRC Press, Boca Raton, FL (1999).
14. M. L. Free and D. O. Shah, Adsorption and desorption of cetyl pyridinium ions at a tungsten-coated silicon wafer surface, *J. Colloid Interface. Sci.*, 208, 104–109 (1998).
15. M. L. Free and D. O. Shah, Enhancement of particle removal and modification of interfacial phenomena using surfactants, in: *Particles on Surfaces 7: Detection, Adhesion and Removal*, K. L. Mittal (Ed.), pp. 405–418, CRC Press, Boca Raton, FL (2002).
16. S. Veeramasesaneni, M. L. Free and J. D. Miller, Usefulness of surfactants in reducing particle adhesion and their effectiveness in cleaning silicon wafers, *J. Adhesion Sci. Technol.*, 12, 185–195 (1998).
17. E. Camerotto, S. Brems, M. Hauptmann, A. Pacco, H. Struyf, P. W. Mertens and S. De Gendt, Influence of surface tension on cavitation noise spectra and particle removal efficiency in high frequency ultrasound fields, *J. Appl. Phys.*, 112, Art. No. 114322 (2012).
18. S. Rojvoranun, C. Chadavipoo, W. Pengjun, S. Chavadej, J. F. Scamehorn and D. A. Sabatini, Mechanistic studies of particulate soil detergency: I. Hydrophobic soil removal, *J. Surfactants Deterg.*, 15, 277–289 (2012).

19. S. Rojvoranun, S. Chavadej, J. F. Scamehorn and D. A. Sabatini, Mechanistic studies of particulate soil detergency: II: Hydrophilic soil removal, *J. Surfactants Deterg.*, 15, 663–677 (2012).
20. A. M. Freitas and M. M. Sharma, Effect of surface hydrophobicity on the hydrodynamic detachment of particles from surfaces, *Langmuir*, 15, 2466–2476 (1999).
21. D. Ng, P. Y. Huang, Y. R. Jeng and H. Liang, Nanoparticle removal mechanisms during Post-CMP cleaning, *Electrochem. Solid State Lett.*, 10, H227-H231 (2007).
22. J. C. Berg *An Introduction to Interfaces and Colloids: The Bridge to Nanoscience*; first edition, pp. 76–80, World Scientific Publishing, Hackensack, New Jersey (2010).

# Index

- Acoustic boundary layer, 247–248
- Adhesion
  - one-dimensional, 159–160
  - two-dimensional, 159, 161, 165, 167, 193
- Adhesion bond, 158–160, 162, 165, 167–168, 170, 173, 179, 187, 189, 193
- Adhesion characterization, 158–159, 161–162, 167, 172, 177, 182, 193
- Adsorption isotherm, 530
- Advanced spray, 329–331
- AFM (atomic force microscopy), 4, 12, 15, 43–45
- Air jet
  - air jet, 283
  - pulsed air jet, 300
  - vibrating air jet, 304
- Air velocity, 283
- ALARA 1146™ strippable coating, 418
- Alumina (aluminum oxide), 535
- Aminophenyl methylene diphosphoric acid (APMDP), 422, 442
- Anisotropic adhesion
  - behavior, 165, 187
- Antique Telescope Society, 429
- AOT (sodium bis(2-ethylhexyl) sulfosuccinate), 488
- ARclean® strippable coating, 417
- ARclear® strippable coating, 417
- Atomized spray, 324–331
- Beryllium removal, 422, 442
- Boltzmann charge distribution, 90
- Brewster windows, 429
- Bumpy particle, 89, 92
- Capillary force, 93
- Capillary forces
  - comparison of, 4
  - non-sphere, flat plate, 23
  - origin of, 4
  - parallel plates, 18–20
  - pressure component, 6–10, 12
  - sphere-plate, 7, 25
  - sphere-sphere, 20–23
  - surface tension component, 10–12
- Capture coating, 420, 438
- CARBICOTE®, 416
  - 946 coating, 414
  - coating, 416
- Carbon nanotubes (CNTs) cleaning, SCCO<sub>2</sub> in, 498–499
- Cauchy plots, 41
- Cavitation, 203–204, 207–212, 215–216, 218, 220–223, 227, 230–231, 234–235, 237–240, 251–252, 254, 257–262, 264–274, 317
  - power intensity, 209, 218, 231, 235
  - degassing, 231–232
- Cavitation erosion, 218, 238–239
- Charge distribution, 90
- Chemical surface modification, 125–130

- chemical vapor deposition (CVD), 129
- wet chemical process, 126–127, 134, 136, 140, 142
- Chemical vapor deposition (CVD), 164, 178
- Chernobyl nuclear accident, 441
- Cleaning chemicals, 203, 211, 227–229, 232–235
  - aqueous cleaning, 225–226, 228, 232–233, 237, 241
  - cleaning chemistry and particle removal, 238
- Cleaning efficiency, 365, 382, 400–405, 407
- Cleaning process parameters, 221
  - frequency and power amplitude, 224, 235
- Cleaning process window, 318–319
- Cohesive powders, 105–106
- Collodion, 411, 413–414, 427–431, 435–436
  - cleaning guidelines, 429–431
  - cleaning optics, 427–429
  - particle sample preparation, 435–436
  - solvent-based coatings, 413–414
- Colloidal probe technique, 132, 134–136
- Commercial  $\text{SCCO}_2$  cleaning systems, 491–492
- Contact angle, 125, 127–128
- Contact angles, 46
- Contact electrification, 53–54
- Contact model, 107–121, 134, 136–145
  - elastic, 113–115, 136–137
  - elastic-plastic, 115–117, 138–139
  - plastic, 118–119
  - unloading, 119–121, 139
- Contact radius, 85
- Contaminants, 211, 219, 221, 227–239
  - organic, 221, 226, 228–229, 232–233, 236
  - inorganic, 228–229, 233, 236
- CorShield® VpCI™ coating, 417
- Coulomb's law, 50
- Critical point, 479, 482, 485, 498
- Critical pressure, 482, 484, 284, 302
- Critical properties, 483, 488
- Critical shear velocity, 96, 97, 98
- Crown formation, 317
- Cryo-aerosol cleaning, 455–456
  - aerosol particle size control, 466–467
  - airflow management, 465
  - cleaning mechanisms, 461–462
  - control of electrostatic charges, 463–465
  - gas purity, 468–469
  - moisture control, 463
  - thermodynamics, 456–461
- Debye interactions, 30–32
- Debye length, 64, 66
- Debye-Hückel approximation, 66
- DeconGel™ coating, 419, 440
- Decontamination factor (DF), 418, 420–421, 437
- Density functional theory, 17
- Derived air concentrations (DACs), 438
- Diffusion and field charging, 91
- Direct megasonic, 262–263
- Discoat 4210 coating, 414–415
- DLPH theory, 33
- DLVO theory, 67
- DMT model, 85
- Doubling effect, 167, 172, 174, 177
- Drag force, 94
- Droplet energy density, 321–324
- Droplet impact
  - liquid film, 318
  - solid surface, 315–317
- Droplet opto-hydrodynamic cleaning (DOC), 340–343, 352
- Dry wiper uses, 393–395
- Drying time, 296
- Dual spray cleaning, 340
- Dynamic pressure, 285, 289, 303

- Eckart streaming, 248–250
- Electro-decontamination
  - system, 421–422
- ElectroDecon™ strippable
  - coating system, 422
- Electrostatic detachment, 96
- Electrostatic forces, , 92
  - aqueous environment, 64–67
  - in bishperical coordinates, 58–64
  - in spherical coordinates, 55–57
  - method of images, 51–53
  - point charges, 50
  - sphere-sphere constant charge, 51
  - sphere-sphere constant potential, 50
  - trapped charge, 53–54
- Environmental Protection
  - Agency, U.S., 413, 438
- Fabric construction
  - knit, 381
  - microdenier, 382
  - non-woven, 383
  - woven, 383
- Flow fluctuation, 282, 307
- Graphene (Gr)
  - mechanical properties of, 164, 180
  - monolayer, 159, 163–164, 178–179, 183
- HaloShield® coatings, 422–423
- Hamaker constant, 177, 180–181, 191
  - experimental measurement methods, 42
  - van der Waals forces, 28–32, 36
- Height of asperities, 298
- Hertz model, 84
- Humidity
  - humidity at deposition, 296
  - humidity in removal environment, 297
- Hydrodynamic drag force,
  - 344–345, 358
- Hydrodynamic forces, 93
- Hydrodynamic torque, 93, 94
- Hydrophilicity
  - definition of, 5
    - effect on capillary forces, 12
- Hydrophobicity
  - definition of, 5
    - effect on capillary forces, 12
- Impact pressure, 345
- Impinging angle, 290
- Indirect megasonic, 262–263
- Inductively coupled plasma
  - mass spectrometry (ICP-MS), 436, 442
- InstaCote CC Strip, 420, 438
- InstaCote CC Wet, 420
- Interferometer, 162, 170, 174, 185
- Intermolecular forces, 522
- Introductory wiper use
  - training, 395–396
- Isotron Radblock™, 421
- JKR model, 84
- Keesom interactions, 30–32
- Kelvin
  - equation, 10–11, 13, 18, 23
  - radius, 10–11
- Laplace pressure, 6–7
- Laser cleaning
  - dry laser cleaning, 339
  - laser shock cleaning, 339
  - steam laser cleaning, 339
- Laser flash shadowgraphy, 345
- Laser windows cleaning, 429
- Laser-induced breakdown, 339–342
- Laser-induced plasma, 339, 342–343
- Laser-induced spray cleaning,
  - nanoscale particle removal, 357–359
  - process parameters, 355–357
- Laser-induced spray jet, 342, 346–351
- Lattice gas, 15–17
- Leaning angle, 174–177, 193
- Liquid jetting, 316
- London interactions, 30–32
- Lyophilicity, 5
- Maugis-Pollock model, 86
- Meniscus
  - ideal, 6–7
    - non-ideal, 23–26

- Mercury removal, 442
- Micelles, 524–526
- Micro liquid jet
  - divergence angle, 350–351, 354
  - forward jet, 346–348, 350
  - jet speed, 350–351, 354
  - spreading jet, 347, 352–354
- Micro-particle, 158–162, 164–165, 167, 172, 178, 184, 193–194
- Molecular dynamics, 17
- Monte Carlo simulations, 15–17
- Nafion (fluorocarbon polymer), 414
- Nano-film, 162–163, 177–178
- Nanospray, 325–331
- National Optical Astronomy Observatories (Tucson, Arizona), 431
- N-methyl pyrrolidone (NMP), 498
- Non-collodion cleaning of optics, 431
- Non-contact technique, 159, 165–165
- Nonlinear and coupled dynamics, 162, 167
- Non-optical cleaning applications, 436
- Non-radioactive decontamination applications, 441–443
- Nonvolatile residue (NVR), 479
- Non-volatile residues (NVRs), 378, 379, 396, 397
- Nostoc muscorum* bacterium, 441
- Optics and non-collodion cleaning, 431–434
- Out-of-plane motion, 160, 162, 167–168, 174, 177, 189
- Particle adhesion and detachment models, 83
- Particle adhesion forces
  - capillary force, 372
  - electrostatic force, 372
  - van der Waals force, 371
- Particle detachment, 95
- Particle manipulation, 184, 186
- Particle packing experiments, 140–146
  - ring shear tester, 140–146
- Particle removal, 259–262, 264–274, 314, 318, 320–321, 323–325, 328, 330
- Particle removal efficiency, 324–326, 328, 331, 355
- Particle removal force
  - experimental, 320–324
  - theoretical, 319–320
- Particle removal forces
  - capillary force, 375
  - drag force, 374
  - net buoyancy force, 375
  - push force, 374
- Passive aerosol generator, 420
- Peak count, 298
- Phase masks cleaning, 434
- Physical cleaning methods
  - acoustic cleaning, 368
  - carbon dioxide snow cleaning, 368
  - PVA brush for cleaning silicon wafers, 367
  - wiper-based cleaning, 369
- Poisson-Boltzmann equation, 65–66
- Polymeric smart coatings, 421
- Polystyrene latex (PSL), 166, 170–171, 178–181, 183–187, 191
- Powder flow properties, 106, 121–124, 134, 141–146
  - flow function, 123–124, 141, 145
- Pressure drop, 288
- Pull-off force, 85
- Quantum field theory, 33
- Quartz crystal microbalance (QCM), 502
- Radioactive decontamination, 436–441
- Rayleigh streaming, 248–251
- RedOxy Peel™ coating, 422
- Relative humidity,
  - effect on capillary forces, 4, 12–15, 23–24, 27
- Removal efficiency
  - instantaneous removal efficiency, 287
  - integrated removal efficiency, 287
  - removal efficiency, 288

- Resonance frequencies, 161, 167,
  - 169–170, 172–180, 182–183
- force, 158, 162, 167–168, 173,
  - 189–190
- moment, 160, 162, 165, 168, 173
- Rocking motion, 162, 167–169,
  - 173–175, 177, 180
- Rolling detachment, 95
- Rolling motion, 159–160, 165,
  - 168, 184–185, 191
- Rough particles, 89
- Savannah River Site (SRS), 437
- Schlichting streaming, 248, 250–251
- SensorCoat smart coating, 421
- SFA (surface forces apparatus), 45
- Shock wave, 315–316, 318–320
- Silicon wafers cleaning, 434
- Single particle experiments, 130–140
  - atomic force microscopy, 131–135
  - nanindentation, 134–140
- Sliding detachment, 95
- Soft spray, 324–329
- Soil cleaning, with ionic liquids
  - and SCCO<sub>2</sub>, 499
- Soluble polysaccharide (SPS), 441
- Solution models, 488
- Solvent-based coatings, 413–415
- Spectral domain, 162, 167, 171–172,
  - 174–177, 180–181
- Stable cavitation, 252, 260
- Stampers for compact discs
  - cleaning, 435
- Streaming, 244, 248–253,
  - 260–261, 264, 266
- Stripcoat TLC Free™ coating,
  - 418, 438–440, 442
- Strippable coatings, 411–413,
  - 421, 424, 426–427, 431,
  - 436–439, 441, 443
- issues, 426
- non-radioactive decontamination,
  - 441
- precision cleaning applications, 427
- properties, 411–412, 414, 420,
  - 423–424, 426, 441
- radioactive decontamination, 418
- solvent-based, 413–414, 424
- surface contaminants, 412–413,
  - 418–420, 430
- UV-curable, 424
- water-based, 411, 413, 415–417,
  - 419–420, 424, 426, 439, 443
- Substrate, 372, 373, 374, 375, 377,
  - 399, 401, 402, 403, 404
- Supercritical carbon dioxide (SCCO<sub>2</sub>), 477
  - advantages, 493–495
  - applications, 477–480, 486–489,
    - 493–494, 496–497, 499, 501, 503
  - cleaning process, 490
  - cleaning systems, 490–491
  - co-solvents, 490
  - costs, 491–493
  - critical point, 490
  - critical pressure, 490
  - critical temperature, 491
  - dipole moment, 482, 488
  - disadvantages, 495–497
  - particle size removed as a function
    - of stream velocity, 489
  - photoresist removal by absorption,
    - 492
  - post-etch residue removal, 497
  - precision cleaning applications,
    - 496–497
  - pressure-enthalpy diagram, 486
  - pressure-temperature phase
    - diagram, 482, 484
  - quadrupole moment, 490–491
  - relevance to particle removal, 477–518
  - solubility considerations, 487
  - solvating power, 482
  - stream velocity, 489
  - surface cleanliness levels, 478, 480
  - surface tension, 477, 483, 485, 493,
    - 501–502
  - thin film removal,
  - triple point, 482, 484
  - variation of density as a function of
    - temperature,

- viscosity, 477, 482–483, 485, 494, 502
- Surface, 411–443
  - contaminants and strippable coatings, 411–451
- Surface acoustic wave (SAW), 159, 18–186, 189–190, 192
- Surface energy, 5, 46, 521
- Surface properties mapping, 164–165, 184
- Surface roughness, 160, 181, 183, 298
- Surface tension, 46
  - contribution to capillary forces, 11–12
  - origin of, 5–6
- Surfactant, 524–540
- Textile terms, 380
- Thin layer, 159, 163
- Threshold limit value (TLV), 494
- Tollmien's equation, 292
- Transducer assembly, 213, 215–216
- Transducers, 203–204, 211–218, 225–227
  - gas-driven transducers, 211
  - liquid-driven transducers, 212
- Transducers electromechanical
  - piezoelectric transducers, 211, 213
  - magnetostrictive transducers, 211, 214
- Transient cavitation, 254, 257–259, 266, 268, 271
- U.S. Department of Defense, 422
- U.S. Department of Homeland Security, 422
- Ultrasonic cleaning, 203, 211, 215, 217, 219–223, 227–228, 234–235, 241
  - mechanism of cleaning, 236
  - particle removal mechanism, 236
- Ultrasonic cleaning systems, 227
- Ultrasonic immersible transducers, 216
  - power requirements, 217
- Ultrasonics, 203–204, 207, 211, 213, 220, 224, 227, 230, 233, 235, 237–241
- Ultrasound, 203–208, 211, 214, 216, 231, 233, 235, 240
- Ultrasound waves, 205–206, 214, 235
  - rarefaction, 205, 207, 210, 215, 219
  - transverse waves, 206
- United States Environmental Protection Agency (EPA), 413, 438
- Universal Photonics coatings, 416–417, 431–432
- UV (ultraviolet) curable coatings, 422–425
- van der Waals forces,
  - and capillary forces, 15, 18
  - general, 4, 27
  - Hamaker constant, 28–32, 36
  - Hamaker's pairwise additive method, 27–30, 32
  - Lifshitz' continuum approach, 32–40
  - plate-plate, 30, 34
  - retarded, 32
  - sphere-plate, 29–30, 34, 36
  - sphere-sphere, 27–30, 34
- van der Waals adhesion force, 105–106, 113, 131–132, 134–135, 141, 144–145
- Vibrational spectroscopy, 159, 164, 178, 183
- Volatile organic compound (VOC), 424
- Wafer cleaning sequence, 246–247
- Water hammer, 316, 318
- Water-based coatings, 415–417
- Whirling-like motion, 174, 176–177, 182
- Wiper-based cleaning advantages, focused cleaning, 369
- Wiper construction material, 384
- Wiper contamination level test methods, 396–398
- Wiper edge types,



- cut-edge, 386
- sealed border, 387
- sealed- or laser-edge, 387
- Wiper selection guidelines, 388–390
  - liquid management, 370
  - surface protector, 370
- Wiping protocol, 390–393
- Work of adhesion, 523, 185,
  - 160–164, 167–168, 173–174,
  - 176–180, 183, 189, 191
- Young equation, 46
- Young-Laplace equation, 6,
  - 11, 13, 18, 23, 25
- Zeta potential, 65



# Also of Interest

## Check out these published and forthcoming related titles from Scrivener Publishing

### **Reviews of Adhesion and Adhesives**

Editor: K.L. Mittal

Quarterly publication. ISSN 2168-0965

[www.scrivenerpublishing.com](http://www.scrivenerpublishing.com)

### **Particle Adhesion and Removal**

Edited by K.L. Mittal and Ravi Jaiswal

Published 2015. ISBN 978-1-118-83153-3

### **Laser Surface Modification and Adhesion**

Edited by K.L. Mittal and Thomas Bahners

Published 2014. ISBN 978-1-118-83163-2

### **Adhesion in Microelectronics**

Edited by K.L. Mittal and Tanweer Ahsan

Published 2014. ISBN 978-1-118-83133-5

### **Advances in Contact Angle, Wettability and Adhesion**

#### **Volume 1**

Edited by K.L. Mittal

Published 2013. ISBN 978-1-118-47292-7

### **Advances in Modeling and Design of Adhesively Bonded Systems**

Edited by S. Kumar and K.L. Mittal

Published 2013. ISBN 978-1-118-68637-9

### **Atmospheric Pressure Plasma Treatment of Polymers**

Edited by Michael Thomas and K.L. Mittal

Published 2013. ISBN 978-1-118-59621-0

**Atomic Layer Deposition**

**Principles, Characteristics, and Nanotechnology Applications**

By Tommi Kääriäinen, David Cameron, Marja-Leena Kääriäinen and Arthur Sherman

Published 2013. ISBN 978-1-118-06277-7

**Encapsulation Nanotechnologies**

Edited by Vikas Mittal

Published 2013. ISBN 978-1-118-34455-2

**Atmospheric Pressure Plasma for Surface Modification**

By Rory A. Wolf

Published 2012. ISBN 9781118016237

**Introduction to Surface Engineering and Functionally Engineered Materials**

By Peter Martin

Published 2011. ISBN 978-0-470-63927-6

# **WILEY END USER LICENSE AGREEMENT**

Go to [www.wiley.com/go/eula](http://www.wiley.com/go/eula) to access Wiley's ebook EULA.